

Lecture Notes in Civil Engineering

Mahendrakumar Madhavan
James S. Davidson
N. Elumalai Shanmugam *Editors*

Proceedings of the Indian Structural Steel Conference 2020 (Vol. 2)

ISSC 2020

 Springer

Lecture Notes in Civil Engineering

Volume 319

Series Editors

Marco di Prisco, Politecnico di Milano, Milano, Italy

Sheng-Hong Chen, School of Water Resources and Hydropower Engineering,
Wuhan University, Wuhan, China

Ioannis Vayas, Institute of Steel Structures, National Technical University of
Athens, Athens, Greece

Sanjay Kumar Shukla, School of Engineering, Edith Cowan University, Joondalup,
WA, Australia

Anuj Sharma, Iowa State University, Ames, IA, USA

Nagesh Kumar, Department of Civil Engineering, Indian Institute of Science
Bangalore, Bengaluru, Karnataka, India

Chien Ming Wang, School of Civil Engineering, The University of Queensland,
Brisbane, QLD, Australia

Lecture Notes in Civil Engineering (LNCE) publishes the latest developments in Civil Engineering—quickly, informally and in top quality. Though original research reported in proceedings and post-proceedings represents the core of LNCE, edited volumes of exceptionally high quality and interest may also be considered for publication. Volumes published in LNCE embrace all aspects and subfields of, as well as new challenges in, Civil Engineering. Topics in the series include:

- Construction and Structural Mechanics
- Building Materials
- Concrete, Steel and Timber Structures
- Geotechnical Engineering
- Earthquake Engineering
- Coastal Engineering
- Ocean and Offshore Engineering; Ships and Floating Structures
- Hydraulics, Hydrology and Water Resources Engineering
- Environmental Engineering and Sustainability
- Structural Health and Monitoring
- Surveying and Geographical Information Systems
- Indoor Environments
- Transportation and Traffic
- Risk Analysis
- Safety and Security

To submit a proposal or request further information, please contact the appropriate Springer Editor:

- Pierpaolo Riva at pierpaolo.riva@springer.com (Europe and Americas);
- Swati Meherishi at swati.meherishi@springer.com (Asia—except China, Australia, and New Zealand);
- Wayne Hu at wayne.hu@springer.com (China).

All books in the series now indexed by Scopus and EI Compendex database!

Mahendrakumar Madhavan · James S. Davidson ·
N. Elumalai Shanmugam
Editors

Proceedings of the Indian Structural Steel Conference 2020 (Vol. 2)

ISSC 2020

 Springer

Editors

Mahendrakumar Madhavan
Structural Steel Research Group
Department of Civil Engineering
Indian Institute of Technology Hyderabad
Sangareddy, India

James S. Davidson
Department of Civil and Environmental
Engineering
Auburn University
Auburn, AL, USA

N. Elumalai Shanmugam
National University of Singapore
Queenstown, Singapore

National University of Malaysia
Selangor, Malaysia

Chennai, India

ISSN 2366-2557

ISSN 2366-2565 (electronic)

Lecture Notes in Civil Engineering

ISBN 978-981-19-9393-0

ISBN 978-981-19-9394-7 (eBook)

<https://doi.org/10.1007/978-981-19-9394-7>

© The Editor(s) (if applicable) and The Author(s), under exclusive license to Springer Nature Singapore Pte Ltd. 2023

This work is subject to copyright. All rights are solely and exclusively licensed by the Publisher, whether the whole or part of the material is concerned, specifically the rights of translation, reprinting, reuse of illustrations, recitation, broadcasting, reproduction on microfilms or in any other physical way, and transmission or information storage and retrieval, electronic adaptation, computer software, or by similar or dissimilar methodology now known or hereafter developed.

The use of general descriptive names, registered names, trademarks, service marks, etc. in this publication does not imply, even in the absence of a specific statement, that such names are exempt from the relevant protective laws and regulations and therefore free for general use.

The publisher, the authors, and the editors are safe to assume that the advice and information in this book are believed to be true and accurate at the date of publication. Neither the publisher nor the authors or the editors give a warranty, expressed or implied, with respect to the material contained herein or for any errors or omissions that may have been made. The publisher remains neutral with regard to jurisdictional claims in published maps and institutional affiliations.

This Springer imprint is published by the registered company Springer Nature Singapore Pte Ltd. The registered company address is: 152 Beach Road, #21-01/04 Gateway East, Singapore 189721, Singapore

Foreword I

Civil infrastructure is universally an area requiring the continued attention of the engineers and architects, be it because of creation of additions, or, the quest for improved quality. The volume of additional infrastructure needed is huge in many countries including India. Fulfilment of this demand has to be backed by an adequate supply of building materials, of which the two that are most commonly in use are either concrete or steel. Structurally, both these have their merits, whether used separately, or as steel-concrete composites. Steel offers the merits of high strength-to-weight ratio, thus reduced deadweights, superior seismic performance and economy in applications requiring longer spans or greater heights, flexibility in planning, rapid construction, easy repairability and so on. Another reason for considering the use of steel as an alternative to concrete wherever possible is the ongoing difficulty in finding adequate quantities of constituents of concrete such as aggregates, river sand and water. In this respect, the substantially increased production of steel in India over the last few decades augers well for the growth of civil infrastructure in the country.

Steel is almost always the major construction material in landmark structures. There is a long list of such examples in both India and abroad. Just to cite a few, the Golden Gate Bridge in San Francisco, the Disney Concert Hall in Los Angeles, the Beijing Olympic Stadium, the Millennium Bridge in London, the Rabindra setu and the Vidyasagar setu in Kolkata, India, the upcoming railway arch bridge across the river Chenab in J&K, India, the tower of unity in Gujarat, India and so on. Today, innovative solutions like steel-concrete composites for flooring systems, columns, beams and shear walls are preferred by structural engineers. However, the quest for the economy has been pushing researchers to explore possibilities to obtain more reliable and optimized solutions. Extensive research is actively carried out around the globe on light gauge steel which is observed as a promising building material. In addition, the reduction of the deadweight of composite slab by using lightweight concrete has been intensively studied by the researchers at IIT Hyderabad. The strengthening of existing steel structures using reinforcements like CFRP and GFRPs is another challenging area of research that is carried out around the globe.

The Structural Steel Research Group, Department of Civil Engineering of IIT Hyderabad has organized this, the First Conference focussed on structural steel

and its applications. This conference envisages boosting the ideology of paradigm shift from conventional wet-based construction to dry-based construction which may offer advantages in meeting rapidly the big demands for additional housing units.



Prof. Prem Krishna
Formerly with Indian Institute
of Technology Roorkee
Roorkee, India

Foreword II

Steel structures are the landmarks of modern societies. Examples include the Golden Gate Bridge in San Francisco, the Disney Concert Hall in Los Angeles, the Beijing Olympic Stadium, the Millennium Bridge or the Orbit in London, Calatrava's train stations and thousands more. Steel structures can provide a high strength-to-weight ratio, ultimate flexibility, airy spaces, rapid construction, long spans, superior seismic performance and much more providing economical as well as optimal solutions compared to concrete structures.

Unfortunately, the use of structural steel in India is very less either due to lack of knowledge in structural steel design or outdated codal provisions. Therefore, on the one hand it is necessary to invest more into R&D sector to understand the science behind the behaviour of structural steel in infrastructure applications and update the existing codal provisions. It would encourage and acknowledge the work of young researchers who are investing their lives for a noble cause of providing an affordable, sustainable and respectable shelter for every citizen of our nation through Light Gauge Steel Framing systems (LGSFs) and fulfilling the government of India's mission "Housing for all". On the other hand, it is necessary to promote special steels like cold-formed steel for mass housing projects in both rural and urban India which can be done by the establishment of a centre of excellence. It would be a wise decision to invest in emerging areas of research like structural steel which can boost up the national economy tremendously. In addition, it is essential to make the new generation of structural engineers feel comfortable in the design of steel structures by creating chair professorships at leading institutes for both knowledge creation and knowledge dissemination.

Today, innovative solutions like steel-concrete composites for flooring systems, columns, beams and shear walls are preferred by structural engineers. However, the quench for the economy has been pushing researchers to carry out a large number of experiments to obtain more reliable and optimized solutions. Extensive research is actively carried out around the globe on light gauge steel which is observed as a promising building material. In addition, the reduction of the deadweight of composite slab by using lightweight concrete has been intensively studied by the researchers at IITH.

The Structural Steel Research Group, Department of Civil Engineering of IIT Hyderabad has organized the First Conference focussed on structural steel and its applications. This conference envisages to encourage the use of structural steel in infrastructure projects in India and explore the unexplored areas of research in special steels like Cold-Formed Steel in India.



Prof. B. S. Murty
Director
Indian Institute of Technology
Hyderabad
Sangareddy, India

Foreword III

Currently, India is second in terms of production of crude steel surpassing Japan and USA. The production and consumption figures for FY 20 are 103.044 MT and 94.140 MT, respectively. The capacity augmentation by Indian steel producers is planned in the same way.

However, at present, India is among a handful of countries which suffer from massive deficit in construction. The per capita consumption of steel being 75 kgs in 2019 (19 kgs only in rural sector) compared to world average of 230 kgs, 636 kgs in China and a wobbling 1039 kgs in S. Korea the potential in India looks positive. The projection of steel consumption in the FY 2031 is predicted to be 196 MT of which 73.9 MT is in building construction only. Application of steel may be explored into areas like infrastructure, rural and urban building et al. The institutes may work in areas of “application” with thrust in developing modular concepts, standard designs, use the results of research in the application field. Use of hot rolled has been pursued for a long time. Advent of cold-formed steel is welcomed as its usage also has a potential. The research in this area and the formulation of proper code and guidebook will ease the designing part culminating to more usage of the same.

The research in the application side needs to be improved in terms of Indian perspective and context. Proper funding from stakeholders and the government needs to be channeled to the research institutes for developing “India specific” applications with steel and helps to make the country be ATMA NIRBHAR.

This conference delves with various topics aiming towards the consumption side, i.e. application of steel. Being the head of this institute that is into the area of increasing the consumption of steel, I look forward to getting newer ideas from Indian and foreign brains so that the outcome from this conference can be converted to tangible gains for the well-being of the country.

We are proud enough to find that an esteemed institute like Indian Institute of Technology, Hyderabad, has selected a topic which is the need of the hour and has gathered experts globally.

I wish the conference a great success. Jai Hind.



Pradip Kumar Mishra
Director General
Institute for Steel Development
and Growth
Kolkata, India

Foreword IV

Steel construction is a key consideration in the design of buildings and infrastructures. Significant advances in research and development have increased the knowledge of the structural performance of steel structures. To know about the innovation and advances, we need a forum for researchers, practitioners and engineers to share and discuss their research, practical experience and innovations related to steel structures with their peers in an open, international conference forum.

International conference, Indian Structural Steel Conference (ISSC 2020), organized by the Structural Steel Research Group, Department of Civil Engineering of IIT Hyderabad is the First Conference focussed on structural steel and its applications are scheduled to be conducted via Air meet on 6–8 January 2022 in online mode, with the association of ASCE India Section and Springer Publications.

The aim of the conference is to provide a common platform to share and discuss novel ideas, technologies and research findings to promote interdisciplinary research and to ignite young brains. The conference provides a forum for discussion and dissemination by researchers and designers of recent advances in the analysis, behaviour, design and construction of steel structures. Research papers were contributed from all around the world, with the research ideas in the area of cold-formed steel, structural steel, steel-FRP composites, steel-concrete composites. Dedicated funding from the government and private sectors towards the development of techniques for steel-intensive infrastructure will expedite sustainable construction practices in India.

The efforts of Prof. Madhavan and his entire team at IIT Hyderabad to proliferate emerging construction systems including steel-intensive structural systems are laudable.

Wishing the conference grand success.



Dr. Shailesh Kr. Agrawal
Executive Director
Building Materials and Technology
Promotion Council
Ministry of Housing and Urban Affairs
Government of India
New Delhi, India

Indian Structural Steel Conference

This international conference, organized by the Structural Steel Research Group, Department of Civil Engineering of IIT Hyderabad is the First Conference focussed on structural steel and its applications. This conference was planned to be held from 25 to 27 March 2020 in Hyderabad but due to COVID-19, it got postponed and held online from 06 to 08 January 2022. This ISSC 2020 conference is being organized with an association of ASCE India Section and Springer.

It will be of interest to steel and aluminium structure designers and manufacturers, trade associations, design engineers, steel fabricators, architects, owners and developers of steel and aluminium structures, researchers, academics and postgraduate students.

Aim and Scope of the ISSC

Steel structures are a fairly vast field covering different constructional engineering branches and various materials used in combination of steel to provide a composite system. The applications of structural steel encompass various industries including construction, automotive, aerospace and marine. However, the development of novel structural materials and technologies, together with the computational tools and design specifications, is necessary for continuous advancement in the use of structural steel in numerous areas. In addition, the role of the construction engineer is also to maintain the existing structures for the desired load and purpose; therefore, there is also a need for new retrofitting techniques using sustainable materials.

Hence, this ISSC 2020 conference aims at providing a forum where researchers, designers and construction engineers, structural steel manufacturing engineers and consultants having explicit backgrounds but encountering similar challenges, joining together in a friendly environment, to discuss and disseminate the most recent advances in the analysis, behaviour, design and construction of structural steel.

Message from the Conference Organizing Secretary

The Structural Steel Research Group at the Indian Institute of Technology, Hyderabad, is glad to announce the inauguration of the first Indian Structural Steel Conference (ISSC) to be held at IIT Hyderabad.

As our nation celebrates the 75th Year of its Independence, many challenges lie ahead in terms of basic infrastructure and the difficulties faced by the millions of fellow citizens without proper housing for a safe livelihood. This conference aims to shed light on some of these challenges and is focussed on sustainability to promote steel-intensive sustainable construction practices for a sustainable India. A galaxy of eminent keynote speakers from across the globe will present their latest research work which will create awareness among researchers, industry leaders and policymakers.

I am grateful to the IIT Hyderabad Former Director Prof. U. B. Desai and Current Director Prof. B. S. Murty for their continuous encouragement to conduct this conference. I thank all the keynote speakers for the acceptance to deliver a technical session in this conference.

Special thanks to Mr. T. V. Narendran, MD and Global CEO of Tata Steel and President of CII and Mr. P. K. Mishra, Director General, Institute for Steel Development and Growth (INSDAG), Ministry of Steel Government of India for accepting to be the chief guest for this conference.

This conference attracted 193 papers from 12 countries. A total of 380 authors from 120 institutions (notably IISc, 11 IITs and 12 NITs) have contributed to this conference.

I would like to express my great gratitude to the reviewers for their excellent work. The editorial team also wish to appreciate the staff at the Indian Institute of Technology Hyderabad who helped to throughout to conduct the conference. Special

thanks are owed to my student's team for their effort on this conference. I wish to express my sincere gratitude to all the presenting authors and participants whose contributions have made this conference possible.

Thank you.

Prof. Mahendrakumar Madhavan
Structural Steel Research Group
Department of Civil Engineering
Indian Institute of Technology Hyderabad
Sangareddy, India

Contents

Restoration Works to Existing Heritage Conservation Building at Upper East Coast Road, Singapore	1
Jeslin Quek and Reshma Rajeev	
Nonlinear Finite Element Analysis of GFRP Fabrics Strengthened RC Deep Beams Using ABAQUS	13
A. Kumari and A. N. Nayak	
Study on Short Steel Circular Hollow Sections Jacketed with Carbon Fiber Reinforced Polymers	25
A. Punitha Kumar, R. Senthil, and S. Srishath	
A Review of Strengthening of RC Beam-Column Junction Using Fiber Reinforced Polymer Composites	41
Pramod Tiwari and Kranti Jain	
Effect of In-plane Concentrated Load on Buckling Behavior of FRP Composite Panels with Cutout	51
K. S. Subash Chandra, K. Venkata Rao, and T. Rajanna	
Comparison of the Behaviour of Axially Loaded Slender Hollow Steel Tubes and Concrete Filled Steel Tubes	67
Rebecca Mary Paul, Madhu M. Karthik, and M. V. Anil Kumar	
Computer Aid for Designing Circular Concrete Filled Double Skinned Tube (C-CFDST) Composite Column	81
Yashpal P. Gajjar and Arth J. Patel	
Effect of Initial Imperfections on the Ultimate Axial Compressive Strength of Concrete Filled Steel Tubular Long Columns	93
Mashudha Sulthana and Arul Jayachandran	
Finite-Element Modelling of Double Plate Flat Composite Shear Wall Under Lateral Load	105
R. Senthilkumar, M. Karthikeyan, and Sneha Liya George	

An Experimental Investigation on Light Gauge Steel Hollow Circular Column infilled with Nano Concrete	123
P. Vasanthi and S. Senthil Selvan	
Behavior of Steel–Concrete Composite Beam Section for Various Parameters	139
Prashant B. Kamate and Ashish P. Khatri	
Experimental Study on Cold-Formed Steel–Concrete Composite Trusses	157
B. L. Thippeswami, S. Waghmare, and S. R. Satish Kumar	
Concrete-Filled Tubular Column: A Comparative Study of EC4 and AISC 360-10	167
Ankit Sachdeva, Arvind Vyavahare, and Gourav Sachdeva	
Structural Performance of Partially Confined Concrete-Filled Steel Circular Tubular Columns Under Cyclic Lateral Loading	181
Prasanta Kar, Arun C. Borsaikia, and Konjengbam D. Singh	
State-of-the-Art Review for Concrete-Encased Steel Columns	195
S. Suresh Babu, Priya, and A. Leema Rose	
Enhancing Structural Properties of Wood and Its Composites by Mechanical Annealing	205
G. Mallikarjunachari and P. Mohammad Asif Khan	
Free Vibration of Bio-inspired Composite Circular Plates—An Annual Ring Model	211
R. Kumar, Vaishali, S. Kushari, T. Mukhopadhyay, and S. Dey	
Review on Strengthening of Reinforced Concrete Slab Using Externally Bonded FRP Composites	221
Atanu Debnath and Subhashish Roy Chowdhury	
Post-earthquake Fire Resistance of Concrete-Filled Tubular Steel Columns	235
Smita Singh and Anil Agarwal	
Finite Element Modelling of In Situ Composite Patch Repair of Cracked Aluminium Aircraft Structures	243
Samanvay Anand and Himanshu Pathak	
The Effect of Steel Fibers on Ductility of Reinforced Concrete Beams	261
Yuvraj Singh, Sushil Bhatia, and Harvinder Singh	
Mode Specific Damping Estimation—An Inverse Damping Modelling Technique	271
Naveen Bharti, Yeturi Pramod Kumar Reddy, and Subhamoy Sen	

Effect of the Imperfection on the Axial Loaded Rectangular CFST Column 285
 R. Manigandan and Manoj Kumar

Numerical Investigation of High-Strength CFST Columns with Slender Sections 297
 Trac Nguyen, Tuan Ngo, and Huu-Tai Thai

Influence of Governing Parameters on Long-Term Behaviour of Prestressed Concrete Bridge with Corrugated Steel Webs 313
 Madhup Pandey and Francis T. K. Au

Module Site Installation and Anchorage—Case Study 333
 Parthasarthi Burman, Sourav Biswas, and Munish Dhawan

Behavior of Pumpable Recycled Aggregate Concrete 345
 K. Vipindasn and B. Rajeevan

Experimental Investigation on the Enhancement of Ductility in SRC Columns 355
 A. Gautham and Dipti Ranjan Sahoo

Numerical Validation on SRC-RC Transfer Columns’ Experiments 367
 Abhishek Jain, Dipti R. Sahoo, and Arvind K. Jain

Unbonded Brace: A Review 375
 Prachi Mishra and Arvind Y. Vyavahare

Engineering Solutions to Mitigate Logistics Changes on a Modular Project 385
 Varun Dhiman and Mangesh Amrut Sakpal

A Numerical Study on the Seismic Response of Circular CFST Column-Beam Exterior Joint with Split Bolt Assembly 393
 P. U. Sreeshma and K. P. Beena

Studies on Steel Beam-to-Column Joints Subjected to Accelerated Corrosion and Cyclic Loads 407
 A. Cinitha, V. Sampath, and G. S. Palani

Response of Steel Knee-Braced Moment Frames Designed Using Ductility-Based Seismic Design Approach with Different Ductility Conditions 421
 Shaktiprasad C. Belaladavar

Prequalifying Criteria for Hollow Structural Steel [HSS] Truss Connections 437
 S. Arul Mary and T. Rama Sindhia

Cold-Formed Steel Frames Using Self-Drilling Screw Connections 453
 Jikhil Joseph and S. R. Satish Kumar

Finite Element Modelling of Screw Connections in Cold-Formed Steel	467
Jikhil Joseph and S. R. Satish Kumar	
Behaviour of Self-Tapping Screws Under Shear	479
M. Divya, R. Senthilkumar, and Prince George	
Spirally Welded Steel Hollow Columns—A Numerical Study	489
K. M. Bharathi, B. Vignesh, and H. Jane Helena	
Effect of Braking Load on Longitudinal Forces in Continuous Welded Rail Considering the Presence of Bridge	499
C. K. Ali Mubarak and Akhil Upadhyay	
Assessment of Efficiency of Steel X-Bracings and Steel Plate Bonding Applied as a Retrofit Measure to Enhance the Seismic Resistance of RC Structures	509
Mohammed Mazharuddin and Y. K. Guruprasad	
Static and Cyclic Behaviour of Beam-Column Endplate Connection with Cellular Beam	523
Dondeti Manideep Reddy, C. Arunkumar, and N. Umamaheswari	
Numerical Study of a Novel Self-lock Connection for Modular Tall Buildings	535
Huu-Tai Thai	
Sustainability by Reverse Joints in Steel Structures (Demountable Modular Shear Connection)	549
Shashidhar S. Shilavantar, Savai Suthar, B. Chaitanya, A. Chiranth, and R. Ravindra	

About the Editors

Prof. Mahendrakumar Madhavan is a Professor in the Department of Civil Engineering, Indian Institute of Technology (IIT) Hyderabad, India. He has obtained Ph.D. and MBA (Finance) from the University of Alabama at Birmingham and his Masters degree from the National University of Singapore. He is a Registered Professional Engineer (PE) in the State of Alabama USA. Prior to IIT Hyderabad, he worked as a Structural Engineer at Alabama Power Company, Birmingham, USA. Prof. Madhavan is an international expert in Structural Steel, Cold-formed steel, and Steel-concrete Composite construction and has published more than 50 peer-reviewed internationally reputed journals and holds membership in the “American Society of Civil Engineers (ASCE) Structural Engineering Institute (SEI) Technical Administrative Committee on Metals” and in “ASCE SEI Cold-Formed Steel Members Committee”. Prof. Madhavan has significantly contributed to the revision of IS 801: Indian Design Code for Cold-formed Steel Members based on the original research work carried out at IIT Hyderabad to fulfil the Government of India’s goal of “Housing for All” through sustainable construction. He is an Editorial board member of the Journal of Structures and is an Associate Editor for the *ASCE Journal of Structural Engineering* and serves as a reviewer for more than ten international journals. Prof. Madhavan is a Fellow of the ASCE, Fellow of the Institution of Civil Engineers (ICE), London and is also the first Indian to be elected as a Fellow of ASCE’s Structural Engineering Institute (SEI).

Prof. James S. Davidson is currently the Gottlieb Professor of Structural Engineering in the Department of Civil and Environmental Engineering, Auburn University, USA. He is an expert in mechanics of materials, advanced stress analysis, finite element methods and stability of structures. He has mentored more than 50 research students including MS and Ph.D., has served as associate editor, review director, and editorial board member on five technical journals, and has served as a reviewer for more than 25 different technical journals.

Prof. N. Elumalai Shanmugam has taught for more than 20 years at the National University of Singapore. Prior to this he taught in College of Engineering, Guindy,

Delhi University, University of Wales (Cardiff) and Polytechnic of Wales. After 50 years of teaching at graduate and undergraduate levels he retired recently from the National University of Malaysia where he taught for nine years. His research interest includes steel-plated structures, steel-concrete composite construction, long-span structures and connections, cold-formed steel structures, etc. He has published more than 200 research papers in International refereed journals conference proceedings and contributed chapters in *Civil Engineering Handbook*, *Structural Engineering Handbook* and *Bridge Manual*. He is a member of the Editorial Board of a number of International Journals.

Restoration Works to Existing Heritage Conservation Building at Upper East Coast Road, Singapore



Jeslin Quek and Reshma Rajeev

Abstract In view of the rising development needs and maintaining the history and character of the places, conservation and restoration of Singapore's built heritage has become significant when continuing to grow as a city of distinction. Regulated by the Urban Redevelopment Authority (URA) of Singapore, a strict set of guidelines are in place for a building which has been demarked for conservation when undergoing restoration or upgrading works to preserve the architectural features. Often, this poses a challenge for the engineers who need to ensure the structural safety of the heritage building constructed decades ago without adopting a formal building code, by complying with the modern building design codes. The paper focuses on the complex and innovative engineering approach adopted to upgrade a conserved building built in the 1950s to be able to withstand the increased design loads. The structural analysis of the single-storey building revealed that the existing reinforced concrete (RC) slabs, beams, columns and pad footings had insufficient capacities to meet the new demand due to the low concrete grade, corrosion of the existing reinforcing steel which resulted in spalling concrete and severe steel sectional losses. A hybrid method including RC jacketing, Tyfo[®] Fibrwrap[®] Systems proprietary Fibre Reinforced Polymer (FRP) Composite Systems and Tyfo[®] Corrosion Inhibitor Systems (CIS) were adopted to successfully restore and conserve the building as per the stipulated requirements.

Keywords Conservation · Upgrading · Innovative engineering approach · Fibre Reinforced Polymer · Hybrid method · Corrosion inhibitor systems

J. Quek (✉) · R. Rajeev
Fyfe Asia Pte. Ltd., Singapore, Singapore
e-mail: jquek@aegion.com

R. Rajeev
e-mail: rrajeev@aegion.com

1 Introduction

Heritage conservation and restoration is gaining importance in Singapore in recent years to commemorate Singapore's past and meet the emerging demand for developments despite the land constraints. The Urban Redevelopment Authority (URA) of Singapore is officially administering the conservation of buildings since 1989. Conserved buildings that narrate the history, culture and traditions of the time during which it was built are to be restored and at the same time meet the present and future demands. These buildings are to retain the original building height, original building profile and original structural and architectural elements when undergoing the conservation and restoration works [1]. As such, the engineers have been facing numerous structural safety issues in restoring and reusing the heritage structures to meet the increased design loads. This is attributed to the deterioration in the strength of structural elements over the years and their insufficient sectional sizes to adapt to the new use. Apart from this, the major challenge for engineers is to comply design with the current code of practice.

The paper elaborates on the restoration works proposed to a single-storeyed reinforced concrete structure that was awarded conservation status by URA. Built in the 1950s, the building was constructed for the residents to enjoy the seaside gatherings. It is the only remaining building marking the former coastline at East Coast [2]. The client had put forward the proposal to change the usage of the building to a gym. The design aspects, methodology and sequencing of the restoration works proposed and duly elaborated in this paper met all the guidelines stipulated by URA to retain its status as a conserved building.

2 Background

Heritage buildings are the most valuable assets of a nation due to their historical and architectural values, cultural uniqueness and tourism prospect [3]. Hence, it is of prime importance to conserve these buildings. Conservation is the process of extending the life span and primary function of heritage buildings [4]. There are various approaches involved in conserving heritage buildings such as restoration, preservation and reconstruction or a combination of these approaches [5]. When conserving these buildings, importance is to be given in choosing the right approach which promotes sustainable development.

Structural safety is one among the vital aspects that is to be considered in conserving heritage buildings. Due to aging, these buildings will be exposed to serious structural defects such as cracking and spalling due to corrosion of reinforcement bars. Corrosion reduces the strength and durability of reinforced concrete (RC) structural elements. As such, these elements may not have adequate capacity to adapt to the intended function. To address these structural issues, researchers have conducted various studies in the past.

Nossoni et al. [6] conducted experimental and numerical studies to investigate the durability enhancement of RC beams against corrosion when bi-directional Glass Fibre Reinforced Polymer (GFRP) composite was used as an overlay on shallow depth surface patch. GFRP overlay detained the outset of cracking, and the corrosion rate was reduced. The main crack actuated in concrete and propagated sideways away from the region of GFRP overlay. As the crack does not open through the concrete cover, the migration of moisture, chloride and oxygen to the corroding bar was detained. Whereas, in the absence of an overlay, the main crack actuated in the patch and propagated downwards towards the bottom of beam. Shallow patch repairs of reinforced concrete beams using a GFRP overlay provided increased durability, thereby reducing the maintenance cost and labour for repatching the beams.

Abdelgader et al. [7] illustrated the advantages of using two-stage concreting (prepacked aggregate grouting) over conventional concreting in the reinforced concrete (RC) jacketing process. The drying shrinkage of two-stage concrete was observed to be one-half of conventional concrete. Reduced shrinkage was attributed to the point-to-point contact of aggregate particles due to prepacking of aggregates and pumping of grout under pressure. Segregation could be avoided, and all voids would be filled with mortar.

El Maaddawy et al. [8] investigated the feasibility of using externally bonded Carbon Fibre Reinforced Polymer (CFRP) laminates to enhance the structural capacity of corroded and damaged RC beams. A layer of flexural laminate together with U-shaped transverse strips was reported to increase the ultimate strength of RC beams at all levels of corrosion induced damage of up to 31% of steel mass loss. The ultimate strength of a RC beam at 30% of steel mass loss was 73% higher than that of similar corroded beam which was unstrengthened and 31% higher than that of similar beam which was non-corroded and unstrengthened.

Jorge et al. [9] studied the influence of anti-corrosive coatings on the bond strength between reinforcement bars and repair mortars. The use of coatings on non-corroded plain bars increased the average bond strength for all types of repair mortars. For corroded plain bars, the average bond strength increased except for aqueous dispersion paintings. For ribbed reinforcement bars, the use of coatings on corroded or non-corroded bars reduced the average bond strength for all types of repair mortars. Application of cementitious coatings was recommended for plain reinforcement bars, whereas it was advised to avoid coatings for ribbed reinforcement bars.

Using observations from the aforementioned studies, the case study presented in this paper detailed the structural and geotechnical aspects of conserving the heritage building. Specific objectives of conservation are detailed in the following section.

3 Problem Statement

The objective is to restore and conserve the building to be able to withstand the increased design loads of a gym. The existing building was a single-storeyed RC structure with brick masonry walls. The first storey cantilevered part was built with RC suspended slab, and the rest of the storey was built with plain concrete non-suspended slab. The roof slab was of ribbed type. The infills between ribs were filled with bricks. The suspended slabs were supported on RC beams which were supported on RC columns. The columns were supported on RC pad footings. According to the URA guidelines of a conserved building, the external wall façade, floor-to-roof height and size of structural elements were to remain. Further, any modification to the building should not affect the cantilevered part, neighbouring property and the public drain (Fig. 1).

Due to the absence of as-built drawings, a structural investigation was required upon the proposal to change the usage of the building. It was inferred from the investigation report that the existing RC slabs, beams, columns and pad footings had low concrete grade, existing steel reinforcement bars were corroded which resulted



Fig. 1 Existing building to be conserved

Fig. 2 Severe corrosion in steel reinforcement bars of slabs and beams



in spalling concrete and severe steel sectional losses (Fig. 2). Further to a preliminary design check, all the structural elements required enhancement in capacities to meet the new demand. This meant major modification that will affect the existing sizes and partial demolition of the existing external wall façade which were not allowed under the URA guidelines of a conserved building. The client desired to do strengthening to the structure to adapt to the new usage. However, it was concluded that strengthening individual elements solely was not feasible to carry the increased design loads.

4 Design

Finite element analysis was conducted on the existing structure to investigate the required design bending moment and/ or shear force on RC slabs and beams and the required design axial load on RC columns. The design Live Load (LL) and Superimposed Dead Load (SDL) were taken as tabulated in Table 1. As per the URA guidelines, conserved buildings must be retained and restored with minimum replacement works. As such, during the design stage emphasis had been given to retaining the structure as far as possible without any demolition.

Based on the analysis and design check, first storey beams and pad footings required conventional sectional enlargement and slabs required structural top up to carry the required design loads. Further, a new foundation was required to provide additional support to the cantilever RC beam. Topping up the slab would affect the floor-to-roof height of the building, whilst increasing the size of beams would

Table 1 Design loadings

Floor level	LL (kPa)	SDL (kPa)
1st storey	5.0	1.7
Roof	0.5	3.0

affect the architectural appearance requiring the external wall façade to be locally demolished. Also, providing an additional foundation would affect the neighbouring property and the public drain.

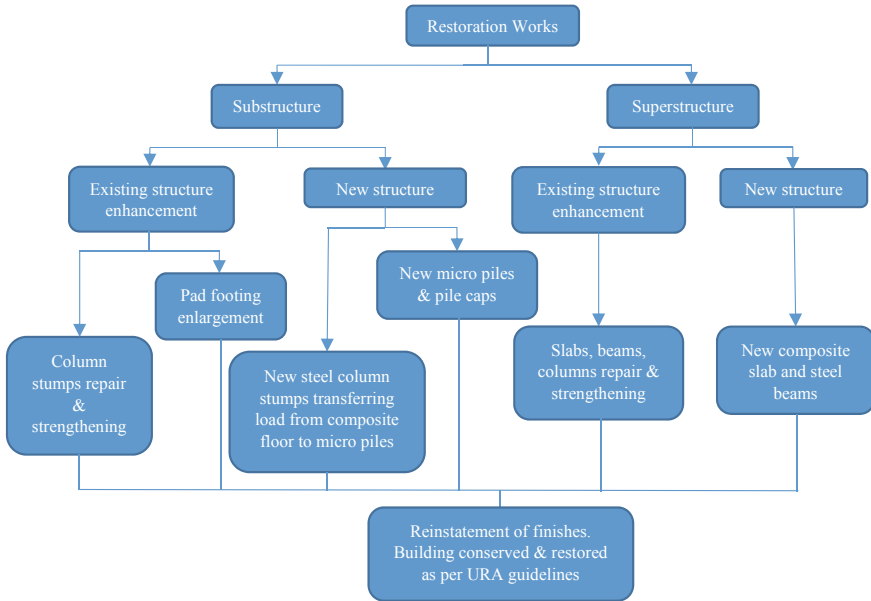
Hence, it was proposed to demolish and reconstruct the first storey slab. A new composite suspended floor system was proposed independent of the existing RC beams transferring load to the new micro-pile through the pile cap. Micro-pile was selected over other foundations due to the space constraints on site where installation of conventional isolated footings can result in overlapping with the existing footings. Additionally, for micro-piles, less excavation was required, and there would be minimal noise and vibration during the installation ensuring less disturbance to the existing structure. After several discussions that focused on the need to hack the slab, the proposal had been approved by the authority. Strengthening was then proposed to the existing slabs, beams and columns to be retained.

The proposed enhancement was achieved through a combination of RC jacketing and the use of Tyfo® Fibrwrap® Systems. Due to severe corrosion, the existing beams required the steel sectional losses to be compensated using new steel reinforcement bars. The existing ribbed roof slab was strengthened by replacing brick infill with concrete and adding steel reinforcement bars. The affected pad footings were strengthened by enlarging the base area and thickness. Tyfo® Corrosion Inhibitor Systems (CIS), a specially formulated material which inhibits corrosion, was used to prevent further corrosion of the existing reinforcing steel and seal the porous concrete. The Tyfo® Fibrwrap® System, proprietary Fibre Reinforced Polymer (FRP) composite systems, was used to enhance the capacity of existing slabs, beams and columns and serve as a protective layer.

5 Methodology

All existing external walls were braced to avoid collapse during the hacking works. Instrumentation was installed to monitor settlements. Existing finishes of the affected elements were removed and exposed to the bare concrete surface. Underground services detection was conducted to determine the location of buried utilities to ensure that all works can proceed safely without damaging or disrupting the services.

5.1 Work Plan



5.2 Materials Used

Tyfo[®] CIS Layer 1 was used to form a passive film over the corroded reinforcement bars to prevent further corrosion. Tyfo[®] CIS Layer 2 was used to seal the porosity of concrete, protect from acid or alkali attack and inhibit the embedded steel corrosion by preventing further penetration of moisture. Glass Fibre Reinforced Polymer (GFRP) with Tyfo[®] S epoxy was used to enhance the capacity of slabs, beams and columns. The types of GFRP composites used were Tyfo[®] SEH-25A and Tyfo[®] SEH-51A. Specifications of the composites are listed in Table 2. Tyfo[®] WR-AFP, Fire-Protection System, was used to provide up to 4 h fire-rating to the installed GFRP composites. Concrete of minimum grade C25/30 and high strength deformed (HSD) bars of yield strength 500 MPa were used for the RC jacketing. For the curved RC beams, 7-wire super steel strands of nominal diameter 12.9 mm, nominal steel area 100 mm² and guaranteed ultimate tensile strength 186 kN were used instead of the HSD bars. The advantages of using steel strands were its higher tensile strength and ease of installation compared to the HSD bar. HSD bars required a higher diameter and need to pre-bend to the required curvature or produced by a series of short straight sections which would require a significant amount of labour and steel to cater for the lap lengths.

Table 2 Specifications of GFRP composites

GFRP composite	Ultimate tensile strength (MPa)	Tensile modulus (MPa)	Thickness per layer (mm)
Tyfo [®] SEH-25A	575	26,100	0.64
Tyfo [®] SEH-51A	575	26,100	1.30

5.3 Procedure

5.3.1 Substructure Works

Holes were cut on the existing first storey slab to install micro-piles. Due to space constraints, a portable rig was used for the micro-pile installation. Drilling was performed until the required depth was reached. The rebar cage was lowered and installed together with a grout hose. Grouting was performed, and the casting of piles was completed.

The first storey slab was saw cut and localized. The slab was then hacked off. Excavation was carried out to expose the first storey beams, footings to be strengthened and pile cap locations. The affected footings were enlarged. Micro-piles were hacked to the required cut-off level. J bolts of the column base plate were put in place together with the reinforcement cage of the pile cap. Pile caps were cast. Steel column stumps were installed.

Tyfo[®] CIS Layer 1 was applied to the concrete substrate of existing column stumps using a roller brush ensuring that all surfaces were covered, and every brush stroke overlapped each other. The previous application was allowed to fully evaporate and penetrate through before proceeding with the next application. The substrate was allowed to dry completely. Then, Tyfo[®] CIS Layer 2 was applied to the concrete substrate using the roller brush. It was ensured that every brush stroke overlapped the previous one. The application was kept speed slow and steady with gentle pressure on the brush allowing the substrate to absorb Layer 2. Each application saturated the substrate and was allowed to dry completely prior to the next application. The system was allowed to cure. Tyfo[®] Fibrwrap[®] System was installed to the affected existing column stumps. Installed Tyfo[®] Fibrwrap[®] Systems were protected using plaster. The excavated soil was then backfilled.

5.3.2 Superstructure Works

All cracks and spalling at the existing first storey beam surfaces were repaired. Concrete cracks were sealed with epoxy injection using an injector system. Locations for the installation of steel strands were marked. 25 mm (Width) × 35 mm (Depth) was saw cut along the length of the beam following the markings for steel strand installation. The concrete was removed to form a groove. Steel strands were installed into the groove. 20 mm (Width) × 25 mm (Depth) was saw cut along the depth and

width of the beam at 300 mm centre-to-centre. The concrete was removed to form a groove. Steel links were installed into the groove. Grooves were patched using polymer modified repair mortar, and inlet ports were inserted at 500 mm centre-to-centre for grouting of epoxy. Curing was allowed for a day. Tyfo® S epoxy was pumped through the inlet port until epoxy oozes out of the next port. The previous port was then plugged. Injection of Tyfo® S epoxy was resumed at the next port, and the process was repeated until the last port was reached. Tyfo® S epoxy was allowed to cure. Grout ports were removed. Tyfo® Fibrwrap® System was installed to the first storey beams. Installed Tyfo® Fibrwrap® Systems were protected using plaster. Steel beams were installed, and the first storey composite slab was cast.

Once the casting of the slab was complete, scaffolding and railing were erected for access to the roof restoration works. The roof slabs and beams were propped. The walls affecting the strengthening works to columns were saw cut and hacked to 50 mm width along the height. Tyfo® CIS Layer 1 and Layer 2 were applied to the concrete substrate of columns using the roller brush. The first storey columns were strengthened using Tyfo® Fibrwrap® Systems, and roof beams were strengthened using RC jacketing. The RC jacketing of roof slab panels was done in parts. The propping erected for the first part was removed. Existing brick infill and spalled concrete were removed. The surface of the existing concrete was roughened to form keys for bonding. Holes were drilled along the existing ribs of the slab to install new steel reinforcement bars. Steel reinforcement bars were installed and anchored to the beams using approved chemical grout. Formwork was fabricated and fixed with proper support/ tie-rods with inlet and outlet grout pipes installed at 500 mm centre-to-centre. Uniformly graded aggregates were prepacked and filled in the formwork. Edges of the formwork were sealed off. Cement grout was pumped in from one end to the other end. Once the grout overflowed from the second nozzle, the first nozzle was nipped, and pressure grouting was continued on the second nozzle. The process was continued until the last nozzle was reached. The last nozzle was sealed after the overflow, and pressure was maintained at 1 bar for 1 min. Grout was allowed to cure. The process was repeated for the other parts of the slabs. Formwork was stripped. Tyfo® CIS Layer 1 and Layer 2 were applied to the concrete substrate of roof slabs and beams using the roller brush. Tyfo® Fibrwrap® Systems were installed to the slabs and beams. Tyfo® WR-AFP Fire-Protection System was applied to the installed Tyfo® Fibrwrap® Systems.

5.4 Challenges Faced

Access to the working elements was the major challenge for this project as the site was congested. The sequence of works was carefully planned to ensure the structural integrity of the structure, at the same time ensuring the successful completion of the project within agreed time frame. The works had to be carried out in two stages, i.e. substructure and superstructure work. The two stages of work could not be executed simultaneously due to constraints on access to working elements. The substructure

work and casting of the first storey slab had to be completed to prop the existing roof slab and beam prior to the roof restoration works. Also, jacketing works of the roof slab were done in parts to ensure necessary propping was in place to prevent any possible collapse during the restoration works. For the temporary bracing of walls, inclined and horizontal bracings had to be adopted without affecting the first storey slab to be hacked.

During drilling for micro-piles, obstruction was encountered below ground. At that stage, the authority's approval was not obtained to hack the first storey slab. Thus, it was not possible to excavate and investigate the obstruction. Only small openings could cut through the existing slab. Further, on visual inspection, the obstruction could be the base of the rubble wall 750 mm from the piling points. Shifting the micro-piles was the only option to ensure the progress of work without any delay. The two micro-piles at the cantilevered side were shifted 1.15 m further into the building to avoid the obstruction. As a result, the new floor system was reframed. Micro-piles carried higher loads, and its length was increased. Steel beam sections at the cantilevered side were also increased.

During the removal of existing finishes, some columns were found to have steel reinforcements that were completely corroded (Fig. 3). This was contrary to the findings from the structural investigation which reported reinforcements to be present. Hence, minimum reinforcements had to be installed to the affected columns for anti-crack requirements.

Fig. 3 Steel reinforcement bars of column reduced to zero section



6 Conclusion

The proposed hybrid method including RC jacketing, Tyfo[®] CIS and Tyfo[®] Fibrwrap[®] Systems restored and conserved the building complying with the existing guidelines of a conserved building. All architectural elements of the building were retained. The cantilevered structure which was unique to Singapore's coastal architecture remained. Any change to the size of structural elements was avoided. The proposed method of jacketing the roof slab by replacing existing brick infill with concrete and adding steel reinforcement bars avoided any deviation to the existing floor-to-roof height. Also, the method of having an independent floor system prevented any change to the existing wall façade.

Further, the restoration works catered the reuse of the building and withstand the required design loads of a gym. Less energy consumption was associated with the current proposal compared to the overall demolition and reconstruction of the structure. Minor modifications adapted the existing building to be compatible to new use complying with the modern building codes. Such restoration works contribute to Singapore's continued progress and development. Besides preserving history, it helps in developing sustainable construction practices. The procedures followed in the present work can be a generalized sustainable guidance for any such future projects.

References

1. Urban redevelopment authority (URA), Singapore (2019) <https://www.ura.gov.sg/Corporate/Guidelines/Conservation>. Accessed 20 Dec 2019
2. Urban redevelopment authority (URA), Singapore (2019) https://www.ura.gov.sg/Conservation-Portal/Explore/History?bldgid=UECR_00001. Accessed 20 Dec 2019
3. Sodangi M, Khamdi MF, Idrus A, Hammad DB, AhmedUmar A (2014) Best practice criteria for sustainable maintenance management of heritage buildings in Malaysia. *Procedia Eng* 77:11–19
4. Idrus A, Khamidi F, Sodangi M (2010) Maintenance management framework for conservation of heritage buildings in Malaysia. *Mod Appl Sci* 4(11):66
5. Harun SN (2011) Heritage building conservation in Malaysia: experience and challenges. *Procedia Eng* 20:41–53
6. Nossoni G, Harichandran RS (2010) Improved repair of concrete structures using polymer concrete patch and FRP overlay. *J Mater Civ Eng* 22(4):314–322
7. Abdelgader HS, Ben-Zeitun AE, Al-Galhud AA (2006) Use of two-stage (pre-placed aggregate) concrete in construction and repair of concrete structures. *Concrete Repair, Rehabilitation and Retrofitting-Alexander* (eds.), pp 869–872
8. El Maaddawy T, Soudki K (2005) Carbon-fiber-reinforced polymer repair to extend service life of corroded reinforced concrete beams. *J Compos Constr* 9(2):187–194
9. Jorge S, Dias-da-Costa D, Júlio ENBS (2012) Influence of anti-corrosive coatings on the bond of steel rebars to repair mortars. *Eng Struct* 36:372–378

Nonlinear Finite Element Analysis of GFRP Fabrics Strengthened RC Deep Beams Using ABAQUS



A. Kumari and A. N. Nayak

Abstract Reinforced concrete (RC) deep beam is widely used in different types of engineering structures, viz. in high rise buildings, offshore structures and foundation pile caps, etc. Deep beam mostly failed under shear rather than flexure. Thus, shear strengthening of deep beam is of a challenging task. In the present paper, both experimental programme and a computer based finite element (FE) analysis of RC deep beam (GFRP strengthened/un-strengthened) is carried out. From both the investigations, the structural behaviour of deep beam in terms of strength enhancement and failure pattern is studied. Thereafter, a comparison has been carried out between those obtained experimental results and the finite element results to check the efficiency of the present numerical FE analysis. From both the studies, it is also evident that the advancement in numerical FE modelling can reduce the number of required test specimens for the resolution of a given problem, recognizing that experiments are time-consuming and expensive.

Keywords ABAQUS · Deep beam · GFRP fabrics · Nonlinear FE analysis · Reinforced concrete · Shear failure

1 Introduction

Most of the rehabilitation works in the construction world consist of repairing of old, deteriorated and partially demolished structures. Many times the degradation of structural members is due to poor design plan, low quality construction, environmental exposure and hence need to meet the present design requirements. In the course of recent decades, retrofitting/strengthening has got a good deal all through the world to

A. Kumari (✉) · A. N. Nayak
Department of Civil Engineering, Veer Surendra Sai University of Technology, Burla,
Sambalpur 768018, India
e-mail: archanakumaripadhi@gmail.com

A. N. Nayak
e-mail: nayakan1964@gmail.com

© The Author(s), under exclusive license to Springer Nature Singapore Pte Ltd. 2023
M. Madhavan et al. (eds.), *Proceedings of the Indian Structural Steel Conference 2020*
(Vol. 2), Lecture Notes in Civil Engineering 319,
https://doi.org/10.1007/978-981-19-9394-7_2

improve the overall strength of concrete members such as reinforced concrete (RC) beams, T-beams, and columns, since the replacement of these deteriorated structures will be highly expensive. In addition to this, Selvaraj and Madhavan [30–33] and Chen et al. [8], investigated on strengthening/retrofitting of steel beams using externally bonded FRP composites in order to improve the structural performance of steel beams. On the other hand, RC deep beams are used as transfer girders in high rise buildings, pile caps, the wall of water tanks, foundations and offshore structures [15–18, 24, 25, 34, 36]. The behaviour of RC deep beam is very complex and is absolutely different from that of RC beams. Normally, shear failure occurs in RC deep beam owing to wide diagonal crack originated in the shear span showing more brittleness in comparison with the slender beam, due to which it needs a thorough investigation. Over the past four decades, numerous experimental and analytical research works are conducted on RC deep beams to study the structural performance such as shear strength, cracking behaviour and failure mode of the deep beams [4, 5, 12, 16, 17, 21, 26, 28, 29, 35, 37, 39]. Furthermore, some notable design guidelines/models [2, 3, 7, 11, 14] are also incorporated to evaluate the shear strength of EB-FRP strengthened concrete beams, which involve either elastic theory or semi-empirical equation. On the other hand, several investigators reported that finite element (FE) method is an alternative powerful and wide-ranging numerical technique for investigating the structural performance of deep beam [6, 10, 13, 19, 20, 22]. Hence, FE modelling is a commonly adopted tool by the researchers for the verification of experimental results.

Therefore, in the present paper an emphasis has been given to present a comparative study to get a complete understanding of the obtained experimental results in support of predicted results obtained from FE analysis by using a commercial FE package ABAQUS 6.12.

2 Summary of the Test Programme

The FE model reported in this paper is validated using the experimental work carried out by the author. A total of three numbers of deep beams are prepared. Keeping one beam as control beam rest two beams are wrapped with two layer and three layers of glass fibre reinforced polymer (GFRP) fabrics in U-shape at shear span only. The details of the dimension and reinforcement details for all the beams prepared are identical as shown in Fig. 1.

The dimensions of the deep beams are 1000 mm in length and 120 mm × 420 mm in cross section. Each beam has four 12 mm dia. High yield strength deformed (HYSD) bars in the tension zone. The compression reinforcement includes two numbers of 8 mm dia. HYSD bars as hanger bars. Four numbers of 8 mm dia. horizontal stirrups and five numbers of 8 mm dia. two legged vertical stirrups are provided as shear reinforcement. Table 1 summarises the mechanical properties of the concrete, steel reinforcement bars, aggregates and EB GFRP sheets used in the

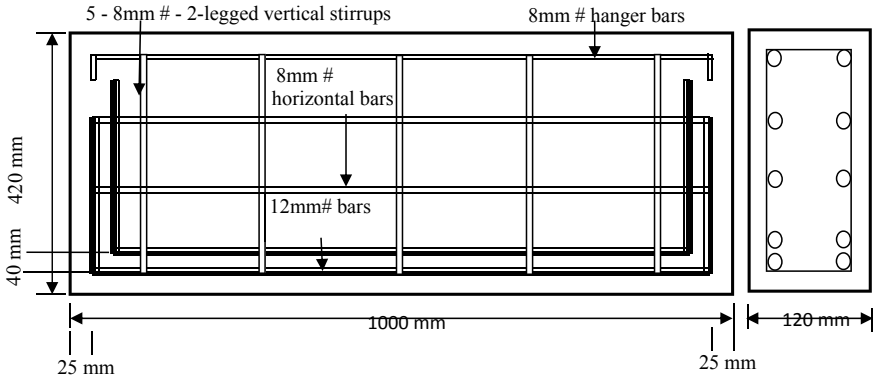


Fig. 1 Details of the dimension and reinforcement of deep beams

Table 1 Material properties

Material	Compressive strength (MPa)	Ultimate strain (mm/mm)	Yield strength (MPa)	Ultimate strength (MPa)
Concrete	30	–	–	–
Steel	–	–	507	667
EB-GFRP	–	2.44	–	290.61

experimental investigation. All beams are tested in a universal testing machine (UTM) under two point loading system as shown in Fig. 2.

3 Numerical Study

A numerical study is performed with the help of the ABAQUS nonlinear FE software. The material modelling and validation of FE model is studied accordingly.

3.1 Material Modelling

3.1.1 Concrete

For concrete, the concrete damaged plasticity (CDP) model accessible in ABAQUS / Explicit is utilized. The CDP model requires the stress–strain relationship of concrete as a contribution to stress versus inelastic strain. For the assessment of stress versus inelastic strain of the concrete the uniaxial compressive stress versus strain model

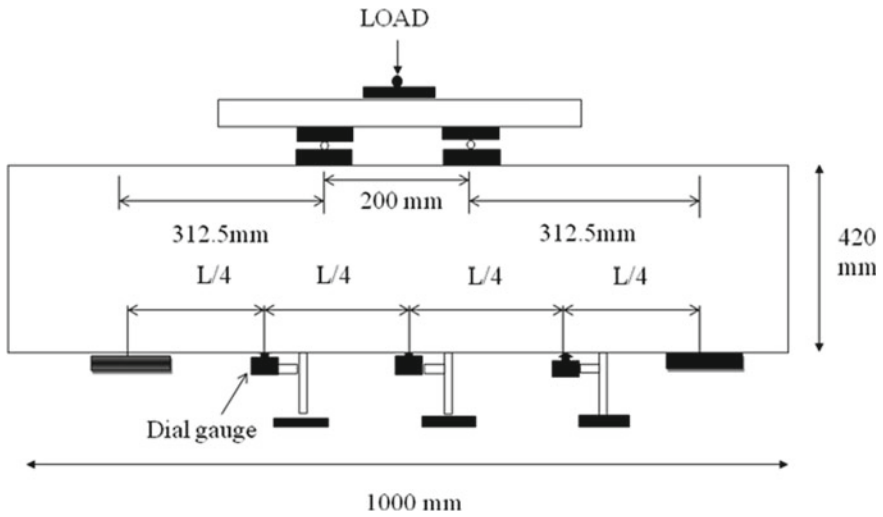


Fig. 2 Schematic diagram for experimental test set-up in UTM

suggested by Popovics [27] is utilized. For concrete under uniaxial tension, tension-stiffening behaviour is accepted to simulate the post-cracking tensile behaviour. The tension-stiffening model suggested by Nayal and Rasheed [23] is utilized. The eight-node brick element with three translational degrees of freedom at each node (C3D8R) is used to model the concrete.

3.1.2 Steel

Both the main and shear steel reinforcements are simulated with three-dimensional, two-node truss elements (T2D3) embedded in concrete region. Reinforcement detailing is shown in Fig. 3.

3.1.3 GFRP Fabrics

In the present study, GFRP fabric and epoxy adhesive is considered as an elastic isotropic material. GFRP fabric is modelled using three-dimensional reduced integration shell element (S4R). The bond between GFRP fabric and concrete is assumed to be perfect bond.



Fig. 3 Reinforcement detail of FE modelling

3.1.4 FE Discretization

The reinforcement details, dimensions, GFRP wrapping pattern, boundary conditions and loading pattern of the deep beam model are similar to the respective experimental beams. The ABAQUS version 6.11 is adopted to simulate the nonlinear finite element model of deep beam specimens. The interfaces between concrete and steel are tied using the ABAQUS tie constraint. The interaction between concrete and steel is done based on the model suggested by Eligehausen et al. [9]. The model suggested by Yuan et al. [38] is used to model the interface between concrete and GFRP. Simply supported type is used for the boundary conditions. Two point loading is modelled for the loading conditions.

3.1.5 Meshing

Equal mesh size is assigned in order to ensure that each of two different materials shares the matching node for all the elements in the FE model. The kind of mesh favoured in the model is structured. FE meshing of deep beam is shown in Fig. 4.

4 Results and Discussion

4.1 *Comparison of Experimental and Numerical Analysis; Validation of FE Model*

The comparison of experimental results and FE analysis are presented in terms of ultimate load and failure mode. The simulated FE model along with loading pattern is shown in Fig. 5. The verified FE results are discussed in the following sections.

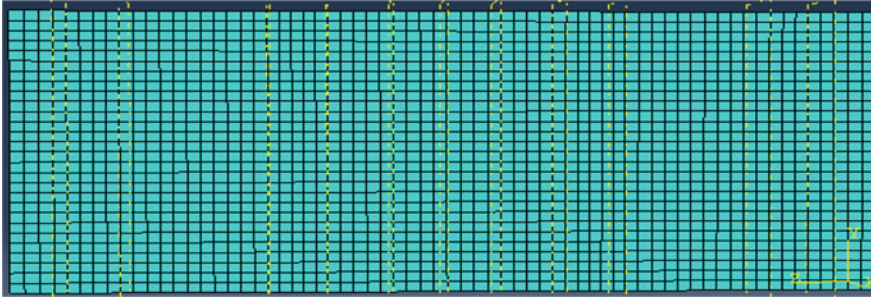


Fig. 4 Meshing of deep beam

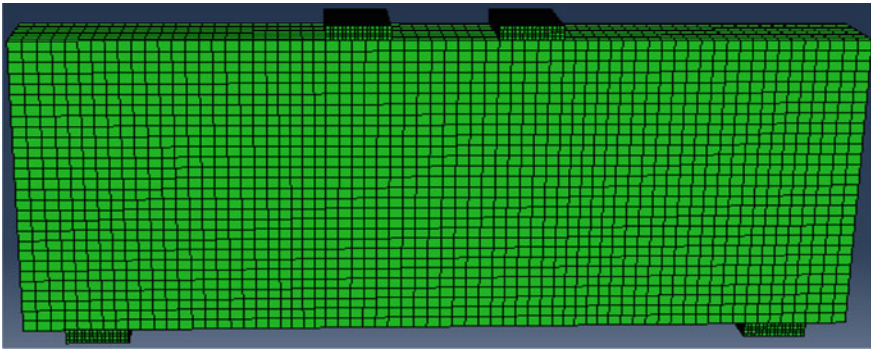


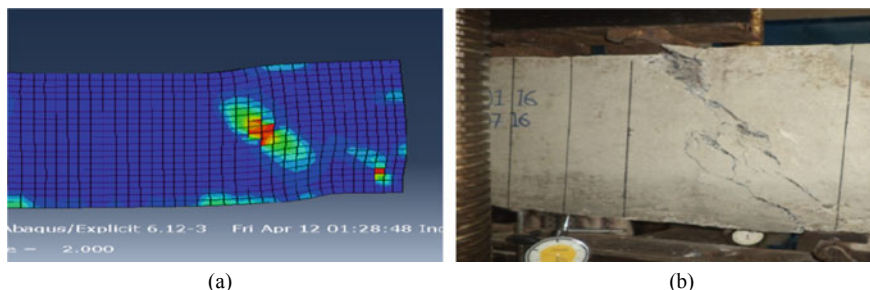
Fig. 5 FE model along with loading pattern

4.1.1 Shear Strength Comparison

The simulated shear strength is compared with the experimental shear strength and is presented in Table 2 along with the failure mode. The shear strength considered in the present study is half of the ultimate load. It is observed that the FE results match with the experimental results very well and the failure mode shows similar trend to that of the experimental failure mode. For the control beam, DB_0 , the predicted shear strength is 175.00 kN (within 14% accuracy from the experimental shear strength). To better understand the effect of increasing the number of GFRP fabric layers during strengthening of the deep beams, as likely the experimental investigation, 2 and 3 layers of GFRP fabrics are selected for numerical FE study. As expected, the predicted shear strength of all the GFRP fabrics strengthened beams is higher than that of the strength predicted by numerical control beam and thicker the GFRP fabric is, the higher is the shear strength observed. It is also observed that the predicted shear strength for deep beams DB_2 and DB_3 are decreased by 14% and 12%, respectively, as compared to their respective experimental beams (Table 2).

Table 2 Comparison of test results

Beam	Experimental shear strength (kN)	Numerical shear strength	Failure pattern	
			Experimental	Numerical
DB ₀	200.00	175.00	Diagonal crack	Diagonal crack
DB ₂	245.00	210.50	De-bonding + diagonal crack	De-bonding + diagonal crack
DB ₃	298.80	263.00	De-bonding + diagonal crack	De-bonding + diagonal crack

**Fig. 6** Failure mode of DB₀ **a** numerical, **b** experimental

4.1.2 Crack Patterns and Failure Mode Comparison

The comparison between experimental and numerical crack pattern as well as failure mode for all the numerically simulated beams are included in Figs. 6, 7, 8, 9 and 10. From Fig. 6, it can be seen that the failure mode of numerical control beam is due to development of shear crack at shear zone, i.e. between the loading point and support point. Comparison of Fig. 6a and b shows identical shear crack pattern appeared at the shear span. The 2-layer GFRP fabric strengthened numerical model is failed by de-bonding of GFRP fabrics at shear span followed by an inclined crack under the wrap as shown in Figs. 7 and 8, respectively. The same failure mode also was observed for the beam DB₃ with three layers of GFRP as shown in Figs. 9 and 10. Thus, it can be concluded that the failure modes of strengthened numerical beams are similar to those seen in case of strengthened experimental beams which are shown in Figs. 7b, 8b, 9b and 10b.

5 Conclusions

This paper presents the effectiveness of strengthening of EB-GFRP fabrics in various layers on RC deep beams. The nonlinear FE analysis is carried out using ABAQUS package in order to predict the real behaviour of deep beam. A comparative approach

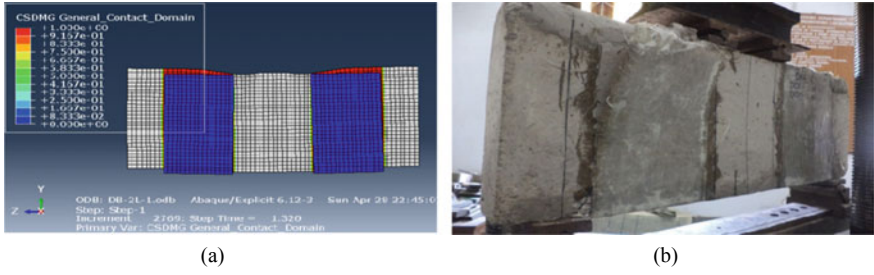


Fig. 7 De-bonding of DB₂ a numerical, b experimental

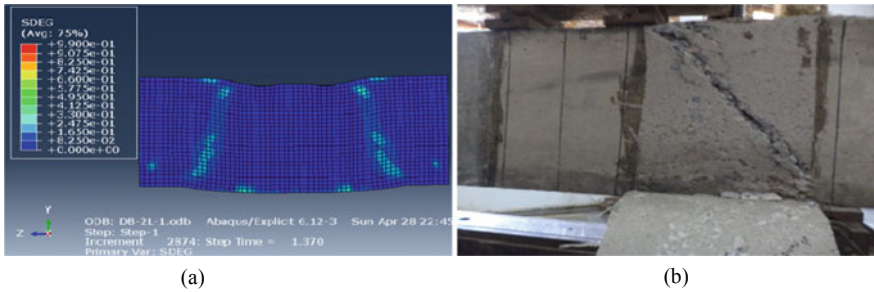


Fig. 8 Cracking pattern of DB₂ a numerical, b experimental

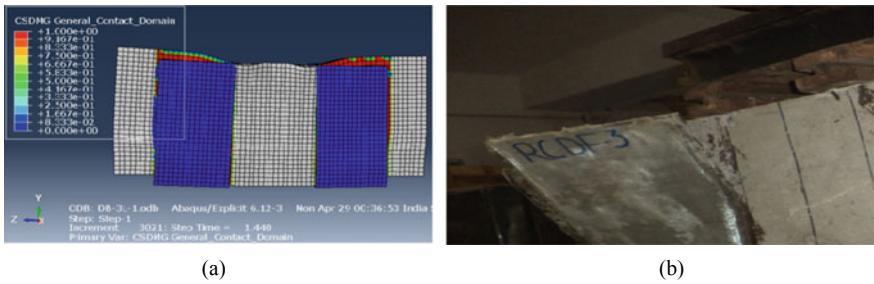


Fig. 9 De-bonding of DB₃ a numerical, b experimental

has been made between the results obtained experimentally and nonlinear FE analysis. Based on the observations of the present experimental study and the comparative approach discussed, the following conclusions have been drawn.

1. The failure of the un-strengthened deep beam is initiated due to development of wide diagonal cracks in the shear span whereas the beams strengthened with EB-GFRP fabrics are mainly failed in shear after partial/fully de-bonding of GFRP fabrics followed by diagonal shear crack underneath the EB-GFRP fabrics. In

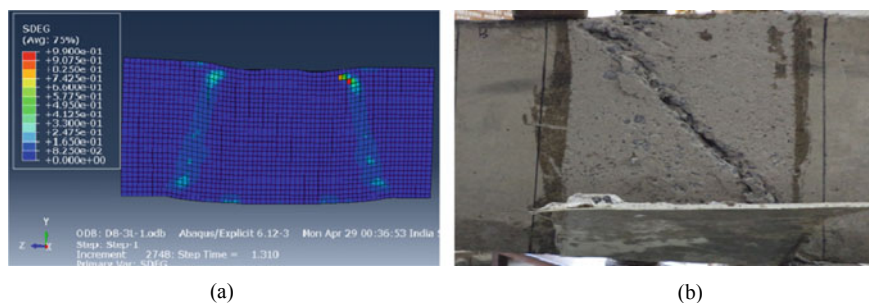


Fig. 10 Cracking pattern of DB₃ **a** numerical, **b** experimental

all beams the diagonal crack initiated at the centre of shear span and propagated towards the support and loading point.

2. Wrapping of EB-GFRP fabrics in various layers has a significant effect on shear behaviour of deep beams in terms of enhancing the ultimate load,
3. The results obtained by FE modelling matches very well with the experimental results, such as ultimate load, crack patterns and failure modes. All these specify that the constitutive models used for concrete and GFRP fabrics by ABAQUS are able to capture the fracture behaviour of GFRP-strengthened deep beam more correctly.

The findings of the present experimental study can be upgraded by carrying out further research on RC deep beams by strengthening the deep beams in different patterns such as strips, grids and with different angle of orientation.

References

1. ABAQUS/Standard v.6.12 SE. Dassault Systèmes Simulia Corp.
2. ACI 440.2R (2008) Guide for the design and construction of externally bonded FRP systems for strengthening concrete structures. American Concrete Institute
3. ACI Committee 318 (2005) Building code requirements for structural concrete and commentary. Farmington Hills, American Concrete Institute
4. Ahmad Shuaib H, Rafeeqi SFA, Fareed S (2011) Shear strength of normal and light weight reinforced concrete deep beams without web reinforcement. *J Emerg Trends Eng Appl Sci (JETEAS)* 2(6):967–971
5. Ashour AF, Yang KH (2008) Application of plasticity theory to reinforced concrete deep beams: a review. *Mag Concr Res* 60(9):657–664
6. Birtel V, Mark P (2006) Parameterised finite element modelling of RC beam shear failure. In: ABAQUS users' conference, pp 95–108
7. Chen JF, Teng JG (2003) Shear capacity of FRP-strengthened RC beams: FRP de-bonding. *Constr Build Mater* 17:27–41
8. Chen Y, Feng R, He K, Chen X, Huang J (2018) Flexural behaviour of concrete-filled stainless steel SHS and RHS tubes strengthened by CFRP. *Thin-Walled Struct* 122:208–229

9. Eligehausen R, Popov EP, Bertoro VV (1983) Local bond stress-slip relationship of deformed bars under generalized excitations. Rep. No. UCBEERC-83/23, Earthquake Engineering Centre, Univ. of California, Berkeley, CA, p 169
10. Enem JI, Ezech JC, Mbagiorgu MSW, Onwuka DO (2012) Analysis of deep beam using Finite Element Method. *Int J Appl Sci Eng Res* 1(2)
11. Fib-TG9.3 (2001) Design and use of externally bonded fiber polymer reinforcement for reinforced concrete structures. Technical report prepared by EBR working party of Task Group 9.3, Bulletin 14, 138
12. Foster SJ, Gilbert RI (1998) Experimental studies on high-strength concrete deep beams. *ACI Struct J* 95(4):382–390
13. Islam SMS, Khennane A (2012) Experimental verification of automated design of reinforced concrete deep beams. In: SIMULIA customer conference
14. Khalifa A, Gold WJ, Nanni A, Abdel Aziz MI (1998) Contribution of externally bonded FRP to shear capacity of flexural members. *ASCE J Compos Constr* 2(4):195–203
15. Kong FK, Robins JP, Cole FD (1970) Web reinforcement effect on deep beams. *ACI J* 67(12):1010–1018
16. Kumari A, Nayak AN (2019) Strengthening of shear deficient RC deep beams using GFRP sheets and mechanical anchors. *Can J Civ Eng*
17. Kumari A, Patel SS, Nayak AN (2018) Shear strengthening of RC deep beam using externally bonded GFRP fabrics. *J Inst Eng (India): Ser A* 99(2):341–350
18. Manuel RF, Slight BW, Suter GT (1971) Deep beam behavior affected by length and shear span variations. *Am Concr Inst J Proc* 68(12)
19. Metwally IM (2015) Three-dimensional nonlinear finite element analysis of concrete deep beam reinforced with GFRP bars. *HBRC J* (in press)
20. Mohamed AR, Shoukry MS, Saeed JM (2014) Prediction of the behavior of RC deep beams with web openings using the finite element method. *Alex Eng J* 53:329–339
21. Mohammadhassani M, Jumaat MZ, Ashour A, Jameel M (2011) Failure modes and serviceability of high strength self compacting concrete deep beams. *Eng Fail Anal* 18(8):2272–2281
22. Najafian HAN, Vollum RL (2013) Automated nonlinear design of reinforced concrete D regions. *Struct Eng Mech* 46(1):91–110
23. Nayal R, Rasheed HA (2006) Tension stiffening model for concrete beams reinforced with steel and FRP bars. *J Mater Civ Eng* 18(6):831–841
24. Oh JK, Shin SW (2001) Shear strength of reinforced high-strength concrete deep beams. *ACI Struct J* 98(2):164–173
25. Paiva De, Siess CP (1965) Strength and behaviour of deep beams in shear. *J Struct Eng Div ASCE Proc* 91:19–41
26. Park JW, Kuchma D (2007) Strut-and-tie model analysis for strength prediction of deep beams. *ACI Struct J* 105:657–666
27. Popovics A (1973) A numerical approach to the complete stress-strain curve of concrete. *Cem Concr Res* 3:583–599
28. Rao GA, Kunal K, Eligehausen R (2007) Shear strength of RC deep beams. In: Proceedings of the 6th international conference on fracture mechanics of concrete and concrete structures (2):693–699
29. Santhakumar AR, Arunachalam NV1972 Strength and behavior of single span reinforced concrete deep beams. *Indian Concr J* 46(11)
30. Selvaraj S, Madhavan M (2017) Strengthening of unsymmetrical open channel built-up beams using CFRP. *Thin-Walled Struct* 119:615–628
31. Selvaraj S, Madhavan M (2018) Retrofitting of structural steel channel sections using cold formed steel encasing channels. *J Perform Constr Facil* 32(4):04018049
32. Selvaraj S, Madhavan M (2019) Strengthening of laterally restrained steel beams subjected to flexural loading using low-modulus CFRP. *J Perform Constr Facil* 33(3):04019032
33. Selvaraj S, Madhavan M (2020) Design of steel beams strengthened with low-modulus CFRP laminates. *J Compos Constr* 24(1):04019052

34. Tan KH, Kong FK, Teng S, Guan L (1995) High-strength concrete deep beams with effective span and shear span variations. *ACI Struct J* 92(4):395–405
35. Tan KH, Kong FK, Teng S, Weng LW (1997) Effect of web reinforcement on high-strength concrete deep beams. *ACI Struct J* 94(5):572–582
36. Tan KH, Lu HY (1999) Shear behaviour of large reinforced concrete deep beams and code comparisons. *ACI Struct J* 96(5):836–846
37. Yang K-H, Ashour AF (2007) Influence of section depth on the structural behaviour of reinforced concrete continuous deep beams
38. Yuan H, Teng JG, Seracino R, Wu ZS, Yao J (2004) Full range behavior of FRP-to-concrete bonded joints. *Eng Struct* 26(5):553–565
39. Zararis PD (2003) Shear compression failure in reinforced concrete deep beams. *J Struct Eng* 131(6):991–991

Study on Short Steel Circular Hollow Sections Jacketed with Carbon Fiber Reinforced Polymers



A. Punitha Kumar, R. Senthil, and S. Srishath

Abstract Carbon fiber reinforced polymer (CFRP) is becoming popular in construction and retrofitting of hollow steel sections due to its axial strength enhancement properties. This paper focuses on the axial behavior of CFRP-jacketed Circular Hollow Sections (CHS). CHS specimens of slenderness ratios—15 and 20, with varying configurations of CFRP laminates are studied. The specimens are subjected to axial static and axial cyclic loading, and the results are recorded. The CFRP-jacketed specimens exhibit an increase in axial strength up to 33.06% for axial static loading and 37.42% for axial cyclic loading. The stiffness of CFRP-reinforced specimens also shows an increase in value up to 65.55% and 42.74% for axial static and axial cyclic loading, respectively. The deformations and the modes of failure of the specimens under axial static and axial cyclic loading are also similar.

Keywords Carbon fiber reinforced polymer · Circular Hollow Section · Axial static loading · Axial cyclic loading · Axial strength · Stiffness · Failure modes

1 Introduction

In the past decade, Fiber Reinforced Polymer (FRP) laminates have become popular for strengthening and retrofitting of concrete structures [14, 15]. Strengthening of metallic structures using FRP has also become popular [8], but it has been limited to strengthening of metallic beams using Carbon Fiber Reinforcement Polymer (CFRP) jackets. Research works on strengthening of steel Circular Hollow Section (CHS) [5–12], Rectangular Hollow Section (RHS) [17], and Square Hollow Section (SHS)

A. Punitha Kumar (✉)
School of Civil Engineering, VIT Vellore, Vellore, India
e-mail: punithakumar.a@vit.ac.in

R. Senthil · S. Srishath
Department of Civil Engineering, Anna University, Chennai, India
e-mail: senthil@annauniv.edu

[2–4] with external CFRP jackets have exhibited significant advantages in the form of improved strength and stiffness of the steel structures.

Bambach et al. investigated the strength of Square Hollow Sections (SHS), with a slenderness value ranging between 1.1 and 3.2, in combination with two different layouts of CFRP matrix configuration. The use of CFRP caused a delay in local buckling and concomitantly caused a significant increase in strength-to-weight ratio of the tubular structure, axial strength and elastic buckling stress [2, 3]. Haedir and Zhao studied the effects of externally bonded orthogonal CFRP structures under axial compression. The CFRP produced an increase in axial section capacity of the tubular columns, and design curves predicting the section capacity of composite steel-CFRP tubular columns were also formulated [7]. FRP confinement is an effective method of strengthening for improving ductility and in preventing elephant's foot buckling near the base of the steel tubular compression member [16]. Bambach inspected the axial capacity and crushing behavior of SHSs, composed of composite steel-CFRP, stainless steel-CFRP, and aluminum-CFRP. The geometries of SHSs and the bonded matrix layouts of CFRP were varied [1]. The compression buckling and axial capacity of SHSs were predicted by a general theory, and it was validated using the experimental results [1]. Shaat and Fam studied the effects of CFRP sheet orientations on 27 short SHSs and long SHSs each under axial loads. CFRP sheets were oriented in longitudinal and transverse directions for short columns, and the sheets were placed in the longitudinal direction for long columns. Short columns with two transverse CFRP layers had the maximum strength gain of 18%. Long columns with three longitudinal layers of CFRP on all four sides achieved a maximum strength gain of 23%. In long columns with CFRP sheets, lateral deflections were reduced. The number of sheets and strength gain of CFRP-jacketed columns did not exhibit any correlation [13]. Punitha Kumar and Senthil conducted a study on the axial strength behavior of CFRP-jacketed CHS specimens of slenderness ratios 30, 35, and 40. Based on 54 specimens, it was observed that the axial capacities were enhanced by 39% for axial static loading and 41% for axial cyclic loading [11].

In this paper, the experimental results of axial static and axial cyclic loading tests of CHSs jacketed by CFRP, with slenderness ratios of 15 and 20, are presented. Two different types of CFRP matrix layouts are used in the experiments: (1) CHSs with one layer of CFRP in both transverse and longitudinal directions and (2) CHSs with two layers of CFRPs in both transverse and longitudinal directions. The experimental results are also compared with the bare CHS specimens.

2 Experimental Specimens

2.1 Nomenclature of the specimens

Each specimen has a character, denoting the type of loading, as its prefix. In case of axial cyclic loading, the letter 'C' is used, and letter 'S' is used for axial static loading. Then, it is followed up by the slenderness ratio. The configuration of the CFRP layers is added as a suffix after a hyphen, and it is represented by the format L_xH_x —L, H, and x denote the longitudinal layer, transverse layer, and number of layer(s) of each orientation. For instance, L_1H_1 denotes the use of one longitudinal and one transverse CFRP layers in the CHS specimen.

2.2 Properties of Specimens

The outer diameter and the thickness of the CHSs of slenderness ratio 15 are 139 mm and 4.3 mm, respectively. For CHS specimens of slenderness ratio 20, the outer diameter and the thickness are 113.8 mm and 4.2 mm, respectively. According to the Indian Code of Practice IS1608-2005, three coupons are prepared for each slenderness ratio to gauge the mechanical properties of the CHSs. Using tension tests, the yield strength, ultimate tensile strength, and Young's modulus are obtained as follows:

1. Slenderness ratio—15: yield strength—394 MPa, ultimate tensile strength—493 MPa and Young's modulus—209 GPa
2. Slenderness ratio—20: yield strength—392 MPa, ultimate tensile strength—504 MPa and Young's modulus—207 GPa.

The thickness of CFRP used in the experiment is 0.117 mm. The tensile modulus and tensile strength of the CFRP, provided by the manufacturer, are 240 GPa and 3800 MPa, respectively.

2.3 Preparation of Specimens

The CHS specimens are roughened by sandblasting, and acetone is used to clean the surfaces. To fix the CFRP layers on the surface of CHS, M-Brace primer, with a hardener to base ratio of 0.25:1, is used as shown in Fig. 1. Then, the specimens are cured at room temperature for 24 h. After curing, the specimens are coated with M-Brace saturant, with a hardener to base ratio of 0.25:1. In case of L_1H_1 configuration, as shown in Fig. 2, one layer of CFRP in longitudinal direction is fixed on the CHS followed by another layer of CFRP in transverse direction. For L_2H_2 orientation,

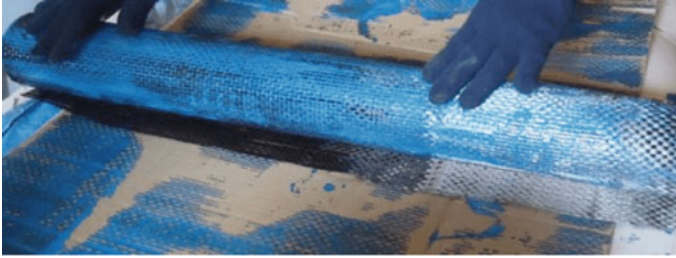


Fig. 1 Longitudinal CFRP laminate

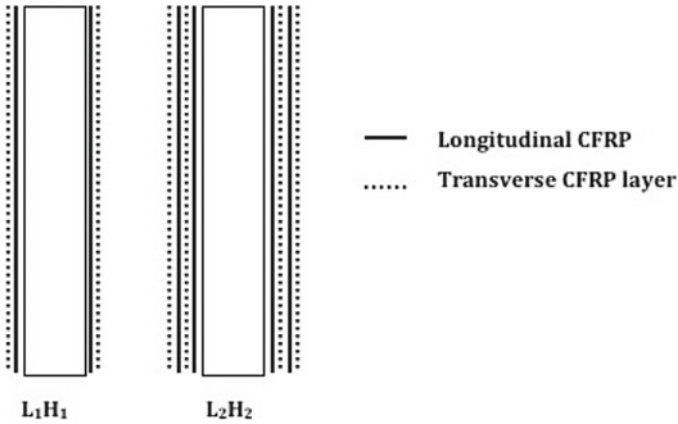


Fig. 2 Longitudinal sectional view of CFRP arrangement for L_1H_1 and L_2H_2 configurations

as shown in Fig. 2, the first layer and third layer are oriented in the longitudinal direction; the second and the fourth layer consist of transverse CFRP layers.

3 Experiment Setup

3.1 Axial Static Loading

1000 kN Universal Testing Machine is used to exert axial static loads on the CHS specimens. Two plates of thickness, 20 mm each, are placed at the ends of the CHS specimen to facilitate uniform distribution of the load. To record the lateral deflection, three dial gauges are attached at the mid-height of the specimen. To obtain the axial displacement, a dial gauge is attached to the bottom of the specimen. At its mid-height, six strain gauges are also fixed, perpendicular and parallel to the direction of loading, to record the circumferential strain and longitudinal strain of the specimen,

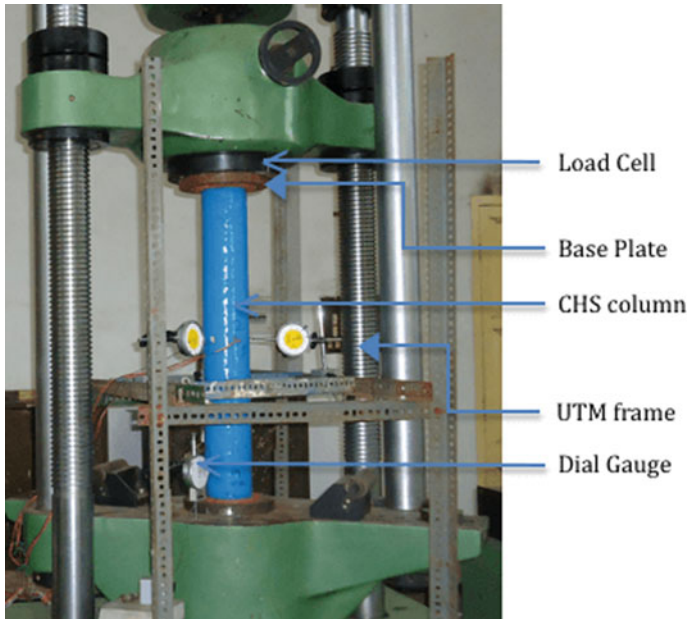


Fig. 3 Experimental setup of CHS specimen for axial static loading

respectively. The load is exerted on the specimen at the rate of 20 kN/min, and the corresponding readings are recorded from the dial gauges and strain gauges. The experimental setup for axial static loading is shown in Fig. 3.

3.2 Axial Cyclic Loading

CHS specimen is placed on the loading frame of 1000 kN capacity for axial cyclic loading. A hydraulic jack is used to exert the load on the CHS specimens. Load cell is placed on the top of the CHS specimen to measure the load values exerted. Dial gauges are attached to record the axial displacements and lateral displacements of the specimen. The load cell and the dial gauge are connected to a data logger to record output. The experimental setup for axial cyclic loading of CHS specimen is shown in Fig. 4.

Figure 5 shows the cyclic loading history of CHS specimens under cyclic loading. Initially, an axial base load equivalent to 10% of axial static ultimate load is exerted. For every cycle that follows, the axial cyclic load is increased by a value equal to 5% of the axial static ultimate load, then it is lowered to the base load. The cycles are carried out till the failure of specimen.

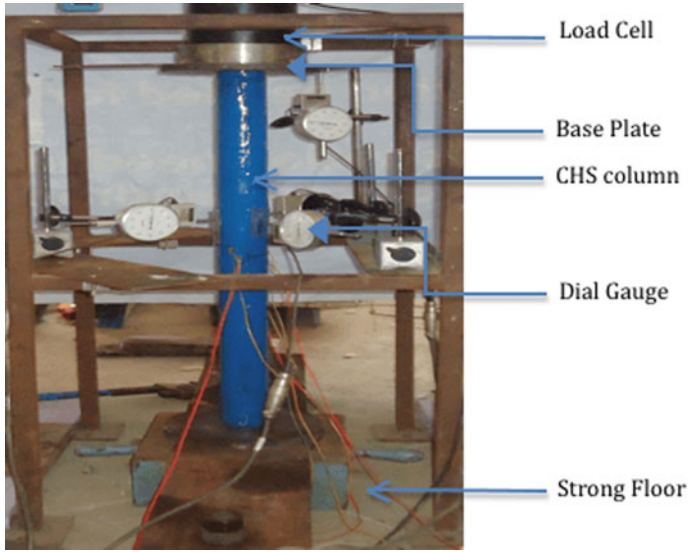


Fig. 4 Experimental setup of CHS specimen for axial cyclic loading

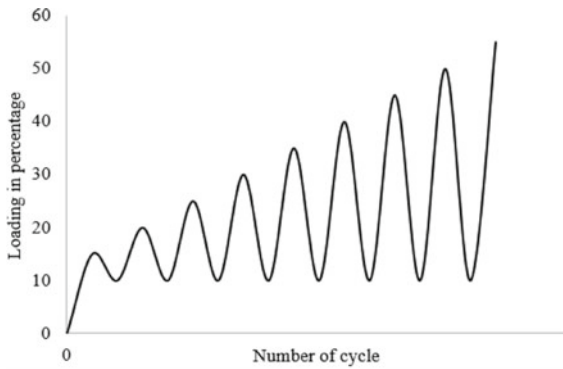


Fig. 5 Cyclic loading history

4 Experimental Results

4.1 Axial Compression Capacity

From Tables 1 and 2, it is evident that the CFRP specimens exhibit significant increase in their axial compressive strength under axial cyclic and axial static loading. On reinforcing the specimens with CFRP, the CHS specimens have shown increments in ultimate load values, in the range of 15.06–33.06%, under axial static loading. A

Table 1 Summary of axial static loading experimental results

Series	Specimen designation	Axial displacement (mm)	Lateral displacement (mm)	Ultimate load (kN)	Increase in ultimate load w.r.t. bare specimen (%)
Series 1	S15-L ₀ H ₀	9.73	2.10	646.27	–
	S15-L ₁ H ₁	8.02	1.50	761.22	17.78
	S15-L ₂ H ₂	7.82	1.40	859.96	33.06
Series 2	S20-L ₀ H ₀	10.22	2.20	566.10	–
	S20-L ₁ H ₁	10.05	2.01	651.40	15.06
	S20-L ₂ H ₂	9.83	1.90	750.30	32.53

Table 2 Summary of axial cyclic loading experimental results

Series	Designation of columns	Axial displacement (mm)	Ultimate load (kN)	Increase in ultimate load w.r.t. bare specimen (%)
Series 3	C15-L ₀ H ₀	8.52	541.84	–
	C15-L ₁ H ₁	8.23	664.48	22.63
	C15-L ₂ H ₂	8.10	733.44	35.28
Series 4	C20-L ₀ H ₀	9.65	485.08	–
	C20-L ₁ H ₁	9.43	566.39	16.76
	C20-L ₂ H ₂	9.28	666.61	37.42

similar observation is noted for CFRP-jacketed CHS specimens under axial cyclic loading, with 16.76–37.42% increase in axial compressive strength values.

4.2 Failure Modes

4.2.1 Axial Static Loading

The failure patterns of CHS specimens of slenderness ratios 15 and 20 are shown in Figs. 6 and 7, respectively. The bare CHS specimens, S15-L₀H₀ and S20-L₀H₀, exhibit failure by elephant's foot buckling at their ends. The specimen S20-L₀H₀ is also characterized by deflection at its mid-height. CFRP-jacketed CHS specimens of slenderness ratios 15 and 20 fail by local buckling. On loading, CFRP layers delaminate at its end, get crushed, rupture, and eventually fail by elephant's foot buckling. Also, there is no significant lateral buckling at the mid-height of the jacketed specimens.

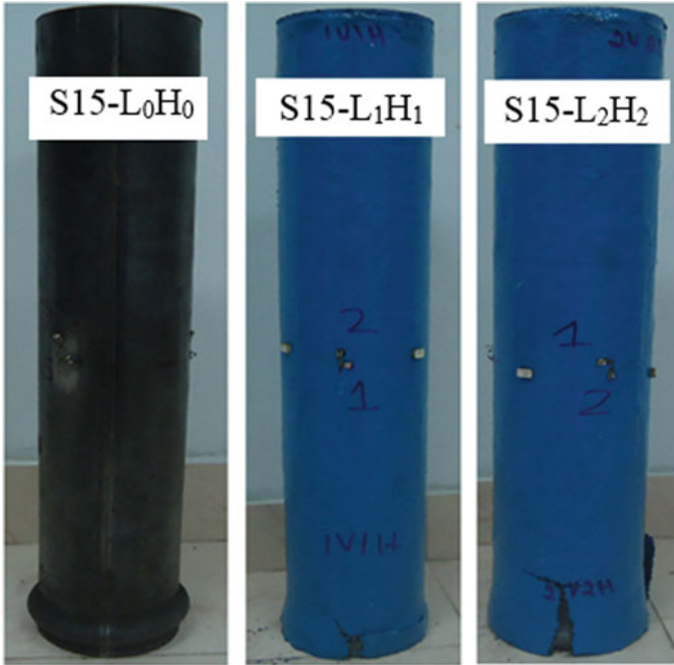


Fig. 6 Failure modes of CHS specimens of slenderness ratio—15 on axial static loading

4.2.2 Axial Cyclic Loading

Failure modes of the specimens under axial cyclic loading, shown in Figs. 8 and 9, are similar to axial static loading. The bare specimens, C15-L₀H₀ and C20-L₀H₀, exhibit elephant's foot buckling at its end. Lateral deflection is also observed at the mid-height of C20-L₀H₀ specimen. On axial cyclic loading, the CFRP-reinforced specimens are characterized by gradual delamination, crushing, rupture of CFRP layers at one end, and eventually fail by elephant's foot buckling. The extents of deformation due to axial cyclic loading for CFRP-jacketed specimens are also similar to that of axial static loading.

4.3 Load–Displacement Behavior

4.3.1 Axial Static Loading

Under axial static loading, the load-lateral displacement curves of the specimens are characterized by steep accession till they reach the ultimate load values. After failure, it is followed by a sharp drop in the load values. In case of load-axial displacement

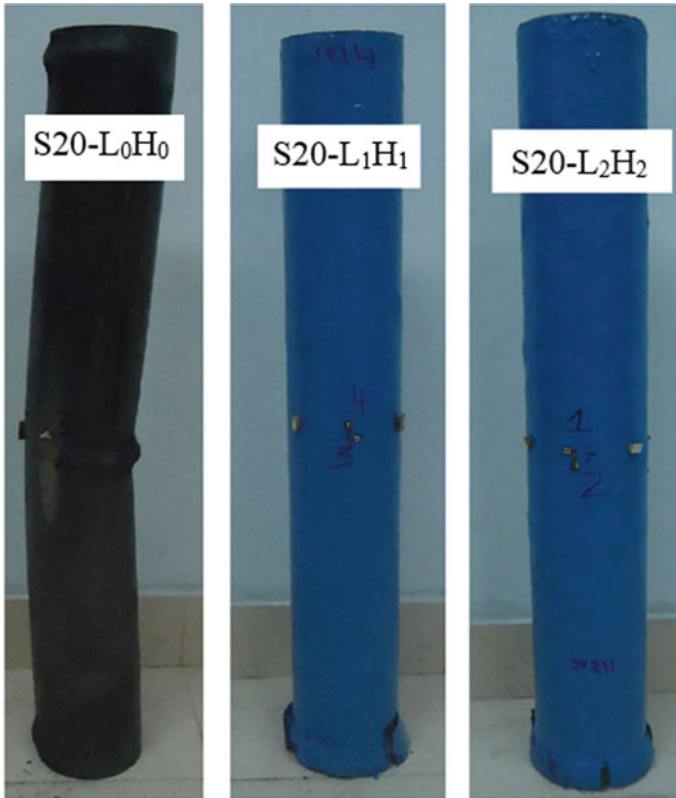


Fig. 7 Failure modes of CHS specimens of slenderness ratio—20 on axial static loading

curves, the rise and fall of the curve are very gradual for the bare specimens, S15-L₀H₀ and S20-L₀H₀. For CFRP-jacketed specimens, the axial displacement curves show a gradual rise, however on CFRP rupture, the fall in the curves is not smooth. From the graphs in Fig. 10, it is evident that the CFRP layers enhance the axial compressive strength of the CHS specimens in axial static loading. In case of L₁H₁ configuration, the ultimate loads for slenderness ratios of 15 and 20 are increased by 17.78% and 15.06%, respectively. The ultimate loads are the highest for S15-L₂H₂ (859.96 kN) and S20-L₂H₂ (750.3 kN) with increments of 33.06% and 32.53%, respectively.

4.3.2 Axial Cyclic Loading

In load-axial displacement graphs as shown in Figs. 11 and 12, initially the curves exhibit a gradual rise with increase in load values. In each cycle, the curve recedes on gradual unloading, and on subsequent loading, the curve rises along different path to the point where it is unloaded. Although the specimens exhibit elasticity in the

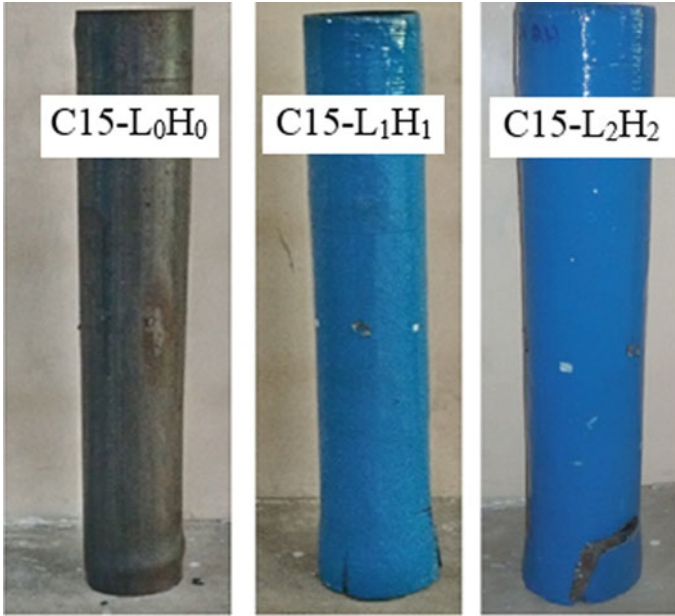


Fig. 8 Failure modes of CHS specimens of slenderness ratio—15 on axial cyclic loading

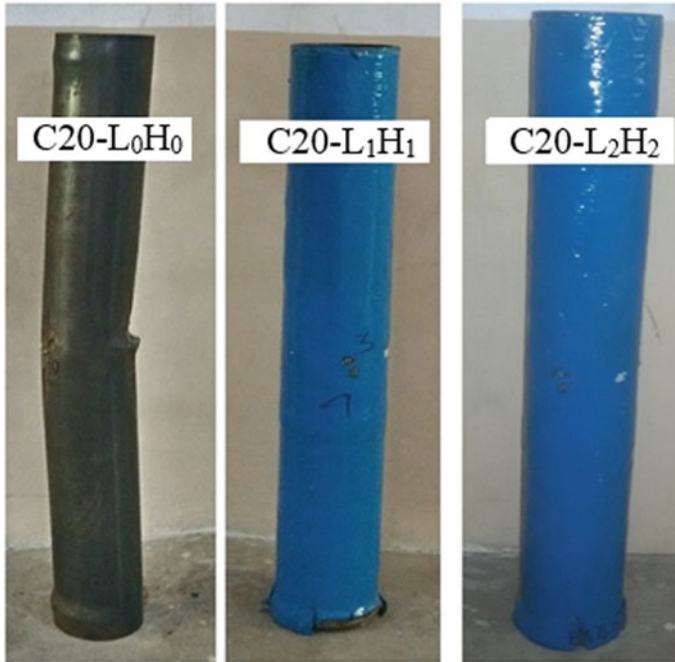


Fig. 9 Failure modes of CHS specimens of slenderness ratio—20 on axial cyclic loading

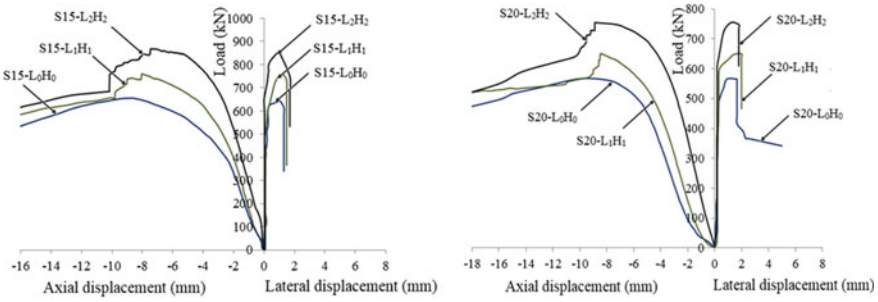


Fig. 10 Load–displacement graphs of CHS specimens of slenderness ratio 15 and 20 under axial static loading

cycles initially, the specimens gradually lose their elasticity with increase in number of loading cycles and become elasto-plastic in nature. This trend is observed till the failure of CHS specimens.

From Figs. 11 and 12, it is evident that with increase in number of CFRP layers, the axial compressive strengths of CHS specimens increase under axial cyclic loading. In case of L_1H_1 configuration, the ultimate loads for slenderness ratios of 15 and 20 are increased by 22.63% and 16.76%, respectively. The ultimate loads are highest for $S15-L_2H_2$ (733.44 kN) and $S20-L_2H_2$ (666.1 kN) with increments of 35.28% and 37.42%, respectively.

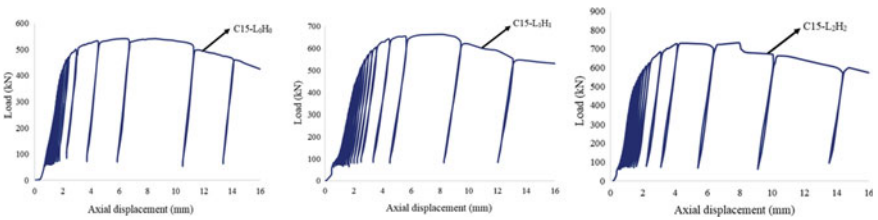


Fig. 11 Load–displacement graphs of CHS specimens of slenderness ratio 15 under axial cyclic loading

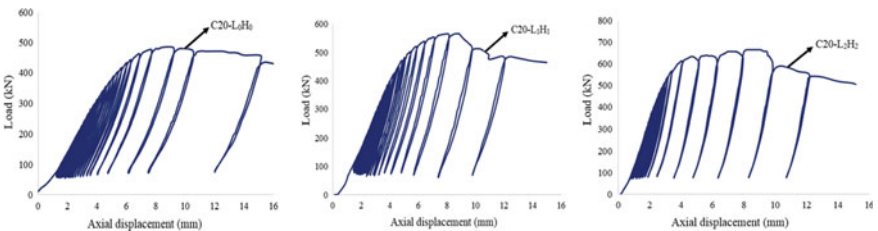


Fig. 12 Load–displacement graphs of CHS specimens of slenderness ratio 20 under axial cyclic loading

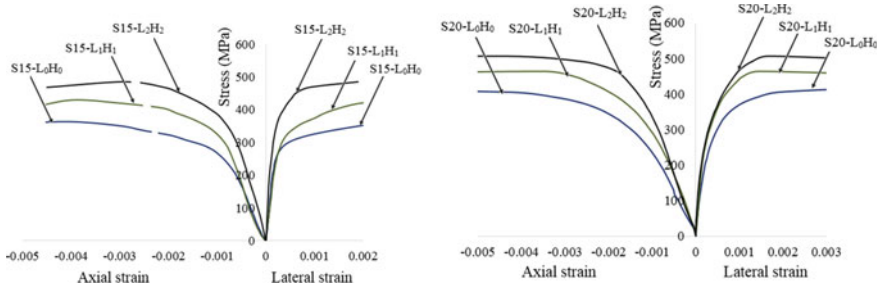


Fig. 13 Stress–strain behavior of CHS specimens of slenderness ratios of 15 and 20 under axial static loading

4.4 Stress–Strain Behavior

The stress–strain graphs of CHS specimens under axial static loading are shown in Fig. 13. On axial static loading, all specimens initially exhibit elastic behavior, characterized by the linear relationship between stress and strain. Beyond elastic limit, the stress and strain cease to exhibit linear relationships. Then, the specimens gradually reach their ultimate stress. From the above shown graphs, the ultimate strength values of the specimens are as follows:

1. Slenderness ratio 15: S15-L₀H₀—355.3 MPa; S15-L₁H₁—418.5 MPa; S15-L₂H₂—472.8 MPa
2. Slenderness ratio 20: S20-L₀H₀—391.7 MPa; S20-L₁H₁—450.7 MPa; S20-L₂H₂—519.1 MPa.

It is evident that, upon addition of new CFRP layers, the ultimate stresses of the specimens are enhanced, when compared with the bare specimens.

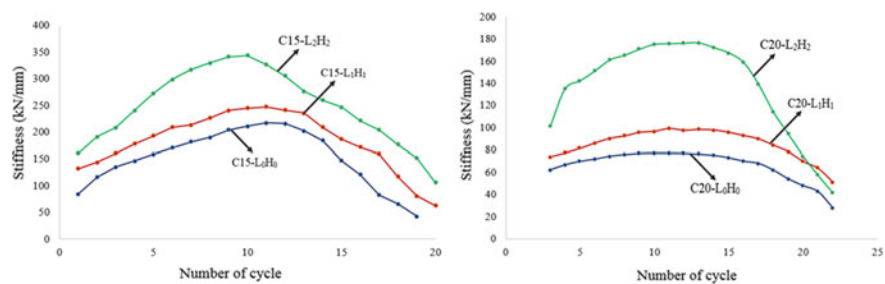
4.5 Influence of CFRP on Stiffness of CHS Specimens

In Table 3, the stiffness of the CFRP specimens is estimated based on calculating the ratio between ultimate load and the corresponding axial displacement. It is evident that there is an increase in stiffness values with increase in the number of CFRP layers for every series. The CFRP specimens on axial static loading show an increase in stiffness value in the range of 16.97–65.55% under axial static loading. For axial cyclic loading, the improvement in stiffness values lies in the range of 19.48–42.74%. The stiffness values of each cycle are shown in Fig. 14, and it is evident that, in general, the stiffness of the specimens is enhanced with increase in number of layers.

From the experimental results, the relationship between ultimate loads and stiffness values is deduced. The presence of high tensile modulus of CFRP plays a significant role in lowering the effect of buckling failure as compared to bare specimens.

Table 3 Stiffness of axial static and cyclic loading specimens

Series	Specimen designation	Stiffness (kN/mm)	Increase in stiffness w.r.t bare specimen (%)
Series 1	S15-L ₀ H ₀	66.42	–
	S15-L ₁ H ₁	94.9	42.87
	S15-L ₂ H ₂	109.96	65.55
Series 2	S20-L ₀ H ₀	55.4	–
	S20-L ₁ H ₁	64.8	16.97
	S20-L ₂ H ₂	76.3	37.72
Series 3	C15-L ₀ H ₀	63.6	–
	C15-L ₁ H ₁	80.7	26.89
	C15-L ₂ H ₂	90.5	42.29
Series 4	C20-L ₀ H ₀	50.3	–
	C20-L ₁ H ₁	60.1	19.48
	C20-L ₂ H ₂	71.8	42.74

**Fig. 14** Stiffness–number of cycles graphs of CHS specimens under cyclic loading

The confining effect of CFRP also delays the occurrence of local or global buckling failure. This delay in failure increases the ultimate load values of CFRP-jacketed specimens.

5 Conclusion

The effects of CFRP reinforcement on CHS specimens with slenderness ratios of 15 and 20 are studied. In total, six specimens of each slenderness ratio are subjected to axial static and axial cyclic loading. Based on the experimental results, conclusions are summarized as follows:

1. As compared to bare CHS columns, the CFRP-jacketed CHS specimens with slenderness ratio of 15 exhibits up to 33.06% increase in axial capacity under axial static loading. Similarly, in case of axial cyclic loading, the increment is even higher with a value of 35.28%.
2. Under axial static loading, the ultimate load value of CFRP-reinforced CHS specimens of slenderness ratio is enhanced by 32.53%, compared to the bare CHS column. Under axial cyclic loading, the presence of CFRP improves its axial strength value by 37.42%.
3. The failure modes of the specimens under cyclic and static loading are similar. In bare specimens, the failure mode is characterized by elephant's foot buckling at its ends, whereas the CFRP-jacketed specimens fail by delamination, crushing and rupture of CFRP layers, followed by elephant's foot buckling at its ends.
4. The CFRP layers significantly improve the stiffness values as compared to the bare specimens, by 16.97–65.55% and 19.48–42.74% under axial static and axial cyclic loading, respectively.

References

1. Bambach MR (2010) Axial capacity and crushing behavior of metal–fiber square tubes–steel, stainless steel and aluminum with CFRP. *Compos Part B: Eng* 41(7):550–559
2. Bambach MR, Elchalakani M, Zhao XL (2009) Composite steel–CFRP SHS tubes under axial impact. *Compos Struct* 87(3):282–292
3. Bambach MR, Jama HH, Elchalakani M (2009) Axial capacity and design of thin-walled steel SHS strengthened with CFRP. *Thin-Walled Struct* 47(10):1112–1121
4. Bambach MR, Elchalakani M (2007) Plastic mechanism analysis of steel SHS strengthened with CFRP under large axial deformation. *Thin-Walled Struct* 45(2):159–170
5. Doi H et al (2003) Deformation capacity of circular tubular beam-columns reinforced with CFRP subjected to monotonic loading. *J Constr Steel* 11:431–438
6. Haedir J, Bambach MR, Zhao XL, Grzebieta R (2009) Strength of circular hollow sections (CHS) tubular beams externally reinforced by carbon FRP sheets in pure bending. *Thin-Walled Struct* 47(10):1136–1147
7. Haedir J, Zhao XL (2011) Design of short CFRP-reinforced steel tubular columns. *J Constr Steel Res* 67(3):497–509
8. Hollaway LC, Cadei J (2002) Progress in the technique of upgrading metallic structures with advanced polymer composites. *Prog Struct Eng Mater* 4:131–148
9. Hong WS, Zhi MW, Zhi MX, Xing WD (2000) Axial impact behaviour and energy absorption efficiency of composite wrapped metal tubes. *Int J Impact Eng* 24:385–401
10. Jiao H, Zhao XL (2004) CFRP strengthened butt-welded very high strength (VHS) circular steel tubes. *Thin-Walled Struct* 42:963–978

11. Punitha Kumar A, Senthil R (2016) Axial behaviour of CFRP-strengthened circular steel hollow sections. *Arab J Sci Eng* 41(10):3841–3850
12. Punitha Kumar A, Senthil R (2015) Behavior of CFRP strengthened CHS under axial static and axial cyclic loading. *KSCE J Civil Eng* 20(4): 1493–1500
13. Shaat A, Fam A (2006) Axial loading tests on short and long hollow structural steel columns retrofitted using carbon fibre reinforced polymers. *Can J Civ Eng* 33(4):458–470
14. Teng JG, Chen JF, Smith ST, Lam L (2001) FRP: strengthened RC structures. Wiley
15. Teng JG, Chen JF, Smith ST, Lam L (2003) Behaviour and strength of FRP-strengthened RC structures: a state-of-the-art review. *Proc Inst Civil Eng–Struct Build* 156:51–62
16. Teng JD, Hu YM (2007) Behaviour of FRP-jacketed circular steel tubes and cylindrical shells under axial compression. *Constr Build Mater* 21(4):827–838
17. Zhao XL, Fernando ND, Al-Mahaidi R (2006) CFRP strengthened RHS subjected to transverse end bearing force. *Eng Struct* 28(11):1555–1565

A Review of Strengthening of RC Beam-Column Junction Using Fiber Reinforced Polymer Composites



Pramod Tiwari and Kranti Jain

Abstract The concrete structure gets deteriorated with time due to its exposure to weather, dynamic loading, fatigue, and creep. So to maintain the strength and serviceability, retrofitting is needed. The steel plates were used previously for strengthening the existing structures, but steel plates tend to corrode with time, so nowadays FRP is the worldwide best solution as a material for strengthening the structure. Different FRP materials, such as a carbon-fiber-reinforced polymer (CFRP), glass fiber reinforced polymer (GFRP), aramid FRP (AFRP), and basalt FRP (BFRP), are available. Carbon FRP (CFRP) and glass FRP (GFRP) are used worldwide due to their lightweight and more tensile strength among all types of fiber. CFRP has more tensile strength as compared to GFRP but is uneconomical. To achieve the approximately same strength as that of CFRP, a multilayer of GFRP glued with epoxy can be used. This paper presents a state-of-the-art review of strengthening the RC beam-column junction under various loading based on experimental as well as computational simulation analysis done by various researchers in recent decades. Strengthening of a beam-column junction in static loading, seismic loading, and weak beam-strong column junction is evaluated experimentally and verified with finite element analysis using Abaqus, Ansys, etc. The ductile behavior of the RC beam-column joint is also reviewed.

Keywords FRP · RC beam-column junction · CFRP · Simulation analysis · Abaqus

P. Tiwari (✉) · K. Jain
Department of Civil Engineering, NIT Uttarakhand, Srinagar, Garhwal, India
e-mail: pramodtiwari.phd19@nituk.ac.in

K. Jain
e-mail: jainkranti8@nituk.ac.in

© The Author(s), under exclusive license to Springer Nature Singapore Pte Ltd. 2023
M. Madhavan et al. (eds.), *Proceedings of the Indian Structural Steel Conference 2020* (Vol. 2), Lecture Notes in Civil Engineering 319,
https://doi.org/10.1007/978-981-19-9394-7_4

1 Introduction

In old structures which are an ordinary moment-resisting frame (OMRF), generally, the principle of a strong column-weak beam is adopted to ensure the plastic hinge formation in the beam rather than at the joint in seismic response as inelastic behavior. There are different types of joints as a monolithic structure described in ACI 352 as shown in Fig. 1. It was also showed that full-scale experimental tests induced lots of expenditure so numerical analysis using FEM is more preferred. In the case of flexure, shear, fatigue, dynamic loading, CFRP is commonly used because of high tensile strength. Reversal loading on the RC beam and slab gives unexpected failures that require further investigation. It has been shown from the previous observation that concrete structure fails at the beam-column joints. So CFRP material used to increase the load-carrying capacity of the beam-column connection. To find the increased capacity in lateral loading, the experimental as well as modeling is done using FEM tools like Abaqus or Ansys [1]. Flexural and shear strengthening of RC beams are tested experimentally and analytically while taking accessibility limitations of all faces wrapped in CFRP into account [2]. In case of strengthening the beam, CFRP sheets are wrapped at the soffit. When tensile force transferred to the bonded sheets, anchorage failure may occur between concrete and sheets. So the U-wrapping of FRP increases the flexural and shear strength, deflection, and stiffness of the RC beam [3]. When the structure is subjected to lateral loads, they required to strengthen the connection of the strong column weak beam with different design philosophies [4]. For ductile behavior of the RC beam-column joint, in special moment-resisting frame (SMRF), extra flexural reinforcement is provided at with 45° bent of top and bottom bar. Because shear reinforcement cannot be provided at the junction so easily then we bent the bar at the joint and extend it to greater length to meet bond length criteria as well as shear strength criteria. According to strong column-weak beam criteria for ductile behavior of joint, plastic hinge formation occurs in the beam with the dissipation of energy absorption, and the column remains unyielded under seismic action [5]. The main design criteria for designing any joints are (1) the ratio of column-beam flexural strength, (2) transverse reinforcement of joint, (3) shear strength, and (4) beam-column anchorage at the joint [6]. If any case there is a weak column strong beam at the joint, it will lead to inelastic action. In such a case of weak columns, there will be flexural yielding of all columns at that level and results in column failure leading to collapse mechanism [7]. So to make a strong joint, confine more reinforcement at the joint as the special moment-resisting frame (SMRF). Based on various test results, different codes recommend the design and detailing procedure of the joint [10,11,NZS3101-2006,EN 1998-1:2003, IS 13920:2016] [8].

In recent trends, FEM nonlinear analysis has made the cyclic behavior very easy and wrapping of FRP sheets, and its composite analysis has also become easier. The joint shear study with FEM tools becomes easy to compute and to know the behavior under different loading conditions [10]. In recent years, various experimental and FEM studies are carried out on beam-column joint strengthening using FRP [5, 10, 11].

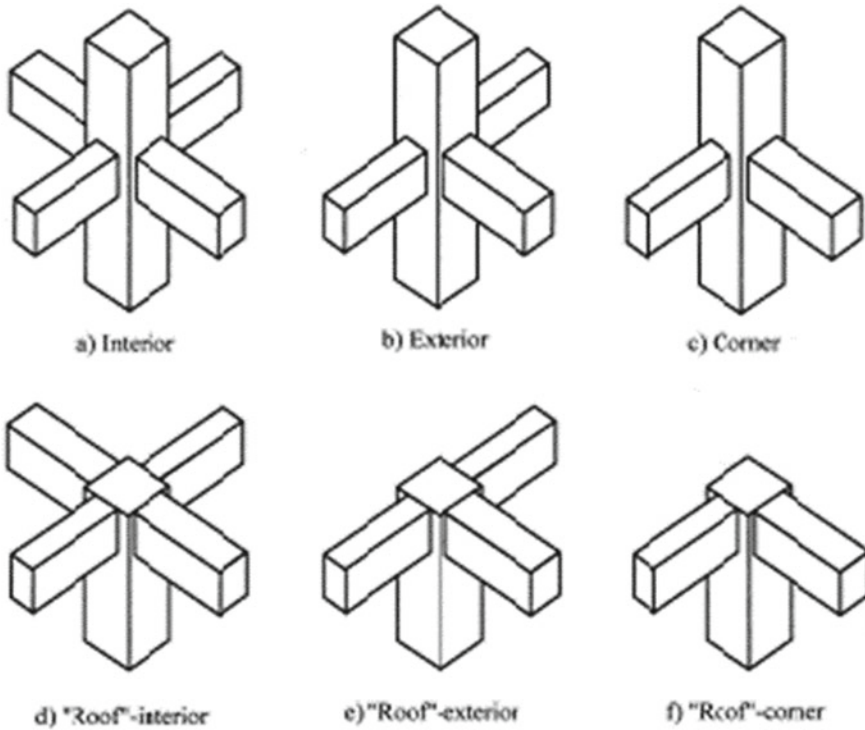


Fig. 1 Different types of beam-column joint as per ACI 352 [9]

2 Literature Review of Design of Beam-Column Junction with FRP

2.1 Background

The various experiments are carried out to strengthen the structure using composite material by taking advantage of FRP as a lightweight material to increase the ductility and strength of joint [12]. Due to insufficient reinforcement at the beam-column joint, the most probable failure may occur at the junction in seismic forces [13]. But in strong ground motion, the junction may fail even in ductile detailing according to codal provision. So extra strengthening is required at beam-column junction to reduce sudden failure. FRP plays a significant role in strengthening the structure at the junction and helps in relocating the plastic hinge point to the desired place.

The data represented in Table 1 shows that all test has been done on a standard dimension of beam and column. The grade of concrete in experiments varies from M15 to M40, and the grade of steel is Fe500 with standard diameter of bar. The

detailing of beam-column junction shows that all detailing has done with seismic codal provisions as extra and shear reinforcement.

Unidirectional and bidirectional CFRP and GFRP fiber are used for strengthening the beam-column joint under static, dynamic, and cyclic loading. The beam and junction wrapped with FRP up to a length of 350 mm from joint and tensile strength of FRP varies from 250 to 3900 MPa as unidirectional and bidirectional with thickness of 0.05 mm as a single layer to 0.5 mm as multilayer FRP. The drift ranges in the experiments from 0.1 to 4% and failure mode were checked accordingly [5, 12–14].

The purpose of doing variety of experiments was to determine the strengthening pattern with FRP even after ductile detailing in strong ground motion. All the experiments were done with a 3D model and prototype to simulate the real field problems. In first stage RC structures tested with ductile detailing and plastic hinge zone were determined, and then FRP was used to relocate the hinge and strengthen the structure with maximum load-carrying capacity.

2.2 Plastic Hinge Formation at the Joint

To find the joint behavior under shear stress, the interior and exterior joint was taken into account and check under three criteria that are flexural strength of beam and column, under reinforced section and the transverse reinforcement provided at the joint. The joint shear failure is due to the inelastic behavior of high shear deformation during the earthquake and leads to a reduction in the axial capacity of the joint. There is beam yielding at the face of the column under cyclic loading [6]. The various new revision of design codes standard gives the design check for the plastic hinge in the column, and the moment of resistant of a column is more than beam including a factor for over strength [15].

2.3 FRP Wrapping to Relocate the Plastic Hinge

The length of the beam and column were designed such that to allow for typical story height and beam up to bending moment diagram. To increase the capacity of a joint in seismic activity, CFRP is used at potential plastic hinge at the end (T_FS1 and T_FS2) of the column. So strengthening of a joint panel can be done by quadriaxial sheet to sustain shear demand and uniaxial sheet can be used in the column to increase the binding capacity of longitudinal bars and in case of the beam to increase the shear capacity in the area of the maximum shear zone [12]. The maximum joint shear stress to the compressive strength of concrete for unreinforced joint without transverse beam, according to ASCE-SEI/41, is given by [11, 16]

$$\tau_{j \max} / \sqrt{f_c} = 0.5.$$

Table 1 Material properties used in literature in experimental setup

References	Specimen	Concrete strength (fc) (N/mm ²)	Beam section (mm)	Column section (mm)	Steel Grade	Top and bottom main reinforcement of beam	Main reinforcement of column	Shear reinforcement (mm)
[5]	CSM0	40	180 × 230	180 × 220	Fe500	2#12mm-Top2#12mm-Bottom	4#12mm	6.5@30 and 6.5@150
	RSM1	45	180 × 230	180 × 220	Fe500	2#12mm-Top2#12mm-Bottom	4#12mm	6.5@30 and 6.5@150
	RSM2	41	180 × 230	180 × 220	Fe500	2#12mm-Top2#12mm-Bottom	4#12mm	6.5@30 and 6.5@150
	CSC1	41	180 × 230	180 × 220	Fe500	2#12mm-Top2#12mm-Bottom	4#12mm	6.5@30 and 6.5@150
	RSC1	37	180 × 230	180 × 220	Fe500	2#12mm-Top2#12mm-Bottom	4#12mm	6.5@30 and 6.5@150
	T_C1	12.6	300 × 500	300 × 300	Fe500	5#16mm-Top3#16mm-Bottom	4#16mm	8@50 and 8@200
	T_C2	16.4	300 × 500	300 × 300	Fe500	5#16mm-Top3#16mm-Bottom	4#16mm	8@50 and 8@200
	T_C3	16.3	300 × 500	300 × 300	Fe500	5#16mm-Top3#16mm-Bottom	4#16mm	8@50 and 8@200
[12]	T_FL1	13.5	300 × 500	300 × 300	Fe500	5#16mm-Top3#16mm-Bottom	4#16mm	8@50 and 8@200
	T_FS1	17.7	300 × 500	300 × 300	Fe500	5#16mm-Top3#16mm-Bottom	4#16mm	8@50 and 8@200
	T_FS2	16.4	300 × 500	300 × 300	Fe500	5#16mm-Top3#16mm-Bottom	4#16mm	8@50 and 8@200

(continued)

Table 1 (continued)

References	Specimen	Concrete strength (fc) (N/mm ²)	Beam section (mm)	Column section (mm)	Steel Grade	Top and bottom main reinforcement of beam	Main reinforcement of column	Shear reinforcement (mm)	
[13]	2DB1	25	200 × 330	230 × 230	Fe500	4#10mm-Top4#10mm-Bottom	6#10mm	6@52.5 and 6@100	
	3DB1	24.2	200 × 330	230 × 230	Fe500	4#10mm-Top4#10mm-Bottom	6#10mm	6mm@52.5 and 6@100	
	2DR1	24.8	200 × 330	230 × 230	Fe500	4#10mm-Top4#10mm-Bottom	6#10mm	6@52.5 and 6@101	
	3DR1	31.2	200 × 330	230 × 230	Fe500	4#10mm-Top4#10mm-Bottom	6#10mm	6mm@52.5 and 6@101	
	2DB2	17.9	200 × 330	230 × 230	Fe500	4#10mm-Top4#10mm-Bottom	6#10mm	6@52.5 and 6@102	
	2DR2	18.9	200 × 330	230 × 230	Fe500	4#10mm-Top4#10mm-Bottom	6#10mm	6mm@52.5 and 6@102	
	2DR3	18	200 × 330	230 × 230	Fe500	4#10mm-Top4#10mm-Bottom	6#10mm	6@52.5 and 6@103	
	2DR4	18.7	200 × 330	230 × 230	Fe500	4#10mm-Top4#10mm-Bottom	6#10mm	6mm@52.5 and 6@103	
	3DB2	17.4	200 × 330	230 × 230	Fe500	4#10mm-Top4#10mm-Bottom	6#10mm	6@52.5 and 6@104	
	3DR2	16.9	200 × 330	230 × 230	Fe500	4#10mm-Top4#10mm-Bottom	6#10mm	6mm@52.5 and 6@104	
	[14]	S33	26	200 × 300	200 × 200	Fe500	3#14mm-Top3#14mm-Bottom	4#14mm	8@45 and 8@150

(continued)

Table 1 (continued)

References	Specimen	Concrete strength (f_c) (N/mm^2)	Beam section (mm)	Column section (mm)	Steel Grade	Top and bottom main reinforcement of beam	Main reinforcement of column	Shear reinforcement (mm)
	S63	24.2	200 × 300	200 × 200	Fe500	3#14mm-Top3#14mm-Bottom	4#14mm	8@45 and 8@150
	S33L	26.3	200 × 300	200 × 200	Fe500	3#14mm-Top3#14mm-Bottom	4#14mm	8@45 and 8@150
	F11	22.8	200 × 300	200 × 200	Fe500	3#14mm-Top3#14mm-Bottom	4#14mm	8@45 and 8@150
	F22	27.2	200 × 300	200 × 200	Fe500	3#14mm-Top3#14mm-Bottom	4#14mm	8@45 and 8@150

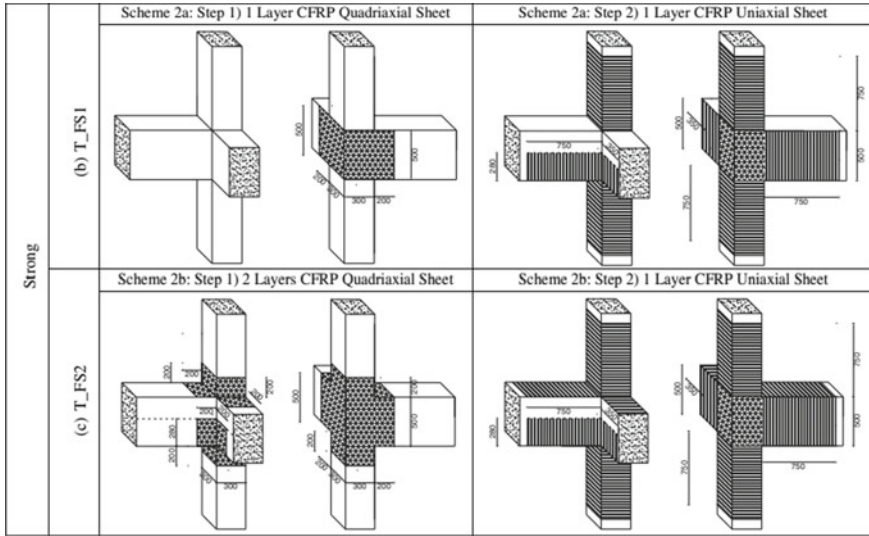


Fig. 2 Various types of FRP strengthening method (units in millimeter) [12]

Some other modified formulae were suggested by Priestley, Park, and Mosalam for joint shear strength. The experiment results compared with formula’s derived from previous experimental results and a guideline may set for further design to the designer.

In Fig. 2, T_FS1 and T_FS2 joint panels are wrapped with quadriaxial FRP sheets and extended up to 200 mm length for proper anchorage. Beam-column junctions wrapped in FRP quadriaxial sheets and having anchorage of 500mm uniaxial sheet as shear confinement in both beam and column are more effective for strengthening than complete quadriaxial sheets. The main debonding failure occurs due to shear failure of concrete so debonding depends majorly on concrete strength. The debonding failure may also occur if FRP length is very small with the member as in Fig. 2 (step 1). Debonding of FRP sheet in case of epoxy becomes a point of concern so the external bond of FRP is becoming popular in recent years [17]. U-wrapping of uniaxial CFRP in the beam would be the one solution to debonding failure [12].

3 Conclusion

As the flexure failure of the FRP wrapped beam generally cannot be governed directly by a simple stress block of concrete given in design codes. Debonding failure is also an important failure, and the most concrete cover comes out with the FRP sheets. Strengthening the column especially circular column with FRP sheets wrapped and fibers are oriented in hoop direction is an ultimate solution [18]. The experimental

result and proposed model are validating and giving the same result for strengthening the beam-column joint with different amount of FRP and its orientation [4]. There is limited research associated with the torsional behavior of the RC beam and the axial application in RC walls [2].

Following conclusions are made with numerous researches carried out for beam-column strengthening:

1. The beam-column joint must be ductile by providing extra steel at joint region to counteract the lateral forces act at the joint and the strength of column should be more than that of connecting beam as strong column and weak beam.
2. FEM model gives an accurate result and simulates actual real field problems. The results are compared such as beam flexural strength, shear strength of joint, bond-slip failure of CFRP-concrete, and longitudinal bar at the joints.
3. New techniques like sensing devices to check the condition of the structural member inside the concrete and simultaneously life of concrete FRP system.
4. FRP possesses high ductility and stiffness so most effective in strengthening the concrete structure under blast load, impact load, and seismic loads.
5. The CFRP sheet helps in relocating plastic hinge from column face to the beam in ordinary moment-resisting frames.
6. The joint shear failure occurs due to the inelastic deformation of joint shear so designed accordingly.
7. In the case of unreinforced joint with plain bar, the deformation of the local failure of the model is majorly due to joint shear strain and rotation of joint.
8. It was noticed by the experiment that for reducing joint deformation the limiting value of strain in FRP should be 1% in design and further investigation needed to set the upper limit.
9. The hairline cracks starts at 0.1–2% drift level and some major cracks about 4–5 mm starts after 2.5–3% drift.
10. The general failure pattern is joint shear failure and beam yielding at the end of FRP layer in the beam. So FRP length may adjusted according to failure point of beam.

References

1. Le-Trung K, Lee K, Shin M, Lee J (2011) Analytical assessment and modeling of RC beam-column connections strengthened with CFRP composites. *Compos Part B: Eng* 42(7):1786–1798
2. Naser M, Hawileh R, Abdalla J (2019) Fiber-reinforced polymer composites in strengthening reinforced concrete structures: a critical review. *Eng Struct* 198:109542. <https://doi.org/10.1016/j.engstruct.2019.109542>
3. Siddika A, Al Mamun MA, Alyousef R, Amran YM (2019) Strengthening of reinforced concrete beams by using fiber-reinforced polymer composites: a review. *J Build Eng* 25:100798
4. Mahini SS, Ronagh HR (2010) Strength and ductility of FRP web-bonded RC beams for the assessment of retrofitted beam-column joints. *Compos Struct* 92(6):1325–1332. <https://doi.org/10.1016/j.compstruct.2009.09.006>

5. Mahini SS, Ronagh HR (2007) A new method for improving ductility in existing RC ordinary moment resisting frames using FRPs. *Asian J Civ Eng (Build Hous)* 8(6):581–595
6. Zhou H (2009) Reconsideration of seismic performance and design of beam-column joints of earthquake resistant reinforced concrete frames. *J Struct Eng ASCE* 135(7):762–773. [https://doi.org/10.1061/\(ASCE\)0733-9445\(2009\)135:7\(762\)](https://doi.org/10.1061/(ASCE)0733-9445(2009)135:7(762))
7. ACI 318-08, Building code requirement for structural concrete and commentary. American Concrete institute
8. Subramanian N (2015) Design of RC beam column joints. *The Master builder* | Oct 2015 | www.masterbuilder.co.in
9. ACI 352-02, Recommendations for design of beam-column connections in monolithic reinforced concrete structures. American Concrete institute
10. Vecchio CD, Ludovico MD, Prota A, Manfredi G (2016) Modelling beam-column joints and FRP strengthening in the seismic performance assessment of RC existing frames. *Compos Struct* 142:107–116. <https://doi.org/10.1016/j.compstruct.2016.01.077>
11. De Risi MT, Ricci P, Verderame GM, Manfredi G (2016) Experimental assessment of unreinforced exterior beam-column joints with deformed bars. *Eng Struct* 112:215–232. <https://doi.org/10.1016/j.engstruct.2016.01.016>
12. Del Vecchio C, Di Ludovico M, Balsamo A, Prota A, Manfredi G, Dolce M (2014) Experimental investigation on exterior RC beam-column joints retrofitted with FRP systems. *ASCE J Compos Constr* 18(4):04014002-1–04014002-13
13. Akguzel U, Pampanin S (2010) Effects of variation of axial load and bidirectional loading on seismic performance of GFRP retrofitted reinforced concrete exterior beam-column joints. *J Compos Constr* 94–104. [https://doi.org/10.1061/\(ASCE\)1090-0268\(2010\)14:1\(94\)](https://doi.org/10.1061/(ASCE)1090-0268(2010)14:1(94))
14. Antonopoulos CP, Triantafyllou TC (2003) Experimental investigation of FRP-strengthened RC beam-column joints. *J Compos Constr* 39–50. [https://doi.org/10.1061/\(ASCE\)1090-0268\(2003\)7:1\(39\)](https://doi.org/10.1061/(ASCE)1090-0268(2003)7:1(39))
15. Uma S, Jain SK (2006) Seismic design of beam-column joints in RC moment resisting frames—review of codes. *Struct Eng Mech* 23(5):579–597. <https://doi.org/10.12989/sem.2006.23.5.579>
16. Ricci P, De Risi MT, Verderame GM, Manfredi G (2016) Experimental tests of unreinforced exterior beam-column joints with plain bars. *Eng Struct* 118:178–194
17. Yuan H, Teng JG, Seracino R, Wu ZS, Yao J (2004) Full-range behavior of FRP-to-concrete bonded joints. *Eng Struct* 26(5):553–565
18. Teng JG, Chen JF, Smith ST, Lam L (2003) Behaviour and strength of FRP-strengthened RC structures: a state-of-the-art review. *Struct Build* 156(1):51–62. <https://doi.org/10.1680/stbu.156.1.51.37880>

Effect of In-plane Concentrated Load on Buckling Behavior of FRP Composite Panels with Cutout



K. S. Subash Chandra, K. Venkata Rao, and T. Rajanna

Abstract Advancement in the material has led to a remarkable upsurge in the permissible stress level of materials. It is more so in the case of recently developed fiber-reinforced laminated composite materials. These panels are highly susceptible to buckle when they are exposed to in-plane loads, especially non-uniform loads. In most of the practical examples, FRP composite panels are provided with cutouts or openings to meet specific functional requirements, such as openings for entry, fuse-lage and some pipeline connections. These panels lead to premature failure depending on size of opening and loading conditions. Hence, it is essential to analyze the effect of in-plane edge load with cutouts. In this article, the effect of concentrated edge loads on buckling behavior of laminated panels with centrally placed circular cutouts has been considered. The plate is modeled by means of a 9-noded heterosis element by including the effect of shear deformation and rotary inertia. The effect of several parameters such as cutout size, the position of concentrated load, orientation of ply and panel thickness is included in this work to examine the buckling behavior of each parameter in detail.

Keywords FRP composite panels · Buckling behavior · Cutouts · In-plane concentrated load · 9-nodded heterosis

1 Introduction

Structural elements made of steel have been in use for more than an epoch ago in the field of civil, mechanical and other engineering fields. These engineering structures are exposed to in-plane edge loads and tend to buckle. Studying the buckling behavior has always been a field of study for slender structures. Development of

K. S. Subash Chandra (✉) · K. Venkata Rao
Department of Mechanical Engineering, GPT Bagepalli, DTE and BMSCE, Bangalore, India
e-mail: siddachandra@gmail.com

T. Rajanna
Department of Civil Engineering, BMSCE, Bangalore, India

© The Author(s), under exclusive license to Springer Nature Singapore Pte Ltd. 2023
M. Madhavan et al. (eds.), *Proceedings of the Indian Structural Steel Conference 2020* (Vol. 2), Lecture Notes in Civil Engineering 319,
https://doi.org/10.1007/978-981-19-9394-7_5

fiber-reinforced composites has motivated much more intensifying survey due to their excellent tailoring material properties and enormous use in the area of other industries such as aviation and space. To have an efficient and reliable design of structures one needs to consider the effect of in-plane loads on buckling on such panels.

The stability of the plate under compression loading has been analyzed by Timoshenko and Gere [15]. Reddy and Phan [11] have analyzed the static stability of laminated plates using shear deformation theory. Deolasi et al. [2] examined the panels buckling characteristics on partial edge loading. Buckling parameters by using woven glass polyester laminate was studied by Komur et al. [6]. Ghannadpour et al. [3] analyzed buckling behavior made up of polymer matrix composites with rectangular perforated cross-ply laminates, which are symmetrically oriented. Singh and Kumar [13] had used quasi-isotropic material subjected to uniaxial compression with different shape of cutouts. Various sized circular cutouts are used with non-uniform edge loads of cross-oriented and quasi-isotropic ply laminates by Soni et al. [14] to study buckling behavior using ABAQUS. Rajanna et al. [8–10] has performed analysis for different loads such as uniaxial and biaxial in-plane loads with circular cutouts of varying orientations of ply. Baba and Baltaci [1] performed analysis using material called E/glass–epoxy composite plates subjected to uniaxial loads, both symmetric and antisymmetric laminated composites are analyzed. Jayashankarbabu and Karisiddappa [4] has done work on buckling behavior of laminated panel by considering the effect of boundary condition by varying panel thickness.

From outline of the previous studies, the laminates buckling behavior has been done on considering the uniform in-plane edge loads. On the contrary, the concentrated loads on the panel edge are not much dealt with. No much comprehensive work has been come across regarding in-plane concentrated edge loads acting on laminated plates with cutouts. The current article gives a brief about the effect of concentrated edge load on laminates with different ply orientations having various sized circular cutouts.

2 Theory and Formulation of Equation

The square laminated panel considered for the study has dimension ' a ' and ' b ' in direction of x and y axes correspondingly, with constant thickness ' t ' and has a central circular cutout of diameter ' d ' as in Fig. 1. It has four lamina; each lamina has a different ply orientation ' θ '. Figure 2 shows the mesh adopted for the present analysis.

Fig. 1 Laminate geometry showing dimensions with a circular cutout

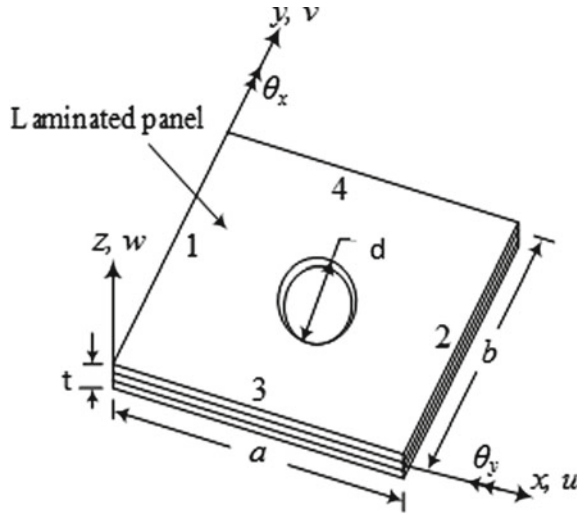
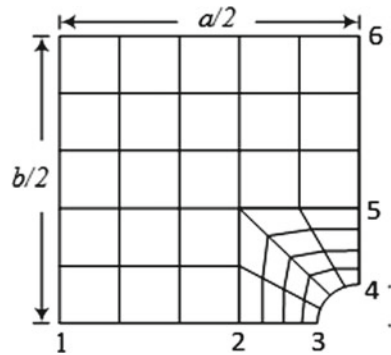


Fig. 2 Mesh pattern adopted for analysis over a quarter plate



2.1 Strain Displacement Relations

Based on the postulates of the hypothesis done by Reissner–Mindlin, the present model is used for the investigation by incorporating the shear deformation effect. The displacement field is taken according to plate theory of first-order shear deformation

$$\{\bar{u}, \bar{v}, \bar{w}\}^T = \{u(x, y), v(x, y), w(x, y)\}s^T + \{z\theta_x, z\theta_y, 0\}^T \quad (1)$$

where \bar{u} , \bar{v} and \bar{w} are displacement components along x , y and z directions, respectively; u , v and w are related mid-plane displacement components along x , y and z axes, respectively; θ_x and θ_y are rotations of normal about y and x -axes, respectively. The equation gives the corresponding strain as,

$$\{\varepsilon\} = \{\varepsilon_l\} + \{\varepsilon_{nl}\} \quad (2)$$

where $\{\varepsilon_l\}$ is the linear strain for deriving the elastic stiffness matrix and $\{\varepsilon_{nl}\}$ is the non-linear strain used to derive geometrical stiffness matrix.

The stress-strain relation for laminates given by equation

$$\{N\} = [C]\{\varepsilon\} \quad (3)$$

where $\{N\} = [\{N_i\}, \{M_i\}, \{Q_i\}]^T$ and $\{\varepsilon\} = [\varepsilon_j \chi_j \gamma_j]^T$ are corresponding stresses and strains respectively and $[C]$ is the constitutive matrix of the laminate and is given by,

$$[C] = \begin{bmatrix} \begin{bmatrix} A_{ij} \\ B_{ij} \\ 0 \end{bmatrix} & \begin{bmatrix} B_{ij} \\ D_{ij} \\ 0 \end{bmatrix} & \begin{bmatrix} 0 \\ 0 \\ S_{ij} \end{bmatrix} \end{bmatrix} \quad (4)$$

where

$$\left(A_{ij}, B_{ij}, D_{ij} \right) = \sum_{k=1}^n \int_{z_{k-1}}^{z_k} (\overline{Q_{ij}})_k (1, z, z^2) dz, \quad i, j = 1, 2, 6 \quad (5)$$

and

$$S_{ij} = \sum_{K=1}^n \int_{z_{k-1}}^{z_k} \alpha (\overline{Q_{ij}})_K dz, \quad i, j = 4, 5 \quad (6)$$

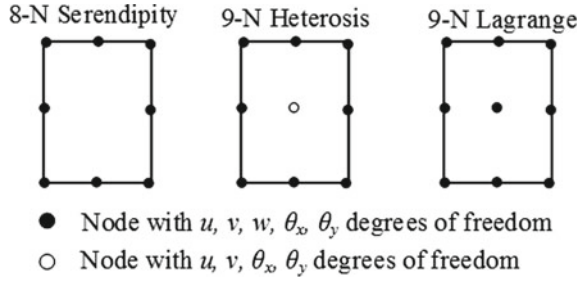
' n ' is the number of ply-layers, $\alpha = 5/6$ is a shear-correction factor [11]. $(\overline{Q_{ij}})_k$ is the stiffness matrix of the k th lamina regarding the plate axes.

2.2 Finite Element Formulation

Finite element formulation is done by employing a 9-noded heterosis element which is a combination of 8-noded serendipity and 9-noded Lagrange element. This element under the present study has 5 degrees of freedom at all edge nodes of an element (u , v , w , θ_x and θ_y) and 4 degrees of freedom at the inner node as shown in Fig. 3.

The different participating matrices of the plate element that are required to perform analysis are as follows:

Fig. 3 Plate elements of different kinds



$$[K_e] = \int_{-1}^1 \int_{-1}^1 [B]^T [C] [B] |J| dr ds \tag{7}$$

$$[K_g] = \int_A [B_g]_j^T [S]_j [B_g]_j dA \tag{8}$$

wherein $[K_e]$, $[K_g]$ are corresponding elastic stiffness, and geometric stiffness matrices, respectively.

2.3 Governing Equations

The structural component under the influence of in-plane load has the governing differential equation of equilibrium as inscribed below:

$$[M]\{\ddot{q}\} + [[K] - P_{cr}[K_G]]\{q\} = \{0\} \tag{9}$$

In case of a problem with only bucking is considered the above equation reduces to a static problem, when $\{\ddot{q}\} = \{0\}$.

$$[K]\{q\} - P_{cr}[K_g]\{q\} = \{0\} \tag{10}$$

By solving the above equation, the Eigenvalues are obtained. These Eigenvalues provide different modes for the buckling loads. The least load is called the fundamental or critical buckling load for that structure.

3 Convergence and Comparative Study

3.1 Evaluation of the Problem

The solution to the issues of stability is obtained by the static approach where there is the extraction of Eigenvalues and vectors from Eq. (10). The global matrix is obtained by assembling various element-level arrays. In this MATLAB code, selective integration is employed to generate an elastic stiffness matrix for an element. In the case of capturing the bending effects 3×3 Gauss rule and 2×2 Gauss rule for shearing effect in order to avoid shear locking within the elements resulting in an error of the problem. The geometric stiffness matrix is generated by performing the plane stress analysis, which is developed due to the application of an in-plane edge load. The full integration of the 3×3 Gauss rule is used to create a geometric stiffness matrix for an element.

In the present work, a simply supported square thin plate ($b/h = 100$) has been considered, whose material property $E_{11} = 25$, $E_{22} = 1.0$, $G_{12} = G_{13} = 0.5$, $G_{23} = 0.2$ and $\nu_{12} = 0.25$ unless otherwise specified. In this study, three different layup schemes are considered which are termed as ‘Angle-Ply’ whose fibers are oriented in $45/-45/45/-45$, ‘Cross-Ply’ whose ply orientations are $0/90/90/0$ and ‘Quasi-Ply’ in $0/45/-45/90$. In the analysis, the buckling loads are calculated by using two sets of boundary conditions as follows:

Simply Supported Boundary Conditions (SSSS)

- For pre-buckling stress analysis: $w = \theta y = 0$ at $x = 0, a$; $w = \theta x = 0$ at $y = 0, b$ and $u = 0, v = 0$ at two nodes along the edges $x = a/2$ and $y = b/2$, respectively.
- For buckling analysis: $u = w = \theta y = 0$ along $x = 0, a$; $v = w = \theta x = 0$ along $y = 0, b$.

Clamped Boundary Condition (CCCC)

- For pre-buckling stress analysis: $w = \theta y = \theta x = 0$ along $x = 0, a$ and $y = 0, b$ and $u = 0, v = 0$ at two nodes along the edges $x = a/2$ and $y = b/2$, respectively.
- For buckling analysis: $u = v = w = \theta x = \theta y = 0$ along $x = 0, a$ and $y = 0, b$.

The critical load in non-dimensional form is presented as follows [11]

$$\gamma_{cr} = \frac{P_{cr} b^2}{E_{22} h^3} \quad (11)$$

where P_{cr} is the absolute critical load.

Table 1 A square laminate with a circular cutout ratio of 0.3 and 0.5 studied for convergence showing the number of elements and its buckling load parameter (γ_{cr}) for a concentrated edge load acting at mid position for simply supported boundary condition

Cutout ratio (d/b)	No. of elements	Compressive buckling loads (γ_{cr}) acting at mid position
0.3 Ply (0/90/90/0)	88	8.001
	112	9.939
	136	7.911
	160	7.891
	184	7.879
	208	7.869
0.5 Ply (45/- 45/45/- 45)	68	18.172
	100	18.789
	132	19.032
	164	19.028
	196	19.091
	228	19.067

3.2 Convergence Studies

In FE analysis, it is necessary to discretize the structure for the proper convergence to obtain the appropriate results. In this regard, convergence studies encourage in achieving the minimum possible number of elements with a particular plate with cutout. Table 1 gives the results of the buckling load parameter (γ_{cr}) for the different number of elements employed in the process of discretization for the cutout ratio of 0.3 and 0.5 for cross-ply and angle-ply, respectively. It is acquired from the results that nearly 160 elements would be sufficient in the case of $d/b = 0.3$ and 164 elements for $d/b = 0.5$ to obtain a reasonably good result.

3.3 Comparative Studies

The precision of the meshed panel is found out by equating the results of previous literature. Table 2 shows the buckling behavior of SSSS edged isotropic panel without cutout under concentrated edge load over different edge positions is related to the ideal solution of Deolasi et al. and that of Rajanna et al. [8, 9]. The comparison of critical buckling loads of uniaxial uniformly distributed load for different cutout ratio (d/b) is made with [3] and Rajanna et al. [8, 9] shown in Table 3. This geometric stiffness matrix of the laminated panel with the cutout is validated for its rightness by agreeing on the present results with the previous studies.

Table 2 Buckling load parameter (γ_{cr}) comparison for concentrated edge load for isotropic solid plate

Aspect ratio (a/b)	Distance from one edge (c/b)	Present	Rajanna et al. [8, 9]	Deolasi et al.
1.0	0.25	36.32	36.33	36.40
	0.5	25.71	25.60	25.72

$E = 210,924 \text{ N/mm}^2; \nu = 0.3$

Table 3 Buckling parameters of cross-ply laminates with circular cutout having $E_1 = 130.0 \text{ GPa}; E_2 = 10.0 \text{ GPa}; E_3 = 10.0 \text{ GPa}; G_{12} = G_{13} = 5.0 \text{ GPa}; \nu_{12} = \nu_{13} = 0.35; \nu_{23} = \nu_{32} = 0.49$

d/b ratio	Present	Rajanna et al. [8, 9]	Ghannadpour et al. [3]
0.1	12.82	12.83	12.80
0.5	6.41	6.40	6.40

4 Results and Discussion

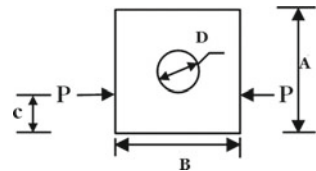
The buckling behavior of the laminated panels with cutout holding 4 layers of ply is studied considering the parameters such as ply orientations, cutout sizes, edge restraints and thickness variation. Concentrated type of loading is done from one edge as shown in Fig. 4 is considered throughout the study. Loading distance ratio (C/B) denoted by ζ and diameter to breadth ratio (D/B) indicated by β .

4.1 Effect of Concentrated Edge Load on Buckling of Cross-Ply Cutout Laminate

The panel with circular cuts of different sized is studied for cross-ply laminates under the action of concentrated load at various loading distance ratio (ζ). The circular cutouts under consideration for study are all centrally placed varying in dimension from $\beta = 0.1$ to 0.7 .

The effect of different sized cutout and loading position on the buckling characteristics of plate has been studied by considering $0/90/90/0$ layup scheme and the numerical results are illustrated in Fig. 5. It is observed from Fig. 5 that the buckling

Fig. 4 Plate with cutout under concentrated load from one edge



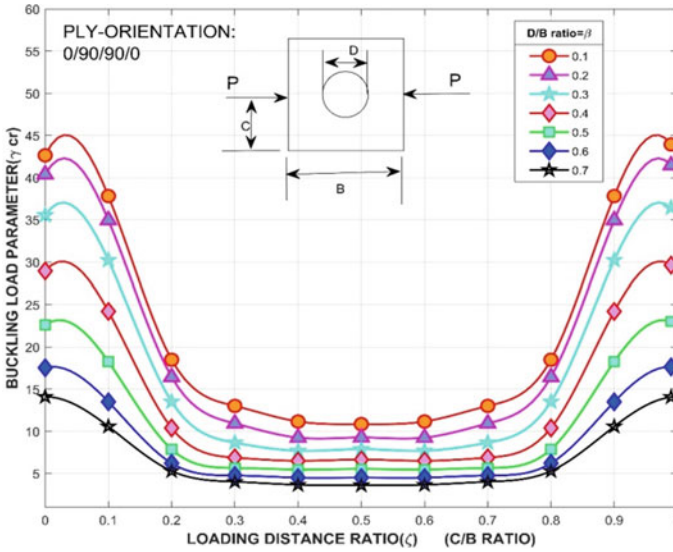


Fig. 5 Effect of cross-ply laminate with different sized cutout on buckling behavior

parameter decreases with the increase in the value of c/b and found lowest at $c/b = 0.5$ and increases thereafter with the further increase in buckling parameter and found highest at $c/b = 0.0$ and 1.0 irrespective cutout size. It is also observed that the value of γ_{cr} decreases with the increase in cutout size irrespective of the position of load. It is worthwhile to mention that for a given cutout size, the plate with the position of load toward the edge shows highest buckling parameter. It may be due to higher stiffness at the edges of plate.

4.2 Effect of Concentrated Edge Loadings on Buckling of Angle-Ply Cutout Laminate

The effect of concentrated edge loads on the bucklings behaviors of angles ply laminates with varying size of circulars cutouts is shown in Fig. 6 by considering angle-ply lay-up scheme. The buckling behavior of angle-ply layup scheme as shown in Fig. 6 is almost similar to that of cross-ply layup scheme as observed in Fig. 5 except when the loading near to the vicinity of edge of plate, wherein higher buckling parameters observed at higher sized cutouts. It may be attributed to the fact that at higher sized cutouts, the redistribution of stress will take place especially for angle-ply layup schemes.

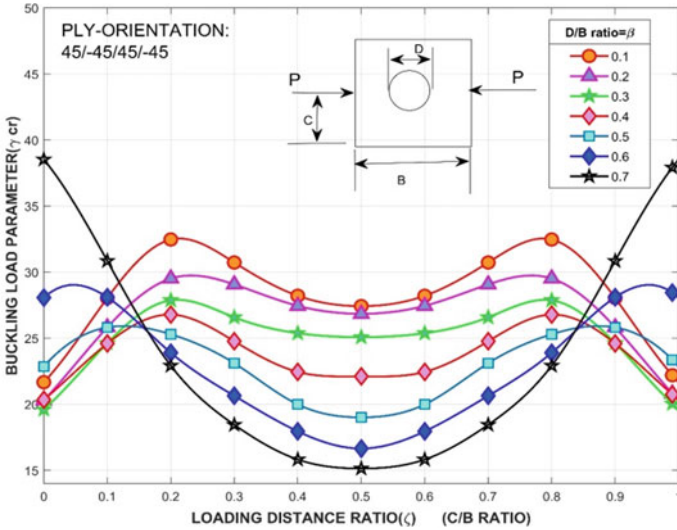


Fig. 6 Effect of angle-ply laminate with different sized cutouts on buckling behavior

4.3 Effect of Concentrated Edge Loadings on Buckling of Quasi-ply Cutout Laminate

The effect of concentrated edge loads on buckling behavior of the quasi-ply laminated cutout panel is shown in Fig. 7. It is noticed from Fig. 7 that the value of γ_{cr} decreases with the increase in cutout size irrespective of loading position. This behavior is almost similar to that cross-ply scheme with higher in the value of buckling parameters. In this case study, the buckling load parameter does not drop much as observed in previous cases where, there is a substantial decrease in buckling resistance at the mid position when compared to extreme edges for $\beta \leq 0.5$ in cross-ply and $\beta \geq 0.5$ in angle-ply.

The panel with all circular cutout sizes has higher buckling resistance at extreme edges compared to mid position. The loading distance ratio $\zeta = 0.1$ and 0.9 has highest buckling resistance for all cutout ratios.

4.4 Effect of Concentrated Edge Loadings on Buckling Behavior of Cutout Laminate of Size $\beta = 0.4$ Considering All Ply Laminates Under Study

Polynomial equations for the cutout ratio, $\beta = 0.4$ for different ply orientations under study are as follows:

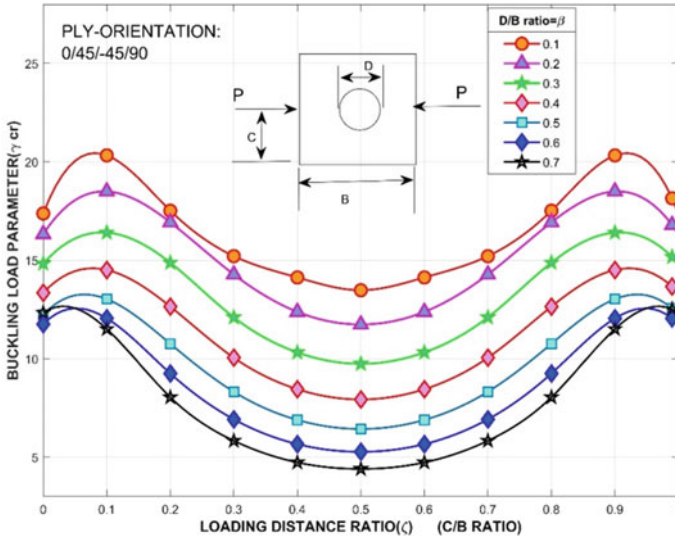


Fig. 7 Effect of quasi-ply laminate with different sized cutouts on buckling behavior

$$\text{Angle - ply: } \gamma_{cr a} = 1.3e^{+03} \times (x)^6 - 3.8e^{+03} \times (x)^5 + 3.9e^{+03} \times (x)^4 - 1.5e^{+03} \times (x)^3 + 90 \times (x)^2 + 49 \times (x) + 20.3.$$

$$\text{Cross - ply: } \gamma_{cr c} = -3.4e^{-07} \times (x)^9 - 2e^{+04} \times (x)^8 + 8e^{+04} \times (x)^7 - 1.4e^{+05} \times (x)^6 + 1.3e^{+05} \times (x)^5 - 7.4e^{+04} \times (x)^4 + 2.5e^{+04} \times (x)^3 - 4.2e^{+03} \times (x)^2 + 1.9e^{+02} \times (x) + 28.$$

$$\text{Quasi - ply: } \gamma_{cr q} = -2e^{+02} \times (x)^4 + 3.9e^{+02} \times (x)^3 - 2.2e^{+02} \times (x)^2 + 26(x) + 14.$$

where γ_{cr} is the critical buckling load and ‘x’ is the concentrated loading distance ratio (ζ). Cross-ply has the highest degree of 9 for the polynomial function and least is in quasi-ply with 4th degree. For a structural design engineer to select the laminate with cutout when the concentrated load is acting more toward the extreme position, then cross-ply configuration would be beneficial. On the other case, if cutout sizes are less than $\beta = 0.5$ and uniaxial concentrated load is acting at center of the edge, then angle-ply would be preferable. Hence, one can tailor to the necessary application (Fig. 8).

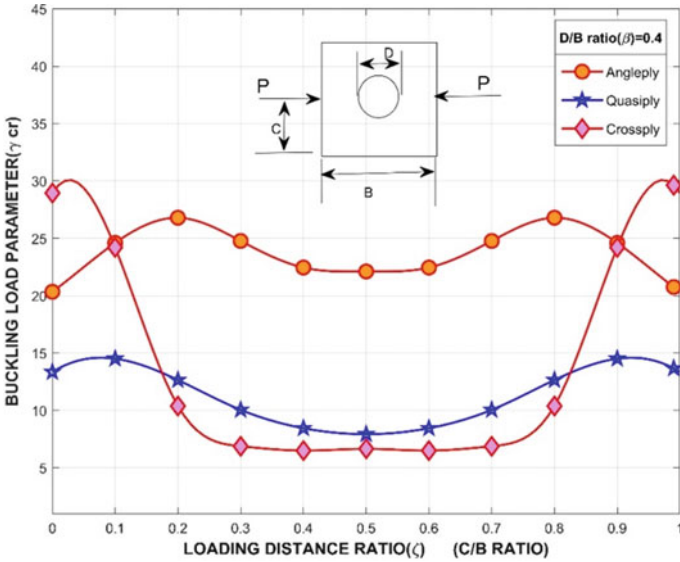


Fig. 8 Effect of all 3 different ply laminates with cutout size (d/b ratio) $\beta = 0.4$ on buckling behavior

4.5 Effect of Angle-Ply Orientations with Varying Configurations

The effect of the concentrated load is analyzed for a cutout ratio 0.4, for different angles of ply orientations. The angles of each ply are made to differ by 15° in $\theta/\theta/\theta/\theta$ laminate where θ is ranged from 0° to 90° and graph is plotted for the same to analyze the buckling behavior (Fig. 9). The concentrated loads are applied at particular loading distance and analyzed for buckling behavior. The highest buckling load parameter (γ_{cr}) is found at different concentrated loading distance ratio (ζ) for each of the ply orientation. For a loading distance ratio $\zeta = 0.2$, γ_{cr} is highest with $(\pm 45)_2$ configuration. The cutout laminate with angle-ply $(\pm 0)_2$ has highest buckling resistance for $\zeta = 0.0$ and decreases as ζ is increased, but this is not the case for all ply orientations, there is shift over in the range after $(\pm 30)_2$. At $(\pm 45)_2$, $\zeta = 0.2$ becomes predominant and while with $(\pm 75)_2$ configuration, $\zeta = 0.5$ has highest buckling resistance due to stress regions are getting redistributed causing an increase in buckling load. In $(\pm 90)_2$, there is no effect of position of concentrated load. This shows that there is a significant effect of ply orientation on buckling behavior.

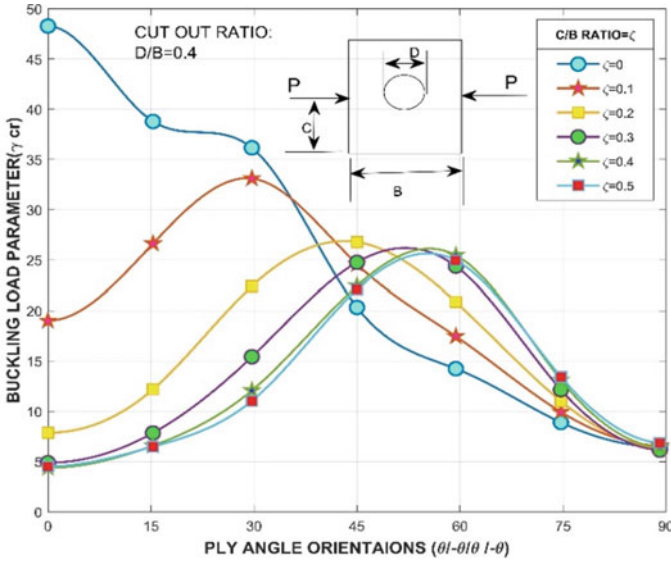


Fig. 9 Effect of varying angle-ply cutout laminate with cutout size $\beta = 0.4$ on buckling behavior

4.6 Effect of the Concentrated Edge Loads on Boundary Condition with Thickness of a Perforated Panel

The effect of concentrated edge loads at different locations on buckling behavior of $(\pm 45)_2$ ply orientated cutout laminate is examined for cutout ratio, $\beta = 0.4$ accounting for panel thickness and boundary conditions. The numerical results for $\beta = 0.4$ are tabulated in Table 4. It is acquainted that in case of thin plate configuration with $B/T = 100$, the resistance to buckling is significantly higher for clamped (CCCC) condition, when compared to that of simply supported (SSSS) cutout panel irrespective of loading parameters. However, this behavior is totally nullified for thick plate configuration ($B/T = 10$), where change in boundary condition will not play any role in the buckling resistance.

Table 4 Effect of loading distance parameter, thickness and boundary conditions on $(\pm 45)_2$ panel

$(D/B \text{ ratio})$ $\beta = 0.4$	$B/T = 100$		$B/T = 20$		$B/T = 10$	
Load distance ratio ($C/B \text{ ratio}$) (ζ)	SSSS	CCCC	SSSS	CCCC	SSSS	CCCC
$\zeta = 0$	20.34	32.38	13.35	13.55	3.56	3.58
$\zeta = 0.1$	24.6	39.00	16.76	19.64	6.53	6.64
$\zeta = 0.2$	26.79	41.15	17.56	19.57	6.03	6.21
$\zeta = 0.3$	24.77	40.94	17.63	19.25	5.62	5.62
$\zeta = 0.4$	22.45	37.79	16.33	18.25	5.21	5.21
$\zeta = 0.5$	22.11	39.3	16.42	18.35	5.16	5.16

5 Conclusions

Finite element buckling analysis was performed on fiber-reinforced composite plates containing centrally located different sized holes. The effect of plates fiber orientations, hole size, thickness and plate support conditions were studied in detail. The key conclusions of the analysis are as follows:

- The buckling resistance of the panel decreases with the increase in cutout size irrespective of position of concentrated load. However, this is not true in the case of angle-ply scheme, wherein the panel with higher sized cutout shows higher buckling resistance only when the loading position toward the extreme edges of the panel.
- The buckling resistance of the angle-ply layup scheme is significantly higher as compared to that of cross-ply and quasi-ply laminate schemes irrespective of cutout size and loading conditions because of the stresses in angle-ply cutout panel is more distributed throughout the panel.
- The buckling resistance of the panel found to be higher when the position of concentrated load toward the vicinity of extreme edges and it is least when the loading position toward the center of the panel.
- Of all the different angle-ply orientations under consideration, $(\pm 45)_2$ has reasonably good minimum range buckling load variation avoiding the extreme critical buckling.
- The position of loading and angle-ply orientation for laminate with cutouts play a significant role on the buckling behavior. However, the maximum buckling resistance is found for the angle-ply scheme for each position of loading case for $\beta = 0.4$ cutout ratio, except for extreme places cross-ply has the highest buckling strength.
- The boundary condition significantly affect the buckling resistance of the cutout panel only in thin plate condition, whereas it is insignificant in thick plate configuration.

References

1. Baba BO, Baltaci A (2007) Buckling characteristics of symmetrically and antisymmetrically laminated composite plates with central cutout. *Appl Compos Mater* 14(4):265–276
2. Deolasi PJ, Datta PK, Prabhakar DL (1995) Buckling and vibration of rectangular plates subjected to partial edge loading (compression or tension). *J Struct Eng* 22(3):135–144
3. Ghannadpour SAM, Najafi A, Mohammadi B (2006) On the buckling behavior of cross-ply laminated composite plates due to circular/elliptical cutouts. *Compos Struct* 75:3–6
4. Jayashankarbabu BS, Karisiddappa (2014) Stability of square plate with concentric cutouts. *Int J Civ Archit Struct Constr Eng* 8(3)
5. Kim JH, Nguyen KH, Choi JH, Kweon JH (2016) Experimental and finite element analysis of curved composite structures with C-section. *Compos Struct* 140:106–117
6. Komur MA, Sonmez M (2015) Elastic buckling behavior of rectangular plates with holes subjected to partial edge loading. *J Constr Steel Res* 112:54–60
7. Leissa W, Ayoub EF (1988) Vibration and buckling of a simply supported rectangular plate subjected to a pair of in-plane concentrated forces. *J Sound Vib* 127(1):155–171
8. Rajanna T, Banerjee S, Desai YM, Prabhakara D (2016) Effects of partial edge loading and fibre configuration on vibration and buckling characteristics of stiffened composite plates. *Latin Am J Solids Struct* 13(5)
9. Rajanna T, Banerjee S, Desai YM, Prabhakara D (2016) Vibration and buckling analyses of laminated panels with and without cutouts under compressive and tensile edge loads. *Steel Compos Struct* 21(1):37–55
10. Rajanna T, Banerjee S, Desai YM, Prabhakara D (2017) Effect of reinforced cutouts and ply-orientations on buckling behavior of composite panels subjected to non-uniform edge loads. *Int J Struct Stabil Dyn* 1850058
11. Reddy JN, Phan ND (1985) Stability and vibration of isotropic, orthotropic and laminated plates according to a higher-order shear deformation theory. *J Sound Vib* 98(2):157–170
12. Selvaraj S, Madhavan M, Dongre SU (2016) Experimental studies on strength and stiffness enhancement in CFRP-strengthened structural steel channel sections under flexure. *J Compos Constr* 20(6):04016042
13. Singh SB, Kumar D (2010) Effect of boundary condition on buckling and post-buckling responses of composite laminate with various shaped cutouts. *Compos Struct* 92:769–779
14. Soni G, Singh R, Mitra M (2013) Buckling behavior of composite laminates (with and without cutouts) subjected to non-uniform in-plane loads. *Int J Struct Stabil Dyn* 13(8)
15. Timoshenko SP, Gere JM (1961) *Theory of elastic stability*. McGraw-Hill, New York

Comparison of the Behaviour of Axially Loaded Slender Hollow Steel Tubes and Concrete Filled Steel Tubes



Rebecca Mary Paul, Madhu M. Karthik, and M. V. Anil Kumar

Abstract Concrete filled steel tubes (CFSTs) are composite members in which concrete is encased within hollow steel tubes (HSTs). To understand the influence of the concrete core on the elastic local buckling stress and the axial strength of the steel tube, finite-element (FE) models of HST and CFST are developed using ABAQUS. From the FE analysis of CFST, it is evident that even for a diameter to thickness ratio (D/t) of 150 which is much higher than the $(D/t)_{\text{limit}}$ for slender members ($D/t = 110$), local buckling is not observed up to the ultimate load. This explains the reason for the highly conservative prediction of slender CFSTs by AISC 360-16. In addition, the yielding of the steel tube occurs before the peak strength of CFST is achieved, and the reduction in the load carrying capacity beyond peak load is due to the crushing of the core concrete. It is also observed that the axial strength of steel in CFSTs can be much lower than that predicted in the literature and codal provisions due to development of hoop stresses.

Keywords Concrete filled steel tube · Hollow steel tube · Buckling · Slender · Finite-element modelling

1 introduction

Concrete filled steel tubes (CFSTs) are composite members where the concrete is filled in hollow steel tubes (HSTs). The presence of concrete in steel tubes improves the performance of concrete and steel compared to their individual performances.

R. M. Paul (✉) · M. M. Karthik · M. V. A. Kumar
IIT Palakkad, Palakkad, India
e-mail: 101803102@smail.iitpkd.ac.in

M. M. Karthik
e-mail: madhu@iitpkd.ac.in

M. V. A. Kumar
e-mail: anil@iitpkd.ac.in

The steel tube not only acts as the longitudinal reinforcement but also provides lateral confinement to the inner concrete. This confinement effect increases the compressive strength and ductility of the concrete core. Besides providing confinement, the steel tube also functions like a formwork which further provides speedy and economical construction, whereas the concrete in CFSTs delays the occurrence of local buckling in steel tubes.

CFSTs are predominantly used as compression members. Since CFSTs have low cross-sectional area to load carrying capacity ratio, they are used as columns for the lower storeys of high-rise buildings. Due to its inherent properties of high strength and ductility, CFSTs are mainly adopted for construction of buildings situated in seismic zones, bridge piers (with internal reinforcements), transmission towers and retrofitting purposes.

Circular CFSTs in which both the steel tube and concrete core are simultaneously loaded, both the constituent materials contribute to its axial load carrying capacity. During the initial stages of loading, as the Poisson's ratio of steel and concrete is different, they do not influence the mechanical behaviour of each other and share the load independently. The development of micro-cracks in concrete at approximately 0.4 to 0.7 f'_c . Chen and Han [1] causes it to dilate more than steel. This increases the Poisson's ratio of concrete, which causes the concrete to apply a lateral pressure on the steel tube. The lateral pressure in-turn introduces tensile hoop stress in steel, which results in a reduction in the axial stresses in the steel tube. On the other hand, the steel tube confines the lateral expansion of the core concrete thereby improving its strength and ductility. Even though there is a reduction in the axial capacity of the steel tube, the overall capacity of the CFST is enhanced due to the increase in strength of concrete due to confinement.

2 Classification of Circular CFSTs

AISC 360-16 [2] classifies circular CFSTs as compact, non-compact and slender based on section slenderness λ , defined as the ratio of overall diameter to the thickness of the steel tube (D/t) of concrete filled steel tubes. Compact sections are those in which yielding of steel happens before buckling, thus providing adequate confinement to the concrete core. Non-compact sections are those in which yielding and local buckling of the steel tube happens simultaneously. Owing to the local buckling of steel tube in non-compact sections, the concrete core does not attain its unconfined compressive strength f'_c . In slender sections, the steel is assumed to buckle locally before yielding, resulting in ineffective confinement of the concrete core. Depending on the section classification, AISC 360-16 [2] proposes different expressions for calculating the ultimate capacity of circular CFSTs based on slenderness limits and is given as:

$$\text{Compact CFSTs, } \lambda \leq \lambda_p = 0.15 E_s / F_y \quad P = F_y A_s + 0.95 f'_c A_c, \quad (1)$$

$$\text{Non - compact CFSTs, } \lambda_p < \lambda \leq \lambda_r = 0.19E_s/F_y \quad P = P_p - \frac{(P_p - P_y)(\lambda - \lambda_p)}{(\lambda_r - \lambda_p)}, \tag{2}$$

$$\text{Slender CFSTs, } \lambda > \lambda_r \leq 0.31E_s/F_y \quad P = F_{cr}A_s + 0.7f'_cA_c, \tag{3}$$

where F_y = yield strength of steel; f'_c = compressive strength of unconfined concrete; A_s, A_c = area of steel and concrete, respectively; E_s = modulus of elasticity of steel; $P_p = P$ as defined in Eq. (1); and the yield load P_y and the critical buckling stress F_{cr} are given as:

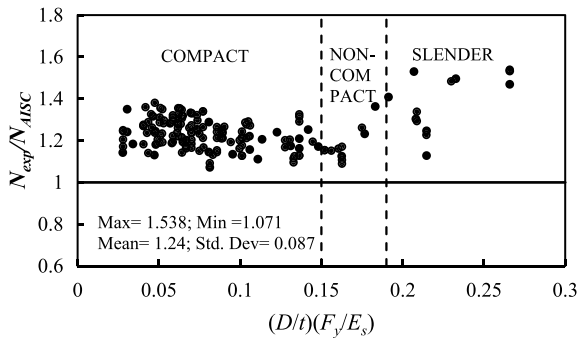
$$P_y = F_yA_s + 0.7f'_cA_c. \tag{4}$$

$$F_{cr} = \frac{0.72F_y}{\left(\frac{D}{t} \frac{F_y}{E_s}\right)^2}. \tag{5}$$

The above expressions are valid for steel strength less than 525 MPa and concrete strength between 21 and 69 MPa.

Figure 1 presents a comparison of the AISC 360-16 [2] expression for the axial load carrying capacity of CFST with the experimental database reported in Lai and Varma [3] and Lai and Ho [4]. It is evident from Fig. 1 that the expressions defined in AISC 360-16 [2] underestimate the axial load carrying capacity of circular CFSTs, particularly for slender sections with a mean and standard deviation of 1.345 and 0.131, respectively. This warrants further investigation on the behaviour of slender CFSTs.

Fig. 1 Comparison of axial load capacity of CFSTs with AISC 360-16 [2]



3 Finite-Element Modelling Details

In order to understand the behaviour of concrete and steel in axially loaded CFSTs, a numerical model is prepared using the finite-element (FE) software, ABAQUS (SIMULIA 2016), that accounts for both material and geometric nonlinearities. FE models of axially loaded slender HSTs and CFSTs are validated and are further adopted to analyse the stresses acting in the steel tubes. The details of the model are presented in this section.

3.1 Geometric Details

Four-noded shell elements with reduced integration (S4R) and eight-noded linear brick elements with reduced integration are, respectively, used for modelling the steel tube and the concrete core of the CFST. The size of the elements is finalised based on the mesh convergence study of HST sections. Optimal mesh sizes are determined based on the ratio of theoretical buckling load P_{Th} to the buckling load P_{FE} generated from the FE analysis and considering the trade-off between accuracy and computational time. The theoretical value of the buckling load P_{Th} is determined using the following equation [5]:

$$P_{Th} = \frac{2E_s}{\sqrt{3}(1 - \mu_s^2)} \frac{t}{D}. \quad (6)$$

where μ_s = Poisson's ratio of steel.

For the present study, a mesh size of 15 mm is adopted. In order to ensure compatibility at the interface between steel and concrete in CFST, the same mesh size is adopted for the concrete core as well.

3.2 Contact Between Steel and Concrete

To ensure compatible deformation between concrete and steel during compression, a hard contact in the normal direction is specified at the interface between concrete and steel [6]. For the tangential contact, the coefficient of friction between concrete and steel is taken as 0.6 as reported by Schneider (1998) and Tao et al. [6].

3.3 Loading and Boundary Conditions

In order to accurately represent the loading condition during experimental tests on CFSTs, loads are applied as uniform displacements at the top nodes of concrete and steel. The boundary conditions at both ends of the CFST are restrained against all translational movements except the axial deformation of the top nodes.

3.4 Geometric Imperfections

Study the effects of geometric nonlinearity on the behaviour of CFSTs, geometric imperfections are incorporated into the FE analysis. In the absence of experimentally measured imperfections, the buckling mode shapes of the steel tube obtained from the buckling analysis of CFSTs may be used. In the present study, the mode shape for the first eigenvalue is used to define the geometric imperfection in the steel tube, with a magnitude of 0.1 times the thickness of the steel tube [3].

3.5 Material Constitutive Relationships

Appropriate material models of steel and concrete are essential to closely simulate the actual behaviour of CFSTs. The concrete in CFSTs gets confined due to the hoop stress applied by the outer steel tube. Therefore, the effects of concrete confinement should also be considered. The constitutive relation of steel and confined concrete is discussed in this section.

3.5.1 Constitutive Relation for Steel

Figure 2a shows the stress–strain relation of steel adopted in this study. The initial modulus of elasticity E_s and Poisson's ratio μ_s is taken as 200 GPa and 0.3, respectively, for defining the elastic portion of the stress–strain relation of steel. Since the stress–strain behaviour of steel considered for the present study is not reported in the literature, the plastic portion is defined by specifying the yield strength F_y up to a strain of $10 \varepsilon_y$, ε_y being the yield strain of steel. Beyond this, the strain hardening part is taken into consideration by specifying the ultimate strength F_u , where the ultimate strain of steel ε_u is taken as 0.15. The ultimate strength of steel is determined using Eq. (7) [7].

$$\frac{F_u}{F_y} = 1 + 2 \left(\frac{150}{F_y} \right)^2. \quad (7)$$

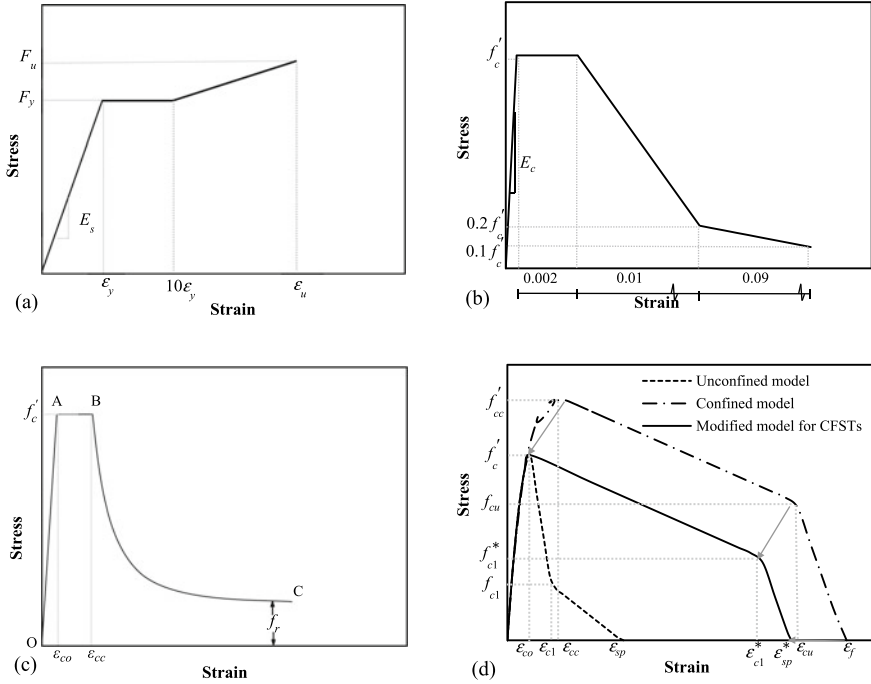


Fig. 2 Stress–strain behaviour of **a** steel; and concrete by **b** Schneider (1998), **c** Tao et al. [6] and **d** proposed

3.5.2 Constitutive Relation for Confined Concrete

The concrete in axially loaded CFSTs, as a result of the confinement offered by the steel tube, is subjected to a triaxial state of stress. Concrete under triaxial stress state can be modelled using the concrete damage plasticity (CDP) model (Lubliner et al. 1989). The CDP model requires several input parameters, which includes the plasticity parameters and the compressive and tensile behaviour of concrete. The plasticity parameters predict the confinement in concrete offered by the outer steel tube. The parameters required to define the plasticity of concrete are the dilation angle ψ , flow potential eccentricity ratio e , ratio of the second stress invariant on tensile meridian to compressive meridian K_c , ratio of biaxial compressive strength to uniaxial compressive strength f_{bo}/f_{co} and viscosity ν . Table 1 presents the plasticity parameters used in the present study that are adopted from literature [6, 8, 9] for modelling concrete in slender CFST specimen.

Table 1 Plasticity parameters for concrete damage plasticity model

f'_c (MPa)	Dilation angle ψ	Eccentricity e	f_{bo}/f_{co}	K_c	Viscosity ν
27.2	37	0.10	1.17	0.72	0.0005

Figure 2b and c presents the stress–strain models proposed by Schneider (1998) and Tao et al. [6] for modelling confined concrete in CFSTs. Schneider proposed a concrete model based on the experimental results of CFSTs, where the stress and strain values of the confined concrete model were retained to be the same for all CFSTs regardless of the confinement offered by the outer steel tube. Tao et al. proposed a three-stage stress–strain model for confined concrete where the post-peak branch is a function of the confining pressure acting on concrete. Since the confining pressure is an unknown at the beginning of the analysis, Tao et al. proposed an empirical equation for the confining pressure based on their numerical studies. In this study, a rational new modification is proposed to the concrete constitutive model based on the confined model proposed by Karthik and Mander [10].

Figure 2d shows the compressive stress–strain behaviour of unconfined concrete adopted in this study [10]. From the preliminary FE analysis of CFST using the unconfined concrete model, it is found that the plasticity parameters of the CDP model and the interaction between steel and concrete only partially account for the increase in compressive strength of concrete due to confinement. Similar observations were also reported by Tao et al. [6] and Lin and Zhao (2019). Hence, a novel methodology is proposed to simulate the confined concrete behaviour accurately. Figure 2d shows the modified stress–strain relation for confined concrete that is adopted in this study. To obtain this, the confinement ratio $K = f'_{cFE}/f'_c$ which is the ratio of peak concrete stress from the FE model f'_{cFE} to the unconfined compressive strength of concrete f'_c extracted from the preliminary FE analysis using unconfined concrete model. The confined concrete model proposed by Karthik and Mander [10] is then defined using the extracted confinement ratio K as shown in Fig. 2d. The post-peak branch of the confined model is then parallelly shifted to the post-peak branch of unconfined concrete to obtain the modified concrete model. Since the FE analysis with the modified stress–strain model of concrete showed a further increase in the confinement ratio, the procedure is iterated until the confinement ratio K defined in the analysis and that obtained from the FE analysis converge. The tensile behaviour of concrete is defined based on the model proposed by Karthik and Mander [10].

3.6 Validation of FE Analysis Methodology

The FE analysis methodology adopted in this study is validated with experimental observations reported in the literature. Towards this, the validation of the FE analysis of both HST and CFST columns is presented in the following sections.

3.6.1 Hollow Steel Tubes

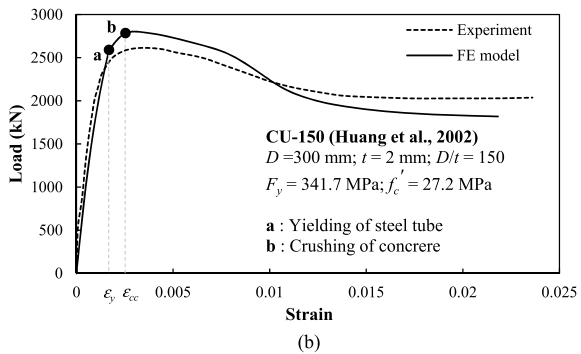
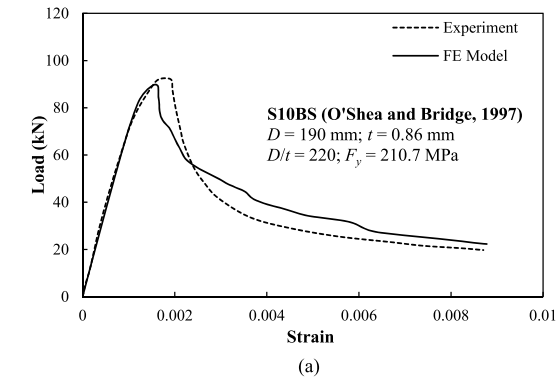
To ensure that the numerical model appropriately simulates the behaviour of hollow steel tubes without any infill, an experimental slender steel tube S10BS [11] with $D/t = 220$ is modelled using the FE method.

Table 2 presents the geometric and material properties of the HST specimen. The effects of geometric imperfections and residual stresses are also incorporated into the analysis. Figure 3a shows a comparison of the load-strain behaviour of the hollow steel tube member obtained from the FE analysis with the experimental test result. The initial part of the load-strain behaviour is modelled quite accurately. The reduction in stiffness of the HST at approximately 70 kN is attributed to the effects of geometric imperfections and residual stresses. Even though the ultimate load simulated by the FE analysis is slightly under predicted (by 3%), the simulated post-peak behaviour agrees quite well with the experimental observations.

Table 2 Details of specimens used for validation of FE models

Specimen	Length (mm)	Diameter (mm)	Thickness (mm)	F_y (MPa)	f'_c (MPa)	P_{Exp} / P_{FE}
SB10S (HST)	665	190	0.86	210.7	–	1.03
CU-150 (CFST)	900	300	2	341.7	27.2	0.94

Fig. 3 Comparison of experimental load versus strain behaviour with FE results. **a** Hollow steel tube, **b** concrete filled steel tube



3.6.2 Concrete Filled Steel Tubes

In order to verify the accuracy of the FE analysis in simulating the behaviour of CFSTs, a slender CFST experimental specimen CU-150 [12] with $D/t = 150$ is considered for validation. Table 2 presents the geometric and material properties of the experimental specimen. Geometric nonlinearities are implemented into the analysis as described earlier. Figure 3b presents a comparison of load versus axial strain behaviour of the slender CFST obtained from the finite-element analysis with the experimental results. The load-strain curve presented in Fig. 3b that is obtained from the FE analysis corresponds to the results from the final iteration, where the confinement ratio K converges to a value of 1.23. The initial slope and the post-peak behaviour simulated by the FE analysis compare well with the experimental results. However, the analysis slightly overpredicts the peak axial load by approximately 6%. Considering the complexities associated with the interaction between the steel tube and the concrete core in CFSTs, the FE analysis simulates the overall behaviour quite well. The load-strain behaviour therefore validates the modelling approach adopted for axially loaded CFSTs.

4 Results and Discussions

Figure 3b shows the key events along the load-strain curve of the axially loaded CFST. In this, point 'a' corresponds to the yielding of the steel tube, where the Von Mises stress reaches the yield strength of steel, and point 'b' corresponds to the ultimate load of the CFST. Figure 3b also shows the strains corresponding to yield stress of steel (ϵ_y) and confined concrete stress (ϵ_{cc}). As evident from the figure, the maximum load capacity of the CFST is attained corresponding to the peak confined concrete strain of ϵ_{cc} . This clearly indicates that the post-peak reduction in the load carrying capacity of CFST corresponds to crushing of the concrete core. The observation is contradictory to the AISC 360-16 [2] classifications of CFSTs, where slender CFSTs are assumed to fail due to the elastic local buckling of the steel tube. This observation alludes that the section classification of CFST may have to be reconsidered. However, further studies are necessary.

Figure 4 presents the failure modes of HST and CFST obtained from the FE analysis. It is observed that at failure, the slender HSTs displays elephant foot buckling at the ends (Fig. 4a). However, in CFSTs along with elephant foot buckling at its ends, the column bulges out at the mid-section due to the dilation of concrete (Fig. 4b).

The validated FE analysis is also used to understand and compare the behaviour of slender HST and CFST with similar geometry and material properties. Towards this, a HST column with similar geometry and material property as that of CFST specimen CU-150 (Table 2) is analysed using the FE technique described earlier.

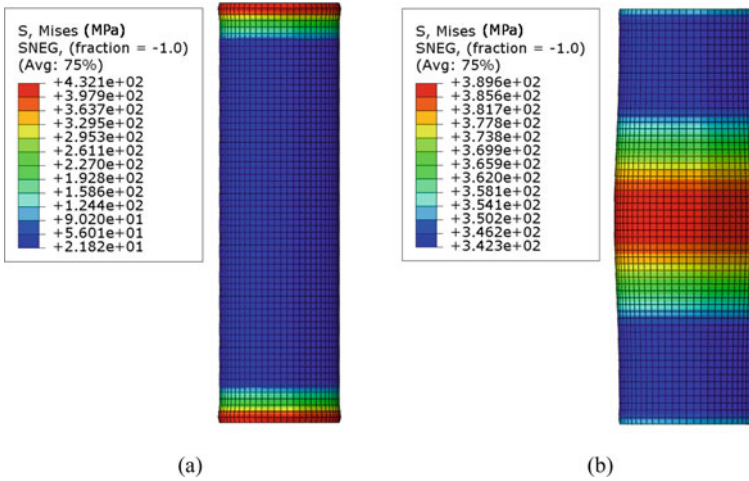


Fig. 4 Failure modes of **a** SB10S (HST) and **b** CU-150 (CFST) obtained from FE analysis

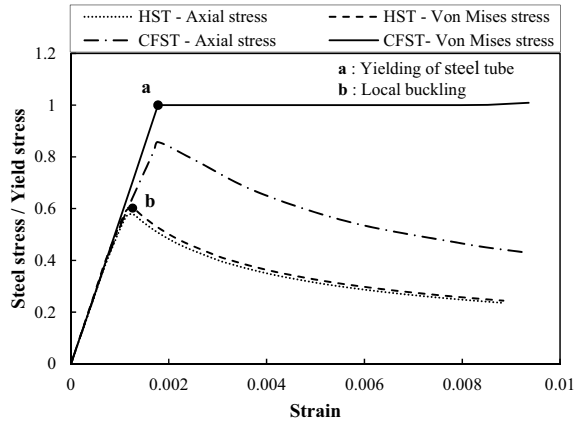
4.1 Comparison of Axial Stress of Steel in Slender HST and CFST

Figure 5 shows a comparison of the axial steel stresses in concentrically loaded slender HST and CFST columns of similar cross-section and material properties. Point ‘a’ corresponds to the yielding of steel tube in CFST, where the Von Mises stress reaches the yield strength of steel, whereas point ‘b’ corresponds to the local buckling of the steel tube in HST. From Fig. 5, it is evident that the maximum steel stress in HST reaches a value of approximately $0.6 F_y$, indicating that slender HST column fails under elastic local buckling as specified by AISC 360-16 [2]. The axial stress in the steel tube of the CFST column reaches a maximum of approximately $0.8 F_y$. However, the Von Mises stress reaches yield and exhibits strain hardening behaviour owing to the presence of hoop stresses that arise due to the lateral expansion of the concrete core. This clearly shows that the steel tube in CFST yields before local buckling.

4.2 Comparison of Existing Expressions for Axial Stress of Steel in CFSTs

Many researchers [13–15] have proposed different expressions for determining the ultimate capacity of axially loaded slender CFSTs. Each of these expressions considers the contribution of both the steel tube and the concrete core towards the axial load capacity of CFST. However, the contribution of steel towards the axial capacity of CFST varies significantly. Table 3 presents the maximum axial stress in

Fig. 5 Comparison of axial steel stresses in HST and CFST



the steel tube corresponding to the ultimate load of axially loaded slender CFST. The table also presents a comparison of the axial stress proposed by the various references $f_{sz, predicted}$ with the axial stress that is obtained from the FE analysis $f_{sz, FE}$. It is evident that most of the current expressions overpredict the axial stress of steel in CFSTs. This is despite the fact that most of these expressions predict the ultimate load capacity of CFSTs quite well.

From Table 3, it is evident that most of the existing expressions (ACI 318–14; [13, 14]) do not consider the reduction in axial stress in steel due to the presence of hoop stress. Even though the expression proposed by Sakino et al. [15] accounts for a reduction in the axial stress in the steel tube, the reduction factor is taken as a constant function of F_y . Among the various expressions predicting the axial stress of steel in CFSTs, the expression proposed in EN 1994-1-1 (2004) is found to fairly predict the axial stress in steel. The reduction factor accounted in EN 1994-1-1 (2004) is taken as a function of relative slenderness of CFST irrespective of whether the column is stub or long. Therefore, from these observations, it is evident that further investigation is necessary to accurately predict the axial stress of steel in CFSTs.

Table 3 Comparison of existing expressions for axial capacity of steel in CFST

References	Axial capacity of steel tube, $f_{sz, predicted}$	$f_{sz, predicted} / f_{sz, FE}$
[16]	F_y	1.26
[2]	F_{cr}	1.19
EN 1994-1-1 (2004)	$\eta_s F_y$	1.04
[13]	F_y	1.26
[15]	$0.89 F_y$	1.12
[14]	$1.47 F_y$	1.86

5 Conclusions

To investigate the changes in the behaviour of steel tubes in axially loaded slender CFSTs in comparison to slender HSTs, a numerical FE-based study was conducted using ABAQUS (SIMULIA 2016). The FE models were developed and validated to simulate the behaviour of axially loaded slender HST and CFST and validated with experimental results. The validated FE models were then further adopted to analyse the steel stresses in HST and CFST columns and to understand the failure mechanism of CFSTs. The following are the major conclusions that can be drawn from the analysis:

- Steel tubes in slender CFSTs are not subjected to elastic local buckling, which is contrary to AISC 360-16 [2] provisions.
- Reduction in the load carrying capacity beyond peak of slender CFST was due to the crushing of concrete core which was preceded by the yielding of the steel tube. Elastic local buckling was not the cause of failure.
- Results from the present study show that further studies are necessary to look into the behaviour of axially loaded slender CFSTs.
- Further studies are also necessary to accurately predict the axial stresses in the steel tubes of CFSTs.

References

1. Chen WF, Han DJ (2007) *Plasticity for structural engineers*. J Ross Publishing
2. AISC 360-16 (2019) *Load and resistance factor design (LRFD) specification for structural steel buildings*. American Institute of Steel Construction, Chicago (IL, USA)
3. Lai Z, Varma AH (2015) Noncompact and slender circular CFT members: Experimental database, analysis, and design. *J Constr Steel Res* 106:220–233
4. Lai MH, Ho JCM (2016) A theoretical axial stress-strain model for circular concrete-filled-steel-tube columns. *Eng Struct* 125:124–143
5. Timoshenko SP, Gere JM (2009) *Theory of elastic stability*. Courier Corporation
6. Tao Z, Wang ZB, Yu Q (2013) Finite element modelling of concrete-filled steel stub columns under axial compression. *J Constr Steel Res* 89:121–131
7. Bannister AC (1998) Contribution to sub-task 2.3: assessment of the occurrence and significance of yield plateaus in structural steels. Report No. SINTAP/BS/19, Brite-Euram BE95-1426
8. Papanikolaou VK, Kappos AJ (2007) Confinement-sensitive plasticity constitutive model for concrete in triaxial compression. *Int J Solids Struct* 44(21):7021–7048
9. Yu T, Teng JG, Wong YL, Dong SL (2010) Finite element modelling of confined concrete-II: plastic-damage model. *Eng Struct* 32(3):680–691
10. Karthik MM, Mander JB (2011) Stress-block parameters for unconfined and confined concrete based on a unified stress-strain model. *J Struct Eng* 137(2):270–273
11. O'Shea MD, Bridge RQ (1997) Local buckling of thin-walled circular steel sections with or without internal restraint. *J Constr Steel Res* 41(2–3):137–157
12. Huang CS, Yeh YK, Liu GY, Hu HT, Tsai KC, Weng YT, Wang SH, Wu MH (2002) Axial load behavior of stiffened concrete-filled steel columns. *J Struct Eng* 128(9):1222–1230

13. Giakoumelis G, Lam D (2004) Axial capacity of circular concrete-filled tube columns. *J Constr Steel Res* 60(7):1049–1068
14. Lu ZH, Zhao YG (2010) Suggested empirical models for the axial capacity of circular CFT stub columns. *J Constr Steel Res* 66(6):850–862
15. Sakino K, Nakahara H, Morino S, Nishiyama I (2004) Behavior of centrally loaded concrete-filled steel-tube short columns. *J Struct Eng* 130(2):180–188
16. ACI 318-14 (2014) Building code requirements for structural concrete (ACI 318-14) and commentary (ACI 318R-14). American Concrete Institute, Farmington Hills (MI, USA)
17. ABAQUS (2017) (Dassault systemes, 2016) Dassault systemes. 2016. ABAQUS/CAE 2017. Dassault Systemes Simulia Corp, Rhode Island, USA
18. EN 1994-1-1 (2001) Design of composite steel and concrete structures. Part 1.1, General rules and rules for buildings. European Committee for standardization: British Standards Institution

Computer Aid for Designing Circular Concrete Filled Double Skinned Tube (C-CFDST) Composite Column



Yashpal P. Gajjar and Arth J. Patel

Abstract Composite structures are becoming a part of modern construction practice. Composite columns sections such as concrete filled tube (CFT), concrete filled double skinned tube (CFDST), and concrete encased steel (CES) have made the high-rise buildings and long bridges, reasonably safer and lighter. Newly evolved CFDST sections, where concrete sandwiched between two steel tubes, have shown improved performance under earthquake loading. The concrete infill enhances the load-carrying capacity and energy absorption and limits steel tube to get locally buckled. Furthermore, these sections provide high bending stiffness, better local and global stability, and enhanced post-peak behavior. Currently, in many countries like China and America, composite structures are constructed in a considerable extent. However, in India, utilization of composite columns is very limited because of lack of committed Indian standard stipulations. Acknowledging multifaceted nature in investigative answer for column element, utilization of load–moment (P–M) interaction curve plays a crucial role in design of composite column. Currently, available composite structure design codes predict the load–moment capacity based on either plastic design or strain compatibility design method. The present study aims to develop theoretical formulations for design of circular concrete filled double skinned tube (C-CFDST) composite column section using plastic method of design approach following Eurocode-4. Computer aid has been developed in Visual Studio 2019 with VB.net language based on proposed theoretical formulations to have a great advantage of computers in obtaining a solution for such complicated problems.

Keywords Composite column · Plastic design · Eurocode-4 · Interaction curve · Computer aid

Y. P. Gajjar (✉) · A. J. Patel
Department of Civil Engineering, School of Engineering, Institute of Technology, Nirma
University, Ahmedabad, Gujarat, India
e-mail: 15bcl035@nirmauni.ac.in

A. J. Patel
e-mail: arth.patel@nirmauni.ac.in

© The Author(s), under exclusive license to Springer Nature Singapore Pte Ltd. 2023
M. Madhavan et al. (eds.), *Proceedings of the Indian Structural Steel Conference 2020*
(Vol. 2), Lecture Notes in Civil Engineering 319,
https://doi.org/10.1007/978-981-19-9394-7_7

1 Introduction

In current scenario of construction industries the use of composite columns in high-rise buildings, bridges, etc., have significantly increased. Filling up the void of thin walled steel tube with stronger material like concrete delays the local as well as global buckling, which leads to improved energy absorption and load carrying capacity. Furthermore the ductility of the composite column also gets improved due to the confinement of filled concrete and restrained steel tube against the local buckling. It is now well established that circular steel tubes provide better confinement to the concrete infill as compared to other shapes of structural steel. However, newly evolved composite section concrete filled double skinned tube (CFDST), in which concrete sandwiched between two steel tubes, has shown improved performance under earthquake loading. Circular concrete filled double skinned tube (C-CFDST) shows high bending stiffness, better local and global stability, and enhanced post-peak behavior, making the use of C-CFDST section more efficient than other shapes. In India, currently available code IS:11384 [1] does not provide any design stipulations for CFDST composite column, which leads to bare minimum use of composite column. In upcoming years it may boost up due to its superiority over the regular reinforced concrete and steel column sections. Currently available literatures, as well as codal stipulations based on either plastic design method or compatibility method to design composite column sections, underestimate or overestimate the actual capacity of the composite column section, which may lead to more conservative (uneconomical) or unsafe design respectively.

Present paper focuses on developing theoretical formulations of P-M (load-moment) interaction curve considering plastic design method. As to design composite column section, based on the needed accuracy, number of positions of neutral axis can be considered and for each of the position of neutral axis, load-moment capacity can be calculated separately and finally integrated to develop P-M interaction curve. By hand this method of calculating the capacity of column section would be the very tedious, extremely difficult, and time-consuming work as presented by Patel and Sheth [2]. Thus, computer aid has been developed in Visual Studio 2019 with VB.net language based on proposed theoretical formulation to have a significant advantage of computers to analyze and design C-CFDST composite column loaded with axial load and biaxial bending moment as per Eurocode-4 [3].

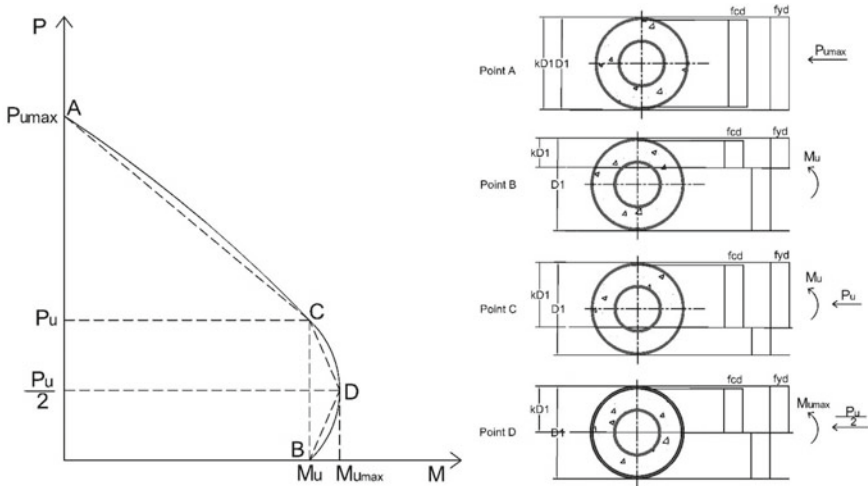


Fig. 1 Simplified interaction curve

2 Theoretical Formulation for Interaction Curve of C-CFDST Composite Column Section

2.1 Simplified Interaction Curve

Interaction curve helps in predicting the safety of a section against given applied design load and moment. Apart, one can recognize the types of failure well before the actual failure. The typical simplified interaction diagram is illustrated in Fig. 1 for C-CFDST composite column considering four illustrative positions of neutral axis. The overall behavior of interaction diagram of C-CFDST shows good matches with a well-established interaction diagram of composite concrete filled column (CFT).

2.2 Theoretical Formulation

Design of CFDST composite column may become accurate and economical if the P-M interaction curves have been plotted by considering various positions of neutral axis with minimal numbers of intervals. In present study, theoretical formulations for C-CFDST composite column is developed following plastic design method as discussed by Johnson [4] and considering neutral axis at various location within the section only. As plastic design method is employed, consideration of neutral axis outside the section will not affect P-M interaction curve, unlike the strain compatibility method suggested by ACI and AISC codes. Various positions of neutral axis may be considered within the section for developing representative equations.

At any one location of the plastic neutral axis in the cross section, axial load-carrying capacity and moment of resistance can be obtained. In this theoretical formulation, the position of plastic neutral axis is denoted as $kD1$, which is a distance from the extreme top fiber, is moving from $kD1 = D1$ (extreme bottom fiber) to the $kD1 = 0$ (extreme top fiber). Furthermore, limited numbers of longitudinal reinforcement bars have been considered in the theoretical formulation for the sake of ease. Based on the steel tubes and arrangement of longitudinal reinforcement bars, seven (07) different cases may arise for calculating the capacity of section at varying position of neutral axis, i.e., (i) $0 < D1 - kD1 \leq t1$; (ii) $t1 < D1 - kD1 \leq (D1/2 - D2/2)$; (iii) $(D1/2 - D2/2) < D1 - kD1 < D1/2$; (iv) $D1 - kD1 = D1/2$; (v) $D1/2 < D1 - kD1 \leq (D1/2 + D2/2)$; (vi) $(D1/2 + D2/2) < D1 - kD1 \leq (D1 - t1)$; (vii) $(D1 - t1) < D1 - kD1 \leq 0$. Generalized set of equations for various locations of plastic neutral axis in the range of $(D1/2 - Y1) < (D1 - kD1) \leq (D1/2 - Y2)$, as shown in Fig. 1, are illustrated.

From Fig. 2, one can calculate area of arc sector for any position of plastic neutral axis with the following equation:

$$\text{Area} = \int_{-R1 \sin \frac{\theta}{2}}^{R1 \sin \frac{\theta}{2}} \int_{R1 \cos \frac{\theta}{2}}^{\sqrt{R1^2 - x^2}} dy dx \tag{1}$$

$$\text{Area} = \frac{R1^2}{2} [\theta - \sin \theta]. \tag{2}$$

Moment of resistance due to arc sector can be calculated as

$$\sum W = \int_{-R1 \sin \frac{\theta}{2}}^{R1 \sin \frac{\theta}{2}} \int_{R1 \cos \frac{\theta}{2}}^{\sqrt{R1^2 - x^2}} y dy dx \tag{3}$$

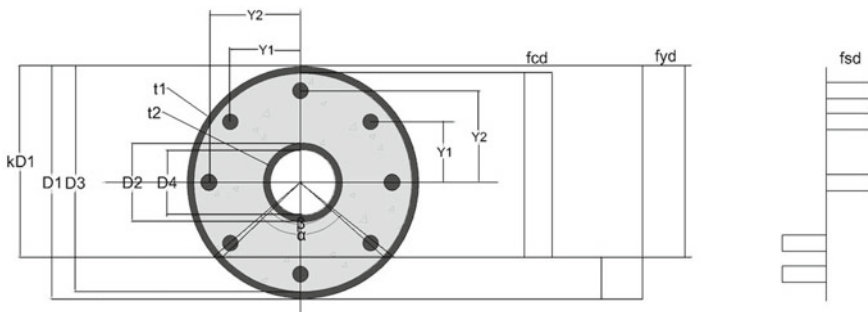


Fig. 2 Plastic neutral axis at $(D1/2 - Y2) < (D1 - kD1) \leq (D1/2 - Y1)$

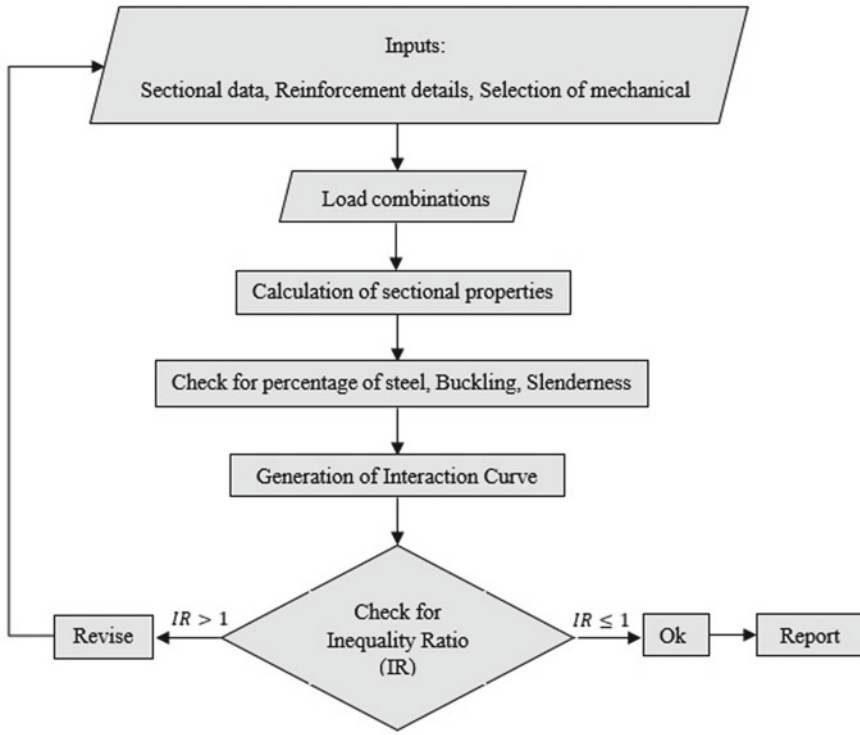


Fig. 3 Flowchart of software module of C-CFDST composite column

$$\sum W = \frac{2}{3} \times R1^3 \sin^3 \frac{\theta}{2}, \tag{4}$$

where

$D1, R1, t1$ = diameter, radius and thickness of outer steel tube, respectively; $D2, R2, t2$ = diameter, radius and thickness of inner steel tube, respectively; $Y1$ = distance between neutral axis and second outer most layer of reinforcement bar; $Y2$ = distance between neutral axis and outer most layer of reinforcement bar.

2.3 Stress Axis is at $(\frac{D1}{2} - Y2) < (D1 - kD1) \leq (\frac{D1}{2} - Y1)$

Compressive force due to steel tube

$$C1 = \frac{f_{yd}}{1000} \left[A_a - \frac{R1^2}{2}(\alpha - \sin \alpha) + \frac{R3^2}{2}(\beta - \sin \beta) \right]. \tag{5}$$

Compressive force due to longitudinal reinforcement

$$C2 = \frac{f_{sd}}{1000} \left[A_s - \frac{\pi}{4} \theta^2 \right]. \quad (6)$$

Compressive force due to concrete

$$C3 = \frac{f_{cd}}{1000} \left[A_c - \frac{R3^2}{2} (\beta - \sin \beta) \right]. \quad (7)$$

Tensile force due to steel tube

$$T1 = \left(f_{yd} \times \frac{A_a}{1000} \right) - C1. \quad (8)$$

Tensile force due to longitudinal reinforcement

$$T2 = \left(f_{sd} \times \frac{A_s}{1000} \right) - C2. \quad (9)$$

Moment of resistance due to steel tube

$$M1 = \frac{2f_{yd}}{10^6} \left[\frac{2}{3} R1^3 \sin^3 \frac{\alpha}{2} - \frac{2}{3} R3^3 \sin^3 \frac{\beta}{2} \right]. \quad (10)$$

Moment of resistance due to longitudinal reinforcement

$$M2 = \frac{2f_{sd}}{10^6} \left[\frac{\pi}{4} \theta^2 \times Y2 \right]. \quad (11)$$

Moment of resistance due to concrete

$$M3 = \frac{f_{cd}}{10^6} \left[\frac{2}{3} R3^3 \sin^3 \frac{\beta}{2} - \left(\frac{M2 \times 10^6}{f_{sd}} \right) \right]. \quad (12)$$

where

$$\alpha = 2 \cos^{-1} \left(\frac{kD1 - \frac{D1}{2}}{R1} \right), \quad \beta = 2 \cos^{-1} \left(\frac{kD1 - \frac{D1}{2}}{R3} \right) \text{ and } R3 = \frac{(D1 - 2t1)}{2}.$$

θ = diameter of longitudinal reinforcement bar; f_{yd} = yield stress of steel section; f_{sd} = yield stress of longitudinal reinforcement; f_{cd} = yield stress of concrete; A_a = area of steel tubes; A_s = area of longitudinal reinforcement bars; A_c = area of concrete section.

The axial load-carrying capacity P_u can be calculated by superimposing the compressive strength and tensile strength of steel tubes, concrete, and reinforcement bars as depicted

$$P_u = C1 + C2 + C3 - T1 - T2. \quad (13)$$

Similarly, the moment of resistance M_u can be obtained as

$$M_u = M_1 + M_2 + M_3. \quad (14)$$

In the absence of longitudinal reinforcement, the axial load and moment of resistance can be calculated as

$$P_u = C_1 + C_3 - T_1 \quad (15)$$

$$M_u = M_1 + M_3. \quad (16)$$

3 General Design Consideration for Software Module

The software module formed such that steel tube, concrete infill, and longitudinal reinforcement material is taken care in Indian context while considering other controlling stipulations as per Eurocode-4. To understand essential steps involved in design of C-CFDST composite column a flow chart as shown in Fig. 3 may be referred. It incorporates steel grades Yst310 to Yst500, concrete of strength classes M20 to M60 considering the materials compatibility as described by Liew et. al. [5]. It applies to isolated columns and compression members in framed structures where the other structural members are either composite or steel members. The steel contribution ratio should be between 0.2 and 0.9. The influence of local buckling of the steel section on the resistance is considered in the design. The longitudinal reinforcement that may be used in the calculation should not exceed 6% of the concrete area. The ratio of the depth to width of the composite cross section should be within limits 0.2 and 5.

3.1 Flowchart for Software Module of C-CFDST

3.2 Inputs of Sectional Details and Load Combinations

Figure 4 shows input tab for geometrical and mechanical features of the steel tube, longitudinal reinforcement, and concrete infill required to develop interaction curve and to calculate the capacity of a section of C-CFDST composite column section. Apart from this, Fig. 5 illustrates how one can input a wide range of various load combinations in a single run for which circular concrete filled double skinned tube column is required to be analyzed and designed.

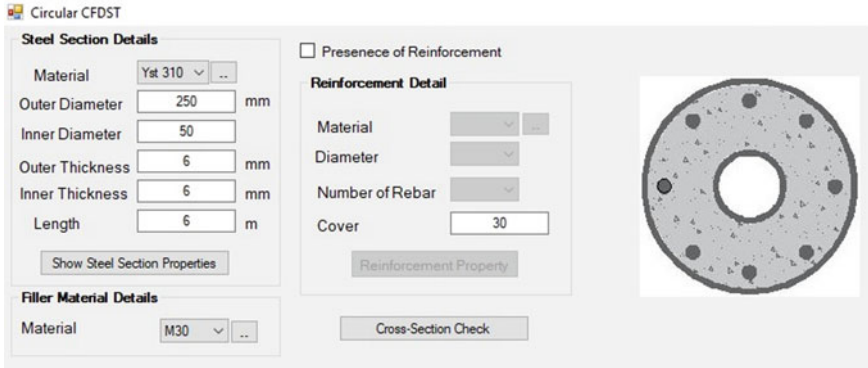


Fig. 4 Inputs of sectional details required for the C-CFDST composite column

Sr. No.	Case	Pu	Mux	Muy	MuxD	MuyD	MuxC	MuyC	I. Ratio	Check
1	Case-1	1200	60	50	60	50	121.4602	121.4602	0.9056	Safe
2	Case-2	500	40	10	40	10	136.483	136.483	0.3663	Safe
3	Case-3	1000	80	100	80	100	128.5979	128.5979	1.3997	Fail

Fig. 5 Load combination input from the structural analysis

3.3 Checks for Longitudinal Reinforcement, Local Buckling, and Slenderness

3.3.1 Check for Longitudinal Reinforcement

As illustrated in Fig. 6a and b, based on usage of reinforcement, composite column sections have been categorized in two means as follows: (a) C-CFDST without reinforcement; (b) C-CFDST with reinforcement.

As per clause 6.7.3 EN 1994 1-1:2004, the maximum percentage of longitudinal reinforcement has been limited to 6%. Percentage of the longitudinal reinforcement bars, P_t , can be calculated as



Fig. 6 a C-CFDST without reinforcement. b C-CFDST with reinforcement

$$P_t = \frac{A_s \times 100}{A_c}, \quad (17)$$

where

A_s Area of longitudinal bars.

A_c Area of concrete.

3.3.2 Check for Local Buckling

Under the axial compression, circular steel section can be susceptible to buckle locally. Eurocode-4 relates the local buckling of the steel section with its aspect ratio. Local buckling can be prevented by limiting the aspect ratio of steel section. The maximum limit for the aspect ratio has been given in Table 6.3 of EN 1994-1-1:2004, which can be given as

$$\max\left(\frac{D}{t}\right) = 90 \frac{235}{f_y}, \quad (18)$$

where

D = diameter of the outer steel section; t = thickness of outer steel section; f_y = yield stress of steel section.

3.3.3 Check for Slenderness

As per clause 6.7.3.3 of EN 1994-1-1:2004, relative slenderness is determined to obtain the strength reduction factor for the slender column. This reduction factor is only used to reduce the axial resistance of the composite column.

$$EI_{\text{eff}} = E_a I_a + E_s I_s + K_c E_c I_c. \quad (19)$$

Plastic resistance to compression based on the characteristic strength of materials, $N_{\text{pl,Rk}}$, can be given as

$$N_{\text{pl,Rk}} = (f_{ck} \times A_c) + (f_{yd} \times A_a) + (f_{cd} \times A_s). \quad (20)$$

Elastic critical normal force, N_{cr} , can be given as

$$N_{\text{cr}} = \frac{\pi^2 EI_{\text{eff}}}{L^2}. \quad (21)$$

Relative slenderness λ can be given as

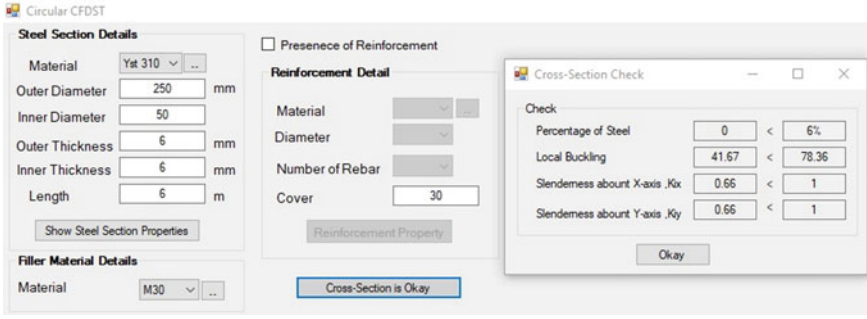


Fig. 7 Section check for the percentage of reinforcement steel, local buckling, and slenderness ratio about X-axis and Y-axis

$$\lambda = \sqrt{\frac{N_{pl,Rk}}{N_{cr}}} \tag{22}$$

$$\omega = 0.5[1 + \alpha(\lambda - 0.2) + \lambda^2]. \tag{23}$$

Reduction factor for the axial compression χ can be given as below which should be less than or equal to 1

$$\chi = \frac{1}{\omega + \sqrt{\omega^2 - \lambda^2}} \leq 1, \tag{24}$$

where

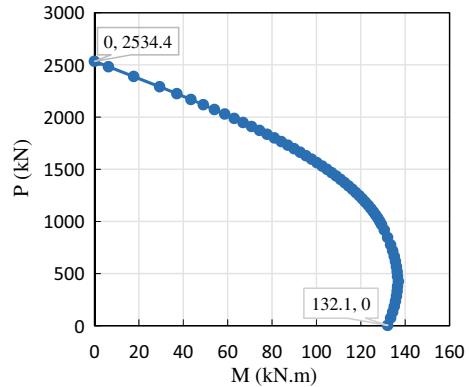
I_a = moment of inertia of steel section about both the axis; I_s = moment of inertia of longitudinal bars; I_c = moment of inertia of concrete; $E I_{eff}$ = effective flexural stiffness; $N_{pl,Rk}$ = characteristic value of the plastic resistance of the composite section to compressive normal force; N_{cr} = elastic critical normal force; λ = relative slenderness; χ = reduction factor; Kc = correction factor that should be taken as 0.6; L = length of the composite column; α = imperfection factor, which can be considered as 0.21 for buckling class a. Following the Eurocode stipulations checks for longitudinal reinforcement, local buckling and slenderness is incorporated in the software module as shown in Fig. 7.

3.3.4 Check for Inequality Ratio

Inequality ratio for the composite column subjected to the axial load with biaxial bending can be obtained as per the clause 6.7.3.7 of EN 1994-1-1:2004, which can be given as

$$\frac{M_{uxD}}{M_{uxL}} + \frac{M_{uyD}}{M_{uyL}} \leq 1, \tag{25}$$

Fig. 8 P-M interaction curve for defined section



where

M_{uxD} Design moment of the composite column about x -axis.

M_{uyD} Design moment of the composite column about y -axis.

M_{uxL} Moment of resistance for the acting axial load, P_u , about x -axis.

M_{uyL} Moment of resistance for the acting axial load, P_u , about y -axis.

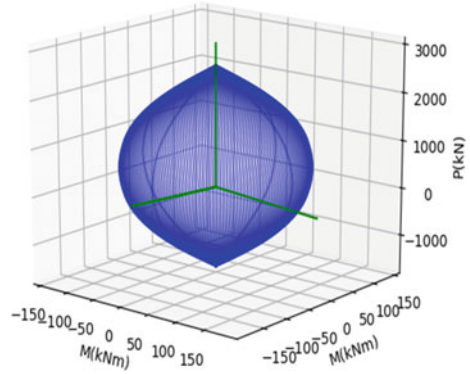
3.4 P-M Interaction Curve

An illustrative P_u - M_u interaction curve has been plotted as shown in Fig. 8 by considering outer steel tube of 250 mm diameter and 6 mm thick, inner steel tube having diameter 50 mm and 6 mm thickness, and steel grade of Yst310 for both tubes. The void in between two concentric steel tubes has been filled with concrete of M30 grade. Furthermore, author has attempted to generate 3D bulb of P_u - M_u interaction curve by varying the inclination of plastic neutral axis in interval of 2° as depicted in Fig. 9.

4 Conclusions

In the present study, the theoretical formulation has been developed to design the concrete filled double skinned tube (CFDST) composite column of circular shape by following a simplified plastic method of design. The simplified approach given by Eurocode-4 predicts only four points to generate interaction curve to design composite columns like concrete filled tube (CFT), which may lead to inaccurate and conservative results. Furthermore, as the analysis and design of composite column sections are tedious and time consuming, an attempt has been made to develop a computer software module to design C-CFDST with confidence within a stipulated

Fig. 9 Three-dimensional (3D) bulb of P-M interaction curve for C-CFDST at an interval of $\theta = 2^\circ$



time specifically for the steel sections available in the Indian construction industry as per EN 1994-1-1:2004 (Eurocode-4). A developed software module can be utilized to analyze and design C-CFDST composite column loaded with axial load and biaxial bending moment as per Eurocode-4. The software module provides comprehensive design flexibility to users for checking the design capacity under variety of load and moment resistance in a single run. A computer program can generate detailed output reports as well as graphs. P-M interaction curves derived using plastic method-based formulations are validated through standard cases that show good agreement.

References

1. IS 11384 (2022) Code of practice for composite construction in structural steel and concrete. New Delhi, 2022
2. Patel A, Sheth R (2020) Development of design aid for non-rectangular reinforced concrete column - C Shape. Technology drivers: engine for growth. CRC PRESS, Ahmedabad, India, pp 159–163
3. EN 1994-1-1 (2004) Eurocode 4: Design of composite steel and concrete structures – Part 1-1: General rules and rules for buildings. Commission of European Communities
4. Johnson RP (2004) Composite structures of steel and concrete. Wiley
5. Richard Liew JY, Xiong M-X, Lai B-L (2021) Design of steel-concrete composite structures using high-strength materials. Woodhead Publishing.

Effect of Initial Imperfections on the Ultimate Axial Compressive Strength of Concrete Filled Steel Tubular Long Columns



Mashudha Sulthana and Arul Jayachandran

Abstract Any deviation from the expected shape and dimension of a steel member before loading is ascribed as an initial imperfection. They are formed in steel components during the manufacturing process, transportation, handling, fabrication etc. Traditionally, they are considered as a significant parameter in determining the actual capacity of slender steel members. International codes like AISC-360 and EC3 has prescribed column curves which includes the effect of initial imperfections in finding the global stability reduction factor for steel column design. A half-sine column profile with a maximum deviation of $L/1500$ and $L/1000$ are used as the initial global imperfections in the development of column curves as per AISC-360 and EC3, respectively. Similar design philosophy is adopted for concrete filled steel tubular long columns in AISC-360 and EC4. However, the experimental data available in literature for concrete filled steel tubular long columns is varying on comparison with code predictions. In this study, the axial compressive capacities of eighteen hollow and concrete filled steel tubular (CFST) long columns tested by the authors is correlated with the initial profile and magnitude of imperfections measured in the steel tubes before the commencement of tests. The axial test capacities of the specimens are around 30% higher than the code predictions. The initial double curvature (full-sine) profile of the steel tubes with very low magnitude in the bow imperfection has triggered concrete confinement in the CFST long columns, which lead to over-strength in the test specimens. Finite element model is developed using ABAQUS to comparatively study this phenomenon and the ultimate load. From this study, it is evident that the initial imperfections have higher significance on the axial behavior of CFST long columns than the hollow steel tubular columns.

Keywords Long columns · Initial imperfection · Composite columns · Column buckling · Concrete confinement · Axial capacity

M. Sulthana (✉) · A. Jayachandran
Department of Civil Engineering, Indian Institute of Technology Madras, Chennai, India
e-mail: mashudha@gmail.com

A. Jayachandran
e-mail: aruls@iitm.ac.in

© The Author(s), under exclusive license to Springer Nature Singapore Pte Ltd. 2023
M. Madhavan et al. (eds.), *Proceedings of the Indian Structural Steel Conference 2020*
(Vol. 2), Lecture Notes in Civil Engineering 319,
https://doi.org/10.1007/978-981-19-9394-7_8

1 Introduction

Since the inception of inelastic column buckling by Engesser in 1889, which demonstrated the deviation of equilibrium state in an axially loaded column above the proportionality limit (in the stress–strain plot), the initial imperfection factors have been considered carefully in the experimental studies of steel column buckling [1]. Shape and magnitude of initial out-of-straightness of the specimens, unavoidable eccentricity in loading, manufacturing process that develops residual stresses etc. have claimed to decrease the actual axial capacity from the predicted buckling loads (Bjorhovde 1972). These imperfection factors are taken into account in the development of column curves that are based on tangent modulus concept. While most of the international standard prescribes multiple column curves (EN1993-1-1 2005 etc.), which are classified according to steel grade, manufacturing process, bending axis and type of cross-section, ANSI/AISC 360(16) gives a unified column curve for design simplicity. The same column curves are used for the design of concrete filled steel tubular (CFST) long columns. Concept of effective tangent modulus is adopted to account for the concrete contribution in the global buckling resistance of the CFST columns. Experimental studies on the CFST long column buckling has confirmed the applicability of the effective tangent modulus method of design [Eq. (1)] with reasonable accuracy (Gardner and Jacobson 1967; Kato 1996; Knowles and Park 1969). A reduction factor is prescribed by design standards in the effective stiffness (EI_{eff}) calculation as shown in Eq. (2), to account for concrete stiffness degradation towards the column buckling. The concrete stiffness reduction factor (C_3) as per ANSI/AISC 360(16) is given in Eq. (3), as a function of steel area ratio of the cross-section, whereas, a blanket value of 0.6 is recommended in EN 1994-1-1 [2].

$$P_{cr} = \pi^2 \frac{EI_{\text{eff}}}{L^2} \quad (1)$$

$$EI_{\text{eff}} = E_s I_s + C_3 E_c I_c \quad (2)$$

$$C_3 = 0.45 + 3 \left(\frac{A_s}{A_g} \right) \leq 0.9 \quad (3)$$

The experimental results from the axial compression test conducted by Galambos and Surovek [3] and Perea [4] for long column CFST are quite different from the analytical results based on Eqs. (1)–(3). The critical buckling loads of test specimens in Galambos and Surovek [3] are about 30% higher than the code capacity equations. Increase found in the test capacity is attributed to higher reliability of design expressions used for predicting the long column CFST axial strength [5]. Similar disparity between the test capacities and analytical predictions are observed in the axial compression tests conducted by Perea [4]. Unlike [3], the various test uncertainties associated with CFST long column like friction in the test crevices, magnitude of initial imperfection, and confinement effect are stated as the reasons of the higher

test loads in Perea [4]. In fact, Eq. (3) has been developed [6] based on the test results by Perea [4]. However, according to the authors, a rational explanation on the test capacities as high as 30% from the analytical predictions is still not addressed in the literature.

Recently, the axial compression tests conducted on concrete sandwiched double steel tubes (CSDST, a variant of CFST) by the first author [7] report test axial capacities that are higher than the analytical predictions. The test results viz., axial capacities, axial load versus lateral displacements and strains are studied in conjunction with the initial profile of the test specimens. The test results have given interesting insights regarding the initial profile of the test specimens and the increased axial capacities. Therefore, the observations from the study related to the influence of initial imperfections are reported in this paper. Results from the numerical models developed in ABAQUS are also presented to comparatively study the behavior of test specimens and interpret their results.

2 Test Specimens and Initial Imperfections

Experiments are primarily conducted to study the axial buckling behavior of concrete sandwiched double steel tubular long columns (CSDST) comparatively with the buckling behavior of CFST. In the code specified method for CFST, effective stiffness (EI_{eff}) is taken as the summation of the stiffness of steel and concrete components with reduction factors applied to the concrete contribution. The extension of this method to CSDST requires an in-depth investigation, as the hollowness in CSDST changes the nature of concrete stress state compared to CFST ([8]; Uenaka et al. 2010; Wei et al. 1995). The experimental studies found in the literature so far on the long column behavior of CSDST (Essopjee and Dundu 2015; Romero et al. 2015; Tao et al. 2004) have reported a lesser buckling load in CSDST on comparison with code equations. Whereas, some of the test results on its contemporary cross-sections, namely, CFST has higher strength compared to code equations. This leads to an extensive study in understanding the buckling load of CSDST in conjunction with the initial imperfection profiles. Therefore, the axial compression tests conducted by the first author on long column CSDST are reported here, and assessed along with numerical studies, in order to get a complete mechanism in the global buckling of long column CSDST.

2.1 Test Specimens

The geometric properties of eighteen specimens selected for the test including hollow steel tube, CFST and CSDST are listed in Table 1. The cross-sections selected for the study are shown in Fig. 1. The length to width ratio (slenderness) is selected such that the specimen fails in global buckling. The cross-sectional dimensions are chosen to

avoid local buckling and a subsequent local–global interaction. There are nine square and nine circular specimens. Hollow steel tube is included in both square and circular types to compare its buckling behavior with CFST and CSDST. The average yield strength of the square and circular tube is 400 N/mm^2 and 520 N/mm^2 , respectively (as found from coupon test). Two types of concrete strength are used for filling the tubes, 40 N/mm^2 and 80 N/mm^2 . The 28-day mean compressive strength of the specimens are presented in Table 1.

2.2 Initial Imperfection Profile

As mentioned in the previous section, for long columns, initial imperfection is an important parameter that influences the ultimate axial capacity of slender columns. Therefore, initial profile of the specimens is measured before the commencement of loading. The specimens are placed on a lathe bed, which is almost perfectly straight, and the initial imperfection of the specimens along the length (global imperfection) is measured using a laser beam with an accuracy of 0.1 mm. The sample initial imperfection profile of a circular and square steel tube is shown in Fig. 2. The steel tubes make a double curvature profile (when the ends were held in position), and the magnitude of bow is in the order of $L/6000$, which is very low compared to the imperfection considered in design codes ($L/1000$) like EC4 etc.

2.3 Axial Compression Capacity

The maximum axial compressive strength of the specimens found from the experiment is shown in Table 2. The test capacities are compared with [9] and [2] based axial capacity equations. Over strength is observed in the test axial capacity (P_{test}) of the specimens when compared to code based equations. Square specimens gives an over strength of about 15% except SS-70-40 that had concreting issues. Circular specimens have an over strength of around 30% for normal strength and 18% for high strength concrete, except C-0-80 and CC-20-80 that are subjected to minor bent during shifting process. Strictly speaking, over strength of the above mentioned magnitude is not possible in long columns as the actual strength will be less than the critical buckling load. However, this phenomenon has also been observed in few other test data reported in literature on the long column behaviour of concrete filled steel tubes [3, 10, 11]. Galambos and Surovek [3] has regarded the axial capacity prediction by code recommendations as conservative, and thereby higher reliability is marked for these predictions [5]. Perea et al. [10] and Xiong et al. [11] have discussed on the impracticality of the long column over strength and corrected the raw test data by considering frictional resistance at the supports. Perceiving these reports, the friction effects are minimized in the present experiment by applying grease in the roller bar. In spite of it, the over strength is found in the tests, which is in fact a multi-factor

Table 1 Geometric and material properties of the specimens

Sp. ID	Nominal size		Measured size					
	Outer tube	Inner tube	D_o	t_o	D_i	t_i	L	f_{cm}
	(mm)	(mm)	(mm)	(mm)	(mm)	(mm)	(mm)	(N/mm ²)
S-0	150 × 150 × 6	–	150	6.08	–	–	3600	–
S-0-40	150 × 150 × 6	–	150	6.08	–	–	3600	51.28
SS-20-40	150 × 150 × 6	32 × 32 × 2	150.65	6.16	32	2	3600	51.28
SS-50-40	150 × 150 × 6	72 × 72 × 4	150.62	6.12	72.22	4	3600	54.83
SS-70-40	150 × 150 × 6	100 × 100 × 4	149.88	6.08	100.3	4.06	3600	57.5
S-0-80	150 × 150 × 6	–	150.32	6.1	–	–	3600	54.17
SS-20-80	150 × 150 × 6	32 × 32 × 2	151.05	6.1	32	2	3600	89.02
SS-50-80	150 × 150 × 6	72 × 72 × 4	150.35	6.14	72.52	3.96	3600	84.95
SS-70-80	150 × 150 × 6	100 × 100 × 4	149.98	6.08	100.3	3.94	3600	87.25
C-0	NB-150 × 5.4	–	166.06	5.18	–	–	3150	–
C-0-40	NB-150 × 5.4	–	166.06	5.18	–	–	3600	58.61
CC-20-40	NB-150 × 5.4	NB-25 × 4	166.34	5.24	33.7	4	3600	57.94
CC-50-40	NB-150 × 5.4	NB-65 × 3.6	166	5.04	76.66	3.58	3600	55.5
CC-70-40	NB-150 × 5.4	NB-100 × 5.4	165.84	5.06	114.1	5.2	3600	60.61
C-0-80	NB-150 × 5.4	–	166	5.22	–	–	3600	84.95
CC-20-80	NB-150 × 5.4	NB-25 × 4	166.36	5.22	33.7	4	3600	84.95
CC-50-80	NB-150 × 5.4	NB-65 × 3.6	165.86	5.24	76.74	3.58	3600	85.47
CC-70-80	NB-150 × 5.4	NB-100 × 5.4	166.32	5.24	114.2	5.22	3600	84.36

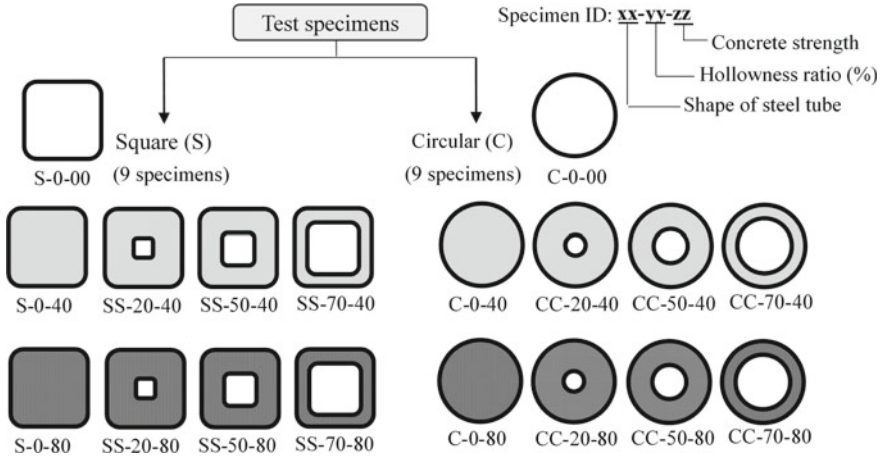


Fig. 1 Cross-sections of test specimens

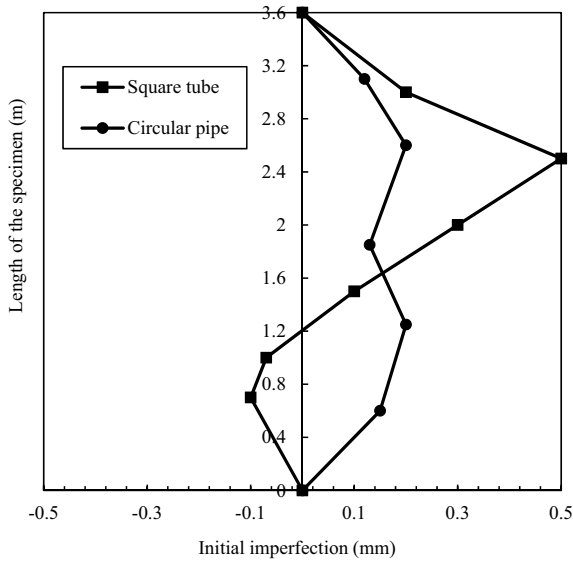


Fig. 2 Initial imperfection profile of a circular and square cross-section

effect. The predominant factor for over strength in this study is contemplated as the initial imperfection profile of the specimen and concrete confinement.

On assessing the initial imperfection profile of the test specimen, it is found that the placement of an initially out-of-plumb steel tube between the roller bars rearranges into a full-sine wave as shown in Fig. 3. A hollow steel tube with full-sine wave as initial imperfection shape ultimately buckles as half-sine wave at failure, and the

Table 2 Test capacity of the specimens compared with code equations

Sp. ID	P_{test} (kN)	P_{EC4} (kN)	P_{AISC} (kN)	$P_{\text{EC4}}/P_{\text{test}}$	$P_{\text{AISC}}/P_{\text{test}}$	χ_{test}	χ_{EC4}	χ_{AISC}
S-0	1016	1061	1026	1.04	1.01	0.72	0.75	0.73
S-0-40	1801	1504	1460	0.84	0.81	0.83	0.69	0.67
SS-20-40	1694	1550	1509	0.92	0.89	0.75	0.69	0.67
SS-50-40	1750	1646	1614	0.94	0.92	0.71	0.67	0.66
SS-70-40	1568	1673	1637	1.07	1.04	0.64	0.68	0.67
S-0-80	1682	1525	1481	0.91	0.88	0.76	0.69	0.67
SS-20-80	1901	1750	1732	0.92	0.91	0.68	0.62	0.62
SS-50-80	1998	1753	1732	0.88	0.87	0.73	0.64	0.63
SS-70-80	1959	1735	1702	0.89	0.87	0.75	0.67	0.66
C-0	885	989	958	1.12	1.08	0.66	0.74	0.72
C-0-40	1726	1308	1317	0.76	0.76	0.76	0.58	0.58
CC-20-40	1557	1352	1373	0.87	0.88	0.64	0.56	0.57
CC-50-40	1771	1341	1363	0.76	0.77	0.74	0.56	0.57
CC-70-40	1803	1503	1532	0.83	0.85	0.67	0.56	0.57
C-0-80	1548	1411	1443	0.91	0.93	0.58	0.53	0.54
CC-20-80	1496	1443	1485	0.96	0.99	0.53	0.51	0.53
CC-50-80	1705	1456	1496	0.85	0.88	0.61	0.52	0.54
CC-70-80	1899	1588	1624	0.84	0.86	0.65	0.55	0.56

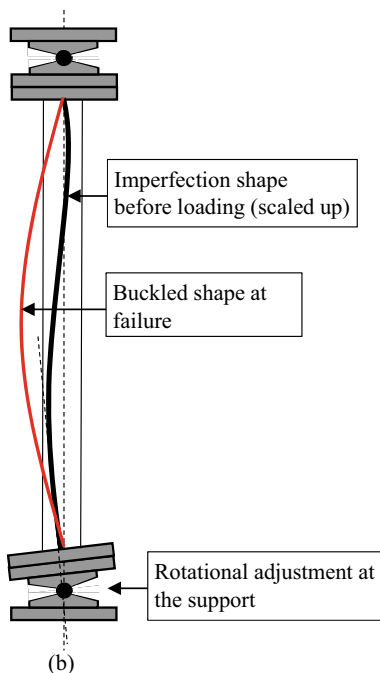
failure load is not greater than the critical buckling load [1]. However, this theory does not hold good for concrete filled steel tubes. The concrete undergoes confinement at the snapping point (i. e. full-sine wave to half-sine wave transformation) towards failure. The occurrence of concrete confinement is further discussed in the following sections.

3 Numerical Study

3.1 Comparison of Test and FE Results

Numerical study is performed using ABAQUS-v6.14 and compared with test results to confirm the presence of concrete confinement and the eventual over-strength effect. The initial imperfection shape of the test specimens is full-sine wave, which snapped to half-sine wave towards failure. Numerically it is simulated by incorporating the first two fundamental modes of buckling (1st—half-sine wave; 2nd—full-sine wave) in the model. Buckling analysis is performed before static analysis to incorporate the initial imperfections. A scale factor of $L/3000$ is considered as the magnitude of 2nd mode of buckling (primary profile from Fig. 2) and 1/10th its value is given for first

Fig. 3 Profile of the test specimen before loading and at failure condition



mode (as shown in Fig. 4). Imperfection is assigned only for the outer steel tube and over-closure pressure is invoked at the steel–concrete interface. The steel tubes and concrete are modelled using shell (S4R) and solid (C3D8R) elements, respectively for the measured geometric properties in Table 1. Elements are meshed in sizes less than 1/13th of the steel tube width [8], and care is taken to avoid element distortion. Loading and boundary conditions are invoked at end plates that are modelled using C3D8R element. Young’s modulus and Poisson’s ratio of 2×10^7 N/mm² and 0.0001 respectively is assigned to the end plates to facilitate complete load transfer to the specimen with negligible end plate deformation. Tie constraint is used to simulate the weld connection between the end plates and the specimen. Surface-to-surface contact property is used to define the compatibility between the steel tubes and concrete infill. A penalty friction coefficient of 0.25 is assigned in the tangential direction [12], and *hard contact* is assigned in the normal direction. Displacement-controlled loading and pinned boundary conditions (restraining x , y and z translations at base; and x and y translation at loading end) are assigned along the central line of end plates to simulate the test conditions. STATIC-GENERAL solver is used for analysis with *CONTACT CONTROL command to avoid convergence issues. The material model selected is explained in Mashudha Sulthana [7].

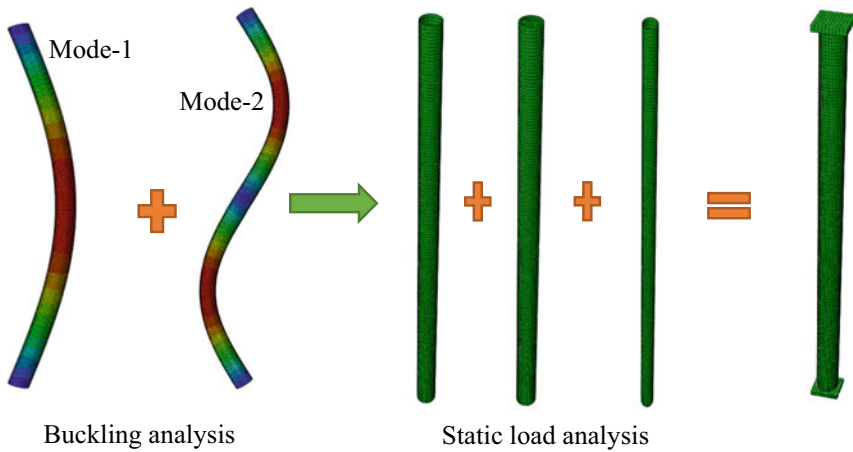


Fig. 4 Simulation of initial imperfection in the present model

3.2 Effect of Initial Imperfection in Ultimate Load

The test and numerical behavior comparison of selective specimens (extreme parameters) namely, CC-70-40 and CC-20-40 are explained here for brevity. The axial compressive load versus lateral deflection curves at the mid-height are presented in Figs. 5 and 6 for the selected specimens. The numerical model where mode-1 alone is considered for initial imperfection (CC-70-40-FE1 and CC-20-40-FE1) has matching initial stiffness with the test results. However, the ultimate axial capacities are not the same. These load values are closer to the code predictions, with no over strength effects. Nevertheless, when mode-2 is simulated as the primary initial imperfection (as measured in the experiment), numerical behavior prediction (CC-70-40-FE2; CC-20-40-FE2) is in good agreement with the test results. The mode transformation or snapping of the specimen profile has become an essential condition for failure, and it has increased the ultimate failure load by delaying the buckling. Further, concrete confinement has occurred during the mode transformation. It should be noted that the hollow steel test specimens (S-0; C-0) which have similar initial imperfection do not exhibit increase in the axial load capacity as explained by Galambos and Surovek [1]. Therefore, this phenomenon is specific to concrete filled steel tubes and it increases the sensitivity of overall (global) initial imperfections on the buckling load of these columns.

Fig. 5 Axial load versus lateral displacement comparison (CC-70-40)

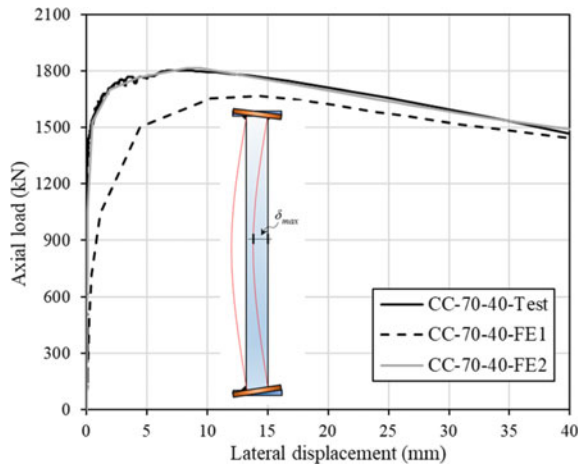
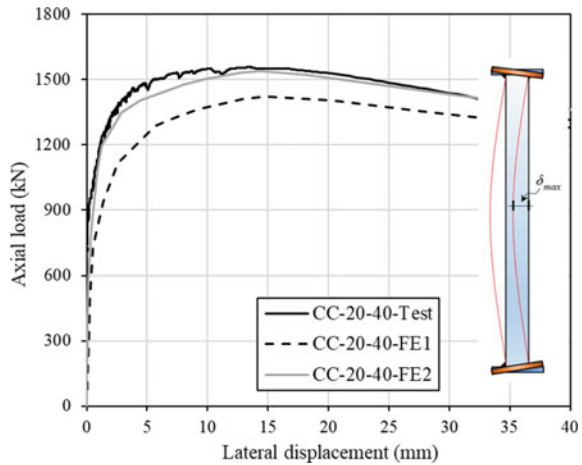


Fig. 6 Axial load versus lateral displacement comparison (CC-20-40)



4 Summary and Conclusions

Experimental results of the axial compression test conducted on concrete filled steel tubular long columns are assessed in this paper. The initial imperfection profile of the test specimen is found to be influencing the ultimate axial capacity of the long column concrete filled steel tubular specimens. The magnitude and shape of the initial profile has greater influence on concrete filled long columns compared to hollow steel tubes. In this test, the initial profile is a full-sine curve rather than a half-sine (which is considered in design codes). The transformation in the specimen profile delays the buckling, leading to concrete confinement action. The phenomenon is also studied numerically.

The over-strength in axial compressive tests is generally considered as higher confidence level in the design equations. However, this is not always true as the test result has to be assessed in conjunction with the initial imperfection and the associated confining effects in the case of concrete filled steel tubular long columns.

References

1. Galambos, T. V. and Surovek, A. E. (2008) *Structural Stability of Steel: Concepts and applications for structural engineers*.
2. EN 1994-1-1 (2004) Eurocode 4 : Design of composite steel and concrete structures Part 1-1 : General rules and rules for buildings, European Committee for Standardization. doi: <https://doi.org/10.1680/dgte4.31517>.
3. Han L-H (2000) Tests on Concrete Filled Steel Tubular Columns with High Slenderness Ratio. *Adv Struct Eng* 3(4):337–344. <https://doi.org/10.1260/1369433001502265>
4. Perea, T. (2010) *Analytical and Experimental Study on Slender Concrete-Filled Steel Tube Columns and Beam-Columns (PhD Thesis)*. Georgia Institute of Technology.
5. An Y-F, Han L-H, Zhao X-L (2012) Behaviour and design calculations on very slender thin-walled CFST columns. *Thin-Walled Structures* 53:161–175. <https://doi.org/10.1016/j.tws.2012.01.011>
6. Denavit MD et al (2016) Stability Analysis and Design of Composite Structures. *Journal of Structural Engineering (ASCE)* 142(3):1–12. [https://doi.org/10.1061/\(ASCE\)ST.1943-541X.0001434](https://doi.org/10.1061/(ASCE)ST.1943-541X.0001434)
7. Mashudha Sulthana, U. (2018) *Concrete-sandwiched double steel tubes under axial compression (PhD Thesis)*.
8. Tao Z, Wang Z, Yu Q (2013) Finite element modelling of concrete- filled steel stub columns under axial compression. *J Constr Steel Res* 89:121–131. <https://doi.org/10.1016/j.jcsr.2013.07.001>
9. ANSI/AISC (2016) ‘Specification for Structural Steel Buildings’.
10. Perea T et al (2013) Full-scale tests of slender concrete-filled tubes: Interaction behavior. *J Struct Eng* 139(7):1249–1262. [https://doi.org/10.1061/\(ASCE\)ST.1943-541X.0000784](https://doi.org/10.1061/(ASCE)ST.1943-541X.0000784)
11. Xiong M, Xiong D, Liew JYR (2017) Behaviour of steel tubular members in filled with ultra high strength concrete. *J Constr Steel Res* 138:168–183. <https://doi.org/10.1016/j.jcsr.2017.07.001>
12. Hu H et al (2003) Nonlinear Analysis of Axially Loaded Concrete-Filled Tube Columns with Confinement Effect. *Journal of Structural Engineering (ASCE)* 129(10):1322–1329. [https://doi.org/10.1061/\(ASCE\)0733-9445\(2003\)129:10\(1322\)](https://doi.org/10.1061/(ASCE)0733-9445(2003)129:10(1322))

Finite-Element Modelling of Double Plate Flat Composite Shear Wall Under Lateral Load



R. Senthilkumar, M. Karthikeyan, and Sneha Liya George

Abstract This paper presents the behaviour and validation of finite-element modelling of double plate flat composite shear wall system subjected to static shear load with experimental results. A flat composite shear wall specimen was tested under static shear load. It is observed in the experiment that the failure of the composite shear wall is due to the buckling of cold-formed steel at the bottom of the compression side of the composite shear wall followed by cracks on the tension side of the exposed concrete surface. The experimental results are validated by numerical modelling of the composite shear wall using the finite-element package. A parametric study is carried out to find the effect of the number of shear studs (spacing of shear studs), yield strength of steel and compressive strength of concrete on the behaviour of the double flat plate composite shear wall. It is found that the load carrying capacity of walls is increased with decrease in spacing of shear studs.

Keywords Composite shear wall · Finite-element modelling · Cold form steel · Shear studs

1 Introduction

A conventional shear wall is a reinforced concrete structural member with dense layers of reinforcement and mainly functions as a lateral load resisting system against earthquakes and wind forces. The heavy quantity of reinforcement decreases the ease in constructability of the structure and increases the weight of the structure which in turn increases the lateral force which acts on it. An innovation over this reinforced concrete shear wall is the composite shear wall which has concrete infill sandwiched

R. Senthilkumar · M. Karthikeyan · S. L. George (✉)
Department of Civil Engineering, NIT, Tiruchirappalli, Tamil Nadu, India
e-mail: 203218027@nitt.edu

R. Senthilkumar
e-mail: senthilr@nitt.edu

© The Author(s), under exclusive license to Springer Nature Singapore Pte Ltd. 2023
M. Madhavan et al. (eds.), *Proceedings of the Indian Structural Steel Conference 2020* (Vol. 2), Lecture Notes in Civil Engineering 319,
https://doi.org/10.1007/978-981-19-9394-7_9

between two steel sheets. The idea behind this composite shear wall initially originated from using profiled sheets in floor structures [1]. There are different kinds of composite shear walls where the sheets are found on both sides of the shear wall [2–9] or only on one side of the wall [9] or even where the steel sheet is embedded in the concrete [10]. One of the main advantages of the composite shear wall is that the use of the steel sheet acts a permanent formwork during its construction. The steel sheets which also act as bracing to the concrete infill help in the increase of the buckling capacity. The prevention of buckling by increasing the composite action will thus ensure the failure of the wall by yielding rather than by buckling. The lateral loads are resisted by the combined action of both the steel sheets and concrete. Studies have been conducted on the composite shear wall to understand about the contributions of the steel plates and concrete separately to the overall ultimate load carrying capacity [11]. In a steel shear wall, the story shear is due to the action of tension field followed by buckling of diagonal due to compression. In a composite shear wall, the concrete wall constraints the steel plate and prevents its buckling before the initiation of yielding. Thus, the steel plate opposes the story shear by yielding in shear. The shear yield limit of steel plate can be essentially more prominent than its ability to oppose shear in yielding of diagonal tension field. The composite action between these is ensured by the usage of shear studs, battens, vertical stiffeners, etc. The bond between the steel sheets and concrete determines the composite action which mainly depends upon the type and the number of shear connectors used [12, 13]. Even though composite system has many advantages, the studies on the same are very limited. In this study, an experimental work on flat cold-formed steel concrete composite wall was carried out to find the behaviour of system, and finite-element model was developed to do the parametric study.

This paper presents the plan and validation of the finite-element model to reproduce the behaviour of the cold-formed steel–concrete composite shear wall dependent on experimental results. Finite-element models were created utilizing the ABAQUS/CAE finite-element programming and validated by the experimental outcomes. Parametric study was completed to research the impact of evaluation of steel, concrete strength and the number of intermediate fasteners. [1, 5–8, 13–18].

2 Experimental Set Up

2.1 Test Matrix

The experimental set up consists of a reaction frame along with a base frame as shown in Figs. 1 and 2. The composite shear wall was attached to the base frame through a steel foundation block using 12 numbers of 16 mm diameter bolts. The load path of the system is in such a way that the loads which come on the wall should be transferred to the base frame on which the reaction frame is mounted. Each connection is designed so that it can transfer, or support, a specific type of load or loading conditions. The

Fig. 1 Schematic diagram of experimental set up

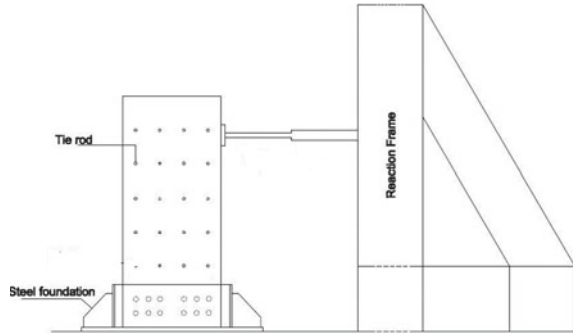


Fig. 2 Experimental set up



connection between the shear wall and foundation is designed based on direct shear and torsional shear application due to lateral load applied at the top end of the shear wall. The foundation block and bolts were designed to resist the shear and moment developed due to applied load. The dimensions of the wall specimen are 425 mm wide and 1250 mm high which are fixed based on laboratory facilities. The thickness of the concrete infill is 125 mm, and the flat cold-formed sheets on either side of the concrete are of 1 mm thickness. Intermediate fasteners were provided along the height and width of the wall to act as shear connectors to increase the composite action between its components. A total number of 24 intermediate fasteners is provided in six rows at a spacing of 110 mm c/c. A hydraulic jack of 200 kN capacity, attached to the side of the reaction frame, was used to apply the static shear load to the wall.

2.2 Material Testing

Tension coupon test was performed on specimens with standard dimensions as per codal provisions of ASTM E 8M-04 [19]. The cutting of mild steel specimen for

Table 1 Material properties of cold-formed steel

Material properties	Cold-formed steel
Young's modulus, Mpa	190,000
Average yield stress, MPa	138
Yiel strain in %	0.78%
Ultimate strain in %	35.5%

tensile coupon was done by EDM wire cutting machine. The material properties of the cold form steel are given in Table 1.

The 28th-day results of the compressive strength test on control cube specimens gave an average compressive strength of concrete as 44.5 MPa, and the split tensile strength tests carried out on the cylinder specimens gave an average split tensile strength of concrete as 4.37 MPa.

2.3 *Fabrication, Casting, Instrumentation and Testing of Composite Shear Wall*

For the fabrication of the wall, a flat wooden board bigger than the dimensions of the steel plate was positioned underneath the steel sheets and the sheets which were positioned face to face were aligned and fixed at all four corners by using four vice-grips pliers. A drill bit was used to make the holes for the intermediate fasteners, whereas a steel hole saw was used for the bigger bolts. While casting, to seal the gap between the sheets, flattened sheets were placed on both the sides and tightened with the steel wires at a spacing of 10 cm along its height. The wall was cast vertically and compacted using needle vibrator (Fig. 3).

Fig. 3 Fabrication and formwork of composite shear wall



Fig. 4 Location of LVDTs on composite shear wall



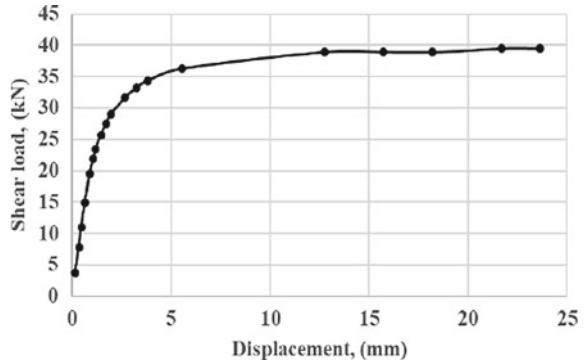
Three LVDTs were used to measure linear displacement which are named as LVDT-1, LVDT-2 and LVDT-3 as shown in Fig. 4. LVDT-1 was placed at the top of the wall to measure the top displacement, and LVDT-2 was placed at the bottom to ensure about the zero displacements of the foundation block. LVDT-3 was used to measure the out of plane displacement and positioned behind the shear wall. The locations of the LVDTs are as shown in Fig. 4. A hydraulic jack of 200 kN was attached to the reaction frame to apply static load to the wall by force-controlled method. A proving ring of 500 kN capacity was placed between the hydraulic jack and the wall.

3 Experimental Results and Discussions

The lateral load versus displacement response of the cold-formed steel–concrete composite shear wall was plotted in Fig. 5.

The initial stiffness of the composite shear wall was found to be 24.59 kN/mm. The ultimate lateral and maximum deflection of the composite shear wall was 39.42 kN and 23.62 mm, respectively. The cold-formed steel concrete specimens failed due to buckling of cold-formed steel at the bottom of the compression side of the composite shear wall followed by cracks on the tension side of the exposed concrete surface. The buckling of cold-formed steel plate started at 29.02 kN and cracks on the tension side of the exposed concrete surface started at 31.61 kN. High ductility was observed in the cold-formed steel–concrete composite shear wall. The portion of the concrete surface in and around the loading area was crushed due to the stress concentration at the loading area. LVTD 2 was kept at the foundation block in the direction of load,

Fig. 5 Load versus displacement graph



and it was observed zero displacements throughout the testing of the composite shear wall.

The displacements obtained experimentally were found to be far more than the expected displacements. This can be mainly attributed towards the failure that was seen surrounding the foundation block of the set up. Apart from the local buckling behaviour observed at the foot of the wall on the compression side of cold-formed sheet under the applied static shear load, the concrete in that region was found to be crushed under compression as shown in the Fig. 6. However, on the tension side of the wall, the sheet was torn around the bolt holes in the bottom area (as shown in Fig. 7) by bearing against the foundation block due to tensile forces acting on it. All these factors contributed towards the unexpected increase in the horizontal displacement of the wall and hence it is failure.

Fig. 6 Buckling of sheets and crushing of concrete at the base of the wall on the compression side



Fig. 7 Tearing of sheet due to bearing of foundation bolts



4 Finite-Element Modelling

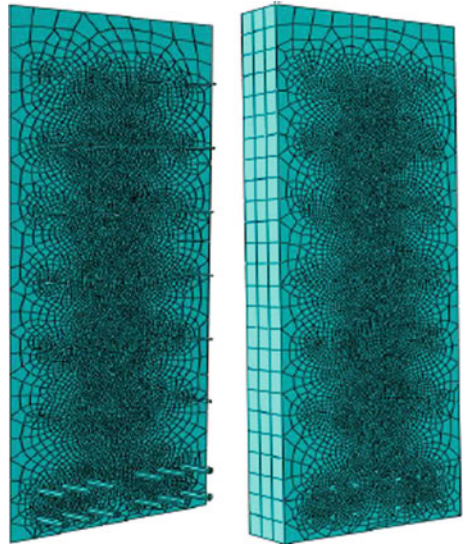
4.1 *Parts, Meshing, Element Assignment and Contact Surfaces*

The finite-element model consists of two instances, i.e. the concrete solid element with cut extrude and two steel faceplates with solid extrude. Concrete and the intermediate fasteners were modelled as three-dimensional (3D) deformable solid element, and the steel plates were modelled as three-dimensional (3D) deformable shell element. The parts are globally seeded by specifying the required size of the element. The meshing algorithm used was swept meshing. The linear hexahedral elements (C3D8R) and linear quadrilateral shell element (S4R) were used for concrete and steel, respectively. The C3D8R element is an eight-node, linear brick and reduced integration with hourglass control, and the S4R element is a four-node general purpose shell, reduced integration with hourglass control and finite membrane strains. Tie constraint was used to model the contact surfaces of the model. A total of 48 contact pairs were modelled between the concrete hole and the surface of the rod and between the surfaces of rod on both the plates (Fig. 8).

4.2 *Loading and Boundary Conditions*

Encastre boundary condition was given at the base edge of the shear wall on both the steel plate and concrete to reproduce fixed end condition, i.e. control in three translational and rotational degrees of freedom. The effects that occurred due to

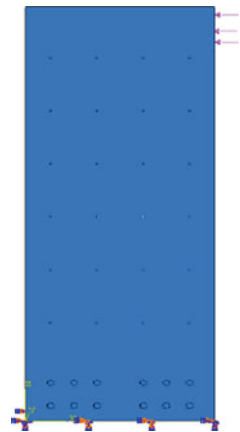
Fig. 8 Meshing of steel and concrete parts



stress concentration around the foundation block were simulated by modelling the bolts that were used in the foundation block.

The load was applied as pressure load on the concrete and as shell edge load on steel plate on the top side of the model (Fig. 9).

Fig. 9 Loading and boundary conditions



4.3 Material Properties

4.3.1 Steel

ABAQUS, while characterizing the material property the nominal stress and strain values are changed over to true stress and logarithmic plastic strain utilizing Eqs. (1) and (2). The material is considered as isotropic and homogeneous.

$$\sigma_{\text{true}} = \sigma_{\text{nom}} \times (1 + \epsilon_{\text{nom}}) \tag{1}$$

$$\epsilon_p = \ln(1 + \epsilon_{\text{nom}}) - \sigma_{\text{true}}/E, \tag{2}$$

where E is the Young’s modulus.

4.3.2 Concrete

The comparable stress–strain graph for confined cement under compressive loading as appeared in Fig. 10 is utilized in the proposed FE model. This methodology resembles the one embraced by Ellobody and Young [20]. The tensile behaviour of the confined concrete is thought to be straight all through its expanding and diminishing stages as given by the stress–strain outline appeared in Fig. 11.

By building up the uni-axial stress–strain graph for confined concrete in both compression and tension, the concrete material property would then be able to be characterized in ABAQUS by characterizing the accompanying two fundamental areas:

- Elastic: The straight portion of the confined concrete’s stress–strain graph is characterized right now. The Young’s modulus of confined concrete and its Poisson’s ratio are characterized below.

Fig. 10 Compressive behaviour of concrete [20]

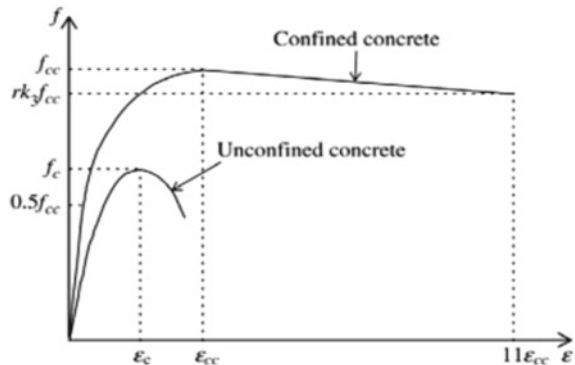


Fig. 11 Tensile behaviour of concrete [20]

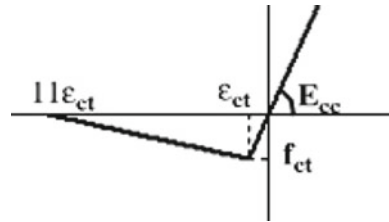


Table 2 Concrete damaged plasticity properties

Dilation angle	Eccentricity	f_{b0}/f_{c0}	K	Viscosity parameter
35	0.1	1.16	0.67	0

- Plastic: There are a few material definition calculations gave by ABAQUS to the nonlinear conduct of concrete materials. The Concrete Damage Plasticity model is used right now in the study. The parameters characterized are presented in Table 2.

5 Finite-Element Validation

Finite-element model was developed and validated with the experimental results based on load and displacement behaviour as shown in Fig. 12. It was found that the finite-element model was the best way to simulate the behaviour of experimental cold-formed steel–concrete composite walls concerning the load–displacement response. The initial stiffness of the FEM results is 30.84 kN/mm, and it is 25.42% more than the experimental results. The ultimate load of the FEM results is 42.84 kN, and it is 8.68% more than the experimental results. This might be because by modelling the shear wall through finite-element method, and it was possible to simulate the fixed end condition at the base of the shear wall better than the actual condition present experimentally.

The failure of the composite shear wall of the FEM results is due to the yielding or buckling of cold-formed steel at the bottom of the compression side of the composite shear wall followed by cracks on the tension side of the exposed concrete surface. The buckling of cold-formed steel plate started at 24.32 kN as shown in Fig. 13. Steel had taken both compressive and tensile forces acting in the shear wall but concrete only takes the compressive forces acting in the shear wall. Steel and concrete attained the maximum stress of 247 MPa and 34.5 MPa (Fig. 14), respectively, at the peak load, and it showed that the cold-formed steel in the composite wall did not attain the failure before reaching its yield stress. So that the number of studs was provided in the composite shear wall not enough to attain the full composite action.

Fig. 12 Validation of experimental and numerical results

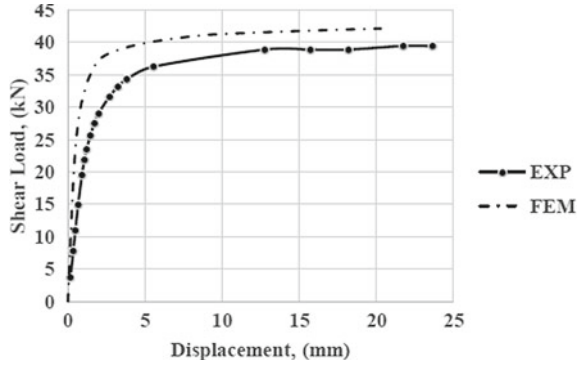
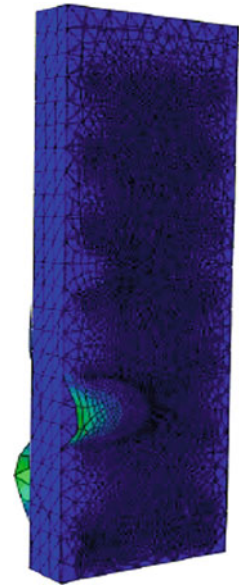


Fig. 13 Buckling behaviour of cold-formed sheet



5.1 Parametric Study

Based on the experimental study, it was found that grade of concrete, grade of steel and number of fasteners are the parameters which affecting the load carrying capacity of wall. To quantify the effect of these parameters, a parametric study was conducted by varying number of intermediate fasteners (24, 12, 6 and 0 No.s), compressive strength of concrete(45, 35 and 25 MPa) and tensile strength of steel (350 MPa and 250 MPa) and presented in Table 3. The nomenclature of the finite-element models is shown in the following Fig. 15.

Where s , is the spacing of shear studs, t_p the thickness of the steel plates used and t_w is the thickness of the wall.

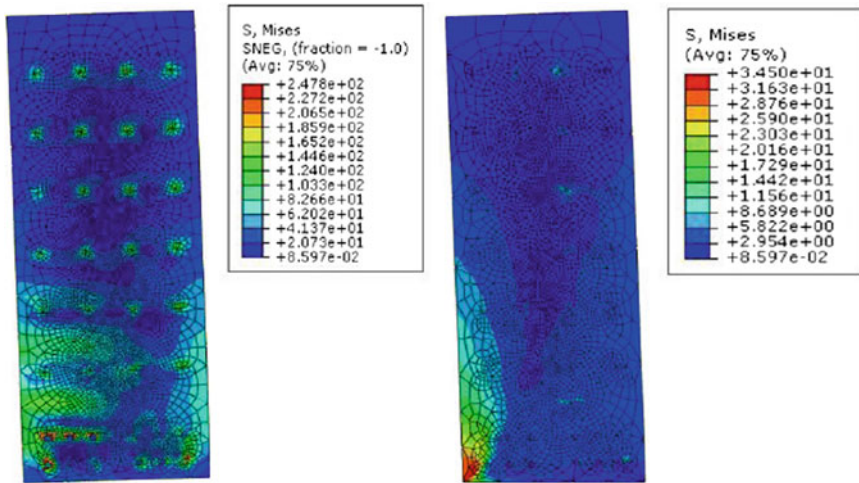


Fig. 14 Contours of stress in steel and concrete

5.1.1 Effect of Intermediate Fasteners

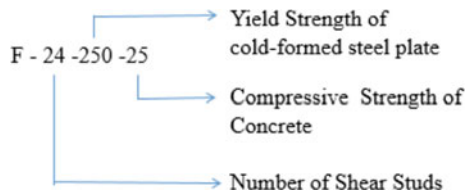
The load capacity of the wall increased with an increase in the number of intermediate fasteners due to enhanced composite action. For the composite shear wall with 250 MPa grade of steel and 25 MPa grade of concrete, the strength enhancement from 0 to 6 numbers of intermediate fasteners was 45.21%, the strength enhancement from 0 to 12 numbers of intermediate fasteners was 52.40% and the strength enhancement from 0 to 24 numbers of intermediate fasteners was 56.54%. This is due to the transfer of stress from the concrete to the steel through the intermediate fasteners. The effect of number of intermediate fasteners on the load carrying capacity of the composite shear wall in Fig. 16. The slenderness of sheet got reduced due to reduction of the spacing of fasteners and as the slenderness ratio decreased the ultimate load increased.

For 24 number of intermediate fasteners, the composite shear wall attained full composite action at the ultimate load as the cold-formed steel reached the 257 MPa that is more than the yield stress. But for zero number of intermediate fasteners, cold-formed steel attained only a maximum stress of 128 MPa (Fig. 17). It can be concluded that this is due to the lack of intermediate fasteners, and there is a minimal effect of composite action between the concrete and the steel, and hence, buckling failure is predominant which leads to the lack of proper stress transfer from concrete to steel (Fig. 18).

Table 3 Shear resistance of the composite shear wall

Test specimen	Number of shear studs	Steel yield strength (MPa)	Concrete compressive strength (MPa)	Stud spacing (s/t_w)	Slenderness ratio (s/t_p)	Ultimate load (kN)
F-0-250-25	0	250	25	–	–	22.92
F-0-250-35	0	250	35	–	–	25.55
F-0-250-45	0	250	45	–	–	27.85
F-0-350-25	0	350	25	–	–	23.48
F-0-350-35	0	350	35	–	–	26.31
F-0-350-45	0	350	45	–	–	28.96
F-6-250-25	6	250	25	2.16	135	33.28
F-6-250-35	6	250	35	2.16	135	39.72
F-6-250-45	6	250	45	2.16	135	45.05
F-6-350-25	6	350	25	2.16	135	36.61
F-6-350-35	6	350	35	2.16	135	44.49
F-6-350-45	6	350	45	2.16	135	50.05
F-12-250-25	12	250	25	1.73	108	34.73
F-12-250-35	12	250	35	1.73	108	41.26
F-12-250-45	12	250	45	1.73	108	46.36
F-12-350-25	12	350	25	1.73	108	40.28
F-12-350-35	12	350	35	1.73	108	47.03
F-12-350-45	12	350	45	1.73	108	54.24
F-24-250-25	24	250	25	1.23	77.14	35.88
F-24-250-35	24	250	35	1.23	77.14	42.05
F-24-250-45	24	250	45	1.23	77.14	47.32
F-24-350-25	24	350	25	1.23	77.14	42.52
F-24-350-35	24	350	35	1.23	77.14	48.49
F-24-350-45	24	350	45	1.23	77.14	54.48

Fig. 15 Nomenclature of finite-element model



5.1.2 Effect of Tensile Yield Strength of Steel

Based on the parametric study on the effect of tensile yield strength of steel, the shear load capacity of the wall increased with the increase of steel yield strength. For the

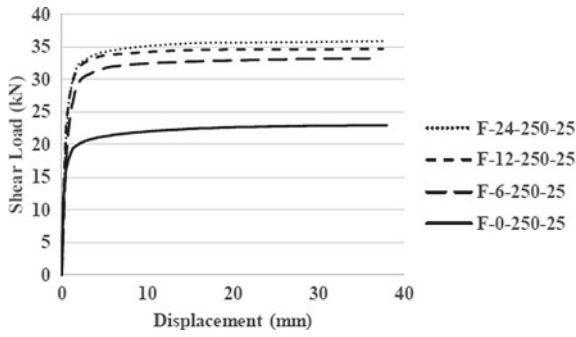


Fig. 16 Load versus displacement (varying number of fasteners, 250 MPa steel and 25 MPa concrete)

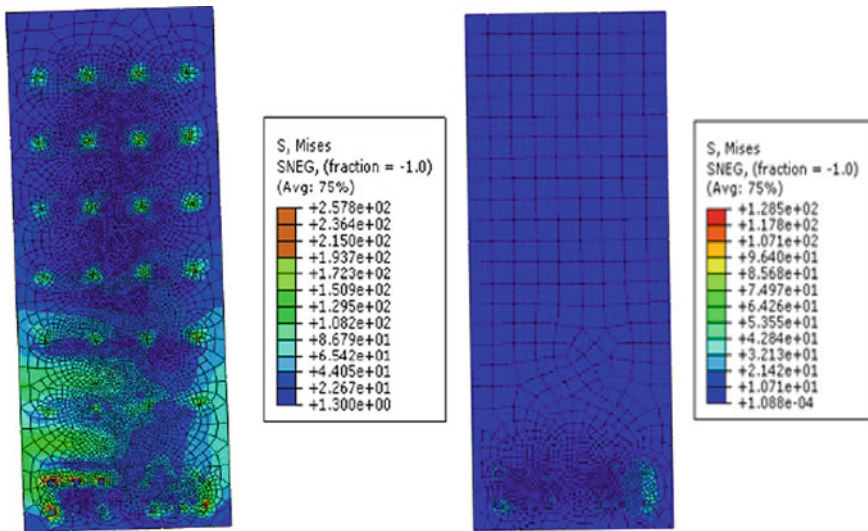


Fig. 17 Stress contours of sheets for varying number of fasteners

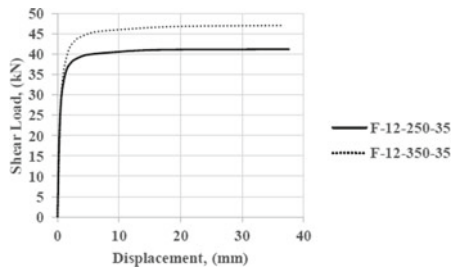


Fig. 18 Load versus displacement (Varying grade of steel, 12 numbers of fasteners and 35 MPa concrete)

composite shear wall of grade of concrete 35 MPa and 12 numbers of intermediate fasteners, the ultimate load carrying capacity of shear wall of 350 MPa steel sheet is 14.1% higher than that of the shear wall of 250 MPa steel sheet. The maximum stress reached in the steel of F-12-350-35 and F-12-250-35 was 355 MPa and 254 MPa, respectively, which is clearly explained the behaviour change in the stress contours in Fig. 19.

For the walls with no intermediate fasteners, the tensile yield strength of steel had no effect on the ultimate load carrying capacity as shown in Fig. 20.

This was because the failure of such walls was governed by buckling of cold-formed steel sheets and hence did not depend on the yield strength of the material.

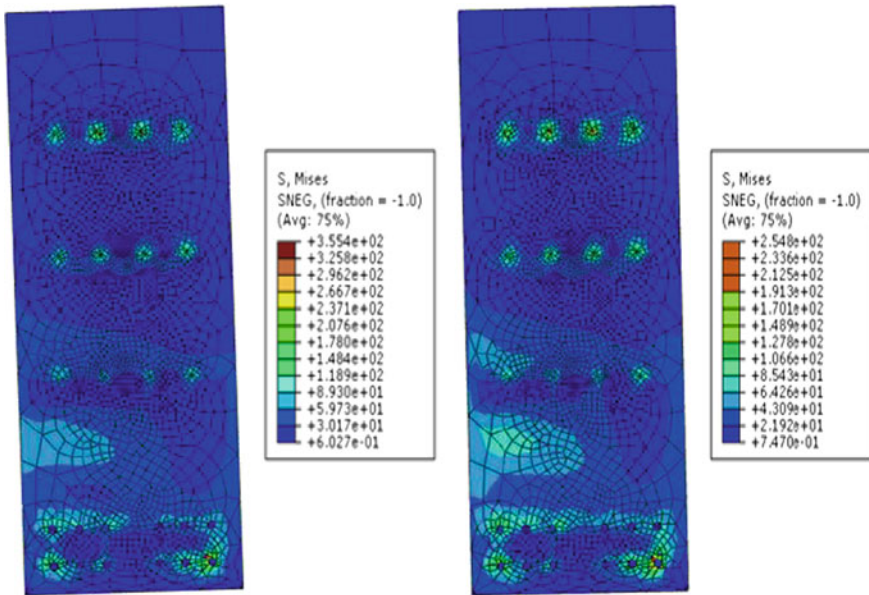


Fig. 19 Stress contours of sheets for varying grade of steel

Fig. 20 Load versus displacement (Varying grade of steel, 0 fasteners and 25 MPa concrete)

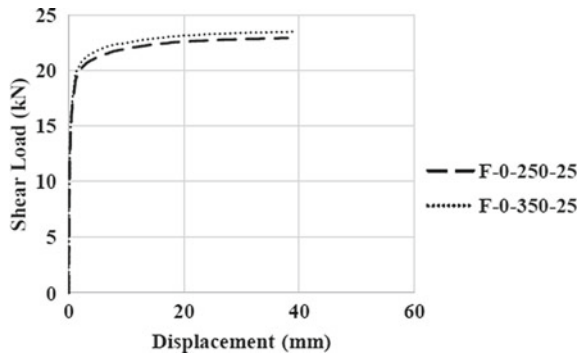
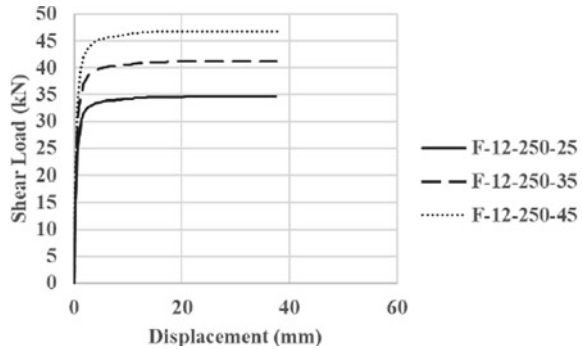


Fig. 21 Load versus displacement (Varying grade of concrete, 12 fasteners and 250 MPa steel)



The composite shear wall with no intermediate fasteners, the grade of concrete was the leading factor for the shear load capacity of the composite shear wall.

5.1.3 Effect of Compressive Strength of Concrete

The parametric study based on the compressive strength of concrete revealed that for the composite shear wall with 12 number of shear studs and 250 MPa grade of steel, the ultimate load carrying capacity increased with the increase in the compressive strength of concrete (Fig. 21). The strength enhancement between 25 and 35 MPa grade of concrete was 18.80%, and the strength enhancement between 25 and 45 MPa grade of concrete was 33.48%.

6 Conclusions

A composite shear wall specimen of 450 mm (wide) and 1250 mm (height) was tested under a static shear load. Finite-element modelling and parametric study were carried out by varying tensile yield strength, grade of concrete and the number of intermediate fasteners. Steel sheet-concrete composite action was enhanced by the study of varying number of intermediate fasteners. The following conclusions were inferred from the study:

- The failure of the composite shear wall was either due to the local buckling on the compression side or by the yielding of the steel sheet. The failure criterion used for the steel sheet was Von Mises yield criterion, and it was observed that the shear stress was closer to the limiting shear stress which implied that yielding of the sheet occurred before the start of local buckling when the number of intermediate fasteners increased which might be a result of enhanced composite action between steel sheet and concrete.

- From the parametric study, it was observed that the increase in the compressive strength was more effective in increasing the ultimate lateral load carrying capacity when compared to the increase in the tensile yield strength of steel.
- For the composite shear wall having no intermediate fasteners, it was observed that the lateral load carrying capacity was mainly based on the grade of the concrete with almost negligible effect on the tensile yield strength of steel due to the lack of composite action and buckling of steels.

References

1. Hossain KM, Rafiei S, Lachemi M, Behdinan K, Anwar MS (2016) Finite element modeling of impact shear resistance of double skin composite wall. *Thin-Walled Struct* 107:101–118
2. Chen L, Mahmoud H, Tong SM, Zhou Y (2015) Seismic behavior of double steel plate–HSC composite walls. *Eng Struct* 102:1–12
3. Eom TS, Park HG, Lee CH, Kim JH, Chang IH (2009) Behavior of double skin composite wall subjected to in-plane cyclic loading. *J Struct Eng* 135(10):1239–1249
4. Ji X, Cheng X, Jia X, Varma AH (2017) Cyclic in-plane shear behavior of double-skin composite walls in high-rise buildings. *J Struct Eng* 143(6):04017025
5. Nie JG, Hu HS, Fan JS, Tao MX, Li SY, Liu FJ (2013) Experimental study on seismic behavior of high-strength concrete filled double-steel-plate composite walls. *J Constr Steel Res* 88:206–219
6. Prabha P, Palani GS, Lakshmanan N, Senthil R (2017) Behaviour of steel-foam concrete composite panel under in-plane lateral load. *J Constr Steel Res* 139:437–448
7. Rafiei S, Hossain KMA, Lachemi M, Behdinan K, Anwar MS (2013) Finite element modeling of double skin profiled composite shear wall system under in-plane loadings. *Eng Struct* 56:46–57
8. Rafiei S, Hossain KM, Lachemi M, Behdinan K (2015) Profiled sandwich composite wall with high performance concrete subjected to monotonic shear. *J Constr Steel Res* 107:124–136
9. Rassouli B, Shafaei S, Ayazi A, Farahbod F (2016) Experimental and numerical study on steel-concrete composite shear wall using light-weight concrete. *J Constr Steel Res* 126:117–128
10. Uy B, Wright HD, Bradford MA (2001) Combined axial and flexural strength of profiled composite walls. *Proc Inst Civ Eng-Struct Build* 146(2):129–139
11. Hossain KA, Wright HD (2004) Experimental and theoretical behaviour of composite walling under in-plane shear. *J Constr Steel Res* 60(1):59–83
12. Yan JB, Li ZX, Wang T (2018) Seismic behaviour of double skin composite shear walls with overlapped headed studs. *Constr Build Mater* 191:590–607
13. Zhang K, Varma AH, Malushte SR, Gallocher S (2014) Effect of shear connectors on local buckling and composite action in steel concrete composite walls. *Nucl Eng Des* 269:231–239
14. Epackachi S, Nguyen NH, Kurt EG, Whittaker AS, Varma AH (2014) In-plane seismic behavior of rectangular steel-plate composite wall piers. *J Struct Eng* 141(7):04014176
15. Hossain KMA, Attarde S, Anwar MS (2019) Finite element modelling of profiled steel deck composite slab system with engineered cementitious composite under monotonic loading. *Eng Struct* 186:13–25
16. Nguyen NH, Whittaker AS (2017) Numerical modelling of steel-plate concrete composite shear walls. *Eng Struct* 150:1–11
17. Qin Y, Shu GP, Fan SG, Lu JY, Cao S, Han JH (2017) Strength of double skin steel-concrete composite walls. *Int J Steel Struct* 17(2):535–541
18. Rabbat BG, Russell HG (1985) Friction coefficient of steel on concrete or grout. *J Struct Eng* 111(3):505–515
19. ASTM E (2001) 8M-04. Standard test methods for tension testing of metallic materials

20. Ellobody E, Young B (2006) Performance of shear connection in composite beams with profiled steel sheeting. *J Constr Steel Res* 62(7):682–694

An Experimental Investigation on Light Gauge Steel Hollow Circular Column infilled with Nano Concrete



P. Vasanthi and S. Senthil Selvan

Abstract This paper deals with the axial load carrying capacity of light gauge steel hollow circular section infilled with Nano concrete. Among the various infill materials, Nano silica is gaining attention in the concrete-filled steel tube (CFST) columns. The main objective of this paper is to study the axial load carrying capacity, relation between the steel and concrete interaction and also the characteristic of hollow steel column, plain and Nano silica infilled steel columns, load–deformation, load–axial strain and load–axial shortening of CFST columns. Nano silica was optimized as 2% in the Nano concrete based on the tests conducted. A total of 21 specimens were tested with a dimension of 50 mm diameter, 1.5 m length and the thickness of the steel tubes were taken as 1.2, 1.6 and 2.0 mm. Experiments were carried out with M30 grade of concrete, and finally, these experimental results are evaluated, and the experimental values are guide lines available validated with the existing codes such as Eurocode4 (EC4-2004), British code (BS5400-2005) and American code (ACI-1999).

Keywords Axial load carrying capacity · Load–deformation · Load–axial strain · Load–axial shortening · Nano concrete

1 Introduction

Concrete is the world's most frequently used construction material. Due to the world's rapid urbanization and population growth, its demand continues. As a result, cement plays an important role because of its size and adhesive properties from various materials used in the production of concrete. Therefore, the mechanism of cement

P. Vasanthi (✉)

Adhi College of Engineering and Technology, Chennai, India
e-mail: vasanthihh@gmail.com

S. S. Selvan

Department of Civil Engineering, SRM Institute of Science and Technology, Chennai, India
e-mail: senthils10@srmist.edu.in

hydration should be properly examined and better substitutes suggested in order to produce concrete with improved properties. Hence, concrete is added to various materials known as cemented additional materials to improve its properties. Some includes fly ash, burnt slag, rice husk, silica fumes and bacteria. Nanotechnology is promising field which improve the characteristics of concrete between the different techniques used. The interest in nanotechnology concept for cement composites is steadily growing. In recent years, many of the researchers have investigated the behaviour of concrete-filled steel tubes and concrete encased sections with various parameters like types of loading, d/t ratio, cross-sectional shapes, material properties, ultimate load carrying capacity and slenderness ratio and compared with analytical results. Lu [1] presented behaviour of high-strength rectangular columns under eccentric loading and has highlighted the failure modes of the column due to slenderness ratio. It was observed that the slenderness ratio increases, and the buckling starts with close to specimen at mid-height of the steel hollow section. Kumutha et al. [2] showed that when the number of layers of GFRP wrap was increased, compressive strength and aspect ratio also increased, but the load carrying capacity of the column decreased. Sakina et al. [3] have tested 114 specimens experimentally both hollow and CFT short columns for the circular and square CFT columns. In case of circular columns, the stress strain relationship of the steel tube is developed as elastic-perfectly relation model. In case of Square CFT columns, increasing of B/t ratio decreasing the yield stress, due to local buckling. Fujimoto [4] showed that in circular CFT columns, the ductility behaviour improved by confining the concrete with in a high-strength steel tube or within a tube having smaller d/t ratio.

Hassanein [5] was investigated the strength and behaviour of concrete-filled double skin steel tubular (CFDST) slender columns under axial compression. Mirmiran [6] showed that reinforced concrete core cast in a composite FRP shell is advantageous in corrosive environments and seismic zones. Saloma et al. explain [7] Nano material concrete is new generation concrete formed of materials of the grain size of Nano scale. Concrete containing Nano silica and Nano clay was high compared to concrete containing silica fume, fly ash and slag. It was showed that the microstructure of the Nano silica concrete was denser and more uniform than that of the conventional concrete. Also, the results show that the additions of Nano silica as cement partial substitute material improve the mechanical behaviour of the concrete. Reshma et al. [8] have highlighted the performance of concrete using Nano silica. It is more effective due to its small size and high surface area when compared to other pozzolana materials, and it is used as supplementary material and highly reactive amorphous material. Georgios Giakoumelis, Lam [9] found that for high-strength CFT columns, the ultimate load was attaining small displacement compared to normal concrete and also highlighted that the concrete strength increases the effects of the bond of the concrete with the steel tube became more critical.

Many researchers have carried out the experimental investigation to study the ultimate strength of the CFST composite columns. The main aim of this study is to improve the performance of the concrete using Nano silica (Nano-SiO₂). The results showed that the addition of Nano silica as cement partial substitute material will improve the mechanical behaviour of the concrete.

2 Material Properties

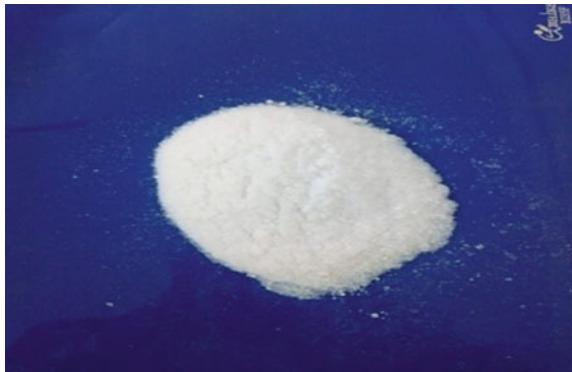
2.1 Concrete

Ordinary Portland cement of 53 grade was used; locally available river sand which satisfies the IS 383-1970 code was used. The coarse aggregate up to 12.5 mm size was used. Normal portable water was used for mixing and curing. The concrete mix proportions were carried out as per IS 10262-2009. The water cement ratio used by conducting concrete slump test. Concrete cube specimens were casted for each batching and tested at the age of 28 days to determine the compressive strength of concrete.

2.2 Nano Silica

In fast growth of construction, concrete plays a vital role in construction materials. In this paper, Nano silica is the additive material in Nano modified concrete as shown in Fig. 1. The presence of Nano silica in concrete will fill the Nano size pores of cement paste and enhances durability of concrete. Replacing of cement 0–3% NS in weight during cement mortar test, 2% Nano silica was optimized at the age of 28 days of compressive strength. Therefore, the presence of 2% NS in the concrete by weight of cement is found optimum Superplasticizer is added to improve the workability of concrete. The superplasticizer polycarboxylate was used in plain and Nano concrete.

Fig. 1 Nano silica



2.3 Steel Tubes

The steel sections used for the test are cold-formed circular hollow sections with the grade of 240 MPa and nominal yield stress 248 MPa. The dimension of the steel tubes is 50 mm diameter and length of the tube is 1.5 m. Three different thicknesses of 1.2, 1.6 and 2.0 are taken for the research. The specimen of the steel tube is shown in Fig. 4.

3 Experimental Study

In the present work, twenty-one specimens are tested, including three hollow steel tube (HST) columns and eighteen CFST columns under axial loading to investigate the structural behaviour. The test parameters for the experiment results are diameter 50 mm, length 1.5 m, diameter to thickness ratio (d/t) 25, 31 and 41.67, for the thickness 1.2, 1.6 and 2.0 mm, load–deformation relationship, load–end shortening and load–axial strain were obtained. Fig. 2 shows the details of experiment conducted.

Concrete-filled steel composite columns are most commonly used in all types of structures such as high rise and medium rise buildings in recent decades. CFST columns are combined by the steel tube and concrete as infill material. Owing to the benefits of CFST columns like the permanent formwork of the structures, reduction of time in construction and reduced construction cost. Furthermore, steel tube gives good confinement to the concrete and increases its ductility and also prevented and eliminates the local inward buckling of the columns. Fig. 3. shows the plain concrete-filled steel tube column (PCFST) and Nano concrete-filled steel tube column (NCFST). Among the various infill materials, recently Nano concrete has more attention in concrete due to several reasons like reducing the cement content, produces dense concrete and reduces segregation and bleeding.

In this paper, the specimen dimension selected as diameter 50 mm, length of specimen 1.5 m with the different thickness are 1.2, 1.6 and 2.0 mm. Hence, the d/t ratio 25, 31 and 41.67 is used. In this CFST columns, M30 grade of concrete is

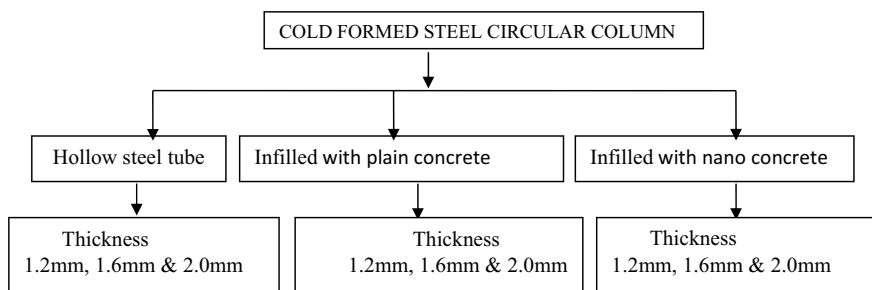


Fig. 2 Details of experiments conducted

Fig. 3 Diagrammatic view of concrete-filled steel tubular columns



Fig. 4 Few specimen of steel tube



taken as infilled with plain concrete; 2% Nano silica as replacement with controlled concrete and along with empty steel tube also tested. The effects of diameter to thickness ratio, load–deformation relationship, load–axial strain relationship and load–axial shortening are carried out. The grade of concrete selected as M30 to study the experimental investigation of hollow circular column. The steel section is infilled with plain and Nano concrete to study the axial load carrying capacity. The experimental results and compared with existing codes like EC4, BS 5400 and ACI (Fig. 4).

3.1 Preparation of Steel Specimen

The circular hollow light gauge steel tube is cut accurately into 1.5 m length. Both the ends of the tubes are surfaced to get a smooth surface. The inner surface of the tube is first cleaned using cloth to remove dust and oil. The outer surface is also brushed and painted with primer coat. The steel tube is covered with a steel plate on one side to avoid the leakage of concrete during the time of filling the tube with concrete. The concrete is filled by steel tube layer by layer; each layer is perfectly compacted using vibrating table to avoid air gaps. The surface is levelled, and the specimen is

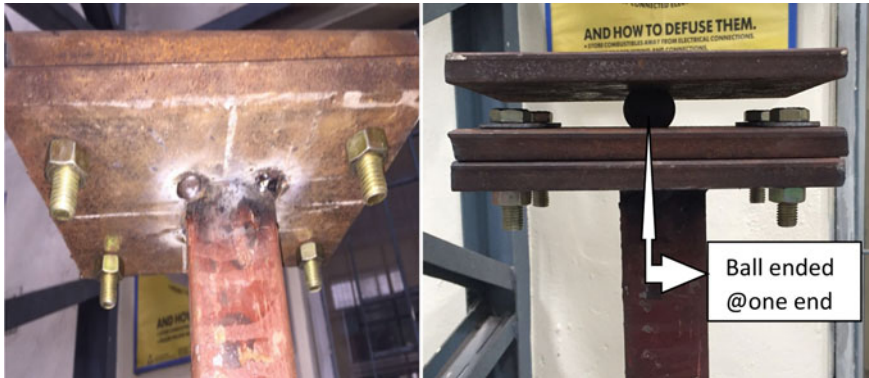


Fig. 5 Welded and ball end condition of columns

kept in room temperature for one day. Then it is cured in water for 28 days. Welded and ball end condition of columns is shown in Fig. 5.

3.2 Parameters for the Test

Parameters for the test are as follows: (1) The thickness of the steel tube such as 1.2 mm, 1.6 mm and 2.0 mm. (2) The tube diameter to thickness (d/t) ratio such as 41.67, 31.25 and 25. (3) Two types of concrete such as of plain and Nano infilled concrete. Specimen dimensions and material properties of CFST columns are shown in Table 1. In this test, the length of the specimen is 1.5 m, and diameter of column is 50 mm. The diameter to thickness (d/t) ratio of steel tubes is one of the most important parameters in the experimental program and is in the range of 41.67, 31.25 and 25. From the tensile coupon test tube, tensile strength is found as 248 MPa. The specimens were classified in to three groups based on filling material such as hollow circular column (HCC), plain concrete circular column (PCC) and Nano concrete circular column (NCC) as shown in Table 2. In specimen representation symbol like HCC 1.2, PCC 1.2, NCC1.2, HCC1.6, PCC1.6, NCC1.6, HCC2.0, PCC2.0 and NCC 2.0 based on thickness.

Table 1 Specimen dimensions details with L/D ratio

S. No.	Dimensions D in mm	Length L in mm	Thickness t in mm	D/t ratio	Stainless steel f_y in MPa
1	50	1500	1.2	41.67	248
2	50	1500	1.6	31.25	248
3	50	1500	2.0	25	248

Table 2 Geometric properties of CFST columns test specimen

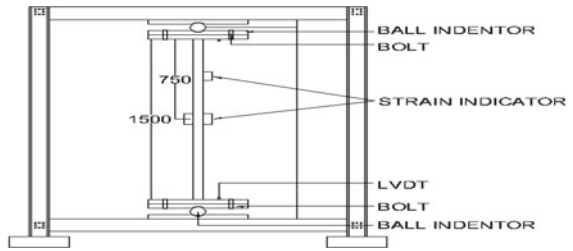
Specimen	Diameter D (mm)	Thickness t (mm)	Area of concrete A_c (mm ²)	Area of steel A_s (mm ²)
Hollow circular column HCC	50	1.2	0	183.97
Plain concrete circular column PCC	50	1.2	1779.52	183.97
Nano concrete circular column NCC	50	1.2	1779.52	183.97
Hollow circular column HCC	50	1.6	0	243.28
Plain concrete circular column PCC	50	1.6	1720.2	243.28
Nano concrete circular column NCC	50	1.6	1720.2	243.28
Hollow circular column HCC	50	2.0	0	301.59
Plain concrete circular column PCC	50	2.0	1661.9	301.59
Nano concrete circular column NCC	50	2.0	1661.9	301.59

3.3 Specimen Test Procedure

Deep grooves are made in the four plates in its centre. Two plates are welded at both sides of the steel tube. Circular hollow, plain and Nano infilled concrete columns are tested in the column loading frame of 500 kN capacity in the Structural Engineering Laboratory of SRM Institute of Science and Technology, Chennai, India. Specimens were fixed in the Instrument. The columns are tested up to failure, total of six strain gauges fitted on the outside surface of the circular tubes, two in centre of the specimen, two in quarter height of the specimen and each one in axial shortening between the two end plates. Using LVDT axial shortening was measured in the composite column specimen.

The objective is to find the maximum deflection at $L/2$ and $L/4$ distance of the column. Each specimen was loaded at 10 kN gradually applied using hydraulic jack through the proving ring. The position of the strain gauges and LVDT position are shown in Fig. 6. As the load increases, strain gauges readings and LVDT readings were manually noted down. The instrumentation and test arrangement setup is shown in Fig. 7. The test is carried out until the specimen fails. Lateral deflections at the mid-height, $L/4$ distance and axial shortening are measured using 0.01 mm least count deflectometer, and the strains were measured using electric strain gauge. The axial shortening values are as shown in Table 3, and Fig. 8 shows the failure modes

Fig. 6 Schematic diagram of test setup



of the tested hollow columns. After the test of all specimens, the specimens were removed and photographed and carefully examined.

Fig. 7 Specimen setup

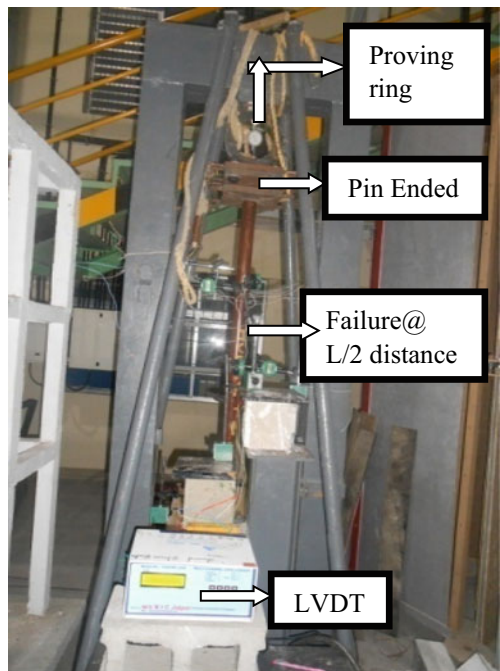
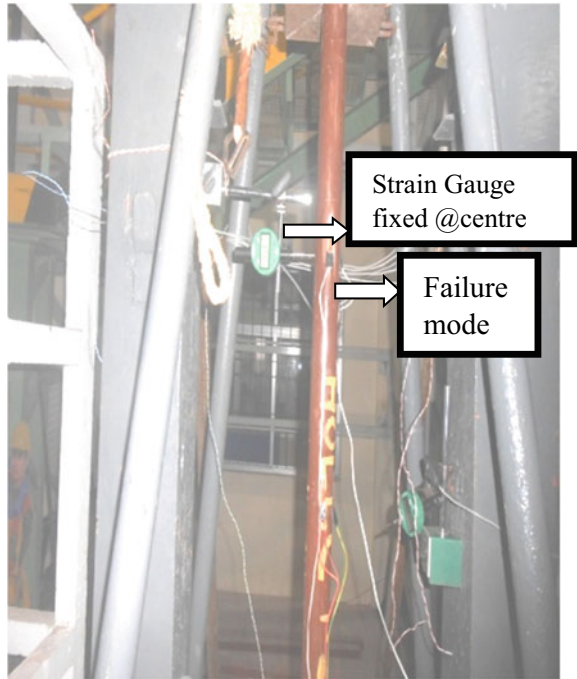


Table 3 Comparison results of experimental, theoretical results

Specimen label	Thickness t (mm)	Test results N_{test} (kN)	Ratio N_{test} / N_{EC4}	Ratio N_{test} / N_{ACI}	Ratio N_{test} / N_{BS5400}	Relative slenderness $\bar{\lambda}$	Axial Shortening (mm)
HCC30	1.2	47.79	1.048	1.047	1.047	0.805	0.0017
PCC30	1.2	114.85	1.098	1.200	1.345	1.219	0.0038
NCC30	1.2	118.98	1.094	1.198	1.348	1.243	0.0032
HCC30	1.6	76.23	1.264	1.263	1.263	0.848	0.0025
PCC30	1.6	126.94	1.082	1.167	1.285	1.183	0.0034
NCC30	1.6	129.63	1.068	1.155	1.276	1.203	0.0030
HCC30	2.0	79.89	1.068	1.068	1.068	0.879	0.0023
PCC30	2.0	135.72	1.046	1.117	1.213	1.159	0.0027
NCC30	2.0	140.83	1.053	1.127	1.229	1.177	0.0025
		Mean	1.091	1.149	1.230		
		Standard deviation	0.0675	0.0678	0.108		

Fig. 8 Hollow specimen failure mode



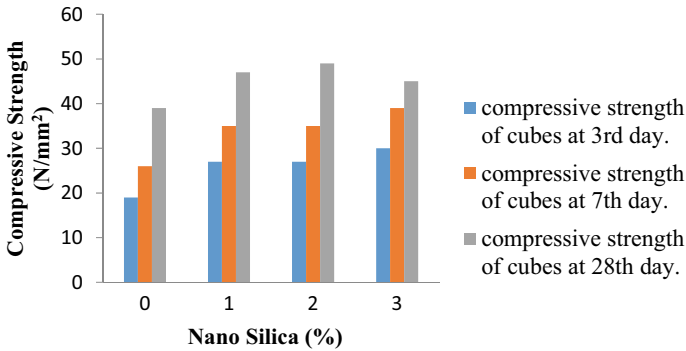


Fig. 9 Compressive strength of plain and Nano concrete

Table 4 Compressive strength of plain and Nano concrete

Percentage of Nano silica used (%)	Compressive strength of cubes at 3rd day (N/mm ²)	Compressive strength of cubes at 7th day (N/mm ²)	Compressive Strength of cubes at 28th day (N/mm ²)
0	19	26	39
1	27	35	47
2	27	35	49
3	30	39	45

4 Results and Discussion

4.1 Effect of Concrete Strength

The compressive strength of concrete was tested and observed for a period of 7 days, 14 days and 28 days. The cube and cylinders were casted different ratios of 0%, 1%, 2% and 3% replacement of Nano silica. Addition of 0.5% of polycarboxylate superplasticizer in both plain and Nano concrete is used for good workability. From these results, it is concluded that 2% replacement of Nano silica is optimum for 28 days of testing. Adding of 2% Nano silica increasing strength 25.64%, when compared to nominal concrete as shown in Fig. 9 and Table 4.

4.2 Load Versus Axial Shortening Behaviour

Figure 10a–c shows the results of concrete filling on the load–axial shortening curves. The different thicknesses of the steel tube are 1.2, 1.6 and 2.0 mm of hollow, infilled column of plain and Nano concrete. The hollow column reached failure at a lower load

than the filled columns (plain and Nano). Composite columns have been observed to have more advantages than unfilled (hollow) columns. Further, the Nano infilled columns enhance the axial shortening as well as lesser buckling than the plain infilled column and unfilled (hollow) column. Figure 10a–c illustrations due to effect of axial shortening, the load and thickness increases but axial shortening are reduced. Due to the utilization of light gauge steel, all composite columns exhibited very ductile behaviour, even after having experienced severe buckling. Fig. 10a–c shows the effect of hollow tube, the thickness of 1.6 and 2.0 mm is increasing 60.55% and 67.165% of load than the 1.2 mm thickness but the effect of plain and Nano infilled column, the thickness of 1.6 mm and 2.0 mm is increasing 8 to 10% and 18% of load than the 1.2 mm thickness. At the same time, axial shortening also decreased due to the effect of filled composite column which is demonstrated in Fig. 10a–c.

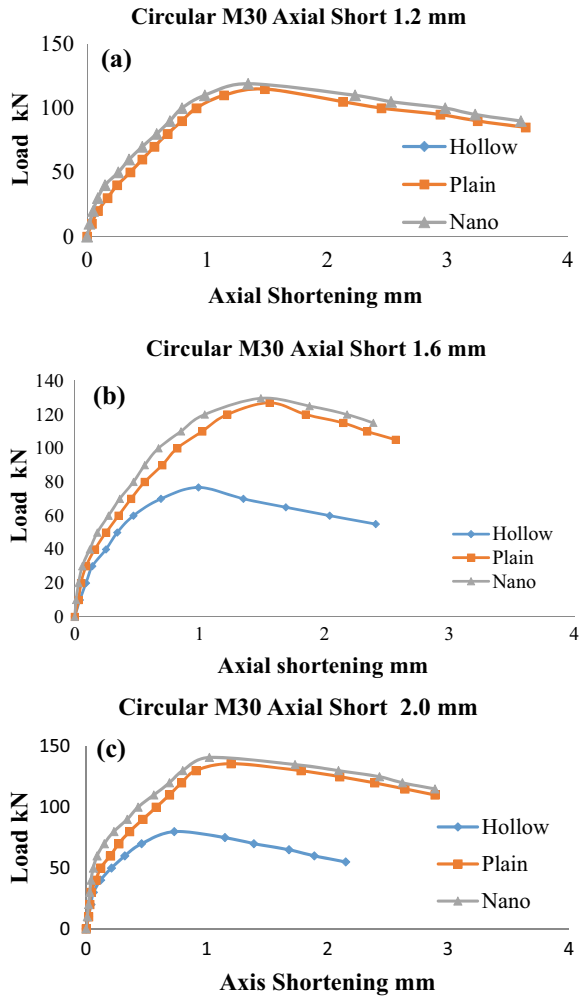
4.3 Behaviour of Load–Axial Strain

Fig. 11a–c shows the load versus strain behaviour of hollow, plain and Nano concrete infilled light gauge steel column. To analyse the behaviour of CFST columns, the axial strains were measured from strain gauges. The axial load (N) versus axial strain (ϵ) relationship changes from three types of type A, type B and type c (8). Initially, the graph is linear for all the thickness. It is observed that there is a considerable growth in the load–axial strain curve of concrete due to the presence of Nano silica. The enhancement of Nano silica is clear in the post-cracking response which improves the long term serviceability of the structure, even though the concrete first crack strength is not increased. Serkan Tokgoz (1) studied the determination of strain values are 0.0035 and 0.004 for plain and steel fibre CFSST columns. Furthermore, in this experimental research was observed due to effect of CFSST columns reached their ultimate capacity at strain values of 0.004 and 0.0048 for the infilled concrete (plain and Nano). The results revealed that the addition on Nano silica in to the concrete had significant effect in the strain. The experimental results of tested column provide significant knowledge to understand the structural behaviour of plain and Nano CFSST columns. The ratio of loads in experimental test results to EC4, ACI and BS5400 is shown in Table 3. It is clearly shows that the mean values of ACI and BS5400 are 5.3% and 12% and are more than the EC4. The standard deviations are less in EC4 and ACI compared to BS5400. The relative slenderness $\bar{\lambda}$ is calculated and represented in Table 3.

4.4 Behaviour of Load–deflection Curves

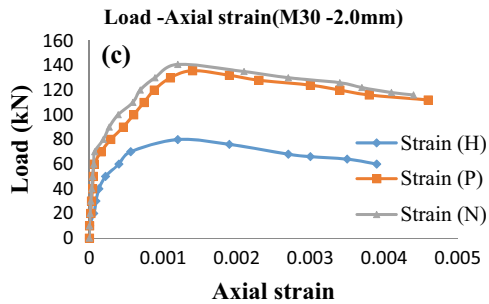
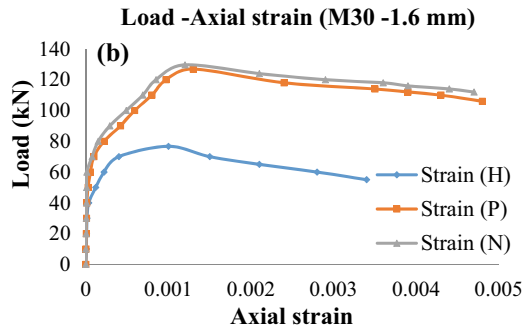
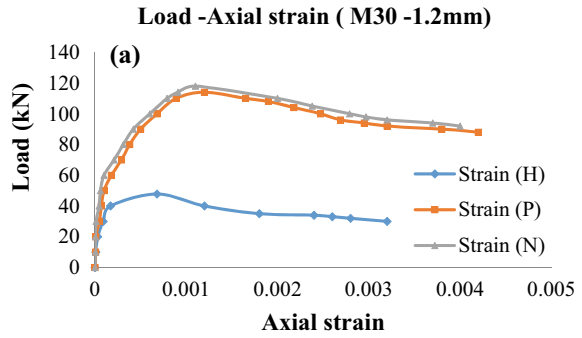
The experimental and theoretical results are illustrated in Table 3. It was assumed that the CFST columns reached their ultimate load versus strain values of plain concrete 0.0035. At this stage, first concrete occurred and steel tubes slightly exceeded the

Fig. 10 **a** Load versus axial shortening curves at 1.2 mm thickness. **b** Load versus axial shortening curves at 1.6 mm thickness. **c** Load versus axial shortening curves at 2 mm thickness



yield strength. The load with lateral deflection relations was obtained at the $L/4$, mid-height of the light gauge tube column specimen. In Fig. 12a–c, the experimental load–deflection curves of hollow infilled plain and Nano concrete for different wall thickness results are plotted in the Fig. 12a–c. Small deflections are monitored at the initial loading stages, and the experimental strength capacity of CFST columns was influenced by concrete compressive strength. The results indicate that the addition of Nano silica has considerable impact on column strength deflection at mid height compared with the quarter span. In addition, for varying the thickness and D/t ratio, maximum deflection will be at the mid-height of the axial loaded columns, in which 2-mm-thick column shows the good response against deformation of Nano CFST columns.

Fig. 11 **a** Load versus axial strain curves @ 1.2 mm thickness. **b** Load versus axial strain curves @ 1.6 mm thickness. **c** Load versus axial strain curves @ 2 mm thickness



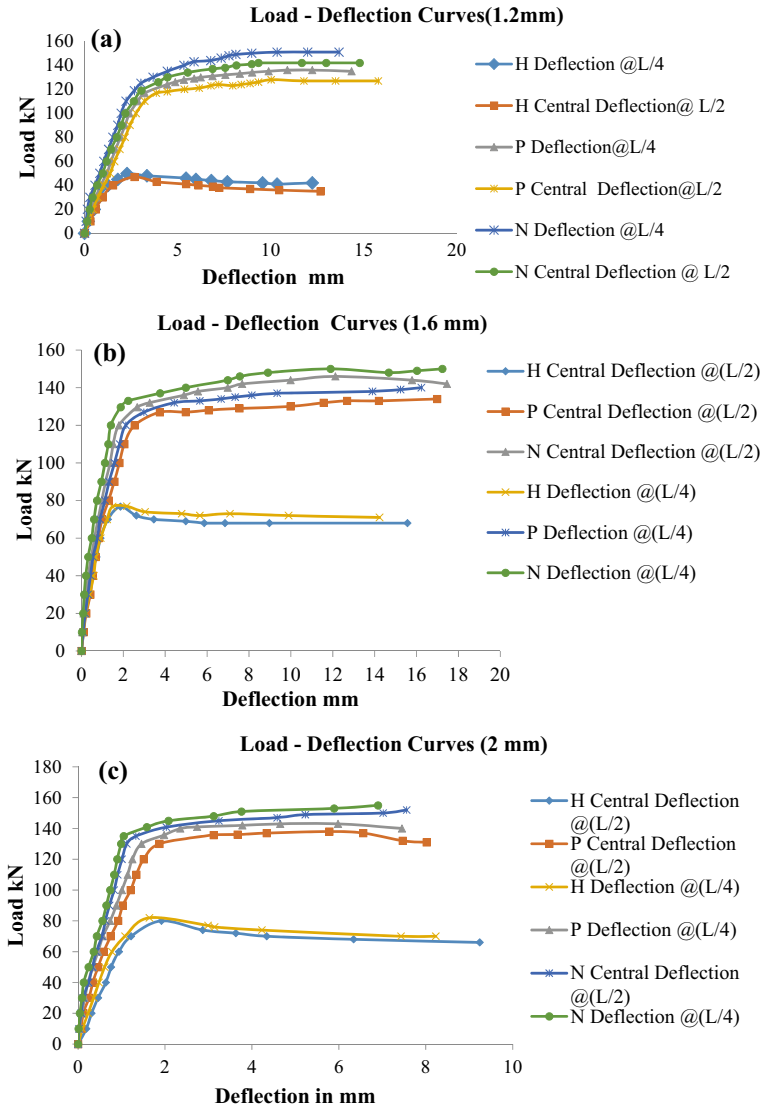


Fig. 12 a Load versus deflection curves at 1.2 mm thickness. b Load versus deflection curves at 1.6 mm thickness. c Load versus deflection curves at 1.2 mm thickness

5 Conclusion

From this experimental investigation, the following conclusions can be drawn.

- (1) Twenty-one circular CFST columns were tested by pin ended support with axial loads applied at the ends, and to determine the structural behaviour of the circular section of the hollow, plain and Nano CFST columns has been tested under the axial load. The strength of the hollow, plain and Nano infill concrete columns using different thickness of 1.2, 1.6, 2.0 mm is found. Load–end shortening, load–axial strain relation, load–deflection behaviour at quarter and mid-height of the span are tested. The tested columns have been analysed and compared with the provisions providing in the existing codes such as EC4, ACI and BS5400 codes.
- (2) In addition, the ultimate strength capacity of CFST column has significance effect on the variation of thickness. The addition of 2% Nano silica reduces the impact of buckling failure.
- (3) The Nano concrete, the strength was increased by 25.64% than the plain concrete. Due to this effect of Nano concrete, buckling also reduced in Nano CFST columns.
- (4) The Nano infilled concrete columns are gaining more benefits and increasing in usage with greater emphasis on durability and life cycle costing.
- (5) The structural stiffness of column having thickness 2.0 mm has more than the other thickness.
- (6) The diameter to thickness ratio and thickness parameters has effects on ultimate strength capacity of plain and Nano CFST columns.
- (7) The experimental strength of the columns is compared with the theoretical values arrives from the various codes such as EC4, ACI and BS5400. From this, EC4 code is related to the experimental values.
- (8) Load versus axial shortening and load versus strain curves represents that load was increased but axial shortening and strain were decreased for the 2 mm Nano infilled concrete tube as compared to the Hollow and Plain infilled concrete.
- (9) In deflection curve represents @ $L/2$ distance the buckling are more compared to the $L/4$ distance of the tube. At the same time, 2 mm thickness infilled Nano concrete is less buckling compared to the other thickness of hollow and plain concrete in filled tube.

References

1. Roeder CW, Cameron B, Broen CB (1999) Composite action in concrete filled tubes. *J Struct Eng* 125(5):477–484
2. Lam D, Gardner L (2018) Structural design of stainless steel concrete filled columns. *J Constr Steel Res* 64:1275–1282
3. Kumutha R, Vaidyanathan R, Palanichamy MS (2007) Behaviour of reinforced concrete rectangular columns strengthened using GFRP. *Cement Concr Compos* 29:609–615

4. Kumaria K, Preethaa R, Ramachandran BD, Vishwakarma V, Georgec RP, Sundaramurthya C, Kamachi Mudalic U, Sivathanu Pill C (2016) Nanoparticles for enhancing mechanical properties of fly ash concrete. In: Recent advances in nano science and technology 2015 (RAINSAT2015) materials today: proceedings vol 3, pp 2387–2393
5. Patal VI, Liang QQ, Hadi MNS (2014) Non linear analysis of axially loaded circular concrete-filled stainless steel tubular columns. *J Constr Steel Res* 101:9–18
6. Lu D (2004) Behaviour of high strength rectangular concrete-filled steel hollow section columns under eccentric loading. *Thin-Walled Struct* 42:1631–1644
7. Tokgoz S (2015) Tests on plain and steel fiber concrete-filled stainless steel tubular columns. *J Constr Steel Res* 114:129–135
8. Saloma AN, Imran I, Abdullah M (2013) Experimental investigation on nano material concrete. *Int J Civ Environ Eng IJCEE-IJENS* 13(3):15–20
9. Reshma S, Siddirajulu S (2015) An experimental investigation on concrete with nano silica and partial replacement of cement with flyash. *Int J Sci Res (IJSR)* 4(7)
10. Elremaily A, Azizinamini A (2002) Behavior and strength of circular concrete-filled steel tube columns. *J Constr Steel Res* 58:1567–1591
11. Kumarpatidar A (2012) Behaviour of concrete filled rectangular steel tube column. *IOSR J Mech Civ Eng* 4(2):46–52
12. Mirmiran A, Shahawy M (1996) A new concrete-filled hollow FRP composite column. *Composites: PART B* 27B 263–268
13. Uy B, Tao Z, Han L-H (2011) Behaviour of short and slender concrete-filled stainless steel tubular columns. *J Constr steel Res* 67:360–378
14. Ellobody E (2013) Nonlinear behaviour of eccentrically loaded FR concrete-filled stainless steel tubular columns. *J Constr Steel Res* 90:1–12
15. Ellobody E, Young B (2006) Non linear analysis of concrete-filled steel SHS and RHS columns. *Thin-Walled Struct* 44:919–930
16. Giakoumelis G, Lam D (2004) Axial capacity of circular concrete-filled steel tube columns. *J Constr Steel Res* 60:1049–1068
17. Ajel HA, Abbas AM (2015) Experimental and analytical investigations of composite stub columns. *Int J Innovative Res Sci Eng Technol* 4(2):185–200
18. Hassanein MF, Kharoob OF, Liang QQ (2013) Circular concrete-filled double skin tubular short columns with external stainless steel tubes under axial compression. *Thin-Walled Struct* 73:252–263
19. Sakino K, Nakahara H, Morino S, Nishiyama I (2004) Behavior of centrally loaded concrete-filled steel-tube short columns. *J Struct Eng* 130:180–188
20. Gardner LD, Burdett (2008) Behaviour of concrete filled stainless steel Elliptical hollow sections. In: Proceeding of the second international symposium on innovative design of steel structures
21. Lu ZH, Zhao YG (2008) Mechanical behaviour and ultimate strength of circular CFT columns subjected to axial compression loads. In: World conference on earthquake engineering, Beijing, 12–17 Oct
22. Sundarraja MC, Prabhu G (2012) Experimental study on CFST members strengthened by CFRP composites under compression. *J Constr Steel Res* 72:75–83
23. Fujimoto T, Mukai A, Nishiyama I, Sakino K (2004) Behavior of eccentrically loaded concrete-filled steel tubular columns. *J Struct Eng* 130:203–212

Behavior of Steel–Concrete Composite Beam Section for Various Parameters



Prashant B. Kamate and Ashish P. Khatri

Abstract Guidelines related to apportioning of steel–concrete composite sections to achieve maximum moment capacity and ductility are not available in present design codes. Study carried out in this paper is useful for apportioning of steel–concrete composite section. In present study, moment–curvature relationship of steel–concrete composite section considering its different parameters are explored. The considered parameters include cylindrical strength of concrete, effective flange width of concrete slab, distribution of area of steel section and confinement of concrete slab. From present study, it is found that for unconfined and confined concrete slab, moment capacity and curvature ductility of symmetric as well as un-symmetric section increase with increase in cylindrical strength of concrete and effective flange width of concrete slab. For same area of steel section, un-symmetric composite section with larger bottom flange area shows higher moment capacity and lower curvature ductility than symmetric composite section. Confinement in concrete slab enhances moment capacity and curvature ductility of symmetric and un-symmetric cross section.

Keywords Steel–concrete composite beam · Moment–curvature · Effective flange width · Unconfined and confined concrete · Curvature ductility · Steel utilization ratio

1 Introduction

Nowadays, use of steel–concrete composite beam section is increasing in design of structures. Increased demand of composite section is due to effective use of concrete and steel material and increased speed of construction. As concrete is only strong in compression and weak in tension, composite section gives composite action only at sagging bending moment location. At this location, steel section is subjected to

P. B. Kamate · A. P. Khatri (✉)
Department of Applied Mechanics, VNIT, Nagpur, India
e-mail: as123khatri@gmail.com

© The Author(s), under exclusive license to Springer Nature Singapore Pte Ltd. 2023
M. Madhavan et al. (eds.), *Proceedings of the Indian Structural Steel Conference 2020*
(Vol. 2), Lecture Notes in Civil Engineering 319,
https://doi.org/10.1007/978-981-19-9394-7_11

139

tension, and concrete is subjected to compression, thus utilizing strength of each material in efficient manner. Composite section made of higher grade of steel gives enhanced moment capacity but limited ductility [17]. Also, concrete in composite section provides resistance to lateral torsional buckling of top flange of steel section [16], but under hogging moment cracking in the slab and local buckling of steel section changes strength and ductility of section [7]. From design point of view, beam section should give maximum ultimate moment capacity and ductility. However, current design codes, such as IS 11384 [4], AISC 360-10 [1] and Eurocode 4 [2] do not contain any guidelines for apportioning of steel–concrete composite beam section relating its maximum moment capacity and ductility. Moment–curvature of composite beams considering slip-behavior is studied by Fabbrocino et al. [3].

In present study, moment–curvature relationship of steel–concrete composite section considering different parameters is explored. The considered parameters are unconfined cylindrical strength of concrete (f_c), effective flange width of concrete slab (b_{ef}), distribution of area of steel section (symmetric and un-symmetric section), and confinement of concrete slab. These moment–curvature relationships are based on fundamental principles of mechanics considering respective stress–strain characteristics of steel and concrete materials. These are explored for the condition where concrete slab of the composite beam section is in compression under static loading and assuming complete interaction between concrete and steel section. Behavior of different cross sections, for unconfined and confined concrete slab, is compared on the basis of ultimate moment capacity of section (M_u) and ultimate curvature ductility (Φ_u) of section. Moreover, the cost of composite construction is affected by cross-sectional area of structural steel as well as concrete. For present study, the effectiveness of cross section of composite beam is determined by a term ‘percentage utilization of steel’ and ‘percentage utilization of concrete’. Percentage utilization of steel is total compressive and tensile force resisted by steel section at failure stage to its capacity when all fibers are yielded expressed in percentage. Percentage utilization of concrete is the ratio of area of concrete under compression at failure stage to total area of concrete expressed in percentage. Hence, behavior of different cross sections, for unconfined and confined concrete, is also compared with percentage utilization of steel and percentage utilization of concrete. The findings of analysis from present study is useful in apportioning of steel–concrete composite section to attain maximum moment capacity and curvature ductility.

2 Methodology

The moment–curvature analysis is performed on the basis of fundamental principles of mechanics. For analysis, program is developed in EXCEL VBA which includes iterative calculations. For analysis, position of neutral axis and strain in farthest point of bottom flange of steel section is assumed. Steel–concrete composite section is divided into number of small strips. As strain distribution across the section is linear, strain in each fiber is calculated using linearity. Stress in each strip of section

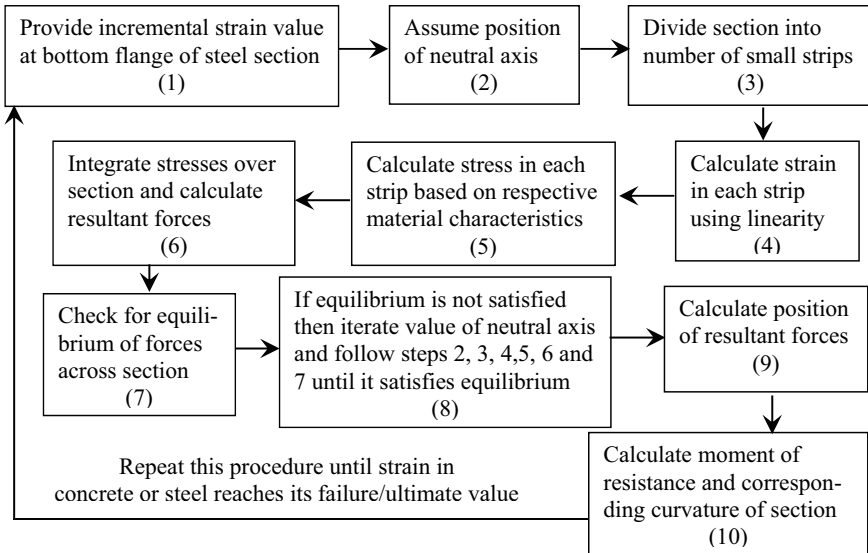


Fig. 1 Flowchart for moment–curvature analysis

is calculated according to appropriate stress–strain characteristics of each material. Stresses over the section are integrated, and resultant compressive and tensile forces are calculated.

For equilibrium of section, tensile force and compressive force on section must be equal. To attain this equilibrium, developed program iterates assumed value of neutral axis and performs similar calculations until satisfaction of equilibrium condition. Finally position of neutral axis for assumed value of strain in bottom flange of steel section is determined. Position of resultant compressive as well as tensile force is determined using integration approach. Figure 1 shows flowchart of step-by-step procedure for moment–curvature analysis of composite section.

Moment of resistance of section is calculated by multiplying resultant force with lever arm between two resultant forces. Curvature of section corresponding to its moment of resistance is calculated by determining ratio of strain in extreme fiber of steel section to its distance from neutral axis. Same procedure is followed for every positive increment of strain at bottom fiber. All possible elastic stages and all stages beyond last elastic stage till its failure are examined for determining moment of resistance and corresponding curvature of section. Failure of section is assumed to occur when strain in extreme fiber of concrete reaches to its failure strain or strain in extreme fiber of bottom flange of steel section reaches to its ultimate value. At failure stage, program gives ultimate moment capacity and ultimate curvature of composite section.

3 Parameter Variables and Material Characteristics

3.1 Parameter Variables

For present study of moment–curvature relationship, different parameters of cross sections are considered. The considered parameters for analysis are cylindrical strength of unconfined concrete (f_c), effective flange width of concrete slab (b_{ef}), distribution of area of steel section and confinement of concrete slab. Symmetric and un-symmetric section is provided with equal area of steel section. Considered steel sections are apporitioned to avoid any local buckling in steel section satisfying clauses of Indian standard IS 800 [6] for E250 grade of steel. Details of considered steel section such as top flange width (b_{tf}), top flange thickness (t_{tf}), bottom flange width (b_{bf}), bottom flange thickness (t_{bf}), depth of web (d_w) and thickness of web (t_w) are provided in Table 1.

Sufficient slab thickness is required to provide confining reinforcement in slab. For present study, considered slab thickness is maximum of thickness required from design considerations and practical provision of confinement reinforcement in slab. For comparison purpose, maximum required slab thickness of 200 mm is provided for all slabs mentioned in Table 1. Considered effective flange widths of steel–concrete composite sections are calculated according to Eurocode 4 [2]. All sections have same web depth and web thickness.

Strength and ductility of confined concrete depend on number of confined longitudinal bars and spacing of longitudinal bars. Assumed details of confining reinforcement in concrete slab and corresponding assumed longitudinal reinforcement in slab along length of beam are provided in Table 2. Reinforcement rings and links of grade Fe415 are provided as confining reinforcement.

Figure 2 shows reinforcement detailing of concrete slab of steel–concrete composite sections. These figures show considered details of spacing of longitudinal reinforcement and detailing of confining reinforcement in slab.

Table 1 Considered parameter in analysis

f_c (MPa)	b_{ef} (mm)	Type of section		Type of concrete
		Symmetric (mm)	Un-symmetric (mm)	
24	1000	$b_{tf} = 230$	$b_{tf} = 130$	Unconfined
40	750	$t_{tf} = 20$	$t_{tf} = 20$	Confined
	550	$b_{bf} = 230$	$b_{bf} = 330$	
		$t_{bf} = 20$	$t_{bf} = 20$	
		$d_w = 310$	$d_w = 310$	
		$t_w = 10$	$t_w = 10$	

Table 2 Details of assumed reinforcement in concrete slab

b_{ef} (mm)	Longitudinal reinforcement on each face of concrete slab	Confining Reinforcement of 8 mm diameter @ 170 mm c/c
1000	7 bars of 12 mm diameter	3 Nos of 2 legged rings + 3 Nos of links
750	5 bars of 12 mm diameter	2 Nos of 2 legged rings + 2 Nos of links
550	4 bars of 12 mm diameter	2 Nos of 2 legged rings

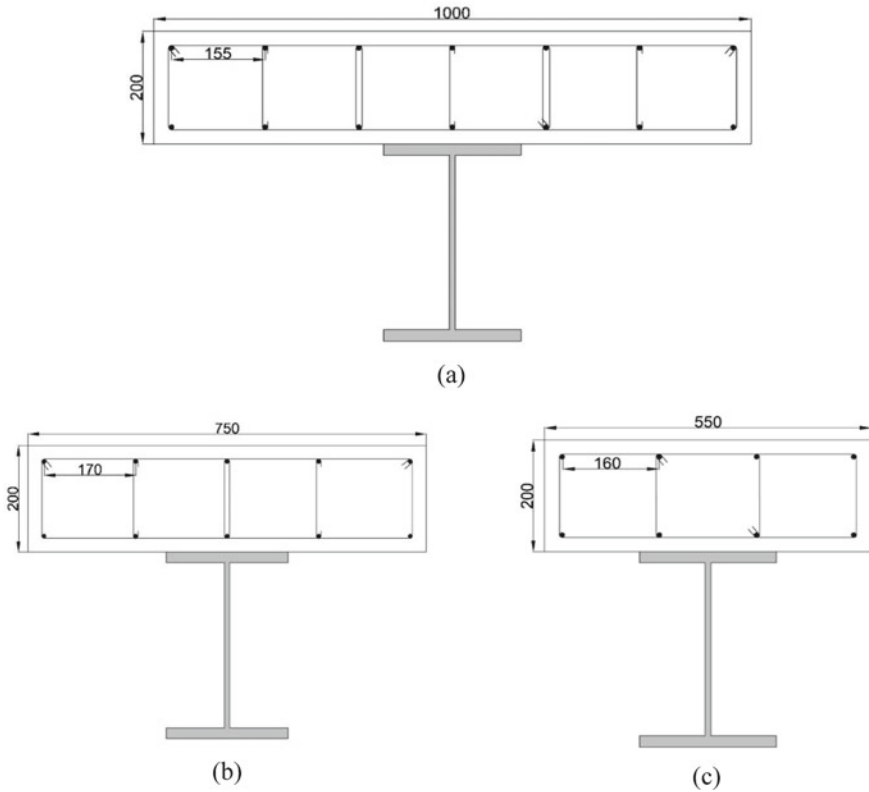
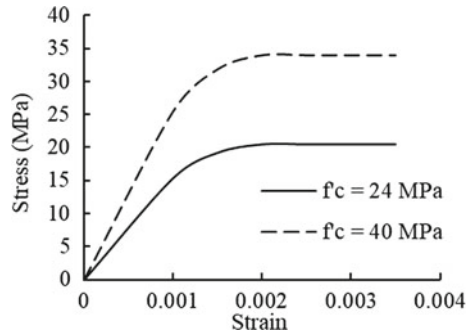


Fig. 2 Considered reinforcement detailing of effective concrete slab width **a** 1000 mm; **b** 750 mm; **c** 550 mm (All dimensions shown in figures are in mm.)

3.2 Material Characteristics

In this section, material characteristics of concrete and structural steel used for the present analysis purpose are discussed. Two different strengths of unconfined

Fig. 3 Idealized stress–strain curve for unconfined concrete in flexural compression



concrete are considered. Stress–strain curve in terms of cylindrical strength is developed for M30 and M50 grade of concretes [5]. Obtained corresponding cylindrical strength for M30 and M50 grade of concrete is 24 MPa and 40 MPa, respectively. Maximum flexural strength of concrete is less than cylindrical strength, and it can be obtained by applying correction factor of 0.85 factor to cylindrical strength of concrete. Considered stress–strain characteristics of concrete and steel used in present study do not include any material safety factors. Design strength can be obtained by applying appropriate material safety factors. Tension capacity of unconfined and confined concrete is neglected.

3.2.1 Unconfined Concrete

IS 456 [5] gives idealized stress–strain relationship of unconfined concrete in terms of cube strength and does not consider strength degradation of concrete after yield point. In present study, properties of unconfined concrete are considered as per IS 456 [5] and expressed in the form of cylindrical strength of concrete. Figure 3 shows idealized stress–strain characteristics of unconfined concrete in flexural compression. The maximum flexural stress in concrete is $0.85f'_c$. This maximum stress in concrete is at strain value of 0.002, and stress in concrete after this strain remains constant up to ultimate strain of concrete, i.e., 0.0035. Legends shown in Fig. 3 for unconfined concrete are in terms of cylindrical strength.

3.2.2 Confined Concrete

Kent and Park [9] and Mander's model [11] give stress–strain characteristics of confined concrete in terms of cylindrical strength of concrete. As Mander's model is used widely in many researches, in present study stress–strain characteristics of confined concrete are considered according to Mander's model [11]. Confined concrete model includes the strength degradation characteristics after attaining the maximum confined strength along with increase in strain values. Confined strength

of concrete and its failure strain depends upon length of leg of ring which mainly depends on spacing of longitudinal reinforcement of slab along its length and amount of confinement provided. For this reason, different confined concrete models for all considered flange widths are presented in Fig. 4.

In Fig. 4, legends are presented in terms of cylindrical strength of concrete, and same is followed in subsequent sections. From these graphs, it is clear that concrete slab with effective flange width of 1000 mm and longitudinal reinforcement spacing of 155 mm has higher value of confined strength and failure strain than others. This is due to more confinement in slab as compared with other considered slabs. So, strength and ductility of confined concrete increase with amount of confinement in it. Also, percentage increase in strength and failure strain of confined concrete are more for lower cylindrical concrete strength than higher cylindrical strength of concrete.

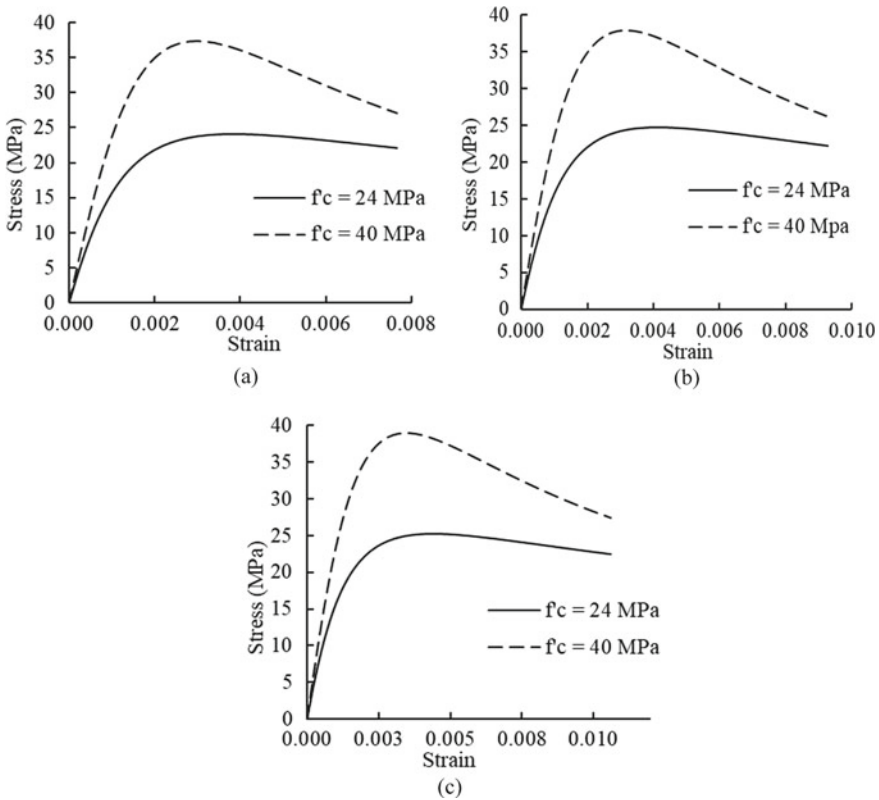
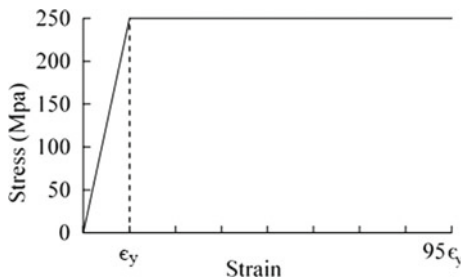


Fig. 4 Stress–strain curve of confined concrete in flexural compression for considered effective flange width **a** $b_{cf} = 550$ mm; **b** $b_{cf} = 750$ mm; **c** $b_{cf} = 1000$ mm

Fig. 5 Bilinear stress–strain characteristics of steel in tension/compression



3.2.3 Structural Steel

Structural steel material of grade E250 is considered for present moment–curvature analysis. Idealized bilinear curve of structural steel without considering effect of strain hardening is used. For considered composite sections, failure of section occurs when strain in concrete slab reaches to its failure strain, and corresponding maximum strain in steel section is much below than strain corresponding strain hardening effect. So, strain hardening effect of structural steel is not considered for present analysis. Figure 5 shows idealized bilinear stress–strain curve of considered structural steel material up to ultimate strain of steel (ϵ_{su}). It is assumed that steel material has same stress–strain characteristics in compression as well as in tension.

4 Analysis Procedure

Tables 1 and 2 show different parameters that are used to define a steel–concrete composite section for analysis. Using combinations of all considered parameters, analysis is carried out. While considering effect of particular parameter, all other parameters of cross section are kept constant. For every defined section, moment–curvature analysis is carried out as per methodology explained under Sect. 2 of this paper. For every increment in strain value, position of neutral axis changes from earlier one and shifts in upward direction, i.e., toward concrete slab. Neutral axis may lie in bottom flange of steel section or in web of steel section or top flange of steel section or in concrete slab of section. Developed program is capable of doing calculations for all position of neutral axis across section.

Figure 6 shows the general stress–strain distribution for intermediate stage after yielding of the composite section. On the basis of strain value in each fiber, analysis of composite section is divided into different stages, i.e., elastic stage and inelastic stage. In elastic stage, strain in all fibers of section is within elastic limit, i.e., linear stress–strain relationship will be followed. At ultimate stage, failure of section occurs when strain in extreme fiber of concrete reaches to its failure strain or strain in extreme fiber of bottom flange of steel section reaches to its ultimate value. For every increment of strain, moment capacity and curvature of section are calculated. Effect

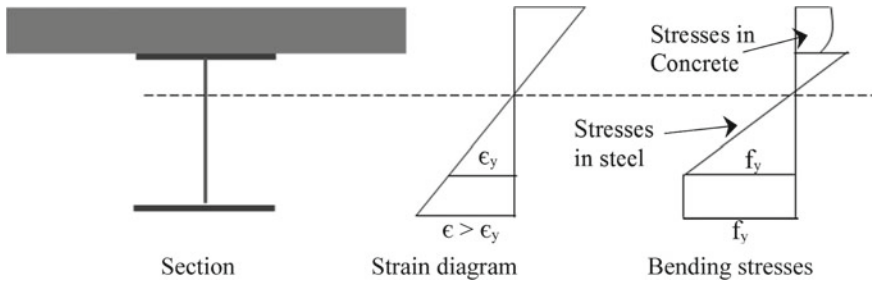


Fig. 6 Stress–strain distribution for intermediate stage after yielding of section

of longitudinal reinforcement in slab on moment–curvature analysis is negligible, so it is not considered in present analysis.

5 Analysis Results

Comparison of analysis results for different parameters is represented on the basis of ultimate moment capacity of section, ultimate curvature ductility, and percentage utilization of steel and concrete materials. In present study, apportioning of composite section results in yielding of steel section before attaining failure strain concrete slab and hence gives ductile failure of section. For this study, composite section gets yielded when strain in steel section reaches its yield strain. For plotting of analysis results, non-dimensional ratios such as moment capacity of section (M) to moment capacity at yielding of section (M_y), i.e., (M/M_y) and curvature of section (Φ) to curvature at yielding of section (Φ_y), i.e., (Φ/Φ_y) are calculated. Results are plotted as moment ratio on Y -axis and curvature ratio on X -axis. Also, ratios corresponding to ultimate moment capacity (M_u/M_y) and ultimate curvature value (M_u/M_y) are represented in tabular form. All considered composite sections have same thickness of concrete slab, same depth of web and same thickness of web as per Table 1.

5.1 Program Validation

Developed program of moment–curvature is validated with analysis software SAP [15]. Moment–curvature analysis for considered composite sections is performed in section designer of SAP 2000. Analysis results of four sections on the basis of developed program for present study and SAP 2000 are tabulated in Table 3. All four sections have thickness of slab as 200 mm, depth of web 310 mm and web as thickness 10 as mm.

From Table 3, it is clear that analysis results of developed program in this study are closely resembles to results of SAP 2000.

Table 3 Analysis results of developed program and SAP [15]

Developed program						SAP [15]	
f'_c (MPa), Concrete type	b_{cf} (mm)	b_{tf} (mm)	b_{bf} (mm)	M_u (kN-m)	Φ_u (m ⁻¹)	M_u (kN-m)	Φ_u (m ⁻¹)
24, unconfined	750	230	230	810	0.019	810	0.018
24, unconfined	1000	230	230	891	0.021	887	0.020
24, confined	750	130	330	981	0.017	985	0.017
24, confined	1000	130	330	1062	0.020	1058	0.019

5.2 Effect of Cylindrical Strength of Concrete and Confinement

In this section, effect of cylindrical strength of concrete for unconfined concrete strength of 24 and 40 MPa and its confinement on moment–curvature ($M-\Phi$) relationship of section is determined. These results are expressed in Fig. 7. All considered sections as per Table 4 have thickness of slab as 200 mm, depth of web as 310 mm and web thickness as 10 mm.

Figure 7a and b gives analysis results for unconfined and confined concrete composite sections, respectively. For both unconfined and confined concrete composite section, curvature ductility enhances with increase in strength of concrete. Also, confined concrete shows more ductility than unconfined concrete.

The results at the ultimate stage for both unconfined and confined steel–concrete composite section are also presented in Table 4. This table contains ultimate moment

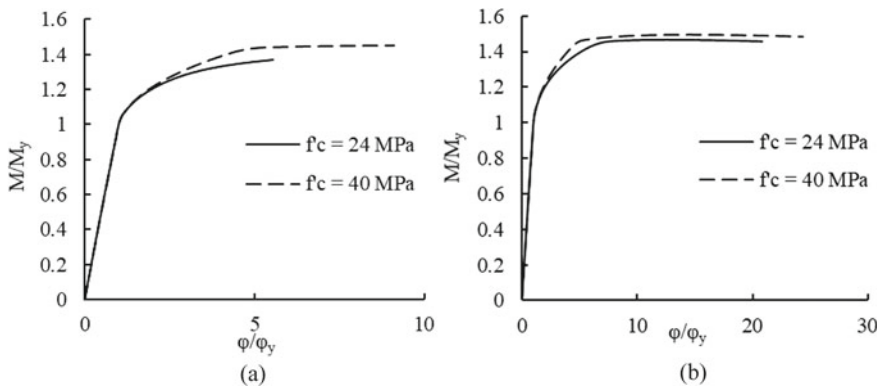


Fig. 7 Effect of cylindrical strength of concrete **a** unconfined; **b** confined

Table 4 Effect of cylindrical strength of concrete and confinement

f_c (MPa), concrete type	b_{cf} (mm)	b_{tf} (mm)	b_{bf} (mm)	M_y (kN-m)	M_u (kN-m)	Φ_u (m^{-1})	$\frac{M_u}{M_y}$	$\frac{\Phi_u}{\Phi_y}$	Steel section utilized (%)	Concrete section utilized (%)
24, unconfined	1000	230	230	650	891	0.021	1.37	5.5	89	84
40, unconfined	1000	230	230	696	1008	0.031	1.45	9.1	100	57
24, confined	1000	230	230	655	956	0.079	1.46	21.6	100	69
40, confined	1000	230	230	686	1021	0.087	1.49	25.1	100	47

capacity of section and ultimate curvature of section. Also, at ultimate stage of composite section percentage utilization of steel and concrete materials are tabulated in Table 4.

From these results, it is observed that in case of unconfined concrete by increasing concrete strength ultimate moment capacity of section is increased. For confined concrete, the effect of concrete strength on ultimate moment capacity is negligible. For confined as well as unconfined concrete percentage of steel section utilized increases with increase in concrete strength.

5.3 Effect of Symmetry of Section and Confinement

In this section, effect of symmetry of section on $M-\Phi$ relationship of composite section with unconfined concrete strength of 24 MPa and confinement thereof is determined. The analysis results for unconfined and confined concrete section are expressed in Fig. 8. All sections as per Table 5 have depth of slab 200 mm, depth of web as 310 mm and web thickness as 10 mm.

From results, it is observed that curvature ductility of unconfined and confined composite section is maximum for symmetric section. Also, confined concrete section shows more curvature ductility than unconfined concrete section for both symmetric and un-symmetric section.

The results at the ultimate stage are also presented in Table 5. This table contains ultimate moment capacity of section, ultimate curvature of section and percentage utilization of steel and concrete materials at ultimate stage of section. It is observed that confined and unconfined un-symmetric composite sections have more yield moment capacity and ultimate moment capacity than symmetric sections. Also, curvature ductility and percentage utilization of steel section are more for composite

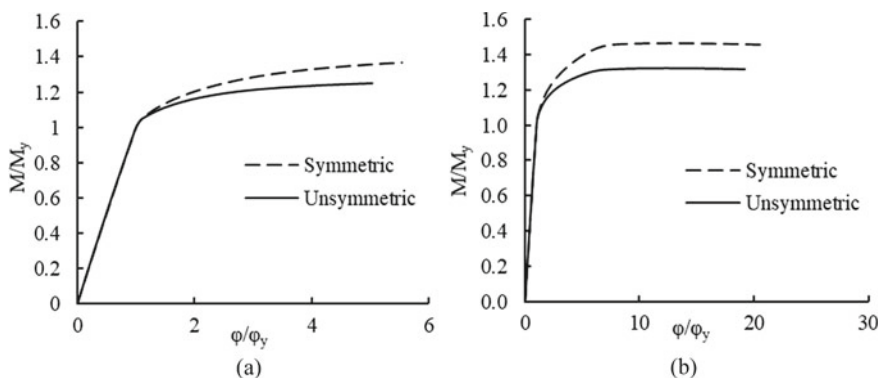


Fig. 8 Effect of symmetry of section **a** unconfined; **b** confined

Table 5 Effect of symmetry of composite section and confinement

f_c (MPa), concrete type	b_{cf} (mm)	b_{tf} (mm)	b_{bf} (mm)	M_y (kN-m)	M_u (kN-m)	Φ_u (m^{-1})	$\frac{M_u}{M_y}$	$\frac{\Phi_u}{\Phi_y}$	Steel section utilized (%)	Concrete section utilized (%)
24, unconfined	1000	230	230	650	891	0.021	1.37	5.5	89	84
24, unconfined	1000	130	330	849	1062	0.020	1.25	5.0	92	86
24, confined	1000	230	230	655	956	0.079	1.46	21.6	100	69
24, confined	1000	130	330	854	1123	0.082	1.32	20.7	100	68

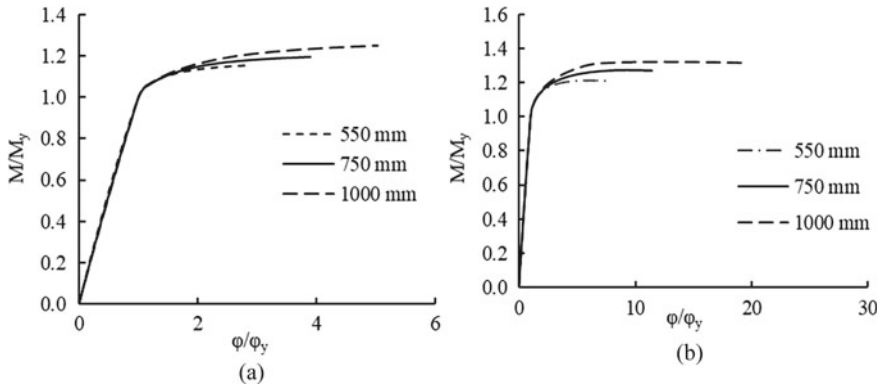


Fig. 9 Effect of flange width of concrete slab **a** unconfined; **b** confined

section of confined concrete. For un-symmetric section, increase in percentage utilization of concrete material is negligible.

5.4 Effect of Flange Width of Concrete Slab and Confinement

In this section, effect of flange width of concrete slab on moment–curvature relationship of composite section with unconfined concrete strength of 24 MPa and confinement thereof is determined. The analysis results for unconfined and confined concrete section are expressed in Fig. 9. As per Table 6, considered sections in this section have thickness of slab 200 mm, depth of web 310 mm and web thickness 10 mm. As un-symmetric section has more yield moment capacity and ultimate moment capacity than symmetric section, effect of flange width of concrete slab on M - Φ relationship is only checked for un-symmetric section.

From results it is clear that curvature ductility of composite section increases with increase in effective flange width of concrete slab. Composite section with confined concrete has more curvature ductility than unconfined concrete section.

The results at the ultimate stage are also presented in Table 6. This table contains ultimate moment capacity of section, ultimate curvature of section and percentage utilization of steel and concrete materials at ultimate stage of section. It is observed that ultimate moment capacity and ultimate curvature of section increases with increase in effective flange width of concrete slab for both confined and unconfined composite sections. Percentage utilization of steel section increases with increase in effective flange width concrete slab. In case of confined concrete section with more effective flange width, percentage utilization of steel section and curvature ductility is more than unconfined concrete section.

Table 6 Effect of effective flange width of concrete section and confinement

f_c (MPa), concrete type	b_{cf} (mm)	b_{lf} (mm)	b_{bf} (mm)	M_y (kN-m)	M_u (kN-m)	Φ_u (m^{-1})	$\frac{M_u}{M_y}$	$\frac{\Phi_u}{\Phi_y}$	Steel section utilized (%)	Concrete section utilized (%)
24, unconfined	550	130	330	781	902	0.015	1.15	2.9	82	100
24, unconfined	750	130	330	818	981	0.017	1.20	3.9	80	100
24, unconfined	1000	130	330	849	1062	0.020	1.25	5.0	92	86
24, confined	550	130	330	787	950	0.036	1.21	7.4	81	100
24, confined	750	130	330	823	1048	0.050	1.27	11.4	98	93
24, confined	1000	130	330	853	1123	0.082	1.32	20.7	100	68

6 Conclusions

Current design codes do not contain any guidelines for apportioning of steel–concrete composite section to give maximum moment capacity and ductility. Program based on principles of mechanics is developed to carry out moment–curvature analysis of steel–concrete composite section. Elastic and inelastic stage analysis is performed by considering respective material characteristics of steel and concrete for different parameters, viz. cylindrical strength of concrete effective flange width of concrete slab, distribution of area of steel section and confinement of concrete slab. Analysis results of sections are compared on the basis of ultimate moment capacity, ultimate curvature and percentage of material utilized. From results it is found that

- Higher strength of concrete results in higher ultimate moment capacity of unconfined composite section.
- For same area of steel section, un-symmetric composite section with larger bottom flange area has more yield moment capacity and ultimate moment capacity but lower ductility than symmetric section for unconfined and confined concrete sections.
- Ultimate moment capacity, curvature ductility of section and utilization of steel section increase with increase in effective flange width of concrete.
- Steel–concrete composite sections with confined concrete have more curvature ductility than unconfined concrete.

Analysis carried out in the present study provides basis for apportioning of steel–concrete composite section to attain maximum moment capacity and curvature ductility.

References

1. Ansi B (2010) AISC 360-10-specification for structural steel buildings. Chicago AISC
2. BS EN 1994-1-1 (2004) Eurocode 4. Design of composite steel and concrete structures. General rules and rules for buildings, pp 1994
3. Fabbrocino G, Manfredi G, Cosenza E (1999) Non-linear analysis of composite beams under positive bending. *Comput Struct* 70(1):77–89
4. Indian Standard, I.S. (1985) IS 11384 1985: code of practice for composite construction in structural steel and concrete. New Delhi
5. Indian Standard, I.S. (2000) IS 456 2000: plain and reinforced concrete. Code of practice (4th revision). New Delhi
6. Indian Standard, I.S. (2007) IS 800 2007: general construction in steel. Code of practice (3rd revision). New Delhi
7. Husain HM, Abdul-Majeed Q, Yousifany AH, Korkess IN (2009) Behavior of composite steel-concrete beam subjected to negative bending. *Eng Technol J* 27(1):53–71
8. Johnson RP (2018) Composite structures of steel and concrete: beams, slabs, columns and frames for buildings. Wiley
9. Kent DC, Park R (1971) Flexural members with confined concrete. *J Struct Div* 97:1969–1990
10. Kisała D (2016) Moment-curvature model for steel plate-concrete composite beams. *Procedia Eng* 161:950–957

11. Mander JB, Priestley MJ, Park R (1988) Theoretical stress-strain model for confined concrete. *J Struct Eng* 114(8):1804–1826
12. Park R, Paulay T (1975) Reinforced concrete structures. Wiley
13. Pauly T, Priestley MJN (1992) Seismic design of reinforced concrete and masonry buildings
14. Saatcioglu M, Razvi SR (1992) Strength and ductility of confined concrete. *J Struct Eng* 118(6):1590–1607
15. SAP C (2000) V-21, Integrated software for structural analysis and design, analysis reference manual. Computer and Structures Inc., Berkeley (CA)
16. Shamass R, Cashell KA (2017) Behavior of composite beams made using high strength steel. In: *Structures*, vol 12, pp 88–101. Elsevier
17. Yakel AJ, Azizinamini A (2005) Improved moment strength prediction of composite steel plate girders in positive bending. *J Bridg Eng* 10(1):28–38

Experimental Study on Cold-Formed Steel–Concrete Composite Trusses



B. L. Thippeswami, S. Waghmare, and S. R. Satish Kumar

Abstract Steel trusses supporting reinforced concrete floors and acting in composite action with it are efficient and functional arrangements for floor systems in buildings. If the truss can be made with cold-formed steel members connected by self-drilling screws the system becomes even more efficient. However, providing suitable shear connection between the truss and the slab becomes a challenge, and in this study, this was attempted by using cold-formed shear connectors connected to the top chord with self-drilling screws. The trusses were simply supported and tested under four-point bending. The truss carried higher loads due to mobilization of composite action with the concrete slab. Failure was ductile by loss of shear connector stiffness leading to local buckling of truss members. However, the truss can be used in lightly loaded floors of long spans as it can satisfy deflection limits. The test results are presented in the form of load-deformation curves and load-slip curves along with photographs showing the failure modes.

Keywords Cold-formed steel · Steel–concrete composite · Shear connector · Composite truss · Self-drilling screw

1 Introduction

Steel construction has evolved over the years to give more efficient forms of construction. One such form of construction is the use of cold-formed steel sections which are characterized by high width-to-thickness ratios and consequently suffer local buckling of cross-sections. Notwithstanding this aspect, they are used widely in construction and are characterized by high strength to weight ratios. Another form of steel construction is to use it in composite action with concrete. Consequently, the combination of cold-formed steel in composite action with concrete holds immense potential as a structural system for lightweight construction. Cold-formed lipped

B. L. Thippeswami · S. Waghmare (✉) · S. R. Satish Kumar
Department of Civil Engineering, Indian Institute of Technology Madras, Chennai, India
e-mail: sachinwaghmare06@gmail.com

© The Author(s), under exclusive license to Springer Nature Singapore Pte Ltd. 2023
M. Madhavan et al. (eds.), *Proceedings of the Indian Structural Steel Conference 2020*
(Vol. 2), Lecture Notes in Civil Engineering 319,
https://doi.org/10.1007/978-981-19-9394-7_12

channels and Z-sections acting composite with concrete have been tried in the recent past with some degree of success. Hot-rolled truss girders and open-web joists are also commonly used in multi-storey buildings as they provide strong and stiff floor systems and at the same time allow the unhindered passage of service lines through their webs. In this study, cold-formed steel trusses acting composite with concrete are investigated experimentally with the objective of using them in light-floor construction.

The most important component of a composite beam is the shear connector which prevents relative slip between the concrete and steel. In hot-rolled steel–concrete composite beams, the stud has emerged as the most commonly used shear connector due to its ease of welding to the beam flange. However, welding studs to cold-formed steel sections is not a viable option due to the thinness of the cold-formed sections. In profiled deck composite slabs, the shear connection between the deck sheet and concrete is achieved by creating indentations in the sheet. The method gives satisfactory results due to the large contact area between the steel sheet and concrete. In order to achieve adequate shear connection between a cold-formed steel section and concrete, the primary challenge lies in creating a simple but efficient shear connector. In this study, a cold-formed shear connector was developed by folding the sheet pieces like a hat section and attaching it to the lipped channel beam section by means of self-drilling screws. Uplift is prevented by inserting a piece of reinforcement into the shear connector. A sufficiently large number of shear connectors are used to get full shear connection. However, the shear connector is quite flexible and loses its stiffness rapidly with increase in load. In spite of this short coming, the beam was able to carry sufficient load and performed better than a pure steel beam. Failure was essentially by large slip in the shear connector leading to the full load coming on the steel truss whose members fail by local buckling.

2 Literature Review

In a pioneering study, Hanaor [1] tested a variety of shear connectors including CFS Channels screwed, bolted, and welded to the concrete slab. He found the resulting beam system to have ductile failure and concluded that a variety of systems are possible to use.

Lakkavalli and Liu [2] carried out push-out tests on pre-fabricated bent-up tabs, pre-drilled holes, and self-drilling screws in cold-formed steel C-sections with partially embedded flanges to evaluate their load-slip characteristics. The specimens exhibited ultimate loads of 60–113 kN achieved between 0.4 and 1.6 mm slips and failed by longitudinal cracks in the concrete. However, they did not report on the initial stiffness of the shear connectors. They also tested full-scale beams under four-point bending and the specimens failed by yielding of the tension flange in a ductile manner. The shear tabs exhibited maximum strength increase of about 19% followed by holes and self-drilling screws.

Mujagic et al. (2007) [3] carried out an analytical and experimental study on the load-slip behaviour, design, and behaviour of composite truss girders with standoff screws as shear connectors. Six full-scale composite trusses with spans from 7.3 to 12.2 m and truss depths of 200 and 500 mm were tested under almost uniformly distributed loads. Three of the trusses failed by flexural yielding of chord members while the other three failed by shearing of the connectors. They also presented an analytical model to estimate the failure loads assuming full shear connection.

Hsu et al. [5] tested cold-formed steel–concrete composite beams with continuous cold-formed furring shear connector screwed to the CFS section. The beams were about 4 m long and exhibited increase in strengths of 14–38% under four-point bending.

Lawson and Toufiq [4] tested cold-formed channel sections acting composite with slab using screws or bolts or perforations in the web as shear connectors. The beam spans were 0.8–1.7 m, and channel depths were 150–300 mm. They reported the increase in shear and flexural strength observed.

3 Test Details

The average yield and ultimate strengths of the cold-formed steel used in angle web members and channel chord members were obtained from coupon tests as 210 and 310 MPa, respectively. Concrete of grade M25 with an average cube crushing strength of 28 MPa and steel reinforcement of grade Fe500D with average yield and ultimate strengths of 515 MPa and 615 MPa, respectively, was used in the slab.

Push-out tests were carried out on the shear connectors in accordance with EC4 to get the load-slip relationship shown in Fig. 1. In this study, two push-out specimens P1 and P2 were tested to failure. Figure 1 also shows the detail of the push-out specimen. A cold-formed steel C section lipped channel was used with the shear connector cast into 250 mm wide \times 300 mm height 80 mm thick concrete slab. Push-out test specimens were cast with mix ratio of 1:1.78:2.95 with a w/c ratio of 0.5. A recess of 50 mm in height was provided between the bottom of the concrete slab and the lower end of the cold-formed steel section to allow for slip during testing. Shear connector on both sides of the flange of the C section for each specimen was embedded in the concrete slab to form the composite system.

Two composite trusses were made with the geometry shown in Fig. 2. The trusses were 2.4 m long and 500 mm deep. The top and bottom chords were of lipped channel sections 100 \times 60 \times 15 \times 2 thick, while the web members were angles of size 70 \times 70 \times 3 mm thick. The members were connected with several self-drilling screws of 6 mm diameter depending on the expected force in the member. The shear connectors were 1 mm thick folded plates and were connected to the top chord using self-drilling screws. Adequate shear connectors were provided to ensure full shear connection. The concrete slab was 500 mm wide and 80 mm thick and nominally reinforced with bars of 10 mm diameter.

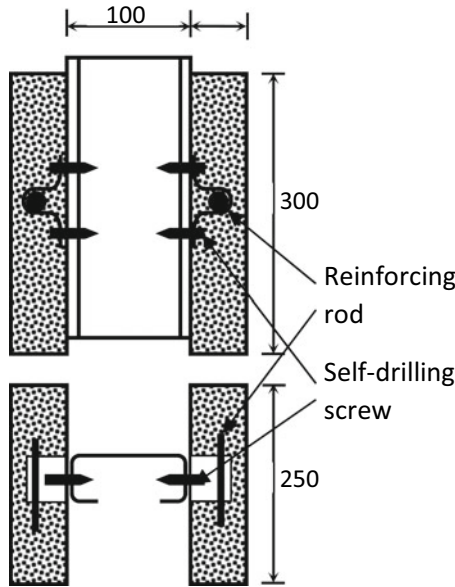


Fig. 1 Push-out test specimen

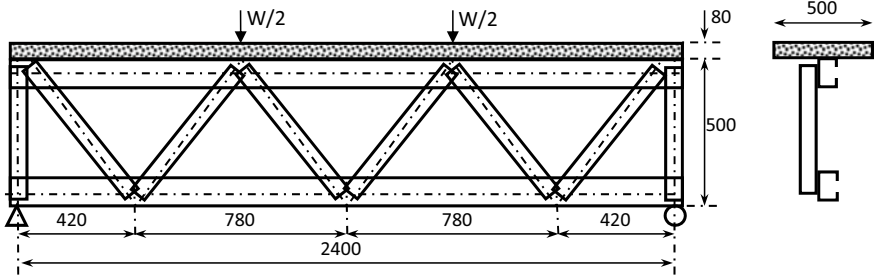


Fig. 2 Cold-formed steel–concrete composite truss details

The composite truss was simply supported over a span of 2.2 m and tested under four-point bending in a beam bending machine of 40 MT capacity. Linear voltage displacement transducers were used at mid-span and under a load point to measure the vertical displacement. Two LVDTs were placed at the end, one on the slab and the other on the top chord so that the difference in the readings gave the end slip. Strain gauges were pasted on the slab reinforcement, top and bottom chords to get the strain variation across the section. Loading was applied gradually, and the data from the load cell, LVDTs, and strain gauges were recorded in a data logger. A photo of the test setup is shown in Fig. 3.



Fig. 3 Photo of the composite truss test setup

4 Experimental Results

Push-out specimens P1 and P2 were kept under the loading ram, and load was applied on the load cell kept above the steel plate. Corresponding to the loads, slip between concrete and steel was recorded continuously using a data logger. The load-slip curves obtained from the push-out tests are shown in Fig. 4 for the two specimens P1 and P2 tested along with the average.

Both specimen exhibited a ductile failure with the shear connector folding up and the screws getting tilted as shown in Fig. 5. The maximum loads attained were 50 kN and 45 kN, respectively, for the two tests. Such a ductile behaviour of shear connector enables the design of partial shear connection between the steel and concrete. However, the loss of strength is a cause for concern as the use of such shear connectors implies that failure of the composite beam or truss is likely to be due

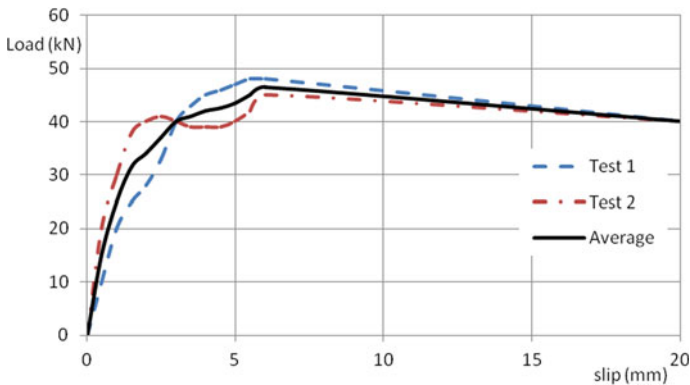


Fig. 4 Load-slip curve for shear connector

Fig. 5 Failure of push-out test specimen



to longitudinal shear at the interface rendering the steel and concrete as independent systems and eventual collapse due to non-composite action.

The four-point bending tests were carried out to observe the behaviour of the composite truss up to failure and the failure mode. Since the truss top chord was connected to the slab through the shear connectors, there was no possibility of lateral-torsional buckling of the truss even though no external support was provided. Both specimens behaved in a similar manner, and their load-mid-span deflection is shown in Fig. 6. As the load was increased, the stiffness reduced gradually due to the deformation of the shear connector. The trusses underwent yielding of the bottom chord at about 80 kN and thereafter lost their stiffness completely. The maximum loads attained by Specimen 1 was 81.3 kN while that attained by Specimen 2 was 111.2 kN, respectively.

The strains measure in Specimen 1 in the top and bottom chords are designated as SG11 and SG12, respectively. Similarly, the strains measured in Specimen 2 in the top and bottom chords are designated as SG21 and SG22, respectively. The load-strain graphs are shown in Fig. 7. The theoretical yield strain can be worked out as $\epsilon_y = f_y/E$, and with $f_y = 210$ MPa and $E = 200,000$ MPa works out to be 1050 microns. It is evident from Fig. 6 that the bottom chord has reached this strain and consequently yielded. However, the load continues to increase further as the steel did not show a well-defined yield plateau. The strain at ultimate stress of 310 MPa works out to be 1550 microns, and this is the point where the load stops increasing.

Although not presented here, the strains measured in the reinforcement also showed that the linear strain profile gets disturbed at about 80 kN load. The tests

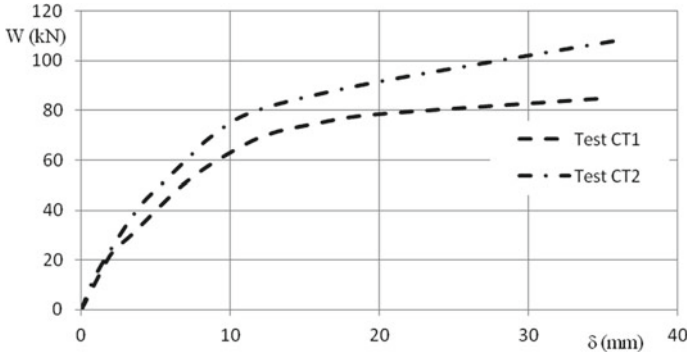


Fig. 6 Load–displacement curves for composite trusses

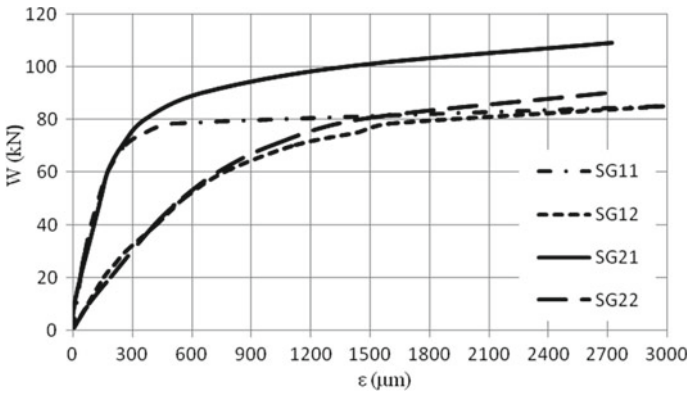


Fig. 7 Load-strain curves

were terminated when the compression members such as the end verticals and diagonals showed significant local buckling. The failure mode is shown in Fig. 8 where a black line is drawn connecting the bottom corners of the slab to indicate that the slab underwent significant bending deformation. However, due to the large span to depth ratio of the slab, no crushing was observed even at the failure point. The locations of local buckling are indicated with white circles in Fig. 7.

Finally, the average load-slip plot obtained for both specimens is shown in Fig. 9. Although there is a gradual decrease in the slope of the curve, the positive slope at collapse indicates that the shear connectors have performed well and are yet to reach their failure.



Fig. 8 Photo at test termination showing deflected shape and local buckling failures

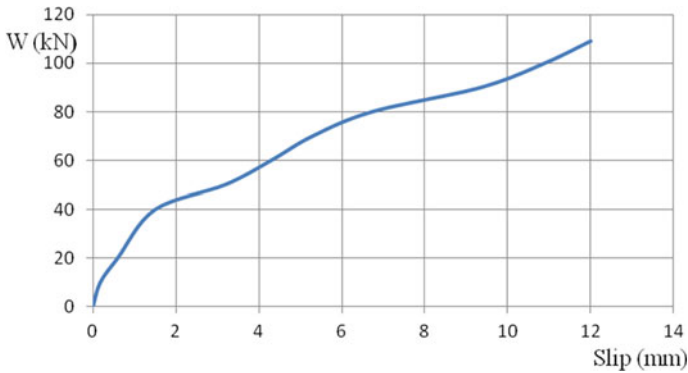


Fig. 9 Load-slip curve

5 Conclusions

The behaviour of cold-formed steel–concrete composite trusses was studied by carrying out tests. The truss and its folded plate shear connector were assembled using self-drilling screws and are easy to fabricate. It has the advantage of being lightweight, having high stiffness, and enabling service lines to pass through and can be used in flooring systems. The truss carried higher loads due to mobilization of composite action with the concrete slab. Failure was ductile by loss of shear connector stiffness leading to local buckling of truss members. However, the truss can be used in lightly loaded floors of long spans as it can satisfy deflection limits. Future studies should be aimed at maintaining the stiffness over larger loads and deflections.

References

1. Hanaor A (2000) Tests of composite beams with cold-formed sections. *J Constr Steel Res* 54(2):245–264
2. Lakkavalli BS, Liu Y (2006) Experimental study of composite cold-formed steel C-section floor joists. *J Constr Steel Res* 62(10):995–1006
3. Mujagic JRU, Easterling WS, Murray TM (2010) Design and behavior of light composite steel–concrete trusses with drilled standoff screw shear connections. *J Constr Steel Res* 66(12):1483–1491
4. Lawson RM, Taufiq H (2019) Partial shear connection in light steel composite beams. *J Constr Steel Res* 154:55–66
5. Hsu CTT, Punurai S, Punurai W, Majdi Y (2014) New composite beams having cold-formed steel joists and concrete slab. *Eng Struct* 71:187–200
6. Baran E, Topkaya C (2014) Behavior of steel-concrete partially composite beams with channel type shear connectors. *J Constr Steel Res* 97:69–78. <https://doi.org/10.1016/j.jcsr.2014.01.017>
7. Youns MA, Hassaneen SA, Badr MR, Salem ES (2016) Composite beams of cold formed steel section and concrete slab. *J Constr Steel Res* 4(4):165–177
8. Tian L-M, Kou Y-F, Hao J-P, Zhao L-W (2019) Flexural performance of a lightweight composite floor comprising cold-formed steel trusses and a composite mortar slab. *Thin-Walled Struct* 144:106361

Concrete-Filled Tubular Column: A Comparative Study of EC4 and AISC 360-10



Ankit Sachdeva, Arvind Vyavahare, and Gourav Sachdeva

Abstract Concrete-filled tubular (CFT) column is a revolutionary combination of steel and concrete. It takes into account the respective merits and overcomes the limiting characteristics of these materials individually. This is being used worldwide from low rise to high multi-storeyed structures, but still its usage in India is limited due to the unavailability of standard specifications. Thus, a detailed study of EC4 and AISC 360-10 on axially loaded CFT column has been carried out, and their comparison has been made. Also, a database of more than 130 experiments from the literature has been created to assess the suitability of above standards for a large range of parameters. It is found that the predictions of EC4 are in good agreement with the experimental results, whereas the AISC 360-10 shows quite conservative results due to disregard of confinement effect of steel tube on concrete. The application range of EC4 can be extended to concrete of higher strength and to a higher diameter to thickness (D/t) ratio of steel tube. Based on the study carried out on the behaviour of various columns from literature, few refinements in the AISC 360-10 and EC4 are suggested incorporating the above discussed requirements which should be further studied.

Keywords Composite column · Concrete-filled tubular column · CFT · EC4 · AISC 360-10

A. Sachdeva (✉)
GEC, Rewa, Rewa, India
e-mail: ankit0508sachdeva@gmail.com

A. Vyavahare
VNIT Nagpur, Nagpur, India
e-mail: ayv@apm.vnit.ac.in

G. Sachdeva
WAPCOS Limited, Bhopal, India

1 Introduction

The concrete-filled tubular column is a combination of hollow steel tube and concrete which eliminates the limitations of the above materials. The concrete filled in the hollow steel reduces the chances of local buckling of steel tube. Also as the concrete is filled in the steel tube, it eliminates the inward buckling of steel tube. Further the steel tube provides a confining pressure on the concrete and thus helps in improving its strength which is a unique and most desired characteristic of CFT columns. From the past studies, it has been observed that the confinement effect of steel tube on concrete strength was not visible for small axial loads when the Poisson's ratio of steel under the load was greater than concrete and the effect comes into picture only after the strain exceeds 0.001 [7]. The CFT columns possess high stiffness, ductility and energy absorption characteristics which make them suitable to be used under earthquake prone zones [23].

A number of researchers have carried out experimental studies covering together a large range of a number of parameters such as length-to-diameter (L/D) ratio, D/t ratio and strength of materials. In order to understand the behaviour of columns, few researchers have tried to compile and create a database of the past studies [7, 17, 23]. These compilations have helped in understanding the general behaviour of CFT columns and thus have been proved as foundation for the formation and revision of design standards.

A number of standards are available across the world which provide guidelines for the analysis and design of a CFT column. Some of them are American standard AISC 360-10, Australian Standard AS 5100.6, Chinese Standard DBJ/T13-51-2010 and European standard Eurocode-4 (EC4). The CFT columns are being utilized worldwide due to its various merits. However, its usage in India is still very limited due to the unavailability of design standard in the country for the CFT columns. The guidelines set by the design standards help the practicing engineers to incorporate these new structural members into the real-time structures with confidence.

The objective of this study is to provide an up-to-date database of relevant and significant experimental studies carried out on the CFT columns by various researchers in the past which covers a vast range of parameters from the past researches. Thus, this database is also utilized further to judge the predictions of EC4 and AISC 360-10 for varying range of parameters for a CFT column which will help in understanding the accuracy of above standards and may be further utilized for the formation of a new standard for a country like India.

2 Design Standards

EC4 and AISC 360-10 are the two design standards which are being used widely for the prediction of capacity of composite members. In this section, a review of prediction method of each code for axially loaded circular concrete filled tubular column has been presented.

2.1 Eurocode 4 (EN 1994-1-1)

The EC4 provides a limit state-based design approach which incorporates partial safety factor for materials and loadings. The guidelines given by EC4 can only be referred for the members who satisfies certain conditions. These conditions are based upon material grade and geometry which are as follows:

- (i) The provisions will be applicable to columns and compression members with steel grades in between S235 to S460 and concrete of strength classes C20/C25 to C50/C60.
- (ii) The steel contribution ratio δ should satisfy the following condition given in Eq. (1)

$$0.2 \leq \delta \leq 0.9 \quad (1)$$

where $\delta = \frac{A_a f_{yd}}{N_{pl,Rd}}$

Here, A_a = Area of steel tube and f_{yd} = Design yield strength of steel tube.

- (iii) Circular concrete filled tubular column should be checked for resistance to local buckling as per the Eq. (2)

$$\text{Max.} \left(\frac{D}{t} \right) = 90 \frac{235}{f_y} \quad (2)$$

EC4 provides two methods for the prediction of capacity of axially loaded CFT columns, namely general method and the simplified method. The general method can be referred for any section and for any member which may be uniform or not, whereas the simplified method can be used only when the section is doubly symmetrical and the member is uniform along its length. Also the relative slenderness $\bar{\lambda}$ should fulfil condition given by Eq. (3).

$$\bar{\lambda} = \sqrt{\frac{N_{pl,Rk}}{N_{cr}}} \leq 2.0 \quad (3)$$

$N_{pl,Rk}$ = Characteristic value of plastic resistance to compression given by Eq. (4)

$$N_{pl,Rk} = A_a f_{yd} + A_c f_{cd} + A_s f_{sd} \quad (4)$$

A_c = Cross-sectional area of concrete; f_{cd} = Design strength of concrete;
 A_s = Area of reinforcement in the column; f_{sd} = Design strength of steel reinforcement.

N_{cr} = Elastic critical force for the relevant buckling mode is given in Eq. (5)

$$= \frac{\pi^2 (EI_{eff})}{l_e^2} \quad (5)$$

(EI_{eff}) = Characteristic value of the effective flexural stiffness of a cross section is given in Eqs. (6) and (7)

$$= E_a I_a + E_s I_s + K_c E_{cm} I_c \quad (6)$$

I_a = Second moment of area of steel tube; I_s = Second moment of area of steel reinforcement.

I_c = Second moment of area of un-cracked area of concrete section.

K_c is a correction factor which works for the reduction of flexural stiffness of the concrete, and its value should be taken equals to 0.6.

$$E_{cm} = 22000 \left(\frac{f_{ck} + 8}{10} \right)^{0.3} \quad (7)$$

f_{ck} = Characteristic compressive strength of concrete

Finally, the design value of the normal force N_{Ed} should satisfy Eq. (8)

$$\frac{N_{Ed}}{\chi N_{pl,Rd}} \leq 1.0 \quad (8)$$

Here, $N_{pl,Rd}$ is the design plastic resistance of the composite section. It is worth mentioning that in the case of concrete filled tubes of circular section the effects of enhancement in strength of concrete due to confinement have been considered in EC4. However, this confinement effect will be taken into account if $\bar{\lambda} \leq 0.5$, and the design plastic resistance will be given Eq. (9)

$$N_{pl,Rd} = \eta_a A_a f_{yd} + A_c f_{cd} \left(1 + \eta_c \frac{t}{d} \frac{f_y}{f_{ck}} \right) + A_s f_{sd} \quad (9)$$

Here, η_a is the steel reduction factor, and η_c is the concrete enhancement factor. The value of η_a and η_c for loading eccentricity less than 10% of the outer diameter of the structural steel tube is given by Eqs. (10) and (11).

$$\eta_a = 0.25(3 + 2\bar{\lambda}) \quad (\text{But } \leq 1.0) \quad (10)$$

$$\eta_c = 4.9 - 18.5\bar{\lambda} + 17\bar{\lambda}^2 \quad (\text{But } \geq 0) \quad (11)$$

In Eq. (8), χ works as a reduction factor which takes into account the second-order effect due to the imperfections of steel tube and is given by Eq. (12).

$$\chi = \frac{1}{\left(\emptyset + \left(\emptyset^2 - \bar{\lambda}^2\right)^{0.5}\right)} \quad (12)$$

2.2 AISC 360-10

American Institute of Steel Construction also provides some provisions to determine the strength of composite sections. This standard allows the use of both limit state design and allowable stress design. However, application of the provisions is subjected to the fulfilment of certain governing conditions provided by the standard which are as follows:

- (i) The compressive strength of concrete (f'_c) should be in the range between 21 and 70 MPa.
- (ii) The minimum yield stress of structural steel and reinforcing bars to be used in strength calculations shall not exceed 525 MPa.
- (iii) The steel section shall comprise at least 1% of the total cross section.

The nominal compression capacity (P_n) of the member of given length for the limit state of flexural buckling based on member slenderness can be determined using Eqs. (13)–(21) as per following classification:

- (i) When $\frac{P_{no}}{P_e} \leq 2.25$

$$P_n = P_{no} \left[0.658 \frac{P_{no}}{P_e} \right] \quad (13)$$

- (b) When $\frac{P_{no}}{P_e} \geq 2.25$

$$P_n = 0.877 P_e \quad (14)$$

P_e = Elastic critical buckling load.

$$P_e = \frac{\pi^2 (EI_{\text{eff}})}{KL^2} \quad (15)$$

EI_{eff} = The effective stiffness of the composite sections

$$EI_{\text{eff}} = E_s I_s + E_s I_{sr} + C_3 E_c I_c \quad (16)$$

$$C_3 = 0.6 + 2 \left[\frac{A_s}{A_c + A_s} \right] \leq 0.9 \quad (17)$$

Here, P_{no} = Nominal compressive strength for the zero length, doubly symmetric axially loaded composite member.

P_{no} is section strength which is different for compact, non-compact and slender section as given below.

(i) For Compact sections

$$P_{no} = P_p$$

$$P_p = f_y A_s + C_2 f'_c \left(A_c + A_{sr} \frac{E_s}{E_c} \right) \quad (18)$$

where $C_2 = 0.95$

(b) For Non-Compact sections

$$P_{no} = P_p - \frac{P_p - P_y}{(\lambda_r - \lambda_p)^2} (\lambda - \lambda_p)^2 \quad (19)$$

Here, λ , λ_p and λ_r are section slenderness ratios determined from Table 1 corresponding to slender, compact and non-compact sections, respectively.

(iii) For Slender sections

$$P_{no} = F_{cr} A_s + 0.7 f'_c \left(A_c + A_{sr} \frac{E_s}{E_c} \right) \quad (20)$$

$$F_{cr} = \frac{0.72 F_y}{\left(\left(\frac{D}{t} \right) \frac{F_y}{E_s} \right)^{0.2}} \quad (21)$$

In the above equations, A_s , A_c and A_{sr} are the area of steel tube, concrete and steel reinforcement in the column.

In comparison of EC4, AISC 360-10 provides a comprehensive classification for cross section of CFT column based on the local buckling which covers a wide range of sections. The classification is shown in Table 1.

Table 1 Limiting diameter-to-thickness ratios for compression members under axial compression. (AISC 360-10)

Element	Width to thickness ratio	Compact/non-compact	Non-compact/slender	Maximum permitted
Round HSS	D/t	$\frac{0.15E}{f_y}$	$\frac{0.19E}{f_y}$	$\frac{0.31E}{f_y}$

3 Assessment of Design Standards Using the Database

A compilation of experimental studies is created which includes only those tests which are having unique characteristics and are comprising axially loaded CFT columns without any reinforcement. The database excludes specimens with non-circular geometry or specimens which are non-axially loaded. Table 2 shows the details of specimens from various experimental studies.

The compilation shows that the majority of the experiments conducted in past were focused on stub columns and the material with low-to-medium strength. Only 28% of the specimens from this database were in the range of practical application length of columns. Also, it is found that there were only 16% of specimens which have been tested with characteristic compressive strength greater than 80 MPa and only 5% of specimens were those incorporating the structural steel tube with characteristic yield strength of 390 MPa or more.

Table 2 Experimental work on axially loaded concrete filled tubular column from literature

S. No.	References	No. of specimens	L/D	D/t	f_{ck}	F_y
1	Ekmekyapar and Eliwi [6]	18	2.63–7.89	19.3–42.2	56–107	270–479
2	Abed et al. [1]	6	2.19	20–53.8	60	354
3	Perea et al.	3	31.4–33.8	55–86	38–88	306–479
4	Dundu [5]	12	7.9–19.7	25–46	32–106	186–479
5	Lee et al. [15]	2	4.89–5.26	25–60	32	343
6	Oliveira et al. [3]	16	3.00–10.00	33.53	30–100	313–537
7	Nardin and Debs [4]	2	9.45	26.2–39.7	48–59	329–355
8	Yu et al. [24]	4	2.96–3.00	45.6	43–77	287–306
9	Giakoumelis and Lam [9]	8	2.61	20.89–30.26	31–105	340–479
10	Gupta et al. [10]	1	47.2	24.89	25	360
11	Zeghiche and Chaoui [25]	15	12.5–25	32	40–106	280
12	Han and Yao [12]	3	3.0–10.0	33.33–66.67	40	256–363
13	Han and Yao [11]	3	3–11.6	44	20–36	185–337
14	O’Shea and Bridge [20]	18	3.4–3.5	58.9–211	38–108	185–363
15	Han [13]	11	32.5–38.5	24	32–47	210–415
16	Schneider [21]	3	4.2–4.4	20–47	24–28	285–360
17	Lin [17]	3	5.33	71–107	23–35	305–340
18	Gardner and Jacobson [8]	2	10.9–14.9	32.9–47.8	21–34	328–340
	Total	130				

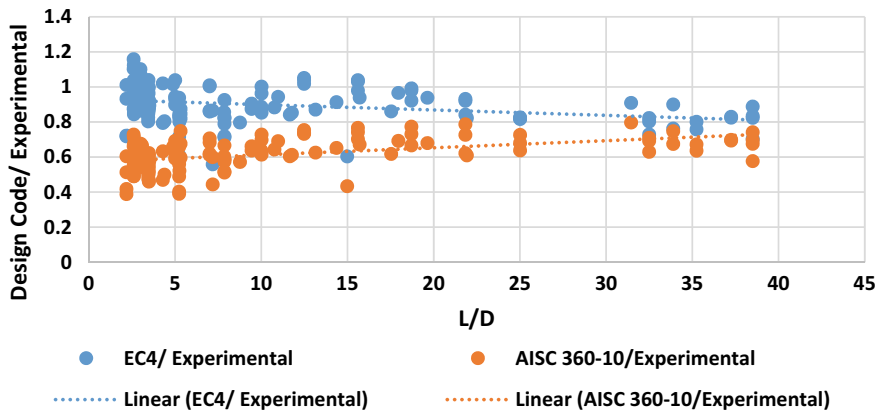


Fig. 1 Plot between the prediction of design standard with L/D of specimen

In order to assess the prediction of the Eurocode 4 and AISC 360-10, a comparison of experimental results for the various specimens has been made with that of the codal predictions, and a graph has been plotted between the ratio of prediction of design standards to experimental result to the ratio of L/D of the specimen which is shown in Fig. 1. It is to be noted that these predictions are without taking into account the partial safety factor for material provided by these codes.

It can be seen from Fig. 1 that for few specimens with L/D less than 5, i.e. for the stub columns, the EC4 over-predicts the strength. When L/D is in between 5 and 20, the predictions of EC4 are quite close to the experimental results, and as we go beyond L/D 20, the predictions of EC4 are continuously towards conservative side. However, if we observe the predictions of AISC 360-10, we can see that it continuously gives very conservative results; however as we increase the L/D ratio, the difference between predicted and experimental value decreases.

The predictions of AISC 360-10 are very conservative because it does not take into account the effect of confinement on concrete by the steel tube which is very significant for short columns which generally fails by crushing. The EC4 does take into account this effect and thus show better results. The longer columns fail by overall buckling which occurs well before the concrete and steel reach their ultimate strength, and thus, the confinement effect does not come into picture. This is the reason behind the improvement of strength prediction of AISC 360-10 for longer columns, and thus, the difference between the predictions of these code reduces in these columns.

The database also includes few specimens which were beyond the applicable limits of EC4. An attempt has been made to observe the prediction of EC4 for such specimens. Figure 2 shows the predictions of EC4 for 24 such specimens.

As can be observed there are a number of specimens in Fig. 2 which are having diameter-to-thickness ratio almost twice to that of the maximum applicable D/t ratio.

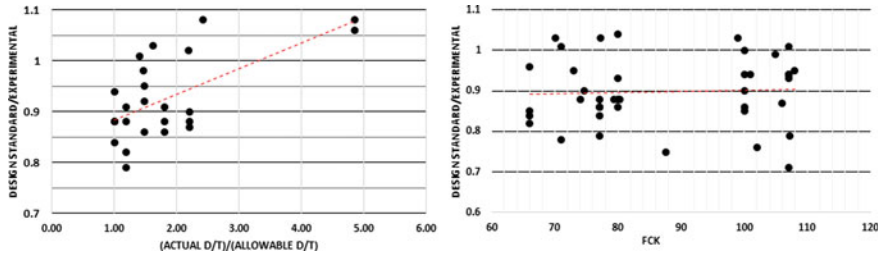


Fig. 2 Predictions of EC4 for specimens beyond the applicable D/t ratio and f_{ck}

The mean of all these specimens was 0.95 which represents that the limit on maximum D/t for the application of EC4 can be extended.

Also, the database includes few specimens which have concrete of characteristic strength beyond the application limit of these standards. The predictions of EC4 for such specimens is shown in Fig. 2. It can be clearly seen that for these specimens which are having concrete characteristic compressive strength of more than 100 MPa the results suggested by EC4 are in a good agreement with the experimental results with a mean of ratio of EC4 to experimental prediction as 0.91. It is to be noted that the upper limit specified by EC4 on usage of concrete is 60 MPa.

4 Strength of Confined Concrete from the Literature

In order to include the effect of confinement on the strength of concrete in AISC 360-10, a detailed study of confinement models suggested by various researchers have been made, and few most relevant are presented.

Mander et al. [18] have presented his study on the circular R.C.C. columns, but this has been taken into account for CFT columns because both of them show similar confinement effect which is better in the case of concrete filled tubular steel columns. Martinez et al. [19] conducted an experimental study on large number of short circular RCC columns confined by spiral reinforcement with high grade of concrete and provided an expression for strength of confined concrete. Attard and Setunge [2] were most probably from the first few authors who had actually gave suggestion regarding the confinement effect on concrete filled tubular column itself. They had carried out a large number of testing on high grade concretes and thus gave a full stress-strain behaviour of both confined and unconfined concrete. Giakoumelis and Lam [9] had carried out an experimental study on the stub concrete filled tubular columns with varying range of concrete characteristic strength. In order to improve the predictions of ACI 318 the author on the basis of regression analysis suggested to incorporate an increase in grade of concrete by 30%. Hu et al. [14] had carried out an analytical study, and based on the previous studies, they had suggested the stress strain relationships for confined concrete.

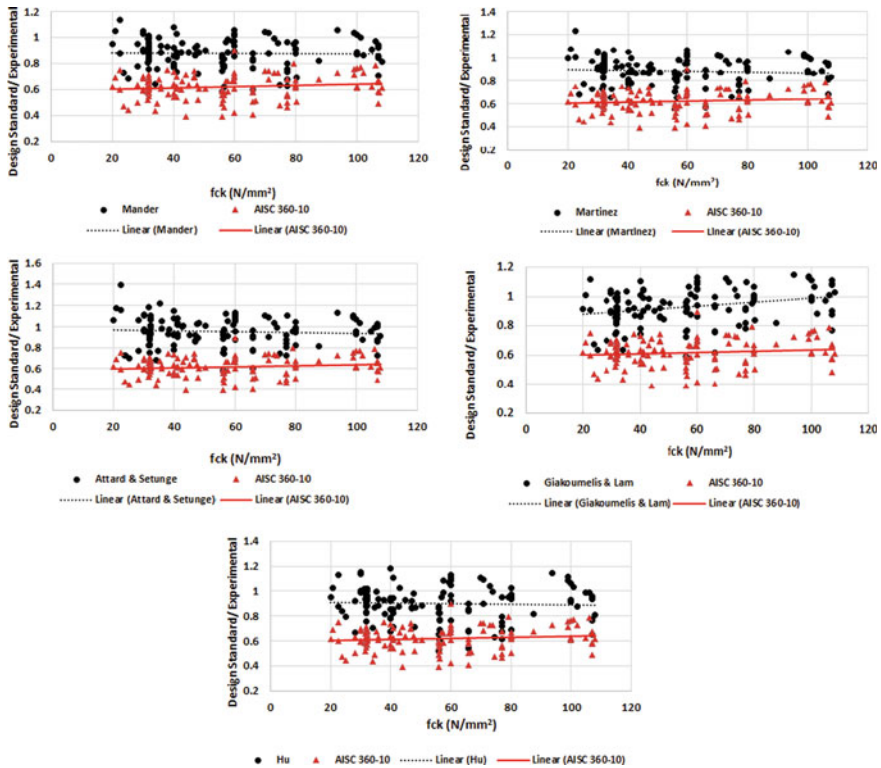


Fig. 3 Predictions of AISC 360-10 with and without the confinement models suggested by various researchers

The expressions for strength of confined concrete provided by above authors are used and incorporated with AISC 360-10 to observe the impact on predictions, and the results are shown in Fig. 3. As can be clearly seen by incorporation of any of the above confinement model, the predictions of AISC 360-10 improve, and it gets closer to the experimental result.

5 Results and Discussion

The predictions of AISC 360-10 by incorporating any of these models have shown a considerable shift towards the experimental values. However, in order to find the best among the discussed confinement models, the mean and standard deviation of predictions after incorporating these models with AISC 360-10 is given in Table 3.

It can be observed from Table 3 that by incorporating any of the above-discussed confinement models the results are improved to a large extent. However, the best results are being observed by incorporation of equation for confined strength of

Table 3 Comparison of various confinement model on different parameters

Parameters	Mander et al	Martinez et al	Attard and Setunge	Giakoumelis and Lam	Hu et al	AISC 360-10
Mean	0.879	0.882	0.951	0.928	0.899	0.619
Standard deviation (σ)	0.109	0.112	0.130	0.118	0.137	0.091
Mean+ σ	0.988	0.994	1.081	1.047	1.035	0.709
Mean- σ	0.769	0.770	0.821	0.810	0.762	0.528
Mean+2 σ	1.097	1.106	1.211	1.165	1.172	0.800
Mean-2 σ	0.660	0.658	0.692	0.692	0.625	0.437

concrete provided by Mander et al. with a mean of 0.879 and a standard deviation (σ) of 0.109. Also, the mean $\pm 2\sigma$ and mean $\pm \sigma$ values by employing Mander et al. [18] is considerably improved from that of current AISC 360-10. Thus, this equation can be incorporated to improve the predictions of AISC 360-10. The equation provided by Mander et al. [18] which gives the strength of confined concrete is as given by Eqs. (22) and (23).

$$f_{cc} = f_{ck} \left(-1.254 + 2.254 \times \sqrt{1 + \frac{7.94 \times f_1}{f_0} - 2 \times \frac{f_1}{f_{ck}}} \right) \quad (22)$$

Here

$$f_1 = \frac{2 \times 0.1 \times f_y \times t}{D} \quad (23)$$

f_1 = Confining stress which is a function of yield strength of steel tube and D/t ratio of tube

In order to take confinement effect into account, the characteristic strength of concrete (f'_c) in Eqs. (18), (19) and (20) will be taken as equal to the value of f_{cc} given by Eq. (22).

The predictions of EC4 were pretty close to the experimental results for the axially loaded CFT columns. Also, it is found that the prediction of EC4 is close to experimental results for various specimens, which are beyond the applicable limits of EC4 on D/t and f_{ck} .

Thus, these limits can be revised. Based on the predictions of EC4 on various specimens, the new limits mentioned in Table 4 can be referred. It is to be noted that the predictions of EC4 are pretty close to the experimental values even for those specimens which are having characteristics beyond the suggested limits. However, more studies on specimens beyond the applicable limits of EC4 should be conducted to have further verification of the suggested limits in Table 4.

Also, as found from the collected literature, there are very few studies conducted on CFT columns with high strength concrete and steel with a total of 16% of studies

Table 4 Suggested limits for D/t and f_{ck}

Parameters	Previously	Suggested
D/t	21,150/ f_y	29,000/ f_y
f_{ck}	60 MPa	90 MPa

with f_{ck} greater than 80 MPa and only 5% with f_y greater than 390 MPa. Thus, more studies in this range should be conducted.

References

1. Abed F, AlHamaydeh M, Abdalla S (2013) Experimental and numerical investigations of the compressive behavior of concrete filled steel tubes (CFSTs). *J Constr Steel Res* 80:429–439
2. Attard MM, Setunge S (1996) Stress-strain relationship of confined and unconfined concrete. *Mater J* 93(5):432–442
3. de Oliveira WLA, De Nardin S, de Cresce El ALH, El Debs MK (2009) Influence of concrete strength and length/diameter on the axial capacity of CFT columns. *J Constr Steel Res* 65(12):2103–2110
4. De Nardin S, El Debs ALHC (2007) Axial load behaviour of concrete-filled steel tubular columns. *Proc Inst Civ Eng-Struct Build* 160(1):13–22
5. Dundu M (2012) Compressive strength of circular concrete filled steel tube columns. *Thin-Walled Struct* 56:62–70
6. Ekmekyapar T, Al-Eliwi BJ (2016) Experimental behaviour of circular concrete filled steel tube columns and design specifications. *Thin-Walled Struct* 105:220–230
7. Furlong RW (1967) Strength of steel-encased concrete beam columns. *J Struct Div* 93(5):113–124
8. Gardner NJ, Jacobson ER (1967) Structural behavior of concrete filled steel tubes. In: *Journal proceedings*, vol 64, no 7, pp 404–413, July 1967
9. Giakoumelis G, Lam D (2004) Axial capacity of circular concrete-filled tube columns. *J Constr Steel Res* 60(7):1049–1068
10. Gupta PK, Sarda SM, Kumar MS (2007) Experimental and computational study of concrete filled steel tubular columns under axial loads. *J Constr Steel Res* 63(2):182–193
11. Han LH, Yao GH (2003) Behaviour of concrete-filled hollow structural steel (HSS) columns with pre-load on the steel tubes. *J Constr Steel Res* 59(12):1455–1475
12. Han LH, Yao GH (2004) Experimental behaviour of thin-walled hollow structural steel (HSS) columns filled with self-consolidating concrete (SCC). *Thin-Walled Struct* 42(9):1357–1377
13. Han LH (2000) Tests on concrete filled steel tubular columns with high slenderness ratio. *Adv Struct Eng* 3(4):337–344
14. Hu HT, Huang CS, Wu MH, Wu YM (2003) Nonlinear analysis of axially loaded concrete-filled tube columns with confinement effect. *J Struct Eng* 129(10):1322–1329
15. Lee SH, Uy B, Kim SH, Choi YH, Choi SM (2011) Behavior of high-strength circular concrete-filled steel tubular (CFST) column under eccentric loading. *J Constr Steel Res* 67(1):1–13
16. Leon RT, Aho MF, Kim DK (2005) A database for encased and concrete-filled columns. *Internal Rep*
17. Lin CY (1988) Axial capacity of concrete infilled cold-formed steel columns
18. Mander JB, Priestley MJ, Park R (1988) Theoretical stress-strain model for confined concrete. *J Struct Eng* 114(8):1804–1826
19. Martinez S, Nilson AH (1984). Spirally reinforced high-strength concrete columns. In: *Journal proceedings*, vol 81, no 5, pp 431–442, Sept 1984

20. O'Shea MD, Bridge RQ (2000) Design of circular thin-walled concrete filled steel tubes. *J Struct Eng* 126(11):1295–1303
21. Schneider SP (1998) Axially loaded concrete-filled steel tubes. *J Struct Eng* 124(10):1125–1138
22. Structural Stability Research Council (SSRC) Task Group 20 (1979) A specification for the design of steel-concrete composite columns. *AISC Engl J* 16(4):101–115
23. Xu F, Chen J, Jin WL (2014) Experimental investigation of thin-walled concrete-filled steel tube columns with reinforced lattice angle. *Thin-Walled Struct* 84:59–67
24. Yu ZW, Ding FX, Cai CS (2007) Experimental behavior of circular concrete-filled steel tube stub columns. *J Constr Steel Res* 63(2):165–174
25. Zeghiche J, Chaoui K (2005) An experimental behaviour of concrete-filled steel tubular columns. *J Constr Steel Res* 61(1):53–66

Structural Performance of Partially Confined Concrete-Filled Steel Circular Tubular Columns Under Cyclic Lateral Loading



Prasanta Kar, Arun C. Borsaikia, and Konjengbam D. Singh

Abstract This paper presents an experimental investigation on partially confined concrete-filled circular steel tubular (PCCFST) columns to explore the use of circular hollow section (CHS) configuration as partial inner confinement to the concrete-filled steel tubular (CFST) column. A total of four columns, three PCCFST and one CFST were tested under combined axial and cyclic lateral loadings. In this study, hysteretic behavior, flexural strength, ductility coefficient, energy dissipation capacity and failure mode of the PCCFST columns were investigated as a function of the height of inner CHS tube. Based on the experimental results, it was seen that the height of the inner CHS has evident influence on the energy dissipation capacity of the column. It has been found that, till 0.5D height of inner steel tube, there is no change in the hysteretic curve. For 1.5D height of inner steel tube, the flexural strength, ductility coefficient and energy dissipation capacity of CFST column were enhanced by 12.2%, 14% and 20.5%, respectively. This shows the structural viability of PCCFST column in the region particularly prone to seismic activity.

Keywords Confined concrete-filled steel tubular column · Partial inner confinement · Axial compression · Cyclic loading

P. Kar (✉) · A. C. Borsaikia · K. D. Singh
Indian Institute of Technology Guwahati, Guwahati, India
e-mail: prasanta2016@iitg.ac.in

A. C. Borsaikia
e-mail: arubors@iitg.ac.in

K. D. Singh
e-mail: darun@iitg.ac.in

1 Introduction

The use of concrete-filled steel tube (CFST) has become very popular and widespread in the past few decades because of its various advantages such as high bearing capacity, ductility, easy construction, time and cost saving [13]. It has better structural performance than those of steel or reinforced concrete. All these advantages have made CFST members widely recognized and have led to extensive use in structures. The continuous confinement provided by the steel to the concrete enhances the core's strength and ductility [7]. The steel tube acts as a longitudinal and lateral reinforcement for the concrete core that increases the strength and inelastic deformation of the concrete. The typical cross sections of CFST members widely used in construction are circular, square and rectangular shapes. Other cross-sectional shapes have also been used for aesthetic purpose such as polygon, round-ended rectangular, elliptical and L-shaped CFST [3–5, 10, 31]. In general, circular CFST members exhibit excellent mechanical behavior than square CFST column because the confinement provided by the circular section member is more effective than square section member.

In recent decades, earthquake has caused major devastation to different civil engineering structures. That has made researcher to investigate the behavior of structural member under seismic loading. Due to the enhanced confinement and ductility, of the CFST members, several works have been initiated to understand the cyclic behavior of CFST members: (e.g., [6, 8, 9, 15, 19, 20, 22, 25, 27, 28]). It was observed that thin-walled CFST exhibits higher energy dissipation and more ductile behavior compared to common reinforced concrete column [29]. CFST is generally considered to possess favorable characteristics for use in region at high seismic risk [21]. CFST members subjected to those tests are found to exhibit local buckling failure at the plastic hinge zone (0.45D–0.95D height), where D is the outer diameter of the steel section, while the remaining part of the member remains undamaged and the post buckling behavior of the CFST member is governed by the deterioration rate of the tube plates in the plastic region [12]. It was reported by Varma et al. [26] that the total energy dissipated by the cyclic specimen was dominated by the flexural energy dissipated in the failure region within 0.8D length from the base of the column (plastic hinge region). Thus, the strength and stiffness of the member are governed by the deterioration rate of the member at the plastic hinge region, while the remaining portion of the test length unloaded elastically. It may be worth mentioning that current earthquake-resistant design requires strong column and weak beam behavior which intrigued the concept of developing a column with higher compressive strength and higher energy dissipating capacity. It was found that the energy dissipation capacity of the hollow steel tube could be enhanced economically by strengthening the plastic hinge zone with cross tie [11]. This work was extended by Hsu and Yu [12], and the same method was applied to the CFST column, which resulted in higher energy dissipation efficiency. It was also observed by Xiao et al. [30] that the seismic behavior of the CFT column can be improved significantly by providing additional confinement of carbon fiber-reinforced polymer (CFRP) wrap at the potential plastic hinge

region. Mao and Xiao [16], fabricated ‘confined concrete-filled steel tube’ (CCFT) columns by providing thick steel sheets externally in the plastic hinge region and found to have enhance energy dissipation capacity. Zhang et al. [32] observed that the seismic performance of ‘hybrid FRP-concrete-steel double skin tubular column’ can be enhanced by filling the inner void in the plastic hinge region. As a research in this direction, in this work an attempt has been made to investigate the effects of partially confined concrete-filled circular steel tubular (PCCFST) columns using additional inner steel tubes. Therefore, the present work mainly focuses on the influence of providing partial confinement of varying height at the base of the CFST column under combined constant axial loading and cyclically varying lateral loading.

2 Description of the Test Campaign

2.1 Specimen Details

The experimental campaign consisted of four columns: three partially confined concrete-filled circular steel tubular (PCCFST) column and one concrete-filled steel tube (CFST) column under combined axial compression and cyclic lateral loading. All these specimens consist of hollow steel tube with outer diameter (D) 114 mm and 3.2 mm thickness (t). The clear height of the specimens was 650 mm (length between the top of the stiff RC (reinforced concrete) footing to the point of lateral loading). All the three PCCFST specimens were provided with one inner steel tube (having outer diameter (D_i) of 60 mm and thickness (t_i) of 3.2 mm) each, welded concentrically at the base plate. The height of inner steel tubes was taken as $-0.5D$, $1D$ and $1.5D$ from the top of footing. No inner steel tube was provided to the CFST specimen. Two separate batches of concrete mix were prepared: one for the RC footing and another for the CFST and PCCFST specimens. All the specimens were subjected to combined constant axial loading and cyclically varying lateral loading. To maintain uniformity for comparison, all the specimens were provided with the same axial load level ($n = 0.02$). The axial load level (n) in this paper is defined by Eq. (1).

$$n = \frac{N_0}{N_u}, \quad (1)$$

where N_0 is the axial load applied to the specimen and N_u is the axial compressive capacity of the specimen. The value of N_u was determined by testing a CFST stub column of same cross section under compression. Nomenclature of the specimen follows the form $Cx-cy-z$, where ‘ Cx ’ represents circular outer steel tube of ‘ x ’ diameter, ‘ cy ’ represents the circular inner steel tube of ‘ y ’ diameter, and ‘ z ’ represents the height of inner steel tube. For example, C114-c60-1.5D means circular outer steel tube of 114 mm diameter provided with a circular inner steel tube of diameter 60 mm

Table 1 Average mechanical properties of steel tube used

Specimen ID	t (mm)	D/t	f_y (MPa)	f_u (MPa)
C114-3.2	3.2	35.6	312	374

Table 2 Mix proportion of concrete

Materials	Cement	Fine aggregate	Coarse aggregate	Water
Quantity (kg/m ³)	400.0	916.1	792.4	208

till 1.5D height from the top surface of footing. The specimen with no inner steel tube was named as C114-c0. Due to the limitation of the test setup, only small-scale specimens could be tested.

2.2 Material Properties

2.2.1 Steel Tubes

Commercially available circular hollow steel tubes were procured locally from the manufacturer ‘Nezone pipes and structures’. All the steel tubes used in the test campaign are cold formed. To evaluate the mechanical properties, a series of coupon specimens were prepared from the extract of circular tubes, and tensile coupon testing was performed as per [2]. The average mechanical properties based on the tensile coupon tests in terms of yield strength, f_y , and ultimate strength, f_u , are given in Table 1.

2.2.2 Concrete

All the specimens were cast using normal grade of concrete. The achieved average concrete strength of all the specimens at the time of test was -31 MPa. To facilitate the workability during compaction, coarse aggregate of maximum size aggregate (MSA) 10 mm were used. Mix proportion of concrete used is given in Table 2. For each batch of concrete mixture, six 150 mm cubes are cast and cured for 28 days.

2.3 Preparation of Test Specimen

Procured circular steel tubes (C114-3.2) were originally of length 6 m. Steel tubes of length 1300 mm were cut from these tubes, which ultimately provided a clear height of 650 mm (Fig. 1). Circular inner steel tubes (c60-3.2) of height H_i (0.5D,

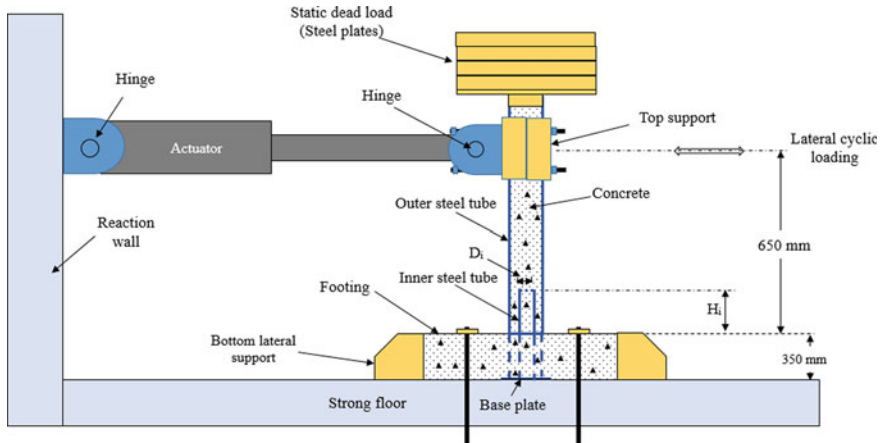


Fig. 1 Test setup

1D and 1.5 D) were also cut from 6 m length original pipe. The diameter (D_i) of inner steel tube of all PCCFST specimens was kept same. The ends of the cut specimens were machined to avoid any undulation. A 200×200 mm square steel base plate of thickness 4 mm was welded at the bottom of the specimen for better grip of the specimen with the footing. Inner circular steel tube was first welded to the center of the base plate at the bottom. A steel 'spacer' was fabricated to ensure uniform spacing between the two concentric tubes. The spacer connected with a wire was then placed on the inner tube and outer tube was placed from top, and both the tubes were welded to the same square base plate. The spacer was then removed once the welding of the outer tube was completed.

Form work for RC footing of length 1550 mm, width 400 mm and depth 350 mm was made to support the bottom of the specimen (so as to achieve a fixed ended support). Two specimens were cast using a single footing. Welded steel tubes were then placed and centered in the form work of the footing to be cast. Welded tubes were then tied to avoid any undesirable shift or movement at the time of casting. The footing of the specimens was first cast using batch 1 concrete mix. The freshly prepared concrete of second batch is then poured to the specimen in three layers, followed by vibration using a 10 mm diameter rod for proper compaction. The embedded length of the specimens into the footing was 350 mm which was $\approx 3D$. As suggested by Lehman and Roeder [14], Stephens et al. [24], the minimum embedded length of $0.75D$ – $0.9D$ is needed to avoid cone pullout failure and allow ductile tearing of the CFST specimen. During the time of concreting, three 150 mm cubes of each batch were also cast. Both the cubes and the CFST were kept for 28 days of curing under ambient temperature. During curing, a very small amount of longitudinal shrinkage of about 2–3 mm occurred at the top surface of the column. Gypsum paste was used to fill this longitudinal gap so that the concrete surface was flush with the steel tube at the top.

2.4 Test Setup and Instrumentation

Schematic diagram of the test setup is shown in Fig. 1. A fixed end support has been provided at the bottom, whereas a hinge support is at the top via the actuator head. The footing was then laterally restrained by two steel supports to confirm no lateral slippage condition during the test. At the top, axial load was applied using four loading plates stacked one above another on a thick plate having square groove on the other face of the plate to hold the specimen. The axial loading was maintained constant throughout the test. Along with constant axial loading, cyclic lateral loading was also applied following AISC 341 [1] loading protocol described in the section below. To impose lateral cyclic displacement to the specimen, a steel support has been made which connects the steel specimen to the MTS actuator (250 kN capacity and 500 mm strokes length). The imposed lateral displacement was measured by an internal measurement system, and the level of applied force was measured using inbuilt load cell in the actuator. Two LVDTs were also used, to measure the lateral displacement at the loading level and footing level. Strain gauges were fixed for each specimen at a height of 50 and 150 mm (on both the diametrically tension and compression side) from the top of RC footing, respectively, to monitor the yielding strain of the outer steel tube at the plastic hinge region. All the tested specimens showed a very ductile behavior, and testing proceeded in a smooth and controlled manner.

2.5 Loading Pattern

Displacement controlled lateral cyclic loading as per AISC 341, 10 (Fig. 2) is applied at the top of the specimen [17, 18, 23]. Six number of cycles were applied for each 0.00375, 0.005 and 0.0075 radians of drift angle (θ , where $\theta = \Delta/L$), followed by four cycles for 0.01 rad drift angle. For the rest of the test, two cycles for each drift angle were provided. A constant loading rate of 1 mm/sec was applied to maintain quasi-static loading condition. After placing the specimen in the strong floor, all the strain gauges, LVDTs are fixed. Bottom support fixed the specimen to the strong floor. Top support connected the MTS actuator to the specimen top to facilitate the transfer of lateral load. Displacement controlled loading as per AISC 341-10 is applied at the sampling rate of 10 Hz. All the data are stored in a data acquisition system. Test continued till the lateral load drops down to 80% of the peak lateral load or the specimen fails (steel tube tearing has occurred).

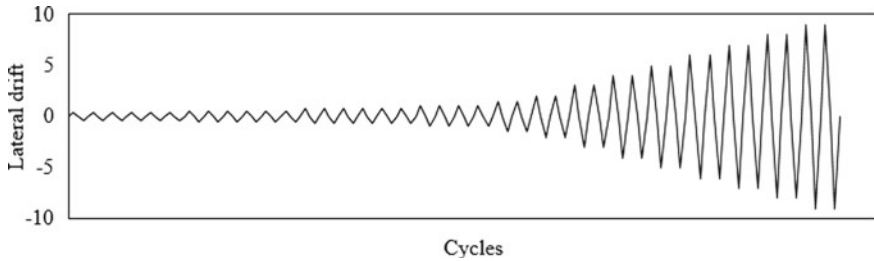


Fig. 2 Cyclic loading protocol (AISC 341-10)

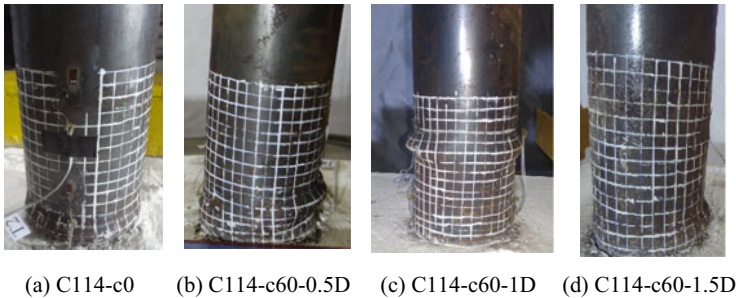


Fig. 3 Failure mode of tested specimen

3 Experimental Results

3.1 General

The experimental observations and results are presented and discussed here in this section (Figs. 3, 4, 5, 6, 7 and 8). The pull direction is defined to be the positive direction, while the push direction to be the negative direction. For the ease of observation, a 10 × 10 mm white grid was plotted on the surface of the outer tube up to a height of 150 mm from the top surface of the RC footing.

3.2 Test Observations

Figure 3 shows the typical failure mode of all the four specimens. Near the bottom of the specimen, formation of plastic hinge can be seen. This plastic hinge may be associated with the occurrence of local buckling. The local buckling in the member’s plastic hinge region may also be related to the decrease of the lateral resistance for increasing level of deformation. The height of occurrence of plastic hinge from the top surface of RC footing was found to vary for different specimen. For the specimen

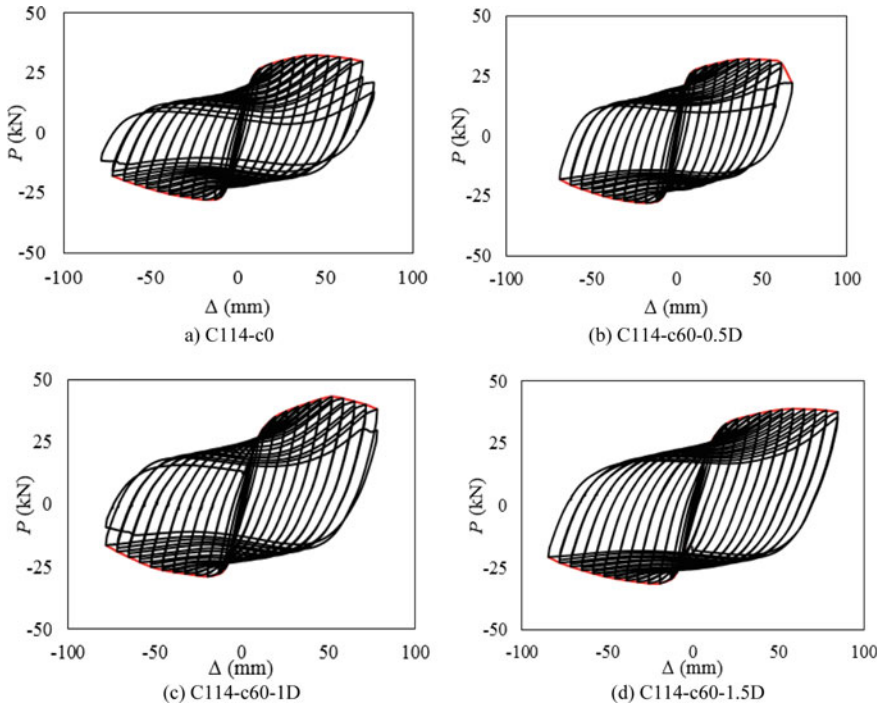


Fig. 4 $P-\Delta$ hysteretic curves

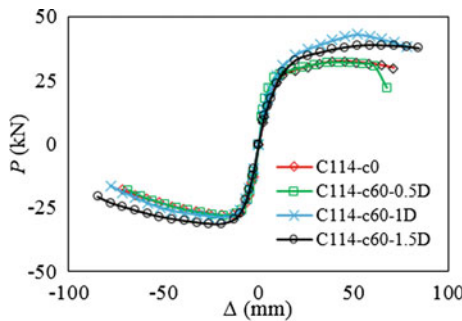


Fig. 5 $P-\Delta$ envelope curves

C114-c0, it has been found that the failure pattern (outward local buckling) is near the base support of the specimen, similar to that reported by Peng et al., 2015, whereas for the specimen C114-c60-0.5D, the buckling has taken place at a region approximately 30–50 mm above the footing surface. For the specimen C114-c60-01D, the buckling region was seen in 90–120 mm segment from the footing surface, but in case of C114-c60-1.5D, buckling was observed to take place at two places, one, near the

Fig. 6 $K-\Delta$ curves

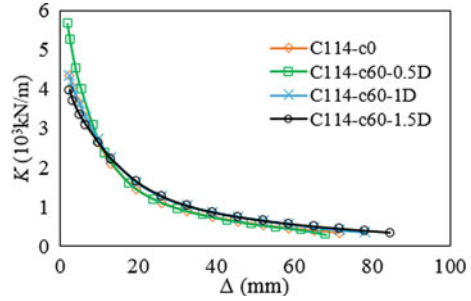


Fig. 7 $E-\Delta$ curves

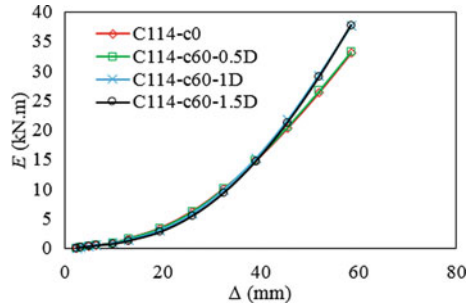
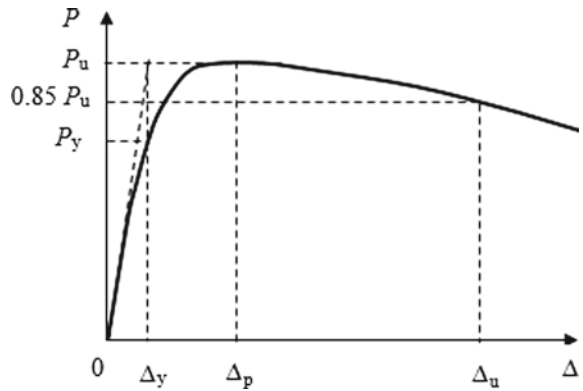


Fig. 8 Typical $P-\Delta$ envelope curve



base support of specimen and another, at around 170 mm. The other local buckling region was not very visible at zero displacement, but when the specimen reached the maximum displacement at the last few cycles, it becomes visible. Local buckling on the outer steel tube was evident at the drift ratio of 5% approximately for all the specimens. After that, with gradual increase in drift ratio the buckling of the outer steel tube became more apparent and formed a local buckled ring gradually at that region. The bulges on the steel tube grew rapidly at the moment when the specimen was close to failure. From the failure modes of all the specimens, it could

be concluded that on providing inner tube to the CFST specimen, the buckling region could be shifted up.

3.3 Lateral Load–Displacement (P - Δ) Hysteretic Curves

The measured lateral load (P) versus displacement at the level of lateral load (Δ) hysteretic curves for all the specimens are shown in Fig. 4. From the figure, it can be clearly seen that there is an initial elastic response and lateral load–displacement relation can roughly be considered as linear. The stiffness gradually degraded, and the response entered into the inelastic range. It has also been observed that with the increase in cycle number, there is a degradation in peak lateral load. However, such drop was not visible, in the pull region, apparently due to the faulty hinge behavior of the actuator/setup. Hence, the test lateral ultimate strength P_u from the push region was taken for ultimate load and ductility coefficient calculation.

3.4 P - Δ Envelope Curves

P - Δ envelope curves for all the tested specimens are shown in Fig. 5. It has been observed that on providing inner steel tube up to a height of 0.5D (C114-c60-0.5D) from the top surface of RC footing, there is no enhancement in the flexural strength of the specimen with respect to the C114-c0 specimen, whereas, for C114-c60-1D and C114-c60-1.5D specimen, it was found to have an enhancement in flexural capacity by 3.5% and 12.2%, respectively, with respect to the C114-c0 specimen. The possible reason could be the partial confinement provided by the inner circular steel tube to the whole region where the plastic hinge was expected to form.

3.5 Stiffness Deterioration

The average secant stiffness has been used as the stiffness of the members at different lateral displacement level. The average secant stiffness of members was calculated using Eq. (2).

$$K_i = \frac{|P_i| + |-P_i|}{|\Delta_i| + |-\Delta_i|}, \quad (2)$$

where P_i and Δ_i are the peak load and corresponding lateral displacement of specimens at the i -th displacement loading level, respectively. + and – sign denote the push and pull directions, respectively. The secant stiffness (K) versus lateral displacement (Δ) curve for all the tested specimens is shown in Fig. 6. It has been observed that the

stiffness of all the specimens drops as the lateral displacement increases. Stiffness deterioration for all the specimens is found to follow similar pattern, although the initial stiffness of PCCFST specimens was slightly higher compared to the CFST specimen.

3.6 Energy Dissipation Capacity

The distribution of cumulative energy dissipation with respect to lateral displacement for all the tested specimen is shown in Fig. 7. Energy dissipated is calculated up to second cycle of the 9% drift angle for all the specimens to maintain the uniformity for the comparison. The energy dissipated by C114-c60-0.5D was found to be slightly higher (0.7%) than the C114-c0, whereas energy dissipated by C114-c60-1D and C114-c60-1.5 was found to have an enhancement of approximately 14% each.

3.7 Ductility Coefficient

The displacement ductility coefficient (μ) of the specimens has been assessed as per the expression given in Eq. 3. It has been observed that for C114-c60-0.5D, C114-c60-1D and C114-c60-1.5D specimens, there is an enhancement in ductility coefficient of 9.1%, 10.2% and 20.5%, respectively, with respect to the C114-c0 specimen.

$$\mu = \frac{\Delta_u}{\Delta_y}, \quad (3)$$

where Δ_y = yield displacement and Δ_u = displacement when the lateral load falls to 85% of the ultimate strength. The P - Δ envelope curve of the tested specimens did not exhibit an obvious yield point. Thus, the displacement corresponding to the intersection of the two tangents between the elastic segment line and peak loading tangent has been taken as yield displacement (see Fig. 8). Computed ductility coefficients are listed in Table 3.

Table 3 Ductility coefficient

Specimen ID	Δ_y	Δ_u	μ
C114-c0	6	49	8.17
C114-c60-0.5D	5.5	49	8.91
C114-c60-1D	6	54	9.00
C114-c60-1.5D	6.3	62	9.84

4 Conclusion

In this paper, the seismic performances of CFST and PCCFST specimens were studied. The following observations and conclusions can be drawn on the basis of limited research reported in the paper.

1. It has been observed that on providing partial confinement to the CFST at plastic hinge region, the buckling region could be shifted up.
2. The lateral ultimate strength of PCCFST specimen has increased on increasing the height of inner steel tube up to 1.5D by 12.2% with respect to the CFST specimen.
3. The energy dissipation capacity of the PCCFST specimens has been found to have enhanced by 14% with respect to the CFST specimen.
4. A ductility coefficient enhancement of 20% has been observed for PCCFST specimens with respect to the CFST specimen.

References

1. American Institute of Steel Construction (2010) Seismic provisions for structural steel buildings. Seismic provisions for structural steel buildings, pp 402
2. ASTM E8/E8M (2016) Standard test method for tension testing of metallic materials, USA
3. Chan T, Huai Y, Wang W (2015) Experimental investigation on lightweight concrete-filled cold-formed elliptical hollow section stub columns. *J Constr Steel Res* 115:434–444
4. Chen J, Chan T, Su RKL, Castro JM (2019) Experimental assessment of the cyclic behaviour of concrete-filled steel tubular beam-columns with octagonal sections. *Eng Struct* 180:544–560
5. Du G, Zhang J, Li Y, Zhang J, Zeng L (2019) Experimental study on hysteretic model for L-shaped concrete-filled steel tubular column subjected to cyclic loading. *Thin Walled Struct* 144:1–14
6. Elchalakani M, Zhao XL (2008) Concrete-filled cold-formed circular steel tubes subjected to variable amplitude cyclic pure bending. *Eng Struct* 30:287–299
7. Elremaily A, Azizinamini A (2002) Behavior and strength of circular concrete-filled tube columns. *J Constr Steel Res* 58:1567–1591
8. Fam A, Frank S, Rizkalla S (2004) Concrete in-filled steel tubes subjected to axial compression and lateral cyclic loads. *J Struct Eng* 130:631–640
9. Gajalakshmi P, Helena HJ (2012) Behaviour of concrete-filled steel columns subjected to lateral cyclic loading. *J Constr Steel Res* 75:55–63
10. Hassanein MF, Patel VI (2018) Round-ended rectangular concrete-filled steel tubular short columns: FE investigation under axial compression. *J Constr Steel Res* 140:222–236
11. Hsu HL, Juang JL (2000) Performance of thin-walled box columns strengthened with internal braces. *Thin-Walled Struct* 37:241–258
12. Hsu H, Yu H (2003) Seismic performance of concrete-filled tubes with restrained plastic hinge zones. *J Constr Steel Res* 59:587–608
13. Han LH, Li W, Bjorhovde R (2014) Developments and advanced applications of concrete-filled steel tubular (CFST) structures. *J Constr Steel Res* 100:211–228
14. Lehman DE, Roeder CW (2012) Foundation connections for circular concrete-filled tubes. *J Constr Steel Res* 78:212–225
15. Liu J, Zhou X, Zhang S (2008) Seismic behaviour of square CFT beam-columns under biaxial bending moment. *J Constr Steel Res* 64:1473–1482

16. Mao XY, Xiao Y (2006) Seismic behavior of confined square CFT columns. *Eng Struct* 28:1378–1386
17. Narendra PVR, Singh KD (2017) Elliptical hollow section steel cantilever beams under extremely low cycle fatigue flexural load—a finite element study. *Thin Walled Struct* 119:126–150
18. Park SH, Choi SM, Kim YS, Park YW, Kim JH (2010) Hysteresis behavior of concrete filled square steel tube column-to-beam partially restrained composite connections. *J Constr Steel Res* 66(7):943–953
19. Patel VI, Liang QQ, Hadi MNS (2014) Numerical analysis of high-strength concrete-filled steel tubular slender beam-columns under cyclic loading. *J Constr Steel Res* 92:183–194
20. Peng Q, Yang T, Yan X (2015) Low cyclic fatigue performance of concrete-filled steel tube columns. *J Cent S Univ* 22:4035–4042
21. Schneider SP, Alostaz YM (1998) Experimental behavior of connections to concrete-filled steel tubes. *J Constr Steel Res* 45:321–352
22. Serras DN, Skalomenos KA, Hatzigeorgiou GD, Beskos DE (2016) Modeling of circular concrete-filled steel tubes subjected to cyclic lateral loading. *Structures* 8:75–93
23. Silva A, Jiang Y, Castro JM, Silvestre N, Monteiro R (2016) Experimental assessment of the flexural behaviour of circular rubberized concrete-filled steel tubes. *J Constr Steel Res* 122:557–570
24. Stephens MT, Lehman DE, Roeder CW (2016) Design of CFST column-to-foundation/cap beam connections for moderate and high seismic regions. *Eng Struct* 122:323–337
25. Usami T, Ge H (1998) Cyclic behavior of thin-walled steel structures—numerical analysis. *Thin-Walled Struct* 32:41–80
26. Varma AH, Ricles JM, Sause R, Lu LW (2002) Seismic behavior and modeling of high-strength composite concrete-filled steel tube (CFT) beam-columns. *J Constr Steel Res* 58:725–758
27. Varma AH, Ricles JM, Sause R, Lu LW (2004) Seismic behavior and design of high-strength square concrete-filled steel tube beam columns. *J Struct Eng* 130:169–179
28. Wang J, Sun Q, Li J (2019) Experimental study on seismic behavior of high-strength circular concrete-filled thin-walled steel tubular columns. *Eng Struct* 182:403–415
29. Wu B, Zhao XY, Zhang JS (2012) Cyclic behavior of thin-walled square steel tubular columns filled with demolished concrete lumps and fresh concrete. *J Constr Steel Res* 77:69–81
30. Xiao Y, He W, Choi K (2005) Confined concrete-filled tubular columns. *J Struct Eng* 131:488–497
31. Yu M, Zha X, Ye J, Li Y (2013) A unified formulation for circle and polygon concrete-filled steel tube columns under axial compression. *Eng Struct* 49:1–10
32. Zhang B, Teng JG, Yu T (2015) Experimental behavior of hybrid FRP—concrete—steel double-skin tubular columns under combined axial compression and cyclic lateral loading. *Eng Struct* 99:214–231

State-of-the-Art Review for Concrete-Encased Steel Columns



S. Suresh Babu, Priya, and A. Leema Rose

Abstract Composite structural members are recently used in major buildings since it possesses considerable load-carrying capacity and notable resistance toward fire and seismic forces. Steel concrete composite systems for structures are composed of concrete that interact with steel sections with the same system. This method is considered as a replacement for conventional method of construction. In a composite member, the steel section and concrete would oppose the extrinsic loading by its action of bonding and abrasion. The concrete encased around or infilled inside the steel specimen used is correlated that the merits of both materials are successfully used in the composite member. Encased columns are formed by I sections or built-up steel sections surrounded by concrete. Their integral behavior provides sufficient strength and stability to the structural system. This paper includes the review of the research work conducted on the buckling effects of encased column, concrete confinement, fire resistance, ductility behavior, and strength of encased column.

Keywords Composite column · Encased · Buckling · Confinement

1 Introduction

A composite structural system is composed of steel specimens and concrete enclosed it that have been described as another possible way of construction to the conventional framed system. The acknowledgement is due to its improved strength and rigidity which can be accomplished with minimum material use. Concrete is familiar for its good behavior in compression and steel in tension. Hence, integrating the above-said materials results in improved strength structurally. In composite construction, steel provides sufficient strength, and concrete provides rigidity. Composite framework additionally offers advantages in time saving for construction.

S. Suresh Babu (✉) · Priya · A. Leema Rose
Department of Civil Engineering, SRM Valliammai Engineering College, Kattankulathur, India
e-mail: sureshbabus.civil@valliammai.co.in

© The Author(s), under exclusive license to Springer Nature Singapore Pte Ltd. 2023
M. Madhavan et al. (eds.), *Proceedings of the Indian Structural Steel Conference 2020*
(Vol. 2), Lecture Notes in Civil Engineering 319,
https://doi.org/10.1007/978-981-19-9394-7_15

A composite structure reduces the depth of the floor and further gives significant benefits of service costs. Such members usually become unsuccessful by the bond between the concrete and steel surface that is commonly referred to as de bonding. The inceptive bond which is given by the adherence of the concrete and steel which is called as chemical bond. After some time the concrete shrinkage sets and adversely affects the chemical bonding and adherence.

Steel and concrete composite building method blends reinforced concrete's rigidity and ductility with the help of rebars to provide an economical building. In general the strength of composite buildings is achieved by the concept that two or many components are mingled in a form that creates an economical structure.

2 Composite Column

A composite column is a structural component which consists of reinforced steel, steel specimen, and concrete in which all the components behave like a single member and withstand compressive load. It is a compression member which can be steel specimen covered with concrete or tubular section filled with concrete. A composite column is broadly categorized into two

1. Concrete-encased steel column
2. Concrete infilled steel column.

2.1 Concrete-Encased Steel Column

Concrete-encased column is a column in which a steel specimen covered with concrete. The concrete around the steel specimen enhances the buckling behavior of it and further provides high strength. This encasement has a major advantage in fire and corrosion protection. Figure 1 shows a steel tube encased with concrete.

Fig. 1 Encased composite column

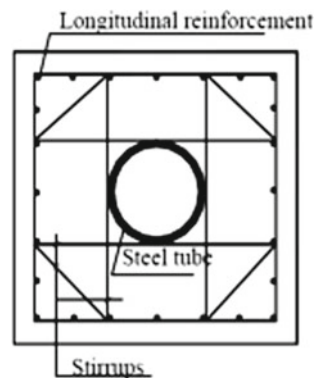
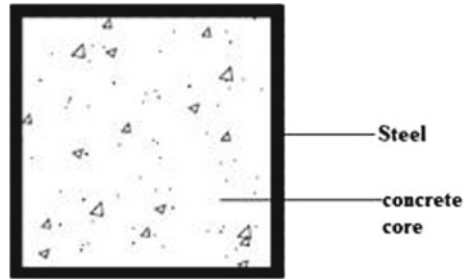


Fig. 2 Concrete infilled column



2.2 Concrete-Filled Tubular Steel Column

A concrete-filled steel column is a compressive structural member which consists of concrete filled inside the tubular steel section as shown in Fig. 2. The filled concrete enhances stability and further increases the resistance of the axial load but possesses limited impact on the tensile strength. These concrete filled columns are highly recommended for rehabilitation works in places which are vulnerable to earthquake.

2.3 Advantages of Using Concrete-Encased Columns

1. The application of concrete-encased column in buildings minimizes the cost of construction, and the accessible space can be elevated.
2. It possess high fire resistance and corrosion resistance property.
3. The constant outer dimensions of the column in all floors make the architectural detailing construction easy.
4. The long-term failures are much smaller in concrete-encased steel columns than in conventional columns.

2.4 Applications of Concrete-Encased Columns

1. Concrete-encased columns are used in many circumstances.
2. The implementation of encased columns are highly recommended in low-rise and high-rise structures.
3. For aesthetic reasons, these columns are used in low-rise structures like granary, stadiums, and other such structures for further fire resistance.
4. These columns interact with spandrel beam to resist horizontal load in high-rise structures.

3 Seismic Performance of Concrete-Encased Column

The seismic efficiency of the concrete-encased column is quite strong under cyclic loading condition. In this paper, the seismic activity of concrete-enclosed steel columns was studied by Xu et al. [1]. This study includes six hexagonal columns which are encased with concrete and is subjected to lateral cyclic loading condition. The column is made of a hexagonal steel tube filled with concrete and is further encased with concrete.

They have used beams which are fixed to fix the foundation to the ground by supporting it laterally. The vertical jack charged axial force. A horizontal actuator is used laterally to provide cyclic loading condition. Initially the axial load was applied and kept constant as the cyclic lateral load was loaded. Since the cyclic loading is applied, the axial load was induced and kept constant. Both strain and displacements were measured during the test.

The testing reveals the damages of the exterior reinforced concrete layer such as compressive failure, flexural crack, shear crack developed diagonally, and punching shear failure. When the height of the exterior reinforced concrete portion decreases, the elastic stiffness and maximum strength of the large columns with variable modes of failure are reduced by 8.1% and 17.9%, respectively. The elastic stiffness and strength of the base of the column were improved by 2.6% and 8.9%, respectively, with the aid of shear studs.

4 Behavior of High-Strength Concrete-Encased Columns

The performance of HSC encased columns is studied by Lai et al. [2]. Three members were casted whose area of cross section is square and rectangular. The members were of 2800 mm height further welded with endplates at its ends. Eight corner bars are employed; additionally the ties were used whose spacing is 100 mm c/c. The two ends of the columns were strengthened by the application of welding the outer steel box specimens and stiffeners to avoid unintended end failure due to stress accumulation. A 10,000 kN actuator was used at a mode of control to load all the specimens monotonically. Three LVDT were mounted at the middle line and the both ends of the endplate which registered vertical deflection. Additionally seven LVDTs were placed across the length of the column to find the horizontal deflection. The axial load is applied in a mode regulated by displacement. To make sure the efficiency of the testing devices, initially loading is given till 30% of the ultimate loading; later the load is subjected at a range of 0.3 mm per minute till the failure of the column. The test members displayed the identical displacement and mode of failure. The concrete crushed in a fragile way at its load of failure; further the concrete cover subjected to spalling which leads to exposed longitudinal bars buckling. The inheritance fragileness of HSC and inadequate confinement of concrete is given by the horizontal rebars which can explain the mode of failure. The experiment results

revealed that the 6 mm ties whose spacing is 100 mm center to center. It is noticed from the experiment that the concrete-encased columns casted up to a grade of C100 reveal fragile failure at its highest load. It is revealed that the regular shear for concrete-encased columns does not provide needed confinement for the HSC encased system which leads to brittle failure.

5 Behavior of Totally Encased Columns Under Fire

In this paper, Paulo et al. [3] investigated the behavior of totally encased columns under fire. The columns which were tested were of three meters height which consists of European wide flange beams section. These columns were fully encased with reinforced concrete. It consists of four longitudinal bars of 12 mm dia. The ties used were of 8 mm diameter whose spacing is 150 mm at the middle region and 100 mm at the corners of the member. The columns were completely encased in concrete and subjected to constant compressive load. A constant compressive force is loaded throughout the test with the help of a hydraulic jack whose capacity is about 3 MN. This hydraulic jack was controlled with the aid of a load cell of capacity 1 MN. The load cell is positioned in the middle of upper beam and hydraulic jack. The fire action was induced with a modular electric furnace which follows the ISO 834 fire curve. This furnace consists of two modules where one is of one meter height and the other module of 0.5 m height which were kept at the top layer of each other which forms a chamber surrounding the column and is of 1.5 m of length and breadth whose height is 2.5 m. The vertical deformations of the member were found using a LVDT. The strain values of the members were also carried out using strain gauges. This strain values further employed to make sure the restraining loads on the specimen. The columns were tested under fire whose critical times were more than one eighty minutes which shows a better thermal resistance. The loading level is indirectly proportional to the critical times. Minimizing the loading level enhances the critical times. The overall cover of concrete and the axis length of reinforcement to the external concrete has a relation on critical times. The cover of concrete which surrounds the steel specimen is directly proportional to the critical times. Increasing the cover of concrete results in increase of critical times.

6 Behavior of Fully Encased Sections Under Monotonic and Cyclic Loading

In this investigation, Campian et al. [4] have experimentally investigated the behavior of encased members subjected to cyclic and monotonic loading. This test included three monotonic loading and nine cyclic loading. The columns used for testing have similar dimensions and were arranged based on their height. The area of cross section

of the encased columns was 220 mm × 170 mm whose height is about 2 and 3 m which results in varying slenderness. The lateral force is enforced to the column at a distance which represents the middle length of the floor. The load is applied cyclically with the help of 280 kN actuators mounted at the left and right end of the free end to represent the lateral earthquake force on the column in both positive and negative range of magnitude. By increasing the loading cycle, the rigidity of the columns were minimized. The initial cracks at the concrete surface are formed by the confining hoops direction. After expelling the concrete, the longitudinal reinforcement was exposed. On the only hand, the monotonic tests found out that elastic displacement $e+y$ reduces with a variety of 16% for the member with HSC compared to the conventional concrete and, and then again, the horizontal force attains to a higher range of 28% better than the column made of normal concrete. The mode of failure was identical for the columns which tested. The column failure made with HSC was intense and fragile compared to the specimens casted using conventional concrete. The totally encased columns are a viable solution for both earthquake and non-earthquake regions since it shows high seismic resistance and further possesses enhanced thermal resistance.

7 Comparing the Behavior of Steel Column and Composite Column

Piotr Lacki et al. compared the behavior of steel column and composite column. An analytical approach was used to construct the composite member as a viable solution to the current steel column. The main column in the structure was made of welded steel H profile. The column of 3.6 m was taken in account. The column experienced compression and uniaxial bending. The axial force was about 2045 kN, whereas the bending moment was 180 kNm which is based upon the combination of loading.

The concentration of stresses in the steel and composite columns is at the base and the head of the column due to the restricting conditions and way of preparing. The structure of the steel member is proposed since after loading the stresses will become higher than the yield strength which is 235 MPa. The analytical approach is used to calculate the load-bearing capacity for the steel reinforced concrete column which is said to be 90%. According to the numerical analysis the steel section stress values in the composite member was 201 MPa which is about 86% of the yield strength. Since the tensile stress of the concrete surface in the head and base of the column results in scratch appearance, the composite column is flexible than the steel column and subjects to lesser deflection.

8 Numerical Modeling

To analyze the concrete-encased column, a finite element analysis software (ANSYS) is used. The finite element analysis software enables us to derive the deflections, stress distribution, and failure pattern of a member.

Initially, a column whose dimension $325\text{mm} \times 325\text{mm} \times 1000\text{mm}$ is modeled using ANSYS workbench by giving all the material properties. In this paper, I have analyzed a composite column where the steel specimen is a cold formed one. A CFS specimen with corrugated web welded back to back to make it a symmetrical section is infilled into the concrete layer. Since the Eurocode does not cover the provisions for cold-formed steel, in the software approach the material properties are allotted for the cold formed specimen. The steel specimen used is generally termed as Supacee section. This section has an added advantage that the corrugations at its web itself acts as a stiffener. The column is further provided with longitudinal and transverse reinforcement to resist the shear force action. After modeling, the member meshes are generated to ensure the process of discretization. The support condition of the column is given to be fixed at both the ends.

Load is applied gradually to the column. The von Mises stress and von Mises strain and the deflection of the concrete-encased column are picturized.

Figure 3 represents the von Mises stress distribution of a concrete-encased column whose maximum stress value is 144.19 MPa and minimum of 6.04 MPa. Whereas the stress distribution in conventional column with a maximum of 165.75 MPa and minimum of 6.62 MPa.

Figure 4 represents the equivalent elastic strain of the concrete-encased column and conventional column.

Figure 5 shows the total deformation of concrete-encased column and conventional column. The maximum deflection of concrete-encased column and conventional column is 1.00 mm and 1.38 mm, respectively.

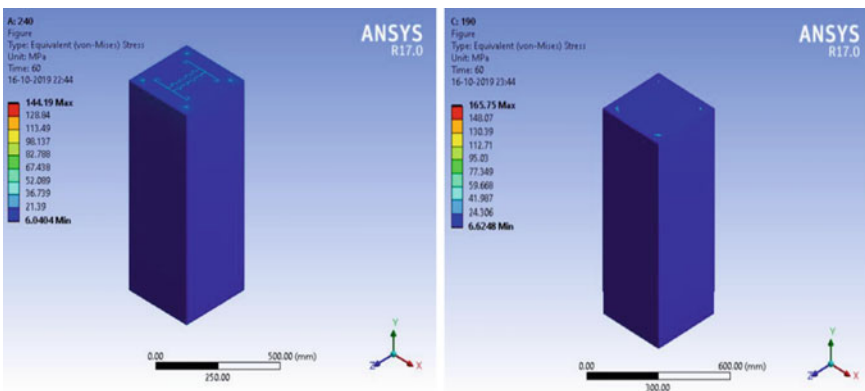


Fig. 3 Equivalent von Mises stress of concrete-encased column (Left) and conventional column (Right)

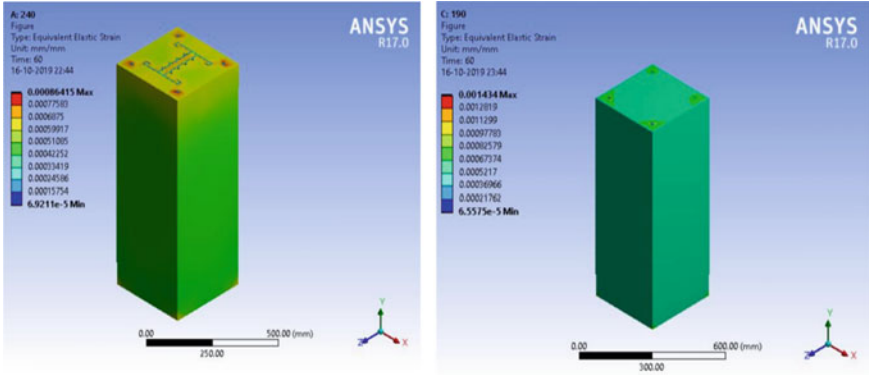


Fig. 4 Equivalent elastic strain of concrete-encased column (Left) and conventional column (Right)

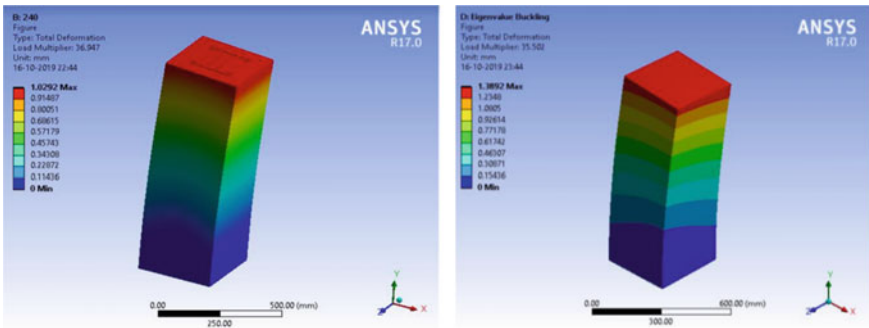


Fig. 5 Total deformation of concrete-encased column (Left) and conventional column (Right)

Specimen	Stress in MPA	Deformation in MM
Conventional column	165.75	1.0
Concrete-encased column	144.19	1.38

From this, it is well known that the composite column resists more stress than the conventional column. These columns have lesser deflection subjected to axial loads. The composite column can give more floor space and carry higher load when compared with the conventional column. Rather than using hot-rolled specimens, cold-rolled specimens can be recommended since they are economical and made in different shapes.

9 Conclusion

This study of composite columns has an eminent advancement. The reviews were recapitulated in this paper. HSC includes major applications which were compared with conventional concrete. The load-bearing ability is comparatively higher in high strength concrete. It is understood that when the eccentricity ratio (e/D) is increased, the ultimate load-bearing ability of columns has reduced in all the series. When the ratio of length to depth is increased, the load-carrying capacity has reduced. Concrete-encased columns shows good resistance toward fire and seismic behavior, and hence, more research has to be carried out in the construction. The work can be extended by giving variation in length-to-depth ratios, confining areas ratio and material properties. These columns can be further investigated under dynamic loading conditions. The fibers can be included in concrete, and its behavior can be studied under composite behavior.

References

1. Xu W, Han L-H, Li W (2016) Seismic performance of concrete encased column base for hexagonal concrete filled steel tube: experimental study. *J Constr Steel Res*, pp 352–369
2. Lai B, Richard Liew JY, Wang T (2019) Buckling behavior of high strength concrete encased steel composite columns. *J Constr Steel Res*, pp 27–42
3. Rodrigues JPC, Correia AJM, Pires TAC (2015) Behavior of composite columns made of totally encased steel sections in fire. *J Constr Steel Res*, pp 97–106
4. Campian C, Nagy Z, Pop M (2015) Behavior of fully encased steel-concrete composite columns subjected to monotonic and cyclic loading. *J Constr Steel Res*, pp 439–451

Enhancing Structural Properties of Wood and Its Composites by Mechanical Annealing



G. Mallikarjunachari and P. Mohammad Asif Khan

Abstract The primary aim of present research work is tuning the mechanical properties of wood and its composites applying mechanical annealing. The application of wood materials and its composites is gradually increasing in various fields, especially in the construction field due to its advantages such as lightweight, less processing cost and, renewable. For instance, magnetic wood composites are successfully applied as electromagnetic shielding, indoor electromagnetic wave absorption in electronic and military fields. Also, wood-plastic composites are using for moisture resistance, resistance to biological agents in biomedical filed. Moreover, recently, wood as a structural material is gaining significant attention to the research community; however, unswerving usage of wood obtained from trees is not strong as a building material; thus, it is necessary to modify its structure. There are various methods to enhance the strength of wood materials; one such method is mechanical annealing. In this work, the wood material is subjected to compressive stresses applying various monotonic load magnitudes P_1 , P_2 , and P_3 . Then mechanical properties are calculated using the 3-point bending test before and after mechanical annealing. Interestingly, central deflection decreased as the load increases. Finite element simulations performed to complement the experimental results. This analysis significantly helps in design of wood and its composites, and also wood can be used as an alternative material for structural steel.

Keywords Wood material · Young's modulus · A critical load of fracture · Mechanical annealing · Finite element method

G. Mallikarjunachari (✉) · P. Mohammad Asif Khan
Department of Mechanical Engineering, Madanapalle Institute of Technology & Science,
Madanapalle, India
e-mail: drmallikarjunachari@mits.ac.in

© The Author(s), under exclusive license to Springer Nature Singapore Pte Ltd. 2023
M. Madhavan et al. (eds.), *Proceedings of the Indian Structural Steel Conference 2020*
(Vol. 2), Lecture Notes in Civil Engineering 319,
https://doi.org/10.1007/978-981-19-9394-7_16

205

1 Introduction

The application of renewable materials such as wood, sheep's wool, and straw bales are gaining significant attention these days. Less manufacturing processes, low cost, and lightweight are the primary advantages of wood materials over structural steel, which involves a series of manufacturing processes and hence high cost. Recently, thin films based on wood cellulose are replaced with polymer films and then successfully applied in packaging and paper industries [3, 5]. The estimated mechanical strength and Young's modulus are 47 MPa and 9.6 GPa respectively which are much higher than the raw wood, and synthetic polymers such as polyethylene, Polypropylene, and Poly (vinyl alcohol) [2, 9]. Due to porous structure and fibrous tissue of these materials make them more versatile in construction field since their mechanical properties can be easily tuned by various synthesis and mechanical routes. There are various methods, such as pre-treatment with water vapor, heat, ammonia, or cold rolling, followed by densification, are successfully applied to enhance the mechanical properties of the wood materials.

Irrespective of length to time scale, mechanical annealing has been demonstrated to be an effective method for enhancing the structural properties of various materials. In general, the degree of densification of a given material depends on the sample size and applied stress level. Recently, this method applied to decrease the dislocation density of the single crystal Al micropillars applying the different stress levels. Chawla et al. [4] studied the mechanical response of Al–Cu alloys before and after mechanical annealing, and their mechanical properties are observed to be significantly improved. The mechanical performance of bulk natural wood is compared with the densified wood (DW) by Song et al. [8, 10]. It is observed 45% DW having 586.6 MPa strength, which is much higher compared to the natural wood, which has 51.6 MPa. Similarly, the work of fracture increases from 0.43 MJ/m³ (for natural wood) to 4.0 MJ/m³ (for DW).

From the literature, it is clearly seen that the application of mechanical annealing is only limited to natural wood materials. In this current work, wood composites are synthesized by varying the concentration of Fe₃O₄ nanoparticles. The mechanical properties are mechanically annealed, applying various stress levels. A three-point bending method [1, 6, 7] is used to find the various properties before and after mechanical annealing. Systematic analysis has been done to find the density, critical load of fracture, and bending modulus and presented here.

2 Synthesis and Methodology

In this research work, raw Neem tree is used for the preparation of samples. Specimens are cut in a way that the length of the specimen is in the tree growth direction. Few specimens prepared for this work are shown in Fig. 1a. The length, width, and

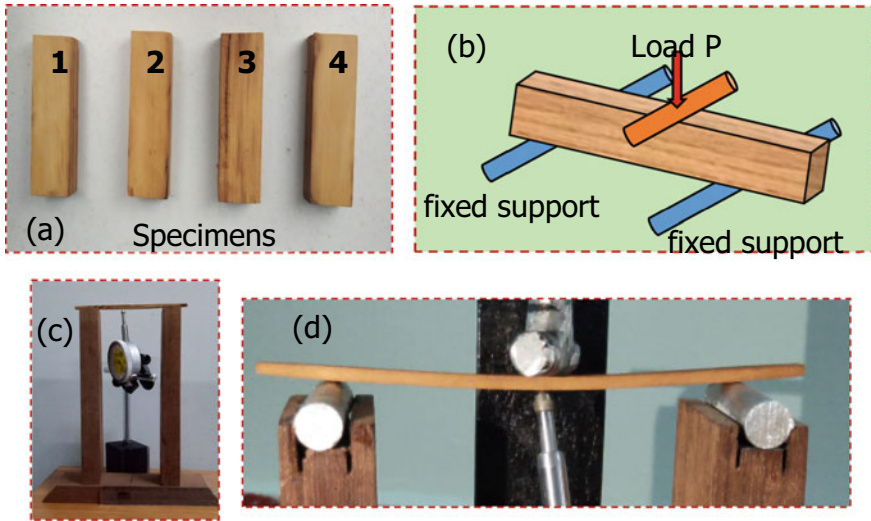


Fig. 1 a Specimens used for this study b schematic diagram showing 3-point bending experiment to find out Young’s modulus and strength c lab made experimental setup which shows the specimen placed on the top and dial indicator to measure the deflection, and d deformed specimen after applying load

thickness of the specimen are 150 mm, 10 mm, and 5 mm, respectively. These specimens are subjected to mechanical annealing of various stress magnitudes. The setup for conducting experiments is schematically shown in Fig. 1b. The central deflection is measured using the dial indicator and from image analysis. The formula used to find Young’s modulus is given in Eq. (2) which is derived from a well-known bending Eq. (1)

$$\text{From deflection of the beam } y_c = \frac{WL^3}{48EI} \tag{1}$$

$$\text{Youngs Modulus } E = \frac{WL^3}{48Iy_c} \tag{2}$$

where L = length of the beam, y_c = central deflection of beam, I = Moment of Inertia, and W = applied load and E = Young’s modulus.

3 Result and Discussions

Wood specimens are compressed to the desired dimensions (reduced dimensions) using hydraulic press subjected to different stress levels. The dimensions before and after mechanical annealing are measured using a micrometer. The measured

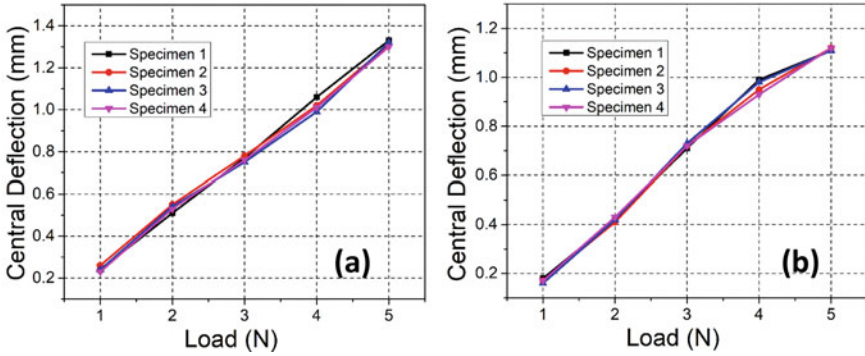


Fig. 2 Variation of central deflection with increase in load **a** before mechanical annealing **b** after mechanical annealing

dimensions are within the tolerance limits of ± 0.05 mm. At least 5 specimens are prepared of reduced dimension. All the samples are tested under temperature $17\text{ }^{\circ}\text{C}$ and RH 60%. Different sets of loads 1–5 N are applied to the specimen to find the central deflection. Same sets of loads are applied to mechanically annealed samples. The variation of central deflection before and after mechanical annealing is shown in Fig. 2a, b. From the plots, it is noticed that the central deflection increases as the load increases before annealing and after annealing. It is also observed that the variation is almost linear with increasing the load. However, irrespective of load magnitude, the central deflection is less for mechanically annealed samples compared with the un-annealed samples. For example, for the same given load, the central deflection is 0.8 mm for a load of 3 N before mechanical annealing, and the central deflection is 0.69 mm for the same load of 3 N after mechanical annealing. A similar trend is observed for loads 1, 2, 4, and 5 N.

Similarly, the wood composites are prepared by adding Fe_3O_4 nanoparticles (with a diameter 300 nm) with different weight percentages. The Young’s modulus (E) is calculated before and after mechanical annealing.

S. No.	Fe_3O_4 weight percentage	Young’s modulus before mechanical annealing (GPa)	Young’s modulus after mechanical annealing
1	0	27	29
2	0.5	30	32
3	1	31	33
4	1.5	32	35
5	2	33	37

4 Conclusions

The density of the wood specimens is increased after subjecting to hydraulic compression of various pressure. The thickness of the specimen is controlled by applying various pressures. It is observed for a pressure of 760 kg/cm² the thickness decreases from 5 to 4 mm. Elastic modulus (E) is calculated using the 3-point bending test. The Elastic Modulus is increased from 27 to 29 GPa for a 1 mm decrease in thickness for 0 wt% Fe₃O₄.

References

1. Anshari B, Guan ZW, Wang QY (2017) Modelling of Glulam beams pre-stressed by compressed wood. *Compos Struct* 165:160–170. <https://doi.org/10.1016/j.compstruct.2017.01.028>
2. Benítez AJ, Walther A (2017) Cellulose nanofibril nanopapers and bioinspired nanocomposites: a review to understand the mechanical property space. *J Mater Chem A* 5(31):16003–16024. <https://doi.org/10.1039/c7ta02006f>
3. Gu W, Liu X, Li F, Shi SQ, Xia C, Zhou W, Li J (2019) Tough, strong, and biodegradable composite film with excellent UV barrier performance comprising soy protein isolate, hyperbranched polyester, and cardanol derivative. *Green Chem* 21(13):3651–3665. <https://doi.org/10.1039/c9gc01081e>
4. Kaira CS, Kantzos C, Williams JJ, De Andrade V, De Carlo F, Chawla N (2018) Microstructural evolution and deformation behavior of Al-Cu alloys: a transmission X-ray microscopy (TXM) and micropillar compression study. *Acta Mater* 144:419–431. <https://doi.org/10.1016/j.actamat.2017.11.009>
5. Keplinger T, Wang X, Burgert I (2019) Nanofibrillated cellulose composites and wood derived scaffolds for functional materials. *J Mater Chem A* 7(7):2981–2992. <https://doi.org/10.1039/C8TA10711D>
6. Li J, Hunt JF, Gong S, Cai Z (2016) Simplified analytical model and balanced design approach for light-weight wood-based structural panel in bending. *Compos Struct* 136:16–24. <https://doi.org/10.1016/j.compstruct.2015.09.045>
7. Li M, Khelifa M, El Ganaoui M (2017) Mechanical characterization of concrete containing wood shavings as aggregates. *Int J Sustain Built Environ* 6(2):587–596. <https://doi.org/10.1016/j.ijbsbe.2017.12.005>
8. Pikul JH, Özerinç S, Liu B, Zhang R, Braun PV, Deshpande VS, King WP (2019) High strength metallic wood from nanostructured nickel inverse opal materials. *Sci Rep* 9(1):1–12. <https://doi.org/10.1038/s41598-018-36901-3>
9. Sirviö JA, Liimatainen H, Niinimäki J, Hormi O (2013) Sustainable packaging materials based on wood cellulose. *RSC Adv* 3(37):16590–16596. <https://doi.org/10.1039/c3ra43264e>
10. Song J, Chen C, Zhu S, Zhu M, Dai J, Ray U, Hu L (2018) Processing bulk natural wood into a high-performance structural material. *Nature* 554(7691):224–228. <https://doi.org/10.1038/nature25476>

Free Vibration of Bio-inspired Composite Circular Plates—An Annual Ring Model



R. Kumar, Vaishali, S. Kushari, T. Mukhopadhyay, and S. Dey

Abstract This paper portrays the natural frequencies and mode shapes of composite circular plate being inspired from the construction of annual rings at stem of the tree. This bio-inspired concentric circular orientation of fibers unlike annual ring model can be utilized as structural components of engineering systems. Each layer of concentric circular fibers indicates the growth per annum. In present study, the simple concentric circular annual ring geometry is considered wherein the annual rings are idealized to construct each layer by graphite-fibers bonded together with epoxy resin in between the subsequent layers. Considering full clamped (FC) and half clamped (HC) boundary conditions, the first five natural frequencies are obtained and the corresponding mode shapes are plotted. The advantages of adopting these novel nature-inspired composites are compared with the conventional laminated composites.

Keywords Annual ring · Composite · Graphite-epoxy · Natural frequency · Mode shapes

1 Introduction

Fiber reinforced composite materials are nowadays extensively used in various fields of applications such as aerospace, automotive, civil, and marine industries. For efficient utilization of such weight-sensitive materials, a prudent understanding of its dynamic and structural behavior is essential. It is also necessary to accurately predict

R. Kumar (✉) · Vaishali · S. Kushari · S. Dey
Department of Mechanical Engineering, NIT Silchar, Silchar, Assam, India
e-mail: rahulkr0629@gmail.com

Vaishali
Department of Mechanical Engineering, Bihar Engineering University, Government Engineering College, Samastipur, India

T. Mukhopadhyay
Department of Aerospace Engineering, Indian Institute of Technology Kanpur, Kanpur, India

© The Author(s), under exclusive license to Springer Nature Singapore Pte Ltd. 2023 211
M. Madhavan et al. (eds.), *Proceedings of the Indian Structural Steel Conference 2020* (Vol. 2), Lecture Notes in Civil Engineering 319,
https://doi.org/10.1007/978-981-19-9394-7_17

its deformation characteristics, stress distribution, buckling behavior, and natural frequencies under various loading conditions. In the past, various researches are carried out investigating the static as well as the dynamic behavior of fiber reinforced composites (FRCs). In addition, the analysis of free vibration and mode shapes has attracted a lot of interest of researchers as the possibility of occurrence of resonance can be predicted, which are the major cause of failure in various structures.

Crawley [1] worked on eight ply graphite-epoxy cantilever plates and analyzed both theoretically and experimentally the natural frequencies and mode shapes of these structures. Later Anderson et al. [2] worked both experimentally and theoretically on twelve ply epoxy-graphite plate and analyzed the natural frequencies and mode shape for the same with different configurations like free, cantilever, and fixed. Ni et al. [3] predicted the dynamic characteristics of hybrid laminated composite beams in FE analysis. It was concluded that natural frequencies are more prominent for thin plates. Dun-xiang et al. [4] worked on laminate composite plates and numerically analyzed natural frequencies, mode shape, and damping value. Kamal et al. [5] worked on laminate composite plate and studied its free vibration characteristics by utilizing shear deformation theory, layered theory, and composite plate theory. Nowadays, natural fibers are used for various purposes, for example, jute is used as reinforcement in many materials [6]. Natural fibers are increasingly used in automotive as packaging materials. Because of the more favorable cost factor and high structural performance, all the leading car manufacturers are switched to use plant fibers for several parts in the automotive sector. In the past, various researchers worked on different types of natural fibers. Kang and Leissa [7], Liew and Yang [8], Zhou et al. [9], So and Leissa [10] presented free vibration analysis of annular and circular plate using Ritz method. Han and Liew [11], Liew et al. [12], Wu et al. [13], and Wang [14] represent the free vibration of annular, circular and sector plates using differential quadrature method. Sharma et al. [15] and Houmat [16] performed free vibration analysis of shear deformable laminated sector plates. McGee et al. [17] derived the exact solutions for the free vibrations of thick annular sector plates having simply supported radial edges. Using the finite element method, Malekzadeh et al. [18] investigated the free vibration of thick annular plates, and Pingulkar and Suresha [19] investigated the free vibration of laminated rectangular composite plates. Soamidas [20] analyzed the buckling of fiber reinforced annular disks subjected to a concentrated tangential edge load. Khare and Mittal [21–23], Liu and Lee [24] performed three-dimensional free vibration analysis of thick laminated circular plates. Powmya and Narasimhan [25] and Zhang et al. [26] performed vibration analysis of composite laminated circular and annular plate. From the above discussion, it can be concluded that many researchers worked both experimentally and analytically on composites structures for analyzing its static and dynamic behavior. It is also observed that a few research works are conducted on dynamic analysis of bio-inspired composite structures.

This paper focuses on the analysis of the natural frequencies and mode shape of a composite annual ring structure. This bio-inspired concentric circle ring model can be utilized in many structural components of a wide range of engineering systems. This annual ring structure is inspired and idealized from nature wherein the annual rings

are constructed at the cross-section of stem of the tree wherein each layer represents the growth per annum. The present study deals with the simple concentric circular annual ring geometry where the annual rings are idealized to construct each layer by graphite-fibers bonded together with epoxy resin in between the layers. Considering half clamped (HC) and full clamped (FC) boundary conditions, the first five natural frequencies are obtained, and the corresponding mode shapes are plotted for the proposed composite structures. The advantages of adopting this novel composite form over the conventional fiber reinforced composite are discussed. Hereafter, the paper is presented in the following sections: Section 2 deals with the methodology, Sect. 3 deals with the results and discussion, and Sect. 4 deals with the concluding remark and future outlook of the present study.

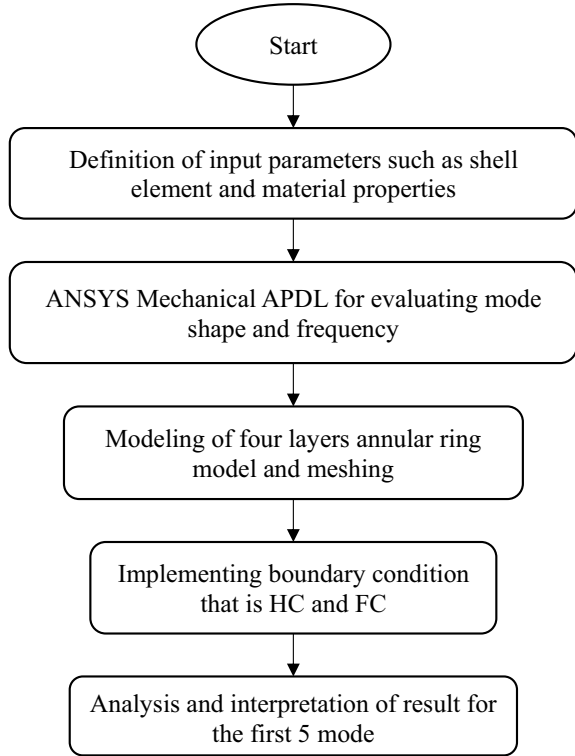
2 Methodology

In the present analysis, ANSYS Mechanical APDL software is employed for designing, meshing, material properties, applying load and modal analysis. First 'Shell 63' is selected for the element type. The element has six degrees of freedom at each node including three translational and three rotational. It includes stress stiffening and large deflection. The element is defined by four nodes, four thicknesses, and orthotropic material properties. The first layer of the composite circular plate was modeled then four layers. In the first layer, total 25 circles were modeled having minimum circle radius of 2 mm to maximum circle radius of 50 mm. The consecutive circle was modeled with an increment of radius 2 mm. Then, four supporting lines of length 100 mm were modeled. The thickness of individual layer was set to 1 mm. So the total thickness of composite was 4 mm. The thickness of the individual circles and supporting lines in the model was set to 0.1 mm in real constant option. The whole model meshed using area quadrilateral meshing. The modal analysis is conducted for the first five natural modes, and Block Lanczos method is employed for the mode extraction. Two types of boundary conditions are considered, namely half peripheral clamping and full peripheral clamping, respectively. The degree of freedom of clamping nodal points are considered as zero in all three translational and three rotational directions. The natural frequencies and mode shapes for the first five natural modes are obtained for both boundary conditions. The completed procedure is represented in the form of a flow diagram as furnished in Fig. 1.

3 Results and Discussions

To verify the accuracy of this work, the present results are first compared with that of the results obtained from the past literature [1]. The material properties for the validation and further analysis are obtained from Crawley [1] as given in Table 1. For validation purpose, 8-layered graphite-epoxy composite plate having two different

Fig. 1 Flowchart showing the analysis for mode shape and natural frequency



dimensions (76 mm × 76 mm) and (152 mm × 76 mm) are considered. Both plates are fixed at one side having dimension 76 mm. In both plates, the nominal thickness of each layer is considered as 0.13 mm, and the orientation of each layer is $[45^\circ/-45^\circ/-45^\circ/45^\circ]_s$. The modal analysis is performed to obtain the natural frequencies for both plates, and it is compared with the results obtained by Crawley [1]. The validation is given in Tables 2 and 3.

For the present analysis, total 25 circles are modeled having an initial circle diameter of 4 mm and a large circle diameter of 100 mm. The increment of consecutive

Table 1 Material properties of graphite/epoxy

Properties	Value
Longitudinal modulus EL	128 GPa
Transverse modulus ET	11 GPa
Poisson's ratio	0.25
Shear modulus GLT	4.48 GPa
Shear modulus GLZ	1.53 GPa
Density	1500 kg/m ³
Nominal ply thickness	1 mm

Table 2 Natural frequency (Hz) of 8-ply graphite-epoxy cantilever plate (76 mm × 76 mm)

Orientation	Mode	Crawley [2]	Present study	% Difference
[45°/-45°/-45°/45°] _s	1	131.20	136.85	4.30
	2	472.00	488.24	3.44
	3	790.50	780.25	- 1.29
	4	1168.00	1287.30	10.21
	5	1486.00	1577.90	6.18

Table 3 Natural frequency (Hz) of 8-ply graphite-epoxy cantilever plate (152 mm × 76 mm)

Orientation	Mode	Crawley [2]	Present study	% Difference
[45°/-45°/-45°/45°] _s	1	31.30	31.65	1.13
	2	185.80	189.50	1.99
	3	214.00	224.30	4.81
	4	533.00	555.59	4.24
	5	653.00	693.54	6.20

circle diameter was 4 mm. Total four supporting lines of length 100 mm are modeled to hold the circles. One layer is completed by providing a thickness of 1 mm. The thickness of individual annual circles and supporting thin plate in each layer is considered as 0.1 mm. After completing one layer, four layers are created and glued together. The model is completed and the two-dimensional view and three-dimensional view along with the meshed model using area quadrilateral meshing are shown in Fig. 2. The model is considered as half clamped and full clamped having zero degrees of freedom on the outer periphery as furnished in Fig. 3. The first five natural frequencies (for both half clamped and full clamped conditions) are determined as depicted in Table 4. Finally, the mode shapes are generated up to the first five modes which are shown in Fig. 4.

The present study is aimed to model the composite circular plate of annual rings (inspired from formation of annual ring in stem of tree). The fiber have the material properties of graphite and bonding material as epoxy. The aim is to find the natural frequencies and mode shapes of the same by applying different boundary conditions.

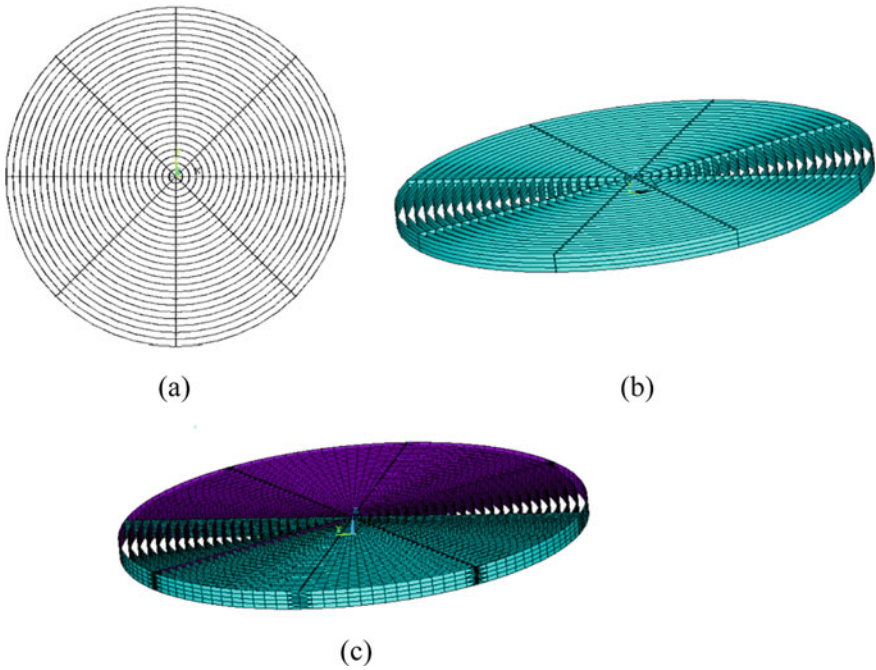


Fig. 2 Annual ring model (a) in 2D view (b) in 3D view (c) after meshing

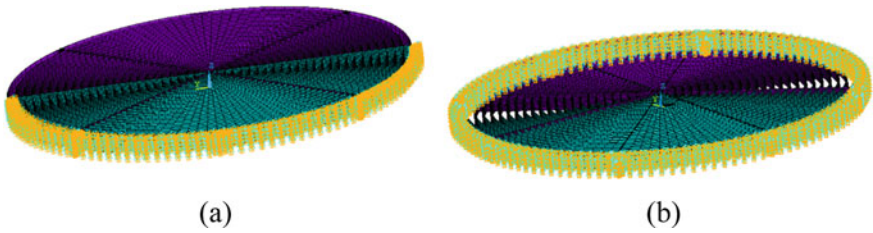


Fig. 3 Annual ring model after meshing (a) half clamped (HC) (b) full clamped (FC)

Table 4 Natural frequency (in Hz) for first five modes of annual ring model

Mode	Natural frequency (Hz) for half clamped	Natural frequency (Hz) for full clamped
First	275.80	370.90
Second	345.76	640.32
Third	536.56	821.98
Fourth	605.43	843.90
Fifth	633.11	911.63

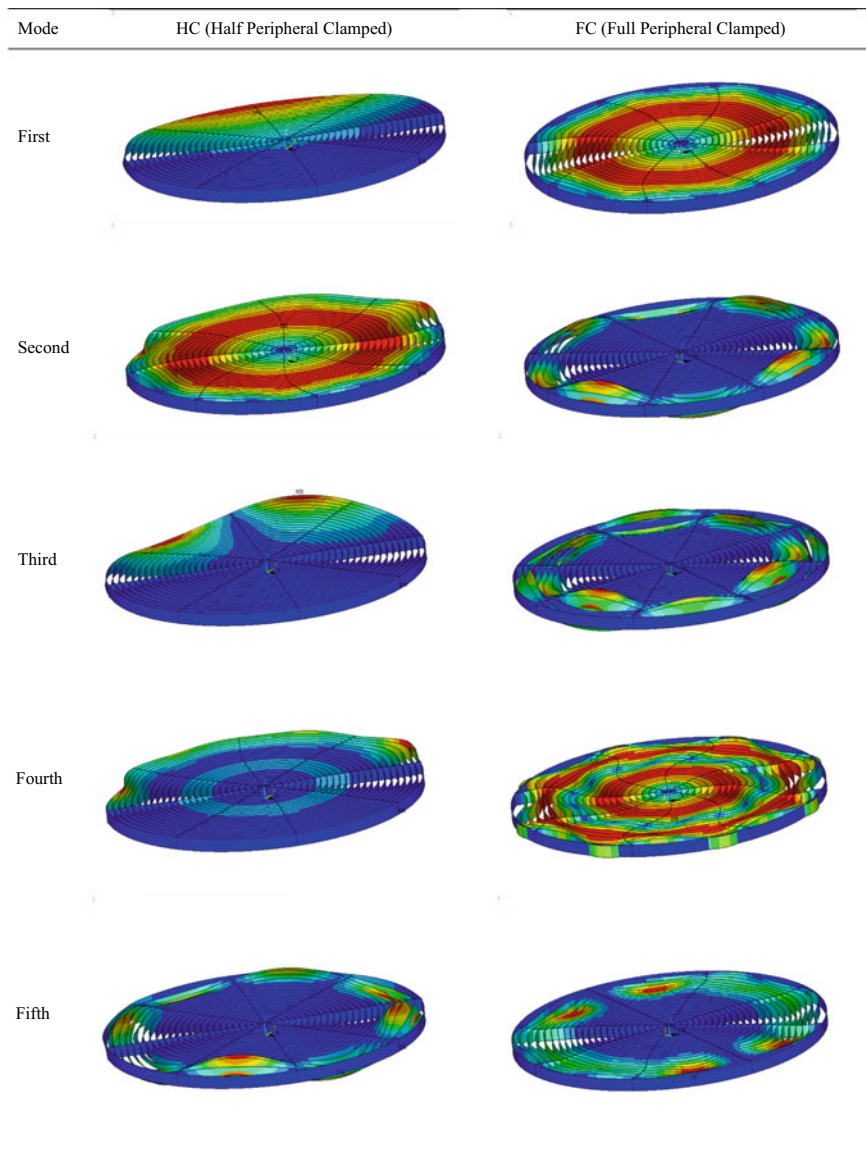


Fig. 4 Mode shapes when the annual ring model is half clamped and full clamped

4 Conclusion

In the present study, commercial CAE software ANSYS is used. Modal analysis is performed for analyzing the natural frequency of four layered graphite-epoxy fiber reinforced composite in ANSYS Mechanical APDL. From the modal analysis, the natural frequency of the first five modes and mode shapes for each mode in both half clamped and full clamped conditions were analyzed. It is observed that the natural frequencies in both cases are varying. It is found that the natural frequency is higher for the fully clamped model as compared to that of the half clamped model. The present analysis focuses on the natural frequency and mode shape of the structure. It helps in attaining higher reliability and safety of the structure. So, further different types of analysis such as structural analysis, buckling analysis can be performed to find out the load at which the model will fail or buckle and should be compared with conventional composite plates. If this annual ring composite shows higher strength, then this type of composite material should be implemented in the future in different broad areas such as aerospace and automobiles.

Acknowledgements The authors acknowledge Ministry of Education (MoE), Govt. of India for providing financial support.

References

1. Crawley EF (1979) The natural modes of graphite/epoxy cantilever plates and shells. *J Compos Mater* 13(3):195–205
2. Anderson TJ, Nayfeh AH (1996) Natural frequencies and mode shapes of laminated composite plates: experiments and FEA. *Modal Anal* 2(4):381–414
3. Ni RG, Lin DX, Adams RD (1984) The dynamic properties of carbon-glass fibre sandwich-laminated composites: theoretical, experimental and economic considerations. *Composites* 15(4):297–304
4. Dun-xiang L, Rong-gen N, Adams RD (1986) The finite element technique for predicting the natural frequencies, mode shapes and damping values of filamentary composite plates. *Appl Math Mech* 7(2):197–213
5. Kamal K, Durvasula S (1986) Some studies on free vibration of composite laminates. *Compos Struct* 5(3):177–202
6. Saravana Bavan D, Mohan Kumar GC (2010) Potential use of natural fiber composite materials in India. *J Reinf Plast Compos* 29(24):3600–3613
7. Kang JH, Leissa AW (1998) Three-dimensional vibrations of thick, linearly tapered, annular plates. *J Sound Vib* 217(5):927–944
8. Liew KM, Yang B (2000) Elasticity solutions for free vibrations of annular plates from three-dimensional analysis. *Int J Solids Struct* 37(52):7689–7702
9. Zhou D, Au FTK, Cheung YK, Lo SH (2003) Three-dimensional vibration analysis of circular and annular plates via the Chebyshev-Ritz method. *Int J Solids Struct* 40(12):3089–3105
10. So J, Leissa AW (1998) Three-dimensional vibrations of thick circular and annular plates. *J Sound Vib* 209(1):15–41
11. Han JB, Liew KM (1999) Axisymmetric free vibration of thick annular plates. *Int J Mech Sci* 41(9):1089–1109

12. Liew KM, Liu FL (2000) Differential quadrature method for vibration analysis of shear deformable annular sector plates. *J Sound Vib* 230(2):335–356
13. Wu TY, Wang YY, Liu GR (2002) Free vibration analysis of circular plates using generalized differential quadrature rule. *Comput Methods Appl Mech Eng* 191(46):5365–5380
14. Wang X, Wang Y (2004) Free vibration analyses of thin sector plates by the new version of differential quadrature method. *Comput Methods Appl Mech Eng* 193(36–38):3957–3971
15. Sharma A, Sharda HB, Nath Y (2005) Stability and vibration of thick laminated composite sector plates. *J Sound Vib* 287(1–2):1–23
16. Houmat A (2008) Large amplitude free vibration of shear deformable laminated composite annular sector plates by a sector p-element. *Int J Non-Linear Mech* 43(9):834–843
17. McGee OG, Huang CS, Leissa AW (1995) Comprehensive exact solutions for free vibrations of thick annular sectorial plates with simply supported radial edges. *Int J Mech Sci* 37(5):537–566
18. Malekzadeh P, Afsari A, Zahedinejad P, Bahadori R (2010) Three-dimensional layerwise-finite element free vibration analysis of thick laminated annular plates on elastic foundation. *Appl Math Model* 34(3):776–790
19. Pingulkar P, Suresha B (2016) Free vibration analysis of laminated composite plates using finite element method. *Polym Polym Compos* 24(7):529–538
20. Soamidas V (2011) Buckling of fiber-reinforced annular disks subjected to a concentrated tangential edge load. *J Emerg Trends Eng Appl Sci* 2(5):835–839
21. Khare S, Mittal ND (2016) Three-dimensional free vibration analysis of thick laminated circular plates. *Int J Eng Sci Technol* 8(2):11–29
22. Khare S, Mittal ND (2017) Three-dimensional free vibration analysis of thick laminated composite circular plates with simply-supported boundary conditions. *Mater Today Proc* 4(9):10054–10061
23. Khare S, Mittal ND (2018) Free vibration of thick laminated circular and annular plates using three-dimensional finite element analysis. *Alex Eng J* 57(3):1217–1228
24. Liu CF, Lee YT (2000) Finite element analysis of three-dimensional vibrations of thick circular and annular plates. *J Sound Vib* 233(1):63–80
25. Powmya A, Narasimhan MC (2015) Free vibration analysis of axisymmetric laminated composite circular and annular plates using Chebyshev collocation. *Int J Adv Struct Eng (IJASE)* 7(2):129–141
26. Zhang H, Zhu R, Shi D, Wang Q (2019) A simplified plate theory for vibration analysis of composite laminated sector, annular and circular plate. *Thin-Walled Struct* 143:106252

Review on Strengthening of Reinforced Concrete Slab Using Externally Bonded FRP Composites



Atanu Debnath and Subhashish Roy Chowdhury

Abstract Strengthening of different components of RC frame structure using fiber-reinforced polymer (FRP) is a very popular and convenient technique to withstand higher load. During last few decades, several researches have been carried out on reinforced concrete slab strengthened using different types of externally bonded FRP composites and adhesives. Various aspects of RC slab strengthened with externally bonded FRP have been reviewed in this paper. Though there is a huge advancement in the technology in the recent past, this topic has not been covered elaborately in previous studies. It covers subjects such as strengthening of punching and flexural strength for different types of slab, strengthening under different type of loading, use of different types of FRP, strengthening of slab with cutout, failure mode, FRP strain, crack load, ultimate load and ductility and assessment of extent of strengthening through finite element analysis. Furthermore, this paper reviews the debonding issues of externally bonded FRP sheet or strip. This paper finally concludes with the future scope of further research.

Keywords Externally bonded fiber-reinforced polymer (EBFRP) · Failure mode · Finite element · RC slab · Strengthening

1 Introduction

Rehabilitation and repairing of old structure is a contemporary research in the field of civil engineering. Strengthening of reinforced concrete structure during their service life is a real difficult problem for civil engineers. These structures require strengthening due to different reasons like increased applied load, deterioration of materials,

A. Debnath

Department of Civil Engineering, Meghnad Saha Institute of Technology, Kolkata, India
e-mail: atanu.debnath@msit.edu.in

S. Roy Chowdhury (✉)

Department of Civil Engineering, Jadavpur University, Kolkata, India
e-mail: subhashishroy.chowdhury@jadavpuruniversity.in

lack of maintenance, environmental damage, etc. Furthermore, design of old structure using the previous codes is structurally unsafe compared to the recent design codes. Since replacement of unsafe structure requires huge amount of man hour, time and investments, strengthening are becoming a popular way of increasing their load-carrying capacity as well as life span. Several strengthening techniques have been applied in different ways such as concrete jacketing, external post-tensioning and externally loaded steel plates. Although these traditional strengthening techniques are able to improve load-carrying capacity of concrete structure, self-weight of repaired structure is increased. Moreover, these techniques are time consuming. Strengthening of concrete structure using EBFRRP has gained popularity worldwide in recent years. Several researches have shown that this method is better than traditional one due to its anticorrosion property, low weight and high strength to weight ratio. Moreover, the process of strengthening is very simple and less time consuming. Till now, several review papers have been published regarding FRP-strengthened concrete structure. But most of these review papers mainly cover strengthening of beam using EBFRRP. To date review of strengthening of RC slab using EBFRRP has not been covered elaborately. The goal of this paper is to collect and review research papers reported regarding strengthening of RC slab using EBFRRP. Several researchers reveal the benefit of use of EBFRRP techniques to strengthen one-way slab [1, 2] as well as two-way slab [3, 4].

Finite element (FE) models for one-way [5, 6] and two-way slab have been developed to compare with experimental data. Extensive research studies have been carried out to investigate the performance of one-way and two-way slab with cutout strengthened by EBFRRP. A lot of studies have focused on strengthening of slab against punching failure. As debonding of FRP is relevant in achieving a successful strengthening, anchoring between FRP and concrete plays an important role. Several researches have covered this area. Use of different types of fiber affects the efficiency of this technique. Not only RC structure, concrete-filled hollow steel structures are also strengthened using FRP [7]. In case of steel structure, use of low modulus CFRP is also a research area [8, 9]. The focus of this paper is to provide a review on the strengthening of RC slab by using EBFRRP. In addition, this work covers the following areas: strengthening of one-way and two-way RC slab using EBFRRP, strengthening of RC slab with cutouts, increase of punching shear strength of flat slab/slab-column connection FRP strain and FE simulation. This paper also discusses the gap of researches and future scope of research.

2 Experimental Studies of One-Way Slab

Seim et al. [10] tested one-way slab and demonstrated that load capacity can be increased by up to 370% due to the use of EBFRRP. But the failure mode changed from ductile to brittle. It also showed that FRP material type and configuration affected the load-carrying capacity. The measured responses of slab were compared with analytical results, and it established a good agreement. The bending capacity

of flexural members depends on the bonding of FRP composites to the members' tension face. Smith et al. [2] reported a series of tests on one-way slab strengthened in flexure with tension face bonded FRP composites anchored with different arrangements of FRP anchors. According to the test results, the load-carrying capacity of FRP anchored slab was 30% more than unanchored one as well as ductility was increased due to use of FRP anchors. Anchors positioned in the shear span were found to be most effective position of anchors. Smith et al. [11] conducted experiments on ten slabs, one of them was controlled slab, nine were strengthened in flexure with FRP plates, and eight of the strengthened slab were anchored with different types and arrangements of FRP anchors. Test results suggested an optimal arrangement of anchors which enhanced the load and deflection capacities up to 44% and 216%, respectively. Intermediate crack debonding failure is a common problem for EBFPR strengthening techniques. Elsanadedy et al. [1] developed an analytical model using artificial neural network and regression model to predict ultimate FRP strain at intermediate crack (IC) debonding. The sensitivity analysis of the above model explored that the three most significant parameters for the prediction of IC debonding strain of FRP-strengthened RC one-way slab were axial rigidity of FRP system, yield strain of steel bars and the ratio of the width of FRP sheet to the width of the rib of slab. Fathelbab et al. [12] analytically examined the performance of RC bridge slab strengthened using several schemes of externally bonded carbon fiber-reinforced polymer (CFRP) under distributed load. From test results, it was clear that strengthening of RC bridge deck using CFRP sheets increased slab strength, but different schemes of CFRP influenced increase of strength. Ali et al. [13] conducted a comparison studies between GFRP sheets, carbon fiber laminate strips and near surface mounted steel rebars as strengthening materials and examined the behavior of strengthened specimens. The experimental results (Table 1) explored that use of GFRP sheet was more effective in respect of crack load and deflection. Moon et al. [5] noticed that accessibility and installation of FRP lamination/sheet to the underside of slab were difficult. So a hybrid composite system was proposed. The system consisted of UHPC, CFRP and shear connectors, and it was applied to the top surface of the floor slab (Fig. 1). Positive moment section of a simply supported slab specimen was strengthened by this new method, and the effectiveness of the proposed method was examined. This hybrid method increased both flexural and shear capacity of slab, and according to the test results, ultimate load-carrying capacity was increased by 70%. Author also conducted a FE analysis of the specimen which matched well with the experiment. The load-carrying capacity of RC slab may be compromised by creating new openings due to functional use. Shehab et al. [14] conducted experimental and analytical studies on strengthening of slab with cutouts. The key parameters of the investigation were opening ratio, CFRP layers, laminates' widths, position of cutouts and the CFRP configuration around cutouts. The experimental result revealed that though EBFPR techniques increased the ultimate load-carrying capacity of cutout slab compared to control one, no. of FRP layers, layer width and area of FRP had a great influence on ultimate load-carrying capacity. The finite element model overestimated the values of the ultimate loads of the tested slabs by 2–3%. This research also formulated equivalent amount of CFRP to replace the loss of steel reinforcement

caused by the cutouts to restore the load-carrying capacity of RC slabs after having cutout. Rehman et al. [15] conducted experimental tests and reported a comparative discussion between control slab (S1), slab strengthened by GFRP (S2) and slab strengthened by CFRP (S3). It was observed from experimental results (Table 2) that slab strengthened by GFRP was more effective in respect of yield load, ultimate load, flexural capacity and ductility. Bond mechanism of EBFPR strengthened slab is an important part of this strengthening technique.

Costa et al. [16] developed a new numerical model which provided important insights on the bond mechanism. The model was also able to predict the composite behavior and strength of the FRP strengthened structure. The proposed model was validated through experimental data which showed good agreement with the model.

Table 1 Comparison among different strengthening methods using FRP

Specimen	Cracking load (ton)	Ultimate load (ton)	Cracking/Ultimate (%)	Max deflection (mm)	Strengthening method
S1	7.1	10.6	67	17.55	Control
S2	10.2	14	72	18.48	GFRP sheets
S3	9.5	15.5	61	18.01	Carbon laminated strips
S4	10.00	17.7	56	19.53	Near surface mounted

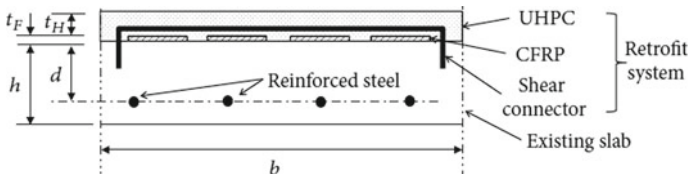


Fig. 1 Hybrid composite system

Table 2 Comparison between effect of use of different FRP materials

S. No.	Specimen	Yield load (kN)	Ultimate load (kN)	Maximum deflection (mm)	% difference in the deflection	Max BM (kN-M)
1	Control	128.64	192	15.2		23.59
2	GFRP sheets	181.44	252	16.45	8.22	30.24
3	CFRP sheets	151.89	249	16.1	5.92	25.8

3 Experimental Studies of Two-Way Slab

EBFRP techniques are applicable for both retrofitting and repairing of two-way slab. Mosalam et al. [3] tested 12 two-way slabs, among those three were controlled unreinforced, one was controlled reinforced, two unreinforced slabs were repaired by two layers carbon/epoxy laminates, two unreinforced slab were retrofitted by two layers carbon/epoxy laminates, two unreinforced slabs were retrofitted by three layers E-glass/epoxy laminates, one reinforced slab was repaired by two layers carbon/epoxy and last one reinforced slab was retrofitted by carbon/epoxy laminates. All the slabs were tested up to ultimate uniformly distributed pressure. The test results reported that the applied method was successful to upgrade structural capacity of both two-way unreinforced and reinforced concrete slab. Moreover in all cases, large deflection was observed during failure which provided enough visual warning. Also in case of two-way slab, the strength is compromised due to cutouts in an existing slab. Choi et al. [17] conducted experiments on two-way slab having central cutouts and strengthened by different orientation (Fig. 2) of GFRP. The test results concluded that all strengthening techniques were able to raise load-carrying capacity approximately by an average of 20%. But diagonally strengthened slab showed to be one of the most effective ways. It was also observed that for all the cases, the reason of failure was IC debonding of GFRP sheet (Fig. 3). Florut et al. [18] also presented analytical and experimental results of investigations on two-way slab having cutout on their sides. But combination of EBFRP and NSM was used as strengthening material. The proposed strengthening system was enabled to increase the load and deflection capacities of the FRP strengthened slab by up to 121 and 57% in relation to unstrengthened reference slab. The test results also showed that use of NSM with EBFRP was enabled to avoid debonding failure. An analytical method named yield line theory was also applied to validate the experimental results, which revealed a good match with the experimental results. Teng et al. [19] introduced a layered four-node, 24 degrees of freedom rectangular composite plate element concept for finite element analysis of FRP strengthened RC slabs. The model was validated by previous years' experimental results. According to the test results obtained from this new layered model, CFRP strengthened RC slab performed the best compared to the GFRP and BFRP strengthened slabs. The load resistance capability was increased with the increase of width of FRP strip as well as thickness of FRP strips slightly affected the flexural responses of FRP strengthened RC slab.

RC slab with central cutout of different shape (circular, square, rectangular) strengthened by CFRP was tested by Elsayed et al. [20]. As per the test results, (i) CFRP laminates were very successful for three types of opening. (ii) Premature debonding of CFRP laminates was a serious issue. (iii) For same opening area and location, circular opening showed the best performance. Al-Fatlawi et al. [21] investigated the effect of opening on a two-way slab strengthened by CFRP sheets under uniformly distributed load. Firstly, only one opening was considered centrally and tested. Then keeping same opening area, two cutouts were considered at different locations. The test results showed that the use CFRP was depended

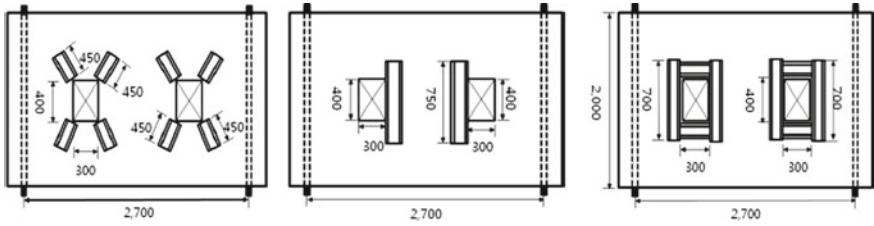


Fig. 2 Different orientation of GFRP

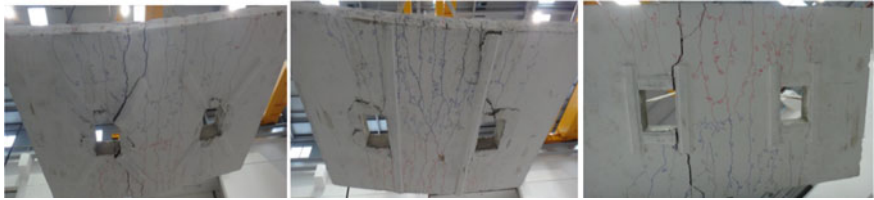


Fig. 3 IC debonding failure for diagonal, parallel and surround strengthening

on the strengthening scheme which improved the cracking load 33.3–8705% and ultimate load 26.2–55.1%. The experimental tests also showed that the specimen with two diagonal diverging opening and strengthened with CFRP performed the best. Two-way four-side fixed supported slabs were strengthened by different FRP materials (CFRP, GFRP, AFRP, BFRP), and ultimate load-carrying capacity were checked under impact load [4]. The specialty of experiments was that first the control slabs were subjected to impact loading up to its first crack and then rehabilitated by different FRP sheets. Performance of rehabilitated slabs was then examined and compared with control slabs. The impact resistance of slabs strengthened by CFRP, GFRP, BFRP and AFRP was increased by 46.75%, 26.74%, 60.09% and 73.44%, respectively. Energy absorption capacity was the highest for AFRP rehabilitated slab comparing with control one.

4 Strengthening of Punching Shear Capacity for Slab-Column Connection/Flat Slab

Punching shear is very common type of failure for internal slab-column connection of a building and flat slab. This type of failure may lead to a progressive failure of adjacent slab-column connections. The aim of strengthening and stiffening of slab-column connection is to improve structural service performance and ultimate capacity. Sharaf et al. [22] investigated the punching shear capacity of interior slab-column connection for varying CFRP amount and configuration. Experiment test results showed that increase in punching shear load was maximum 15% than the

control one. According to the results, punching shear load capacity was almost proportional to the area of CFRP strips. Use of CFRP strips also increased the stiffness of the specimens. An analytical model was also developed to predict the capacity of specimens strengthened with CFRP strip and compared with experimental results and different design codes. Load-carrying capacity predicted by the proposed model was the closest to the experimental results. A new technique which consisted of combination of shear bolts and EBFPR was applied to improve the punching shear capacity [23]. Test results revealed that the use of EBFPR alone increased the shear capacity from 16 to 32%, use of shear bolts alone increased the same from 23% but combination of both increased the punching shear capacity between a minimum of 32% and a maximum of 77%. This technique also improved the ductility of the specimen. An analytical model was also proposed and compared with the experimental results, which established a good agreement.

Soudki et al. [24] conducted experimental test on six square slabs strengthened by CFRP sheets externally bonded at tension face. The variables of test were the configuration and amount of CFRP. According to the test results, the most efficient configuration was skew orientation. It was also observed that the strengthened specimen exhibited stiffer responses. An analytical model was developed, and punching capacities of the test specimens were also evaluated. Results were obtained from the model agreed with the experimental results. Farghaly et al. [25] presented a numerical model which simulated the experimental slabs strengthened by EBFPR to improve punching shear capacity. The test results reported that use of FRP increased the punching shear capacity of a two-way slab up to 40%. The numerical simulation tool predicted the ultimate load and deflection with good accuracy. It also gave a better understanding of debonding behavior. A simple set of equations were also developed for design purpose which were verified by existing experimental results. Halabi et al. [26] investigated behavior of interior slab-column connections subjected to eccentric loading. Experimental studies were carried out, and test results revealed that ultimate flexural strength was increased by 75%. Increase of eccentricity markedly decreased the ultimate capacity of slab-column connection. Abbas et al. [27] presented experimental test results of a set of one-way slab strengthened by externally bonded CFRP and textile-reinforced mortar (TRM) separately. From test results, it was observed that load-displacement profile had two peak loads and one peak followed by a plateau in control. The reason behind the second plateau was the combined action of the aggregate interlock and dowel action of the back face rebar and the strengthening layers. The first peak load was the ultimate punching load which was increased by 9–18% for strengthened slab. But there was significant increase in the second peak load and energy absorption for both the strengthening system (CFRP and TRM). An analytical model was also developed and compared with experimental results which established a good agreement. Azizi et al. [28] tried a new technique to strengthen flat slab against punching shear failure. The grooving technique and externally bonded reinforcement in groove (EBRIG) method was used for bar, and externally bonded reinforcement on groove (EBROG) and externally bonded reinforcement (EBR) (Fig. 4) method was applied for FRP sheet. To know the efficiency of this new technique, 15 numerical models were simulated developing FE models using computer program. One was

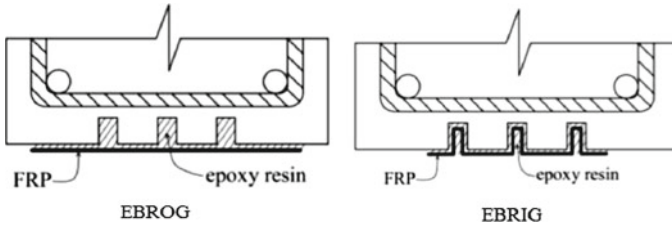


Fig. 4 EBROG and EBRIG

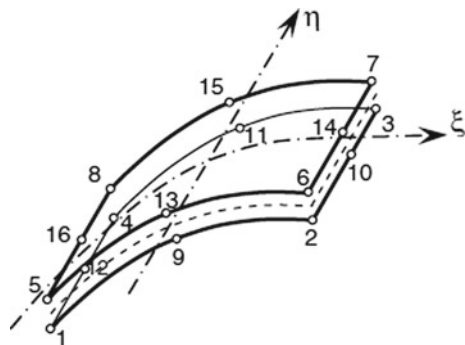
control specimen, and remaining fourteen specimens were strengthened by above-mentioned method. Slab strengthened by EBRIG (bar) in two directions increased punching shear capacity 28–33%, whereas EBRIG (bar) in one direction and EBR (FRP) in other direction increased punching shear capacity 18–53%. The best results came out from the combination of EBRIG (bar) and EBROG (FRP), and the punching shear capacity was increased by 23–63%.

5 Finite Element Simulation

The finite element method (FEM) is a very popular and acceptable approach to analyze a structure a structure. ABAQUS and ANSYS are very common computer program by which finite element analysis (FEA) of RC slabs has been carried out. FEM is generally used to predict the ultimate load-carrying capacity, failure pattern and strain in material, etc. Ebead et al. [29] used ABAQUS to simulate a FE model of a two-way slab strengthened using FRP. An incremental elastic plastic concrete model was implemented for concrete. The strain rate of concrete and compressive stress was decomposed into elastic and plastic strain. In this study, cracks were assumed to be smeared. The column was modeled as 3D solid brick elements. Both the steel and FRP were modeled as rebars. Slab support was modeled as nonlinear spring. The analytical results were validated by experimental results which established a good agreement. A finite element method was applied to predict the behavior of both control and rehabilitated slab strengthened by carbon/epoxy and glass/epoxy [3]. The FE models were developed considering eight-node quadrilateral shell elements based on isoparametric degenerated solid approach. A layered version of shell element was used to represent FRP composite strips. The thickness of each element was subdivided into several layers, and full bond was assumed between different layers. So the model did not consider delamination issue. The deformed shape and corresponding contour plot for axial stress in the bar were also shown. Comparison with experimental results confirmed the validity of the FEA. Elsayed et al. [30] developed FE model of the mechanically fastened FRP-strengthened two-way concrete slab with and without cutouts. Finite element software package ADINA (2004b) was used to describe the nonlinear stress–strain relationship for the concrete. To describe the behavior of

cracked concrete, smeared crack approach was employed. The steel reinforced was modeled as bilinear elastic–plastic material. The FRPs were simulated as linear elastic material until failure. The challenging part of this model is to describe FRP/concrete interface. The analytical model of the interface was ‘bearing slip’ model which was illustrated schematically. Izadi and Behbahani [31] used FE software package ABAQUS to study the behavior of GFRP strengthened RC slab. Total 36 models were developed of different width and configuration of GFRP strips. A comparison study reveals that width, spacing and orientation of GFRP strips have significant effect on slab deformation. An analytical model was developed to simulate the mechanism of punching shear strength of two-way slab externally strengthened with FRP [25]. A three-dimensional nonlinear finite element program named 3D CAMUI was used in this study. Newton Raphson solution was applied for nonlinear solutions. Smeared crack model was applied to simulate the crack mechanism. A 20-node solid element with eight Gauss integration points was used to represent concrete and reinforcement elements. The interfacial bond was modeled as a 16-node isoparametric joint element with four Gauss integration points (Fig. 5). The finite element analysis was validated by experimental results, and it was found that the numerical simulation tool simulated the ultimate load and deformation of strengthened slab with reasonable accuracy. A linear and nonlinear FEA for strengthened slab using several schemes of FRP sheets was carried out by ANSYS FE program [12]. SOLID65 element was used to model plain concrete material, Link8 element was used to model the reinforcing steel bar, and SOLID64 layered structural solid element was used to model the CFRP materials. Again smeared crack model was adopted by ANSYS to simulate the crushing and cracking behavior. ANSYS model was verified with existing experimental results, and it revealed very good agreement between FE model and results from published papers. A comparison study was conducted by Martin et al. [32] between FE analysis using LUSAS FE software package and Queen’s University Belfast (QUB) arching theory to predict load capacity of FRP strengthened RC slab. The result shows LUSAS prediction is more accurate than QUB arching theory. An analytical model was developed by Smith and Gravina [33] to predict the IC debonding failure of EBFPR strengthened RC slab. Though the results establish a good correlation with test data yet it requires more investigations using FE software package.

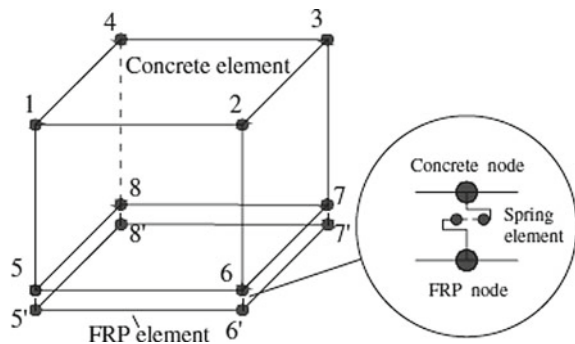
Fig. 5 16-node isoparametric joint element



Teng and Zhang [34] developed two nonlinear FE models (FE-S and FE-C) to analyze FRP-strengthened RC slab under static and cyclic load, respectively, using the FE software package ANSYS. The concrete, steel and FRP were modeled using solid, link and shell elements, respectively. FRP/concrete interface was modeled using spring elements (Fig. 6). The proposed model included material and geometric nonlinearity, but it assumed full bond between steel and concrete. FEM-C model considered the gradual degradation of each material under cyclic loading. Both the models were validated through existing numerical examples and demonstrated to be reasonably effective. A new layered method was developed for nonlinear FEA of FRP-strengthened RC slab [19]. Timoshenko's composite beam functions were adopted to explain the flexural behavior of the layered plate element. Each layer had four nodes with 24 DOF, and each layer was assumed in a state of plane stress. Perfect bond was considered between FRP, steel and concrete. Three existing experimental results were considered to validate the proposed FE analysis which demonstrated good agreement between them.

A polymeric hybrid composite system made of UHPC and CFRP was modeled for nonlinear FE analysis using a computer software package ABAQUS [5]. The concrete and HPC were modeled using eight-node solid elements. Four-node shell and two-node truss were used for CFRP sheet and rebar, respectively (Fig. 7). EMBEDDED option was used to embed the rebar and FRP sheet into the concrete. As concrete includes many nonlinear responses, STABILIZE option in ABAQUS was used to ensure the convergence of the solution. This model showed good agreement with the experimental results. Shehab et al. [14] developed a FE ANSYS model to simulate a one-way RC slab with cutouts. 3D eight-node solid element (SOLID65) was used to model concrete and resin. SOLID185 elements were used for modeling the CFRP composite. To model the steel, LINK180 was used. No slippage condition was considered between concrete and steel. Creep, shrinkage and temperature such time depended parameters were not considered in these studies. The percentage of error in results was $\pm 3\%$ comparison to the experimental results. A finite element model which was able to simulate the complex behavior of FRP-strengthened RC slab was developed by Costa et al. [16]. This model also simulated the interaction between the strengthening materials and cracks. The proposed model automatically simulated the

Fig. 6 Spring element model



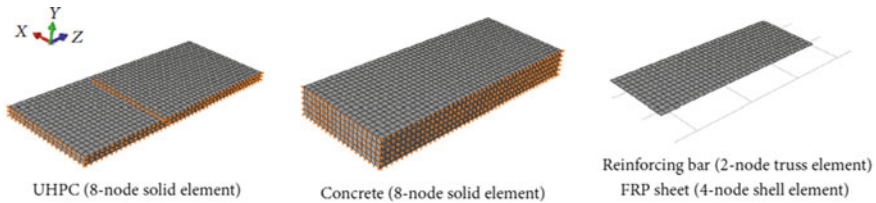


Fig. 7 Finite element model

material separation induced by crack opening. This model was validated with experimental data as well as sensitivity analysis was also carried out which revealed the well acceptance of this model. FEA of FRP-strengthened RC slab with FRP anchors was carried out by Yang et al. [6]. ABAQUS was used to develop the FE model. The FRP plate and concrete block were modeled by two-node truss element where four-node cohesive elements were used to model the FRP to concrete bonded interface as well as the FRP anchor. The results obtained from FE analysis showed a good agreement with the experimental test results. Azizi et al. [28] developed 15 FE models to simulate the behavior of flat slab strengthened with the combination of EBRIG (bar), EBROG (FRP) and EBR (FRP). Shit and Roychowdhury [35] carried out a parametric study involving the numerical analysis of a RC slab with or without FRP laminates and reported that the diagonal position of FRP at the tension face of the slab contributed the highest stiffness and ultimate load carrying capacity, coverage of 50–55% area gave satisfactory improvement and increase in the thickness of FRP at the diagonal location resulted maximum extent of strengthening rather than the other two considered locations.

6 Conclusion

In this paper, current and relevant researches conducted by other researchers were reviewed in terms of strengthening of one-way slab, two-way slab and flat slab using EBFRR. This study covered the following:

1. Though EBFRR is a successful technique to increase flexural capacity, shear capacity and punching shear capacity of one-way/two-way/flat slab, there are several parameters like amount of FRP, configuration of FRP, number of FRP layers, anchoring procedure and type of FRP, etc., which control the strength of FRP-strengthened slab. So there is need of proper optimization analysis of the same.
2. Debonding and delamination are common failure reasons for maximum slab strengthened by EBFRR. So further examination is required for a user-friendly and powerful anchoring system.
3. For slab with cutouts, shape of cutouts and position of cutouts affect the load-carrying capacity of a strengthened slab.

4. There are no guidelines in IS Code for design of FRP-strengthened RC slab.
5. Reasonable agreement between FE analysis and experiments surely proves the advantage of this repairing and retrofitting system. But to understand the characteristics of strengthened slab under failure mode, shear load and flexural still require further investigations. This issue can be solved by FEA in a reliable way.

Several researches have been carried out for simply supported one-way and two-way slab, but more researches are required for one-way and two-way slab having fixed support at two sides and four sides, respectively.

References

1. Elsanadedy HM, Abbas H, Al-Salloum YA, Almusallam TH (2014) Prediction of intermediate crack debonding strain of externally bonded FRP laminates in RC beams and one-way slabs. *J Compos Constr* 04014008:1–16
2. Smith ST, Hu S, Kim SJ, Seracino R (2011) FRP-strengthened RC slabs anchored with FRP anchors. *Eng Struct* 33:1075–1087
3. Mosalam AS, Mosalam KM (2003) Strengthening of two-way concrete slabs with FRP composite laminates. *Constr Build Mater* 43:43–54
4. Reddy J, Patankar MA (2017) Study on strengthening by rehabilitation of cracked RC slabs using different FRP sheets under impact loading. *Int J Res Eng Technol* 7(1):15–23
5. Moon J, Reda MM, Kim JJ (2017) Flexural strengthening of RC slabs using a hybrid FRP-UHPC. *Adv Mater Sci Eng* 2017:1–7
6. Yang J, Smith S, Wang Z, Lim YY (2018) Numerical simulation of FRP-strengthened RC slabs anchored with FRP anchors. *Constr Build Mater* 172:735–750
7. Chen Y, Feng R, He K, Chen X, Huang J (2018) Flexural behaviour of concrete-filled stainless steel SHS and RHS tubes strengthened by CFRP. *Thin-Walled Struct* 122:208–229
8. Selvaraj S, Madhavan M (2020) Design of steel beams strengthened with low-modulus CFRP laminates. *J Compos Constr* 24(1):04019052
9. Selvaraj S, Madhavan M (2019) Retrofitting of steel beams using low-modulus carbon fiber reinforced polymer laminates. *J Constr Steel Res* 105825
10. Seim W, Horman M, Horman V, Seible F (2001) External FRP poststrengthening of scaled concrete slabs. *J Compos Constr* 5(2):67–75
11. Smith ST, Zhang H, Wang Z (2013) Influence of FRP anchors on the strength and ductility of FRP-strengthened RC slabs. *Constr Build Mater* 49:998–1012
12. Fathelbab FA, Ramadan MS, Al-Tantawy A (2014) Strengthening of RC bridge slabs using CFRP sheets. *Alex Eng J* 53:843–854
13. Ali T, Yehia S (2016) Study on strengthening of RC slabs with different innovative techniques. *Open J Civ Eng* 6:516–525
14. Shehab HK, Eisa AS, Ei-Awady KA (2017) Strengthening of cutouts in existing one-way spanning R. C. flat slabs using CFRP sheets. *Int J Concr Struct Mater* 11(2):327–341
15. Rehman MA, Dhoke SV, Shirbate SR (2018) Experimental study on strengthening of RCC slab by using CFRP & GFRP Sheets. *Int J Eng Dev Res* 6(2):60–68
16. Costa DD, Costa R, Ranzi G (2018) Assessment of the behavior of FRP strengthened RC slabs using a discrete crack model. *J Compos Constr* 22(6):04018045
17. Choi Y, Park I, Kang SG, Cho C (2013) Strengthening of RC slabs with symmetric openings using GFRP composite beams. *Polymers* 5:1352–1361
18. Florut S, Sas G, Popescu C, Stoian V (2014) Tests on reinforced concrete slabs with cut-out openings strengthened with fibre-reinforced polymers. *Composites* 66:484–493

19. Teng X, Zhang X (2014) Nonlinear finite element analyses of FRP-strengthened reinforced concrete slabs using a new layered composite plate element. *Compos Struct* 114:20–29
20. Elsayed AA, Amer N (2015) Experimental analysis of centrally opened two-way slabs strengthened with carbon fiber laminates. *Concr Res Lett* 6(4):189–203
21. Al-Fatlawi ARS, Abed HA (2015) CFRP Strengthening of concrete slabs with and without openings. *Int J Sci Technol Res* 4(8):132–146
22. Sharaf MH, Soudki KA, Dusen MV (2006) CFRP Strengthening for punching shear of interior slab–column connections. *J Compos Constr* 10(5):410–418
23. Harajli MH, Soudki KA, Kudsi T (2006) Strengthening of interior slab–column connections using a combination of FRP sheets and steel bolts. *J Compos Constr* 10(5):399–409
24. Soudki K, El-Sayed A, Vanzwol T (2012) Strengthening of concrete slab–column connections using CFRP strips. *J King Saud Univ* 24:25–33
25. Farghaly AS, Ueda T (2011) Prediction of punching shear strength of two-way slabs strengthened externally with FRP sheets. *J Compos Constr* 15(2):181–193
26. Halabi Z, Ghrib F, El-Ragaby A, Sennah K (2012) Behaviour of RC slab column connections strengthened with external CFRP Sheets and subjected to eccentric loading. *J Compos Constr* 1943-5614.0000343
27. Abbas H, Abadel AA, Amusallan T, Al-Solloum Y (2015) Effect of CFRP and TRM strengthening of RC slabs on punching shear strength. *Lat Am J Solids Struct* 12:1616–1640
28. Azizi R, Talaeitaba SB (2019) Punching shear strengthening of flat slabs with CFRP on grooves (EBROG) and external rebars sticking in grooves. *Int J Adv Struct Eng* 11:79–95
29. Ebead U, Marzouk H, Lye LM (2002) Strengthening of two-way slabs using FRP materials: a simplified analysis based on response surface methodology. In: 2nd world engineering congress. Sarawak, Malaysia, pp 1–6
30. Elsayed WE, Ebead UA, Neale KW (2009) Mechanically fastened FRP strengthened two-way concrete slabs with and without cutouts. *J Compos Constr* 13:198–207
31. Izadi H, Behbahani HP (2017) Deformation behavior of reinforced concrete two-way slabs strengthened with different widths and configurations of GFRP. *Civ Eng J* 3(11):1121–1132
32. Martin T, Taylor S, Robinson D, Cleland D (2019) Finite element modelling of FRP strengthened restrained concrete slab. *Eng Struct* 187:101–119
33. Smith ST, Gravina J (2007) Modeling debonding failure in FRP flexurally strengthened RC members using a local deformation model. *J Compos Constr* 11(2):184–191
34. Teng X, Zhang X (2015) Nonlinear finite element analyses of FRP-strengthened concrete slabs under fixed-point cyclic loading. *J Compos Constr* 04014057:1–10
35. Shit F, Roychowdhury S (2019) A numerical study on the behaviour of reinforced concrete slab strengthened with frp laminates using finite element approach. In: Rao ARM, Ramanjaneyulu K (eds) Recent advances in structural engineering, vol 2, pp 675–686. Select proceedings of SEC 2016. Springer, Singapore

Post-earthquake Fire Resistance of Concrete-Filled Tubular Steel Columns



Smita Singh and Anil Agarwal

Abstract Following an earthquake, a building's capacity to withstand fire greatly diminishes, and the risk of fire also increases significantly. Although fire following an earthquake has a severe effect on structure, the subject has not been studied well. In this paper, the behaviour of concrete-filled steel tube (CFST) columns is presented under fire loading followed by an earthquake by using ABAQUS, a finite element-based analysis tool. The steps involved in numerical modelling were cyclic analysis and sequentially coupled thermal stress analysis. The output from the cyclic analysis was used as an input for the sequentially coupled thermal stress analysis. The results from the numerical analysis showed that the column with residual deformation failed early than the undamaged column.

Keywords Concrete-filled steel tubular (CFST) · Post-earthquake fire · Finite element modelling · Fire resistance

1 Introduction

Earthquakes are one of the most devastating forms of natural calamity. But if an earthquake event is followed by a fire, it can cause even more damage than the earthquake. Numerous cases of fire have been documented in the past following the earthquake. In the early twentieth century, a devastating fire followed the San Francisco, California earthquake in 1906 and the Tokyo earthquake in 1923 caused significant damage to both cities [1]. Although no post-earthquake large-scale fires have been reported recently, there are numerous episodes of isolated post-earthquake fires that cause significant damage [2]. Hundreds of fires have been reported after

S. Singh (✉) · A. Agarwal
Structural Group, Department of Civil Engineering, IIT Hyderabad, Hyderabad, India
e-mail: ce17resch11007@iith.ac.in

A. Agarwal
e-mail: anil@iith.ac.in

the 1994 Northridge, the 1995 Kobe and the 1989 Loma Prieta earthquake. Recently, Davidson 2012 reported several conflagrations after the 2011 Japan earthquake [3].

Several researchers have studied the behaviour of CFST columns under seismic loading and fire loading separately, but no one has studied the behaviour under the combined action of both scenarios. Therefore, there is a need to study the behaviour of the CFST column under the post-earthquake fire scenario.

The seismic behaviour of eight circular CFST columns was studied by Han and Yang [4] experimentally. A constant axial load was maintained, while the cyclic load was increased based on the ATC-24 protocol. They have also done the numerical analysis to validate the experimental results. A parametric study was also done to study the effect of several parameters on the behaviour of the moment versus curvature response, and lateral load versus lateral displacement relationships for the CFST columns.

Both experimental and numerical studies were conducted by Imani et al. [5, 6] to study the effect of fire loading followed by an earthquake on the concrete-filled double-skin tube (CFDST) columns. Numerical predictions matched significantly with experimental results. They inserted a horizontal discrete crack model at the location of maximum tensile stress to incorporate the pinching phenomenon of the hysteresis behaviour.

A research group at the National Research Council of Canada (NRCC) conducted experimental investigations on the circular and square columns of length 3810 mm [7]. The tested columns were filled with plain concrete, and their cross-section varied from 141.6 to 406.4 mm. The specimens were tested under fixed boundary conditions and were subjected to axial loading.

Talebi et al. [8] developed and validated a nonlinear 3D FE model for investigating the behaviour of CFST columns subjected to post-earthquake fire. They reported that CFT columns use benefits of the composite action between the steel tube and in-filled concrete, and can behave in a ductile manner.

CFST column has shown good resistance under cyclic as well as fire loading conditions. This study expands on these previous studies by investigating the behaviour of CFSTs numerically when exposed to fire after an earthquake.

2 FE Model Under Fire Loading

To model the fire resistance of the CFST column, a three-step sequentially coupled thermal stress analysis method was used. The validity of the finite element model was done against the experimental results of CFST columns performed by Lie and Chabot [7]. Two columns labelled as C-26 and C-23 were randomly selected to validate the numerical model under fire loading. Column length was 3810 mm out of which 3048 mm length was exposed to fire. The end plates of columns C-26 and C-23 had thicknesses of 38 mm and 25 mm, respectively. One square column labelled as S-1 with fixed boundary conditions was tested in our structural engineering lab at

IIT Hyderabad and was also used to validate the FE model for fire loading. Details of the selected CFST column are described in Table 1.

Thermal and ambient properties of concrete and steel were taken from Euro code [9, 10], and the stress–strain properties of steel and concrete are shown in Fig. 1. The modulus of elasticity and Poisson’s ratio ($\mu = 0.3$) were used to model the elastic properties of steel. A classic metal plasticity material model implemented in ABAQUS [11] was used for modelling the plastic behaviour of steel which follows von Mises yield and associated plastic flow. Drucker–Prager yield criteria available in ABAQUS is adopted to model the plastic behaviour of concrete.

To account for an initial geometric imperfection, the first mode shape obtained from the buckling analysis was amplified by a factor $L/1000$ and was considered as an initial imperfection.

The heat transfer analysis was done on the column to simulate the standard ASTM E119 1-1 fire curve [12]. The elemental model used for heat transfer analysis was 3-D eight-node solid element (DC3D8) for steel and concrete. Results of the heat transfer analysis in terms of the nodal time–temperature curve were applied as a boundary condition in the stress analysis. In the stress analysis, 3-D eight-node elements (C3D8R) were used for meshing steel and concrete. Sensitivity analysis showed that the mesh size of 20 mm gives results with reasonable accuracy.

The finite element (FE) model showed good agreement with the experimental results as can be seen in Fig. 2. Maximum fire resistance time and axial displacement for column C-23 were 163 min and 36 mm, respectively. The experimental

Table 1 Detail of the CFST columns for validating FE model under fire

Column		L (mm)	$D \times t$ (mm)	f_c (MPa)	f_y (MPa)	E_s (GPa)	N_o (KN)
C-26	Lie and Chabot	3810	323.9×6.35	24.3	350	200	1050
C-23	Lie and Chabot	3810	273.1×12.7	27.4	350	200	525
S-1	–	1800	$150 \times 150 \times 6$	25	310	200	384

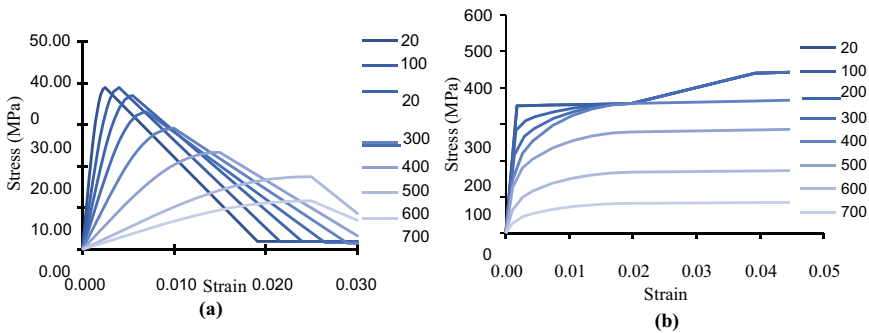


Fig. 1 Stress–strain curve at elevated temperature **a** concrete **b** steel

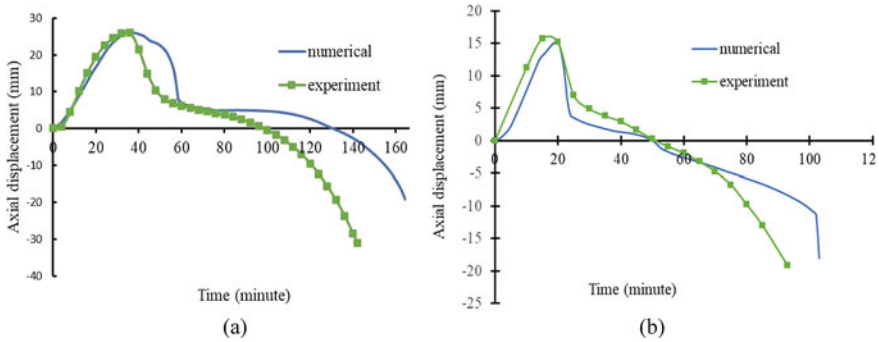


Fig. 2 Comparison of the axial displacement versus time curve for **a** C-23 **b** S-1

graph shows comparable values as 143 min and 36 mm. Column SC-26 experienced the maximum fire resistance time and axial displacement at 102 min and 15.23 mm, respectively, against their corresponding experimental values were 93 min and 15.7 mm. The experimental graph of column S-1 shows the fire resistance time as 87 min, while the numerically simulated model showed 96 min as shown in Fig. 2b.

3 FE Model Under Cyclic Loading

The effect of earthquake loading was investigated by subjecting the CFST column to seismic loading. A 3-D FE model was modelled in ABAQUS. The validity of the numerical model was checked by the experimental results of CFST columns conducted by Han and Yang [4]. They have studied the behaviour of eight CFST column under cyclic loading, and columns labelled as SC2-3 and SC2-4 were selected in this study for numerically validating the ABAQUS model. Both the columns had a diameter of 114 with a thickness of 3 mm and an overall length of 1500 mm. The compressive strength of concrete was 38.9 MPa, and yield strength of steel was 308 MPa. The axial load applied on the composite specimen SC2-3 and SC2-4 was 286 kN and 429 kN, respectively.

Boundary conditions and axial loading were applied through the 16 mm thick steel plates modelled at the columns endings. Loading was applied sequentially. First, the applied axial load was kept constant throughout the analysis, and then, cyclic loading is applied according to ATC-24 [13] loading protocol to simulate the seismic behaviour. Cycles were applied in levels of Δy , $1.5 \Delta y$, $2 \Delta y$, $3 \Delta y$, $5 \Delta y$, $7 \Delta y$ and $8 \Delta y$, where Δy was the yield displacement of the CFST column, and Δy was used as obtained in the test [4].

The elastic behaviour of steel was modelled using the modulus of elasticity as 200 GPa and Poisson's ratio as 0.3. For modelling the plastic nature of the steel, kinematic hardening model was used. The behaviour of concrete in tension as well as in compression was done according to EN 1992 1-1. The 3D eight-node solid

element (C3D8R) is used to model the concrete core, steel tube, and steel plate. Figure 5 shows the FE model. Mesh sizes of 20 and 10 mm (near the support) were used.

Figures 3 and 4 show a difference between the results of the predicted and experimental results in terms of lateral load versus lateral deformation. A comparison of the hysteresis curve from the numerical model and experiments shows comparable results. Results also show that by increasing axial load level displacement ductility also decreases (Fig. 5).

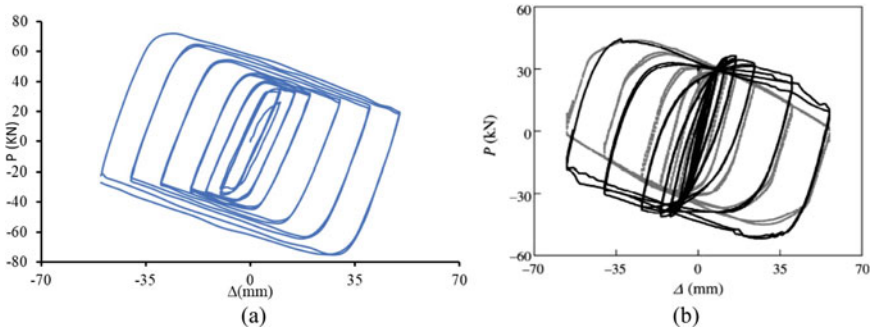


Fig. 3 Lateral displacement versus lateral load for column SC2-3 in a numerical model b experiments

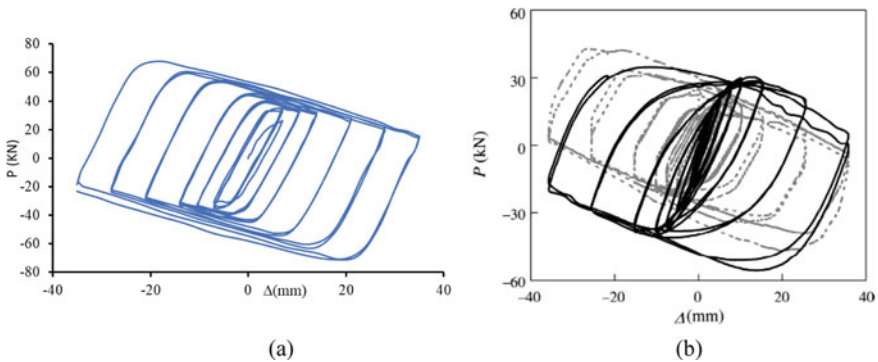


Fig. 4 Lateral displacement versus lateral load for column SC2-4 in a numerical model b experiments

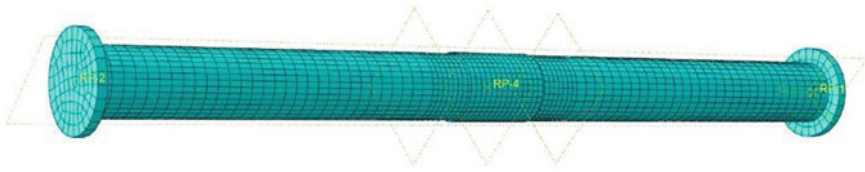


Fig. 5 Whole finite element model

4 FE Model Under Post-earthquake Fire Loading

Now the numerically calibrated model was used to study the effect of fire followed by an earthquake. Information regarding the CFST column selected for the post-fire earthquake study is as follows. The column had a cross-section of 150 * 150 mm, a thickness of 6 mm, concrete cylinder strength of 30 MPa, yield strength of steel 380 MPa and an axial load of 384 kN. The column selected for the post-earthquake fire behaviour was 1800 mm, and boundary conditions and loading were applied through the endplates.

To simulate the post-earthquake fire behaviour of columns, first cyclic analysis was conducted, and then residual deformations generated after the cyclic analysis were used as input for the sequentially coupled thermal stress analysis. To apply the cyclic loading, FEMA 461 loading protocol was used [14]. Thermal stress analysis and cyclic analysis follow the techniques defined in Sects. 2 and 3.

From Fig. 6, it can be observed that as we increase the damage due to cyclic loading, the fire resistance of the column decreases.

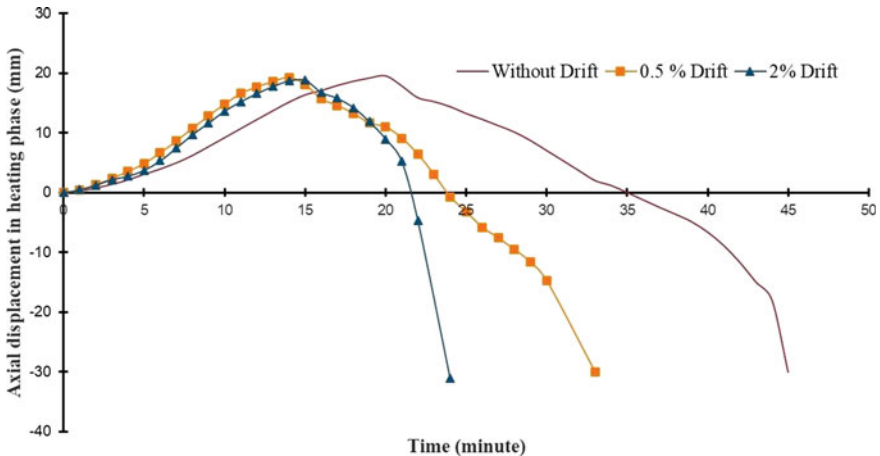


Fig.6 Axial displacement versus time for column with different damage levels

5 Conclusion

This paper studies CFST columns under varying levels of cyclic loading but with constant axial load. The analysis results show that as the damage level increases, the fire resistance of CFST columns decreases. A numerical study on one column does not provide a clear picture of fire behaviour after an earthquake. Hence, further numerical and experimental studies on the post-earthquake behaviour of CFST columns need to be done. Thermal and general properties of the material derived from the Eurocode were accurate enough to model the behaviour of CFST columns.

References

1. Scawthorn C (1986) Fire following earthquake. *Fire Saf Sci* 1:971–979
2. Scawthorn CR (2008) The shakeout scenario supplemental study: fire following earthquake. SPA Risk LLC
3. Davidson R (2012) Post-earthquake fires in the March 2011 Japan earthquake and tsunami. Proc. 2012 Japan and New Zealand RAPID and Research Needs Workshop, NSF, Arlington, VA, Feb. 9–10
4. Han LH, Yang YF (2005) Cyclic performance of concrete-filled steel CHS columns under flexural loading. *J Constr Steel Res* 61(4):423–452
5. Imani R, Mosqueda G, Bruneau M (2014) Experimental study on post-earthquake fire resistance of ductile concrete-filled double-skin tube columns. *J Struct Eng* 141(8):04014192
6. Imani R, Mosqueda G, Bruneau M (2015) Finite element simulation of concrete-filled double-skin tube columns subjected to postearthquake fires. *J Struct Eng* 141(12):04015055
7. Lie TT, Chabot M (1992) Experimental studies on the fire resistance of hollow steel columns filled with plain concrete. National Research Council of Canada, Institute for Research in Construction.
8. Talebi E, Korzen M, Hothan S (2018) The performance of concrete filled steel tube columns under post-earthquake fires. *J Constr Steel Res* 150:115–128
9. EN, B. (2004) 1-1, Eurocode 2: design of concrete structures. Part 1-1: General rules and rules for buildings. European Committee for Standardization (CEN)
10. EN, C. (2005) 1-2, Eurocode 3: design of steel structures. Part 1.2: General rules–structural fire design. Comité Européen de Normalisation, Brussels, Belgium
11. ABAQUS Standard User’s Manual (2013) The Abaqus Software is a product of dassault systèmes simulia corp., Providence, RI, USA Dassault Systèmes, Version 6.14.1, USA
12. ASTM, A.S. (1990) E119-88: standard methods of fire test of building construction and materials. American Society for Testing and Materials, Philadelphia, PA
13. Council A (1992) Guidelines for cyclic seismic testing of component of steel structures. ATC-24, Redwood City, CA
14. Applied Technology Council (ATC) (2007) Interim testing protocols for determining the seismic performance characteristics of structural and non-structural components. Federal Emergency Management Agency (FEMA) 461, Washington, DC

Finite Element Modelling of In Situ Composite Patch Repair of Cracked Aluminium Aircraft Structures



Samanvay Anand and Himanshu Pathak

Abstract Composite patch repair is a very effective and promising way to repair the cracked structure in order to increase their service life and structural integrity. There are a number of parameters which govern the performance of composite patch repair. In this work, symmetrical and un-symmetrical patch has been studied over the side crack on the aluminium aircraft panel. Contour integral technique has been implemented to model crack front discontinuity in the physical geometry. In order to check effectiveness of proposed computational model, benchmark problem has been solved with bonded patch structure. Further, few 3D patch repaired structures have been numerically solved to optimize patch repairing parameters like patch size, patch shape, adhesive material and patch configuration. In situ patch problems are analysed for cured thermal distribution in the patch repaired area over both symmetrical and unsymmetrical patch configuration. As a result of curing process, there is a variation in temperature throughout the repaired area; therefore, thermal residual stresses played a major role in structural integrity of repaired configuration. Numerical results are presented in the form of curing temperature contours, induced thermo-mechanical stress and fracture parameters like stress intensity factor (SIF). A decrease in SIF pattern has been observed in symmetrical patch as compared to unsymmetrical patch repair configuration. The patch curing temperature makes significant effect over SIF.

Keywords Finite element modelling · Composite patch repair · Thermo-mechanical loading · Stress intensity factor · Thermal stresses

S. Anand · H. Pathak (✉)
School of Mechanical and Materials Engineering, IIT Mandi, Mandi, India
e-mail: himanshu@iitmandi.ac.in

S. Anand
e-mail: t18144@students.iitmandi.ac.in

© The Author(s), under exclusive license to Springer Nature Singapore Pte Ltd. 2023
M. Madhavan et al. (eds.), *Proceedings of the Indian Structural Steel Conference 2020*
(Vol. 2), Lecture Notes in Civil Engineering 319,
https://doi.org/10.1007/978-981-19-9394-7_20

243

1 Introduction

Recent boom in the demand of airline industry has made it more susceptible towards the structural damage due to increased duty hours. Metallic aircraft components are very likely to undergo damage in the form of cracks, and a crack is more dangerous if it is under fatigue loading. Crack initiates from unsuspected region of local stress concentrations. Replacement of the cracked component is very costly particularly if there is need to disassemble the entire damaged structure [4]. Traditional method of repair for damaged aircraft structures involves the use of riveted or bolted metallic patches, but these methods provide a major drawback. Following are some of the major drawbacks of conventional fastening techniques [5]:

- Stress concentration due to drilled holes which also amplifies the fatigue cracking.
- Internal damages such as wear of the hydraulic lines and electrical wirings due the drilling of holes.
- Fretting damage due to poor mechanical fastening process which also amplifies the fatigue cracking.

Composite patch materials are more advantageous over metallic alloy fasteners for the repair process of damaged aircraft structures due to their high directional stiffness, high failure strain and durability under cyclic loading, low density and excellent formability [5].

One can control the crack formation by selecting a better material and manufacturing technique, but most of the times in spite of having these conditions cracks do appear in the structures. One alternative in order to deal with this problem is by selecting a better design parameter. Calculation of stress intensity factors (SIFs) is the most important parameter while designing a repair for cracked structures, because it helps in finding out the accurate life of the structure while in service. Calculation of SIFs near the cracked area by analytical method is a very tedious job; therefore, numerical method is getting the attention towards analysing and simulating these crack problems. Finite element method is one of the numerical techniques in order to simulate the fracture problems [1].

Rachid et al. [11] used the numerical technique in order to show the effect of different shape of patches on the mode-I SIF and hence concluded that the efficiency of a rectangular shaped patch can be increased if it is converted into an “H” or “arrow” shape. Ramji et al. [12] used FEM numerical technique in order to study the effect of patch shape which is applied over an inclined central crack and showed that there is a drastic decrease in mode-I and mode-II SIF by the introduction of double-sided composite patch repair. Curing is one the most important steps in the in situ patch repair process [6]. Kim et al. [8] used FEM to simulate the curing process of patched aluminium panels. They supplied the curing heat in the form of induction heating and compared the results of induction cured joints over composite bonded joints. Inspection of repaired structures is also very important in order to rely upon their structural integrity. Daryabor and Safizadeh [7] studied this inspection technique by using FEM numerical technique in order to find out the effect of defect type, shape and

depth over the detection ability of the test. The results obtained from the simulation in the form of heat transfer over the repaired region showed the appropriate heating procedure in order to inspect the repaired metallic structures. Sometimes it is very important to maintain the perfect shape of the repaired area as it was before the fracture and here the role of scarf repair comes into picture. Asrafi et al. [3] used FEM to examine the composite scarf repairs where the adhesive was cured by the resistance-assisted heat generation process. Two heat generation techniques were chosen for curing. In the first technique, adhesive is cured by placing the resistive heater at the bond line, and in the second sample, the resistive heater is placed above the outer surface of scarf patch. This embedded heating technique provided lower in-bond temperature gradients in the scarf repairs. Albedah et al. [2] calculated the SIF at different disbond length and with different crack length and thus showed that an increase in initial disbond width can decrease the fatigue life of the repair. The numerical result also showed that there is an increase in the SIF value in the presence of initial disbond; however, the proposed FE model has some deficiency since the natural growth of the artificial disbond was not taken into account.

On the basis of literature review, it has been found out that composite patch repair over aluminium panels is a very promising technique to regain the strength of cracked aluminium structures. People have mainly worked in the area of different repair techniques, patch shapes and patch sizes under mechanical loading condition, but very few of them focused upon the effect of thermal parameters on repair process like effect of curing temperatures on the bond strength and thermal stresses which generates due to the application of curing temperature. Also there is very less work regarding the combination of different loading conditions over the repaired structures like thermo-mechanical loading condition which plays a very crucial role when there is need to design a repair process for real patch repair scenario. To ensure an efficient and optimize patch repair, following objectives have been led down for the present study:

- To develop and implement finite element model for in situ patch repairing problem using Abaqus.
- To investigate optimized design parameter for symmetrical and unsymmetrical patch repaired configuration.
- Effect of patch size, patch shape and adhesive material have been analysed for fracture parameter.
- In situ patch problems are analysed for cured thermal distribution in the patch repaired area over both symmetrical and unsymmetrical patch configuration.

2 Numerical Modelling

2.1 Problem Formulation

In this section, mathematical formulation for the considered model has been presented. The thermo-elastic governing equation for the problem is given as [10]:

$$\nabla(-k\nabla T) + \mathbf{Q} = 0 \tag{1}$$

$$\nabla : (\mathbf{D} : (\nabla_s \mathbf{u} - \alpha(T - T_{ref})\mathbf{I})) + \mathbf{b} = 0 \text{ in } \Omega. \tag{2}$$

The applied boundary conditions are (Fig. 1)

$$\boldsymbol{\sigma} \cdot \mathbf{n} = \bar{\mathbf{t}} \text{ on } \Gamma_t \tag{3a}$$

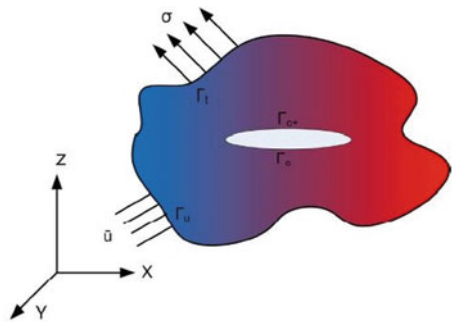
$$\boldsymbol{\sigma} \cdot \mathbf{n} = 0 \text{ on } \Gamma_{c^+} \tag{3b}$$

$$\boldsymbol{\sigma} \cdot \mathbf{n} = 0 \text{ on } \Gamma_{c^-} \tag{3c}$$

$$\mathbf{u} = \bar{\mathbf{u}} \text{ on } \Gamma_u \tag{3d}$$

$$\mathbf{D} = \frac{E}{(1 + \nu)(1 - 2\nu)} \begin{bmatrix} (1 - \nu) & \nu & \nu & 0 & 0 & 0 \\ \nu & (1 - \nu) & \nu & 0 & 0 & 0 \\ \nu & \nu & (1 - \nu) & 0 & 0 & 0 \\ 0 & 0 & 0 & (0.5 - \nu) & 0 & 0 \\ 0 & 0 & 0 & 0 & (0.5 - \nu) & 0 \\ 0 & 0 & 0 & 0 & 0 & (0.5 - \nu) \end{bmatrix}. \tag{4}$$

Fig. 1 Problem domain with crack and boundary condition



Here \mathbf{Q} is the heat source, k is the thermal conductivity, \mathbf{u} is the field displacement, \mathbf{n} is the outward normal unit vector on the boundaries, $\boldsymbol{\sigma}$ is Cauchy stress tensor, \mathbf{b} is the body force per unit volume, \mathbf{D} is the constitutive matrix of the material, ∇_s is symmetric gradient operator, T is the domain temperature field, T_{ref} is the reference temperature of thermal strain, α is the thermal expansion coefficient, and \mathbf{I} shows the identity tensor.

2.2 Finite Element Modelling of Repaired Aluminium Panel

The finite element modelling of repaired aluminium panel has been done by Abaqus software. Crack is introduced with the help of contour integration technique. The mesh is refined near the crack tip in order to accurately model the gradient stress field. Twenty nodes are created around the circle of crack, and five nodes are created over the radius of the circle of crack which makes a total of 630 nodes and 420 elements around the crack tip. Composite patch and adhesive are meshed with hexagonal-dominated element shape with the help of structured mesh. The total number of elements taken in thickness direction for patch and adhesive is 2 and 1, respectively. The element type taken for aluminium panel, composite patch and adhesive is eight-noded thermally coupled brick having trilinear displacement and temperature (C3D8T). The elastic material properties taken are given in Table 1 [9, 12], and the thermal material properties are given in Table 2. The numerical simulations have been done for three patch shapes, namely circular, square and rectangular. In case of square patch, the side length is taken as 15 mm, for circular patch the diameter is taken as 15 mm, for rectangular patch the vertical side is taken as 20 mm, and the horizontal side is taken as 15 mm. The computational algorithm for present study is shown in Fig. 2. The complete model geometry along with applied boundary conditions is shown in Fig. 3 [2].

Table 1 Elastic material properties

Material	E_x (GPa)	E_y, E_z (GPa)	ν_{xy}, ν_{xz}	ν_{yz}	G_{xy}, G_{xz} (GPa)	G_{yz} (GPa)	ρ (kg/m ³)
Aluminium	73.1	–	0.3	–	–	–	2700
Boron/Epoxy	208	25.4	0.167	0.032	7.2	4.9	1600
AV138/HV998	4.59	–	0.47	–	–	–	1700
Araldite 2011	1.16	–	0.41	–	–	–	1290
Araldite 2015	2	–	0.33	–	–	–	1400

Table 2 Thermal material properties

Material	K_{11} (W/mK)	K_{22} (W/mK)	K_{33} (W/mK)	α_{11} (m/K)	α_{22} (m/K)	α_{33} (m/K)
Aluminium	250	–	–	2.4×10^{-5}	–	–
AV138/HV998	0.35	–	–	6.7×10^{-5}	–	–
Araldite 2011	0.22	–	–	8.5×10^{-5}	–	–
Araldite 2015	0.22	–	–	8.5×10^{-5}	–	–
Boron/Epoxy	11.1	0.87	0.87	4.5×10^{-6}	2.3×10^{-5}	2.3×10^{-5}

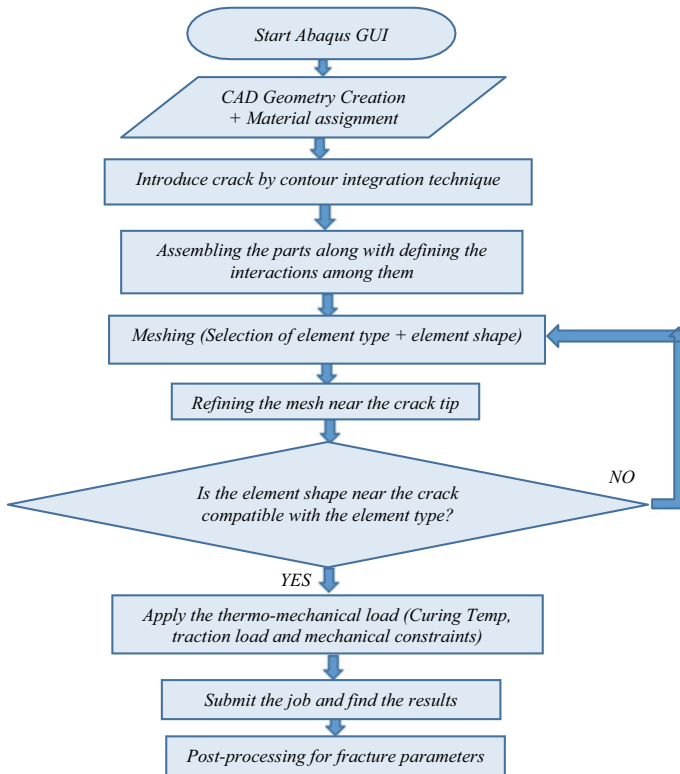


Fig. 2 Computational flow chart for patch repairing model

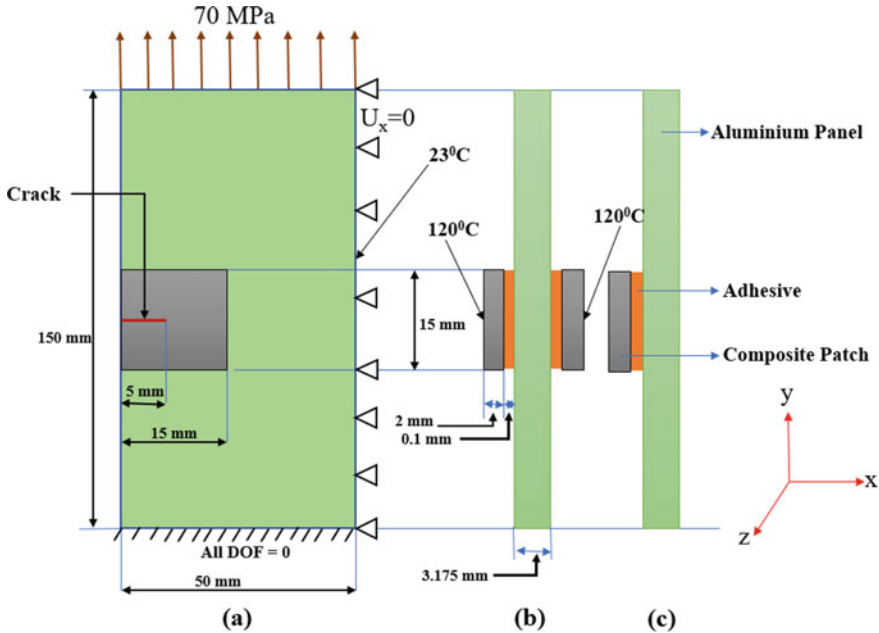


Fig. 3 **a** Front view of square patch repaired model, **b** side view of symmetrical patch repair configuration and **c** side view of un-symmetrical patch repair configuration

2.3 Mesh Sensitivity Analysis

In this section, a mesh sensitivity analysis has been done on symmetrical square patched repair configuration under thermo-mechanical loading condition. For this study, six different sets of elements were taken in mesh topology. Fine mesh refinement has been taken around the crack tip to model high gradient stress fields in problem geometry. Figure 4a clearly shows that as the number of elements increases, the SIF gets converged and characteristics of obtained results (SIFs) are stable with respect to mesh refinement. The elemental aspect ratio has also been recorded for different number of total elements taken.

From Fig. 4b, it can be seen that the elemental aspect ratio for all the number of elements taken is in between the range of 2–4. The elemental aspect ratio which has been taken in this study is 2.9, and this can be calculated by dividing the maximum dimension to the minimum dimension of the hexahedral element taken around the crack tip. It has been found that element aspect ratio at high gradient stress region is almost constant with mesh refinement. The aspect ratio dimension is healthy enough to simulate the considered problem.

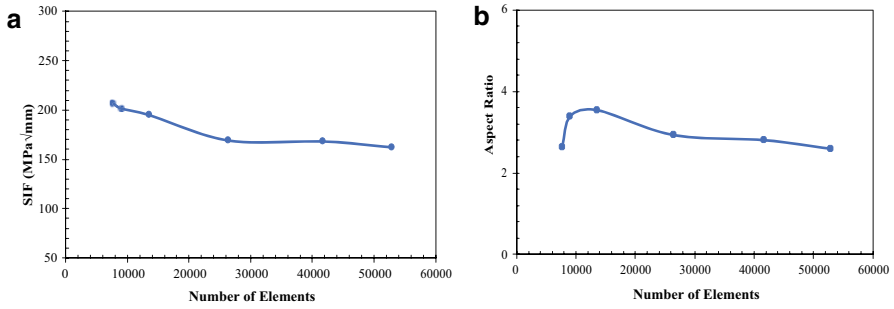


Fig. 4 a SIF variation with mesh refinement for symmetrical square patch repair and b elemental aspect ratio variation with mesh refinement for symmetrical square patch repair

3 Results and Discussions

3.1 Benchmark Problem Study

In this part of the paper, a benchmark problem study has been done in order to check the effectiveness of proposed computational model. The work of Ramji et al. [12] is taken as the reference of this benchmark study. Two results of the paper have been validated. The first one is the variation of mode-I SIF (K_I) near the crack over the thickness of the un-patched aluminium plate, and the second one is the variation of mode-I SIF (K_I) near the crack over the thickness of the square patched aluminium plate. While obtaining the first result, crack is introduced by using contour integration technique, and for the second result, the crack is introduced by using the XFEM technique. The validated results are shown in Fig. 5. From the presented results, it can be concluded that results obtained by implemented computational approach are quite accurate and agree with the available reference results [12].

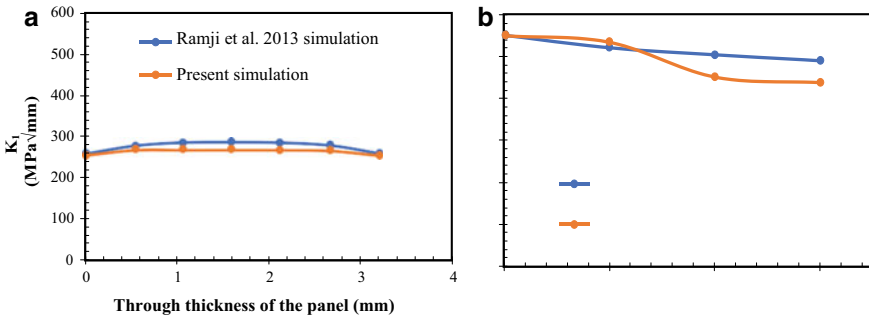


Fig. 5 a SIF variation along thickness of panel without patch repairing and b SIF variation along thickness of panel with patch repairing

3.2 Un-symmetrical Patch Repair Model Under Thermo-mechanical Loading

3.2.1 Patch Thickness Effect

In this section, the effect of different patch thickness has been studied. The adhesive used here is AV138/HV998 having 0.1 mm thickness. From Fig. 6, it can be observed that as the patch thickness increases, the SIF near the crack tip decreases, and this phenomenon becomes very less significant when the thickness of patch increases further. Also, there is an increase in SIF along the thickness of the aluminium panel starting from the patched side to un-patched side, and this is due to corner singularity effect [12]. The effect of patch shapes on von Mises stress is shown in Fig. 7, which clearly shows that von Mises stress decreases when there is a shift in patch shape from circular to square and again from square to rectangular. It has been observed that increment of patch thickness (0.5, 1, 2 and 3 mm) reduces the induced SIFs.

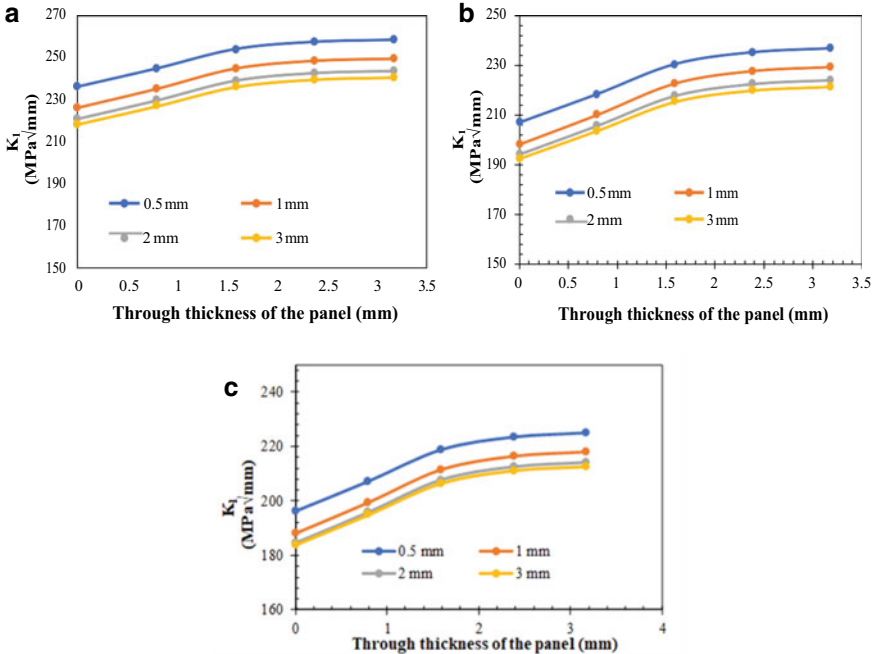


Fig. 6 a SIF variation along panel thickness for circular patch repairing, b SIF variation along panel thickness for square patch repairing and c SIF variation along panel thickness for rectangular patch repairing

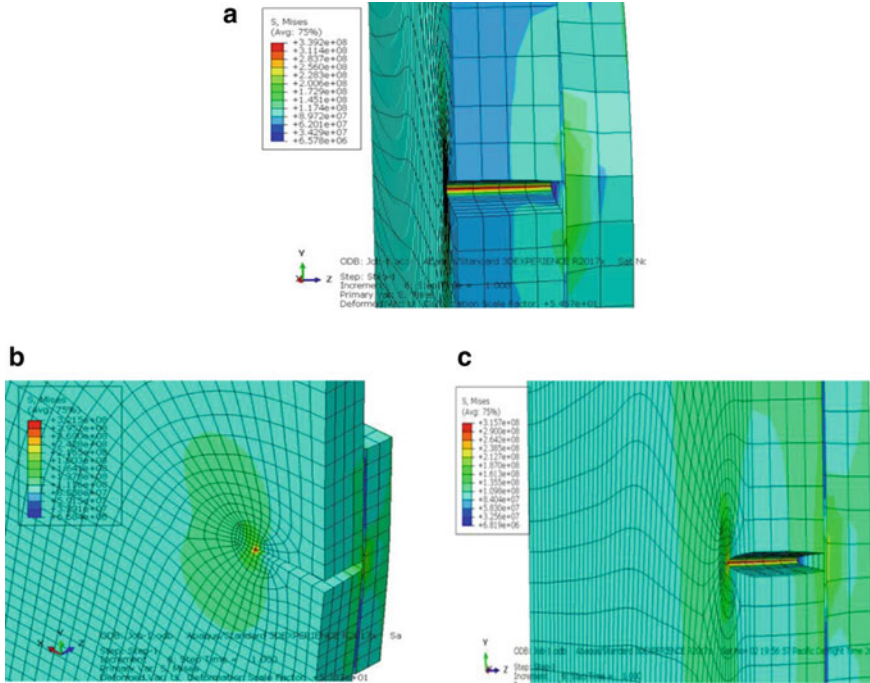


Fig. 7 a von Mises stress variation near the crack for 2-mm-thick circular patch repairing, b von Mises stress variation near the crack for 2-mm-thick square patch repairing and c von Mises stress variation near the crack for 2-mm-thick rectangular patch repairing

3.2.2 Patch Shape Effect

Further, the patch model has been investigated for patch shape effect analysis. From Fig. 6, it can be concluded that value of SIF is decreasing when there is shift in shape from circular to square and again from square to rectangle. This shift in SIF clearly says that rectangular patch can provide better structural integrity as compared to the square and circular shape patch.

Figure 8 shows the variation of temperature around the crack and within the patched repaired configuration for un-symmetrical patch repairing model. This variation in temperature helps in designing the best possible patch repair process so that there are minimum thermal stresses developed in the patched structure. The temperature contour data also helps in the selection of best adhesive and patch combination for the repair process.

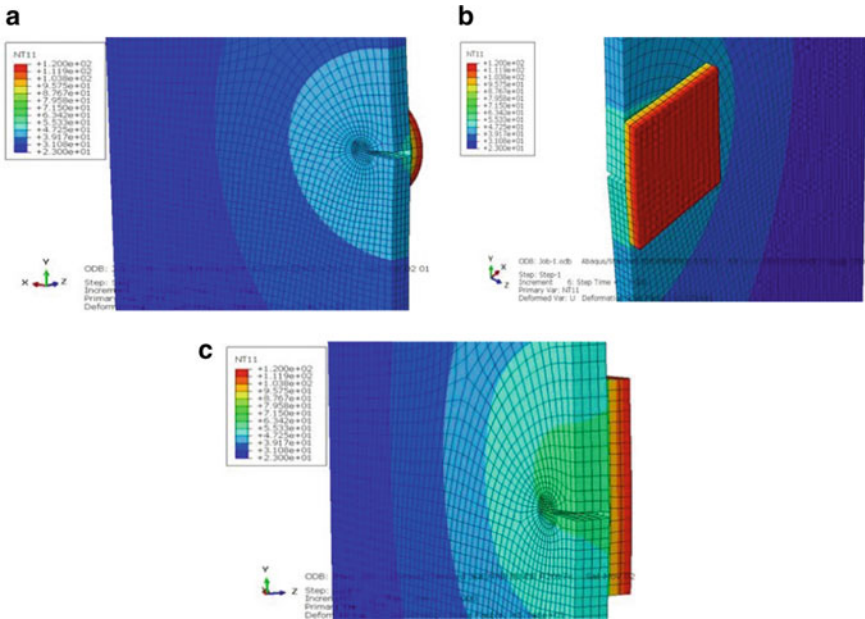


Fig. 8 a Temperature distribution due to patch curing for 2-mm-thick circular patch repairing, b temperature distribution due to patch curing for 2-mm-thick square patch repairing and c temperature distribution due to patch curing for 2-mm-thick rectangular patch repairing

3.3 Symmetrical Patch Repair Model Under Thermo-mechanical Loading

During the modelling of symmetrical patch, all the parameters and materials of patch, adhesive and aluminium panel have been kept exactly same as that of un-symmetrical patch repair case.

3.3.1 Patch Thickness Effect

The symmetrical patch repairing model has been analysed for patch thickness effect. From Fig. 9, it can be clearly seen that the trend of induced SIFs with respect to patch thickness in a symmetrical patch repair configuration is similar to the un-symmetrical patch. However, symmetrical patch repairing induces lesser SIFs as compared to un-symmetrical patch repairing model. In symmetrical patch repairing case, there is a reduction in SIF at the edge near patch and it peaks up at the centre, and this is due to the corner singularity effect. Figure 10 shows the variation of von Mises stress around the crack location. It has been found that rectangular patch configuration induces lesser magnitude of stress field; it can be due to the additional area of rectangular shape which controls the further opening of the crack.

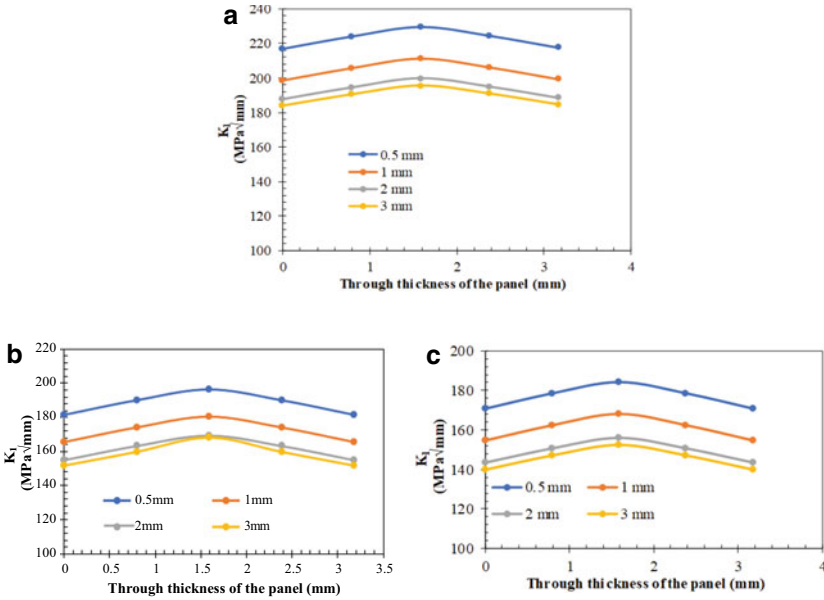


Fig. 9 a SIF variation with patch thickness along panel thickness for symmetrical circular patch repairing, b SIF variation with patch thickness along panel thickness for symmetrical square patch repairing and c SIF variation with patch thickness along panel thickness for symmetrical rectangular patch repairing

3.3.2 Patch Shape Effect

Further, the symmetrical patch model has been investigated to see effect of patch shape on fracture parameter (SIF). From Fig. 9, it can be concluded that value of SIF is decreasing when there is shift in shape from circular to square and again from square to rectangle. This shift in SIF clearly says that rectangular patch can provide better structural integrity as compared to the square and circular shape patch.

Figure 11 shows the variation of curing temperature around the crack and within the patched repaired configuration for symmetrical patch repairing model. This variation in temperature helps in designing the best possible patch repair process so that there are minimum thermal stresses developed in the patched structure.

3.4 Effect of Loading Environment on Patch Repairing

In this section, symmetrical patch domain has been further investigated under thermal (T), mechanical (M) and thermo-mechanical (TM) loading conditions. It can be seen from the graphs in Fig. 12 that the SIF of thermo-mechanical loading is much more as compared to the other two loading conditions, so it needs more design attention.

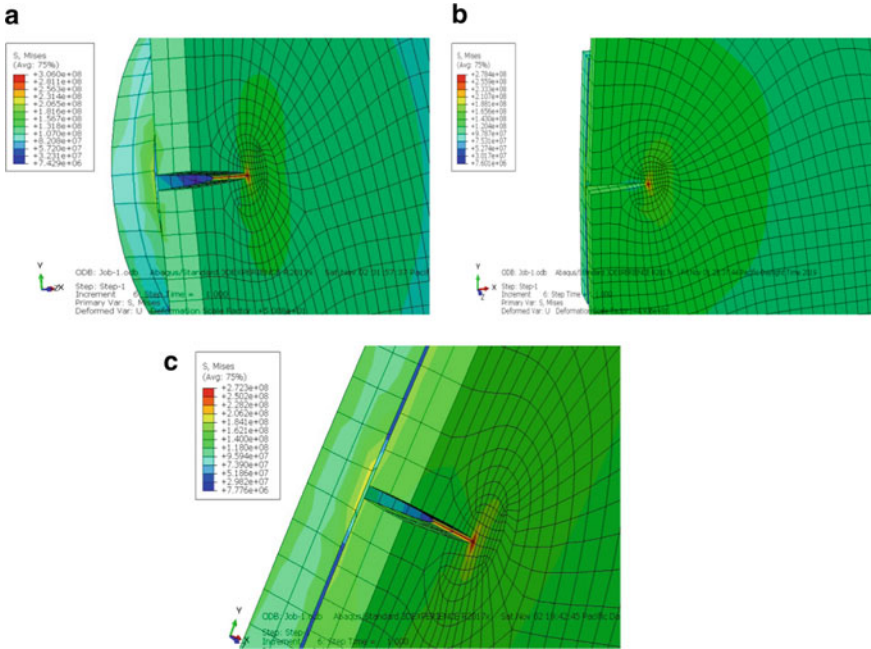


Fig. 10 **a** von Mises stress variation near the crack for symmetrical circular patch repairing, **b** von Mises stress variation near the crack for symmetrical square patch repairing and **c** von Mises stress variation near the crack for symmetrical rectangular patch repairing

From here also, it can be observed that rectangular patch is the best patch since SIF value is less for all the loading conditions as compared to the other patched configurations.

3.5 Effect of Adhesive Material and Adhesive Thickness on Patch Repair

In this section, effects of adhesive materials and adhesive thickness have been investigated for structural integrity of patch repaired model. Thermo-mechanical loading along with symmetrical square patch having 2 mm thickness has been chosen to compare different results. SIF behaviour along the crack front has been illustrated in Fig. 13. The thickness of the adhesives used is 0.1 mm. From Fig. 13, it can be seen that AV138/HV998 is the best adhesive since the induced SIF is less as compared to other adhesive material, and this is due to the fact that this adhesive has the highest shear modulus among all considered adhesive materials. In Fig. 14, the adhesive used for the comparison is AV138/HV998, and it can be seen from here that the thickness

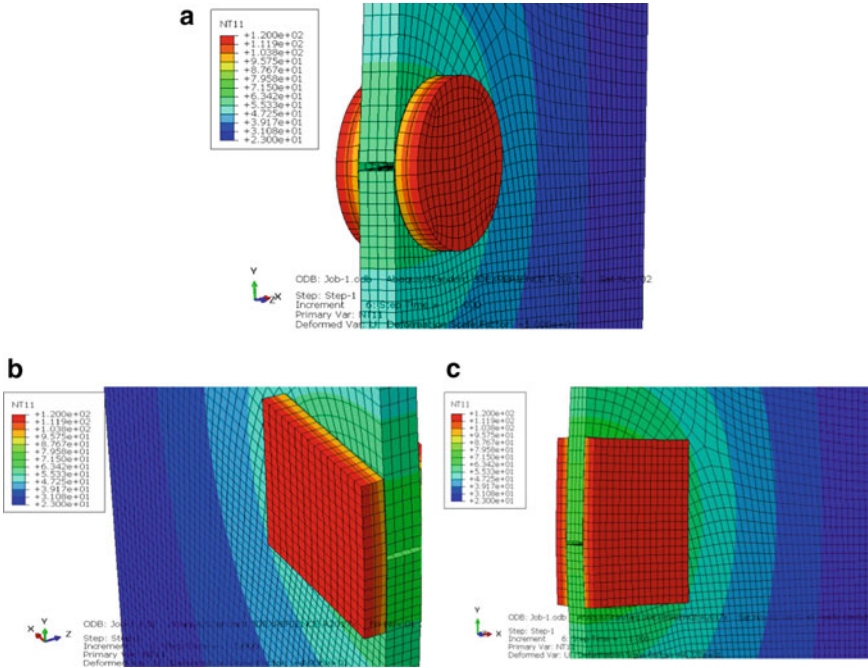


Fig. 11 a Temperature distribution due to patch curing for symmetrical circular patch repairing, b temperature distribution due to patch curing for symmetrical square patch repairing and c temperature distribution due to patch curing for symmetrical rectangular patch repairing

of the adhesive material decreases with SIF. However, lower value of the adhesive thickness may create adhesion problem between patch and plate.

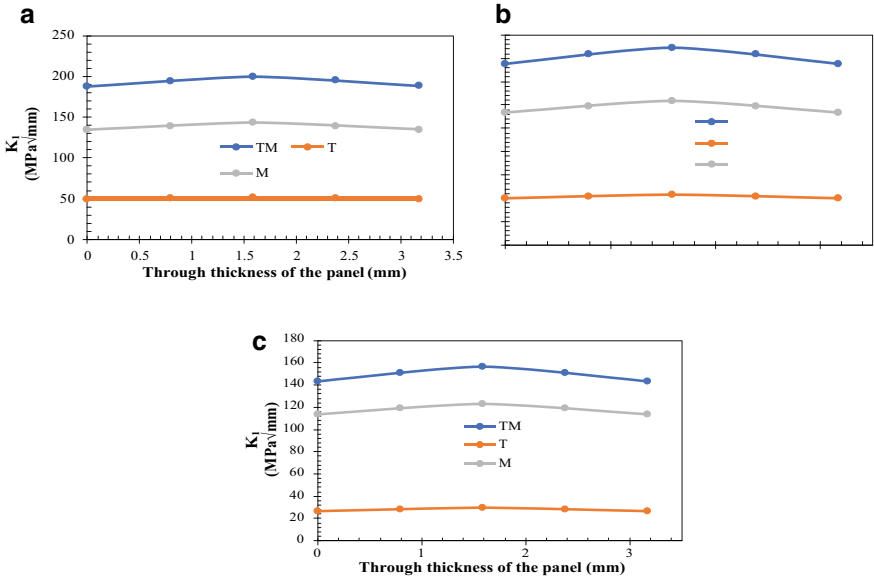


Fig. 12 a SIF variation with applied loading conditions for symmetrical circular patch repairing model, b SIF variation with applied loading conditions for symmetrical square patch repairing model and c SIF variation with applied loading conditions for symmetrical rectangular patch repairing model

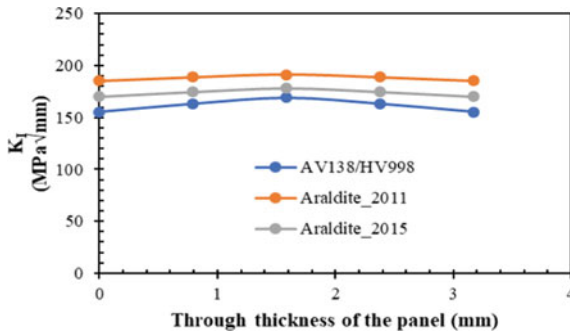


Fig. 13 SIF variation with adhesive materials for symmetrical square patch repairing model

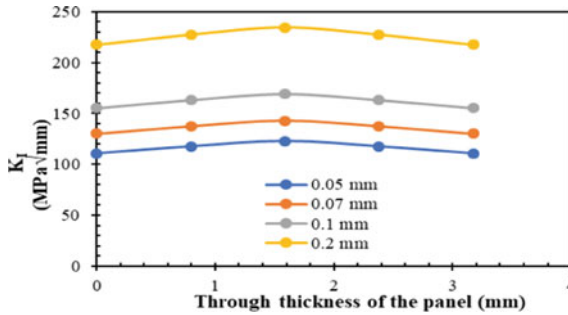


Fig. 14 SIF variation with adhesive thickness for symmetrical square patch repairing model

4 Conclusion

This work describes the computational modelling of in situ bonded composite patch repairing of cracked aluminium structure under thermo-mechanical loading. Based on present numerical simulation, following salient conclusion can be drawn:

- Substantial reduction in stress intensity factor is observed due to the presence of bonded patch.
- Increase in patch thickness reduces the stress intensity factor at the crack front.
- Reduction in adhesive thickness decreases the SIF. However, lower value of the adhesive thickness will create adhesion problem between patch and plate.
- Stress intensity decreases with the increase in adhesive shear modulus, but high value of adhesive modulus may fail in adhesion.
- A decrease in SIF pattern has been observed in symmetrical patch as compared to unsymmetrical patch repair configuration.
- The patch curing temperature makes significant effect over induced SIF at crack front.
- Rectangular patch shape is the best patch shape among all three patches under investigation.
- The presented work can be further extended to crack propagation and fatigue investigation.

Acknowledgements Authors are grateful for the support from the Aeronautics Research & Development Board (DRDO), New Delhi, India, for funding this research through grant file no. 1051914. Financial support received from Indian Institute of Technology (IIT) Mandi is gratefully acknowledged.

References

1. Akin JE (1976) The generation of elements with singularities. *Int J Numer Meth Eng* 10(6):1249–1259
2. Albedah A, Bouiadjra BB, Benyahia F, Mohammed SMK (2018) Effects of adhesive disbond and thermal residual stresses on the fatigue life of cracked 2024—T3 aluminum panels repaired with a composite patch. *Int J Adhes Adhes* 87:22–30
3. Ashrafi M, Smith BP, Devasia S, Tuttle ME (2017) Embedded resistive heating in composite scarf repairs. *J Compos Mater* 51(18):2575–2583
4. Baker AA (1984) Repair of cracked or defective metallic aircraft components with advanced fibre composites—an overview of Australian work. *Compos Struct* 2(2):153–181
5. Baker AA (1988) Crack patching: experimental studies, practical applications. In: *Bonded repair of aircraft structures*. Springer, Dordrecht, pp 107–173
6. Chong HM, Liu SL, Subramanian AS, Ng SP, Tay SW, Wang SQ, Feih S (2018) Out-of-autoclave scarf repair of interlayer toughened carbon fibre composites using double vacuum debulking of patch. *Compos A Appl Sci Manuf* 107:224–234
7. Daryabor P, Safizadeh MS (2016) Investigation of defect characteristics and heat transfer in step heating thermography of metal plates repaired with composite patches. *Infrared Phys Technol* 76:608–620
8. Kim M, Kim H, Lee W (2015) Repair of aircraft structures using composite patches bonded through induction heating. *Adv Compos Mater* 24(4):307–323
9. Papataniasiou TK, Markolefas SI, Filopoulos SP, Tsamasphyros GJ (2011) Heat transfer in thin multilayered plates—Part II: Applications to the composite patch repair technique. *J Heat Transfer* 133(2):021303
10. Pathak H (2017) Three-dimensional quasi-static fatigue crack growth analysis in functionally graded materials (FGMs) using coupled FE-XEFG approach. *Theoret Appl Fract Mech* 92:59–75
11. Rachid M, Serier B, Bouiadjra BB, Belhouari M (2012) Numerical analysis of the patch shape effects on the performances of bonded composite repair in aircraft structures. *Compos B Eng* 43(2):391–397
12. Ramji M, Srilakshmi R, Prakash MB (2013) Towards optimization of patch shape on the performance of bonded composite repair using FEM. *Compos B Eng* 45(1):710–720

The Effect of Steel Fibers on Ductility of Reinforced Concrete Beams



Yuvraj Singh, Sushil Bhatia, and Harvinder Singh

Abstract The ductility of structural elements is of prime importance to avoid brittle or catastrophic failure. Being strong in compression and weak in tension, concrete is very well known to be quasi-brittle material. Incorporating steel as reinforcing bars hence becomes crucial for making concrete worth using as a structural material. Furthermore, extensive research has been carried out worldwide on the use of short discrete fibers to enhance concrete's tensile strength. Among several synthetic and metallic fibers, steel fibers emerge as an attractive option due to its high tensile strength and amazing crack-bridging potential. In this study, an experimental investigation was directed toward evaluating the effect of steel fibers when used along with traditional reinforcing bars on the ductility of reinforced concrete beams. For studying the effect of steel fibers on the ductility of reinforced concrete beams, a set of specimens was cast with varying percentages of steel fibers, i.e., 0, 0.5, 1, and 1.5%. The specimens were tested under three-point bending, and the load–deflection profiles were obtained for each case. The ductility index and flexural toughness for each case were determined using load–deflection profiles. It has been found that the presence of steel fibers enhances the ductility and flexural toughness of reinforced concrete beams significantly which was evident from its crack arresting potential leading to larger post-peak load deformations.

Keywords Cracks · Ductility · Ductility index · Flexural toughness · Reinforced concrete beam · Steel fibers

Y. Singh (✉) · S. Bhatia · H. Singh
Department of Civil Engineering, Guru Nanak Dev Engineering College, Ludhiana, India
e-mail: uvraj_23@yahoo.co.in

Y. Singh
I. K. Gujral Punjab Technical University, Kapurthala, India

© The Author(s), under exclusive license to Springer Nature Singapore Pte Ltd. 2023
M. Madhavan et al. (eds.), *Proceedings of the Indian Structural Steel Conference 2020*
(Vol. 2), Lecture Notes in Civil Engineering 319,
https://doi.org/10.1007/978-981-19-9394-7_21

1 Introduction

Concrete is undoubtedly one of the most versatile building materials. To be used as a material for structural elements, steel is incorporated into it to compensate for its low tensile strength. Apart from conventional steel reinforcement, the inclusion of fibers into the concrete matrix has been widely researched over the years to enhance concrete's performance [2, 3, 5, 7, 9, 10]. And as far as ductility is concerned, it is of utmost importance to prevent catastrophic failures especially when structures are subjected to seismic forces. Among various fibers, steel fibers are known for their exceptionally high tensile strength and crack-bridging potential. Therefore, the inclusion of steel fibers is expected to have a positive impact on the ductility of concrete. Furthermore, apart from ductility, another important parameter determining the performance of a material is its toughness. And as far as reinforced concrete beams subjected to bending load is concerned, the total energy absorbed by the element before fracture can be termed as Flexure Toughness of the beam [6, 8]. Therefore, both ductility as well as the flexural toughness are the two important deciding parameters for adjudging the performance of concrete structural elements. It has been reported that unlike conventional RC members in flexure, the failure of a fiber-reinforced concrete member takes place when the strain in its extreme tensile face exceeds the ultimate strain value; however, it can be made to fail by crushing of the concrete, as in conventional RC members, when steel bars and fibers are used together to reinforce it [7]. Furthermore, it has also been reported that the inclusion of steel fibers acts to suppress crack propagation, and with the increase in the longitudinal reinforcement ratio, the shear capacity increases significantly [9, 10]. Keeping the crack-bridging potential of steel fibers in mind, and to explore its use in addition to conventional reinforcement in RC members, the results of an experimental investigation aimed to determine the influence of steel fibers in addition to the conventional reinforcement on ductility as well as the flexural toughness of RC beams has been presented in this paper.

2 Experimental Design

2.1 *Materials and Methodology*

To determine the influence of the addition of steel fibers on ductility and toughness of reinforced concrete beams, four sets consisting of a total of twelve under-reinforced concrete beams with dimensions 1000 mm × 100 mm × 150 mm were cast containing different amounts of steel fibers, i.e., 0, 0.5, 1, and 1.5% in addition to the conventional tensile reinforcement. Two bars of Fe 415 grade having 10 mm dia. each were incorporated as illustrated in Fig. 1. For casting of specimens, OPC 53 grade cement was used. A concrete mix having a 28-day cubic characteristic compressive strength

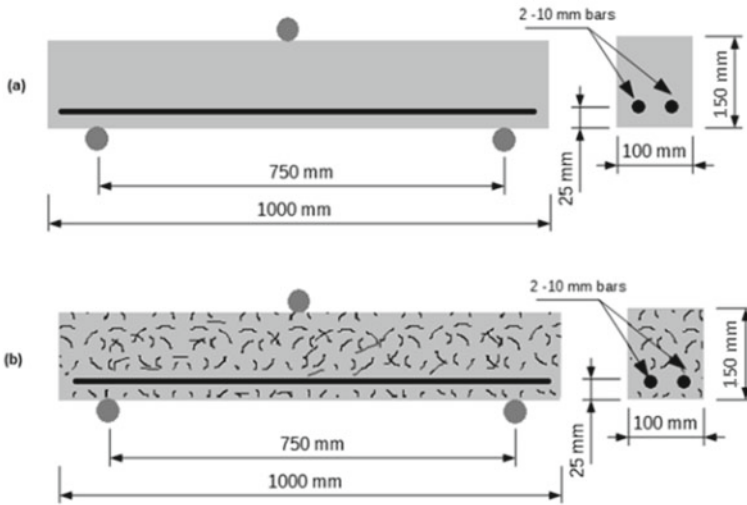


Fig. 1 Details of beam specimens: **a** RC beam and **b** steel fiber RC beam

of 30 MPa was used for the preparation of the specimens. The concrete mix proportion was found to be 1:1.322:2.342 with a w/c ratio of 0.42. The mixing procedure was carried out in several steps. Initially, the sand and coarse aggregates were mixed together with half of the total water content to achieve a saturated surface-dry condition. Then, the cement and the remaining water were added to the mixture, and it was mixed thoroughly. The fibers were gradually sprinkled into the mix to get a homogeneous mix of good workability [1]. The hooked-end steel fibers with 50 mm length, 1 mm diameter, and an aspect ratio of 50 mm were used. On inclusion of steel fibers, the workability reduced, but, in the concrete mix, any sort of admixtures/additives was avoided to capture the influence of steel fibers alone.

2.2 Experimental Testing

All test specimens have been subjected to three-point loading using a displacement-controlled universal testing machine. The details of the beam specimens are illustrated in Fig. 1. Following this, load-deformation profiles for each case have been obtained. To determine the influence of steel fibers on the ductility of reinforced concrete beams, the ductility index was worked out. Ductility of a reinforced beam is referred to as its capacity to undergo higher plastic deformations and considerable loads beyond steel yielding until failure without showing sudden brittle failure [2]. In the present investigation, two ductility indices have been calculated to capture the most practical representation of the ductility. One is referred to peak ductility index which is calculated by the ratio of deformation at the peak load to that at the yield

load, whereas the other is referred to as ultimate ductility index which is measured as the ratio of the deformation at the ultimate load to that at the yield load [4]. Furthermore, the toughness of the RC beam under bending is also determined which is referred to as the overall energy absorbed by a beam under bending before fracture. It has been measured in terms of Joules as the total area under the load-deformation plot.

3 Results and Discussion

Flexural testing was performed on the test specimens to obtain the load-deformation profiles. To determine the effect of steel fibers on the ductility of RC beams, ductility indices have been calculated. Following this, the flexural toughness of the RC beams has also been worked out to capture the influence of steel fibers (SFs) on the overall performance of RC beams.

3.1 Load-Deformation Profiles

The load-deformation profiles of the beam specimens subjected to flexural loading project the effectiveness of steel fibers in enhancing the flexural capacity and the deformation post the peak load as well. Figure 2 and Table 1 illustrate that the peak load attained in the case of beams with 0, 0.5, 1, and 1.5% steel fibers (SFs) is 25.1 kN, 28.5 kN, 30.6 kN, and 33.9 kN, respectively.

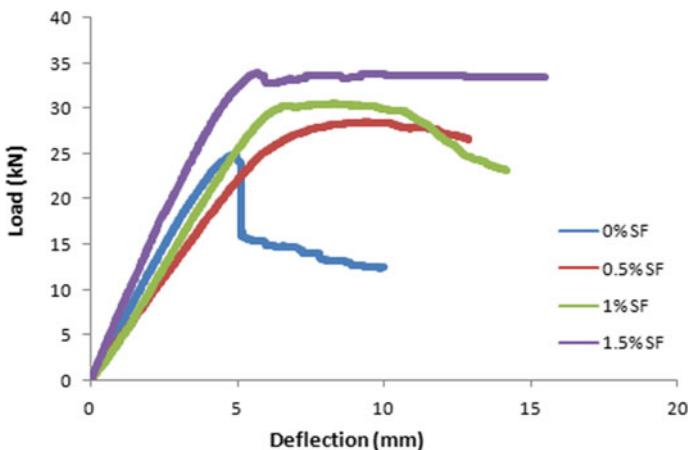


Fig. 2 Comparison among load-deformation profiles of all tested beams

Table 1 Peak load attained in all cases

Fiber content (%)	0% SF	0.5% SF	1% SF	1.5% SF
Peak load (kN)	25.1	28.5	30.6	33.9

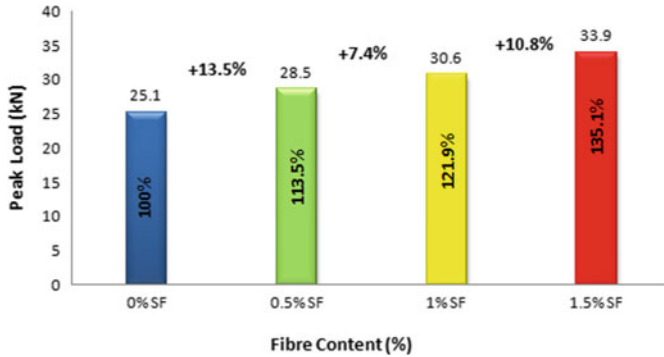


Fig. 3 Percentage augmentation in the peak load due to the inclusion of steel fibers

This increase in the peak load is accounted for due to the existence of steel fibers which delays the first cracking load and yield load due to its large tensile strength and crack arresting potential. Hence, with the inclusion of 0.5, 1, and 1.5% steel fibers, the load-carrying capacity has been increased to 113.5%, 121.9%, and 135.1%, respectively, as compared to the RC beam without steel fibers. Furthermore, it has been observed that the augmentation in the flexural capacity is more pronounced between 0 and 0.5% SFRC beam where the load-carrying capacity increases by 13.5% which further increments by 7.4 and 10.8% on increasing the dosage of steel fibers to 1% and 1.5%, respectively (Fig. 3).

3.2 Displacement Ductility

Besides the higher peak load, the deformation post the peak load is crucial to prevent catastrophic/brittle failure of the structural elements. This deformation referred to as ductility has been determined in terms of ductility index in this investigation. From the load–deflection profiles, two ductility indices (DI) were found, namely, peak ductility index (μ_p) and ultimate ductility index (μ_u) which are calculated as the ratio of deformation at the peak load (Δ_p) and deformation at the ultimate load (Δ_u) to the deformation at yield point (Δ_y), respectively. Many researchers have taken ultimate load as the peak load, but in the present investigation, in an attempt to determine more realistic value of ductility index, and to capture the effect of steel fibers on post-peak load deformations, ultimate load has been taken as the 80% of the peak load post the peak load is attained, or the breaking load, whichever is larger [2].

In other words, load post the peak load and 20% less than it is taken as the ultimate load in this study. Table 2 tabulates the deformations corresponding to yield, peak, and ultimate loads from the load-deformation profiles as illustrated in Fig. 2. From pattern obtained, ultimate DI (μ_u) appears more realistic to capture the influence of the steel fibers on the ductility of RC beams. It has been noticed that a considerable increase in the yield load on the inclusion of SFs in the concrete matrix can result in comparatively higher deflections corresponding to yield point, resulting in showing lesser percentage increase in the peak DI (μ_p) which is inversely proportional to deflection corresponding to yield point. This is the reason that the peak DI (μ_p) lies in between the range of 1 and 2 for all cases. On the other hand, the ultimate DI (μ_u) which is measured as the ratio of deformation at the ultimate load (Δ_p) to the deformation at yield point (Δ_y) captures more realistic results as far as the post-peak deformations are concerned. Figure 4 illustrates that the ultimate DI (μ_u) increases to 161.5, 174.4, and 248% in the case of 0.5, 1, and 1.5% inclusion of steel fibers when compared to RC beam without steel fibers. Furthermore, it can be noticed that the ultimate DI (μ_u) is maximum in the case of an RC beam containing 1.5% SF. The ultimate DI (μ_u) increased by 61.5% and further by 7.9 and 42.6% on increasing the dosage of fibers from 0.5% to 1.5%, respectively. Thus, the presence of steel fibers results in enhanced ductility of RC beams containing conventional reinforcement.

Table 2 Ductility indices of RC beams with different fiber contents

Fiber content (%)	Δ_y (mm)	Δ_p (mm)	Δ_u (mm)	$\mu_p = \frac{\Delta_p}{\Delta_y}$	$\mu_u = \frac{\Delta_u}{\Delta_y}$
0	4.40	4.94	5.13	1.12	1.17
0.5	6.80	9.48	12.88	1.39	1.89
1	6.40	9.90	13.07	1.55	2.04
1.5	5.32	10.05	15.50	1.89	2.91

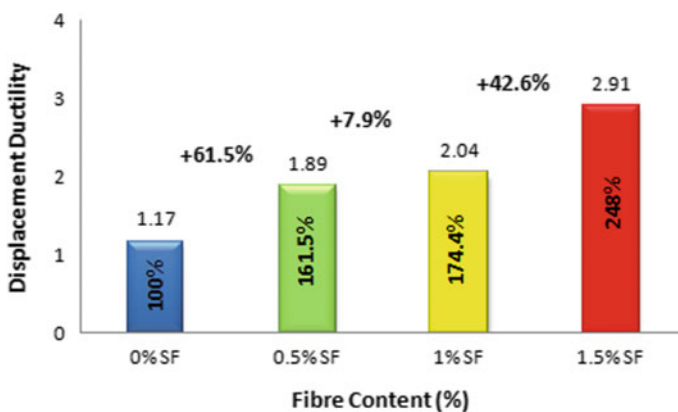


Fig. 4 Percentage augmentation in the ductility due to the inclusion of steel fibers

3.3 Flexural Toughness

As discussed, the ductility of a material is undoubtedly very crucial for post-peak load performance to prevent brittle failure. Another important parameter deciding the overall performance of a material is referred to as the toughness of a material [8]. A material may have high ductility but low strength like gold, while on the other hand, a material may have a high strength but low ductility as in the case of ceramic or glass. As a structural material is desirable to be tough, it needs to have high strength and high ductility as well. Therefore, besides ductility, the toughness of the RC beam under bending is also determined in this study and is termed as flexural toughness. Flexural toughness is referred to as the overall energy absorbed by a beam under bending before fracture. It is measured in terms of Joules as the total area under the load-deformation plot. As tabulated in Table 3, the flexural toughness of RC beams is 74.38, 268.81, 295.99, and 438.72 J in case of the beam containing 0%, 0.5%, 1%, and 1.5% SFs, respectively. As illustrated in Fig. 5, the inclusion of steel fibers enhances the flexural toughness to 361.4, 397.9, and 589.8% in the case of 0.5%, 1%, and 1.5% SFs, respectively, when compared to the RC beam without SFs. Furthermore, it has been observed that on adding 0.5% SF, the flexural toughness augments by 261.4% which further increments by 10.1 and 48.2% on increasing the content of steel fibers to 1 and 1.5%, respectively. Therefore, it has been observed that besides ductility, the inclusion of steel fibers has a considerable effect on increasing the flexural toughness of the RC beam.

Table 3 Flexural toughness of RC beams with different fiber contents

Fiber content (%)	0% SF	0.5% SF	1% SF	1.5% SF
Flexural toughness (J)	74.38	268.81	295.99	438.72

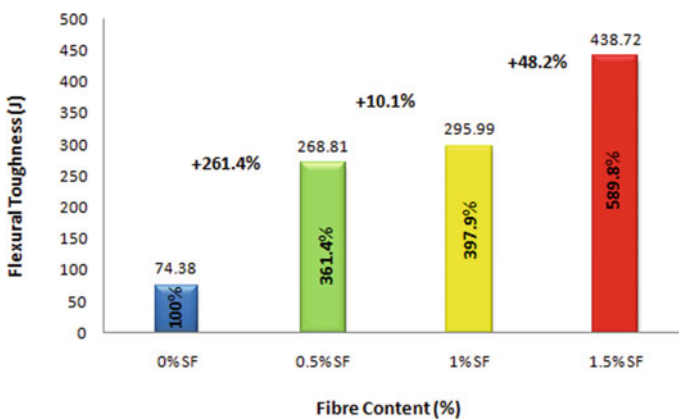


Fig. 5 Percentage increase in the flexural toughness due to steel fiber addition

It is therefore anticipated that the steel fibers would play a crucial role in enhancing the performance of RC structural elements, especially the ones exposed to severe exposure conditions like corrosive environment. From the results, it has been observed that the steel fibers provide enhanced toughness and ductility which would also be instrumental in the case of deterioration/corrosion of the embedded conventional rebars and would, therefore, prevent catastrophic failure. A study on the effect of the corrosive environment on the toughness and ductility of the RC beam with and without steel fibers is hence proposed to be conducted for quantitative results and better insight.

4 Conclusions

The following conclusions have been made from the present investigation:

- (a) Inclusion of steel fibers increases the flexural capacity of the RC beam due to steel fiber's crack-bridging potential resulting in delaying the first cracking load and the yield load.
- (b) On increasing the fiber content up to 1.5%, the ductility index of RC beam increases indicating a better post-peak load deformation and hence improved ductility.
- (c) The addition of steel fibers augments the total energy absorbed before the fracture occurs, which is measured in terms of flexural toughness.
- (d) Enhanced ductility and toughness of RC beams accounted due to the presence of steel fibers provide an indication toward its potential application in the structural elements in addition to the conventional reinforcement, especially in the case of exposure to the corrosive environments.

Hence, the steel fibers' tendency to enhance both the peak load and ductility of RC beam resulting in the augmented flexural toughness improves the overall performance of the RC beams.

Acknowledgements The experimental investigation was conducted in the concrete technology laboratory of Guru Nanak Dev Engineering College, Ludhiana. The authors are grateful for the support and assistance provided by Guru Nanak Dev Engineering College, Ludhiana; I K Gujral Punjab Technical University, Kapurthala; and TEQIP III (a Government of India Project assisted by the World Bank).

References

1. ACI (1993) ACI 544.3R-88: guide for specifying, proportioning, mixing placing, and finishing steel fibre reinforced concrete. American Concrete Institute, Detroit

2. Ahmad A, Sallal A, Mustafa O (2019) Experimental investigation on the effect of steel fibers on the flexural behaviour and ductility of high-strength concrete hollow beams. *Adv Civil Eng* 2019:13. Article id 8390345
3. Altun F, Haktanir T, Ari K (2007) Effects of steel fiber addition on mechanical properties of concrete and RC beams. *Constr Build Mater* 21(3):654–661
4. Apeh JA, Okoli OG (2016) Evaluation of ductility index of concrete beams reinforced with rebars milled from scrap metals. *Concr Res Lett* 7(2):56–68
5. Jhatial AA, Sohu N, Bhatti K, Lakhari MT, Oad R (2018) Effect of steel fibres on the compressive and flexural strength of concrete. *Int J Adv Appl Sci* 5(10):16–21
6. Rilem TC (1985) Determination of the fracture energy of mortar and concrete by means of three-point bend tests on notched beams. *Mater Struct* 18(106):285–290
7. Singh H (2016) Flexural modelling of steel-fibre-reinforced concrete member with conventional tensile rebars. *Struct Build* 169(SB1):54–66
8. Taylor M, Lydon FD, Barr BIG (1997) Toughness measurements on steel fibre-reinforced high strength concrete. *Cement Concr Compos* 19:329–340
9. Vandewalle L (2000) Cracking behaviour of concrete beams reinforced with a combination of ordinary reinforcement and steel fibers. *Mater Struct* 33(3):164–170
10. Xue X, Hua X, Zhou J (2019) Test and prediction of shear strength for the steel fiber-reinforced concrete beams. *Adv Mech Eng* 11(4):1–14

Mode Specific Damping Estimation—An Inverse Damping Modelling Technique



Naveen Bharti, Yeturi Pramod Kumar Reddy, and Subhamoy Sen

Abstract Composites are extensively used in various fields such as civil, aerospace, naval due to their high specific stiffness and strength. These properties are adversely affected due to damage. For damage detection, vibration-based methods are generally used which use modal parameters, i.e. modal frequencies, mode shapes and modal damping ratios. These modal parameters depend on the physical properties of the system, i.e. mass, stiffness and damping. Among these properties, damping is the most sensitive to damage. Therefore, the occurrence of damage should be sensed through changes in damping. Further, in order to localize the damage, a support model for damping is needed to spatially isolate the origin of the changes. Unfortunately, damping depends on numerous known and unknown physical phenomena that makes it difficult to model or estimate. In this study, first variation of modal damping ratios with damage in a composite column has been shown. Then, a new model of damping, called mode specific damping, is proposed. The performance has been checked through numerical simulations and compared with the Rayleigh model of damping.

Keywords Damping estimation · Inverse problem · Composite structures · Structural vibration

N. Bharti (✉) · Y. P. K. Reddy · S. Sen
i4S Laboratory, Indian Institute of Technology Mandi, Mandi, India
e-mail: nvnbhrt17@gmail.com

Y. P. K. Reddy
e-mail: yeturipramod@gmail.com

S. Sen
e-mail: subhamoy@iitmandi.ac.in

1 Introduction

Use of composites is increasing in various fields, such as aerospace, civil, naval. This is due to their higher specific stiffness and strength over conventional materials and also due to the fact that their properties can be altered as required for a specific application. The mechanical properties of the composites are adversely affected due to presence of damage. Detection of damage in the composites in their service conditions, therefore, becomes important. There exist offline non-destructive evaluation (NDE) methods, such as acoustic, ultrasonic and magnetic field-based methods, radiographs which demands that the damage location should be known in advance and is also accessible. These requirements obviously limit their real field application.

To overcome these shortcomings, vibration-based damage detection is used that provides information on the structural level. Common modes of damage in composite include matrix cracking, fibre breakage, fibre matrix debonding and delamination which induce unique changes in the vibrational properties of the composites. Typically, vibration-based methods utilize the information stored in the modal domain structural response, i.e. modal frequencies, mode shapes and modal damping ratio which in turn depend on the physical properties of the structure, i.e. mass, stiffness and damping. The basic strategy is that a damage that alters the physical properties of a structure will eventually lead to inducing changes in modal parameters, especially, system damping which is found to be very sensitive to damage. Ideally, the occurrence of damage should therefore be sensed through changes in damping. Further, in order to localize the damage, a support model for damping is needed to spatially isolate the origin of the changes. Of course, this model needs to be precise to ensure accuracy in damage localization. Unfortunately, damping depends on numerous known and unknown physical phenomena that makes it difficult to model or estimate. The most common approach to model damping is to assume it to be viscous. A further idealization of constant modal damping for first two modes leads to Rayleigh damping model. However, Rayleigh damping assumes existence of all possible modes in the response and therefore does not differ based on existence or absence of a particular mode. Further, the idealization of equal damping ratio for the first two modes most often does not conform to the reality.

Viscous damping is, however, not the only linear model of vibration damping. Any model which makes energy dissipation non negative can serve as an alternative to represent the damping in the structure. Several efforts have been made to incorporate non-viscous damping models. Bagley and Torvik [2], Torvik and Bagley [13], Gaul et al. [5], Maia et al. [9] have considered damping modelling in terms of fractional derivatives of the displacements. The above-mentioned damping models can be said to be a part of what can be called a forward approach, i.e. to find a damping model based on the mechanisms contributing to damping in the structure. Several damping identification methods are available which are based on the reverse approach, i.e. to estimate damping from the vibration response of the structure.

Lee and Kim [8] identified the damping, mass and stiffness matrices from the dynamic stiffness matrix obtained by inverting the frequency response function matrix. Chen et al. [3] made use of normal FRFs extracted from complex FRFs for identifying the system matrices. Instrumental variable method by Fritzen [4] provides an iterative solution for estimation of the system matrices using an “instrumental variable” chosen by the user. Matrix perturbation method developed by Phani and Woodhouse [11] identified damping matrix using modal parameters obtained from FRFs for the diagonal elements and a perturbation expansion for the off-diagonal elements. Adhikari [1] used complex frequencies and complex mode shapes deduced from FRFs to find the viscous damping matrix. Lancaster [7] proposed the use of complex modal parameters provided the eigen vectors are normalized in a specific manner. The drawback of this method lies in the fact that the normalization requires the knowledge of the damping matrix which needs to be estimated. To overcome this problem, an iterative procedure has been proposed by Pilkey [12]. Minas and Inman’s method [10] comprises of finding the stiffness and mass matrix by finite-element method and damping matrix from complex modes determined experimentally. Ibrahim [6] used finite-element modelling and complex modal parameters to find out the improved mass, stiffness and damping matrices. The complex modes are converted into real modes to obtain the corrected mass matrix which is then used to find the stiffness and damping matrices.

Phani and Woodhouse [11] carried out a survey of the existing frequency domain damping identification methods. They classified the methods into three major groups: matrix methods, modal methods and enhanced methods. The matrix methods make use of the FRF matrix directly while the modal methods use the modal parameters extracted from FRFs to estimate the damping matrix. The enhanced methods are designed to improve the performance of the matrix methods. The performance of the methods was judged considering the effect of noise, level of damping present, modal truncation and spatial incompleteness.

In this study, we attempted to prove the fact that damage indeed alters the damping property of a composite structural system. For this, behaviour of a composite column has been analysed using Ansys APDL software. The acceleration and frequencies are found out by transient and modal analysis, respectively. Using these as inputs in time domain decomposition method (TDD), the mode shapes and damping ratios are obtained. For various damage cases, the changes in frequencies and damping ratios have been shown. It has been also demonstrated that how damping changes the distribution of damping ratios over different modes which strengthens the need of a new damping model.

Subsequently, a new method of model-based damping estimation is proposed which takes basis on the existing Rayleigh model of damping that assumes a fixed modal damping value for the first two modes, and the damping corresponding to remaining modes is allowed to take shape based on the structural configuration. This study attempts to find the damping occurring in each mode using the reverse approach, i.e. to find the damping using the vibration response of the structure. Frequency response function of the structure has been selected as the target function that the model has to comply using constrained optimization technique.

2 Methodology

2.1 Modelling of Composite Column

The column consists of a steel tube with concrete inside it. The length of column is 3 m with 0.3 m diameter. No extra reinforcement has been provided. This composite is modelled using Ansys APDL software (version 17.2). Shell 281 element type has been used for the steel tube component and solid 65 element for the concrete component. Boundary condition is given as fixed for all the nodes at the base of the column. This model is supplied with no specific damping model, and the damping is allowed to arise from the internal friction between the steel casing and the concrete cylinder. The dynamic load is applied on top of the column at all the nodes. Six different cases have been analysed: undamaged column, damage in concrete at the top and bottom (two cases), damage in steel at the top and bottom (two cases) and damage in concrete at the top with damage at the steel–concrete interface. The parameters used for modelling are given in Table 1.

The following figure shows the finite-element model of the composite column (Fig. 1).

Table 1 Parameters used for modelling in ANSYS

Material	Element type	Dimensions	Poisson's ratio	Density (kg/m ³)	Friction
Steel	Shell 281	Length = 3 m Thickness of tube = 0.005 m	0.3	7850	0.01
Concrete	Solid 65	Length = 3 m Thickness of concrete = 0.29 m	0.3	2400	0.01

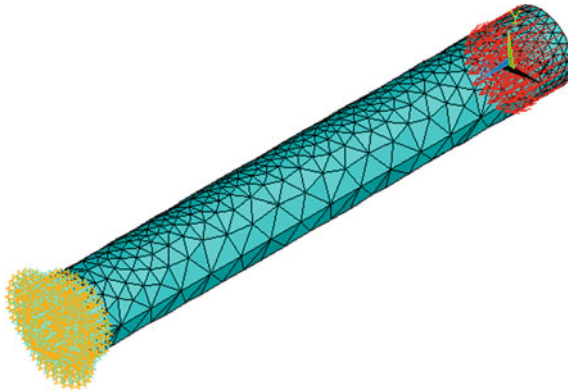


Fig. 1 Finite-element model of the composite column showing the geometry, boundary condition and loading

Transient analysis is performed on this column under a dynamic load, and its transverse acceleration responses are collected at the centre of the column at a sampling frequency of 300 Hz for 2000 time steps. The frequency and damping ratios are then estimated using time domain decomposition of the time series data. The variation of frequencies and damping ratios with damage is shown in Tables 2 and 3, respectively.

It can be seen from Table 2 that the frequencies decrease on introduction of damage, thereby indicating the presence of damage. In a similar way, damping can also be used as an indicator of damage. From Table 3, it is visible that the modal damping ratios in case of damaged cases are greater than the undamaged case. Also, under the Rayleigh model of damping, it is assumed that the damping for the first two modes should ideally be same or nearly similar at least. This is found to be true for the undamaged case as well as for the first damage case. This assumption is however found not to be complying with other damage cases where the first two modal damping values are significantly different. This clearly indicates that, with a Rayleigh model-based assumption, the damping estimation may lead to a very wrong result, which can finally lead to a false estimation of damage for a damping-based damage estimation approach.

Table 2 Frequencies obtained from modal analysis (Hz)

Undamaged	Concrete damaged at top	Concrete damaged at bottom	Steel damaged at top	Steel damaged at bottom	Concrete damaged at top with different friction
17.358	16.635	16.840	10.163	10.323	16.635
17.362	17.082	17.339	10.420	10.612	17.082
103.530	99.301	100.29	60.683	61.434	99.301
103.550	101.740	103.16	62.075	63.357	101.740
154.75	148.76	152.47	91.020	91.571	148.76
218.69	218.34	219.06	133.25	134.15	218.34

Table 3 Damping ratios obtained from TDD method

Undamaged	Concrete damaged at top	Concrete damaged at bottom	Steel damaged at top	Steel damaged at bottom	Concrete damaged at top with different friction
0.0150	0.0153	0.0150	0.0134	0.0127	0.0194
0.0149	0.0153	0.0221	0.0233	0.0214	0.0148
0.0026	0.0028	0.0028	0.0045	0.0046	0.0056
0.0026	0.0029	0.0030	0.0044	0.0047	0.0057
0.0015	0.0016	0.0016	0.0028	0.0030	0.0041
0.0013	0.0014	0.0013	0.0022	0.0021	0.0045

2.2 Mode Specific Damping

The previous section presents the need for a new and more flexible damping model which can cater for varying modal damping on inclusion of damage in the structure. For this reason, the theory for mode specific damping is developed in this study. The equation of motion of a multi degree of freedom system is as follows:

$$M\ddot{x} + C\dot{x} + Kx = F. \quad (1)$$

A modal expansion of the displacement vector x has the form:

$$x = \sum_{r=1}^n \phi_r q_r = \phi q, \quad (2)$$

where ϕ and q are the mode shape and dynamic displacement response matrices. Using this modal expansion Eq. (1) becomes

$$M\phi\ddot{q} + C\phi\dot{q} + K\phi q = F. \quad (3)$$

Pre-multiplying by ϕ^T

$$\phi^T M\phi\ddot{q} + \phi^T C\phi\dot{q} + \phi^T K\phi q = \phi^T F \quad (4)$$

$$M_n\ddot{q} + C_n\dot{q} + K_n q = F_n, \quad (5)$$

where M_n , C_n , K_n and F_n denote the modal mass, damping, stiffness and force matrices.

In order to model the damping with Rayleigh damping model, a linear combination of stiffness and mass matrices is assumed which leads to the following expansion:

$$M_n\ddot{q} + \phi^T (\alpha K + \beta M)\phi\dot{q} + K_n q = F_n \quad (6)$$

$$M_n\ddot{q} + \phi^T \alpha K\phi\dot{q} + \phi^T \beta M\phi\dot{q} + K_n q = F_n \quad (7)$$

$$M_n\ddot{q} + \alpha K_n\dot{q} + \beta M_n\dot{q} + K_n q = F_n. \quad (8)$$

The values of α and β are calculated as a function of the first two modal frequencies with an assumption that the first two modes are getting damped by an equal damping ratio. It can be clearly seen that irrespective of the modes, the values of α and β remain constant which makes the model very rigid and relying only on first two modes of vibration.

Mode Specific Damping

Mode specific damping is an improvement over the Rayleigh damping in the sense that the parameters α and β are considered to vary for each mode. Therefore, Eq. (8) can be written individually for each mode as:

$$M_n \ddot{q} + \alpha_n K_n \dot{q} + \beta_n M_n \dot{q} + K_n q = F_n.$$

The value of these parameters can then be found employing certain constrained optimization techniques such that overall this model yields similar frequency response function as of the real system. In the following, this model has been tested on several benchmark test cases collected from highly cited articles of Lee and Kim [8] and Phani and Woodhouse [11].

2.2.1 Simulation Examples

Two simulation examples are considered in this article. The first example case is taken from Lee and Kim’s article [8]. The system is a three degrees of freedom mass-spring-damper system of discrete masses and springs as shown in Fig. 2 with $m_1 = 10, m_2 = 14, m_3 = 12$ kg, $k_1 = 2000, k_2 = 3000, k_3 = 2500$ N/m. The damping for this system is assumed to be proportional viscous damping with $c_1 = 2, c_2 = 3, c_3 = 2.5$ Ns/m. The second example is a test cases taken from Phani and Woodhouse’s article [11]. The considered system is a four degree of freedom mass-spring-damper system with non-proportional viscous damping as presented in Fig. 3 with $m = 1$ kg, $c = 0.02$ Ns/m, $k = 1$ N/m.

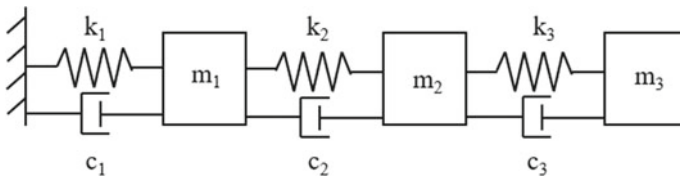


Fig. 2 Example 1

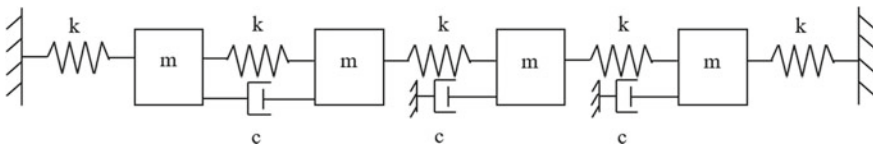


Fig. 3 Example 2

2.2.2 Simulation Procedure

The dynamic simulation for these example systems under a spectrum of dynamic load cases (impulse, harmonic and random) has been done in MATLAB. Acceleration response of the system is found out employing explicit Newmark Beta algorithm with average acceleration assumption. The response is sampled at a very low sampling frequency of 10 Hz since the structural fundamental frequencies also lie within a very narrow band of 0–5 Hz. Next, the frequency response function of the system is obtained from the vibration response of the system using modal analysis of the response. The assumed example cases with actual damping matrix are considered as the “real” system for this validation study. To estimate this “real” system, optimization technique is employed starting from an initial guess for the mode specific damping model which is in turn a function of the α_n and β_n . This frequency response function corresponding to the “real” system is considered as the target which is to be achieved using an iterative optimization procedure. Finally, an optimized set of α_n and β_n is obtained as the end result of the employed optimization technique for which the generated frequency response function optimally matches with the actual frequency response function. The damping model corresponding to these estimated α_n and β_n is then assumed as the estimated damping model. The estimated model is then compared with the actual one using four different error norms as described in the article of Phani and Woodhouse [11]. These test cases have been repeated for several load cases: random force, sinusoidal force and impulse force.

3 Results and Discussions

The actual and the identified damping matrices are shown in Table 4 for the first example case under all three assumed loading conditions. The corresponding frequency response functions associated to original and estimated under all load cases are also presented in Figs. 4, 5 and 6. The original model for this test case corresponds to proportional damping which has been easily estimated under all load cases with very accurate precision. Interestingly, in most of the cases, the original FRF graphs have almost been superimposed by the estimated one, which shows the excellent capability of the proposed method to replicate a proportional damping case. In the following, the proposed method has been employed to replicate a non-proportional damping with a flexible proportional damping model, and attempts have been made to investigate the success of this approximation.

For the second example case, the estimated damping matrices under different load cases have been presented along with the actual one in Table 5. Unlike the previous example, the estimated damping is obviously not as accurate as for the previous example. However, if the diagonal elements of the estimated damping matrices are considered, it can be found that the proposed method has successfully estimated the actual values with sufficient accuracy. The same can also be demonstrated through

Table 4 Original and identified damping matrices for example 1

Actual modal damping matrix	Identified matrix (Random force)	Identified matrix (Sinusoidal force)	Identified matrix (Impulse force)
$\begin{bmatrix} 0.037 & 0 & 0 \\ 0 & 0.3283 & 0 \\ 0 & 0 & 0.7359 \end{bmatrix}$	$\begin{bmatrix} 0.037 & 0 & 0 \\ 0 & 0.3283 & 0 \\ 0 & 0 & 0.7359 \end{bmatrix}$	$\begin{bmatrix} 0.037 & 0 & 0 \\ 0 & 0.3283 & 0 \\ 0 & 0 & 0.7359 \end{bmatrix}$	$\begin{bmatrix} 0.037 & 0 & 0 \\ 0 & 0.3283 & 0 \\ 0 & 0 & 0.7359 \end{bmatrix}$

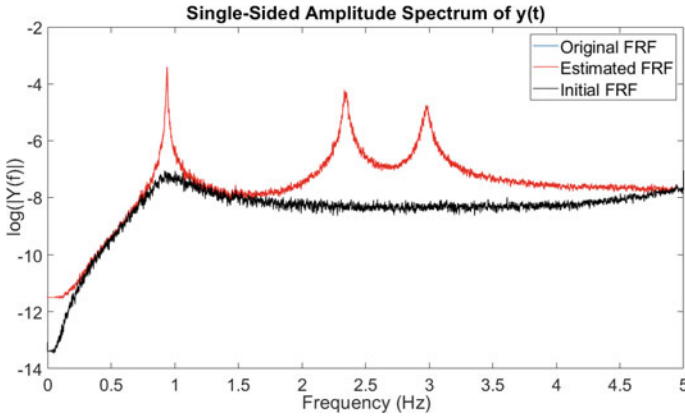


Fig. 4 Frequency response function of example 1 for random force

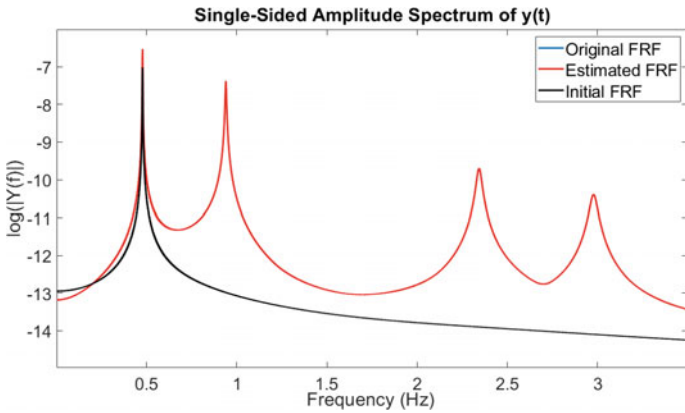


Fig. 5 Frequency response function of example 1 for sinusoidal force

the comparison between the actual and the estimated FRFs, presented in Figs. 7, 8 and 9.

Eventually, it can be concluded that even with a proportional damping assumption, the estimated damping model has sufficiently captured the actual damping which is actually non-proportional. Estimation of a full non-proportional damping matrix can be a very tedious job which can however be simplified using the proposed method with a proportionality assumption.

Comparison with Rayleigh damping model

The proposed model has further been compared with existing Rayleigh damping model. No significant benefit of the proposed algorithm has been found as long as the damping model is proportional and the first two modal damping ratios are equal,

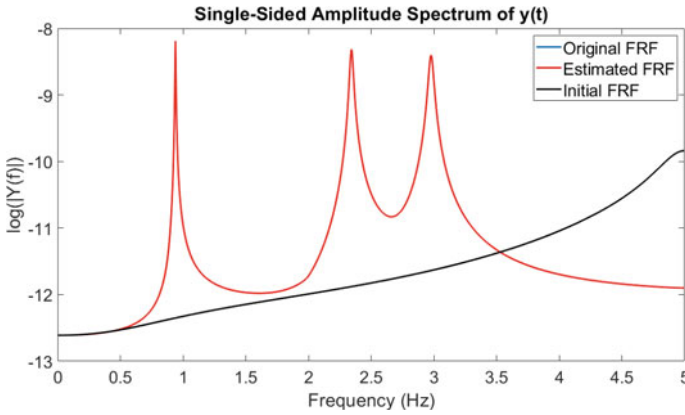


Fig. 6 Frequency response function of example 1 for impulse force

Table 5 Original and identified damping matrices for example 2

Actual modal damping matrix	Identified matrix (Random force)
$\begin{bmatrix} 0.0111 & 0.01 & 0.0045 & 0 \\ 0.01 & 0.0111 & 0 & 0.0045 \\ 0.0045 & 0 & 0.0289 & 0.01 \\ 0 & 0.0045 & 0.01 & 0.0289 \end{bmatrix}$	$\begin{bmatrix} 0.0112 & 0 & 0 & 0 \\ 0 & 0.0111 & 0 & 0 \\ 0 & 0 & 0.0295 & 0 \\ 0 & 0 & 0 & 0.0290 \end{bmatrix}$
Identified matrix (Sinusoidal force)	Identified matrix (Impulse force)
$\begin{bmatrix} 0.0110 & 0 & 0 & 0 \\ 0 & 0.0111 & 0 & 0 \\ 0 & 0 & 0.0290 & 0 \\ 0 & 0 & 0 & 0.0301 \end{bmatrix}$	$\begin{bmatrix} 0.0111 & 0 & 0 & 0 \\ 0 & 0.0111 & 0 & 0 \\ 0 & 0 & 0.0290 & 0 \\ 0 & 0 & 0 & 0.0292 \end{bmatrix}$

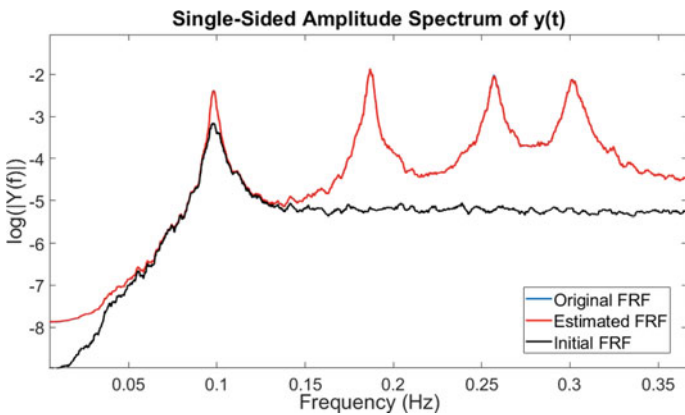


Fig. 7 Frequency response function of example 2 for random force

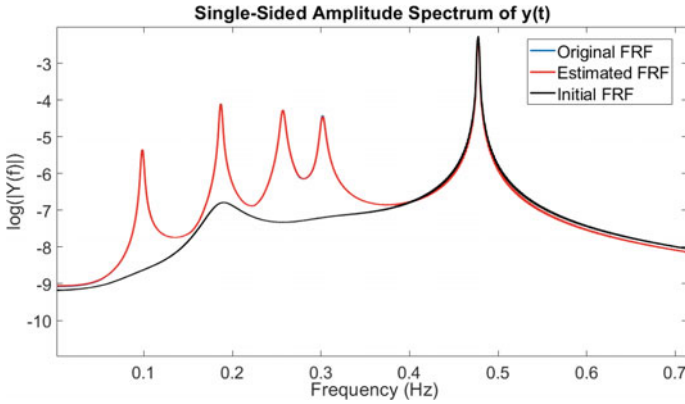


Fig. 8 Frequency response function of example 2 for sinusoidal force

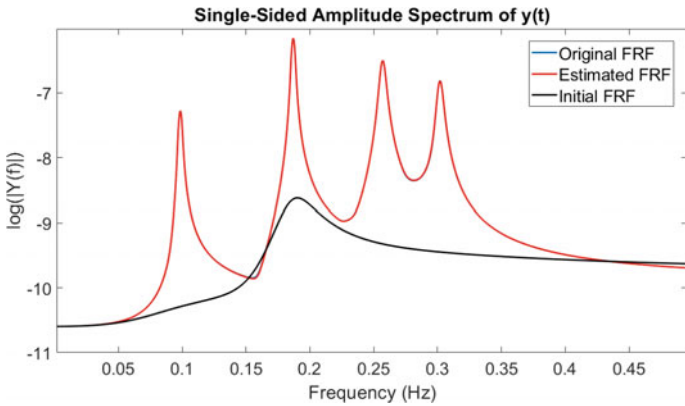


Fig. 9 Frequency response function of example 2 for impulse force

which however complies with the fundamental assumption of Rayleigh damping model. The result for this case is not reported in this article for the sake of brevity.

For non-proportional damping, with impulse load case, Rayleigh model is found to be failing in estimating the actual model severely. The value of damping ratio required for the Rayleigh model is obtained from the frequency response function using half power bandwidth method. The actual and estimated damping matrices are presented in Table 6. However, the proposed mode specific damping model estimated the actual damping with much better accuracy. The comparison between the damping models has been presented in the following in physical domain.

Further, to compare the estimation, we employed a set of error norms as demonstrated in Phani and Woodhouse’s article [11]. The result is presented in Table 7. Again, it can be verified that the proposed method outperforms the Rayleigh damping model in all measures of the considered norms.

Table 6 Comparison of damping matrix obtained from Rayleigh damping model and mode specific damping model

C (Actual)	$\begin{bmatrix} 0.02 & -0.02 & 0 & 0 \\ -0.02 & 0.02 & 0 & 0 \\ 0 & 0 & 0.02 & 0 \\ 0 & 0 & 0 & 0.02 \end{bmatrix}$
C (Rayleigh model)	$\begin{bmatrix} 0.0394 & -0.0144 & 0 & 0 \\ -0.0144 & 0.0394 & -0.0144 & 0 \\ 0 & -0.0144 & 0.0394 & -0.0144 \\ 0 & 0 & -0.0144 & 0.0394 \end{bmatrix}$
C (Mode specific damping model)	$\begin{bmatrix} 0.0200 & -0.0081 & 0.0001 & 0.0040 \\ -0.0081 & 0.0201 & -0.0041 & 0.0001 \\ 0.0001 & -0.0041 & 0.0201 & -0.0081 \\ 0.0040 & 0.001 & -0.0081 & 0.0200 \end{bmatrix}$

Table 7 Comparison of performance of Rayleigh damping model and mode specific damping model

Norm	Rayleigh model	Mode specific damping model
Absolute norm	1.0046	0.3638
Modal norm	0.9686	0.0042
Spatial norm	0.707	0.8090

From the entire validation study, it is evident that the mode specific damping model estimates the actual damping better than the Rayleigh damping model. Obviously, there are some departures between the estimated and original damping matrices for non-proportional damping cases which however can be accepted since the non-proportional damping estimation is computationally expensive which might jeopardize the damping-based damage estimation approach.

4 Conclusion

In this article, it has been demonstrated that the change in the damping ratios can be used as an indicator for the presence of damage. For a damping-based damage detection approach, therefore, an accurate model of damping is required for damage detection. It has been established that the assumption of same damping ratio for the first two modes with Rayleigh damping model is not necessarily true, as is evident in the finite-element modelling of the composite column. Finally, it has been found

that the proposed mode specific damping model performs better than the Rayleigh model especially when the damping is non-proportional.

References

1. Adhikari S (2001) Damping models for structural vibration. Doctoral dissertation, University of Cambridge
2. Bagley RL, Torvik J (1983) Fractional calculus—a different approach to the analysis of viscoelastically damped structures. *AIAA J* 21(5):741–748
3. Chen SY, Ju MS, Tsuei YG (1996) Estimation of mass, stiffness and damping matrices from frequency response functions
4. Fritzen CP (1986) Identification of mass, damping, and stiffness matrices of mechanical systems
5. Gaul L, Klein P, Kemple S (1991) Damping description involving fractional operators. *Mech Syst Sig Process* 5(2):81–88
6. Ibrahim SR (1983) Dynamic modeling of structures from measured complex modes. *AIAA J* 21(6):898–901
7. Lancaster P (1960) Free vibration and hysteretic damping. *Aeronaut J* 64(592):229–229
8. Lee JH, Kim J (2001) Identification of damping matrices from measured frequency response functions. *J Sound Vib* 240(3):545–565
9. Maia NMM, Silva JMM, Ribeiro AMR (1998) On a general model for damping. *J Sound Vib* 218(5):749–767
10. Minas C, Inman DJ (1991) Identification of a nonproportional damping matrix from incomplete modal information. *J Vib Acoust* 113(2):219–224
11. Phani AS, Woodhouse J (2007) Viscous damping identification in linear vibration. *J Sound Vib* 303(3–5):475–500
12. Pilkey DF, Inman DJ (1997) An iterative approach to viscous damping matrix identification. In: *Proceedings of the 15th international modal analysis conference*, vol 3089, p 1152
13. Torvik PJ, Bagley DL (1987) Fractional derivatives in the description of damping materials and phenomena. In: *The role of damping in vibration and noise control*, pp 125–135

Effect of the Imperfection on the Axial Loaded Rectangular CFST Column



R. Manigandan and Manoj Kumar

Abstract Due to the gradual increase in axial load on the rectangular concrete-filled steel tube (CFST) column, initially, the steel tube and concrete core remain in contact all around; however, at higher loads, a gap between steel tube and concrete core is developed along the periphery of column except at corners. This gap leads to local buckling of steel tube, and as a consequence, the confinement effect to concrete is lost, and it is known as one of the major imperfection in CFST. This paper aims to study the effect of aspect ratio of column section and thickness of steel tube on imperfection. In this paper, three aspect ratios, namely 1.0, 1.25 and 1.5, have been considered while the thickness of the tube is varied from 2 to 4 mm at the interval of 1 mm. For the column with various aspect ratios and tube thickness, the variation of imperfection with axial load has been plotted in terms of the non-dimensional parameter denoted as gap ratio. For the column with rectangular cross section, the gap ratio at any face of the column is defined as the ratio of the gap and the length of that face. For the three-dimensional finite-element analysis of CFST using the ABAQUS, the steel tube and concrete core have been discretized into shell and solid elements, respectively, and the contact between the inner side of steel tube and the surface of the concrete core has been considered rough, and the friction coefficient is taken as 0.25. Based on the numerical study, it has been concluded that the axial load carrying capacity of the rectangular CFST column is reduced significantly with an increase in imperfection.

Keywords Rectangular column · Composite column · Concrete-filled steel tube (CFST) · Imperfection

R. Manigandan · M. Kumar (✉)
Department of Civil Engineering, BITS Pilani, Pilani, India
e-mail: manojkr@pilani.bits-pilani.ac.in

R. Manigandan
e-mail: p20180444@pilani.bits-pilani.ac.in

© The Author(s), under exclusive license to Springer Nature Singapore Pte Ltd. 2023
M. Madhavan et al. (eds.), *Proceedings of the Indian Structural Steel Conference 2020* (Vol. 2), Lecture Notes in Civil Engineering 319,
https://doi.org/10.1007/978-981-19-9394-7_23

285

1 Introduction

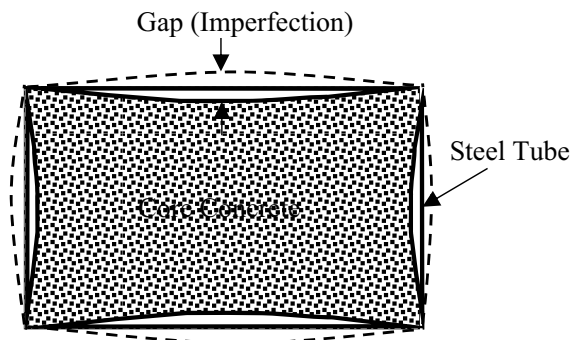
Due to the great economic reason, the use of a concrete-filled steel tube (CFST) column is widely spreading in various fields of construction. It not only provides a high loading capacity [19], but it also increases the stiffness of the column since the steel located in the periphery of the column (away from the centroid), where it makes the maximum contribution to the moment of inertia. The CFST column was used in the high rise and multi-story buildings; also, the mechanical strength of the steel tube enhances the significant confinement to the concrete core.

Moreover, the confinement effect has a significant improvement in the ductility of the concrete core [18]. The contact between the steel tube and concrete core was significant indicative of the structural behavior in the CFST column, which also resists the local buckling. In the seismic condition, the steel tube acts as a lateral and longitudinal reinforcement to the CFT column resists in bending moment, shear, and tension.

In recent research on the CFST column [4, 7, 15] in the real-time CFST member, the gap between the steel tube and concrete core was due to the creep and shrinkage [10]. The gap is generally classified into a circumferential and curved segment, as shown in Fig. 1. The circumferential gap is formed vertically toward the column; it is mainly due to the improper curing of the concrete. The curved segment gap is formed at the edges in a horizontal direction due to the pumping of the concrete [6].

In previous research, an experimental and numerical modeling has been investigated to study the structural response of the CFST stub column by considering the initial imperfections of the circular CFST column, which demonstrated in a significant decrease in the confinement effect of concrete and the load carrying capacity of the CFST column due to the gap between the steel tube and concrete core [13]. However, the research on the effect of the imperfection on the behavior of axially loaded RCFST columns remains unreported. Also, so far, no specification or standard is providing the design approach that takes into consideration the effect of gaps for RCFST columns.

Fig. 1 Rectangular gap segment



To fill this research gap, the primary investigation was focused on the gaps between the steel tube and concrete core in the structural behavior of the axially loaded RCFST column [4]. The main aim of the research is to investigate the influence of the gap on the performance of axially loaded RCFST columns; to establish an authentic FEM model and study the structural response of the composite columns with gaps, and the ultimate strength of axially loaded CFST columns by considering the effect of gaps.

2 Numerical Analysis

2.1 General

A finite-element analysis (FEA) model based on the software ABAQUS is developed to study the structural behavior of the RCFST columns with core concrete of initial imperfection.

2.2 Modeling of Steel Tube Material

In this analysis, the Poisson's ratio μ_s and the elastic modulus E_s of the steel tube are assumed to be $\mu_s = 0.3$ and $E_s = 200$ Gpa. The steel tube is simulated by an elastic-perfectly plastic model of uniaxial behavior. The stress-strain curve is represented as a trilinear curve. The curve has three parts with three linear curves, as shown in Fig. 2. The first part of the curve is elastic in nature up to the yield point with slope equal to the elastic modulus of steel (usually 200 GPa). The second part is constant at yield stress (f_y), which is plastic in nature. The third part of the curve shows the strain hardening ε_t in steel, by ending up to ultimate stress f_{ult} and ultimate strain ε_u of steel. The ultimate strain in the steel tube of specimen ε_u is assumed to be 0.2 [7]

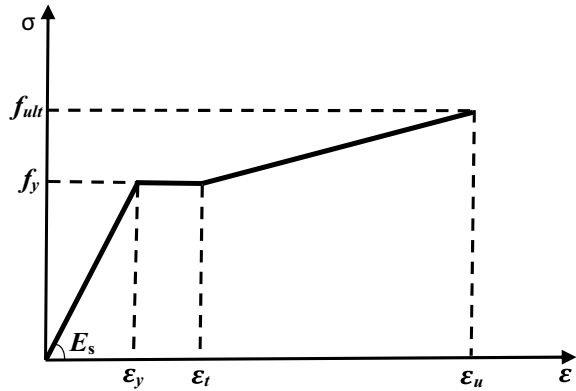
$$\varepsilon_t = 10\varepsilon_y \quad (1)$$

The RCFST is modeled using 3D solid elements. The outer steel is modeled using eight-node 3D solid elements with reduced integration (C3D8R) [3]. Tao et al. proposed a σ - ε model for the structural steel with the validity range of f_y from 200 to 800 MPa, in which the ε_y is the yield strain, and ε_u is the ultimate strain corresponding to the ultimate strength [17].

$$P = E_p \left(\frac{\varepsilon_u - \varepsilon_p}{f_u - f_y} \right), \quad (2)$$

in which E_p is the initial modulus of elasticity at the of the strain hardening and can be taken as $0.02E_s$ [5]

Fig. 2 Idealized trilinear stress–strain curve for steel



2.3 Modeling of the Concrete Core

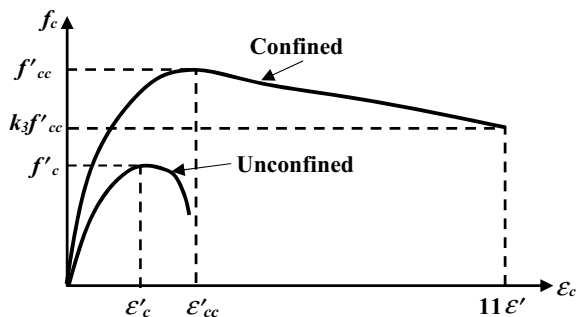
The Poisson’s ratio of the concrete under uniaxial compressive stress ranges from 0.2 to 0.5, with the representative value of 0.9 to 0.20 [8]. In this study, the Poisson’s ratio of concrete has taken as $\mu_c = 0.2$, and elastic modulus is calculated by Eq. 3 [8]. The stress–strain curve for confined concrete compared with unconfined concrete is shown in Fig. 3. The stress–strain relation of the concrete core is also divided into three parts. First part of the curve is linear up to stress ($K_3 f'_{cc}$) with Young’s modulus E_c calculated by using formula according to ACI (1999) [18].

$$E_c = 4700\sqrt{f'_{cc}} \tag{3}$$

$$f'_{cc} = f_c + k_1 f_1 \tag{4}$$

$$\epsilon'_{cc} = \epsilon'_c \left[1 + k_2 \frac{f_1}{f_2} \right], \tag{5}$$

Fig. 3 Stress–strain curve of confined and unconfined concrete



where f'_{cc} = compressive strength of concrete in a confined state, f'_c = compressive strength of concrete in the unconfined state, ε'_{cc} = strain in confined concrete, ε'_c = strain in unconfined concrete, k_1 and k_2 are constants and can be assumed as 4.1 and 20.5, respectively [12]. The value of f_1 for rectangular CFST can be evaluated using empirical Eqs. 6 and 7.

$$\frac{f_1}{f_y} = 0.055048 - 0.001885 \left[\frac{H}{t} \right] \quad \text{for } 17 \leq \frac{H}{t} \leq 29.2 \quad (6)$$

$$\frac{f_1}{f_y} = 0 \quad \text{for } 29.2 \leq \frac{H}{t} \leq 150, \quad (7)$$

where f_y = yield strength of the steel tube, H = width of the RCFST specimen (Longer dimension), t = thickness of the steel.

The following equations can express the second part of the curve for confined concrete:

$$f = \frac{E_c \varepsilon_c}{1 + (R + R_E - 2) \left[\frac{\varepsilon'_c}{\varepsilon'_{cc}} \right] - (2R - 1) \left[\frac{\varepsilon'_c}{\varepsilon'_{cc}} \right]^2 + R \left[\frac{\varepsilon'_c}{\varepsilon'_{cc}} \right]^3} \quad (8)$$

$$R_E = \frac{E_c \varepsilon_c}{f_{cc}} \quad (9)$$

$$R = \frac{R_E (R_\sigma - 1)}{(R_E - 1)^2} - \frac{1}{R_E}. \quad (10)$$

R_ε and R_σ are constants, which are assumed as 4.0. The last part of the curve is assumed to be linear up to the ultimate strength and ultimate strain of confined concrete [14]

$$f_u = k_3 f'_{cc} \quad (11)$$

$$\varepsilon_u = 11 \varepsilon'_{cc}. \quad (12)$$

The value of K_3 for rectangular and square concrete-filled steel tube can be calculated as:

$$K_3 = 0.000178 \left[\frac{H}{t} \right]^2 - 0.02492 \left[\frac{H}{t} \right] + 1.2722 \quad \text{for } 17 \leq \frac{H}{t} \leq 70 \quad (13)$$

$$K_3 = 0.4 \quad \text{for } 70 \leq \frac{H}{t} \leq 150. \quad (14)$$

The FE model is presented by Han et al.; the constant values of 30°, 0.1, 1.16, and 2/3 were used for χ , e , K_c , and f_{b0}/f_c , respectively. By default, in ABAQUS using

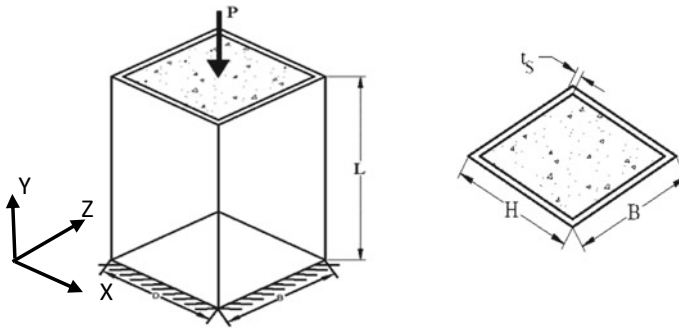


Fig. 4 Geometry of rectangular CFST column

the “Penalty” method, frictional constraints are enforced with a stiffness having a finite value. In case the sticking stiffness is infinite, the elastic slip will be zero.

2.4 Boundary Condition

The asymmetric boundary condition is enforced on the symmetric planes, which $u = 0$ on the plane normal to the x -axis, $w = 0$ on the plane normal to the z -axis, and $v = 0$ on the bottom surface normal to the y -axis. The top surface of the column is restrained with $u = w = 0$ but allows the displacement to take place in the y -direction, as shown in Fig. 4. The corner of the column is assumed to be 90° , and corner radii are not considered. The uniform compressive loading is applied in the y -direction at the top surface of the column.

Where L , H , B , and t_s are the length, width, breadth, thickness of steel tube column respectively, and P is the axially applied force.

2.5 Interaction Between the Steel and Concrete Surface

It is modeled by general surface to surface element with steel as a slave surface and concrete as a master surface. The friction coefficient used in all analyses is 0.25 [11]. Though the contact between the concrete and steel is allowed to separate, it is not allowed to penetrate each other.

3 Simulation of Rectangular and Square Concrete-Filled Steel Column

The geometry and material properties of the rectangular and square CFST columns are given in Table 1, and the graphs are potted for the axial load versus displacement for the column with imperfection and without imperfection.

Table 2 shows the lateral confining pressure f_1 and the material degradation parameter k_3 for all the cross-sectional geometries. Since the larger lateral dimension to thickness ratio for all the sections is more than 29.2 and less than 150, the value of f_1 is zero for all the sections. The value of k_3 increases with decrease in larger lateral dimension to thickness ratio irrespective the strength of concrete [8] which infers that as the tube thickness increases, steel tube provides stronger lateral confinement to the concrete core and consequently the degradation of concrete after peak strength diminishes [16].

While analyzing the CFST with imperfection, an initial imperfection of 5 mm (1% of length of column) was introduced in the analysis in order to examine the effect of imperfection on strength of column. The comparison of axial load-deformation response and axial load carrying capacity of CFST column with or without imperfection determined using the ABAQUS is shown in Figs. 5–7 and Table 2 respectively. It may be observed from Table 2 that imperfection in columns results in reduction of axial load carrying capacity. The reduction in strength due to imperfection depends

Table 1 Geometry and material properties of the CFST column

Cross section	H (mm)	B (mm)	Tube thick., t (mm)	Larger dim. (H or B) to thickness ratio	Length L (mm)	Steel (f_y) (MPa)	Concrete (f_c) (MPa)	Confined concrete (f_{cc}) (MPa)
Square (S1)	100	100	2	50	500	250	40	40
Rectangular (R1)	125	100	3	42	500	250	40	40
Rectangular (R2)	150	100	4	38	500	250	40	40
Square (S2)	100	100	2	50	500	250	45	45
Rectangular (R3)	125	100	3	42	500	250	45	45
Rectangular (R4)	150	100	4	38	500	250	45	45
Square (S3)	100	100	2	50	500	250	50	50
Rectangular (R5)	125	100	3	42	500	250	50	50
Rectangular (R6)	150	100	4	38	500	250	50	50

Table 2 Effect of imperfection on failure strength of columns of various geometries

Cross section	(H/t) or (B/t)	f_1	k_3	Failure strength of column (ABAQUS) (kN)		Strength reduction due to imperfection (%)
				Without imperfection	With imperfection	
Square (S1)	50	0	0.40	835.3	737.8	11.67
Rectangular (R1)	42	0	0.54	1085.7	1009.3	7.03
Rectangular (R2)	38	0	0.59	1384.6	995.0	28.14
Square (S2)	50	0	0.40	1125.4	953.1	15.31
Rectangular (R3)	42	0	0.54	1084.4	975.83	10.01
Rectangular (R4)	38	0	0.59	1444.7	1212.8	16.05
Square (S3)	50	0	0.40	1201.2	1008.2	16.07
Rectangular (R5)	42	0	0.54	1133.4	1061.1	6.38
Rectangular (R6)	38	0	0.59	1483.5	1377.6	7.14

on larger side to thickness ratio as well as on the strength of concrete filled in tube. In general, the reduction in strength due to imperfection varies between 6 and 16%; however, for the column having minimum value of larger dimension to thickness ratio (i.e., 38) and filled with low strength concrete (40 MPa), the reduction in strength was observed 28% as shown in Table 2. Furthermore, it may be observed from the Table 2 that the effect of imperfection is minimum in case of rectangular cross section with larger lateral dimension to thickness ratio 42 (Figs. 5–7).

4 Strength Comparison with Eurocode

Eurocode-4 is recently developed guidelines adopted for the design of composite columns. The design theory is proposed by the code, which is mainly based on the rigid plastic method of analysis, which assumes fully yielded steel and entirely crushed concrete. The code uses a column curve to determine the effect of slenderness in rectangular CFST columns. In Eurocode-4, the confinement is related to slenderness ratio ($\bar{\lambda}$) and eccentricity (e) of the applied loading. Eurocode-4 includes a design mechanism for both concrete encased and steel-filled tubular columns. Eurocode-4 [9] gives ultimate axial load equations for both square and rectangular concrete-filled columns. To check the local buckling of CFST columns, the limiting values of the specimen are governed by the equations given in Table 3.

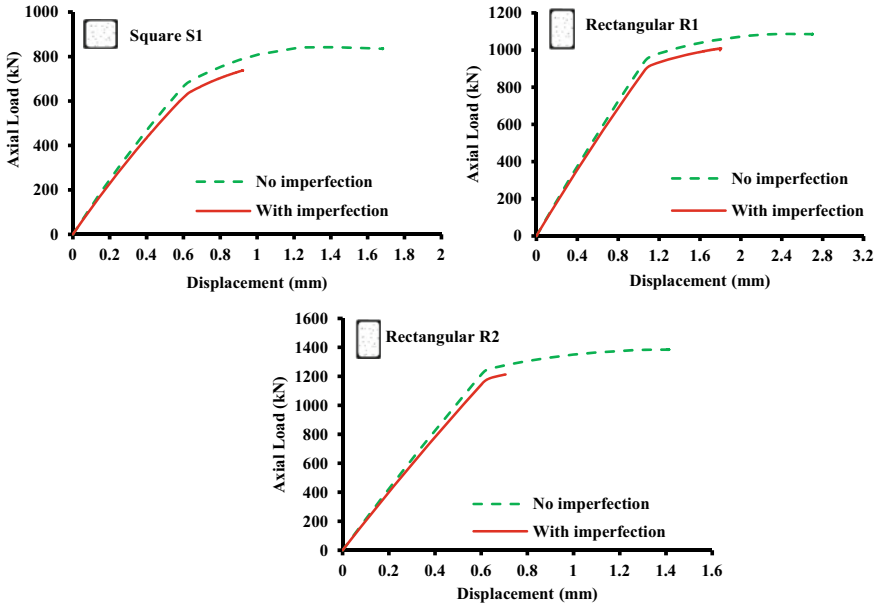


Fig. 5 Axial load versus displacement of thickness 2, 3, 4 mm ($f_{ck} = 40$ MPa)

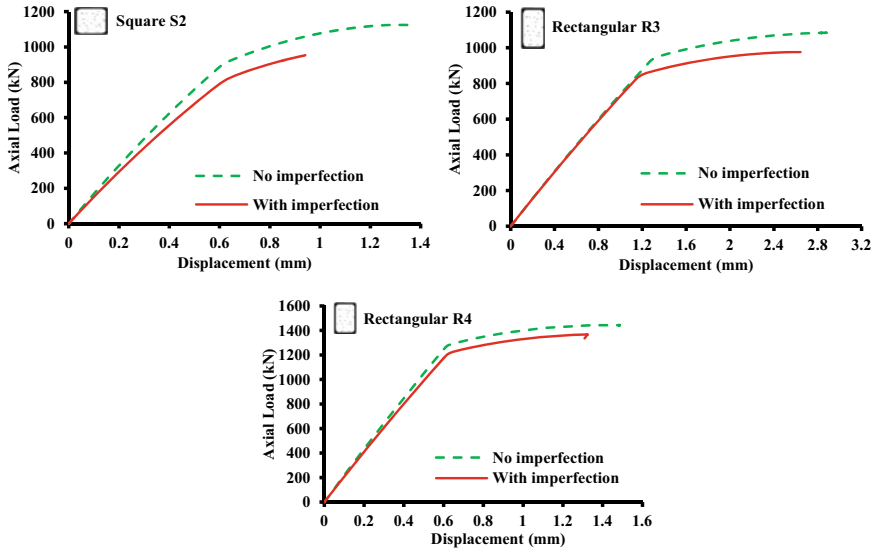


Fig. 6 Axial load versus displacement of thickness 2, 3, 4 mm ($f_{ck} = 45$ MPa)

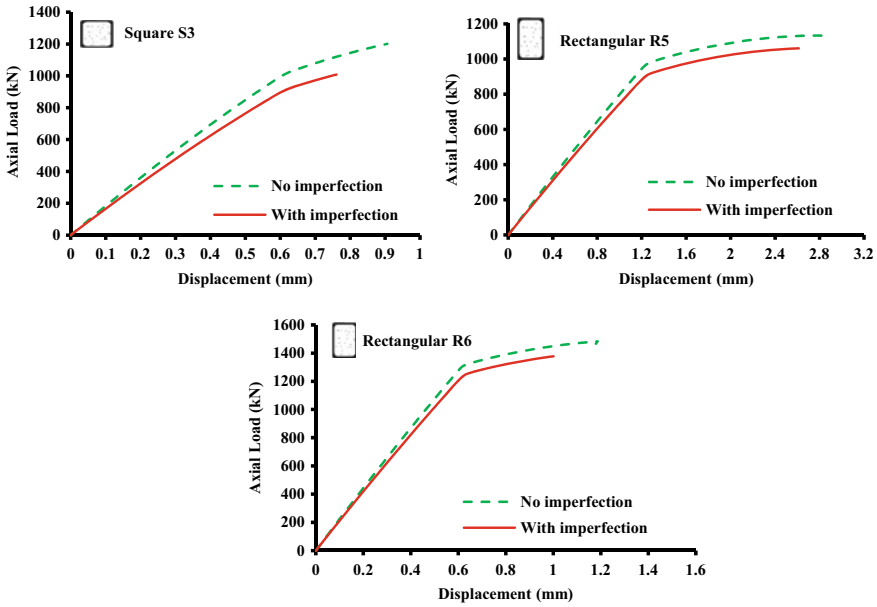


Fig. 7 Axial load versus displacement of thickness 2, 3, 4 mm ($f_{ck} = 50$ MPa)

Table 3 Maximum values of (H/t) and (B/t) for steel strength f_y (in N/mm^2) (Eurocode-4)

Shape	Cross section	(B/t) or (H/t) ratio
Rectangular		$\text{Max } \frac{H}{t} \leq 52\sqrt{\frac{235}{f_y}}$
Square		$\text{Max } \frac{B}{t} \leq 52\sqrt{\frac{235}{f_y}}$

A comparison of failure strength of CFST according to numerical analysis (FEM) and Eurocode-4 (EC-4) for the no imperfection case is summarized in Table 4. It may be observed from Table 4 that for the steel tubes filled with low strength concrete (40 MPa) namely S1, R1 and R2, the EC-4 overestimates the failure strength; however, for the remaining six steel tubes filled with relatively higher strength of concrete (45 and 50 MPa) namely S2, R3, R4, S3, R5, R6, the EC-4 underestimates the failure strength. Thus, the EC-4 should not be used for the steel tubes filled with low strength concrete (40 MPa or less); however, for steel tubes filled with higher

Table 4 Comparison of failure strength according to numerical analysis and Eurocode for no imperfection case

Cross section	Failure strength in (kN) according to		Difference in failure strength (%)
	Eurocode	FEM	
Square (S1)	919	835.3	-9.11
Rectangular (R1)	1118	1085.7	-2.89
Rectangular (R2)	1411	1384.6	-1.87
Square (S2)	1004	1125.4	+12.09
Rectangular (R3)	1017	1084.4	+6.63
Rectangular (R4)	1315	1444.7	+9.86
Square (S3)	1077	1201.2	+11.53
Rectangular (R5)	1128	1133.4	+0.49
Rectangular (R6)	1334	1483.5	+11.21

strength concrete (45 and 50 MPa), EC-4 may be used which will enhance the factor of safety in design.

5 Conclusions

In this paper, the effect of imperfection in square and rectangular shaped tubes filled with various strength of concrete was examined via the finite-element analysis using the commercial software ABAQUS. Moreover, to check the adequacy of the Eurocode for the design of square and rectangular section CFST with no imperfection, the axial load carrying capacity of the CFST columns with no imperfection determined using finite element was compared with EURO code. Based on the numerical results, the following conclusions are drawn.

The imperfection (gap) between the steel tube and concrete core tends to induce a significant reduction in the failure strength of axially loaded CFST columns with rectangular and square cross section. For the various cross-sectional shapes considered in this study, it was observed that due to imperfection (1% of length of column), the failure strength of CFST may decrease up to 28% compared to CFST column with no imperfection. The effect of imperfection is found minimum in case of rectangular cross section with larger lateral dimension to thickness ratio 42.

Moreover, the study showed that EC-4 should not be used for the steel tubes filled with low strength concrete (40 MPa or less) since it overestimates the strength; however, for steel tubes filled with higher strength concrete (45 and 50 MPa), EC-4 underestimates the strength and may be used for design purpose which will further enhance the factor of safety in design.

References

1. ABAQUS (2013) Abaqus analysis user's manual version 6.13. ABAQUS Inc
2. Eurocode 4 (2004) Design of composite steel and concrete structures, Part 1-1: General rules structural rules for buildings. Brussels: EN1994-1-1, CEN
3. Gajalakshmi P, Jane Helena H (2014) Experimental and computational study of SFRC in-filled steel circular columns under axial compression. *Asian J Civil Eng* 15(2):231–244
4. Goode CD, Lam D (2011) Concrete—filled steel tube columns—tests compared with Eurocode 4. In: *Composite construction in steel and concrete VI—Proceedings of the 2008 composite construction in steel and concrete conference*, vol 41142, January 2014, pp 317–325. [https://doi.org/10.1061/41142\(396\)26](https://doi.org/10.1061/41142(396)26)
5. Güneyisi EM, Gültekin A, Mermerdaş K (2016) Ultimate capacity prediction of axially loaded CFST short columns. *Int J Steel Struct* 16(1):99–114. <https://doi.org/10.1007/s13296-016-3009-9>
6. Han LH, Yao GH (2004) Experimental behaviour of thin-walled hollow structural steel (HSS) columns filled with self-consolidating concrete (SCC). *Thin-Walled Struct* 42(9):1357–1377. <https://doi.org/10.1016/j.tws.2004.03.016>
7. Han LH, Ye Y, Liao FY (2016) Effects of core concrete initial imperfection on performance of eccentrically loaded CFST columns. *J Struct Eng (United States)* 142(12):1–13. [https://doi.org/10.1061/\(ASCE\)ST.1943-541X.0001604](https://doi.org/10.1061/(ASCE)ST.1943-541X.0001604)
8. Hu HT et al (2003) Nonlinear analysis of axially loaded concrete-filled tube columns with confinement effect. *J Struct Eng* 129(10):1322–1329. [https://doi.org/10.1061/\(ASCE\)0733-9445\(2003\)129:10\(1322\)](https://doi.org/10.1061/(ASCE)0733-9445(2003)129:10(1322))
9. Huang CS et al (2002) Axial load behavior of stiffened concrete-filled steel columns. *J Struct Eng* 128(9):1222–1230. [https://doi.org/10.1061/\(ASCE\)0733-9445\(2002\)128:9\(1212\)](https://doi.org/10.1061/(ASCE)0733-9445(2002)128:9(1212))
10. Kim CS et al (2017) Effect of sustained load on ultimate strength of high-strength composite columns using 800-MPa steel and 100-MPa concrete. *J Struct Eng (United States)* 143(3):1–16. [https://doi.org/10.1061/\(ASCE\)ST.1943-541X.0001676](https://doi.org/10.1061/(ASCE)ST.1943-541X.0001676)
11. Krishan AL, Astafeva MA, Chernyshova EP (2018) Strength calculation of short concrete-filled steel tube columns. *Int J Concr Struct Mater* 12(1). Springer Singapore. <https://doi.org/10.1186/s40069-018-0322-z>
12. Li P, Zhang T, Wang C (2018) Behavior of concrete-filled steel tube columns subjected to axial compression. In: *Advances in materials science and engineering*, Hindawi. <https://doi.org/10.1155/2018/4059675>
13. Liao FY, Han LH, He SH (2011) Behavior of CFST short column and beam with initial concrete imperfection: experiments. *J Constr Steel Res* 1922–1935. <https://doi.org/10.1016/j.jcsr.2011.06.009>
14. Lu ZH, Zhao YG (2008) Mechanical behavior and ultimate strength of circular cft columns subjected to axial compression loads. In: *The 14th world conference on earthquake engineering (1999)*
15. McCann F, Gardner L, Qiu W (2015) Experimental study of slender concrete-filled elliptical hollow section beam-columns. *J Constr Steel Res* 113:185–194
16. Schneider SP (1998) Axially loaded concrete-filled steel tubes. *J Struct Eng ASCE* 124(10):1125–1138
17. Tao Z, Wang ZB, Yu Q (2013) Finite element modelling of concrete-filled steel stub columns under axial compression. *J Constr Steel Res* 89:121–131. Elsevier Ltd
18. Xue JQ, Briseghella B, Chen BC (2012) Effects of debonding on circular CFST stub columns. *J Constr Steel Res* 64–76. <https://doi.org/10.1016/j.jcsr.2011.08.002>
19. Zeghiche J, Chaoui K (2005) An experimental behaviour of concrete-filled steel tubular columns. *J Constr Steel Res* 61(1):53–66. <https://doi.org/10.1016/j.jcsr.2004.06.006>

Numerical Investigation of High-Strength CFST Columns with Slender Sections



Trac Nguyen, Tuan Ngo, and Huu-Tai Thai

Abstract Concrete filled steel tube (CFST) columns have been widely used in structures largely subjected to compression such as high-rise buildings. To achieve taller constructions, engineers have improved CFST columns performance by applying high-strength materials to make the columns slender. Although the current standards [1, 2, 4] have taken CFST columns into practice, there are restrictions in the material strength and the section slenderness. To solve the problem, this paper presents a numerical examination of CFST columns fabricated from high-strength materials as well as slender sections under axial compression. For verification, a finite element (FE) model, taking into account the initial local imperfection, residual stress on a tube, the confinement effect of filled concrete and the buckling and post-buckling behavior of steel, was developed for CFST columns. Ultimate strengths obtained from numerical analysis were compared with practical code and experimental results to verify its reliable prediction. A parametric study of CFST columns with different concrete compressive strengths f'_c , steel yield stresses f_y and the width to thickness ratios B/t was also presented in the paper.

Keywords Concrete filled steel tube column · High-strength concrete · High-strength steel · Slender section · Stub column · Finite element

T. Nguyen · T. Ngo · H.-T. Thai (✉)
The Department of Infrastructure Engineering, The University of Melbourne, Melbourne,
Australia
e-mail: tai.thai@unimelb.edu.au

T. Nguyen
e-mail: tnguyentan@student.unimelb.edu.au

T. Ngo
e-mail: dtngo@unimelb.edu.au

1 Introduction

Composite structural members have been developed as the most common option that applied to high-rise buildings and many great constructions in modern times. They are the combination of two or more materials with considerably different properties to form structural members taking advantage of the constituent materials. CFST column is such a steel–concrete composite member in that concrete core not only restricts the local buckling of the outer tube but also is confined laterally. The stiffness and ultimate strength of CFST columns can be enhanced considerably so that they are appropriate to structures subjected to great compression (Fig. 1).

To reach the record heights, engineers have had to apply high-strength materials to high-rise buildings. For instance, Taiwan Taipei 101, one of the world's tallest building, was built on eight mega CFST columns with 570 MPa high-strength steel and 70 MPa high-strength concrete. The application of high-strength materials may lessen the column size or, in other words, make the column slender. This would not only save materials but also create more spaces or floor areas which are extremely important for modern buildings in terms of the high cost of land. Furthermore, the premanufactured steel tubes play a role as lateral reinforcement and long-term formwork for the concrete core, resulting in simpler and more rapid construction.

Despite great benefits of high-strength materials for CFST columns, the current standards still have restrictions in the material strength and the section slenderness of steel tube into practice. For example, Eurocode 4 [4] (EC4) assigns a maximum 460 MPa to the steel yield stress and 50 MPa to the concrete compressive strength or American code AISC 360-16 [1] only allows the steel yield stress up to 525 MPa and concrete compressive strength up to 69 MPa. The highest material strengths are of lately Australian/New Zealand standards, AS/NZS 2327 [2], with 690 MPa steel

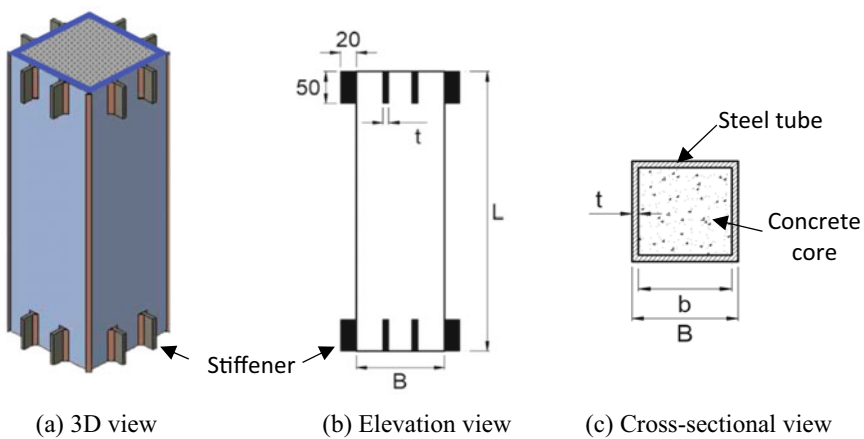
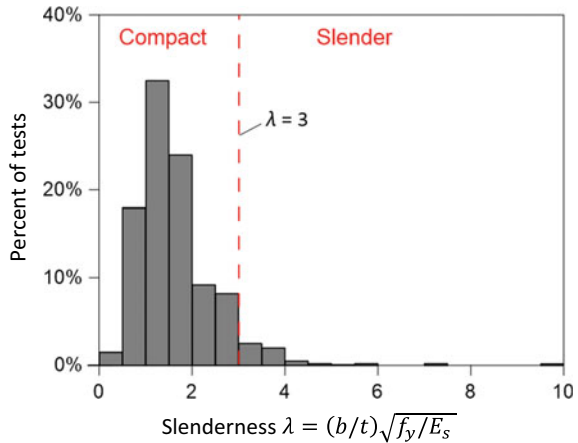


Fig. 1 Typical schematic view of a square CFST specimen

Fig. 2 Distribution of the rectangular specimen among over 3100 test data by Thai et al. [17]



yield stress and 100 MPa concrete compressive strength. It is a fact that design codes have not catch up the development of high-strength materials in CFST columns. In addition, according to the statistics among over 3100 recent CFST column tests by Thai et al. [17], the percentages of ultra-high-strength concrete (compressive strength $f'_c > 90$ MPa) and high-strength steel (yield stress $f_y > 460$ MPa) are consist of only 12.5% and 13.6%, respectively. Furthermore, these tested CFST columns were mostly classified as compact sections, as shown in Fig. 2, which also indicates the current limitation of CFST design.

This paper presents a numerical investigation of CFST columns in that non-linear FE models by using the commercial software ABAQUS have been verified with EC4 and 34 test results. It is also a further attempt to examine the impact of slenderness and high-strength materials on the ultimate strength of CFST columns. In addition, FE models of CFST columns were considered the existence of the initial local imperfection of steel tubular, the materials confinement effect and the residual stress. The paper also provides a parametric study of CFST columns with different concrete compressive strengths f'_c , steel yield stresses f_y and the width to thickness ratios B/t .

2 Finite Element Analysis

2.1 Element Type and Boundary Conditions

To simplify the modeling and analyzing, the one-eighth part of the CFST specimen has been used to reduce the calculation time. One-eighth of a specimen is a reasonable simplified model because of the symmetry of square or circular cross-section and boundary conditions. Both concrete core and steel tube were modeled by 8-node

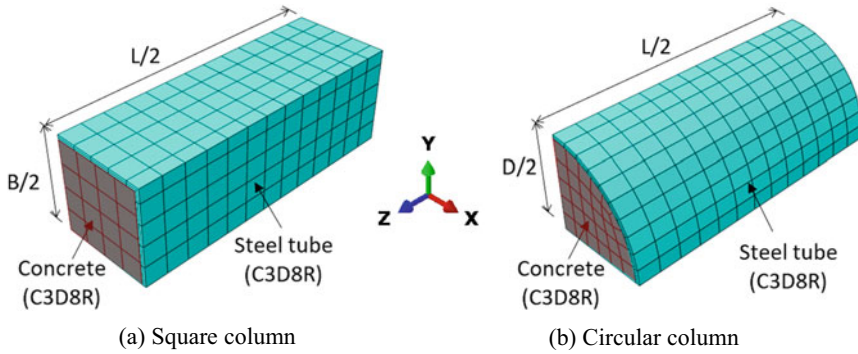


Fig. 3 FE model of a 1/8 of CFST column

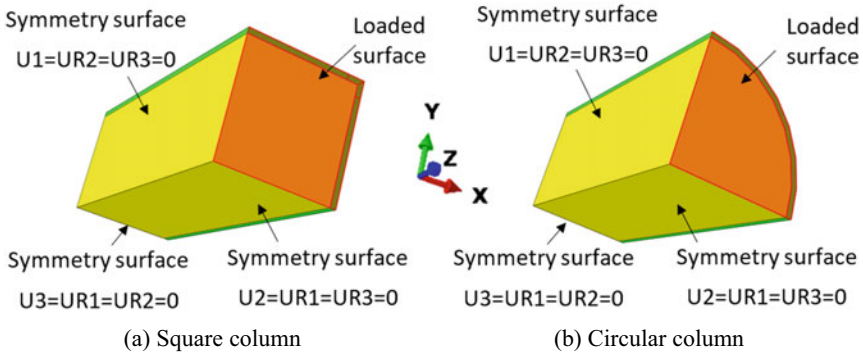


Fig. 4 Boundary conditions of a 1/8 of CFST column

linear brick, reduced integration element (C3D8R), as shown in Fig. 3. Figure 4 shows the boundary conditions of a simplified model.

The “hard” contact was applied in normal direction as the steel–concrete interaction in which the inner steel tube and outer concrete core were respectively master and slave surfaces. The “hard” contact relationship minimizes the penetration of the concrete surface into the steel surface and does not allow tensile stress to transfer across the interaction face. The frictional coefficient was taken as 0.25 in the tangential behavior.

2.2 Initial Local Imperfection and Residual Stress

Steel tubes in CFST columns are manufactured whether by welded plates or hot-rolled and cold-rolled steel, as shown in Fig. 5. Each manufacturing ways has a different influence on finished products. Especially for welded steel tubes, their initial local

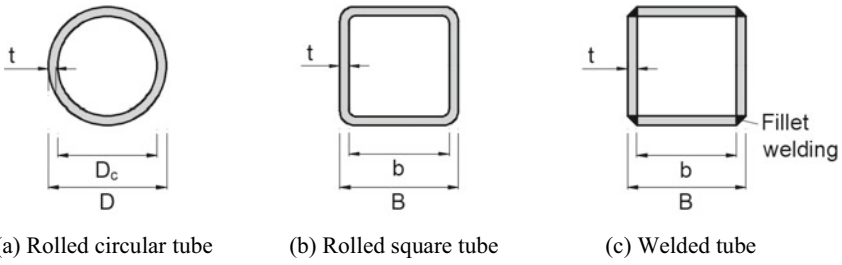


Fig. 5 Different types of steel tube

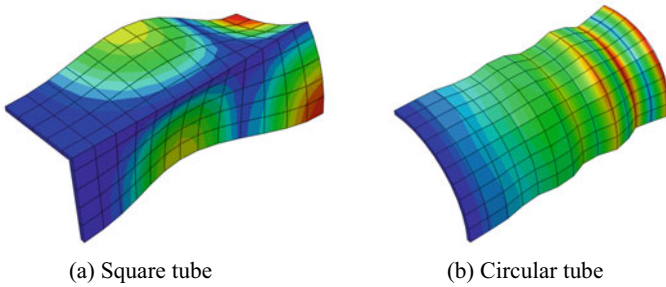


Fig. 6 First buckling mode shape of square and circular tube

imperfection factor, significantly dependent on worker’s skills and types of welding, is much larger than rolled tubes. Therefore, to determine the imperfection factor of a steel tube, it is required to consider how it was manufactured. According to [16], it is assumed that the first buckling mode shape of steel tube, obtained from the Euler buckling analysis, is the local initial imperfection, as shown in Fig. 6. The magnitude of the initial imperfection was taken in the range of 0.1–0.5 multiplied by the thickness of steel tube t .

Residual stresses on steel tubes, caused by plastic deformation after thermal loads or welding processes, have been studied in the past. Khan et al. [7] proposed a model for residual stress distribution, as shown in Fig. 7. In the model, the tensile residual stress (σ_{RST}) was 0.72 and 1.07 times its yielding stress for lightly and heavily welded steel sections, respectively. The compressive residual stress σ_{RSC} and the tensile residual stress width b_t can be obtained by

$$\sigma_{RSC} = 3.6607 f_y \left(\frac{b_t}{t} \right)^{-0.924} \tag{1}$$

$$b_t = \frac{b_1 \sigma_{RSC}}{2(\sigma_{RST} + \sigma_{RSC})} \tag{2}$$

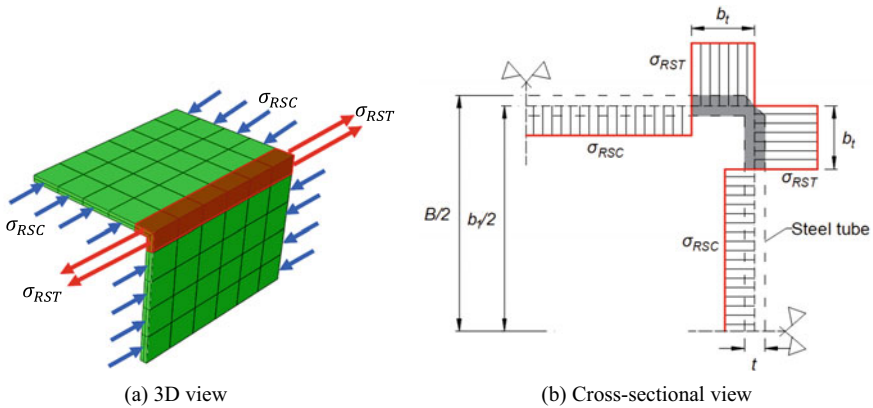


Fig. 7 The residual stress distribution on tube cross-section

where f_y is the yield stress of the steel, b_1 is the width of a box section between the centerlines and σ_{RST} is the tensile residual stress.

2.3 Material Properties

2.3.1 Stress–Strain Models for Filled Concrete

Sakino et al. [13] proposed a model to express the filled concrete properties in which the stress–strain curves of an identified concrete can be varied by their shape of cross-section. For the same kind of concrete, Fig. 8 points out that the circular CFST column could provide filled concrete extra stress at higher strain than the square column does. This can be explained by the ability to evenly distribute pressure on the wall of the circular tube. In other words, concrete could be confined better in circular than square CFST.

On the other hand, compared to a plain concrete column with the same width, concrete in square CFST columns presented a similar performance at the early stage of elastic and buckling. The major difference between them is in the post-buckling of the stress–strain curve since there is no confinement effect in plain concrete.

2.3.2 Stress–Strain Models for Steel Tube

For square CFST column, there are three different stress–strain curves depending on the types of hollow square steel tubes, proposed by Sakino et al. [13]. These types are classified through the slenderness of steel sections $\lambda = (B/t)\sqrt{f_y/E_s}$: type 1 with $\lambda \leq 1.54$, type 2 with $1.54 < \lambda < 2.03$ and type 3 with $\lambda \geq 2.03$, as shown in Fig. 9a. For circular CFST column, the stress–strain relationship of the steel tube

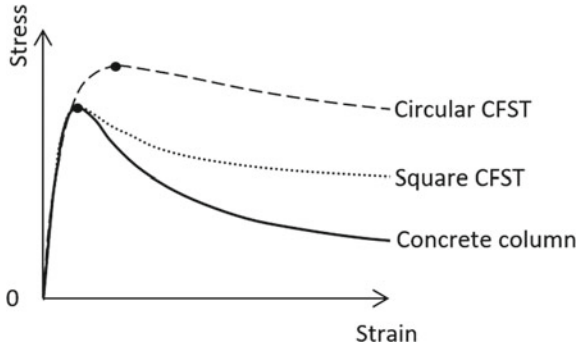


Fig. 8 Stress–strain models for concrete in plain, square and circular CFST columns with $B/t = D/t$

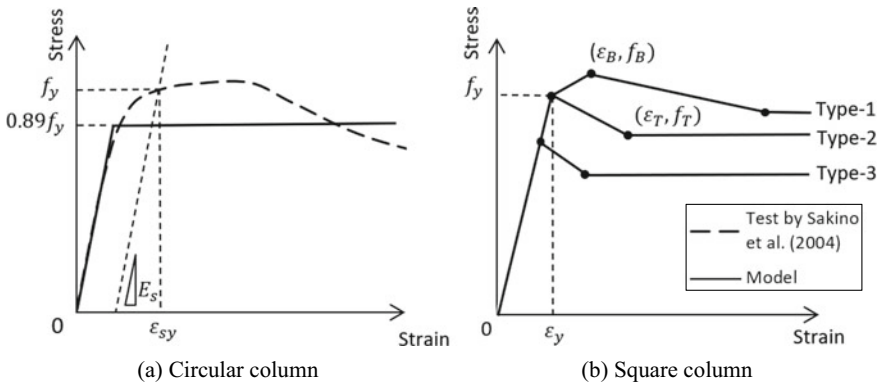


Fig. 9 Stress–strain model of steel tubes in CFST columns

is developed as an elastic perfectly plastic relation model as shown in Fig. 9b. The maximum stress of the circular tube is $0.89f_y$.

3 Verification of Finite Element Model

3.1 Mesh Convergence

The size of a model element is determined based on the column width B and length L . For the square CFST column with width of 215 mm, length of 4.4 mm, concrete compressive strength of 262 MPa and steel yield stress of 41 MPa, the medium mesh size ($B/10$ and $L/30$) provided a reasonable ultimate load in that the test result to FE prediction N_{test}/N_{FE} is 0.977 and the time of process is only ten minutes. It

Table 1 Comparing mesh sizes

Mesh	Fine	Medium	Coarse
Size	$B/30-L/90$	$B/12-L/30$	$B/6-L/16$
Time (min)	140	10	6
$N_{\text{test}}/N_{\text{FE}}$	0.982	0.977	0.918

took more than two hours to run one case of fine mesh ($B/30$ and $L/90$) but the FE result is 0.982 which was not considerably improved. Although the coarse mesh model ($B/6$ and $L/16$) took only six minutes to run, $N_{\text{test}}/N_{\text{FE}}$ of 0.918 obtained from this model is not an accurate prediction. As a result, for efficiency and precision of numerical calculation, the medium element size was assigned as $B/10$ and $L/30$ in the cross-sectional longitudinal direction, respectively (Table 1).

3.2 Evaluation of FE Results

Thirty-four experiment results in recent papers, including 20 square and 14 circular CFST tests, were recorded for verifying. For all specimens, the values of the ultimate strength are summarized in Tables 2 and 3. The testing values were compared to the predictions of the EC4 and FE method. The ratio of the test result to EC4 prediction ($N_{\text{test}}/N_{\text{EC4}}$) has mean values of 0.995 and 1.027 with standard deviation values of 0.088 and 0.130 for square and circular, respectively. Meanwhile, the mean ratios of the test result to FE prediction for square and circular columns ($N_{\text{test}}/N_{\text{FE}}$) are 1.020 and 1.007 with standard deviation values of 0.037 and 0.280 which are more accurate than EC4.

Where B is the width of rectangular sections, D is the outside diameter of circular sections, L is the length of a CFST columns, t is the thickness of steel tubular sections, λ is the slenderness of steel sections and N_{EC4} , N_{FE} and N_{test} is the ultimate strengths of CFST columns calculated by EC4, FE analysis and obtained from experiment, respectively.

It is noted that EC4 only predicts the maximum load of CFST columns while FE analysis provides load–displacement relationships, as shown in Figs. 10 and 11. Furthermore, Fig. 12 indicates that the ratio of $N_{\text{test}}/N_{\text{FE}}$ is closer to one than the ratio of $N_{\text{test}}/N_{\text{EC4}}$ which proves the reasonable predictions of FE analysis.

Table 2 Circular columns results by FE, EC4 and experiment

No	References	D (mm)	t (mm)	D/t	f_y (MPa)	f'_c (Mpa)	N_{EC4} (MPa)	N_{FE} (MPa)	N_{test} (MPa)	$\frac{N_{test}}{N_{EC4}}$	$\frac{N_{test}}{N_{FE}}$
C1	Chen et al. [3]	114	2	57	270	130	1482	1508	1535	1.036	1.018
C2	Han et al. [5]	200	2	100	404	85.2	2928	2974	3011	1.028	1.012
C3	O'Shea and Bridge [12]	190	1.5	126.7	306	80.2	2536	2534	2603	1.026	1.027
C4	Sakino et al. [13]	222	6.5	34.2	823	77	7004	7612	7304	1.043	0.960
C5	Sakino et al. [13]	450	3	150	262	40	7788	6885	6870	0.882	0.998
C6	Sakino et al. [13]	450	2.96	152	279	41.1	8034	6870	6985	0.869	1.017
C7	Sakino et al. [13]	337	6.5	51.8	823	85.1	14,190	14,002	13,776	0.971	0.984
C8	Sakino et al. [13]	360	4.54	79.3	525	85.1	11,752	11,283	11,505	0.979	1.020
C9	Sakino et al. [13]	300	3	100	262	40	3782	3412	3277	0.867	0.960
C10	Sakino et al. [14]	100	0.52	192.3	244	17.9	204	239	242	1.186	1.013
C11	Sakino et al. [14]	100	0.52	192.3	244	37.4	351	373	389	1.110	1.045
C12	Tomii et al. [18]	150	3.2	47	287	28.7	1095	1092	1073	0.980	0.983
C13	Uenaka et al. [19]	158.7	0.9	176.3	221	18.7	516	694	700	1.356	1.008
C14	Xiong et al. [21]	220	5	44	380	193.3	8331	8232	8664	1.040	1.052
Mean value											
Standard deviation											
0.130											
1.027											
0.028											

Table 3 Square columns results by FE, EC4 and experiment

No	References	B (mm)	t (mm)	B/t	f_y (MPa)	f'_c (MPa)	N_{EC4} (MPa)	N_{FE} (MPa)	N_{test} (MPa)	$\frac{N_{test}}{N_{EC4}}$	$\frac{N_{test}}{N_{FE}}$
S1	Chen et al. [3]	100	2	48	350	130.8	1480	1509	1581	1.068	1.048
S2	Han et al. [5]	150	2	73	404	81	2205	2042	2060	0.934	1.009
S3	Han et al. [5]	200	2	98	404	50.9	2198	2051	2054	0.934	1.001
S4	Han et al. [5]	250	2	123	404	50.9	3256	3083	3100	0.952	1.005
S5	Han et al. [5]	250	1.87	131.7	282	60	3529	3147	3400	0.963	1.080
S6	Inai and Sakino [6]	265	6.5	38.8	835	80.3	10,711	8895	8990	0.839	1.011
S7	Khan et al. [8]	75	5	13	762	100	1489	1642	1636	1.099	0.996
S8	Khan et al. [8]	100	5	18	762	100	2258	2397	2632	1.166	1.098
S9	Khan et al. [8]	150	5	28	762	113	4425	4630	4833	1.092	1.044
S10	Khan et al. [8]	200	5	38	762	113	7051	6766	7478	1.061	1.105
S11	Lee et al. [10]	300	6	48	369	40	5921	6293	6298	1.064	1.001
S12	Lee et al. [9]	300	5	58	746	70.5	10,330	8643	8686	0.841	1.005
S13	Lee et al. [11]	180	4.2	40.9	559	70.8	3736	3564	3590	0.961	1.007
S14	Sakino et al. [13]	175	6.5	24.9	835	77	5679	5436	5366	0.945	0.987
S15	Sakino et al. [13]	215	4.4	46.9	262	41	2714	2480	2424	0.893	0.977
S16	Tao et al. [15]	250	2.5	98	270	58.3	3542	3504	3495	0.987	0.998
S17	Tao et al. [15]	250	2.5	98	342	67	4238	3915	4040	0.953	1.032
S18	Uy [20]	306	3	100	300	38	4511	4552	4581	1.016	1.006
S19	Yamamoto et al. [22]	100	2.3	41.5	324	53.7	780	832	851	1.091	1.023
S20	Yamamoto et al. [22]	200	4.5	42.4	324	53.7	3099	3285	3201	1.033	0.974
Mean value										0.995	1.020
Standard deviation										0.088	0.037

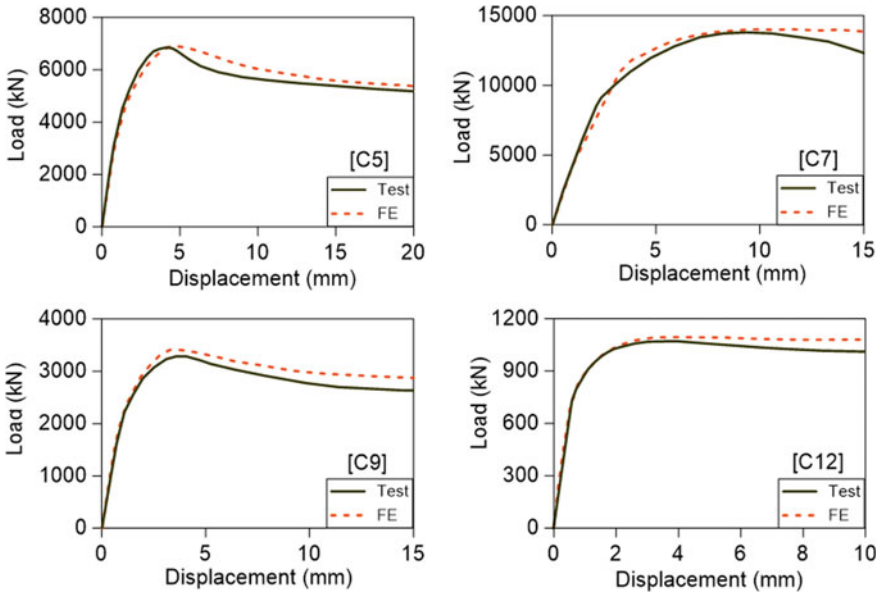


Fig. 10 Load–displacement of circular CFST columns

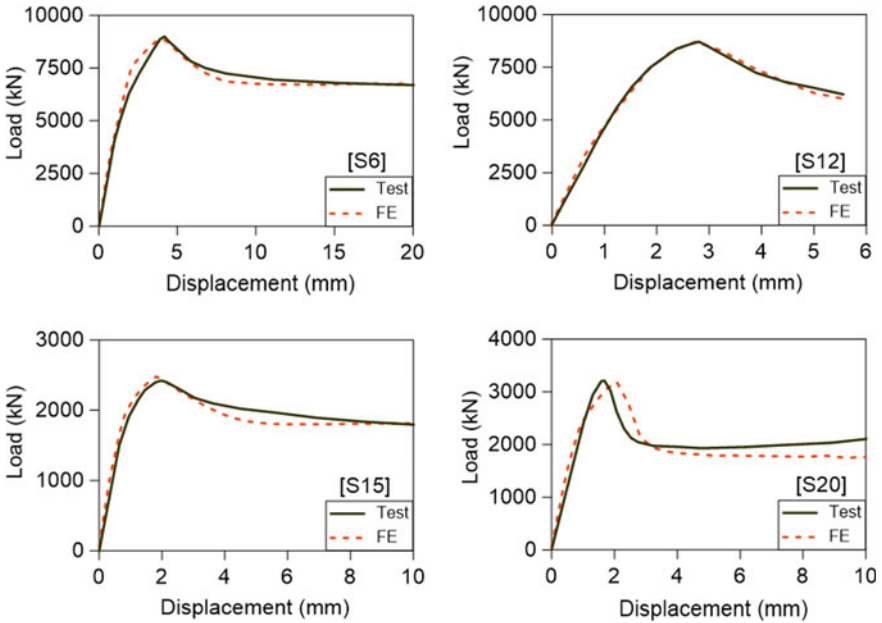


Fig. 11 Load–displacement of square CFST columns

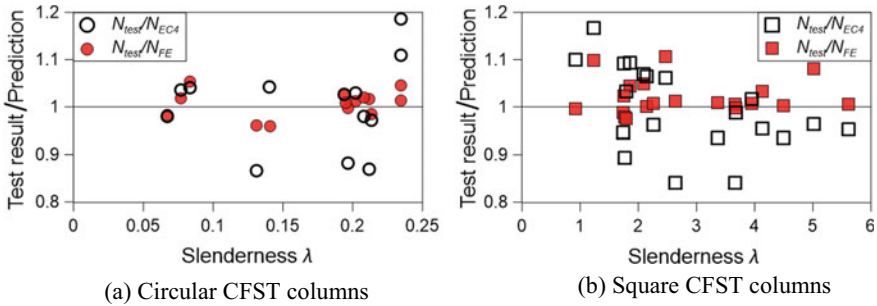


Fig. 12 Comparing the predictions of EC4 and FE to test results for CFST columns

4 Parametric Study

4.1 Concrete Strength

Figure 13 shows the numerical results of ultimate strength of square CFST columns with different width to thickness ratios ($B = 300$ mm and $t = 3, 10$ and 17 mm) and various concrete compressive strengths ($f_c = 30, 50, 100$ and 150 MPa) but remained steel yield stress of 690 MPa. Varying values of width to thickness ratios of $17.65, 30$ and 100 represent the types of CFST sections which are compact, non-compact and slender, respectively. All three types of CFST column show an increase in the ultimate strength corresponding to the use of higher concrete strength.

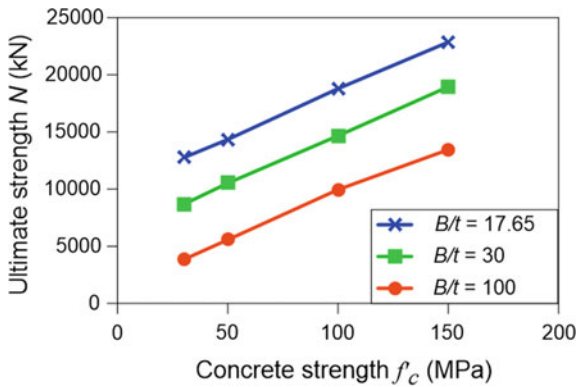
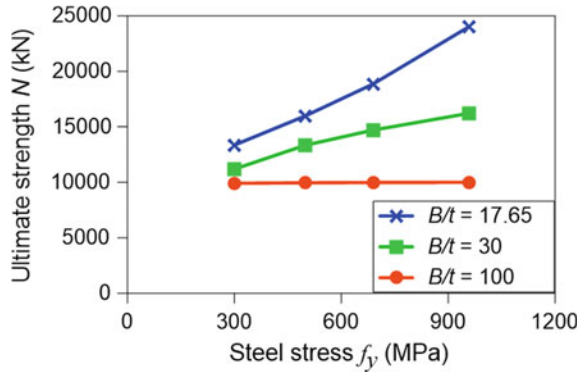


Fig. 13 Ultimate strength over different concrete strengths

Fig. 14 Ultimate strength over different steel stresses



4.2 Steel Stress

A parametric study on steel stress was conducted similarly to the study of concrete strength but the remained parameter is concrete strength of 100 MPa and the steel had yield stresses of 300, 500, 690 and 960 MPa. The numerical results show a disparity of three CFST section types under the increase of steel stress. The compact section ($B/t = 17.65$) had a significant improvement in ultimate strength than non-compact section ($B/t = 30$) because of the stronger effect of thin outer steel to the filled concrete confinement. On the other hand, there is limited change in the ultimate load when applying higher strength steel to the slender CFST section ($B/t = 100$). This is because the buckling propensity which limits the structural strength so that the effects of steel strength could be ignored in slender CSFT (Fig. 14).

4.3 Width to Thickness Ratio

Figure 15 exhibits the consideration of width to thickness ratio and sectional slenderness to square CFST columns which have a width of 300 mm and tube thickness of 3, 10 and 17 mm based on numerical analysis. As the width to thickness ratio increases, the ultimate load tends to be lower regardless of material strength. However, the rate of CFST ultimate strength reduction differentiates between kinds of steel. The ultimate strength of the CFST column with 960 MPa steel decreases intensively from $B/t = 30$ and is mostly equal to the CFST column with 690 MPa steel when $B/t = 100$. This variation is suitable to the above parametric study on steel strength which shows that compact and non-compact sections could take advantage of high-strength steel more effectively than the slender section.

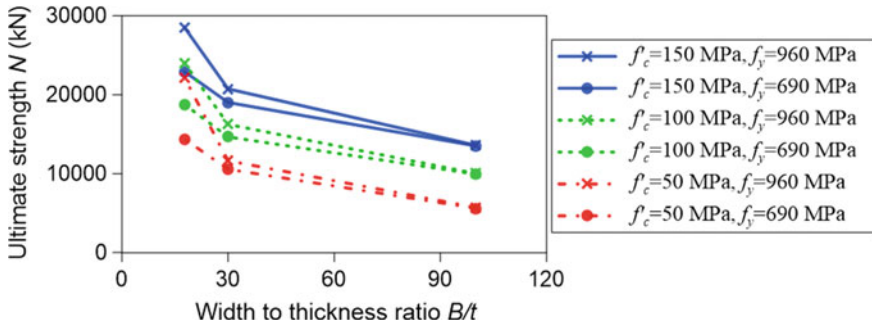


Fig. 15 Ultimate strength over different width to thickness ratios and material strengths

5 Conclusion

Thirty-four recent CFST column tests, in that most of them are slender section and high-strength materials, were verified by the FE method and EC4 in the study. The initial local imperfection, the residual stress of the outer tube and the stress–strain models for concrete and steel were applied to FE model of CFST columns. They have a significant effect on the numerical analysis which can help to obtain reliable results. Furthermore, FE predicted the ultimate strengths of the experiment CFST columns more conservatively than EC4 for wide-ranging material strengths and member slenderness.

A parametric study on material strengths and width to thickness ratios shows that the non-slender section can benefit the CFST column strength by the effect of concrete infill confinement and local buckling restraint for steel tube. Moreover, unlike compact and non-compact sections which their ultimate strengths are limited by the material strength, the slender column may restrict its strength because of its buckling propensity. While high concrete strength has a positive impact on the ultimate strength of all CFST column types, the application of high-strength steel is only effective on non-slender CFST columns. To avoid the waste of material, it is necessary to design a slender limitation that assigns a highest yield stress of steel applied to slender CFST columns.

Acknowledgements This research was supported by the University of Melbourne, Department of Infrastructure Engineering. The financial support is highly acknowledged.

References

1. ANSI/AISC 360-16 (2016) Specification for structural steel buildings. American Institute of Steel Construction, Chicago, IL
2. AS/NZS 2327 (2017) Composite steel-concrete construction for buildings. Standard Australia/Standard New Zealand

3. Chen S, Zhang R, Jia L-J, Wang J-Y, Gu P (2018) Structural behavior of UHPC filled steel tube columns under axial loading. *Thin-Walled Struct* 130:550–563
4. Eurocode 4, I.S EN 1994-1-1 (2005) Design of composite steel and concrete structures. Part 1. 1: General Rules and Rules for Buildings. Brussels, Belgium
5. Han LH, Yao GH, Zhao XL (2005) Tests and calculations for hollow structural steel (HSS) stub columns filled with self-consolidating concrete (SCC). *J Constr Steel Res* 61(9):1241–1269
6. Inai E, Sakino K (1996) Simulation of flexural behavior of square concrete filled steel tubular columns. In: Proceedings of the third joint technical coordinating committee meeting, U.S.-Japan cooperative research program, Phase 5: Composite and hybrid structures, Hong Kong, National Science Foundation, Arlington, Virginia, 12–14 Dec 1996
7. Khan M, Paradowska A, Uy B, Mashiri F, Tao Z (2016) Residual stresses in high strength steel welded box sections. *J Constr Steel Res* 116:55–64
8. Khan M, Uy B, Tao Z, Mashiri F (2017) Behaviour and design of short high-strength steel welded box and concrete-filled tube (CFT) sections. *Eng Struct* 147:458–472
9. Lee HJ, Choi IR, Park HG (2016) Eccentric compression strength of rectangular concrete-filled tubular columns using high-strength steel thin plates. *J Struct Eng* 143:04016228
10. Lee S-H, Choi Y-H, Kim Y-H, Choi S-M (2012) Structural performance of welded built-up square CFST stub columns. *Thin-Walled Struct* 52:12–20
11. Liu D, Gho WM, Yuan J (2003) Ultimate capacity of high-strength rectangular concrete-filled steel hollow section stub columns. *J Constr Steel Res* 59(12):1499–1515
12. O'Shea MD, Bridge RQ (1997) Design of thin-walled concrete filled steel tubes. University of Sydney, Department of Civil Engineering, Research report No. R758
13. Sakino K, Nakahara H, Morino S, Nishiyama I (2004) Behavior of centrally loaded concrete-filled steel-tube short columns. *J Struct Eng* 130:180–188
14. Sakino K, Tomii M, Watanabe K (1985) Sustaining load capacity of plain concrete stub columns confined by circular steel tubes. In: Proceedings of the international speciality conference on concrete-filled steel tubular structures, ASCCS, Harbin, China, pp 112–118
15. Tao Z, Han LH, Wang DY (2008) Strength and ductility of stiffened thin-walled hollow steel structural stub columns filled with concrete. *Thin-Walled Struct* 46(10):1113–1128
16. Thai HT, Uy B, Khan M, Tao Z, Mashiri F (2014) Numerical modelling of concrete-filled steel box columns incorporating high strength materials. *J Constr Steel Res* 102:256–265
17. Thai S, Thai HT, Uy B, Ngo T (2019) Concrete-filled steel tubular columns: Test database, design and calibration. *J Constr Steel Res* 157:161–181
18. Tomii M, Yoshimura K, Morishita Y (1997) Experimental studies on concrete filled steel tubular stub columns under concentric loading. In: Proceedings of the international colloquium on stability of structures under static and dynamic loads, Washington DC, USA, 17–19 May 1977, pp 718–41
19. Uenaka K, Kitoh H, Sonoda K, Hayami M (2003) Experimental study on concrete filled double tubular steel columns under axial loading. In: Advances in structures, Balkema Press, pp 877–882
20. Uy B (2000) Strength of concrete filled steel box columns incorporating local buckling. *J Struct Eng* 126(3):341–352
21. Xiong MX, Xiong DX, Liew JYR (2017) Axial performance of short concrete filled steel tubes with high- and ultra-high-strength materials. *Eng Struct* 136:494–510
22. Yamamoto T, Kawaguchi J, Morino S (2000) Experimental study of scale effects on the compressive behavior of short concrete-filled steel tube columns. In: Composite construction in steel and concrete IV conference, Banff, Alberta, Canada, 28 May–2 June 2000

Influence of Governing Parameters on Long-Term Behaviour of Prestressed Concrete Bridge with Corrugated Steel Webs



Madhup Pandey and Francis T. K. Au

Abstract The influences of critical parameters affecting the long-term behaviour of prestressed concrete bridge with corrugated steel webs (PCBCSW) have been presented in this paper. A calibrated finite element numerical model was used to conduct a detailed parametric study. A total of eleven critical parameters were comprehensively studied using age-adjusted elasticity method (AAEM) to investigate their influence on the serviceability aspect of PCBCSW. Due to large shear deformation and negligible axial stiffness of corrugated steel webs, the Euler–Bernoulli and Timoshenko beam theories are not valid for this type of bridge, thus, the sandwich beam model proposed by Chen [5] was extended by Pandey [11] by duly considering the concrete creep and shrinkage as well as tendon relaxation models of different international codes. It has been found that the long-term deflection of PCBCSW was larger than the identical bridge with flat steel web, and comparable to those with the concrete web. However, the long-term prestress loss of PCBCSW was similar to those of conventional bridges.

Keywords Age-adjusted elasticity method · Corrugated steel webs · Long-term behaviour · Prestressed concrete bridges · Sandwich beam theory · Time-dependent behaviour

M. Pandey (✉)

Department of Civil and Environmental Engineering, The Hong Kong Polytechnic University, Hong Kong, China

e-mail: madhup.pandey@polyu.edu.hk

F. T. K. Au

Department of Civil Engineering, The University of Hong Kong, Pokfulam Road, Hong Kong, China

e-mail: francis.au@hku.hk

1 Introduction

Bridge engineers and researchers have been looking for efficient structural forms under the performance-based concept to satisfy various attributes, including serviceability, safety, economy, constructability, durability, etc. Prestressed concrete bridges with corrugated steel webs (PCBCSW) have emerged as one of the promising bridge forms due to their remarkable advantages such as lightness, high buckling strength of steel webs, efficient prestressing of concrete, and easy maintenance [5]. Corrugated steel webs provide high shear buckling resistance and high transverse stiffness without the need for stiffeners as required in conventional flat steel webs. Extensive analyses of the local, global, and interactive buckling of corrugated steel webs show that they have reasonable post-buckling shear capacities. Apart from the high shear resistance, they are also less susceptible to geometric imperfection. Owing to the high buckling strength, the corrugated steel webs can be thinner than conventional flat steel webs. Because of the ‘accordion effect’ of corrugated steel webs, the axial stiffness is negligible and prestress can be introduced efficiently to the upper and lower concrete flanges. This configuration, therefore, provides excellent structural efficiency with the concrete flanges mainly taking bending and the corrugated steel webs mainly taking shear [5].

Steel webs enable substantial weight reduction and hence longer spans than those of bridges with conventional concrete webs. To further reduce the weight of the flanges, high strength concrete can be employed. The light weight of this bridge form makes it ideal not only for girder bridges but also for cable-stayed bridges. Despite various merits of the corrugated steel webs, there are also some concerns about this type of bridge. PCBCSW are known to have lower stiffness than those with conventional concrete webs, which leads to larger deflections. Owing to large shear deformation and negligible axial stiffness of corrugated steel webs, the assumption that plane section remains plane is not valid, and therefore, the conventional Euler–Bernoulli and Timoshenko beam theories cannot be applied to this form of bridges [10]. Therefore, a sandwich beam theory was developed by Chen [5] to investigate the full-range behaviour of PCBCSW considering geometric and material nonlinearities. In the development of numerical models using sandwich beam theory, special emphasis was placed on the modelling of corrugated steel webs, external prestressing tendons, diaphragms, and interaction between web shear deformation and local flange bending.

In order to study the long-term behaviour of PCBCSW, [11] extended the proposed numerical model [5] by duly considering the concrete creep and shrinkage as well as tendon relaxation models of different codes EN 1992-1-1 [7], ACI-209.2R [1], RILEM B3 Model (2001), AS-3600 [2], HK-COP (2013), and HK-SDMHR [9] using both single-step (age-adjusted elasticity method; AAEM and time integration methods). Subsequently, the numerical model to predict the long-term behaviour of PCBCSW was then verified using the experimental results. For more details, reference can be made to [6, 11] and Pandey and Au [12]. Upon validating the numerical model, a detailed parametric study was then undertaken using AAEM

to investigate the effects of various governing parameters affecting the long-term behaviour of PCBCSW, which is particularly detailed in this paper.

2 Bridge Section Considered for Parametric Study

The parametric study was carried out in accordance with EN 1992-1-1 [7] and EN 1991-2 [8] on a real size bridge with cross-sectional details shown in Fig. 1.

In addition to the overall dead load (DL) of the structure, the bridge is subjected to live load (LL), and external prestress force (P). The nominal yield stress of the strand material was taken as 1860 MPa, and the applied prestress force in each tendon was assumed to be 70% of the nominal yield stress, i.e. $0.70 \times 1860 \times 0.0075 \times 1000 = 9765$ kN. The live load was determined in accordance with load model 1 (i.e. LM 1) as per EN 1991-2 [8]. Also, as per EN 1991-2 [8], when the traffic width ranged from 5.4 to 6.0 m, then a provision of two lanes with equal lane width has been recommended. In addition, as per EN 1991-2 [8], an equivalent uniformly distributed load equal to 67.83 kN/m was taken as LL in this study. For detailed calculations, reference can be made to [11]. Moreover, Table 1 summarizes various standard dimensions and design parameters used in the parametric study.

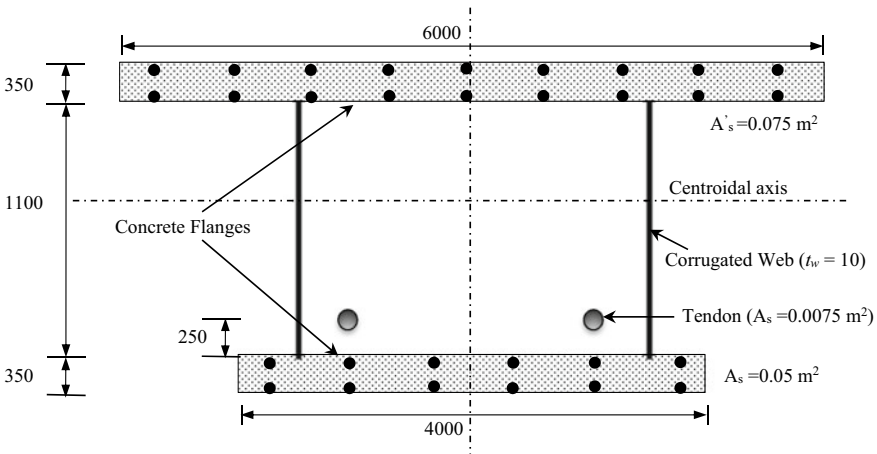


Fig. 1 Cross-sectional details of PCBCSW for parametric study

Table 1 Standard dimension and design parameters used for the parametric study

Clear span (m)	30	Web number	2
Total depth (m)	1.8	Web thickness	0.01 m
Upper flange depth (m)	0.350	Web depth	1.1 m
Upper slab width (m)	6.0	Web spacing	3 m
Lower flange depth (m)	0.350	End block thickness	0.50 m
Lower slab width (m)	4.0	Diaphragm number	2
Loading nature	(DL+LL+P)	Area of each prestress tendon	0.0075 m ²
Time of investigation	5 years	Yield stress of strand	1860 MPa
Mean RH considered	80%	Length of corrugation of steel web	0.566 m
E value of strand	200 GPa	Projected length of corrugation of steel web	0.500 m
E value of rebar	200 GPa	Eccentricity of tendons	0.445 m
Permissible compressive stress limit	0.45 f_{ck}	Permissible tensile stress limit	10% of (0.9 f_{ck})
Area of rebar in top flange (A'_s)	0.075 m ²	Area of rebar in bottom flange (A_s)	0.050 m ²
Permissible mid-span deflection = Span/250			

3 Governing Parameters Considered for Parametric Study

A total of eleven governing parameters was considered for the parametric study. The effects of these parameters were numerically examined for a period of five years. The parameters include—aggregate type; relative humidity; specimen age at first load application; aggregate-cement ratio; cement type; concrete compressive strength; ambient temperature; water-cement ratio; prestress force; cross-section type; and effects of creep, shrinkage, and tendon relaxation.

3.1 Aggregate Type

The type and quality of aggregates used in concrete mix design possess a significant influence on the serviceability limit state of a concrete structure, as coarse and fine aggregates together constitute around 70–75% of concrete by volume and 75–80% of concrete by mass. They hold a remarkable impact on both fresh and hardened properties of concrete. Generally, the majority of international codes have overlooked the importance of aggregate type and estimate the elastic modulus of concrete (E_c) using only the cube or cylinder strength of the concrete mix. However, EN 1992-1-1 [7] suggested some factors to obtain E_c value based on aggregate type. In accordance with EN 1992-1-1 [7], E_c value obtained for quartzite aggregate should be increased

by 20% for basalt aggregate and should be reduced by 10 and 30% for limestone and sandstone aggregates, respectively. Figures 2 and 3 present the variations of prestress force and mid-span deflection with time for different types of aggregates. From Fig. 2, it can be seen that, after 5 years, reduction in prestress force was maximum for sandstone aggregate (7.90%) and minimum for basalt aggregate (6.62%). Similarly, from Fig. 3, it can be noticed that, after 5 years, the maximum mid-span deflection corresponded to sandstone aggregate (27.82 mm), and the minimum corresponded to basalt aggregate (20.47 mm). Aggregates with a large value of E_c possess higher structural stiffness, and consequently, such aggregates observe less volumetric deformation as well as less reduction of prestress force and mid-span deflection.

Fig. 2 Prestress force versus time [11]

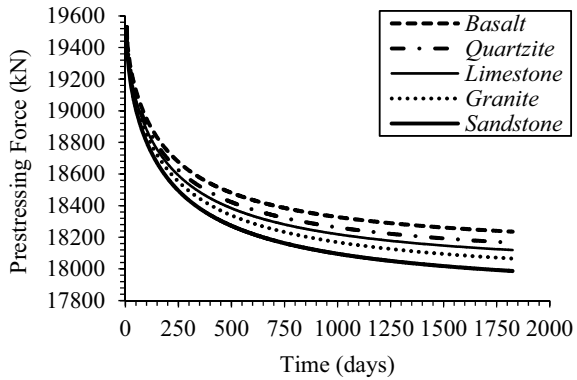


Fig. 3 Mid-span deflection versus time [11]

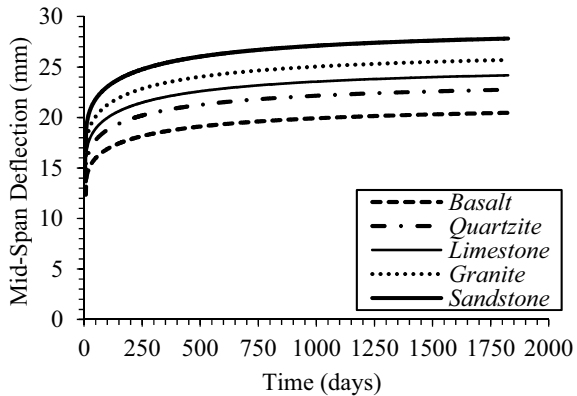
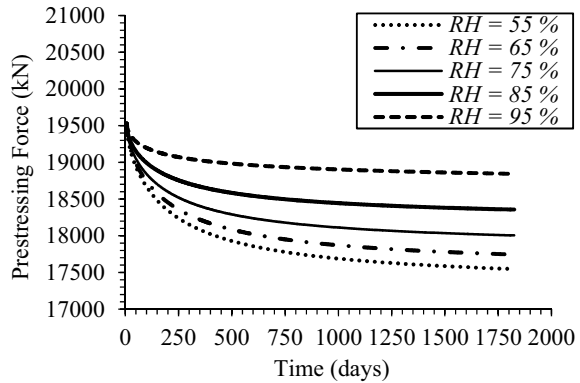


Fig. 4 Prestress force versus time [11]



3.2 Relative Humidity

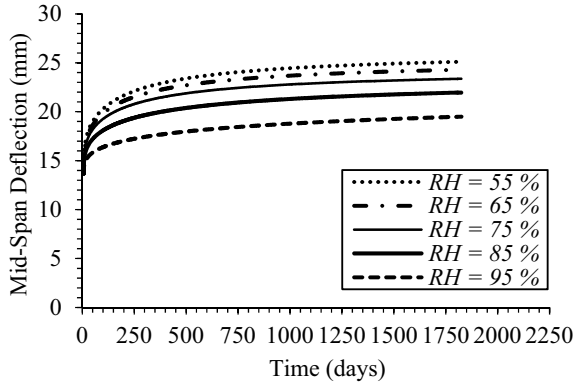
Once concrete curing is over, and it enters the drying phase, the free water inside the concrete will rush towards the surface. As the moisture evaporates from the surface, concrete mass will shrink at different rates across its cross-section. However, as the relative humidity (RH) of the surrounding increases, the evaporation rate of water loss from the concrete matrix decreases. Owing to this decrease in the evaporation rate, the free water available in capillary pores cannot easily evaporate, and in turn, it will contribute to the hydration of the concrete mix. Therefore, the strength and stiffness of concrete members will increase with the increase in RH, and the specimen will observe less deformation. Consequently, there would be less reduction in the prestress force and smaller mid-span deflection due to an increase in RH.

Figures 4 and 5 present the variations of prestress force and mid-span deflection with time for different percentage of RH. From Fig. 4, it can be seen that, after 5 years, reduction in prestress force was maximum for RH = 55% (10.16%) and minimum for RH = 95% (3.51%). Similarly, from Fig. 5, it can be noticed that, after 5 years, the maximum mid-span deflection corresponded to RH = 55% (25.11 mm), and the minimum corresponded to RH = 95% (19.50 mm).

3.3 Specimen Age at First Load Application

The long-term phenomena become less significant with the increase of maturity (or hardening) of concrete at its first load application. In other words, the older the specimen at its first loading time, the lesser it will have serviceability problems, as with the increase in maturity, concrete strength and stiffness will increase. Consequently, the structural member will observe less deformation. Therefore, as concrete becomes more mature at its first loading time, the long-term prestress loss and mid-span deflection significantly reduce. This study was based on the assumption that the

Fig. 5 Mid-span deflection versus time [11]



combined actions of external load effects were in the working stress range, as in the non-linear range, micro-cracking will occur in the structure. However, at the same time, the strength of concrete will also increase due to continual hydration. Therefore, the overall elastic behaviour in such a situation depends on the domination of either concrete strength or micro-cracking. If the strength gain due to continual hydration is more than the strength loss due to micro-cracking, then there would be less chances of failure under such loading. The younger the concrete, the more it possesses the reserve potential for future strength development to cope with the strength loss due to micro-cracking.

Figures 6 and 7 present the variations of prestress force and mid-span deflection with time for different concrete ages at the first application of load (T_0). From Fig. 6, it can be seen that, after 5 years, reduction in prestress force was maximum for $T_0 = 7$ days (6.99%) and minimum for $T_0 = 1095$ days (1.09%). Similarly, from Fig. 7, it can be noticed that, after 5 years, the maximum mid-span deflection corresponded to $T_0 = 7$ days (22.76 mm), and the minimum corresponded to $T_0 = 1095$ days (15.93 mm).

Fig. 6 Prestress force versus time [11]

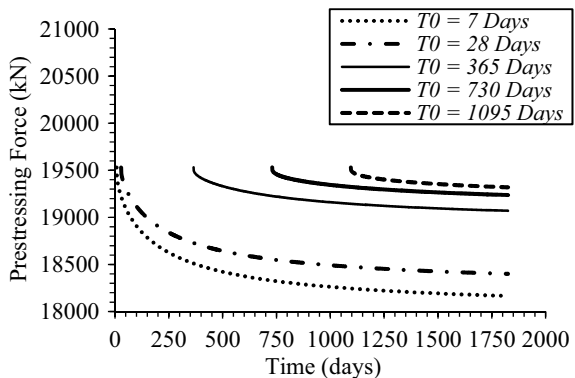
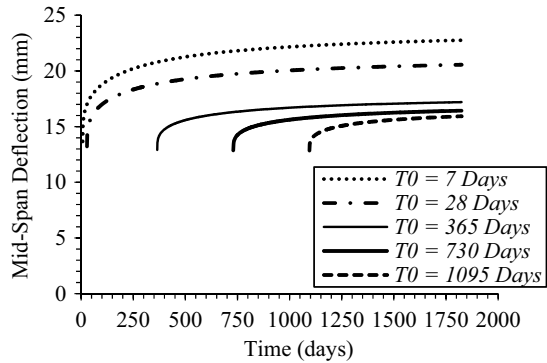


Fig. 7 Mid-span deflection versus time [11]



3.4 Aggregate-Cement Ratio

A concrete mix usually has 70–75% of aggregate content by volume. Due considerations should be given in the selection of shape, size and proportion of coarse and fine aggregates in order to minimize the total specific area occupied by the aggregates. Therefore, correct proportioning of coarse aggregate, fine aggregate and cement is highly desirable. Keeping the total volume of the design mix unchanged, concrete creep and shrinkage deformation decreases as the aggregate-cement ratio (a/c) increases due to the high stiffness of the aggregates. In other words, in a lean concrete (i.e. where a/c ratio is high), cement mortar per unit surface area of the aggregate is less. Therefore, due to the reduced lubrication effect, considerable restraint will occur during the mobility of aggregates. On the contrary, in a rich concrete (i.e. where a/c ratio is low), the lubricating effect is more due to the large amount of cement mortar. Consequently, less restraint will occur during the mobility of aggregates. Hence, as the aggregate-cement ratio (a/c) increases, prestress loss and deflection reduces.

Figures 8 and 9 present the variations of prestress force and mid-span deflection with time for different values of a/c ratio. From Fig. 8, it can be seen that, after 5 years, reduction in prestress force was maximum when $a/c = 2$ (10.31%) and minimum when $a/c = 6$ (7.76%). Similarly, from Fig. 9, it can be noticed that, after 5 years, the maximum mid-span deflection corresponded to $a/c = 2$ (35.29 mm), and the minimum corresponded to $a/c = 6$ (29.59 mm).

3.5 Cement Type

Three cement classes are described in EN 1992-1-1 [7], namely Class R, Class S, and Class N, where symbols R, S, and N denote rapid, slow and normal hardening cement, respectively. The setting rates of different concrete mixes differ due to variations in the fineness of cement particles as well as due to the use of chemical and mineral

Fig. 8 Prestress force versus time [11]

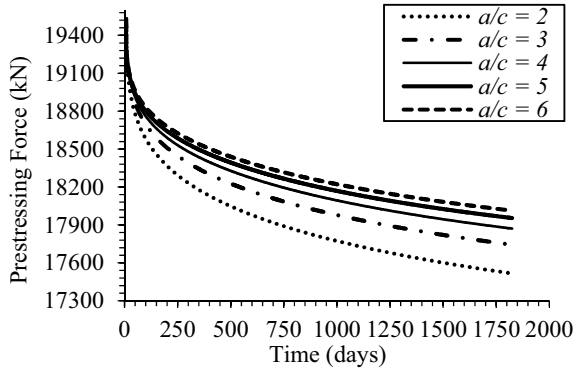
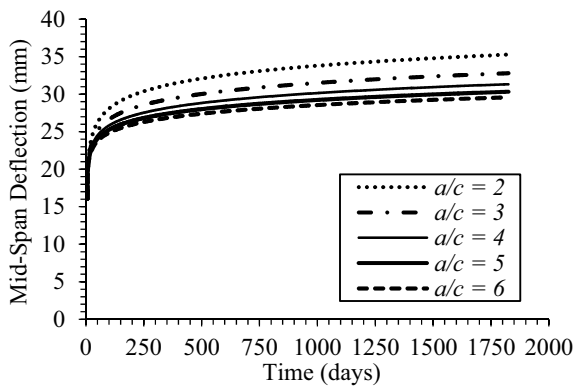


Fig. 9 Mid-span deflection versus time [11]



admixtures. As per EN 1992-1-1 [7], different values of coefficient s have been assigned to different cement types, which in turn are used to determine the mean concrete cylinder strength $f_{cm}(t)$ and secant modulus of elasticity of concrete $E_{cm}(t)$ at time t . In addition, the coefficient s is used to calculate the effect of cement adjusted age of concrete $\beta(\tau_0^c)$ on the notional creep coefficient (θ_0). Moreover, the coefficient s is also used to calculate basic drying shrinkage strain $\varepsilon_{cd,0}$. Although, in the early days, the strength of concrete that uses rapid hardening cement would be two to three times that of concrete that uses normal hardening cement, however, the long-term strength of concrete that uses slow hardening cement could still be larger than other types.

Figures 10 and 11 present the variations of prestress force and mid-span deflection with time for different types of cement. From Fig. 10, it can be seen that, after 5 years, reduction in prestress force was maximum for rapid hardening cement (6.99%) and minimum for slow hardening cement (5.94%). Similarly, from Fig. 11, it can be noticed that, after 5 years, the maximum mid-span deflection corresponded to slow hardening cement (24.52 mm), and the minimum corresponded to rapid hardening cement (22.76 mm).

Fig. 10 Prestress force versus time [11]

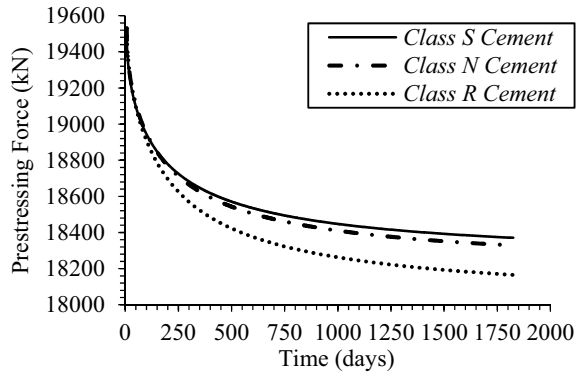
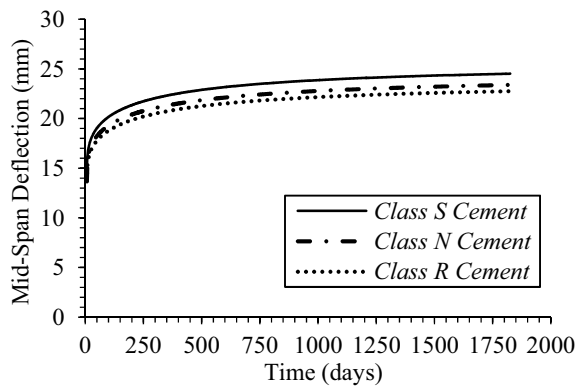


Fig. 11 Mid-span deflection versus time [11]



3.6 Concrete Compressive Strength

In this investigation, the compressive strength of concrete (f_{ck}) varied from 45 to 85 MPa. Generally, the elastic modulus of concrete (E_c) linearly increases with the compressive strength of concrete. Therefore, with the increase in f_{ck} , there will be less reduction in prestress force and deflection with time.

Figures 12 and 13 present the variations of prestress force and mid-span deflection with time for different values of compressive strength of concrete (f_{ck}). From Fig. 12, it can be seen that, after 5 years, reduction in prestress force was maximum for $f_{ck} = 45$ MPa (8.20%) and minimum for $f_{ck} = 85$ MPa (6.03%). Similarly, from Fig. 13, it can be noticed that, after 5 years, the maximum mid-span deflection corresponded to $f_{ck} = 45$ MPa (26.02 mm), and the minimum corresponded to $f_{ck} = 85$ MPa (19.89 mm).

Fig. 12 Prestress force versus time [11]

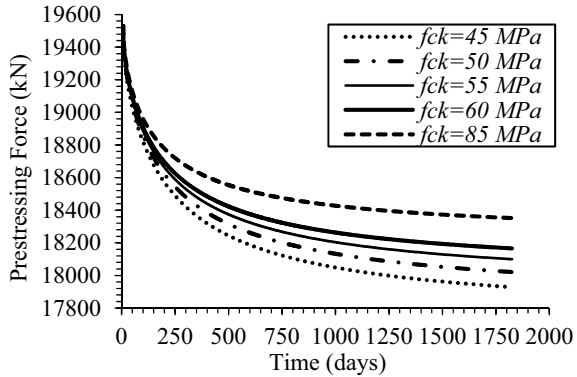
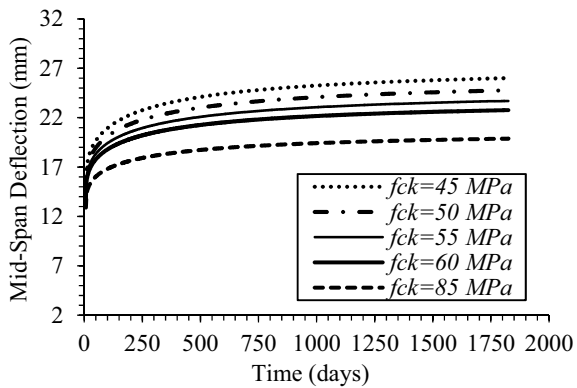


Fig. 13 Mid-span deflection versus time [11]



3.7 Ambient Temperature

The increase in ambient temperature has the following main effects on concrete creep and shrinkage:

- (a) It increases the hydration rate of cementitious gel, which in turn increases the hardening of concrete and reduces concrete creep development rate.
- (b) It accelerates the formation and breaking of bonds between cementitious gel particles due to the creep effect, which in turn will accelerate the concrete creep development rate.
- (c) It increases the surface evaporation rate, which in turn will significantly increase the drying shrinkage rate.

The dominance of the above actions depends on temperature increment. For small temperature increments, action (b) dominates, while for large temperature increments, action (a) dominates. However, action (c) will contribute to both small and large temperature increments. EN 1992-1-1 [7] permits the use of its provisions for a temperature range varying from -40 to $+40$ °C. The compressive strength and

Fig. 14 Prestress force versus time [11]

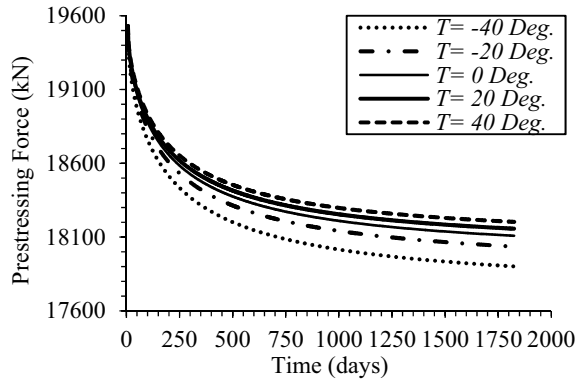
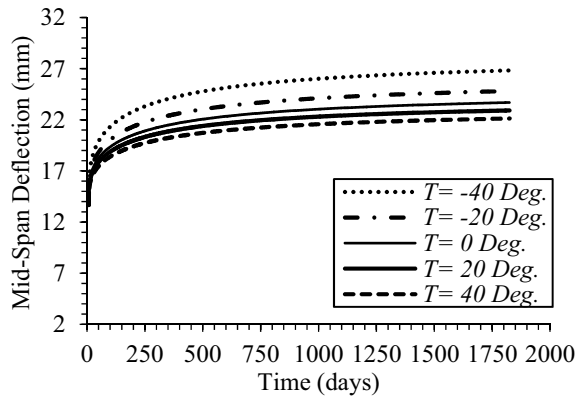


Fig. 15 Mid-span deflection versus time [11]



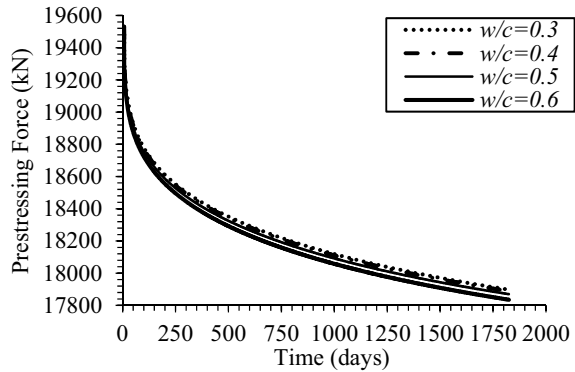
stiffness of concrete members increase with the increase of ambient temperature. Consequently, concrete member will observe less volumetric deformation, and there will be reduced prestress loss and deflection. Figures 14 and 15 present the variations of prestress force and mid-span deflection with time for different values of ambient temperature (T). From Fig. 14, it can be seen that, after 5 years, reduction in prestress force was maximum for $T = -40\text{ }^{\circ}\text{C}$ (8.34%) and minimum for $T = 40\text{ }^{\circ}\text{C}$ (6.79%).

Similarly, from Fig. 15, it can be noticed that, after 5 years, the maximum mid-span deflection corresponded to $T = -40\text{ }^{\circ}\text{C}$ (26.83 mm), and the minimum corresponded to $T = 40\text{ }^{\circ}\text{C}$ (22.14 mm).

3.8 Water-Cement Ratio

Both creep and shrinkage phenomena are directly affected by the water-cement ratio of the concrete mix. Keeping the total volume of the concrete mix unchanged, with

Fig. 16 Prestress force versus time [11]



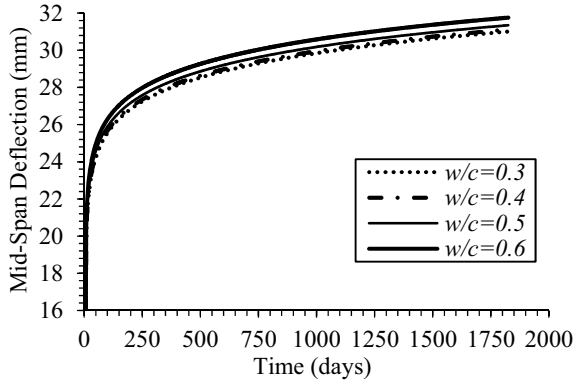
the increase in w/c ratio, the size of capillaries within the concrete matrix increases. Subsequently, additional water will then move towards the gel pores, reducing the density of cementitious gels. As a result, concrete strength reduces appreciably when the value of the w/c ratio reaches 0.60. When water is added to the concrete mix, the solid framework of C–S–H will undergo compression to balance the capillary tension due to adsorbed water, which will lead to volumetric contraction of the concrete member. As the C–S–H structure itself exhibits very little creep, thus, the main factor responsible for the creep effect is the movement of interlayer water, which contributes to the basic creep phenomenon. Therefore, with the increase in w/c ratio, water will start moving to the outside surface, and the large porosity so caused will provide more creep deformability to the concrete matrix. Hence, with the increase in the w/c ratio, there will be more prestress loss and deflection.

Figures 16 and 17 present the variations of prestress force and mid-span deflection with time for different values of w/c ratio. From Fig. 16, it can be seen that, after 5 years, reduction in prestress force was maximum when $w/c = 0.6$ (8.68%) and minimum when $w/c = 0.3$ (8.35%). Similarly, from Fig. 17, it can be noticed that, after 5 years, the maximum mid-span deflection corresponded to $w/c = 0.6$ (31.76 mm), and the minimum corresponded to $w/c = 0.3$ (31.01 mm).

3.9 Prestress Force

In this investigation, the applied prestress force was varied by two approaches. In the first approach, the total cross-sectional area of tendons (A_p) was kept constant, which was equal to 0.015 m², and the ratio of effective prestress (f_{pe}) to yield stress of tendon (f_{py}) was varied from 0.50 to 0.90. On the contrary, in the second approach, f_{pe}/f_{py} was kept constant equal to 0.70, and the total cross-sectional area of tendons (A_p) was varied from 0.010 to 0.030 m². In this study, tensile and compressive stresses of concrete were duly checked and kept under the permissible limits given in EN 1992-1-1 [7]. The relaxation in the tendon is generally directly proportional to $f_{pe}/$

Fig. 17 Mid-span deflection versus time [11]



f_{py} ratio. With the increase of f_{pe}/f_{py} ratio, relaxation losses will be higher. However, as the effect of prestressing is opposite to those of creep and shrinkage, therefore, overall, less prestress loss was observed. Further, with the increase of f_{pe}/f_{py} ratio, overall deflection at mid-span will decrease, as it will counteract sagging due to dead and live loads.

Figures 18 and 19 present the variations of prestress force and mid-span deflection with time for different values of f_{pe}/f_{py} and A_p . From Fig. 18, it can be seen that, after 5 years, reduction in prestress force was maximum when $f_{pe}/f_{py} = 0.5$ (9.41%) and minimum when $f_{pe}/f_{py} = 0.9$ (6.67%). Similarly, from Fig. 19, it can be noticed that, after 5 years, the maximum mid-span deflection corresponded to $f_{pe}/f_{py} = 0.5$ (31.7 mm), and the minimum corresponded to $f_{pe}/f_{py} = 0.9$ (20.65 mm). From Fig. 20, it can be seen that, after 5 years, reduction in prestress force was maximum when $A_p = 0.03 \text{ m}^2$ (9.70%) and minimum when $A_p = 0.01 \text{ m}^2$ (6.01%). Similarly, from Fig. 21, it can be noticed that, after 5 years, the maximum mid-span deflection corresponded to $A_p = 0.01 \text{ m}^2$ (29.94 mm), and the minimum corresponded to $A_p = 0.03 \text{ m}^2$ (1.98 mm).

Fig. 18 Prestress force versus time [11]

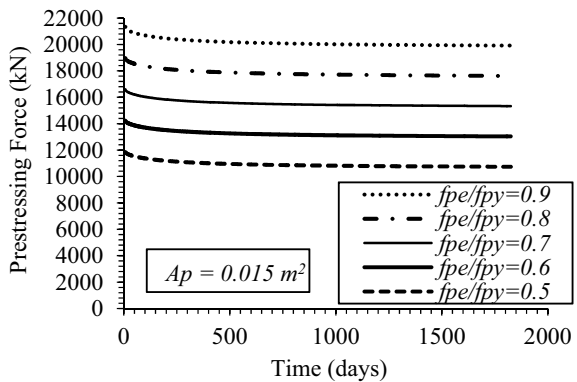


Fig. 19 Mid-span deflection versus time [11]

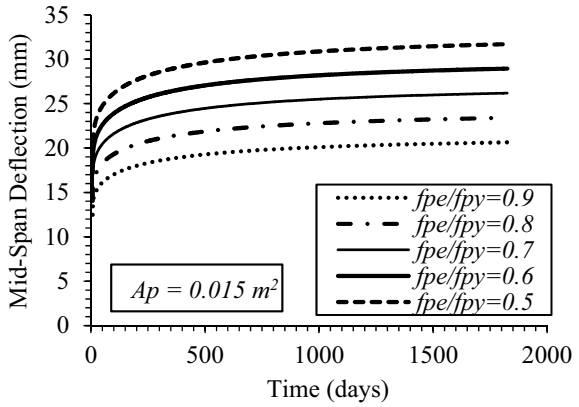


Fig. 20 Prestress force versus time [11]

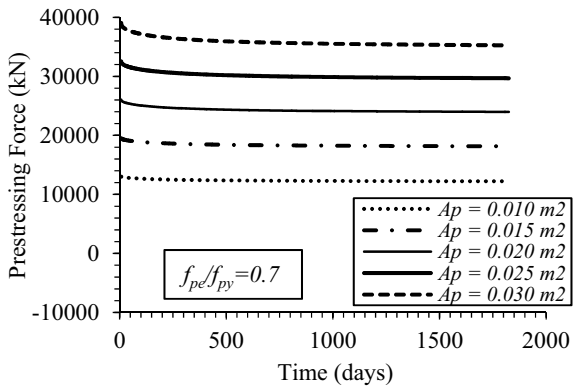
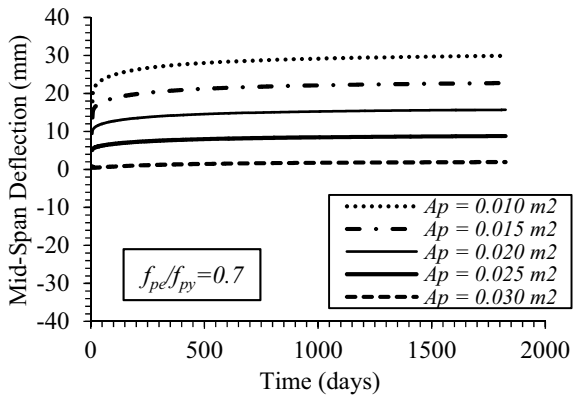


Fig. 21 Mid-span deflection versus time [11]



3.10 Cross-Section Type

Three types of cross-sections were studied in this study, namely cross-section with corrugated steel webs (case 1), cross-section with flat steel webs (case 2) and cross-section with flat concrete webs (case 3). Each of these cross-sections was analysed for two types of load combinations, i.e. DL and DL+LL. Figures 22 and 23 present the deflected shape of real bridges of span length equal to 30 m and different cross-section types for DL and DL+LL, respectively. It can be seen that each cross-section has two curves, the lower curve corresponds to the instantaneous deflection on the seventh day, while the upper curve corresponds to the final deflection after 5 years. It can clearly be seen from Fig. 22, that at instantaneous loading, the cross-section with flat steel web has hogging along the entire length. However, after 5 years, sagging can be seen at the mid-span due to long-term deflection. On the other hand, cross-sections with corrugated steel web and concrete web have sagging almost along the whole span both after seven days as well as after 5 years. The total long-term mid-span deflections after 5 years for cases 1, 2, and 3, when subjected to only DL, were 3.55 mm, 0.78 mm, and 7.31 mm, respectively.

Fig. 22 Deflection versus span for DL [11]

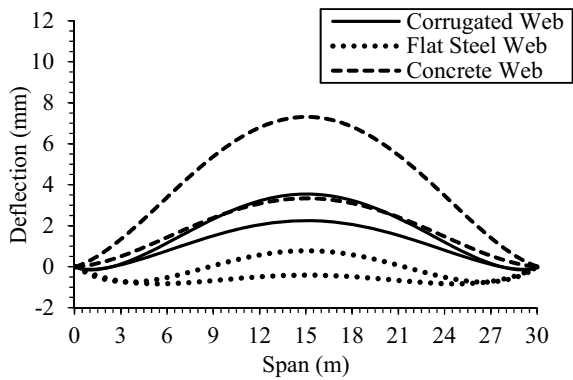


Fig. 23 Deflection versus span for DL+LL [11]

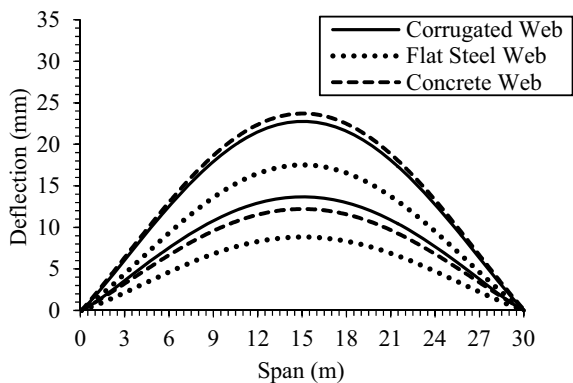


Figure 23 presents the deflected shapes of bridges with different cross-sections along their entire spans for DL+LL combination. The total long-term mid-span deflections after 5 years for cases 1, 2, and 3, when subjected to DL+LL, were 22.76 mm, 17.53 mm, and 23.72 mm, respectively.

Figures 24 and 25 present the variations of mid-span deflection with time for real bridges of span length equal to 30 m and different cross-section types for DL and DL+LL, respectively. When only subjected to DL, the mid-span deflection was maximum for cross-section with concrete web and minimum for cross-section with flat steel web. However, when subjected to DL+LL, the difference between the mid-span deflections of cross-sections with concrete and corrugated steel webs became negligible. The net long-term mid-span deflections (i.e. total deflection—instantaneous deflection), after 5 years, for cases 1, 2, and 3, when subjected to DL+LL, were 9.08 mm, 8.68 mm, and 11.50 mm, respectively.

For different cross-sections, the variations of prestress force in tendons with time for DL and DL+LL are shown in Figs. 26 and 27, respectively. Referring to only DL case, the maximum prestress loss, after 5 years, was found corresponding to

Fig. 24 Mid-span deflection versus time for DL [11]

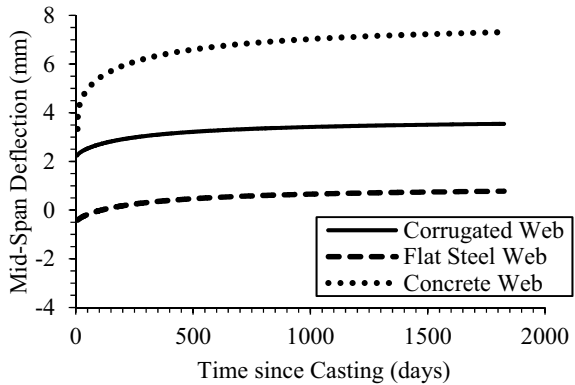


Fig. 25 Mid-span deflection versus time for DL+LL [11]

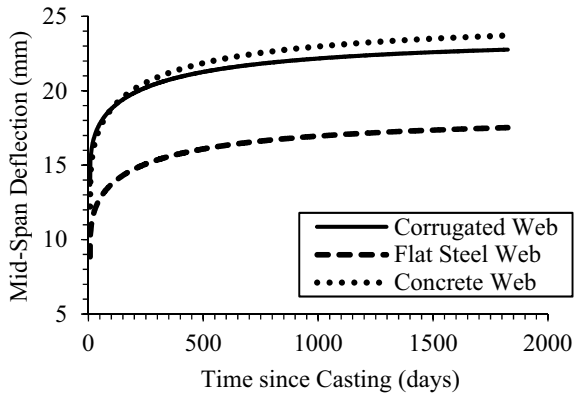


Fig. 26 Prestress force versus time for DL [11]

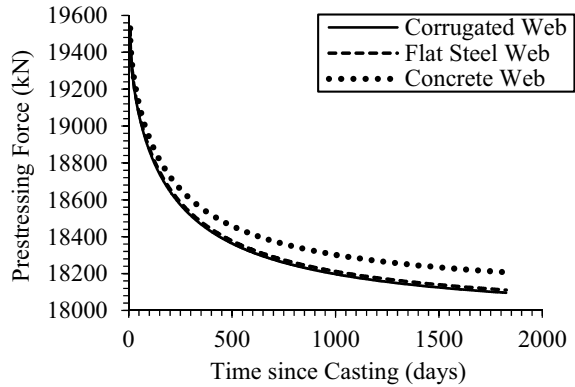
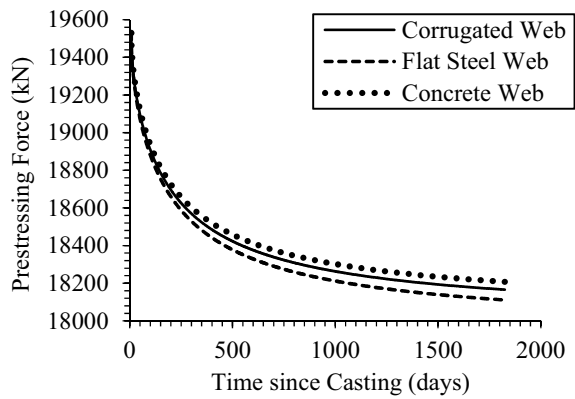


Fig. 27 Prestress force versus time for DL+LL [11]



the corrugated steel web, which was equal to 7.34%. However, when subjected to DL+LL, the maximum prestress loss, after 5 years, was found corresponding to the flat steel web, which was equal to 7.26%. After 5 years, and for DL+LL case, the difference between the prestress losses became negligible for cross-sections with corrugated steel web and concrete web.

3.11 Effects of Creep, Shrinkage, and Tendon Relaxation

The effects of creep, shrinkage, and relaxation were individually considered on a real corrugated steel web bridge for a period of 5 years.

Figures 28 and 29 present the variations of prestress force and mid-span deflection with time for individual and combined effects of creep, shrinkage, and relaxation. With regard to prestress loss, it can be noted that the effect of creep was significantly smaller than the combined effects of creep and shrinkage. After including the effect

of shrinkage, the cumulative action of creep and shrinkage significantly enhanced the prestress loss and deflection of the bridge. It is evident that after including the effect of relaxation negligible changes were observed for both prestress loss and deflection of the bridge. It was primarily due to the fact that the effect of relaxation was relatively small compared to the overall effects of concrete creep and shrinkage. From Fig. 28, it can be noted that the values of prestress loss, after 5 years, corresponding to creep, creep+shrinkage, and creep+shrinkage+relaxation were 2.60%, 7.16%, and 7.16%, respectively. Similarly, from Fig. 29, it can be noted that the values of mid-span deflection, after 5 years, corresponding to creep, creep+shrinkage, and creep+shrinkage+relaxation were 12.17 mm, 13.15 mm, and 13.15 mm, respectively.

Fig. 28 Prestress force versus time [11]

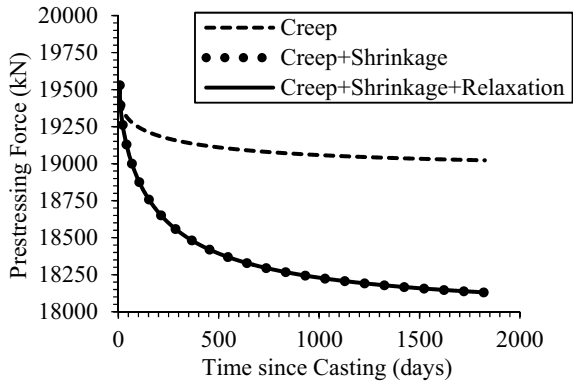
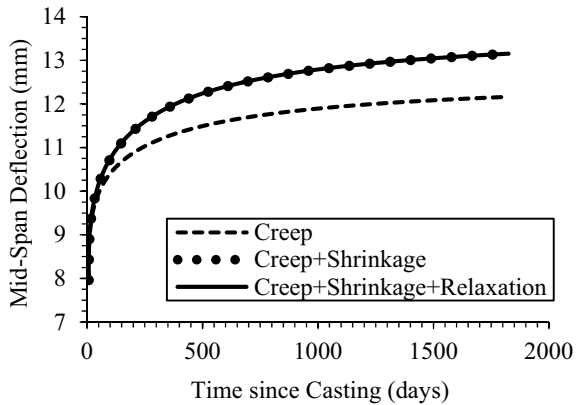


Fig. 29 Mid-span deflection versus time [11]



4 Conclusions

The main conclusions drawn from this investigation are as follows:

- The long-term deflection of PCBCSW is larger than the identical bridge with flat steel web and comparable to those with the concrete web.
- Long-term prestress loss of PCBCSW was similar to those of conventional bridges.
- The influence of shrinkage is much more pronounced compared to the influences of creep and tendon relaxation.
- Age of concrete at first load application, relative humidity and temperature of the surrounding atmosphere, aggregate type, and compressive strength of concrete are the most governing parameters which influence the long-term behaviour of prestressed concrete bridge with corrugated steel webs (PCBCSW).
- Due to low axial stiffness of corrugated steel webs, influence of applied prestress force is significant on the long-term behaviour of PCBCSW.

Acknowledgements The work reported in this paper was supported by the Research Grants Council (RGC) of the Hong Kong Special Administrative Region (RGC Project HKU 710111E).

References

1. ACI 209.2R (2008) Guide for modelling and calculating shrinkage and creep in hardened concrete
2. Australian Standard (2009) AS 3600. Concrete structures
3. Bazant ZP (2001) Criteria for rational prediction of creep and shrinkage of concrete. *ACI Concr Int* ACI 23:38–39
4. Buildings Department, Hong Kong (2013) Code of practice for structural use of concrete
5. Chen X (2016) Full-range behaviour of prestressed concrete bridges with corrugated steel webs. HKU Theses Online
6. Chen XC, Pandey M, Bai ZZ, Au FTK (2017) Long-term behavior of prestressed concrete bridges with corrugated steel webs. *J Bridg Eng* 22(8):04017040
7. EN:1992-1-1 (2004) Eurocode 2: Design of concrete structures—Part 1–1: General rules and rules for buildings
8. EN:1991-2 (2003) Eurocode 1: Actions on structures—Part 2: Traffic loads on bridges
9. Highways Department, Hong Kong (2013) Structures design manual for highways and railways
10. Machimdamong C, Watanabe E, Utsunomiya T (2004) Analysis of corrugated steel web girders by an efficient beam bending theory. *Struct Eng Earthq Eng* 21(2):131s–142s
11. Pandey M (2015) Time-dependent behaviour of prestressed concrete bridge with corrugated steel web. HKU Dissertation
12. Pandey M, Au FTK (2022) Time-dependent behaviour of prestressed concrete bridge with corrugated steel webs—experimental and numerical investigations. In: First Indian structural steel conference, IIT Hyderabad, India

Module Site Installation and Anchorage—Case Study



Parthasarthi Burman, Sourav Biswas, and Munish Dhawan

Abstract Module concept construction, common in offshore projects, is one of the most advanced forms of construction approach currently being implemented in large scale on various onshore Oil and Gas and Chemical projects. The concept involves fabrication, assembly and pre-commissioning at offsite location (commonly known as Module Fabrication yard) where modularized process blocks are constructed with 95% steel and piping, 85% of electrical and 95% instruments on Module. Modules, once fabricated at Module Fabrication Yard, are transported to the site through barge (marine transportation, wherever applicable). Modules are loaded onto/off loaded from barge using Self-Propelled Module Transporter (SPMT). Once modules are offloaded, they are transported to the site thru SPMT for “setting procedure” where modules are rested on pedestal and “anchored”. This paper discusses on various methods of Module anchoring which may vary based on “Module type”, “site environment condition”, “constructability preferences” highlighting design assumptions, challenges (constructability, if any).

Keywords Modules · Anchorage · SPMT

P. Burman (✉) · S. Biswas · M. Dhawan
Fluor Daniel India Pvt. Ltd., Gurugram, India
e-mail: partha.s.burman@fluor.com

S. Biswas
e-mail: sourav.biswas@fluor.com

M. Dhawan
e-mail: munish.dhawan@fluor.com

© The Author(s), under exclusive license to Springer Nature Singapore Pte Ltd. 2023
M. Madhavan et al. (eds.), *Proceedings of the Indian Structural Steel Conference 2020*
(Vol. 2), Lecture Notes in Civil Engineering 319,
https://doi.org/10.1007/978-981-19-9394-7_26

333

1 Introduction

Module concept construction, common in offshore projects, is one of the most advanced forms of construction approach currently being implemented in large scale on various onshore Oil and Gas and Chemical projects. The concept involves fabrication, assembly and pre-commissioning at offsite location (commonly known as Module Fabrication yard) where modularized process blocks and pipe racks are constructed with 95% steel and piping, 85% of electrical and 95% instruments on module. All cabling, wiring, testing and loop check of a process block are performed at Module Fabrication yard with “Plug and Play” at site.

Modules, once fabricated at Module Fabrication yard, are transported to the site through barge/marine transportation, wherever applicable. Modules are loaded onto/off loaded from barge using Self-Propelled Module Transporter (SPMT). Once modules are offloaded, they are transported to the site thru SPMT for “setting procedure” where modules are rested on pedestal and “anchored”. This paper discusses on various methods of Module anchoring which may vary based on “Module type”, “site environment condition”, “constructability preferences”.

Anchorage is defined as connection between superstructure elements (i.e., base plate) and substructure elements (i.e., pedestal). Anchoring provides a medium for transmission of loads from the structure to the foundation and thus to the soil. Anchoring process for modules is different from stick-built structure as concrete or foundation casting is completed significantly earlier than steel installation, and also, pedestal surface may not have protrusion, unlike stick built structures to avoid hindrance in SPMT movement during module installation.

2 Objective

The objective of this case study is to begin a thought process of a possible solution for design of Module anchorage during proposal or Front-End Engineering Design (FEED). This study summarizes innovative concepts applied in different executed projects which varies based on environmental condition and defined acceptable limits of tolerance. The study also recommends various checkpoints for each case which shall be kept in mind or discussed and closed appropriately with construction and logistics prior to implementation of the concept.

3 Module Anchorage Case

3.1 *Welding of Module Base Plate to Embed Plate*

3.1.1 Connection Detail

Welding of module base plate to steel embedded plate on top of pedestal is one of the common methods of anchorage. This concept may/shall be applicable to all modules—from light-weight pipe racks to large process modules. Site welding may not be preferred if steel is galvanized with zinc coating due to damage to galvanization. Touch-up painting shall be required for painted steel structure after welding of the base plate to embed steel plate (Fig. 1).

During setting of concrete, anchor rods are placed and casted with the concrete with projection. Embed steel plate with over-sized hole is placed on top of pedestal carefully such that bolt hole on embed aligns with anchor rod. After placing the steel plate, the projected anchor rod above steel plate is cut off and embedded anchor rod is connected with the steel plate through welding at bolt holes' location. Welded connection is grinded to make the surface smooth. Prior to arrival of the module, steel plate is further grinded as per vertical alignment measurement received from the fabrication yard. The vertical alignment is necessary to level the module with adjacent modules. Non-shrink grout provided through grout holes on steel plate (Fig. 2).

Upon arrival, module is placed on pedestal carefully using SPMT. Column base plate is welded with embed plate on two sides as shown in Fig. 3, and remaining edges are seal welded.

Fig. 1 Site photograph showing welding anchoring method



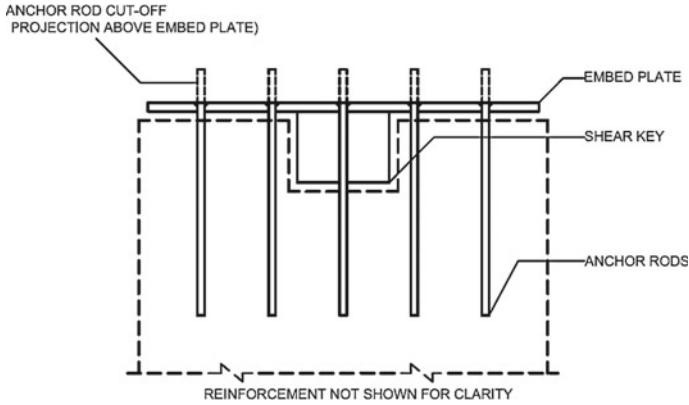


Fig. 2 Embed plate connection with concrete pedestal

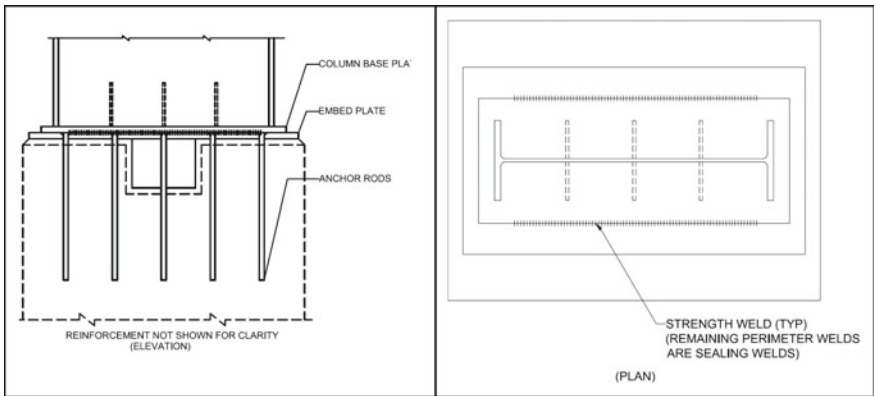


Fig. 3 Module column base plate connection with embed plate

3.1.2 Check Points

Following points shall be considered during thought process and prior to implementation of the concept for construction favorable and cost-efficient implementation.

- (a) *Steel Coating*: Welding does not go along with galvanization; hence, coating philosophy may drive module anchoring method.
- (b) *Shim or Vertical alignment*: Site effort and cost shall be evaluated to finalize the option of grinding embedded steel plate to achieve vertical alignment or leveling. Alternate options may be worked out with construction team to support cost-efficient execution, if applicable.
- (c) *High Seismic Zone*: Strength and applicability of embedded anchor rods and its connection with embed plate shall be validated for high seismic site environmental condition.

- (d) *Accessibility*: Engagement with construction team to determine accessibility requirement or challenges for connection of internal column base plate to embedded plate.

3.2 Shear Lug Concept

3.2.1 Connection Detail

The concept of shear lug anchoring can be applied to all type of modules from pipe rack to very large process structures. The method provides sufficient erection tolerances for the construction and can be a choice of anchoring for steel foundation system, i.e., steel pile cap and piles. However, this system can also be implemented in concrete foundation system by installing it on embedded plate at top of the pedestal (Fig. 4).

Module column is placed on top of steel plate or embedded plate in case of concrete pedestal through SPMT. Shim plate is placed between the base plate and pile cap plate with its thickness determined as per vertical alignment data from the fabrication. Once shim plate is provided and leveling is achieved, shear lugs are placed at location and field welded to steel cap plate (Fig. 5). The perimeter around shear lug is closed with a seal plate, and gap between shear lug and structural column is filled with sealant. Shear lug is installed on cap plate maintaining a gap of at least 3 mm in all directions from structural base plate.

Fig. 4 Site photograph showing shear lug module anchorage



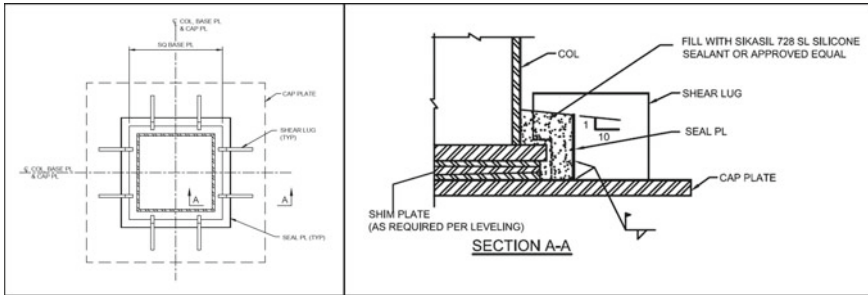


Fig. 5 Shear lug detail and connection with embed or steel cap plate

3.2.2 Check Points

Following points shall be considered during thought process and prior to implementation of the concept for construction favorable and cost-efficient implementation.

- (a) *Pedestal Size*: Large concrete pedestal shall be required owing to embed plate dimension to accommodate shear lug.
- (b) *Accessibility*: Engagement with construction team to determine accessibility requirement or challenges for connection of internal column base plate with embedded plate.
- (c) *High Seismic Zone*: Strength and applicability of embedded anchor rods and its connection with embed plate shall be validated for high seismic site environmental condition. This is only applicable when shear lug concept is used on concrete foundation.

3.3 Coupler Anchor Bolt

3.3.1 Connection Design

The concept of coupler anchor bolt has been implemented for pipe rack modules and light-weight process modules. Its efficacy for very large module shall be checked and designed for. This concept is implemented to enable SPMT movement over pedestal, and thus, anchor rods cannot be left projected like stick built structures. Anchorage using coupling nut may be a preferred option for galvanized coated steel. However, this concept has limitation if steel foundation system is used (Fig. 6).

Anchor rod in this concept can be divided into two parts: permanent and temporary. During the casting and setting of concrete pedestal/foundation, coupler and embedded (or permanent) anchor rod is placed and set. Top of coupler shall flush with top of pedestal. Coupler is covered with a temporary plate and “temporary” bolt assembly to hold the plate (see Fig. 7).



Fig. 6 Site photograph of coupler anchor bolts

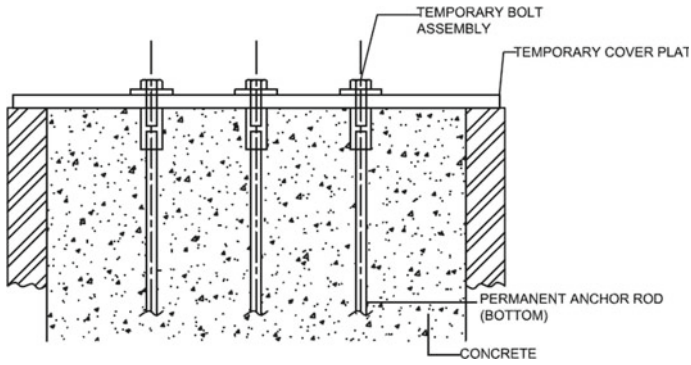


Fig. 7 Coupler anchor bolt details

Prior to the arrival of the module, the temporary plate and bolts are removed to provide smooth surface on top of pedestal and enable SPMT movement. Structural column/base plate is placed over the pedestal using SPMT. Module column/base plate is placed over concrete pedestal using SPMT, and upper anchor bolt is tightened using double nut and square washer. Washer is field welded to the base plate (see Fig. 8). Grouting is done through grout hole provided in the base plate.

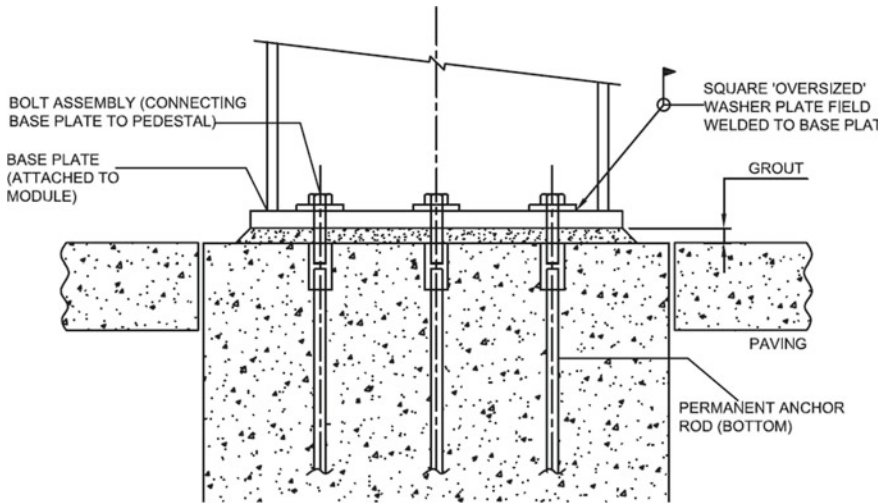


Fig. 8 Module column and base plate connection using coupler anchor bolt

3.3.2 Check Points

Following points shall be considered during thought process and prior to implementation of the concept for construction favorable and cost-efficient implementation.

- (a) *Erection tolerance*: Alignment with the construction team on challenges of erection tolerance for upper anchor bolts once modules are placed.
- (b) *Vertical alignment and Shims*: Alignment with the construction on how vertical alignment shall be achieved to level the module per data from the fabrication yard.
- (c) *Accessibility*: Engagement with construction team to determine accessibility requirement or challenges for connection of internal column.
- (d) *High Seismic Zone*: Strength and applicability of coupling nut shall be validated for high seismic site environmental condition.

3.4 Spherical Bearing System

3.4.1 Connection Detail

The concept is used in structural applications to accommodate thermal, seismic and mechanical expansion and rotation. This option may be applied to site with extreme temperature variation. The basic assumption in structural design is to consider zero tension at column support location (Fig. 9).



Fig. 9 Site photograph for bearing assembly module anchorage

Spherical bearing system is proprietary and procured from specialized vendor such as Lubron, etc. The system accommodates thermal, seismic, mechanical expansion and rotation. They have exceptionally low coefficient of friction and high load capability for heavy duty and structural application. These bearings are designed to accommodate unidirectional and omnidirectional sliding movement and are recommended for applications subjected to limited angular misalignment (Fig. 10).

Elements include

- Concave spherical recess designed to accommodate rotation and angular deflection.
- Sole plate is an upper plate affixed to the superstructure.

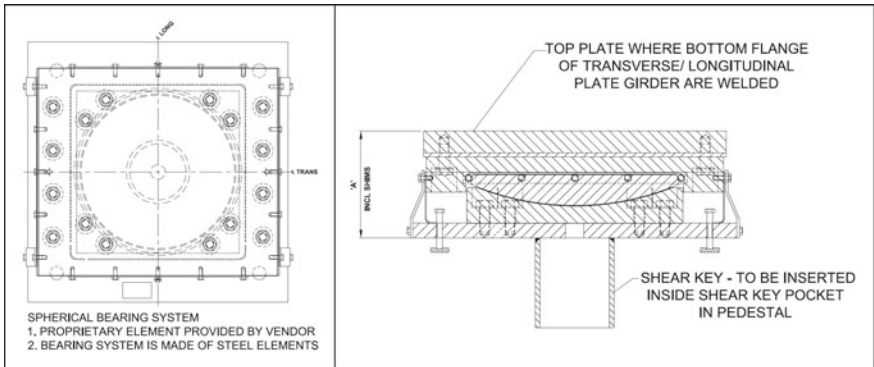
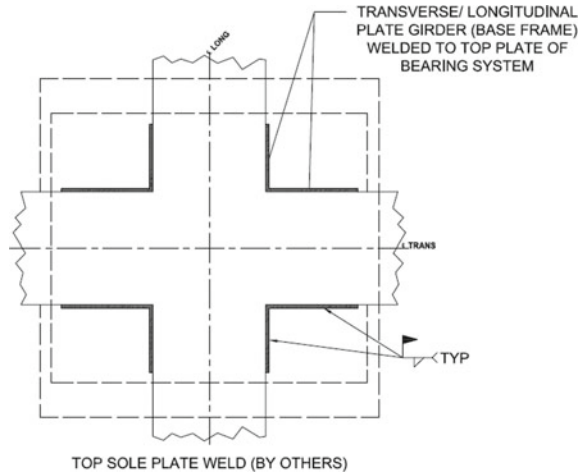


Fig. 10 Bearing assembly detail

Fig. 11 Connection detail between module base and bearing assembly



- Base plate is the lower steel plate which shall be affixed to the supporting substructure.
- Anchor bolts and welded studs for affixing the bearing assembly to the superstructure and supporting substructure.

Spherical bearing system is placed on top of concrete pedestal and connected using welded stud. Module base frame plate girder bottom flange is welded to the bearing plate (see Fig. 11).

3.4.2 Check Points

- Cost*: Bearing system is a proprietary element, and thus, cost evaluation shall be done for most cost-efficient execution.
- Construction tolerance*: Special attention to plate girder deflection during transportation which directly impacts rotational alignment of the bearing system thus may impact shear capacity.
- Structural framing*: Framing of structural system for zero tension at column location.

4 Special Focus

Apart from check points highlighted for each case, few key points shall be considered in thought process and discussed with construction and logistics appropriately and addressed. These are:

- Projection of pedestal above ground may pose a challenge in SPMT movement to install the module. Hence, extent of pedestal above ground shall be worked with construction and/or logistics to minimize impact or hindrance to SPMT movement. As discussed, if SPMT movement is permitted over pedestal, then surface of pedestal shall be smooth without a trace of projected anchor bolts. Pedestal shall be designed for maximum wheel load SPMT under this circumstance.
- For buried or on-grade module, accessibility (challenges) to the internal columns or plate girder bottom for its connection with the foundation shall be discussed and addressed with the construction. Measures such as removable grating at anchoring location can be provided in agreement with the construction team. A special attention shall be given on opening dimension for proper accessibility to weld or bolt the module base. In design model, opening in grating shall be represented as obstruction volume in the beginning of the project so that other disciplines may not place their elements at same location.
- For cost-efficient execution and to align with the project goals, focus shall be on minimum site work and maximum site safety to reap maximum benefit of modularization.

5 Summary

The section summarizes the detail of the projects where each case of anchorage was implemented.

Case	Site condition	Type of modules	Type of foundation	Cost elements
1. Coupler anchor bolts	1. Seismic—no 2. Temperature variation—applicable	1. Pipe rack modules 2. Large modules 3. Process modules are buried	Concrete	1. Anchor bolts 2. Couplers 3. Temporary plates 4. Temporary cover bolts
2. Welding	1. Seismic—no 2. Temperature variation—applicable	1. Pipe rack modules 2. Large modules 3. Elevated base frame	Concrete	1. Anchor rods/ embedded studs 2. Embed plate 3. Site welding

(continued)

(continued)

Case	Site condition	Type of modules	Type of foundation	Cost elements
3. Shear lug	1. Seismic—yes 2. Temperature variation—applicable	1. Pipe rack modules 2. Large modules 3. Elevated base frame	Steel	1. Shear lugs 2. Sealant 3. Site welding
4. Spherical bearing system	1. Seismic—no 2. Temperature variation—applicable	1. Pipe rack modules 2. Large modules 3. Elevated base frame	Concrete	1. Bearing system (proprietary) 2. Site welding

6 Conclusion

The intent of this case study is to share different approaches for the design of module base plate to the foundation connection based on its application and implementation in various projects. Prior to detail engineering phase or during FEED, these approaches may be reviewed to identify the most suitable design applicable to the project based on

- Site environmental condition.
- Construction feasibility and accessibility.
- Cost-efficient execution with minimum site effort.
- Site safety.

Acknowledgements The authors wish to recognize the valuable input provided to this paper by various structural engineers from Fluor Daniel India Private Limited. The authors are also grateful to Structural department manager, Mr. Sandip Gatkhal, for his valuable suggestions.

Behavior of Pumpable Recycled Aggregate Concrete



K. Vipindasn and B. Rajeevan

Abstract The increase in urbanization has led to the depletion of natural materials and increase in demolition of old structures. By suitably reusing the demolition waste materials, the demand for natural resources can be reduced. This paper aims to find mechanical properties of pumpable concrete made by partially replacing the natural aggregates with recycled concrete aggregates. The study was based on a pumpable M20 grade concrete mix. The tests were conducted on three types of mixes with 0, 25 and 50% of recycled aggregate concrete. It was observed that the compressive, tensile and flexural strength of pumpable concrete made with recycled aggregate showed improved compressive and tensile strengths.

Keywords Aggregate · Pumpable · Concrete · Recycle · Strength

1 Introduction

Due to rapid urbanization, huge amount of natural aggregates and other construction materials are used for the construction of civil structures. The higher demand of materials and the ecological problems of mining of natural aggregates, the availability of natural resources is decreasing very rapidly. The mining, processing and transportation of these aggregates affect the environment adversely. Also, the disposal of demolition waste requires large area of land. If the demolition waste can be reused, the demand of natural aggregates can be reduced to a certain extent. The construction cost can be reduced by reuse of demolition wastes. It is found that the recycled aggregate concrete (RAC) exhibits similar properties as that of natural aggregate.

The particle size of recycled aggregate (RA) is similar to that of natural aggregates (NAs). However, the specific gravity and water absorption of RA and NA are found

K. Vipindasn (✉) · B. Rajeevan
Government College of Engineering Kannur, Kannur, India
e-mail: vipindasn2012@gmail.com

B. Rajeevan
e-mail: rajeevan@gcek.ac.in

© The Author(s), under exclusive license to Springer Nature Singapore Pte Ltd. 2023
M. Madhavan et al. (eds.), *Proceedings of the Indian Structural Steel Conference 2020*
(Vol. 2), Lecture Notes in Civil Engineering 319,
https://doi.org/10.1007/978-981-19-9394-7_27

345

to be different due to the presence of mortar remains in RA. The water absorption of RA was observed to be between 3 and 6%. It was found that the strength of RAC is less than that of NA. The mortar content in RAC ranges from 25 to 65% [1]. The increase in mortar content also increases the water absorption of RAC. The mortar portion of RCA is generally porous in nature due to various reasons such as water–cement ratio and age of parent concrete [2]. The initial water absorption of RA is ten times higher than that of NA.

The density of recycled aggregate (RA) is lesser than that of natural aggregate (NA) due to the higher porous behavior of mortar. RAC is mainly used for non-structural members since the durability and strength of RAC are less than that of concrete made from natural coarse aggregate. For the construction of high-rise structures, high slump mixes are required for pumping and this study aims to check the suitability of developing pumpable concrete with RA.

Xiao et al. [3], Etxeberria et al.[4], Padmini et al. [5], Yin et al. [6], Somna et al. [7] and Ozbakkaloglu et al. [8] found that the strength of RAC reduced with increase in RA content. A marginal increase in strength of concrete was observed with 60% of RAC [9]. The increase in compressive strength with RAC was attributed to the higher water absorption of RAC. In general, the strength reduction was due to the development of cracks in concrete made from RAC. However, it was found that surface treatment enhances the mechanical property of RAC [10–12].

2 Experimental Program

The study explored the possibility of using recycled aggregate (RA) in pumpable concrete. It aims to find the mechanical properties of pumpable concrete using aggregates extracted from demolition wastes. This study includes the collection of RA, testing of materials, mix design, casting and testing of specimens to find the tensile strength compressive strength of pumpable concrete made from RA. A representative image of RA is shown in Fig. 1.

2.1 Materials

Ordinary Portland Cement of 53 grade was used in the present study. The fine aggregates used in the study were river sand and coarse aggregate which conform to IS.383:2016. The fine aggregate falls within grading zone II. Coarse aggregates of size 20 and 10 mm were used to get an optimum 10 mm downsize particle of 35% in coarse aggregate mix. Rheobuild 924 KL was used as superplasticizer with a specific gravity of 1.22. Potable water was used for mixing and curing of concrete specimens. Recycled concrete aggregates of nominal size 20 mm were collected manually from demolition wastes.



Fig. 1 Recycled concrete aggregate

The grading of recycled aggregate (RA) was determined in order to get similar particle size distribution as that of crushed natural aggregate. The RA was directly used for the present study without any treatment or pre-wetting.

2.2 Material Properties

The various tests conducted on aggregates were sieve analysis, water absorption, void ratio, specific gravity and porosity to determine their physical properties. The water absorption of natural aggregate (NA) and recycled aggregate (RA) was different. OPC 53 grade cement showed a specific gravity of 2.85 and an initial setting time of 120 min. The final setting time was 360 min.

From the sieve analysis, it was observed that the fine aggregate lies in the grading zone II and the NA and RA showed similar distribution of particles, and the 10 mm downsize aggregate in NA and RA was 1% and 16%, respectively. According to Indian standards, the 10 mm downsize aggregates should not be less than 25% in 20 mm aggregates. Thus, 10 mm-sized aggregates were also used. From the study of Knaack and Kurama [13], it was observed that the specific gravity of RA decreases with increase in mortar content. The specific gravity of different materials was 2.8 for 20 mm NA, 2.81 for 10 mm NA, 2.65 for 20 mm RA and 2.25 for FA. It was found that the specific gravity of RA was 5.26% lower than that of NA.

Water absorption of aggregate is the minimum amount of water required to make an aggregate to Saturated Surface Dry (SSD) condition. The water absorption of aggregates observed from the study were 0.5% for 20 mm NA, 0.5% for 10 mm NA, 4.61% for RA and 1% for FA. As per Indian standards, the fine aggregate and natural aggregates conform to its recommended water absorption levels. The water absorption of RA was more than ten times that of the natural aggregates. The higher

Table 1 Mix proportions

Mix	Cement (kg)	FA (kg)	RA (kg)	20 mm (kg)	12 mm (kg)
0% RAC	322	618	0	722	482
25% RAC	321	616	295	473	414
50% RAC	320	614	581	221	360

water absorption of RA was due to the mortar content in the aggregates as mentioned in the study of [2].

2.3 Mix Proportions

The present study compared three high slump mixes with RA content 0, 25 and 50%. About 10 mm aggregates were used to get a total of 35% of 10 mm downsize material, since both 20 mm NA and RA were insufficient. From the various trials conducted, it was observed that the water–cement ratio for 150 mm slump of NA used mix was 0.51, 25% RAC-used mix was 0.53 and in 50% RAC mix, the water–cement ratio was 0.55. The final mix for M20 concrete with 150 mm slump is shown in Table 1.

From the final mix, the total weight of mix reduced with increase in RA content that the weight of mix with 25% RAC was reduced by 0.8% and that with 50% RAC was reduced by 1.57%. The increase in RA content reduced the weight of the mix. Slight initial bleeding was observed in whole mixes, but bleeding in RAC-used mix was less than that in natural aggregate-used mix, due to the higher water absorption of RAC.

2.4 Casting of Specimen and Curing

To investigate the mechanical property such as tensile strength and compressive strength of concrete, six cubes of size 150 × 150 × 150 mm were cast to get the 7th and 28th day compressive strength of concrete. The tensile strength of concrete was determined using two indirect methods, namely split tensile strength test and flexural strength test. For determining split tensile strength, three cylinders of size of 150 mm diameter and 300 mm height were cast. Three beams with 150 × 200 × 700 mm were cast to determine flexural strength. The specimens were cast and demolded after 24 h. The specimens were wet cured for 28 days. Figure 2 shows the cast specimens.

Water absorption was considered while mixing of concrete for better mix proportion. If RA is used in the dry state without considering water absorption, RA will absorb water during mixing, casting and setting time, which may lead to development



Fig. 2 Cast specimens

of shrinkage cracks in some cases. For mixes with high slump, generally the water content should be a little bit high and the water absorption of RA reduces the water content in the mix which may lead to a strength increase of concrete as reported by [14].

2.5 Compressive Strength of Specimen

About 150 mm size cubes were used for determining the compressive strength of concrete. Many researchers such as Yin et al. [6], Agrela et al. (2011), Mwasha and Ramnath [15], Xiao et al. [3] and Ozbakkaloglu et al. [16] found that the compressive strength of concrete with RAC was less when compared to normal concrete. In the present study, a 3000 kN capacity compression testing machine (CTM) was used to find the compressive strength of concrete.

2.6 Tensile Strength

Indirect test methods such as split tensile strength test, one-point or two-point loading test on beams were used to determine the tensile strength of concrete. For split tensile strength test, 150 mm diameter and 300 mm length cylinder was used. After curing of cylinder specimens for 28 days, the tensile strength of concrete was determined as per the guidelines mentioned in IS 386:2016.

The flexural strength of RAC was evaluated by beam flexure test using the two-point loading method. Two beams of size 150 × 150 × 700 mm were used for the experiment. After the curing of 28 days, the beams were taken out and were kept

Table 2 Compressive strength of mixes

Mix	7th day strength (MPa)	28th day strength (MPa)
0% RAC	13.33	26.22
25% RAC	14.22	27.33
50% RAC	14.22	27.77

for one hour for surface drying. The flexural strength is expressed as the modulus of rupture of concrete in MPa.

3 Results and Observations

The various test results obtained were analyzed in the following sections.

3.1 Compressive Strength

The compressive strength test results are shown in Table 2. From Table 2, it is observed that with increase in the percentage of recycled aggregate, RAC exhibited higher strength than the ordinary concrete.

From the present study, it was observed that the compressive strength of mixes with recycled aggregates (RAs) was slightly higher than the compressive strength of concrete made with natural coarse aggregates. In particular, the concrete should have achieved a minimum compressive strength of 16.9 N/mm^2 (65% of design compressive strength), but the mix with 0% RAC achieved 50% and mixes with 25 and 50% RAC achieved only 54%. All three mixes failed to achieve a compressive strength of 16.9 N/mm^2 in the 7th day. However, at 28 days all the three specimens reached their respective mean target strength (26.6 N/mm^2). About 0% RCA-used mix exhibited least compressive strength and the mix with 25% RAC exhibited 4.23% higher strength than normal mix. The mix with 50% RAC attained 5.91% higher strength than normal mix. These studies showed that the higher water absorption of RAC will absorb more water from mix and which in turn with the existing mortar remains on RA led to increase in compressive strength.

3.2 Tensile Strength

The split tensile strength of different mixes obtained from experimental study is shown in Table 3.

Table 3 Split tensile strength

Mix	28th day strength (MPa)
0% RAC	3.33
25% RAC	3.36
50% RAC	3.42

Table 4 Flexural strength

Mix	Modulus of rupture (MPa)
0% RAC	3.29
25% RAC	3.47
50% RAC	3.56

As observed from Table 3, there was not much influence of RA on the split tensile strength of concrete. All the specimens showed similar split tensile strength with little variation. However, mix with 50% RAC attained 2.7% higher tensile strength than normal mix.

The flexural strength of each specimen obtained from beam flexure tests is shown in Table 4.

The flexural strength of mixes with RA showed improved values than that of mix without RA. The mix with 25% RAC had 2.43% and mix with 50% RAC had 9.1% more flexural strength than that of mix without RAC. The flexural strength of concrete is 10–20 percentage of compressive strength of mix, and generally, it lies near to 15% for flexural strength test. The flexural strength of mix without RAC is 12.55% of its compressive strength, mix with 25% RAC is 12.70% and mix with 50% RAC is 12.82%, respectively. All the three mixes possessed almost similar characteristics. It was observed that mixes with RA had almost similar flexural strength behavior as that of normal concrete.

4 Conclusions

The following conclusions were drawn from the present study:

1. Water absorption of recycled aggregates (RA) were more than ten times that of natural aggregates due to the presence of mortar remains.
2. Specific gravity of RA was 5.26% less than that of natural aggregate.
3. When RA was used to replace natural aggregates, the density of concrete decreased with increase in RA content and the mix proportioning showed a 0.8% density reduction for each 25% addition of RA.

4. The compressive strength of concrete increased with increase in RA content in concrete. For 25% and 50% RAC mix, the strength increased by 4.23% and 5.91%, respectively.
5. The tensile strength also increased with increase in RA content. All the three mixes exhibited similar range of tensile strength when compared with the compressive strength of mix.

From this study, it is concluded that the recycled aggregate concrete for high slump concrete (pumpable concrete) is a better substitute for natural aggregates. The incorporation of RA to the mix improved the mechanical properties of concrete. Thus, the use of recycled aggregates in concrete with high slump is recommended. This leads to a more sustainable use materials as disposal of demolishing waste is finding difficult nowadays. Based on the present study, replacement of natural coarse aggregates up to 50% with recycled aggregate is recommended without any significant loss in strength.

References

1. Marinkovic SB, Ignjatović IS, Radonjanin VS, Malesev MM (2012) Recycled aggregate concrete for structural use—an overview of technologies, properties and applications. In: Innovative materials and techniques in concrete construction. Springer, Dordrecht, pp 115–130
2. Malesev M, Radonjanin V, Broceta G (2014) Properties of recycled aggregate concrete. *Contemp Mater* 2(5):239–249
3. Xiao J, Li J, Zhang C (2005) Mechanical properties of recycled aggregate concrete under uniaxial loading. *Cem Concr Res* 35(6):1187–1194
4. Etxeberria M, Vázquez E, Marí A, Barra M (2007) Influence of amount of recycled coarse aggregates and production process on properties of recycled aggregate concrete. *Cem Concr Res* 37(5):735–742
5. Padmini AK, Ramamurthy K, Mathews MS (2009) Influence of parent concrete on the properties of recycled aggregate concrete. *Constr Build Mater* 23(2):829–836
6. Yin J, Chi Y, Gong S, Zou W (2010) Research and application of recycled aggregate concrete. In: *Paving materials and pavement analysis*, pp 162–168
7. Somna R, Jaturapitakkul C, Chalee W, Rattanachu P (2011) Effect of the water to binder ratio and ground fly ash on properties of recycled aggregate concrete. *J Mater Civ Eng* 24(1):16–22
8. Ozbakkaloglu T, Gholampour A, Xie T (2017) Mechanical and durability properties of recycled aggregate concrete: effect of recycled aggregate properties and content. *J Mater Civ Eng* 30(2):04017275
9. Nandhini KU, Jayakumar S, Kothandaraman S (2017) Studies of the mechanical and structural properties of concrete with recycled concrete aggregates. In: *AEI 2017*, pp 349–367
10. Katz A (2004) Treatments for the improvement of recycled aggregate. *J Mater Civ Eng* 16(6):597–603
11. Zhang H, Zhao Y, Meng T, Shah SP (2015) Surface treatment on recycled coarse aggregates with nanomaterials. *J Mater Civ Eng* 28(2):04015094
12. Zhang J, Shi C, Li Y, Pan X, Poon CS, Xie Z (2015) Performance enhancement of recycled concrete aggregates through carbonation. *J Mater Civ Eng* 27(11):04015029
13. Knaack AM, Kurama YC (2011) Design of normal strength concrete mixtures with recycled concrete aggregates. In: *Structures congress*, pp 3068–3079

14. Agrela F, Alaejos P, De Juan MS (2013) Properties of concrete with recycled aggregates. In: Pacheco Torgal F, Tam VWM, Labrincha JA, Ding Y, de Brito J (eds) Handbook of recycled concrete and demolition waste. Woodhead Publishing, Oxford
15. Mwashia A, Ramnath R (2018) Manufacturing concrete with high compressive strength using recycled aggregates. *J Mater Civ Eng* 30(8):04018182
16. Ozbakkaloglu T, Gholampour A, Xie T (2018) Mechanical and durability properties of recycled aggregate concrete: effect of recycled aggregate properties and content. *J Mater Civ Eng* 30(2):04017275
17. Proportioning-Guideline ISCM (2019) IS 10262: 2019. Bureau of Indian Standards, New Delhi
18. IS.383:2016, Specification for coarse and fine aggregates. Bureau of Indian Standards, New Delhi

Experimental Investigation on the Enhancement of Ductility in SRC Columns



A. Gautham and Dipti Ranjan Sahoo

Abstract The use of Steel-Reinforced Concrete (SRC) columns in regions of high seismic intensity has been on the rise in the recent decades. SRC columns offer notable improvements in the axial load-carrying capacity, lateral ductility and moment-resisting capacity over conventional reinforced concrete (RC) columns. The presence of the encased structural steel enhances the lateral deformation capacity of the column, while the exterior RC section prevents the encased steel from weathering. The current study is focused on performing an experimental investigation to assess the level of enhancement in the lateral ductility of the SRC columns over their RC counterpart. Two test specimens, one each of SRC and RC sections, were cast together and tested in the laboratory under fully reversed lateral cyclic displacements. The SRC column was designed using the provisions of Euro Code 4 for encased structural components, while the RC section was designed according to IS 456. The materials used in the specimens were M30 grade concrete and Fe500 grade steel for the longitudinal bars. Rolled steel section ISMB100 was adopted as the encased structural steel in the SRC specimen. The transverse reinforcement provided in accordance to IS 13920 with ductile detailing was maintained at the same percentage for both the specimens. The hysteresis response, lateral ductility, energy dissipation and moment contributions of steel and RC sections of the SRC column specimen were compared with those obtained for the RC section. For the same cross-sectional dimensions of the concrete, the level of improvement in the lateral ductility of the SRC column over the RC specimen is compared. From the findings of this study, it was observed that the presence of the encased steel significantly improved the lateral ductility, while the lateral capacity was 50% higher than that of the RC specimen. In terms of energy dissipation potential, the SRC column dissipated 2.5 times more energy than the RC column.

A. Gautham (✉)

Department of Civil Engineering, Indian Institute of Technology Delhi, New Delhi, India
e-mail: gautham.a@nitpy.ac.in

D. R. Sahoo

Department of Civil Engineering, National Institute of Technology Puducherry, Karaikal, India
e-mail: drsahoo@civil.iitd.ac.in

Keywords SRC columns · Encased columns · Cyclic loading · Hysteretic performance

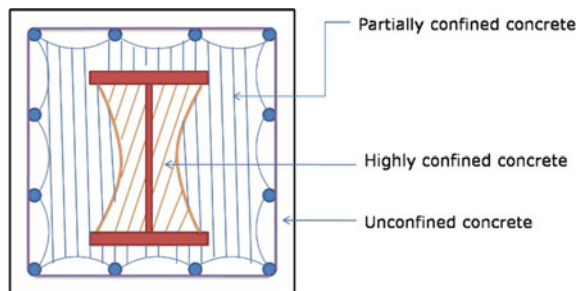
1 Introduction

Multi-storied reinforced concrete-framed structures having irregularities in plan or stiffnesses tend to perform poorly in regions of high seismicity. In such structural configurations, the reinforced concrete frame components are not sufficient to withstand the additional lateral forces and moments acting on them thereby leading to premature local failure of the component which in turn might lead to an overall structural collapse if the irregularity is located at a critical region of the framed structure. In the event of severe earthquakes, the structural components are expected to withstand high lateral forces and have sufficient lateral ductility and seismic energy dissipation capacities.

This structural deficiency of RC components in resisting the high seismic forces has led researchers to look for alternate constructional features. Steel–concrete composite structural components which encompass the merits of both RC and structural steel components have been on the rise as an effective replacement of deficient RC counterparts. The high lateral ductilities, axial load-carrying capacities and greater dissipation of seismic energies have made the Steel-Reinforced Concrete (SRC) columns convenient for use in regions subjected to high and infrequent earthquakes. The composite action of SRC columns ensures that the exterior concrete component protects the encased structural steel section from actions of weathering, while the encased steel sections offer higher lateral ductilities and energy dissipations.

State-of-the-art research on the experimental behavior and numerical predictions of SRC columns subjected to axial loads, eccentric loads, combined axial force and moments have been explored by several research groups [5, 9, 10, 13]. The presence of structural steel in the cross-section introduces an additional zone of confinement in the section. Figure 1 shows the regions of confinement in a cross-section of an encased column. This additional confinement improves the axial and lateral load-carrying capacities of the SRC column components [6, 12, 15].

Fig. 1 Regions of confinement in an SRC column



The validity of the various available design codes for composite structures was tested by El-Tawil and Deirlein [6] and his research group who were able to find unconservative results when using the design guide of ACI while AISC provisions led to an overconservative design. They inferred that EuroCode 4 guidelines best predicted the axial and moment capacities of SRC columns. Experimental investigation on the seismic behavior of the encased column components was carried out by several researchers [2, 4, 14, 15] and validated the claim that SRC columns perform better seismically by having higher lateral displacement capacities, increased shear strengths and greater energy dissipation capacities. The enhanced lateral ductility of these encased columns makes them ideal for regions prone to severe quake loads.

Wang et al. [16] tested SRC column specimens under combined axial and lateral cyclic loading and developed hysteretic models for predicting the cyclic behaviors. Chen et al. [3] conducted experiments on SRC columns subjected to a combined torsion and bending in cyclic loading and concluded that the combination of bending and torsion resulted in plumper hysteresis curves enabling higher dissipation of seismic energies. [11] developed a unified method for prediction of the axial force—moment interaction of SRC columns which was better than the EuroCode 4 predictions for high strength concrete specimens.

Experimental results of an SRC column and a RC column having identical cross-sectional dimensions subjected to gradually increasing slow cyclic displacements are presented in this paper. Both the specimens were cast together in the laboratory using design guidelines of [8] for the RC column and EC4 [7] for the SRC column. Rolled steel section ISMB100 was used as the encased section in the SRC column. The transverse reinforcement ratio was kept constant in both specimens to ensure their identical contribution in the lateral ductility of the specimens. The hysteresis response, failure patterns and modes of failure, lateral ductility and energy dissipation capacities of both specimens were compared.

2 Experimental Program

This section gives a brief description of the overall experimental program which includes preparation of specimen samples, installation of the test setup, placement of strain gauges and sensors and generating the loading protocol for the lateral displacements.

2.1 Description of Test Specimens

Two specimens were designed to be tested in the experimental program. One SRC section is having rolled steel section ISMB100 which accounted for 1.62% of the overall cross-sectional dimension of the column which was 300×300 mm. The other specimen was cast together with the SRC specimen as a plain RCC column having

the same cross-sectional dimensions and material properties. Table 1 gives the values of the material properties of the concrete, reinforcements and structural steels used in the specimens. Both specimens had identical longitudinal reinforcement of six numbers of 16 mm diameter bars and transverse reinforcements of 8 mm diameter having a spacing of 100 mm c/c.

Figure 2 illustrates the details and dimensions of the test specimens. Both the column specimens were cast along with footing beams having a cross-section of 350 × 350 mm and having eight numbers of longitudinal reinforcement bars. The concrete used in the specimens was M30 grade, while the longitudinal and transverse reinforcements were Fe500 grade steel. The structural steel used in the SRC column was of mild steel material.

Table 1 Material properties and details of test specimens

Specimen	Concrete grade	Grade of longitudinal steel	Structural steel	Grade of encased steel	Stirrup detailing
SRC	M30	Fe500	ISMB100	Fe250	φ 8@100
RC	M30	Fe500	–	–	φ 8@100

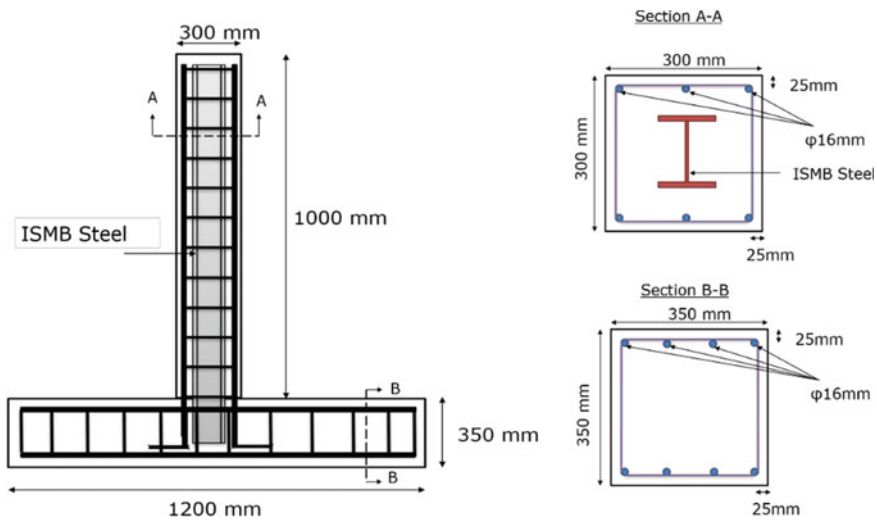


Fig. 2 Illustration of the test specimen and column cross-section

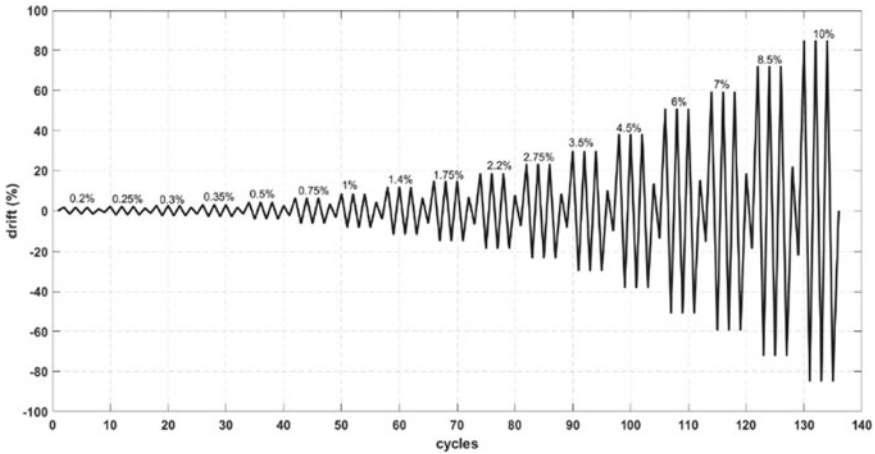


Fig. 3 Cyclic displacement history

2.2 Test Setup and Loading Protocol

The prepared test specimens were attached to the strong floor to ensure fixed boundary conditions. Lateral restraints were provided at the end of either face of the footing beam to prevent their transverse movement during the application of the lateral displacement cycles. The lateral displacement cycle was applied at the top end of the column specimens using a 250 kN actuator having a stroke length of 250 mm.

The cyclic displacements' protocol which was adopted for this study was in accordance with the guidelines of ACI Committee 374.1-50 (2006) [1] and was fully reversed at the end of each cycle. The pattern consisted of three cycles of one particular drift level followed by one cycle of a lower drift. This pattern was progressively increased until imminent collapse of the specimens. Figure 3 shows the cyclic displacement history adopted for the current experimental program. Owing to the higher ductility of SRC columns, the final drift level of 4.5% as suggested by ACI guidelines was extrapolated to 10%. The lateral cyclic displacements in terms of drift levels are as follows: 0.2, 0.25, 0.3, 0.35, 0.5, 0.75, 1, 1.4, 1.75, 2.2, 2.75, 3.5, 4.5, 6, 7, 8.5 and 10%. In either case, the test was terminated when the lateral load capacity reduced by 25% of the peak load irrespective of whether the cyclic history was completed.

2.3 Measurement Sensors

At the time of casting the specimens, before concreting was done, 120 Ω uniaxial strain gauges were fixed at prime locations of the column specimen particularly near the potential plastic hinge zone. The approximate plastic hinge region was assumed

as half the depth of the column cross-section measured from the base of the column-footing junction. Strain gauges were installed in all the six longitudinal reinforcement bars for both specimens as well as the structural steel section at the plastic hinge zone. The strain gauges were connected to a data acquisition system which continuously recorded the measured strains for the duration of the experimental program. Sensors placed inside the actuator helped to measure the lateral displacements imparted and the corresponding base resistance in terms of lateral force on the specimens.

3 Test Results

This section describes in detail the results of the experimental program which was conducted on the SRC and RC column specimens. The failure patterns, modes of failure, lateral ductilities and hysteresis behaviors of both the specimens were observed and compared in this section.

3.1 Failure Modes and Patterns

Both the prepared test specimens were subjected to the same lateral displacement history. For the SRC specimen, visible cracks started forming only after a drift of 0.75% at which horizontal flexural cracks started to develop in the plastic hinge zone. In subsequent drifts, the previously developed cracks extended and deepened. The first shear cracks occurred at a drift of 1.4% from the existing flexural cracks and they developed further at a drift of 2.2%. At 2.75% drift, the corners of the column-footing junction started cracking and separation of the base started to occur. Severe cracking with crack widths of about 5 mm occurred at a drift of 3.5%. The drift of 6% was critical as the existing shear cracks widened and the specimen witnessed severe spalling of concrete at the base of the column in the plastic zone. The first fracture of a longitudinal reinforcement bar occurred in the third cycle of the 7% drift by which all the other rebars had already been exposed and showed clear indications of buckling. At the 8.5% drift, the lateral load-carrying capacity of the column reduced to less than 75% of the peak capacity of the column which was decided as the failure point of the specimen. The overall failure mode of the specimen was predominantly in flexure with certain degree of shear cracking. Hence it could be assumed to have a mixed flexure-shear mode of failure. Figure 4 shows the crack propagation in the specimen at various drift levels.

The RC specimen which was also subjected to the same loading protocol showed similar damage patterns in the initial drift levels. Initiation of flexural cracks was at 0.75% drift as with the SRC specimen. Shear cracks initiated at 1.4% drift after which the flexural cracks stopped propagating and widening of cracks occurred only in the shear direction. The corners of the specimen at the junction of column-footing started cracking at 1.75% drift and subsequently started spalling off at 2.75% drift.

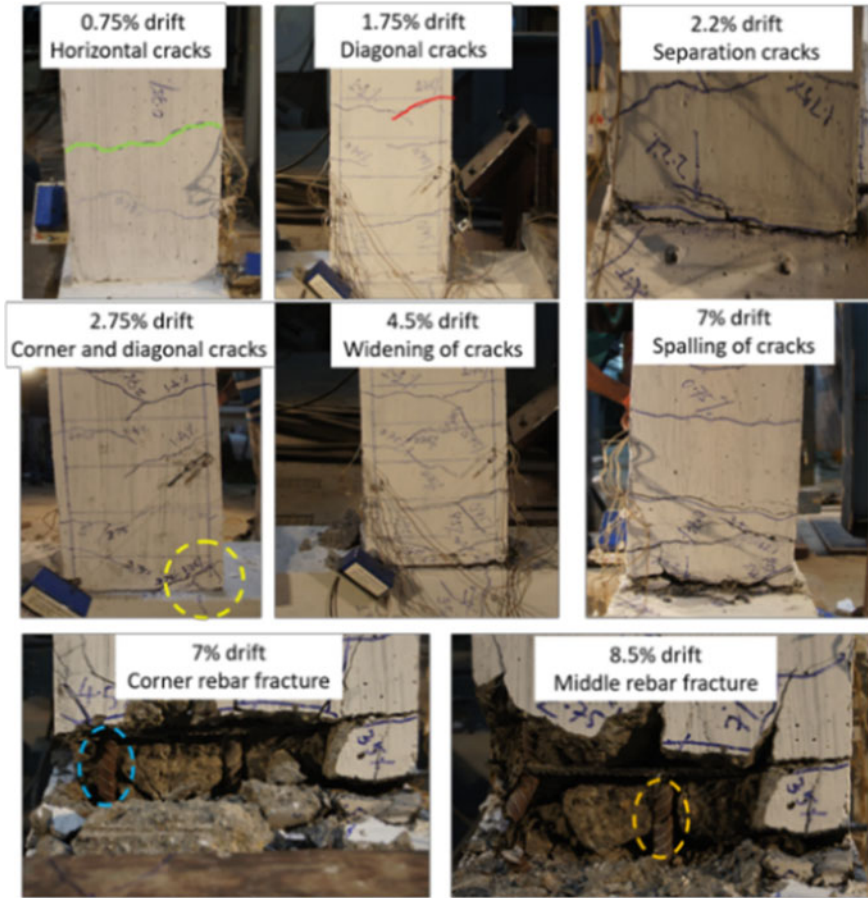


Fig. 4 Damage propagation in SRC column

Even at this drift, the specimen could be seen to bulge out of the plane in the plastic zone. At 3.5% drift, the shear cracks became severe and propagated deeper into the column sections. The longitudinal reinforcements were exposed at 4.5% drift and showed visible signs of buckling. The transverse stirrups had opened up near the base and at the level of the plastic hinge zone indicating initiation of shear failure. The test was continued up to 6% drift at which the lateral load reduced to less than 25% of the lateral capacity of the column and the test was terminated. Figure 5 shows the crack patterns and mode of failure of the RC column specimen. From the figures and the crack patterns observed, it was evident that the specimen failed in shear-dominated failure mode.

From the failure patterns and failure modes, it could be observed that the presence of encased steel sections in a shear-deficient RC column could increase the shear capacity of the column thereby preventing its premature shear failure. With only

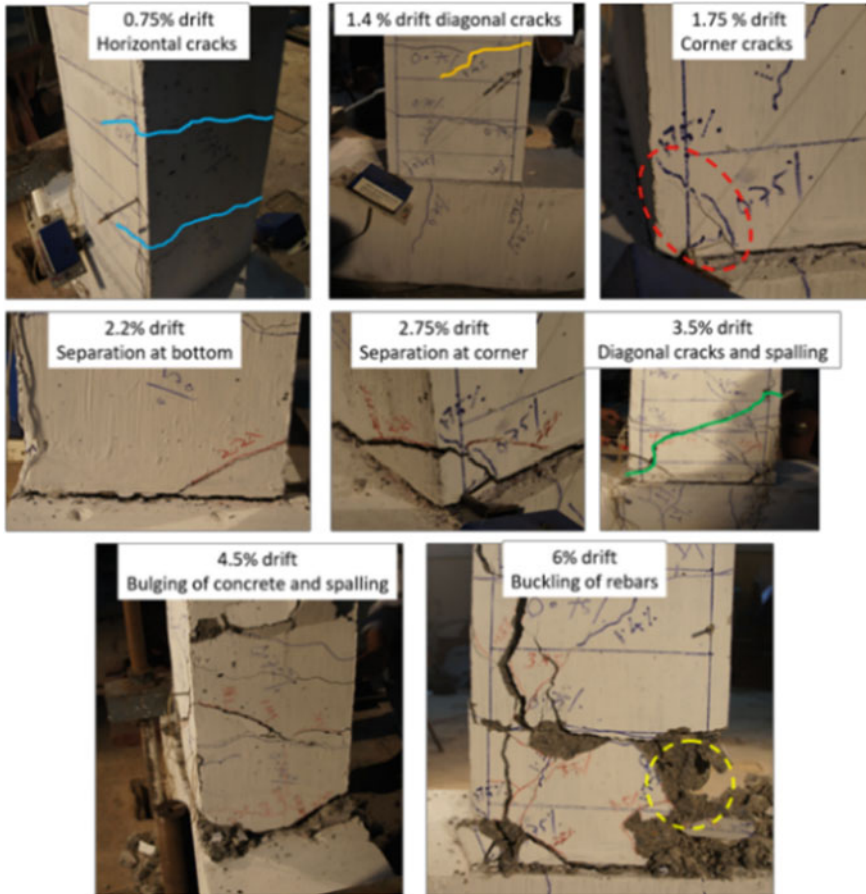


Fig. 5 Damage propagation in RC column

1.62% of structural steel by cross-sectional area, the failure mode was shifted from shear-dominated failure to flexure dominated. If higher percentage of encased steel could be used, the shear failure could be avoided completely.

3.2 Hysteresis Response

Figure 6 illustrates the hysteresis responses of both the SRC and RC specimens tested in the laboratory in lateral cyclic displacements. The RC specimen showed pinched hysteresis curves with degrading stiffness in the subsequent cycles typical of reinforced concrete structural elements. On the other hand, the SRC column exhibited stable spindle-shaped hysteresis behavior with little to no pinching effects in the later

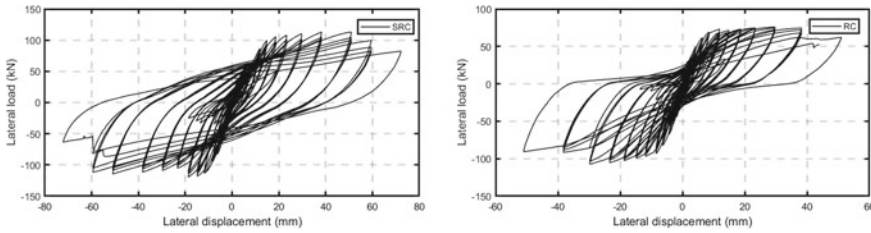


Fig. 6 Hysteresis response of SRC and RC columns

drifts. Degradation of stiffness was gradual and lateral load-carrying capacity was higher for the encased column in comparison to the RC specimen.

The yield drifts of both the specimens were at 1.34% and 0.64%, respectively, indicating that the SRC column behaved elastically for higher drifts in comparison to the RC component thereby delaying the yielding of the column. The encased column also exhibited improvement in the lateral strength and lateral deformation capacities. The lateral strength of SRC column was nearly 50% higher than the RC column having same cross-sectional dimensions. The SRC column sustained the lateral load for a higher drift level than the RC column signifying an improvement in the lateral ductility of the encased column specimen.

3.3 Lateral Stiffness

The column specimens were tested in cyclic displacements under displacement control starting from very small drifts gradually increasing the magnitude until ultimate failure of the specimens. The smaller drift cycles are required in order to capture the elastic behavior of the column specimens from which the elastic initial stiffness could be calculated. For each lateral drift, the effective lateral stiffness particular to that drift was calculated using Eq. 1 as the ratio of the resisting load to the corresponding recorded drift, whose values were taken as the average of the positive and negative loading cycles.

$$K_{\text{eff}} = \frac{(F^+ - F^-)}{(D^+ - D^-)} \tag{1}$$

The plots showing the degradation of the lateral stiffness in the subsequent drifts for both the tested columns are shown in Fig. 7. There was a marginal improvement in lateral stiffness with the lateral stiffnesses of SRC and RC columns being 22.06 kN/mm and 21.11 kN/mm, respectively. The low percentage of encased structural steel resulted in the improvement in lateral stiffness being insignificant in comparison to RC column.

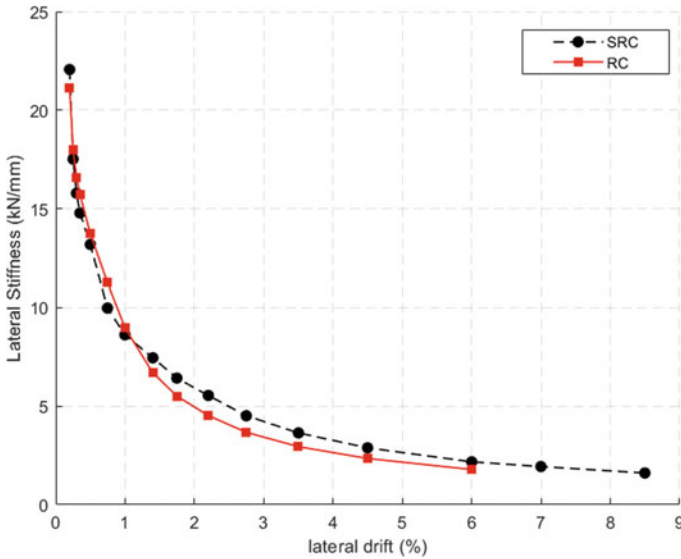


Fig. 7 Comparison of stiffness degradation

3.4 Energy Dissipation

The seismic performance of a structural component is said to be adequate if it is able to dissipate large seismic energies from the ground accelerations. Slow cyclic test is a sort of pseudo-dynamic test which gives an indication of the energy dissipated by the structural system from its cyclic hysteresis curves. The energy dissipated per loop of the hysteresis curve is calculated by measuring the area enclosed by the loop in that cycle. From the experimentally obtained hysteresis curves, the enclosed areas were determined numerically using trapezoidal integration schemes.

The energy dissipation plots of the both the test specimens are shown in Fig. 8. The cumulative energies dissipated at the end of the experiment for the SRC and RC specimens were 33.92 and 13.19 kNm. The total energy dissipated by the SRC column was nearly 2.5 times than that by the RC column. This highlights the significance of the encased steel section which for the same overall cross-sectional dimensions of the column was able to dissipate significantly higher energies even at a small encased steel ratio of 1.62% thus making them suitable for seismically active regions.

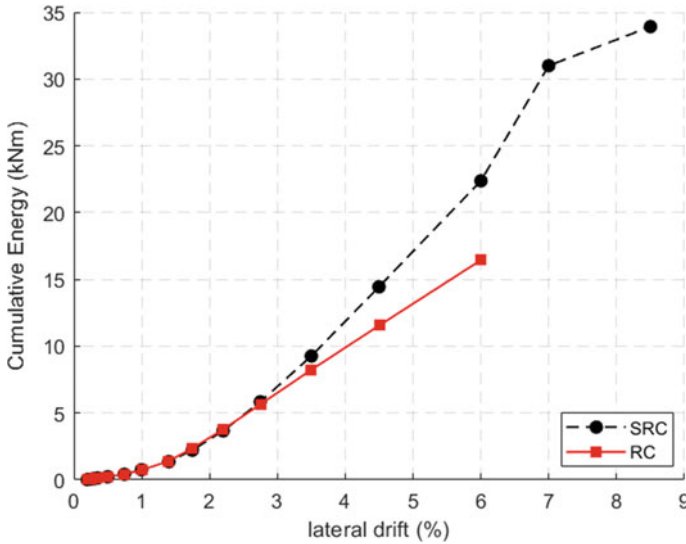


Fig. 8 Energy dissipation plots

4 Conclusions

The observations and inferences following the experimental evaluation of the SRC and RC column components in lateral cyclic loading lead to the following conclusions. The failure modes, hysteretic response, lateral stiffness and total dissipated energies of both the specimens were compared in this experimental study.

- The encased structural steel section in the cross-section was able to prevent a premature shear failure in the column as witnessed in the pure RC column specimen. The overall mode of failure was shifted from a shear-dominated failure to predominantly flexure dominated.
- For the same percentage of transverse steel, the encased column was able to withstand higher lateral drifts up to 8.5%, while the RC column failed at a lower drift of 6%.
- The increase in lateral strength and stiffness of the SRC column in comparison to the RC column was 50% and 4.5%, respectively. The lower increase in lateral stiffness could be attributed to the lower percentage of encased steel in the cross-section.
- Comparing the energy dissipation curves of both the specimens, it could be observed that the SRC column was able to dissipate significantly higher lateral energies of the order 2.5 than the RC column.

References

1. ACI Committee, and International Organization for Standardization (2008) Building code requirements for structural concrete (ACI 318-08)
2. Campian C, Nagy Z, Pop M (2015) Behavior of fully encased steel-concrete composite columns subjected to monotonic and cyclic loading. *Procedia Eng* 117(1):444–456. <https://doi.org/10.1016/j.proeng.2015.08.193>
3. Chen S, Peng W, Yan W (2018) Experimental study on steel reinforced concrete columns subjected to combined bending-torsion cyclic loading. *Struct Design Tall Spec Build* 27(11):e1479. <https://doi.org/10.1002/tal.1479>
4. Chen C, Wang C, Sun H (2014) Experimental study on seismic behavior of full encased steel-concrete composite columns. *J Struct Eng* 140(6):1–10. [https://doi.org/10.1061/\(ASCE\)ST.1943-541X.0000951](https://doi.org/10.1061/(ASCE)ST.1943-541X.0000951)
5. Dundar C, Serkan Tokgoz A, Tanrikulu K, Baran T (2008) Behaviour of reinforced and concrete-encased composite columns subjected to biaxial bending and axial load. *Build Environ* 43(6):1109–1120. <https://doi.org/10.1016/j.buildenv.2007.02.010>
6. El-Tawil S, Deirlein G (1999) Strength and ductility of concrete encased composite columns. *J Struct Eng* 125(9):1009–1019
7. European Committee for Standardization (1994) Eurocode 4: design of composite steel and concrete structures. CEN
8. IS 456 (2000) IS 456 : 2000 - plain and reinforced concrete - code and practice. Bureau of Indian Standards, pp 144. [https://doi.org/10.1061/\(ASCE\)CF.1943-5509.0000280](https://doi.org/10.1061/(ASCE)CF.1943-5509.0000280)
9. Karimi K, El-Dakhkhni WW, Tait MJ (2012) Behavior of slender steel-concrete composite columns wrapped with FRP jackets. *J Perform Construct Facilit* 26(5):590–99. [https://doi.org/10.1061/\(ASCE\)CF.1943-5509.0000280](https://doi.org/10.1061/(ASCE)CF.1943-5509.0000280)
10. Kim C-S, Park H-G, Chung K-S, Choi I-R (2014) Eccentric axial load capacity of high-strength steel-concrete composite columns of various sectional shapes. *J Struct Eng* 140(4):04013091. [https://doi.org/10.1061/\(ASCE\)ST.1943-541X.0000879](https://doi.org/10.1061/(ASCE)ST.1943-541X.0000879)
11. Lai B, Richard Liew JY, Le Hoang A, Xiong M (2019) A unified approach to evaluate axial force-moment interaction curves of concrete encased steel composite columns. *Eng Struct* 201:109841
12. Mirza S, Lacroix E (2004) Comparative strength analyses of concrete-encased steel composite columns. *J Struct Eng* 130(12):1941–1953. [https://doi.org/10.1061/\(ASCE\)0733-9445\(2004\)130:12\(1941\)](https://doi.org/10.1061/(ASCE)0733-9445(2004)130:12(1941))
13. Morino S, Matsui C, Watanabe H (1984) Strength of biaxially loaded SRC columns. In: *Proceedings of the U.S./Japan joint seminar*, vol January 1985, pp 185–94
14. Ricles, James M, Paboojian SD (1995) Seismic performance of steel-encased composite columns. *J Struct Eng* 120(8):2474–94
15. Ricles JM, Paboojian SA (1992) Behavior of composite columns under seismic conditions. In: *Earthquake engineering, tenth world conference*, pp 3431–36
16. Wang B, Huo G, Sun Y, Zheng S (2019) Applied sciences hysteretic behavior of steel reinforced concrete columns based on damage analysis. <https://doi.org/10.3390/app9040687>

Numerical Validation on SRC-RC Transfer Columns' Experiments



Abhishek Jain, Dipti R. Sahoo, and Arvind K. Jain

Abstract This paper presents the numerical validation of experiments' transfer columns in hybrid structures with steel-reinforced concrete (SRC) columns in some stories while having reinforced concrete (RC) columns in the others. These hybrid structures may be subjected to localised story failure mechanism in an earthquake if they are not detailed properly. A numerical validation was carried in the ABAQUS software package. The parameters from the experiments were input in the software to get the backbone curve that would match with the experimental results. Once validation is complete, this model can be further used for conducting a parametric study.

Keywords SRC-RC structures · Steel-reinforced concrete columns · Hybrid column · Composite column · Finite element modelling · ABAQUS validation

1 Introduction

Structures with composite columns have been accepted worldwide as a building option with construction speed of structural steel and still bear the positive aspects of a conventional reinforced concrete (RC) buildings. However, there are a lot of scenarios where the requirement of project is to have a hybrid structure with some stories having RC columns and rest of them having steel-reinforced concrete (SRC) columns. The transfer column is generally treated as the RCC column in design with embedding the structural steel emerging from the SRC stories. The depth of

A. Jain (✉) · D. R. Sahoo · A. K. Jain
Department of Civil Engineering, Indian Institute of Technology, Delhi, India
e-mail: abhishek.jain@civil.iitd.ac.in

D. R. Sahoo
e-mail: drsahoo@civil.iitd.ac.in

A. K. Jain
e-mail: akjain@civil.iitd.ac.in

structural steel embedment, detailing at the structural steel curtailment zone and its end connections are important parameters for the research.

Suzuki et al. [1] addressed the issue with research on the SRC-RCC transfer column by conducting experiment varying the embedment of structural steel in the transfer column. They observed the diagonal style crack occurring where the steel was truncated towards the compression zone of the column capital. It was observed that only the specimen with 3/4th embedment could surpass the strength of 'pure' RCC section and rest failed before attaining the strength. Wu et al. [2] subjected 16 SRC-RC transfer columns and a RC column to cyclic lateral force along with axial load to research failure mechanism and bearing capacity. The parameters varied were embedment length, lateral ties spacing at steel truncation zone, axial loads and size of structural steel. Three modes of failure: shear, shear-compression, shear-tension and bending failures were observed in different sections, and shear capacity formulae for each of the cases were explored. Wu et al. [3] proposed a theoretical formula for minimum extension length concluding that the ductility coefficient and deformation capacity are highest when embedment length is 3/5th of the total specimen length. Huang et al. [4] compiled the experimental results of the two research papers mentioned above and validated them in ABAQUS software package. The authors developed a formula for predicting the shear capacity of the columns and a modification in the equation provided by national standard of formula so that it would underpredict the shear capacity of transfer columns. Zhang et al. [5] simulated hybrid columns in Seismostruct software which found out that as the embedment increased, higher number of shear cracks appeared in the column, and similarly as axial load ratio increased beyond 40%, there was a decrease in the lateral load bearing capacity of the column.

The effect of end conditions like base plate, shear studs and axis of loading is yet to be discovered for the SRC-RCC column. This research paper focusses on finite element modelling of SRC-RC column in ABAQUS and is establishing a baseline for carrying out parametric study.

2 Finite Element Modelling (FEM)

2.1 Geometrical Modelling

The geometric modelling approach of the SRC column was followed from Ellobody et al. [6] and Huang et al. [4]. The concrete solid section was divided in three parts: unconfined concrete cover, partially confined concrete which is effectively confined by lateral ties spacing and highly confined concrete from structural steel section. However, the additional confinement due to the structural steel is not achieved in the case of the lateral load parallel pertaining to minor axis. The structural steel was also modelled as a solid element while all the reinforcements were modelled as wires.

2.2 Material Modelling

2.2.1 Steel

The structural steel and reinforcement steel were modelled with kinematic hardening.

2.2.2 Unconfined Concrete

Popovic's model was used for the material model for unconfined concrete. The model was modified as per [7] and applied in the analysis:

$$f_c = \frac{f_{co}\lambda\left(\frac{\varepsilon_c}{\varepsilon_o}\right)}{\lambda - 1 + \left(\frac{\varepsilon_c}{\varepsilon_o}\right)^{\lambda d}} \text{ where } \lambda = \frac{E_c}{E_c - \left(\frac{f_c}{\varepsilon_o}\right)} \quad (1)$$

$$\text{when } d = 1, \frac{\varepsilon_c}{\varepsilon_o} \leq 1, d = 0.67 + \frac{f_c}{62} \geq 1, \frac{\varepsilon_c}{\varepsilon_o} > 1 \quad (2)$$

E_c is the initial tangent modulus = $5000\sqrt{f_c}$ MPa and $\varepsilon_{co} = 0.002\varepsilon_{co} = 0.002$.

2.2.3 Partially Confined Concrete

The model used for stimulating the partially confined concrete is as given by Mander et al. [8]:

$$f_c = \frac{f_{co}x\left(\frac{\varepsilon_c}{\varepsilon_o}\right)}{r - 1 + x^r}, \quad (3)$$

$$\text{where } x = \frac{\varepsilon_c}{\varepsilon_{cc}}, r = \frac{E_c}{E_c - E_{sec}} \text{ and } E_{sec} = \frac{f_{cc}}{\varepsilon_{cc}}, \quad (4)$$

where f_{cc} and ε_{cc} are calculated as per improved model of Mander et al. [8] which was further improved by Denavit et al. [9]:

$$f_{cc} = Kf_{co}, \quad (5)$$

$$\varepsilon_{cc} = \varepsilon_{co}(1 + 5(K - 1)), \quad (6)$$

$$K = 1 + Af_1\left(0.1 + \frac{0.9}{1 + Bf_1}\right), \quad (7)$$

$$A = 6.8886 - (0.6069 + 17.275r)e^{-4.989u}, \quad (8)$$

$$B = \frac{4.5A}{5(0.9849 - 0.6306e^{-3.8939u}) - 0.1A} - 5, \quad (9)$$

$$f_1 = \frac{f_{11} + f_{12}}{2f_{co}}, \quad (10)$$

$$u = \frac{f_{11}}{f_{12}}, f_{11} \leq f_{12}, \quad (11)$$

where f_{11} and f_{12} are the lateral confining pressures from the lateral ties and reinforcement bars as calculated by Mander et al. [8].

2.2.4 Highly Confined Concrete

The material model followed was same as partially confined concrete. However, the value of f_{cc} and ε_{cc} is calculated as per the paper from Wei et al. [10].

$$f_{1s} = K_s f'_{1s}, \quad (12)$$

where f_{1s} is the lateral confining pressure provided by the steel section.

$f_{11} = f_{12} = f_{1s}$ for lateral loading at the major axis of steel section.

$$f'_{1s} = \frac{f_{yst}t^2}{\sqrt{9t^4 + 3l^2t^2}}, \quad (13)$$

$$K_s = \frac{(b_f - t_w)(d_s - 2t_f) - 1/3(d_s - 2t_f)^2}{(b_f - t_w)(d_s - 2t_f)} \quad (14)$$

2.2.5 Tension Modelling of Concrete

The fracture energy can be defined as per

$$G_f = G_{f0}(f_t)^{0.7} \text{N/mm where } f_t = 0.1f_{ck}. \quad (15)$$

G and G_{f0} range from 0.025 to 0.058 for maximum aggregate size 8–32 mm.

The cracking strain for concrete is defined as $\varepsilon_{cr} = \frac{f_t}{E_o}$

$$\varepsilon_1 = \varepsilon_{cr} + \frac{w_1}{l_c} \quad w_1 = 0.8 \frac{G_f}{f_t} \quad (16)$$

$$\varepsilon_u = \varepsilon_{cr} + \frac{w_u}{l_c} \quad w_u = 3.6 \frac{G_f}{f_t} \quad (17)$$

$$\text{where } l_c = \sqrt[3]{V} \text{ and } E_o = 5500\sqrt{f_c}. \quad (18)$$

2.3 Interaction and Constraints

The lateral and longitudinal reinforcement interface was modelled with embedment constraint constraining the translation degrees of freedom and pore pressure degree of freedom to the interpolated values of the corresponding degrees of freedom of the host element. The interactions between structural steel and concrete section were simulated with penalty friction as tangential behaviour with a coefficient of 0.25 and normal behaviour with hard contact.

2.4 Meshing Scheme

The solid element was meshed with eight-noded brick element with reduced integration (C3D8R) with element deletion and limiting maximum degradation. All the reinforcements were modelled with truss element with two-node linear displacement (T3D2). The mesh size was taken as $25 \times 25 \times 25$ mm for all elements.

3 FEM Validation

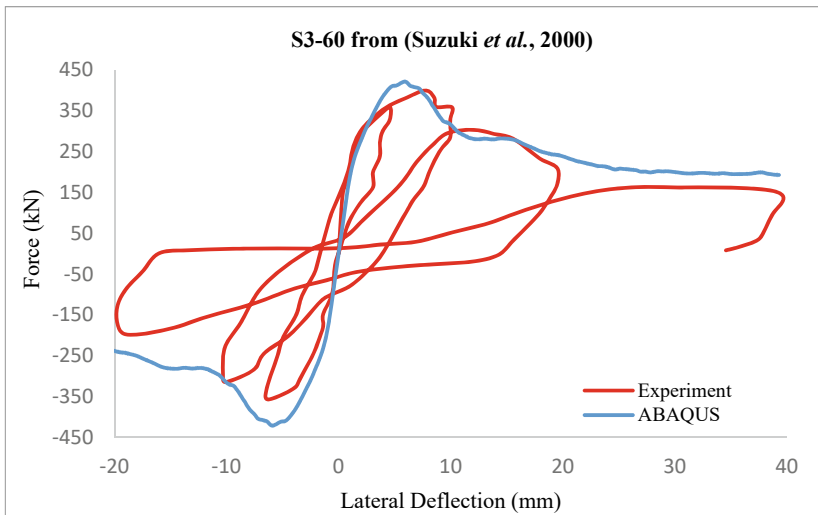
An experiment study was conducted by Suzuki et al. [1] and Wu et al. [2]. It is important to validate the experiment with the ABAQUS study before starting a parametric study. Table 1 has the geometric and material details for the specimen published. The same was input in ABAQUS package a validation (Table 2).

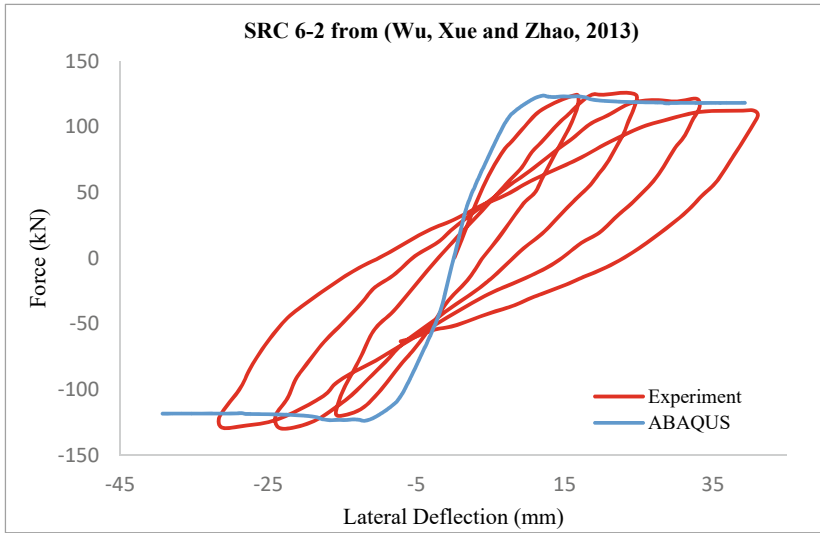
Table 1 Geometric details of the research papers being validated (mm)

	Suzuki et al. [1] S3-60 specimen	Wu et al. [2] SRC 6-2
Gross size	275 × 275	160 × 220
Structural steel size ($D \times t_w \times B_f \times t_f$)	204 × 12 × 200 × 12	140 × 5.5 × 80 × 9.1
Clear specimen height	1200	1000
Embedment length	600	600
Reinforcement bars	8 nos.–19 φ	4 nos.–16 φ
Lateral ties at truncation	10 φ @120 c/c	6.5 φ @48 c/c
Lateral ties throughout	10 φ @120 c/c	6.5 φ @96 c/c
Axial load ratio	0.15	0.2

Table 2 Material details of the research papers being validated

	Suzuki et al. [1] S3-60 Specimen	[2] SRC 6-2
Concrete cube strength	25.9	59.1
Structural steel	228	292.7
Longitudinal reinforcement	755	358.3
Lateral ties	363	292.7





Similarly, a fair match was observed in the failure mechanism with plotting tension damage and observing the contour patterns. While a predominantly shear failure was observed in S3-60, a flexural shear failure was observed for the SRC 6-2 specimen. As in the research papers, SRC 6-2 crack pattern was not shown, the failure patters for another specimen S6-4 were matched to show the validation of the ABAQUS model (Fig. 1).

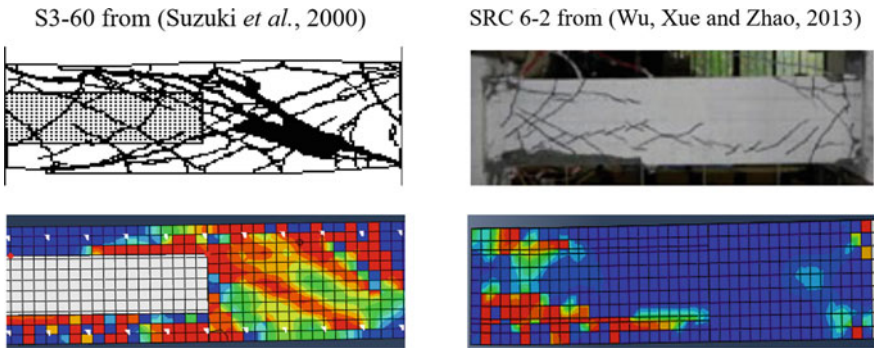


Fig. 1 Failure mechanism in the experiments and the simulation

4 Conclusions

SRC-RC transfer column is an important research area for finite element analysis to study the failure mechanism. It is highly important to conduct experiments and then numerically validate the finite element model with the experimental results. These models then can be used for parametric study to get the optimum detailing and embedment length for these structures.

Numerical validation including backbone curve and failure mechanism validation was successful for the two separate sets of experiments proving efficacy of the ABAQUS software package to be used for this research problem.

References

1. Suzuki H, Nishihara H, Matsuzaki Y, Minami K (2000) Structural performance of mixed member composed of steel reinforced concrete and reinforced concrete. In: The 12th World Conference of Earthquake Engineering, China: Beijing
2. Wu K, Xue JY, Zhao HT (2013) Failure mechanism and bearing capacity of transfer columns in SRC-RC hybrid structures. *Eur J Environ Civ Eng* 17(sup1):s205–s228
3. Wu K, Xue J, Nan Y, Zhao H (2018) Analysis on extension length of shape steel in transfer columns of SRC-RC hybrid structures. *Int J Steel Struct* 18(3):910–923
4. Huang W, Zhou Z, Liu J (2017) Analytical deformation characteristics and shear capacity of SRC-RC transfer columns. *J Constr Steel Res* 138:692–700
5. Zhang H, Cao P, Wu K, Xu C, Ren L (2019) Lateral bearing capacity and stiffness calculation method of SRC-RC columns. *KSCE J Civ Eng* 23(5):2158–2174
6. Ellobody E, Young B (2011) Numerical simulation of concrete encased steel composite columns. *J Constr Steel Res* 67(2):211–222
7. Collins MP, Mitchell D, Macgregor JG (1993) Structural design considerations for high-strength concrete. *Concr Int* 15(5):27–34
8. Mander JB, Priestley MJ, Park R (1988) Theoretical stress-strain model for confined concrete. *J Struct Eng* 114(8):1804–1826
9. Denavit MD, Hajjar JF, Leon RT (2011) Seismic behavior of steel reinforced concrete beam-columns and frames. In: Structures congress, pp 2852–2861
10. Wei H, Jiang Q, Zhi Z (2016) Numerical simulation of the seismic performance of steel reinforced concrete columns by considering the lateral confining pressure. *Eng Mech* 33(5):157–165

Unbonded Brace: A Review



Prachi Mishra and Arvind Y. Vyavahare

Abstract Braces have been considered as the most desirable choice among the engineers as earthquake- and wind-resistant elements for the construction of steel-framed structures, whenever they are acceptable from the architectural point of view. The major drawback of conventional bracing is that it loses strength under compression due to buckling. Braces normally have slip-type hysteresis, and because of this, they cannot give suitable energy absorption. Buckling-restrained brace (BRB) is specially designed to restraint global buckling, and the pressure member is expected to yield before buckling. BRB is designed on a very simple concept which is to restrain the buckling behavior of the brace so that it perform the same behavior in tension as well as compression. As a result, BRB shows stable and nearly symmetrical characteristic. BRBs are emerging in these decades as an innovative and economical solution for the energy dissipation in the earthquake- and wind-resistant construction of steel-framed buildings. This paper presents a brief summary on the development of the unbonded braces and discusses the basic history, concept and applications of BRBs. Various configurations and the buckling behavior of the brace under different buckling modes are presented. The stability criteria for different failure modes are considered. It was found that the torsional buckling is the most critical mode for stability of the brace. Limitations of the brace are also discussed in brief.

Keywords Buckling · Innovative · Bracing · Earthquake · Conventional · Hysteresis

P. Mishra (✉)
Visvesvaraya National Institute of Technology, Nagpur, India
e-mail: er.prachimt@gmail.com

A. Y. Vyavahare
Applied Mechanics Department, Visvesvaraya National Institute of Technology, Nagpur, India

© The Author(s), under exclusive license to Springer Nature Singapore Pte Ltd. 2023
M. Madhavan et al. (eds.), *Proceedings of the Indian Structural Steel Conference 2020*
(Vol. 2), Lecture Notes in Civil Engineering 319,
https://doi.org/10.1007/978-981-19-9394-7_30

375

1 Introduction

Braces have been used by the engineers to reduce the effect of wind and earthquake impacts on the buildings. Conventional braces, when subjected to larger compressive forces, experience considerable buckling and lose strength. When the buckling is restrained, the braces show symmetrical hysteretic performance both in tension as well as compression. Also, braces with larger cross-section no longer possess their inherent rigidity control function. The energy dissipation capacity of braces can be noticeably increased if buckling can be avoided in them. All these troubles influenced researchers to develop a brace that can restrain buckling and they come up with a new type of brace called buckling-restrained brace (BRB). BRB is based on a very simple concept that is to control buckling so that the braces show almost symmetrical hysteretic behavior. BRB is also known as the unbonded braces. They do not buckle because of an enclosing outer steel tube and concrete which in combination have an ability to re-establish the original condition. Due to this property, BRBs have become a popular choice among the engineers for wind- and earthquake-resistant structures in the last few decades all over the world and specially Japan.

The most important feature that makes BRB unique is its stable and repeatable hysteretic behavior. This makes it to be a better choice than conventional bracing by improving the energy dissipation capability and strengthening the structure it is provided to (Fig. 1).

A BRB is made up of the following parts:

1. Buckling restraining device (BRD)—this is the covering tube which carries the axial force. Earlier mortar-filled steel was used as BRD. On the other hand, the new-generation BRD is made with overall steel and therefore is comparatively lighter.
2. Core—it is the main component of BRB which restrains buckling.
3. Unbonding material—in order to provide some space for the expansion of the core member due to compression, an unbonding material is coated in between the core member and the restraining device. It is also helpful in reducing the adhesion between the core and the restraining part (Fig. 2).

Fig. 1 Response of a buckling-restrained brace and a conventional steel brace [27]

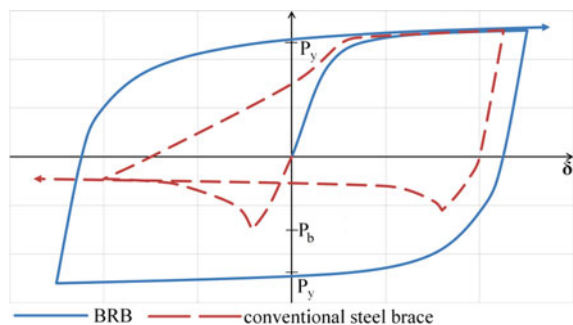
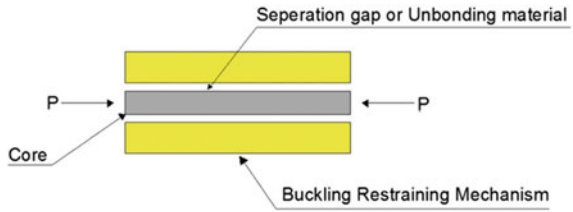


Fig. 2 Parts of a BRB [8]



2 History of BRB

The concept of BRB was first conceptualized by a Japanese engineer, Wakabayashi et al. [25]. He also designed the first BRB in which a flat steel plate was sandwiched between reinforced concrete panels. BRB was devised in Japan in the 1970's. Mochizuki et al. [13] experimented on the buckling behavior of a diagonal bracing enclosed with reinforced concrete. He used some shock absorbing material to prevent the concrete and bracing adhering to each other. Fujimoto et al. [6] made the use of above concept and developed the first practical BRB. They used rectangular-shaped outer tubes made up of steel and filled with mortar for restraining and found out the optimal debonding material specifications to attain stable and repeatable hysteretic performance. To grab the basis characteristics of the brace, an experiment was performed before taking them in practical application. The experiment was conducted by [23] in the late 1980s in Japan. A specimen was made with rolled steel core of yield stress 2880 kg/cm^2 and an outer carbon steel pipe of yield stress 3700 kg/cm^2 . Concrete was used as a filler material. Expandable polystyrene was used as a debonding material in order to prevent adhering of the core and the concrete (Fig. 3).

Five specimens of dimension $90 \times 19 \text{ mm}$ with different outer tube cross-sections were tested for compression. Each brace was placed in a frame and a horizontal force was applied with 110 kN actuator. Cyclic loading was applied to the core member with the displacement varying from $1/400$ to $1/50$. Table 1 gives the experimental and theoretical results. It can be seen in the table that the specimens whose buckling strength of the outer tube is greater than the yield load of the core, they do not buckle and the specimens whose buckling load of the outer tube is less than that of the yield load of the core, they show buckling.

It was further concluded that the unbonded braces show considerable restraining to the global buckling as long as the Euler crippling load of the outer mechanism exceeds the yielding load of the core. Many other experiments were conducted on the unbonded braces by other researchers also. Hasegawa et al. conducted a shake table test on two braces in the 1990s in Japan. The first BRB practical application was

Fig. 3 Dimensions of the specimen [7]

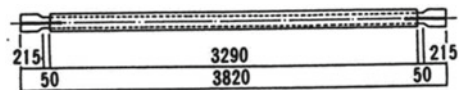


Table 1 Theoretical and experimental values

S. No.	Tube dimension (mm)	Theoretical yield strength		Experimental results			Buckling			
		Buckling load of tube P_e (ton)	Yield load of core P_y (ton)	P_e/P_y	Tensile yielding load P_t (ton)	P_t/P_y	Compressive yielding load P_c (ton)	P_c/P_y	Load P_{cr} (ton)	P_{cr}/P_e
1	150 × 150 × 4.5	171.0	48.5	3.53	48.6	1.00	51.5	1.06	–	–
2	150 × 100 × 4.5	67.4	48.5	1.39	48.3	1.00	51.8	1.07	–	–
3	150 × 100 × 3.2	50.2	48.61	1.03	47.6	0.98	49.3	1.01	–	–
4	150 × 75 × 4.5	35.0	48.5	0.72	48.3	1.00	–	–	46.5	0.95
5	150 × 75 × 3.2	26.2	47.87	0.55	47.9	1.00	–	–	43.1	0.90

employed in two 10- and 15-story steel-framed office buildings. By 1990, more than hundred buildings in Japan accepted and used BRB of which most of the buildings were taller than 15 stories. Meanwhile, in 1995 Wada proposed a new concept of “damage tolerant” design. In this concept, he introduced BRBs as energy dissipating elasto-plastic damper within an elastic main frame. The acceptance and application of BRB in Japan increased mainly after the 1995 Kobe earthquake. The good response and increasing demand in Japan within a very small time inspired the researchers to transfer the technology to USA. The first practical application of BRB in USA was with the construction of a building at UC Davis in 1998 whose testing took place in 2000 at UC Berkeley. In couple of years, several projects using BRB were executed. One of the major reason of acceptance of BRB in USA was the 1994 Northridge, California earthquake. This incident considerably altered the seismic research, design and construction of steel buildings in the USA. By the year 2002, the Seismic Provisions for Structural Steel Buildings included a direction for the design of buckling-restrained braced frames. The braces have also found their use in the New Zealand after 2010–2011 Canterbury earthquakes. The major part of the Christchurch Central Business District has been totally rebuilt with seismic devices in the year 2017. Frames with unbonded braces have been used in buildings making up nearly 40% of the total newly constructed floor area. It is now becoming a modern belief that constructing seismic resistant structures only to minimize loss of lives is not sufficient. Instead, structures should be constructed to incur least damage to the structure as well.

3 Stability Analysis of BRB

For the stability analysis of BRB, it has to be identified in three different buckling modes.

1. Global stability of the brace under axial compression.
2. Higher modes buckling of inner core.
3. Torsional buckling of the inner core.

An analysis was made on a steel composite brace which was encased by a reinforced concrete element to predict the elastic buckling behavior, and it was found that the global stability of BRB can be predicted directly from Euler theory of buckling. It was discovered that the critical load of BRB is simply the Euler buckling load of the outer tube. Thus, the brace is assumed to be stable for global buckling mode when the Euler crippling load of the tube, P_e , is greater than the yielding load of the core, i.e.,

$$\frac{P_e}{P_y} > 1, \quad (1)$$

$$\text{where } P_e = \frac{\pi^2 EI_{\text{tube}}}{KL^2} \quad (2)$$

$$\text{and } P_y = \sigma_y A_{\text{core}}, \quad (3)$$

Where EI_{tube} = flexural rigidity for the outer tube.

KL = effective length of the brace.

σ_y = yield stress of the inner core.

A_{core} = cross-section area of the inner core.

For the local buckling mode, the efficiency of the unbonded brace can be improved when the buckling of the inner core along the restrained length does not take place. Wada et al. gave an equation for the critical load for the local buckling of the core

$$P_{\text{cr}} = 2\sqrt{\beta E_i I_i}, \quad (4)$$

where $E_i I_i$ = flexural rigidity for the inner steel core.

β = distributed spring constant.

High-order buckling of the inner steel core can be avoided when

$$P_{\text{cr}} \geq \sigma_y A_i \quad (5)$$

$$\text{which requires } \beta \geq \frac{\sigma_y^2 A_i^2}{4E_i I_i}, \quad (6)$$

where A_i = cross-section area of the inner core.

It was observed that in higher modes, the critical load of the inner steel core does not depend upon the end conditions of the core.

The part of the core that extends from the casing may undergo torsional buckling which is the third and the most critical mode of buckling for BRB. Many researches have been made and some are still under progress on the torsional buckling behavior of the unbonded braces. Researchers have proven that the critical load causing torsional buckling of the extruded part in BRB does not depend upon the length of the extension.

4 Configuration

BRB can have different configurations depending upon the arrangement of the enclosing steel core. It can have an encasing by a steel tube or a reinforced concrete component. It may also have encasing of precast concrete components. Different type of cross-sections of BRBs have been used till date. Various types include H-section, crisscross section, circular section, wide flange section, bolt connected panels, etc. (Fig. 4).

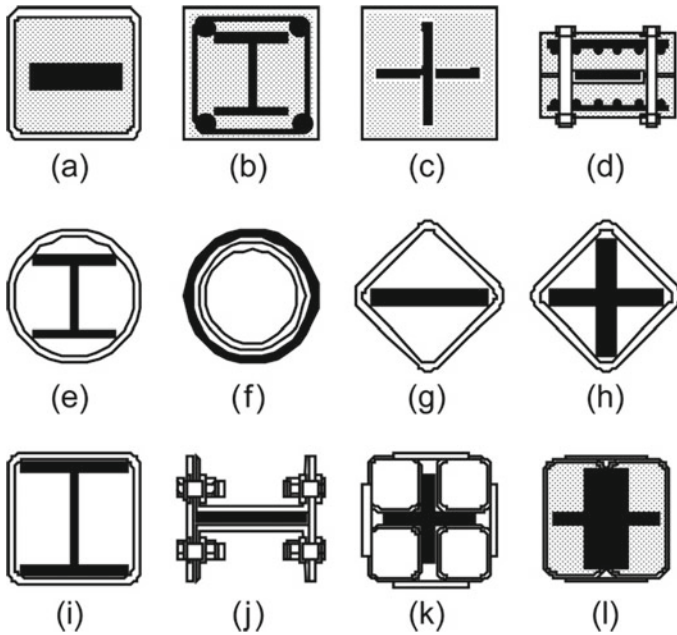


Fig. 4 Various cross-sections of BRB [26]

The researchers had devised and tested various other types of cross-sections also. Whatever be the configuration, the main aim of the outer tube is to provide lateral support to the inner core member to restrain global buckling, whereas the inner core carries axial force. A layer of separation material is provided in between the steel and concrete interface so as to allow the brace to move freely. This also restricts the shear transfer due to contraction and expansion of the core member. Since the adhesion between the steel and concrete is restricted, the name is being given unbonded brace to BRB.

5 Application

Due to its stable hysteretic property and strong energy dissipation capability, BRB has become popular choice among the engineers for seismic construction. A number of buildings in Japan have been constructed using BRB as a structural member. Practically, BRB was first used in the construction of No. 2 Nippon steel building in Chou-Ku, Tokyo (1989). By the year 1990, BRB was being used in more than hundred buildings in Japan (Fig. 5).

BRBs are being used as damage-tolerant structures. A 40-story office building, Triton Square Project, Tokyo (1992), was built using this concept only. A 26-story hotel building, Raguza Tower Osaka was constructed using reinforced concrete



Fig. 5 No. 2 Nippon steel building in Chou-Ku, Tokyo [19]

panels encasing unbonded brace. Due to the increasing demand and great response to the unbonded braces, the technology was then transferred to USA after a testing at UC Berkeley in 2000. Apart from fresh constructions, BRBs have proven to be equally worthy for the retrofitting of the existing buildings. To improve the seismic performance of buildings, several retrofit projects have been developed in various countries. Application of unbonded braces started much later in Europe and is still few in numbers. BRB has been used worldwide in countries such as Japan, China, USA, Taiwan, Turkey, Chile, Romania, Iran, Canada, Italy and New Zealand. In the Christchurch rebuild of New Zealand, about forty percent of the construction used BRB as a structural element. A large number of buildings under construction at the time of the survey used BRBs as their structural systems. In non-ductile moment frames, BRBs are often installed in the perimeter as an external frame. Such type of retrofits is generally difficult to apply. For such type of situations, “integrated facade engineering” is being proposed [20]. This concept combines the structural retrofit, facade design and environmental design and includes improvements on seismic performance using seismic energy dissipation devices as BRBs. BRBs also have their application in trusses and spatial structures. Toyota stadium is an example of BRBs applied to the supporting structure of a spatial structure. Also, the application of BRBs in the construction of a number of bridges has been made in the recent years. Recently, BRBs have been used in a rocking or spine frame commonly identified as “strong-back system”.

6 Limitations

Apart from so many innovative and economical applications of BRB, there are some drawbacks or limitations in using the unbonded braces. There is no criteria developed so far to detect and check the damaged braces. The extent of damage in the brace is difficult to predict after any seismic event. Out-of-plane and in-plane local bulging failure is also observed. Also, the design codes developed by various countries do not give the complete guidelines for the design of BRB. Further studies regarding the reliability of brace connections to the frame are required. Several countries have still not defined any codal provision for the design of the unbonded braces.

7 Conclusion

This paper gives a brief summary of unbonded braces. It discusses about the different buckling modes of BRB, its application in several countries specially Japan. In Japan BRB is considered as dampers rather than braces. It is observed that BRB shows uniform hysteretic behavior. BRB does not require any type of strengthening of foundation or structural members. Further, it was observed that a key limit state corresponding to the design of unbonded braces is to avoid flexural buckling. It can be concluded that as long as the Euler crippling load of the outer tube is greater than the yielding load of the inner core, the global stability of the brace is ensured. It is observed that if the local buckling of the inner core along the restrained length is prevented, the brace is more effective. Furthermore, the restraint conditions for the local buckling of the core member can be critical for the stability and strength of the brace, if the wall thickness of the outer tube is comparatively smaller than the cross-section of the core member. The plastic torsional buckling mode is considered to be the most critical stability mode for the brace. The extruded yielding portion should have a width to thickness ratio less than 5 to avoid torsional buckling.

References

1. Bruneau M, Macrae G (2017) Reconstructing christchurch: a seismic shift in building structural systems. The Quake Centre, University of Canterbury
2. Cameron Black J, Makris N, Ian Aiken D (2004) Component testing, seismic evaluation and characterization of buckling-restrained braces. *J Struct Eng* © ASCE 130(6), 880–894
3. Chia-Ming U, Bruneau M (2018) State-of-the-art review on seismic design of steel structures. *J Struct Eng* © ASCE 144(4):03118002
4. Ding Y, Zhang Y, Zhao J (2008) Tests of hysteretic behavior for unbonded steel plate brace encased in reinforced concrete panel. *J Const Steel Res* 65(2009):11601170
5. Fahnestock L A, Sause R, Ricles JM (2007) Seismic response and performance of buckling-restrained braced frames. *J Struct Eng* 133(9):1195–1204

6. Fujimoto M, Wada A, Saeki E, Watanabe A, Hitomi Y (1988) A study on the unbonded brace encased in buckling-restraining concrete and steel tube. *J Struct Construct Eng AIJ* 34B:249–258 [in Japanese]
7. Fujimoto M, Wada A, Saeki E, Takeuchi T, Watanabe A (1990) Development of unbonded brace. *Q Column* 115:91–96
8. Hoveidae N, Rafezy B (2012) Overall buckling behavior of all-steel buckling restrained braces. *J Constr Steel Res* 79(2012):151–158
9. Jinkoo K, Hyunhoon C (2003) Behavior and design of structures with buckling-restrained braces. *Eng Struct* 26(2004):693–706
10. Kim J, Seo Y (2004) Seismic design of low-rise steel frames with buckling-restrained braces. *Eng Struct* 26(2004):543–551
11. Macrae G, Bruneau M (2017) Reconstructing Christchurch: a seismic shift in building structural systems. *Quakecentre Report*
12. Makris N, Black C, Aiken I (2002) Component testing, stability analysis and characterization of buckling restrained unbonded braces. Final report to Nippon steel corporation, Tokyo, Japan. Pacific Earthquake Engineering Research centre
13. Mochizuki S, Murata Y, Andou N, Takahashi S (1979) Experimental study on buckling of unbonded braces under axial forces: parts 1 and 2. In: *Summaries of technical papers of annual meeting*. Architectural Institute of Japan, pp 1623–1626 [in Japanese]
14. Qu Z, Xie J, Cao Y, Li W, Wang T (2019) Effects of strain rate on the hysteretic behavior of buckling-restrained braces. *J Struct Eng* 146(1):06019003
15. Quang LG, Ying-Zhi S, Jiang J, Fei-Fei S, Chang J (2019) Experimental study on two-level yielding buckling-restrained braces. *J Constr Steel Res* 159(2019):260–269
16. Rahai AR, Alenia MM, Salehi SMF (2008) Cyclic performance of buckling restrained composite braces. *Int J Civ Eng* 7(1), March 2009
17. Ravi KG, Satish Kumar SR, Kalyanaraman V (2006) Behaviour of frames with non-buckling bracings under earthquake loading. *J Constr Steel Res* 63(2007):254–262
18. Sabelli R, Mahin S, Chang C (2003) Seismic demands on steel braced frame buildings with buckling restrained braces. *Eng Struct* 25(2003):655–666
19. Shimuzo et al (1997) Design method to prevent buckling of low yield strength steel tube brace and fracturing of joints (part 1 & 2). In: *Summaries of technical papers of annual meeting, vol III*, Architectural Institute of Japan, C1, Structural Engineering Section, pp 781–784 [in Japanese]
20. Takeuchi et al (2009) Local buckling restraint condition for core plates in buckling restrained braces. *J Constr Steel Res* 66(2010):139–149
21. Tremblay R, Bolduc P, Neville R, DeVall R (2006) Seismic testing and performance of buckling restrained bracing systems. *Can J Civ Eng* 33(1):183–198
22. Wada et al (1994) Damage tolerant structures ATC-15 proceedings of fifth US Japan workshop on the improvement of building structural design and construction practices. ATC, Redwood City, California
23. Watanabe A, Hitomi Y, Saeki E, Wada A, Fujimoto M (1988) Properties of brace encased in buckling-restraining concrete and steel tube. In: *Processing of ninth world conf. on earthquake eng*, vol IV, pp 719–24
24. Wakabayashi M, Nakamura T, Katagihara A, Yogoyama H, Morisono T (1973) Experimental study on the elastoplastic behavior of braces enclosed by precast concrete panels under horizontal cyclic loading—parts 1 & 2. In: *Summaries of technical papers of annual meeting, vol 6*. Kinki Branch of the Architectural Institute of Japan, pp 121–128 [in Japanese]
25. Wakabayashi M, Nakamura T, Katagihara A, Yogoyama H, Morisono T (1973) Experimental study on the elastoplastic behavior of braces enclosed by precast concrete panels under horizontal cyclic loading—parts 1 & 2. In: *Summaries of technical papers of annual meeting, vol 10*. Architectural Institute of Japan, Structural Engineering Section, pp 1041–1044 [in Japanese]
26. Xie Q (2004) State of the art of buckling-restrained braces in Asia. *J Constr Steel Res* 61(2005):727–748
27. Zsarnóczy A (2013) Experimental and numerical investigation of buckling restrained braced frames for Eurocode conform design procedure development. Budapest University of Technology and Economics

Engineering Solutions to Mitigate Logistics Changes on a Modular Project



Varun Dhiman and Mangesh Amrut Sakpal

Abstract The intent of this paper is to highlight the impact of developments in Transportation philosophies of modular structures as the project phases into advanced stages. The design parameters and logistics information get more refined when logistics contractor starts developing execution philosophy for the transportation of modules. It becomes more important that the mitigation measures are there in place to minimize effect on cost and schedule of the project. Modes of transportation discussed in this document are land and sea transportation for a large modularization project. For land transportation of modules, propelled module transporters (PMT)/self-propelled module transporters (SPMT) trailers were used. Mechanical properties of these trailers were defined in the beginning of the project. Modules were transported through water using barges/vessels. Sea accelerations were provided by logistics contractor for analysis and design of modular structures. The modules were fixed on barges/vessels with the help of sea fasteners. Sea fasteners and bulkhead capacities were also provided by logistics contractor. Module support reactions were then checked against these capacities. There was wide range of parameters which had an impact on the design of modules. It was important to mitigate them with effective and efficient solutions since fabrication was at advanced stage. Some of the revised parameters were sea accelerations' coefficients, capacities of vessel/barges, capacities of SPMT/PMT, supporting configurations, etc. Various methods had been employed to screen the changes that were not having any detrimental impact on design of a structure. Also, several re-evaluation methods to mitigate the changes impacting the design were implemented.

Keywords Module logistics · Modularization · Land and sea transportation · PMT · SPMT · Barges

V. Dhiman (✉) · M. A. Sakpal (✉)
Department of Civil Structural, Fluor Daniel India Pvt. Ltd., Gurgaon, India
e-mail: Varun.Dhiman@fluor.com

M. A. Sakpal
e-mail: Mangesh.Amrut.Sakpal@fluor.com

1 Introduction

This section briefly describes various parameters and late developments which impacts project schedule and cost. This study is based on a large-scale modularization project with skids, modules and pipe racks weighing from 500 to 4000 MT. Due to the size of the project, a rigorous planning was needed which had to be dynamic based on different situations and timelines of module transportation. To support logistic contractor and efficient execution, an engineering team always remained equipped with methods to handle any dynamic changes required. There are some scenarios for respective modes of transportation faced in this project which are listed in Sects. 1.1 and 1.2. The impact on project and methods of mitigating these scenarios are discussed in Sects. 2 and 3 respectively.

1.1 Sea Transportation

Some scenarios impacting the sea transportation design are listed below:

- Revisions in values of sea accelerations and sea fastening details of a module on barges/vessels. See Fig. 1 for more details on sea accelerations.
- Addition of different types of vessels for sea transportation such as module carrying vessel (MCV). These were introduced at a later date for transporting heavier modules and had larger capacities than barge.
- Details of grillage design from logistics were unknown at the initial phase of project. Some of the detailing aspects of sea fastening plates were dependent on the grillage design.

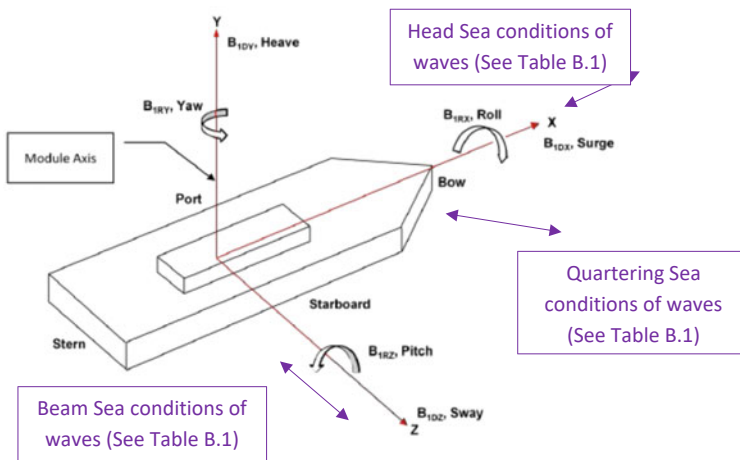


Fig. 1 Sea acceleration components for sea/ocean transportation

1.2 Land Transportation

Some scenarios impacting the land transportation design are listed below:

- (a) Trailer grouping patterns required modifications for some modules at developed stages of project (longitudinal to transverse and vice versa).
- (b) Variation in number of axles for overall length or within trailer grouping based on available SPMT units (4-axle or 6-axle units).
- (c) Maximizing the use of standard length SPMT for different length modules. This was required to support and reduce efforts for logistics (Fig. 2).
- (d) Configuration of wheels disengagement; see Fig. 3. These were requested from logistics contractor for distributing the load evenly on all SPMT axles.
- (e) Change in trailer type (e.g. use of third-generation SPMT having weaker spine instead of fourth generation as per initial basis of design). This was governed by availability at the time of transportation.
- (f) Power pack unit (PPU) information and configurations (1PPU/2PPU) were received at a later stage which caused interference with cantilever portion in some of the PAUs.

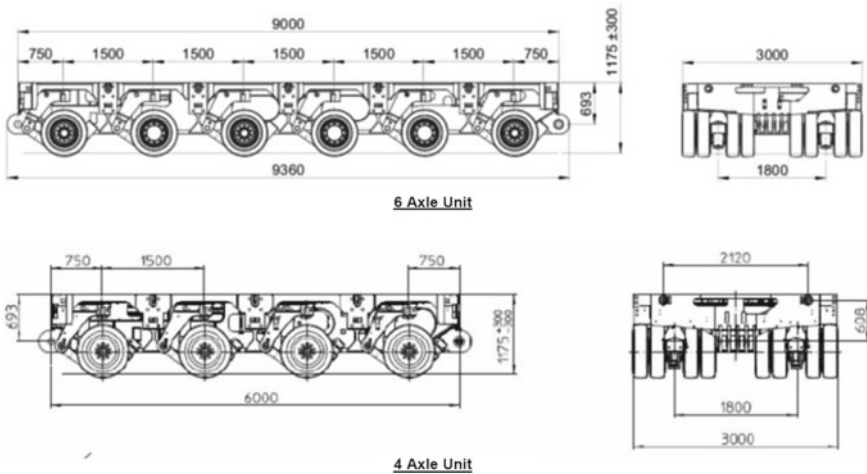


Fig. 2 Different axle arrangements of SPMT (dependent on Logistics Contractor)

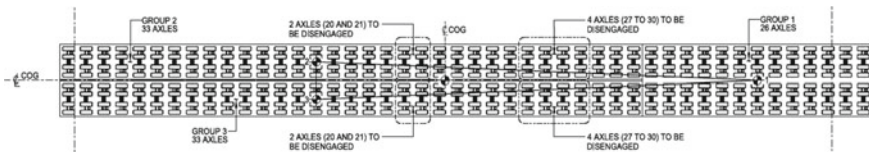


Fig. 3 Typical disengagement of SPMT axles for redistribution of load in land transportation analysis

2 Impact and Mitigation Measures

All of such developments at different phases of the project resulted in rework in engineering to check the adequacy of structure design under revised conditions. These developments certainly impact the project and require additional efforts such as listed below:

- (a) Re-analysis of a structure/module for various cases
- (b) Connection re-validation
- (c) Coordination efforts
- (d) Updating the drawings as needed.

Some engineering and logistics solutions were devised which helped in minimizing the changes/modifications in already fabricated steel or issued deliverables for fabrication. These solutions are described in Sect. 3 of this document.

3 Engineering and Logistics Solutions

3.1 *Engineering Solutions*

Following were some of engineering solutions implemented.

3.1.1 Reserved Capacity Utilization

Reserved capacity of steel sections was utilized in two different ways: firstly by reducing the design margins and secondly by the requesting actual material properties of fabricated steel sections. Design margins were kept and updated based on maturity level of design parameters available during engineering phase. When reducing the design margins did not help then actual material strength were requested from fabricator based on test reports. In general, actual material strengths were higher than the theoretical values. This information was received in the form of Mill certificates of specific steel sections in question. It had helped in avoiding the strengthening requirements at many instances and thus minimizing the efforts in fabrication yard for already fabricated steel.

3.1.2 Use of Voyage-Specific Accelerations

For few modules, sea fastening reactions were exceeding the sea fastener capacities. Voyage-specific accelerations were requested for such modules. This has also helped the engineering team in mitigating sea fastening reaction exceedances which were comparatively less than the considered values.

3.1.3 Implementation of Barge/Vessel Deck Stiffness

Initially, modules were designed with pinned base conditions (i.e. without considering deck stiffness). These are simplified boundary conditions. But by using relative stiffness of structure and vessel deck; heave (compression), uplift reactions and roll reactions potentially got reduced. Stiffness for barges/vessels was requested from logistics contractor and used in structural analysis of affected modules.

3.1.4 COG Offset Analysis

Originally for COG Offset, push and pull forces were applied on structure to develop stresses in consideration of probable COG Offset in fabricated module to analytical module. This is simplified and efficient method to start analysis with, as it involves lesser time and effort and produces conservative results. But later in order to mitigate changes impacting design, more precise method of analysis was implemented on some modules. In this method instead of applying COG Offset loads on module, module was actually moved to extreme ends of defined COG envelope. This gave more realistic stresses development in the module. However, it takes more engineering efforts. The procedure is shown schematically in Fig. 4, showing SPMT spine beam locations with respect to module. Case 1 indicates COG of SPMT group is aligned with COG of module. In cases 2 and 3, SPMT group is moved to edges of COG envelope for considering stress development in module for COG Offset scenarios.

The resulting STAAD files (3 no's) had been verified individually with single COG location by applying the total dead load at the preferred COG location for that STAAD file case. For cases 2 and 3, the dead load COG was moved on edge of COG envelope by applying equivalent moment in basic load cases. This approach gave more accurate analysis and reduced conservatism. But this should be done specifically when needed. This is time-consuming and generalizing this method for entire project can affect overall productivity on the project.

3.1.5 Four-Corner Analysis

To simplify barge transportation analysis, horizontal centre of gravity (COG) Offset are not used and instead dead load increase factors were used. But then sea reactions exceeded the available sea fasteners capacity in some cases. To resolve this exceedance, four-corner analysis was used. In this method the load increase factors were dropped. In four-corner method, COG of module is shifted at four corners of COG envelope and then analysis was performed with actual dead loads. This led to reduction of sea fastening reactions in modules.

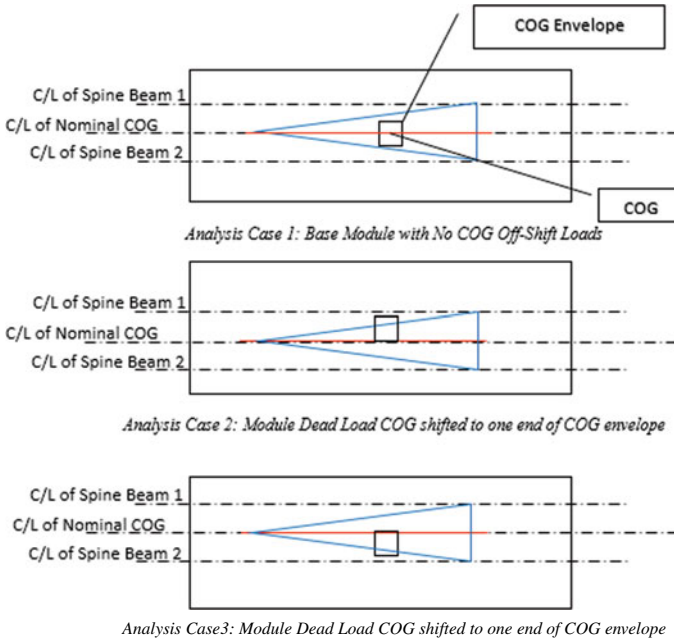


Fig. 4 Nominal COG locations with respect to COG envelope for module analysis

3.2 Logistics Solutions

Apart from engineering solutions described in above section, there were some solutions which were implemented by retrieving voyage-specific parameters from logistics contractor. The following are the solutions used.

3.2.1 Limiting the Sea States with Journey Management

Sea accelerations are generally average values of certain longer duration periods. So some critical modules were decided to be transported in selective days when sea accelerations were lower than average values used for design. This resulted in lower module support reactions to be within vessel specific capacities.

3.2.2 Use of Stronger Ocean-Going Vessels (OGV)

Using stronger ocean-going vessels (OGV) for heavier modules was another method adopted. This solution was implemented when all other methods of reducing sea fastening reactions were exhausted.

3.2.3 Positioning of Module on Barge/Vessel

Positions of modules on barges can also be planned in a manner where barge displacement values are lower (sag/hog values). This helped in reducing overall stresses developed in structure during sea transportation due to lower barge deck displacements.

4 Conclusion

It is important to acknowledge and identify the developments impacting the design in a project coming at mature stage. These can be either due to lack of information in the beginning of a project or due to changed conditions at a later stage. To minimize these at a later stage rigorous and continuous follow-up sessions should be arranged. This helps in getting maximum information at the earliest and reduces the impact on project. In this document, few typical reasons are stated which might require re-engineering to be done to minimize changes in deliverables or fabricated steel. Furthermore, it becomes imminent that contingencies should be taken into consideration for re-validation of structures. This will reduce risks related to project costs and schedules.

A Numerical Study on the Seismic Response of Circular CFST Column-Beam Exterior Joint with Split Bolt Assembly



P. U. Sreeshma and K. P. Beena

Abstract The concrete-filled steel tube (CFST) is a composite member consisting of a steel tube and concrete infill. CFST combines the advantages of both steel and concrete member as they are placed concentrically. Circular CFST columns show better performance compared to square one, as they provide more confinement to concrete infill. But the application of circular CFST columns is limited, due to the difficulties in assembling the connection. Split bolt assembly avoids the complications in the circular CFST column connections and improves the efficiency of the joint compared to straight bolt assembly. Split bolt assembly allows the intersection of through bolts at the same level. In this work, the seismic response of an exterior semi-rigid stiffened extended endplate connection between circular CFST column and I-beam with split bolt assembly is studied under displacement-controlled cyclic loading. The numerical study was conducted to investigate the influence of axial load level and split bolt angle on the joint behaviour. Initial stiffness of joint increases with increase in axial load level but has negligible effect on moment capacity of the joint.

Keywords CFST column · Split bolt assembly · Semi-rigid · Extended endplate · Cyclic loading · Axial load level

1 Introduction

The concrete-filled steel tube (CFST) is a composite member consisting of a steel tube filled with concrete. In the last few decades, CFST columns have been widely used in engineering applications because of their excellent structural performance obtained

P. U. Sreeshma (✉) · K. P. Beena
Trivandrum, India
e-mail: sreeshmapu999@gmail.com

K. P. Beena
e-mail: beenakp@cet.ac.in

from the positioning of steel tube and concrete core concentrically. The steel tube provides confinement [2] and thus increases the strength and stiffness of concrete core, and the concrete in turn reduces the possibility of local buckling of tube wall. Steel tube acts as a formwork, thus increasing the speed of construction. The provision of steel tube provides the benefits of both longitudinal reinforcement and transverse confinement; hence, the traditional longitudinal and transverse reinforcement can be avoided. Circular CFST columns have better performance compared to square CFST columns as the circular tube provides more confinement to concrete core. In square- and rectangular-shaped tubes, due to the weak confining effect the concrete core and the steel tube do not keep in contact with each other during the ultimate loading stage. In the case of circular sections, local buckling is not likely to occur due to this strong confining action [3]. The application of CFST circular columns is limited even though it has a better performance compared to square CFST columns due to the practical difficulties faced in connecting the circular CFST column to beams.

Seismic response of a CFST structure depends upon the beam-column connections as they are critical elements in transferring beam loads to column and ensuring structural safety [14]. The connection between CFST column and steel beam can be exterior or interior connections. In exterior connection steel beam is directly attached to the skin of the steel tube and hence experiences heavy distortion in the tube wall at the connected region [5]. High weld stresses are developed in the welded connection during a seismic event and lead to brittle failure. Welded connections are widely used for exterior joint. In interior connections, the steel beam is allowed to pass through the CFST column by cutting an opening in the tube wall [9]. This connection provides interference with the concrete and is difficult to construct in the field.

Rigid connections are completely welded connections, which is effective in transferring bending moment, shear force and axial load between beam and CFST column [8]. But the relative rotation between beam and column is negligible. Rigid connections are expensive to make due to the inclusion of many stiffening elements and need of heavy welding. To avoid extensive welding and to improve the performance of joint, connections using high-strength bolts are used in CFST structures [6]. A semi-rigid endplate connection helps to avoid weld failure and requires only shop welding and on site bolting works [7]. The semi-rigid connection with an extended reinforcement bar or bolts helps to transmit the stresses to concrete core. As an alternative solution to the problems associated with through beam connections, through bolted connections are also used. Through bolted connection allows a bolt rod to pass through the CFST column and act as a tie rod, which increases the concrete confinement and making it to actively participate in lateral stability [11]. It is difficult to get the grip between steel tube and bolt head while providing straight bolt assembly in a circular CFST column. One solution to avoid the technological difficulties is the provision of curved endplates [12]. Split bolt assembly is used to provide through bolts in circular CFST column connections. This will allow the diametrical intersection of bolts at the same level. Stiffeners are provided where large load-carrying capacity of the joint is required, and it also helps to shift the location of plastic hinge away from the column face and reduces stress concentration at the column face.

From an extensive review of the available literature on CFST beam-column joint, it was found that fewer studies are so far reported in the area of circular CFST beam-column joint compared to square one. Studies on split bolt assembly in circular CFST columns are very rare in the literature. Since circular CFST columns with split bolt assembly improve the structural seismic performance significantly, an extensive research is needed in this field.

The main objective of the study is to investigate the seismic behaviour and failure modes of a stiffened extended curved endplate connection between circular CFST column and steel beam with split bolt assembly. The seismic behaviour of this connection depends on many parameters such as material, geometry and loading. It is difficult to consider all parameters by experiment. Hence, in this study the commercial software ABAQUS is used to simulate the seismic behaviour of I-beams in through bolted beam-column connections and to calibrate this behaviour with experimental results available in the literature. The study focuses on the influence of axial load level of CFST column and angle of split bolt assembly on the joint behaviour.

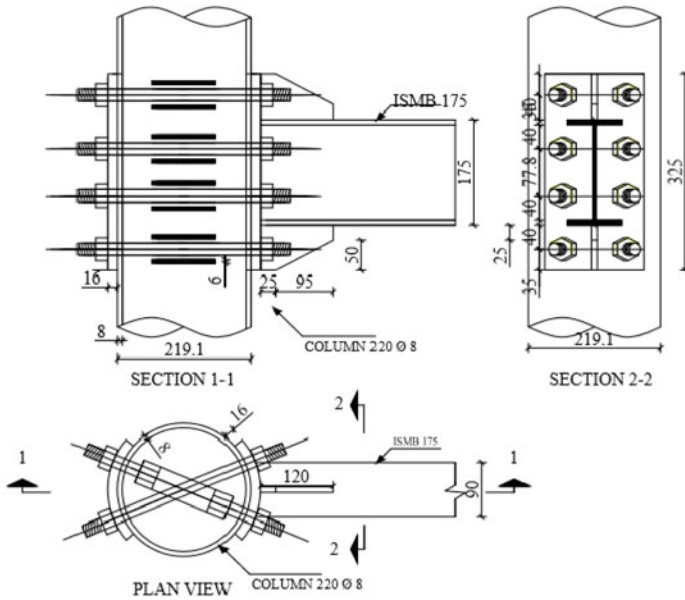
2 Finite Element Model

A finite element model was developed using ABAQUS software for the through bolted curved extended endplate connection between circular CFST column and steel beam with vertical stiffeners and split bolt assembly. The details of joint are given in Table 1.

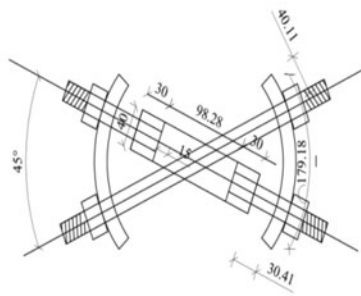
The joint shown in Fig. 1 consists of a circular tube of 220 mm diameter and 8 mm thickness with 300 Grade and beam ISMB 175 with 250 Grade. The beam was welded to 16 mm thick curved extended end plate. 10 mm thick triangular stiffeners with 120 mm length were provided above and below the top and bottom flanges. 20 mm rod 8.8 Grade High Strength Friction Grip is used to form through bolts.

Table 1 Details of joint

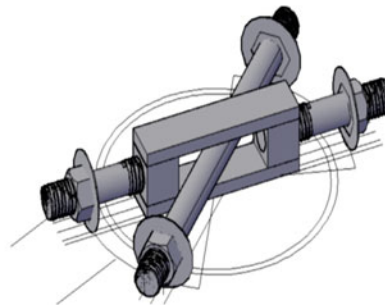
Component	Dimensions	Length (mm)	Thickness (mm)
Steel tube	220 mm dia	1500	8
Concrete core	204 mm dia	1500	–
I-beam	ISMB175	800	$t_w = 5.5, t_f = 8.6$
End plate	158 mm × 325 mm	–	16
Stiffener	120 mm × 75 mm	–	10
Through bolt	M20	Shank length = 252	–



(a) Details of specimen.



(b) Details of split bolt assembly.



(c) Split bolt assembly (3D view).

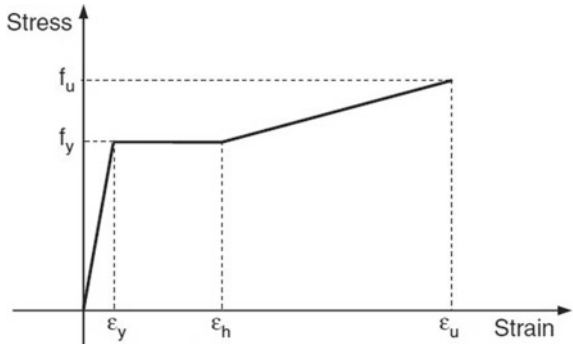
Fig. 1 Joint details [1]

2.1 Material Model

2.1.1 Material Model of Steel

The elastic–plastic model was used to describe the behaviour of the steel. Tri-linear stress–strain curve proposed by Zhong et al. [13] as shown in Fig. 2 was used for tube, end plate, beam, stiffener and bolt. The “plastic” option available in ABAQUS allows to use a multi-linear stress–strain curve. The first part of the tri-linear curve

Fig. 2 Stress–strain model of steel [13]

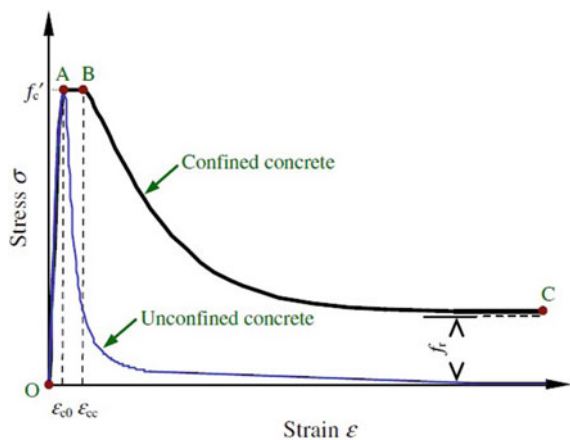


represents the elastic curve up to the proportionality limit stress defined by Young’s modulus and Poisson’s ratio. Poisson’s ratio is taken as 0.3 and Young’s modulus as 200 GPa. After the onset of yielding, steel is assumed to be fully plastic until strain hardening.

2.1.2 Material Model of Concrete

The confined concrete model proposed by Zhong et al. [13] was adopted in the FE analysis. Figure 3 shows the uniaxial stress–strain curve used to define the parameters required in “concrete damaged plasticity” model available in ABAQUS. Uniaxial tensile response was assumed to be linear until the tensile strength of concrete was reached and was taken as 0.1 times the cylinder compressive strength. At this point, plastic strain was zero.

Fig. 3 Stress–strain model for confined concrete [13]

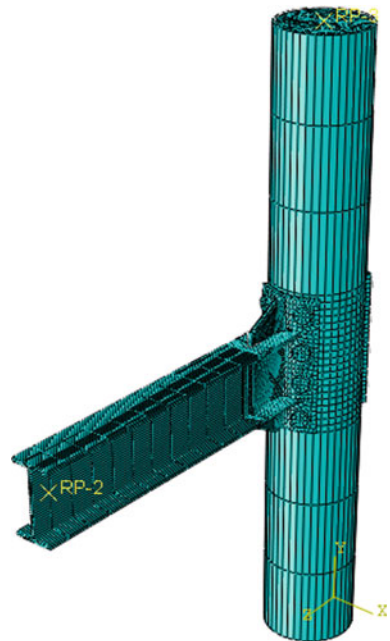


2.2 Geometric Model

In the FE model, three-dimensional 8-node linear brick element with reduced integration and hourglass control (C3D8R) was used for all the components of the joint. This element is not susceptible to shear locking, which makes the model stiffer. Structural meshing technique was used to have a proper element shape [10].

The different parts were assembled together by contact relations and constraints between the surfaces to form the analytical model of CFST beam-column joint. The interaction between the different surfaces among steel parts and concrete core was given through the “contact pair” algorithm, where the surfaces can contact and separate each other but are not allowed to penetrate. The curved surfaces which come into contact including the steel tube inside surface to concrete core outside surface, endplate to steel tube outside surface, bolt head to endplate, bolt shank to bolt holes on the steel tube, bolt shank to bolt holes on the endplate and bolt shank to concrete core were defined with hard contact and coulomb friction model in the normal and tangential directions [4]. The coefficient of friction between the two surfaces in the model has moderate effect on the joint behaviour and was taken as 0.2 for better convergence. The welded connection between beam and end plate, beam and stiffener, stiffener and endplate are simulated using the “tie” constraint, which allows to couple all degrees of freedom for the welded components. A schematic view of the FE model developed is shown in Fig. 4.

Fig. 4 Finite element model of joint



For boundary conditions, all three rotational degrees of freedom were allowed at both ends of the column. The translational degrees of freedom except the vertical displacement were restrained at the loading end of the column. All the three translational degrees of freedom were restrained at the other end of the column.

A nonlinear quasi-static analysis of the joint was performed. Material, geometrical and boundary nonlinearities are considered in the analysis. In order to reflect the actual loading condition, three loading steps were adopted in the FE analysis to apply different loads including bolt pretension force, column axial load and beam load. Bolt pretension force of 100 kN was applied firstly at the centre of the bolt. Second step was to apply a constant axial load equal to 15% of the axial load-carrying capacity of the CFST column at the top of the column through the reference point (RP-3 in Fig. 4) of the “rigid body constraint”. In the third step, displacement-controlled cyclic load was applied at a distance of 50 mm from the tip of the beam through a reference point (RP-2 in Fig. 4) using ANSI/AISC 2002 loading protocol as given in Fig. 5. This reference point acts as a loading plate as it is connected to the slave nodes in the beam at a section through the “multipoint constraint” option available in ABAQUS.

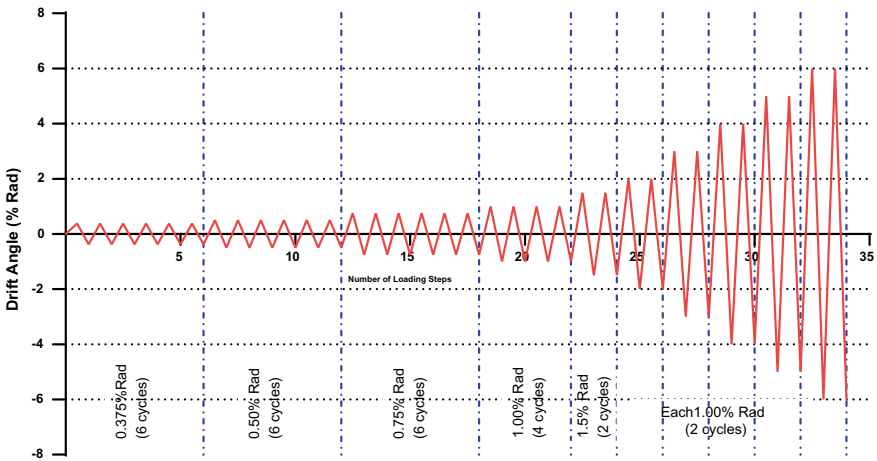


Fig. 5 Loading protocol

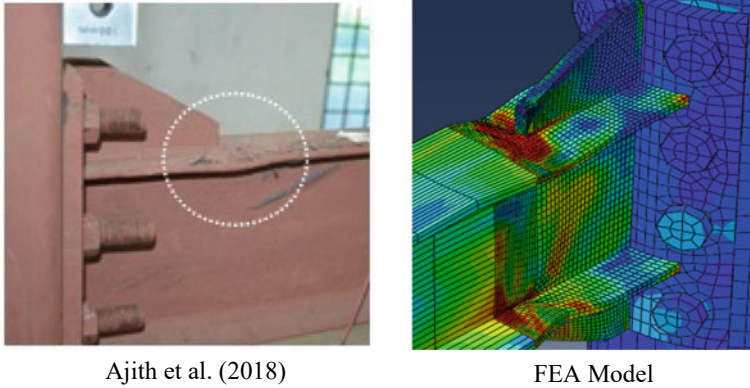


Fig. 6 Failure modes of joint

3 Results and Discussion

3.1 Failure Mode

The deformed shapes observed in the experiment by [1] and numerical studies are compared in Fig. 6. The joint failed in strong joint, strong column–weak beam mode. As expected severe local buckling occurs in the flanges and web of the beam at the end of vertical stiffener, indicating the formation of an obvious plastic hinge. From the experimental and numerical results, the failure modes of the joint are ductile in nature. It can be concluded that the energy is dissipated mainly through beam flexural yielding and subsequent buckling in both experimental and numerical results.

3.2 Moment-Rotation Relationship

The hysteresis loop obtained from numerical study using moment and angular rotation is shown in Fig. 7. Moment at the column face was calculated by multiplying the force at the tip of the beam with distance between the column face and loading line. The total rotation of the joint was contributed by beam, column and panel zone. But the major contribution for joint rotation might be from beam as the design philosophy of strong joint, strong column and weak beam was followed. The curve showed good hysteresis behaviour with no pinching effect. The hysteresis curve obtained was plumb in shape with increase in loop area indicating that the joint has good energy dissipation capacity.

As it is difficult to validate a hysteresis curve, each maximum load points in a loading cycle was used to construct a moment-rotation envelope curve for the joint as shown in Fig. 8. Peak minimum rotation observed was greater than 0.04 rad, which

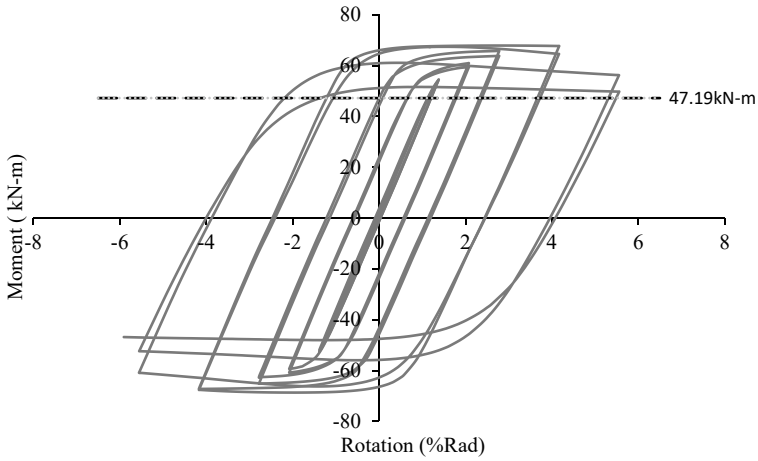


Fig. 7 Moment-rotation hysteresis curve

satisfies the guidelines provided by AISC 341-10 for composite special moment resisting frame. In Table 2, a comparison between numerical and experimental data for moment capacities and initial stiffness is shown. Numerical results are overestimated. But the shapes of curves obtained in both cases are similar. The comparison indicates that the current FE model has reasonable prediction accuracy and can be used for further parametric study.

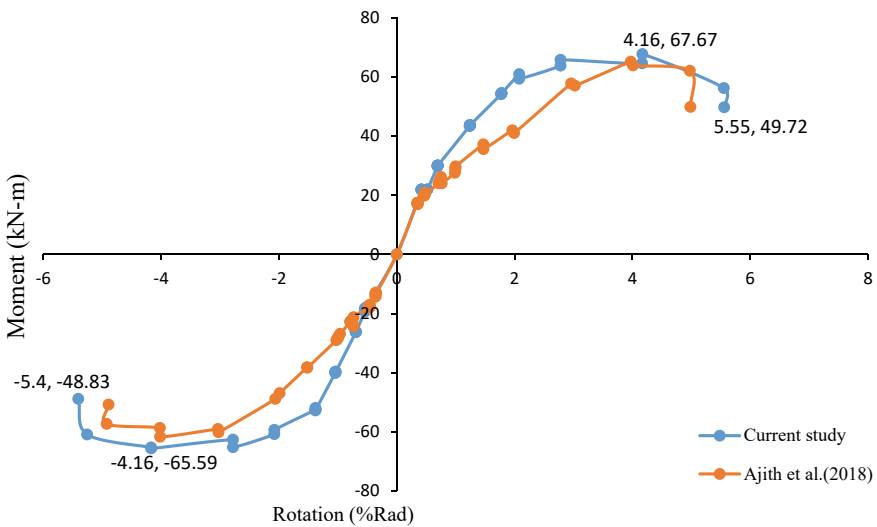


Fig. 8 Moment-rotation envelope curve

Table 2 Validation of results

	M_u (kN-m)		$\theta_{r,u}$ (rad)		S_{ini} (kN-m/rad)	
	H	S	H	S	H	S
FEA	67.66	65.59	4.16	4.16	44.88	35.00
[1]	65.12	61.66	3.97	4.04	44.8	34.09

Note: M_u = ultimate moment; $\theta_{r,u}$ = rotation at ultimate moment; S_{ini} = initial stiffness; H = hogging; S = sagging

3.3 Effect of Axial Load Level

The current FE model was used to study the influence of axial load level in the moment capacity and initial stiffness of the joint. Axial load level of CFST column can be defined as,

$$n = N/N_u, \quad (1)$$

where N and N_u are the axial compressive load and ultimate axial compressive load applied to CFST column, respectively.

To study the effect of axial load level on joint behaviour, models were analysed for axial load levels of 0.05, 0.15 and 0.25. The moment-rotation curves obtained from the analysis are shown in Fig. 9. The initial stiffness of the connection increases with increase in axial load level, but has negligible effect on the ultimate moment capacity of the joint. The initial stiffness was enhanced by 27% in positive and negative displacement when the axial load level increases.

3.4 Effect of Angle of Split Bolt Assembly

A split bolt assembly consists of two through bolts passing diametrically and intersect each other at the same level. The model which is validated has a split bolt assembly with 45° angle between the bolts. Finite element model of the bolted joint with angle of split bolt assembly 35°, 45° and 55° is developed for investigating the effect of the bolt angle on the behaviour of joint. Moment-rotation envelopes are developed for these values of angle of split bolt assembly which is shown in Fig. 10. It is observed that, increase in the angle of split bolt assembly enhances both initial stiffness and ultimate moment capacity of the joint. This is because when the angle of split bolt assembly increases, pitch of the bolts also increases so that the portion of the panel zone confined by the split bolt assembly also increases. That will result in a strong panel zone with increased moment capacity and stiffness of the joint. It was found that as the angle of split bolt assembly increases, moment capacity and initial stiffness of the joint were found to be enhanced by 12 and 39% in positive and negative displacement.

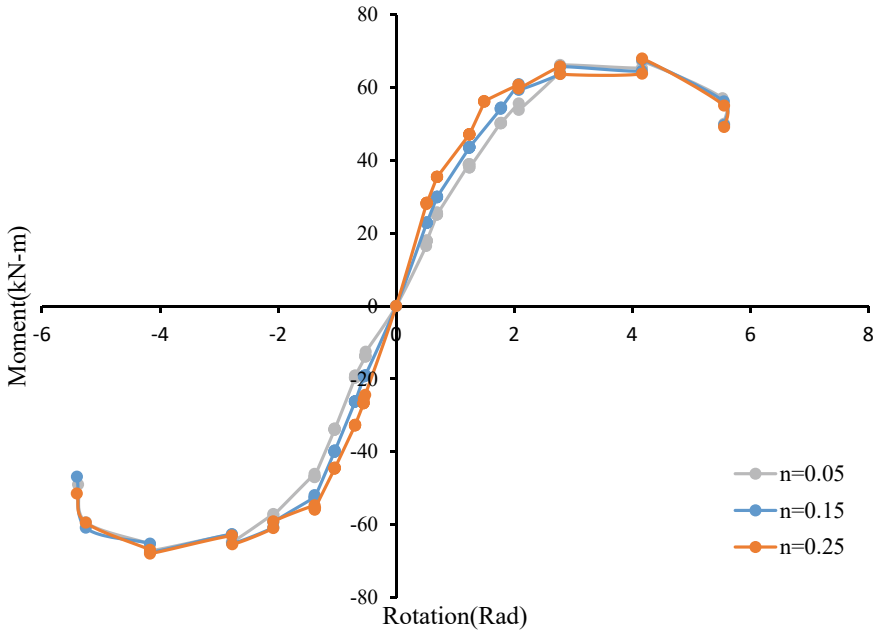


Fig. 9 Effect of axial load level

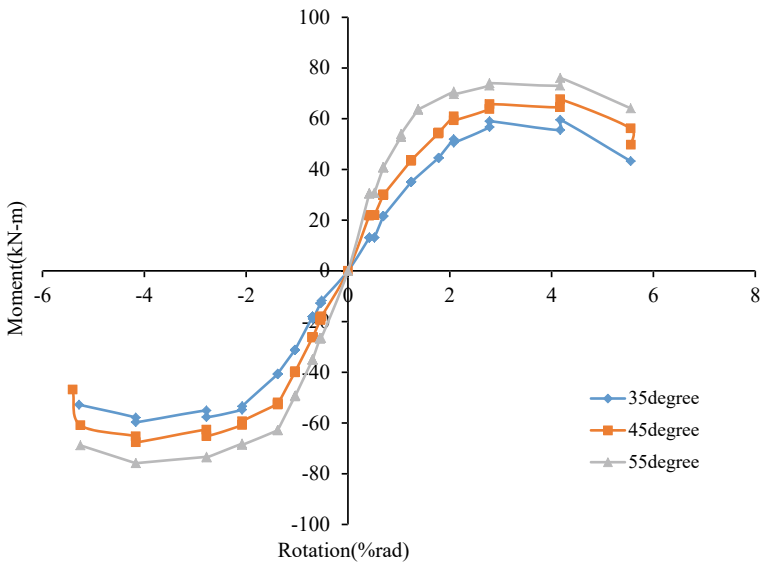


Fig. 10 Effect of angle of split bolt assembly

4 Summary and Conclusions

The behaviour of a stiffened curved extended endplate connection between circular CFST column and I-beam with split bolt assembly under displacement-controlled cyclic load is explored in this study. The FE model of the joint was generated using a confined stress–strain model of concrete and a tri-linear model of steel. The accuracy of model was verified using the experimental results of Ajith et al. [1] in terms of the moment versus rotation relationship and deformed shape. The effect of axial load level and angle of split bolt assembly on the joint behaviour was studied.

The principal conclusions of the present work on the behaviour of CFST beam-column exterior joint are stated below:

1. Nonlinear FEA can be used to predict the ultimate strength and failure modes of circular CFST beam-column exterior joint with sufficient accuracy.
2. The FEA model showed a flexural failure of beam which satisfied the design criteria of strong joint, strong column and weak beam.
3. The total rotation of the joint observed was greater than 0.04 rad in both positive and negative cycle which satisfy the guideline provided by AISC 341-10 for composite special moment resisting frame.
4. Moment versus rotation curve shows a stable behaviour with increase in loop area, indicating the ductile behaviour of joint.
5. The initial stiffness of the joint was found to increase by 27% for positive and negative displacement when the axial load level increases, but it has negligible effect on the moment capacity of the joint.
6. Moment capacity and initial stiffness of the joint were found to be increased by 12 and 39% in positive and negative displacement with increase in angle of split bolt assembly.

References

1. Ajith MS, Beena KP, Sheela S (2018) Comparative study on hysteretic performance of semi through connections in CFT beam-column joint. In: International conference on infrastructure development: issues, innovations and way forward (ICID), pp 81–89
2. Hoang V-L, Jaspert J-P, Demonceau J-F (2015) Extended endplate to concrete filled rectangular column joint using long bolts. *J Constr Steel Res* 113:156–168
3. Hu HT, Huang CS, Chen ZL (2005) Finite element analysis of CFT columns subjected to an axial compressive force and bending moment in combination. *J Constr Steel Res* 61:1692–1712
4. Jingfeng W, Zhang N (2017) Performance of circular CFST column to steel beam joints with blind bolts. *J Constr Steel Res* 82:33–47
5. Kharoob OF, Ghazy MF, Yossef NM (2017) Behavior of beam- high performance fiber reinforced CFST column joint. *Thin-Walled Struct* 113:217–227
6. Lee J, Goldsworthy HM, Gad EF (2010) Blind bolted T-stub connections to unfilled hollow section columns in low rise structures. *J Constr Steel Res* 66(8–9):981–992
7. Li X, Xiao Y, Wu YT (2009) Seismic behavior of exterior connections with steel beams bolted to CFT columns. *J Constr Steel Res* 65:1438–1446

8. Schneider S, Alostaz Y (1998) Experimental behaviour of connections to concrete-filled steel tubes. *J Constr Steel Res* 45:321–352
9. Sheet IS, Umaranim G, MacRae GA (2013) Experimental investigation of CFT column to steel beam connections under cyclic loading. *J Constr Steel Res* 86:167–182
10. Thai H-T, Vo TP, Nguyen T-K, Pham CH (2017) Explicit simulation of bolted endplate composite beam-to-CFST column connections. *Thin-Walled Struct* 119:749–759
11. Wu L-Y, Chung L-L, Tsai S-F, Lu C-F, Huang G-L (2007) Seismic behavior of bidirectional bolted connections for CFT columns and H- beams. *Eng Struct* 29:395–407
12. Yao H, Goldsworthy H, Gad E (2008) Experimental and numerical investigation of the tensile behavior of blind-bolted T-stub connections to concrete-filled circular columns. *J Struct Eng* 134(2):198–208
13. Zhong T, Wang Z-B, Qing Y (2013) Finite element modelling of concrete-filled steel stub columns under axial compression. *J Constr Steel Res* 89:121–131
14. Zhong T, Wei L, Bo-Lin S, Lin-Hai H (2017) Behaviour of bolted end-plate connections to concrete-filled steel column. *J Constr Steel Res* 134:194–208

Studies on Steel Beam-to-Column Joints Subjected to Accelerated Corrosion and Cyclic Loads



A. Cinitha, V. Sampath, and G. S. Palani

Abstract The behaviour of welded beam-to-column joints has widely been studied around the world in recent times as they are predominantly used in the construction of modern steel structures. Basically, the joint consists of an I-section as the beam, while a square hollow section as a column. There has been a dearth of literature on studies pertaining to the behaviour of such welded joints exposed to corrodants and cyclic loads. This served as an impetus to carry out experimental studies to evaluate the behaviour of welded steel beam-to-column joints that were subjected to accelerated corrosion and cyclic loading for the purpose of evaluation for seismic applications. The welded zone was corroded to the extent of causing a loss of 10% to the weight of the steel structure by applying a current of 18A. Sixteen loading cycles conforming to the seismic protocol load were applied to the beam. It was observed that the corroded welded joint failed at a lower load. The unequal distribution of the stresses and the plastic deformation at the corroded welded zone lead to the brittle fracture and ultimately to the failure of the joint.

Keywords Square hollow section · Beam-to-column connection · Corrosion · Cyclic load · Brittle fracture

A. Cinitha (✉) · G. S. Palani
CSIR-Structural Engineering Research Centre, Chennai, India
e-mail: cinitha@serc.res.in

G. S. Palani
e-mail: pal@serc.res.in

V. Sampath
Department of Metallurgical and Materials Engineering, Indian Institute of Technology Madras,
Chennai 600 036, India
e-mail: vsampath@iitm.ac.in

1 Introduction

Welded joints consisting of square hollow section columns and I-beams are widely used in high-rise buildings due to the symmetry of sections, which enables them to resist horizontal forces in both directions without the need for the use of braces [1–3]. The use of welded joints has been widely adopted in recent years in the design of steel-framed structures and has proved to be economical. In areas of high seismicity such joints are adequate to provide sufficient ductility, strength and energy dissipation [5–7]. Moreover, high buckling resistance of the hollow sections makes them an appropriate choice for columns of seismic moment-resisting frames [8–10]. The reduction in thickness and loss of weight due to localization of corrosion of beam-to-column joints have not adequately been addressed hitherto. Damage arising from corrosion leads not only to a decrease in the service life of the structure but also a reduction in its strength and stiffness [11–16]. The reduction in strength and stiffness increases the probability of structural failure leading to catastrophic failure with attendant loss of human life or injury. The catastrophic collapse of both Silver Bridge in 1987 and that of the Mianus River Bridge in 1983 in the USA indicated the paramount importance of predicting the remnant life of steel structural components that have undergone various levels of corrosion. The deterioration due to corrosion could generally range from progressive weakening of the steel structures over a long period of time resulting in catastrophic structural failure. Wang et al. [17] studied the inelastic cyclic behaviour of corrosion damaged welded beam-to-column joints and reported significant reduction in seismic performance due to severe pit formation in weld zones with increasing severity of corrosion levels. This paper presents an analysis of the experimental study of the behaviour of welded steel beam-to-column joints subjected to accelerated corrosion and cyclic loading.

2 Experimental Test Program

Experimental investigations were carried out to assess the performance of welded steel beam-to-column joints that were subjected to accelerated corrosion and cyclic loading. To start with a welded steel I-beam to hollow column joint was fabricated. The welded joint consisted of a box column of $220 \times 220 \times 6$ mm (grade 400 steel) of height 1500 mm with two end plates of size $640 \times 640 \times 16$ mm and an ISMB200 beam (grade 320 steel) of 2100 mm length, as shown in Fig. 1. ISA $80 \times 80 \times 6$ mm sections were used as cleat and seat angles to join beams to columns by adopting MIG welding technique. During welding adequate precautions were taken to minimize distortions arising from heat concentration in localized areas. The welded joints represent corner beam-to-column joints of typical industrial shear frame. The control specimen was labelled BCJ-1, while that was corroded to cause a reduction in weight to the extent of 10% as BCJ-2. A distance of 400 mm on either side of the column from the face of the joint region together with a horizontal region on the

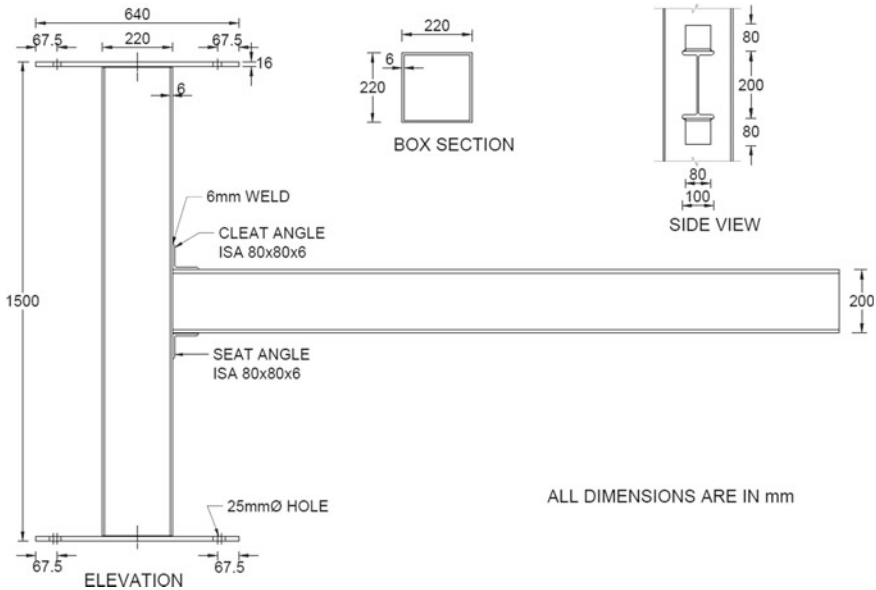


Fig. 1 Schematic diagram showing welded beam-to-column joint

beam (i.e. 400 mm from the face of the joint) was allowed to undergo accelerated chloride-induced corrosion.

The selected regions of beam-to-column joint acted as the anode and a specially fabricated stainless steel section acted as the cathode with a 3.5% NaCl solution being used as the electrolyte as shown in Fig. 2. The welded joint area was corroded so as to cause a loss of 10% in theoretical weight of the targeted area of corrosion by applying a direct current of 18A. A specially fabricated experimental set-up was used to test the cyclic behaviour. The column was loaded axially to apply a load of 300 kN using a hydraulic jack, and the load was maintained at the same level right through the experiment. Sixteen loading cycles adhering to the seismic protocol as per ANSI/AISC 341-16 [18] were applied to the beam from a distance of 1000 mm from the face of the column. An ultrasonic thickness gauge and a micrometre were used to measure the thickness of the beam-column joint (specimen). An electronic balance was used to measure the weight of the uncorroded and corroded BCJ-2 as illustrated in Fig. 3. The thickness measurements of the control (uncorroded/reference) and the corroded BCJ-2 samples were tabulated in Table 1. Figure 4 shows the beam-to-column joint instrumented with elastic and post-yield strain gauges, LVDTs and non-contact LVDTs to investigate the mechanical performance and strain distribution.

The initial weight of the specimen BCJ-2 was found to be 185.4 kg. The weight of the specimen after corrosion was found to be 184.2 kg. The experimental set-up for cyclic loading is shown in Fig. 5. The cyclic loading protocol adhering to ANSI/AISC 341-16 is shown in Fig. 6.

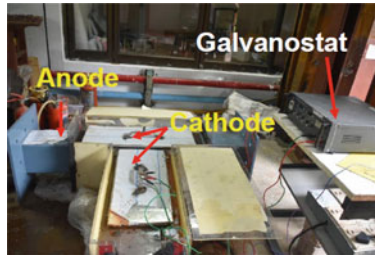


Fig. 2 Photograph showing the experimental set-up used for conducting accelerated corrosion tests



Fig. 3 **a** Photograph showing the experimental set-up used for measuring the weight of corroded BCJ-2 specimen. **b** Photograph showing the experimental set-up used for measuring the thickness of corroded BCJ-2 specimen using ultrasonic thickness gauge. **c** Configuration of beam-to-column joint with notations

2.1 Experimental Set-Up to Simulate Accelerated Corrosion

The galvanostatic method was used to induce corrosion in the specimen BCJ-2. The experimental set-up consisted of a DC power source, an anode, a cathode, a standard calomel electrode and an electrolyte. The targeted regions to be corroded in BCJ-2 were considered as the anode and a specially fabricated stainless steel hollow square box section of $320 \times 320 \times 1$ mm (T-in shape to cover both targeted column and beam region to be corroded) was considered to be the cathode. The positive terminal of the DC power source was connected to the anode, and the negative terminal was connected to the cathode. The current was passed through the electrolyte facilitating electrochemical reactions to take place at the anode as well as the cathode. Thus, the corrosion of targeted region of BCJ-2 specimen [19] was achieved.

In order to assess the mechanical properties of steel, tensile specimens were extracted from beam and column sections by wire cutting adhering to the specifications of ASTM E8M [20] and subjected to accelerated corrosion of varying degrees. The dimensional details of the coupons are shown in Fig. 7. In all 16 specimens were made, with 8 specimens each from the beam and the column, respectively. The

Table 1 Location and thickness (mm) of measurement carried out at each face of the column, angle and beam for control (uncorroded/reference) and corroded specimens for beam-to-column joint

Col-UC	Col-F1	Col-F2	Col-F3	Col-F4
6.00	5.70	5.60	5.83	5.67
<i>Location and thickness of measurement carried out at each face of the column</i>				
6.00	5.73	5.53	5.53	5.70
6.00	5.83	5.47	5.47	5.53
6.00	5.80	5.63	5.63	5.63
6.00	5.83	5.90	5.90	5.83
ISA80-UC		ISA80-L1	ISA 80-L2	
<i>Cleat and seat angle leg thickness (mm)</i>				
6.10		5.63	5.63	
6.10		6.07	5.70	
Beam	Beam-UC	Beam-R1	Beam-R2	Beam-R3
Top Flange	13.17	10.33	10.13	10.07
Web	6.30	6.20	6.23	6.27
Bottom Flange	11.23	9.23	9.30	9.23

Note UC, uncorroded; F1,F2,F3,F4 are faces considered in box column member; ISA80-L1, Avg thickness measured in cleat angle; ISA 80-L2, Avg thickness measured in seat angle; R1, R2 and R3 are three regions considered to measure the thickness in corroded beam specimen

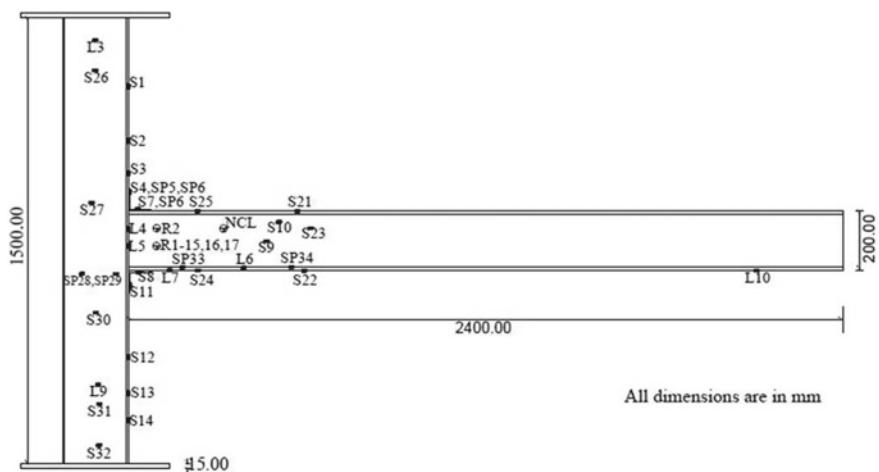
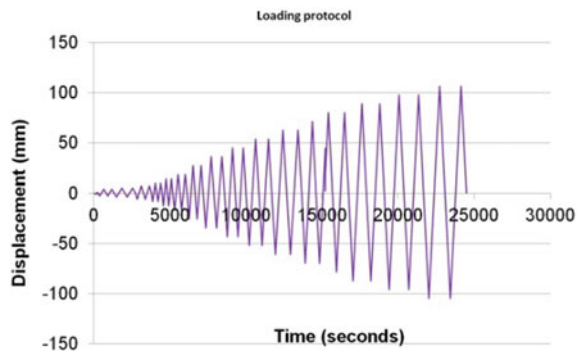


Fig. 4 Location of strain gauges in a welded beam-to-column joint



Fig. 5 Experimental set-up used for cyclic loading

Fig. 6 Cyclic loading protocol as per (ANSI/AISC 341-16)



specimens were then corroded to undergo a weight loss of 0%, 10%, 15% and 20%, respectively, by accelerated corrosion with each group consisting of two specimens. Tensile tests were carried out on corroded coupons to find out the residual strength.

The accelerated corrosion tests were carried out on the specimens by keeping the gauge length region of the coupon as the anode and a steel strip extracted from the same metal as the cathode. They were placed in a 3.5% NaCl solution. The experimental set-up for the accelerated tests is shown in Fig. 8. The specimens were corroded to achieve varying degrees/levels of corrosion. In both tensile specimens extracted from beam and column sections, due to uniform corrosion there was a

Fig. 7 Dimensional details of tensile specimen

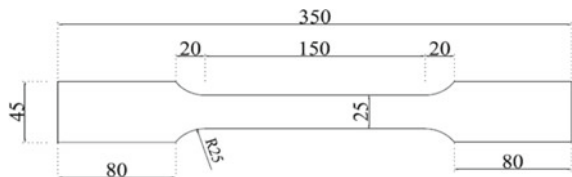




Fig. 8 Experimental set-up used for accelerated corrosion of tensile specimens used in the studies

reduction in thickness of the specimens and the actual thicknesses after corrosion were measured (adopted appropriate surface cleaning methods to remove the rust flakes) using a micrometre. In order to consider the average area, the average thickness and width measurements were taken at three different corroded regions. Strain gauges of 5 mm gauge length were attached to the specimens, and tensile tests were carried out using a hydraulic UTM of 250 kN capacity in order to determine the stress versus strain behaviour. The stress is estimated by dividing the applied load by the average cross-sectional area of the specimen along the gauge length. The test results are presented in the form of stress versus strain plots as shown in Fig. 9. The thickness, weight and yield and ultimate tensile strength values of the specimens are tabulated in Tables 2 and 3. The chemical composition analysis of the samples extracted from the beam and column specimens is given in Table 4.

3 Discussions on Experimental Investigations

The tensile tests were conducted on tensile specimens extracted from the beam and column sections and exposed to different degrees of accelerated chloride-induced corrosion. The strain gauges were attached to the specimens and experiments were carried out in order to determine the stress vs. strain characteristics. In this study, the extent of corrosion was determined by the ratio of the change in weight of the steel specimen due to corrosion to the weight of the initial steel member. The stresses

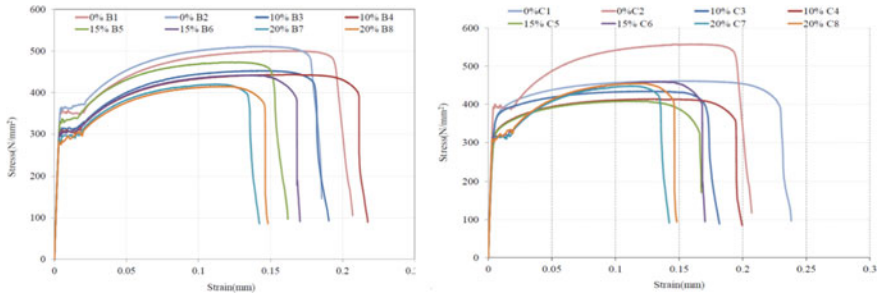


Fig. 9 Stress versus strain behaviour of uncorroded and corroded tensile coupons extracted from **a** beam and **b** column sections

were obtained by dividing the applied load by the cross-sectional area at the average thickness and width along the gauge length. By varying the percentage of corrosion from 0 to 20%, it was observed in tensile specimens extracted from ISMB200 section that the yield and ultimate strength and percentage elongation were reduced by 8–16%, 9–17% and 15–25%, respectively. Similarly, by varying the percentage of corrosion from 0 to 20% it was observed in tensile specimens extracted from BOX $220 \times 220 \times 6$ mm section that the yield and ultimate strength and percentage elongation were reduced by 5–24%, 9–16% and 7–25%, respectively. The behaviour of the welded joint simulated transfer of shear and moment to the column with the column being acted upon by an axial load. The control specimen (BCJ-1) as well as the specimen corroded to cause a loss in weight of 10% (BCJ-2) were capable of reaching 0.1 rad drift angle, which is greater than 0.04 rad specified by AISC 341–16 as demonstrated by the moment versus rotation characteristics as shown in Fig. 10.

The plastic deformation and strain accumulation resulted in fracture of cleat and seat angles in joint zone. The failure modes observed in cleat and seat angles are as shown in Figs. 11 and 12. The combination of high stress and low fracture toughness of the steel is construed to be the primary cause of the fracture of the base metal initiating from the toe of the weld access hole. The site of crack initiation and the failure modes are the same for both BCJ-1 and BCJ-2. However, due to non-uniform distribution of the residual stress during the process of heating to perform welding and the cooling accompanying welding to normal temperature may be the major reason for asymmetric behaviour of BCJ-1. An asymmetrical hysteresis behaviour was also observed for BCJ-2. Strength and stiffness reduction are observed in both the cases. A reduction of 33% in strength is observed for BCJ-2 as compared to uncorroded BCJ-1, which implies that practising engineers need to take necessary precautions during the design stage of such welded joints that are envisaged to be used in marine environments. It can be observed that crack initiation occurred closer to seat angle in BCJ-1 while at the same time tearing of seat angle from the column surface and also bottom beam flange separation from the column surface occurring around the 18th cycle when the displacement amplitude was 88 mm. This was followed by tearing of cleat angle at about the 18th cycles when the displacement amplitude was 105.6 mm.

Table 2 Thickness, weight and yield and ultimate stress values of uncorroded and corroded samples extracted from beam sections measured before and after corrosion

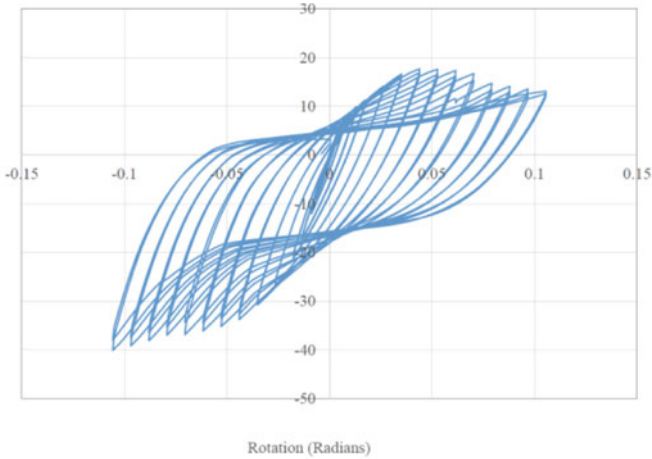
Sample ID	Before corrosion				After corrosion			Strength values		
	Weight (g)	Thickness (mm)	Gauge length (mm)	Corrosion (%)	Reaction time (min)	Weight (g)	Thickness (mm)	Gauge Width (mm)	F_y (MPa)	F_u (MPa)
B1	592.12	6.45	25.12	0	–	592.12	6.45	25.120	340.30	504.95
B2	601.04	6.11	25.17	0	–	601.04	6.11	25.170		
B3	589.87	6.187	24.847	10	176 min & 14 s	573.74	6.03	24.240	305.63	447.22
B4	582.48	6.097	25.047	10	175 min & 05 s	566.32	6.09	24.640		
B5	598.28	6.197	25.010	15	258 min & 58 s	578.67	5.82	24.200	300.06	436.35
B6	580.83	6.073	25.167	15	259 min & 09 s	558.74	5.89	24.160		
B7	602.50	6.493	25.117	20	248 min & 01 s	572.45	6.20	24.630	284.18	416.49
B8	606.04	6.510	25.580	20	376 min 28 s	574.81	6.37	23.580		

Table 3 Thickness, weight and yield and ultimate stress values of uncorroded and corroded specimens extracted from column sections measured before and after corrosion

Sample ID	Before corrosion			Corrosion%	Reaction time	After corrosion			Strength values	
	Weight (g)	Thickness (mm)	Gauge width (mm)			Weight (g)	Thickness (mm)	Gauge width (mm)	F_y (MPa)	F_u (MPa)
C1	569.14	5.81	25.04	0	-	569.14	5.81	25.010	405.99	507.28
C2	571.72	6.07	25.01	0	-	571.72	6.07	24.990		
C3	576.28	5.987	25.183	10	170 min & 23 s	560.74	5.840	24.200	386.50	458.92
C4	569.46	6.040	25.083	10	171 min & 15 s	554.18	5.850	24.830		
C5	569.77	6.020	25.140	15	256 min & 36 s	549.18	5.820	24.120	320.17	455.41
C6	566.27	5.933	24.927	15	250 min & 45 s	543.89	5.65	24.220		
C7	570.13	6.037	24.920	20	340 min & 6 s	547.51	5.68	24.170	304.83	423.03
C8	569.00	5.953	24.983	20	336 min & 13 s	545.61	5.70	24.010		

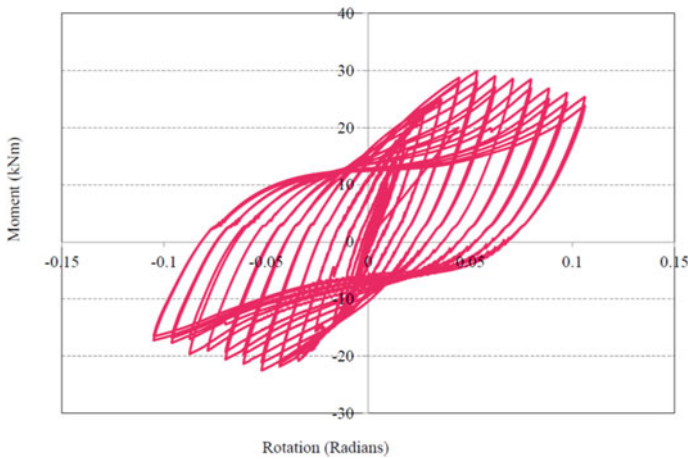
Table 4 Chemical composition of ISMB200 and BOX 220 × 220 × 6 (wt.%) with Fe as the base material

Element (wt.%)	C	S	P	Si	Mn	Si	Fe
ISMB200	0.22	0.028	0.038	0.17	0.52	0.17	Bal
BOX 220 × 220 × 6	0.07	0.02	0.025	0.04	0.4	0.04	Bal



(a) Control specimen

BCJ-2



(b) BCJ-2

Fig. 10 Moment versus rotation characteristics of control specimen (BCJ-1) and 10% corroded specimen (BCJ-2)

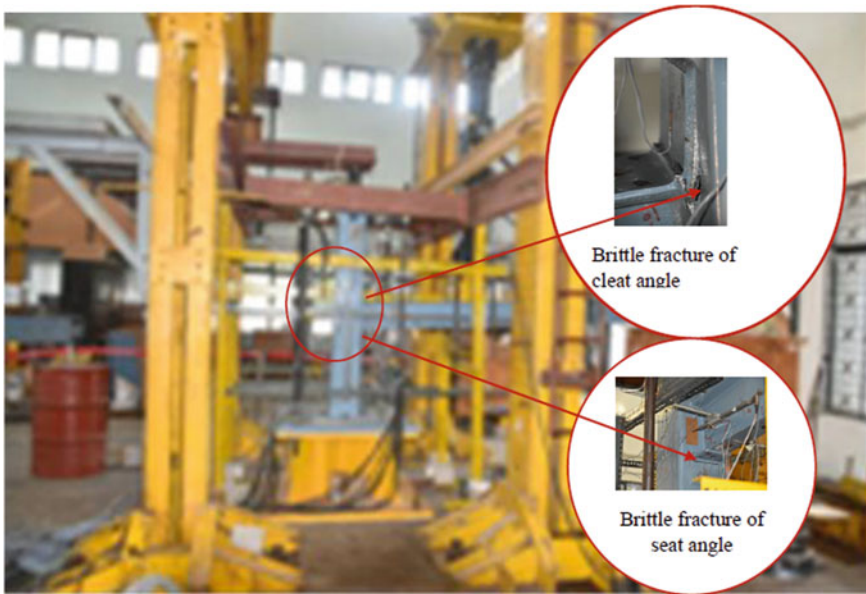


Fig. 11 Failure mode of control specimen BCJ-1 specimen

It was observed for the BCJ-2 specimen that tearing of cleat angle from the column surface and top beam flange initiated at about 15th cycle when the displacement amplitude was 44 mm. Subsequently, the fracture was observed at the cleat angle at about 18th cycle when the displacement amplitude was about 79.2 mm. The test was conducted till 18th cycle with the displacement amplitude being 105.6 mm.

4 Summary

An experimental investigation of the welded beam-to-column joint exposed to corrosion and cyclic loads is presented in this paper. Based on experimental studies on tensile specimens exposed to varying degrees of corrosion and monotonic loads, it is inferred that as the percentage of material deterioration increases with the degree of corrosion, the safe bearing capacity and ductility (measured in terms of percentage elongation) reduces significantly. It was observed that crack initiation occurred closer to seat angle in BCJ-1, around the 18th cycle, while the displacement amplitude was 88 mm, followed by tearing of cleat angle. In BCJ-2 specimen, tearing of cleat angle from the column surface and bottom beam flange occurred around the 15th cycle when the displacement amplitude was 44 mm and subsequently the fracture took place at the cleat angle. The results of cyclic loading test on uncorroded and corroded beam-to-column joints show the corrosion damage and greatly reduce the

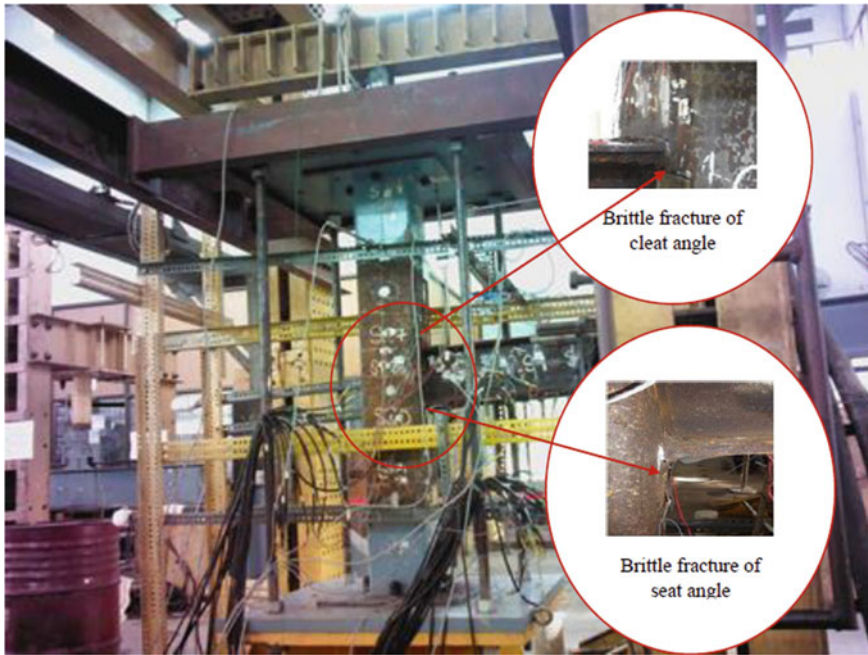


Fig. 12 Failure mode of BCJ-2 specimen

strength and ductility of the joint. The excessive accumulation of plastic deformation resulted in the fracture of the welded regions of the joints in both the cases.

References

1. Morita K (1990) Analysis on strength of unstiffened beam flange to RHS column connections based on the combined yield line theory. E Niemi tubular Structures. In: The third international symposium, Elsevier Science Publishers Ltd
2. Sun Kim UK, Suk Lee J, Bong Kwon Y (1994) Behaviour of connections between SHS Columns & W-section Beams. In: International specialty conference. Missouri University of Science and Technology, pp 705–723
3. Song QY, Heidarpour A, Zhao X-L, Han L-H (2015) Performance of unstiffened welded steel I-beam to hollow tubular column connections under seismic loading. *Int J Struct Stab Dyn* 15(1):113–123
4. Saoula A, Meftah SA, Mohri F, Daya EM (2016) Lateral buckling of box beam elements under combined axial and loads. *J Constr Steel Res* 116:141–155
5. Erfani S, Asnafi AA, Goudarzi A (2016) Connection of I-beam to box-column by a short stub beam. *J Constr Steel Res* 127:136–150
6. FEMA-355D (2000) State of the art report on connection performance. Federal emergency Management Agency Washington (DC)
7. Lyse I, Gibson GJ (1937) Effect of welded top angles on beam-column connections. *Welding J* 16 [Report No.13 (37-2), Fritz Laboratory Reports, Paper 1189]

8. Taras A, Greiner R (2010) New design curves for lateral torsional buckling-proposed based on a consistent derivation. *J Constr Steel Res* 66:648–663
9. EN 1993-1-1 (2005) Design of steel structures. Part 1-1: general rules and rules for buildings. European Committee for Standardization, Brussels
10. EN 1993-1-3 (2006) Design of steel structures, part 1–3: general rules-supplementary rules for cold-formed members and sheeting. European Committee for Standardization, Brussels, Belgium
11. Klinesmith ED, McCuen HR, Pedro A (2007) Effect of environmental conditions on corrosion rates. *J Mater Civ Eng* 19(2):121–129
12. Beaulieu LV, Legeron F, Langlois S (2010) Compression strength of corroded steel angle members. *J Constr Steel Res* 66:1366–1373
13. Appuhamay JMRS, Kaita T, Ohga M, Fujii K (2011) Prediction of residual strength of corroded tensile steel plates. *Int J Steel Struct* 11:65–79
14. Ajide Makinde AF (2011) Microstructural analysis of selected corroded materials from Nigeria oil and gas industry. *Am J Mater Sci* 1(2):108–112
15. Xu SH, Qin GC, Zhang ZX (2016) Experimental research on hysteretic characteristics of steel plates artificially corroded by neutral salt spray. *Adv Mater Sci Eng* 1:1–10
16. Wang H, Xu S, Wang Y (2018) Effect of pitting degradation on ductile fracture initiation of steel butt-welded joints. *J Constr Steel Res* 148:436–449
17. Wang H, Xu S, Li A, Kang K (2018) Experimental and numerical investigation on seismic performance of corroded welded steel connections. *Eng Struct* 174(1):10–25
18. ANSI/AISC 341-16 (2016) Seismic provisions for structural steel buildings. American Institute of Steel Construction, Illinois
19. Cinitha A, Umesha PK, Palani GS, Sampath V (2018) Compression behaviour of steel tubular members under simulated corrosion and elevated temperature. *Int J Steel Struct* 18(1):139–152
20. ASTM E8/E8M-16a (2016) Standard test methods for tension testing of metallic materials. AASHTO No.T68. An American National Standard
21. Nakashima M, Suita K, Morisaka K, Maruoka Y (1998) Tests of welded beam-column subassemblies, global behaviour. *J Struct Eng* 124(11):1236–1244

Response of Steel Knee-Braced Moment Frames Designed Using Ductility-Based Seismic Design Approach with Different Ductility Conditions



Shaktiprasad C. Belaladavar

Abstract This paper presents ductility-based seismic design approach for design of steel knee-braced moment frames (KBMF) and influence of ductility in the design process. Knee-braced moment frame is a hybrid energy dissipating frame which has combined characteristics of moment-resisting frames (MRF) and concentrically braced frames (CBF). In the proposed ductility-based seismic design approach, target displacement ductility ratio and target yield mechanism are the design criteria and the inelastic behaviour of the structure has been incorporated into the design process. A KBMF is designed using Indian Standard (IS) codes and three KBMFs are designed using the ductility-based seismic design approach for different target drifts and ductility conditions. Nonlinear static pushover analysis (NSPA) and nonlinear time history analysis (NTHA) are conducted to assess the effectiveness and study the responses of the frames under strong ground motions. The analytical test results show that the ductility-based seismic design approach produces frames with desirable and predictable structural responses.

Keywords Knee-braced moment frame (KBMF) · Ductility-based seismic design · Displacement ductility ratio · Target yield mechanism · Nonlinear static pushover analysis (NSPA) · Nonlinear time history analysis (NTHA)

1 Introduction

Knee-brace is a stiffener between a column and a beam; it provides greater rigidity in a building frame under lateral loads. Knee-braced moment frame (KBMF) is a hybrid steel structure which combines key characteristics of moment-resisting frame (MRF) and concentrically braced frame (CBF). In MRFs, the beams are rigidly connected to columns and the resistance to lateral forces is mainly due to the rigid frame action by the development of bending moment and shear force, but this causes large lateral

S. C. Belaladavar (✉)
Bengaluru, India
e-mail: belaladavar.shakti@gmail.com

© The Author(s), under exclusive license to Springer Nature Singapore Pte Ltd. 2023
M. Madhavan et al. (eds.), *Proceedings of the Indian Structural Steel Conference 2020*
(Vol. 2), Lecture Notes in Civil Engineering 319,
https://doi.org/10.1007/978-981-19-9394-7_34

421

deformability and the performance of the MRFs is dependent on the quality of materials and workmanship, particularly at the beam-to-column connections. MRFs create no architectural obstruction, and they also provide a stable hysteric behaviour. CBFs deliver excellent stiffness but they are dependent on the post-buckling behaviour of the braces, as post-buckling behaviour is complex and not well understood it is assumed that there will be considerable strength degradation post-buckling in the braces and the CBFs also create architectural obstructions which hampers the aesthetic value of the frame. In order to overcome the deficiencies of the MRFs and CBFs, the KBMFs were developed which is an innovative energy dissipating frame that creates much less architectural obstruction than any other braced frames and also provides lateral stiffness to the frame. KBMF is easy to construct and post an earthquake the damaged knee-brace can be easily replaced.

During major earthquakes, the structures designed to current codes are expected to undergo large inelastic deformations. The seismic design approach employed in the current codes is generally based on elastic structural behaviour and accounts for inelastic behaviour in an indirect manner. In the existing force/strength-based approach for the design of KBMF ductility is implicitly achieved through response reduction factor, R and the strength demand is increased through an occupancy importance factor, I .

In this study, a ductility-based seismic design approach using performance-based plastic design (PBSD) method which is based on energy balance concept is presented, where the inelastic activities are accounted for in the design process. Initially, an elastic KBMF is designed by Indian Standard (IS) code provisions; later three KBMFs are designed by ductility-based seismic design approach using performance-based plastic design (PBSD) method for different target drifts and ductility conditions.

2 Geometry and Loadings of the Test Steel KBMF

Four-storey hypothetical steel KBMF is considered for the present study. The occupancy of the building is for "Office" purpose. The span of the frame is 20 m along both X- and Y-directions. The total height of the frame is 12 m, the height of each storey is 3 m, and the height of all the columns is 3 m placed at 5 m c/c. The slabs are of M25 grade. Figure 1 represents typical plan and elevation of the test KBMF, and Table 1 illustrates the section sizes and loadings considered for the test KBMF. In the frame, the beams and columns are designed to resist the gravity loads and the knee-braces are designed to resist the lateral loads, i.e. earthquake loads. The location of the hypothetical test building is in Dharwad town, India, with earthquake zone of category III. The imposed loads are calculated using IS 875 (Part 2): 1987, design of structural members is carried out using IS 800: 2007 and the earthquake loads are calculated using IS 1893-Part 1: 2016 by "Equivalent static method".

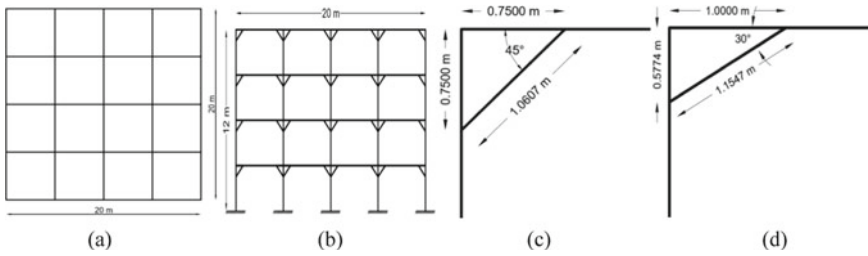


Fig. 1 **a** Plan of the test steel KBMF; **b** elevation of the test steel KBMF; **c** geometry of knee-braced section designed by elastic method; **d** geometry of knee-braced section designed using ductility-based seismic design approach

Table 1 Section sizes and loadings considered in the test steel KBMF

Slab thickness	0.1250 m	Live load (floor)	4.0000 kN/m ²
Area of slab	25.0000 m ²	Live load (roof)	1.5000 kN/m ²
Unit weight of slab	25.0000 kN/m ³	Dead load (structural wall)	13.8000 kN/m
Unit weight of wall	20.0000 kN/m ³	Dead load (parapet wall)	3.0000 kN/m
Height of wall	3.0000 m	Dead load (floor finish)	1.0000 kN/m ²
Height of parapet wall	1.0000 m	Dead load (wpc)	1.5000 kN/m ²
Thickness of wall	0.2300 m	Importance factor, I	1.0000
Thickness of parapet	0.1500 m	Response reduction factor, R	4.0000
Earthquake zone factor, Z	0.1600		

3 Design of KBMF by Elastic Method

The test steel KBMF is designed by elastic method using IS codes, the beams and columns are designed to resist gravity loads ((Dead load) + (Live load)) and the knee-braces are designed to resist the lateral loads, i.e. earthquake loads. The knee-brace is placed at a distance of 3H/4 from the base of the column, and the geometry of the knee-brace is represented in Fig. 1. The knee-brace makes 45° with the beam and column. The beams are designed using Eq. (1); the columns are designed using Eqs. (2–5) based on the end conditions. Knee-brace as a tension member is designed using Eq. (6) and as a compression member using Eqs. (2–5) based on the end conditions. The largest section among the tension and compression member is selected as the knee-braced member. The beam, column and knee-braced member sections of the designed frame are represented in Fig. 2.

$$Z_{reqd} = \frac{(M \times \gamma_m)}{f_y} \tag{1}$$

For compression member with both ends fixed:

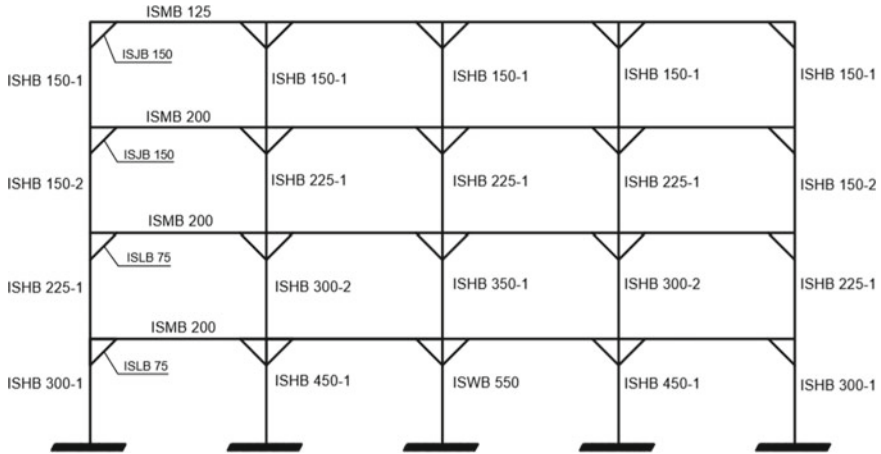


Fig. 2 Member sections of KBFM designed by elastic method

$$P_{cr} = \frac{(2\pi^2 EI)}{l^2} \tag{2}$$

$$L = .7 \times l \tag{3}$$

For compression member with one end fixed and the other end hinged:

$$P_{cr} = \frac{(1.4\pi^2 EI)}{l^2} \tag{4}$$

$$L = .85 \times l \tag{5}$$

$$T_d = \frac{f_y A}{\gamma_{M_o}}, \tag{6}$$

where Z_{reqd} is required section modulus; M is the maximum moment acting on the beam; γ_m is the factor of safety, i.e. 1.15; f_y is the yield strength of the steel i.e. 250,000 kN/m² for mild steel; P_{cr} is the critical load of the compression member; E is Young's modulus; I is the moment of Inertia; L is the effective length of the column member; l is the actual length of the column member; T_d is the design strength of the tension member; A is the gross area of the section; γ_{M_o} is the partial safety factor for failure, i.e. 1.15.

4 Design of KBMF by Ductility-Based Seismic Design Approach

The test steel KBMF is designed using ductility-based seismic design approach by performance-based plastic design (PBPD) method. PBPD method which is based on energy balance concept is used in the present study. In this method, target displacement ductility ratio (μ_s) and target yield mechanism are the design criteria. All the inelastic activities are confined to the knee-braces which are the designated yield members (DYMs) and the beams–columns are the non-designated yielding members (non-DYMs) which are designed to remain elastic.

The design procedure of PBPD method [5] is given below:

- Select a desired yield mechanism and target drift for the structure consistent with the intended performance objectives for the design earthquake hazard. Estimate the yield drift ratio, Θ_y , for the structure.
- Estimate the natural period, T , of the structure given by Eq. (7) and assume an appropriate vertical distribution of design lateral forces.
- With the information from the above steps along with the design spectral acceleration value, S_a , calculate the design base shear, V , by equating the work needed to monotonically push the structure to the target drift (no pushover analysis needed) to the energy needed by an equivalent EP-SDOF to be displaced up to the same drift.
- Use the plastic method to design the structural members that are expected to dissipate the earthquake energy in-elastically, i.e. designated yielding members (DYMs). Members that are required to remain elastic, i.e. non-designated yielding members (non-DYMs) are designed by a capacity design approach.

4.1 Target Displacement Ductility Ratio (μ_s)

Target displacement ductility ratio (μ_s) is given by Eq. (8), and it is dependent on the target drift (Θ_u) for which the KBMF is designed; target drift is selected based on the earthquake zone in which the frame is located such as low drift values for regions with high earthquake activities and high drift values for regions with moderate earthquake activities. The yield drift (Θ_y) which is given by Eq. (9) [1] is varied throughout the frame in order to prevent uneconomic design.

4.2 Target Yield Mechanism

As part of pre-selected yield mechanism, inelastic activities are confined within the DYMs and the global yield mechanism also includes plastic hinge formations at column bases since plastic hinges are formed at these locations during a major

earthquake. In the present KBMF, all the inelastic activities are confined to the knee-braced sections, whereas the beams and columns are designed to remain elastic.

4.3 Design Base Shear (V)

In the current code practice, the design base shear is calculated using earthquake zone factor (Z), response reduction factor (R) which accounts for ductility and an occupancy importance factor (I) which accounts for increase in strength demand thus unable to utilize the significant inelastic deformation capacity of the structures. But in the PBPD method, design base shear is based on the inelastic state of the structure. Using the energy balance concept, after the formation of the pre-selected yield mechanism the structure is monotonically pushed up to a target drift and it is equated with the energy needed by an equivalent EP-SDOF to be displaced up to the same drift to calculate the design base shear of the structure. Equations (10–12) are used in calculation of the design base shear of the frame.

4.4 Design Lateral Forces

It is necessary to incorporate inelastic behaviour of the structures in the design process to obtain desirable and predictable structural response. The design lateral force distribution in PBPD method is based on maximum storey shears and frames designed with this lateral force distribution exhibit uniform inter-storey drifts throughout the height of the structure. Whereas the structures designed according to current code procedures undergo large deformations in inelastic range under major earthquakes leading to different lateral force distributions from those given by code formulas. Equations (13–15) are used for calculation of the lateral force distribution in the frame.

4.5 Design of Designated Yielding Member (DYM)

DYMs are the members in a structure where all the inelastic activities are confined and are designed by plastic method. The DYMs can be replaced post an earthquake while the other members of the structure remain elastic and unaffected. In the present KBMF, the knee-braces are the DYMs, and the required brace strength is very large when the values of L_k/L (length of knee portion/length of the beam portion) are small. The minimum required strength occurs when L_k/L is in the range of 0.13 to 0.25 for all values of the brace angle [6]. Considering large bay openings for utility, the angle of the brace with the beam is taken as 30° and the L_k/L ratio of 0.23 is considered.

Figure 1 gives the geometry of the knee-brace and their design is carried out using Eqs. (16–19).

4.6 Design of Non-Designated Yielding Member (Non-DYM)

Non-DYMs are the members in a structure that are designed to remain elastic. The non-DYMs are designed to resist combined gravity loads and maximum expected strength of the DYM accounting for reasonable strain-hardening and material over-strength. In the present KBMF, beams and columns are the non-DYMs and they are designed by capacity design approach [4]. In the design of columns column tree approach is employed, Fig. 3 shows the forces considered in design of beams, exterior columns and interior columns. Figure 4 [2] represents PBPD flowchart for KBMF.

$$T = \left(\frac{0.09H}{\sqrt{d}} \right) \quad (7)$$

$$\mu_s = \frac{\theta_u}{\theta_y} \quad (8)$$

$$\theta_y = .25 + \left(0.012 \times H \times \left(\frac{h_i}{lb} \right) \right) \quad (9)$$

$$\frac{V}{W} = \frac{-\alpha + \sqrt{\alpha^2 + 4\gamma \left(\frac{s_a}{g} \right)^2}}{2} \quad (10)$$

$$\alpha = \left(\sum_{j=1}^n (\beta_i - \beta_{i+1}) h_i \right) \left(\frac{w_n h_n}{\sum_{j=1}^n w_j h_j} \right)^{0.75T^{-0.2}} \left(\frac{\theta_p 8\pi^2}{T^2 g} \right) \quad (11)$$

$$\gamma = \frac{(2 \times \mu_s) - 1}{R_\mu^2} \quad (12)$$

$$F_i = C'_{vi} V \quad (13)$$

$$C'_{vi} = (\beta_i - \beta_{i+1}) \left(\frac{w_n h_n}{\sum_{j=1}^n w_j h_j} \right)^{0.75T^{-0.2}}, \quad \text{when } i = n, \beta_{n+1} = 0 \quad (14)$$

$$\beta_i = \frac{v_i}{v_n} = \left(\frac{\sum_{j=1}^n w_j h_j}{w_n h_n} \right)^{0.75T^{-0.2}} \quad (15)$$

$$V_i = \sum F_i \quad (16)$$

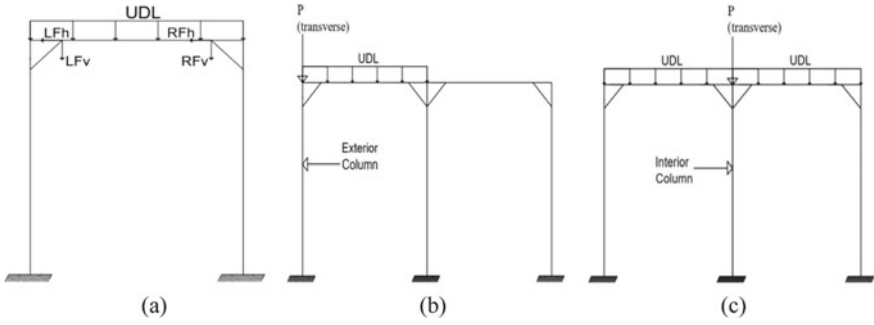


Fig. 3 **a** Forces considered in the design of beams; **b** forces considered in the design of exterior columns; **c** forces considered in the design of interior columns

$$\frac{(V_{\text{storey shear}})_i}{0.9 \cos \alpha_i} \leq (P_y + 0.5 P_{cr})_i \tag{17}$$

$$P_y = F_y \times A_g \tag{18}$$

$$P_{cr} = F_{cr} \times A_g, \tag{19}$$

where T is the fundamental period; H is the total height of the structure; d is the base dimension; h_i is the height at i th level from base; lb is the bay length of the brace; V is the total design base shear; W is the total seismic weight of the structure; g is the acceleration due to gravity (9.81 m/s^2); β_i is the shear distribution factor at i th level; w_j is the seismic weight at j th level; h_j is the height at j th level from base; w_n is the seismic weight at n th level, i.e. top level; h_n is the height at n th level, i.e. top level from base; θ_p is the inelastic drift ($\Theta_u - \Theta_y$); γ is the energy modification factor; R_μ is the ductility reduction factor, it is time period (T) and ductility ratio/factor (μ_s)-dependent; F_i is the lateral force at level i ; V_i, V_n are the storey shear forces at i th and n th level; $V_{\text{storey shear}}$ is the storey shear; α is the angle of brace with beam; P_y is the nominal yield strength; P_{cr} is the nominal compressive strength; F_y is the yield strength, i.e. $250,000 \text{ kN/m}^2$; F_{cr} is the compressive strength; A_g is the gross area.

4.7 Design of KBMF for 2% Target Drift with Varying Ductility by PBD Method

The test steel KBMF is designed by PBD method with target drift of 2%, and the target displacement ductility ratio (μ_s) is varied throughout the structure. The

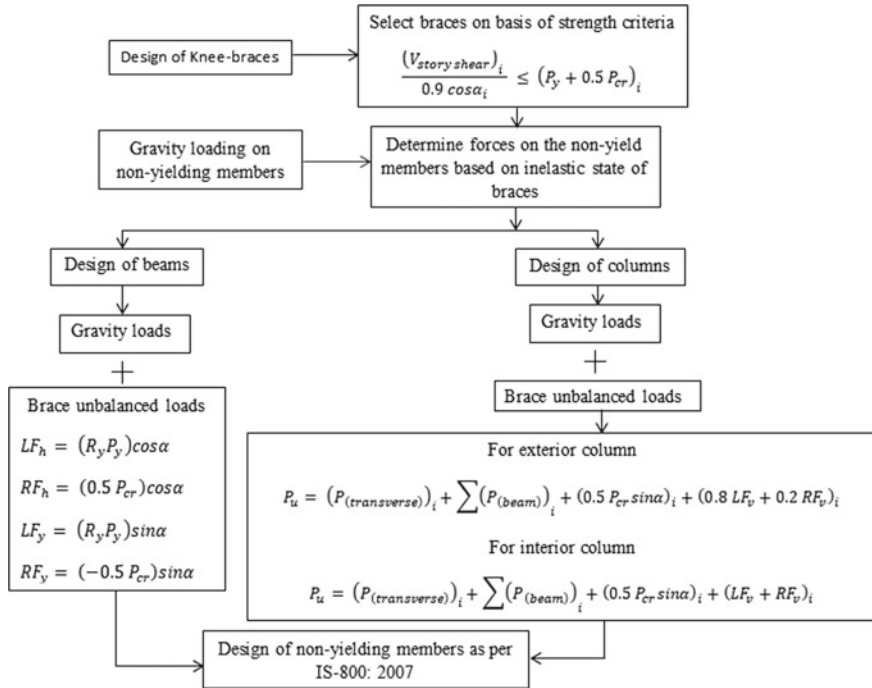


Fig. 4 Performance-based plastic design flowchart for KBMF

parameters used in the design are illustrated in Table 2. The beam, column and knee-braced member sections of the designed frame are represented in Fig. 5.

Table 2 Calculated parameters used in design of PBPD KBMF for target drift of 2% with varying ductility

Parameters	For 2% target drift			
Sa/g	2.5000			
T (s)	0.2415			
Yield drift, θ_y	0.0047	0.0041	0.0036	0.0030
Target drift, θ_u	0.0200	0.0200	0.0200	0.0200
Inelastic drift, θ_p	0.0153	0.0159	0.0164	0.0170
Ductility factor, μ_s	4.2918	4.8544	5.5866	6.5789
Ductility reduction Factor, R_μ	2.7539	2.9511	3.1895	3.4868
Energy modification factor, γ	1.0000	1.0000	1.0000	1.0000
A	17.9040	18.5342	19.1645	19.7948
V/W	0.3425	0.3313	0.3208	0.3109
Design base shear, V (kN)	4700.8800	4546.6341	4402.0302	4266.2051

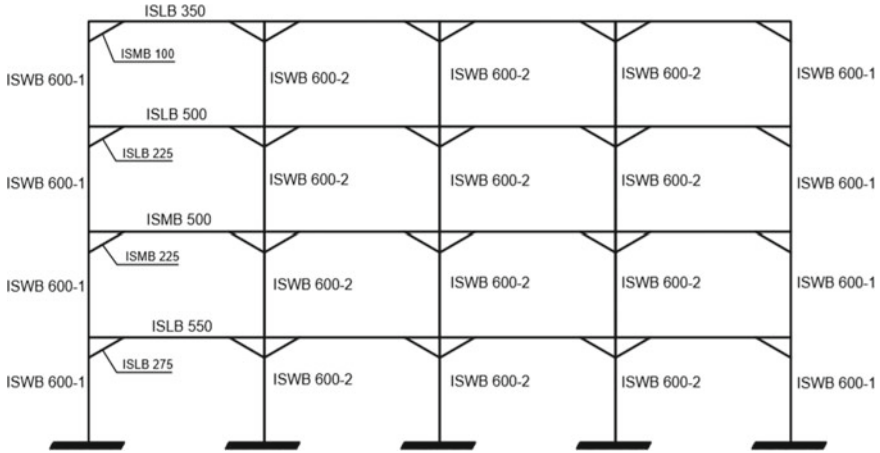


Fig. 5 Member sections of KBMF designed by PBPD method with 2% target drift and ductility varied throughout the structure

4.8 Design of KBMF for 3% Target Drift with Varying Ductility by PBPD Method

The test steel KBMF is designed by PBPD method with target drift of 3%, and the target displacement ductility ratio (μ_s) is varied throughout the structure. The parameters used in the design are illustrated in Table 3. The beam, column and knee-braced member sections of the designed frame are represented in Fig. 6.

Table 3 Calculated parameters used in design of PBPD KBMF for target drift of 3% with varying ductility

Parameters	For 3% target drift			
Sa/g	2.5000			
T (s)	0.2415			
Yield drift, θ_y	0.0047	0.0041	0.0036	0.0030
Target drift, θ_u	0.0300	0.0300	0.0300	0.0300
Inelastic drift, θ_p	0.0253	0.0259	0.0264	0.0270
Ductility factor, μ_s	6.4378	7.2816	8.3799	9.8684
Ductility reduction Factor, R_μ	3.4461	3.6828	3.9699	4.3286
Energy modification Factor, γ	1.0000	1.0000	1.0000	1.0000
A	29.5754	30.2057	30.8359	31.4662
V/W	0.2098	0.2055	0.2014	0.1974
Design base shear, V (kN)	2879.7697	2820.4968	2763.5993	2708.9380

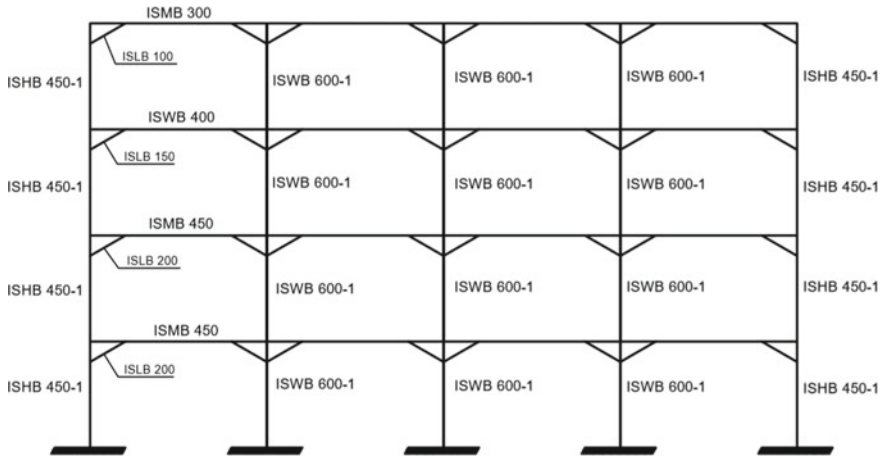


Fig. 6 Member sections of KBMF designed by PBPD method with 3% target drift and ductility varied throughout the structure

Where F_h is the horizontal component; $F_y = F_v$ is the vertical component; LF_h is the horizontal component due to left brace; RF_h is the horizontal component due to right brace; LF_v is the vertical component due to left brace; RF_v is the vertical component due to right brace; P_u is the total load used for column design; $P_{(transverse)}$ is the tributary factored gravity load (1.2 DL + LL); $P_{(beam)}$ is the tributary factored gravity load from the beam, i.e. ($= \frac{1}{2} (W_u) L$).

4.9 Design of KBMF for 3% Target Drift with Constant Ductility by PBPD Method

The test steel KBMF is designed by PBPD method with target drift of 3% and the target displacement ductility ratio (μ_s) is maintained constant throughout the structure. The parameters used in the design are illustrated in Table 4. The beam, column and knee-braced member sections of the designed frame are represented in Fig. 7.

5 Results and Discussions

The effectiveness of the designed KBMFs in terms of seismic performance is assessed through nonlinear static pushover analysis (NSPA) and nonlinear time history analysis (NTHA). NSPA is conducted for gravity loading (1.5(dead load) + 1.5(live load)) condition with the check for P- Δ effects included to determine the maximum

Table 4 Calculated parameters used in design of PBPD KBMF for target drift of 3% with constant ductility

Parameters	For 3% target drift with constant ductility			
Sa/g	2.5000			
T (s)	0.2415			
Yield drift, θ_y	0.0047	0.0047	0.0047	0.0047
Target drift, θ_u	0.0300	0.0300	0.0300	0.0300
Inelastic drift, θ_p	0.0253	0.0253	0.0253	0.0253
Ductility factor, μ_s	6.4378	6.4378	6.4378	6.4378
Ductility reduction Factor, R_μ	3.4461	3.4461	3.4461	3.4461
Energy modification Factor, γ	1.0000	1.0000	1.0000	1.0000
A	29.5754	29.5754	29.5754	29.5754
V/W	0.2098	0.2098	0.2098	0.2098
Design base shear, V (kN)	2879.7697	2879.7697	2879.7697	2879.7697

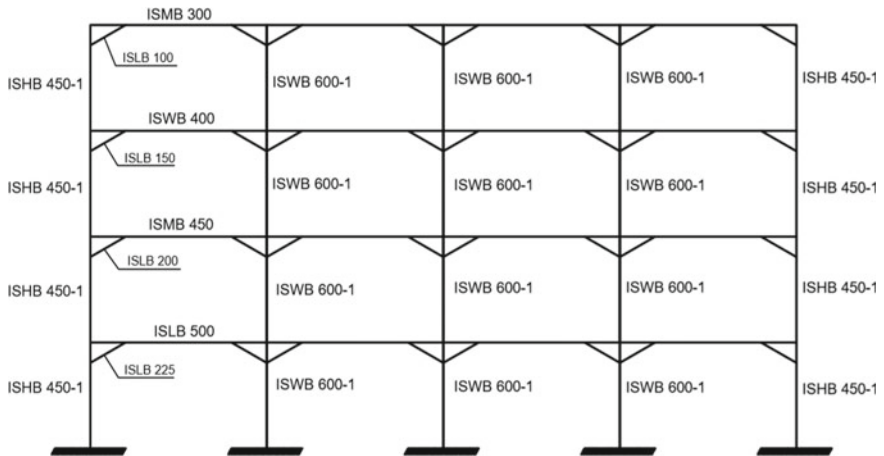


Fig. 7 Member sections of KBMF designed by PBPD method with 3% target drift and constant ductility throughout the structure

base force of the frames, in NSPA displacement is maintained constant and the base force is varied and Fig. 8 represents the pushover curves for all the KBMFs. NTHA is conducted for 1940 El Centro and 2001 Gujarat earthquake, the response of the KBMFs under both the earthquakes in terms of displacement is studied and are presented in Figs. 10 and 11. The inelastic activities in the KBMFs under both NSPA and NTHA are indicated by the formation of plastic hinges which represents the yielding of the particular frame member, and Fig. 9 represents the plastic hinge formations in the frames.

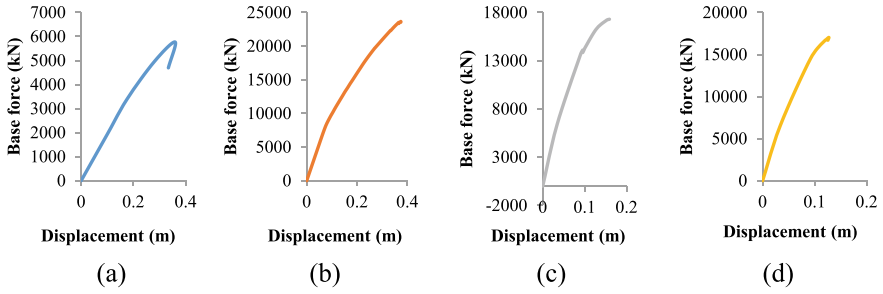


Fig. 8 Pushover curve **a** elastic method; **b** PBPD method with 2% target drift and varying ductility; **c** PBPD method with 3% target drift and varying ductility; **d** PBPD method with 3% target drift with constant ductility

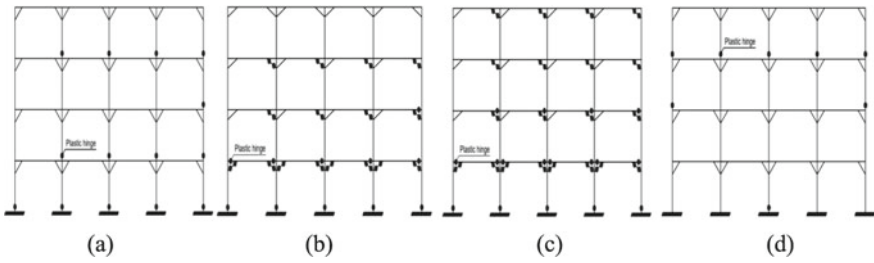


Fig. 9 Plastic hinge formation at collapse under NSPA **a** elastic method; **b** PBPD method for 2% target drift with varying ductility; **c** PBPD method for 3% target drift with varying and constant ductility; **d** plastic hinge formation for elastic method KBMF under El Centro earthquake

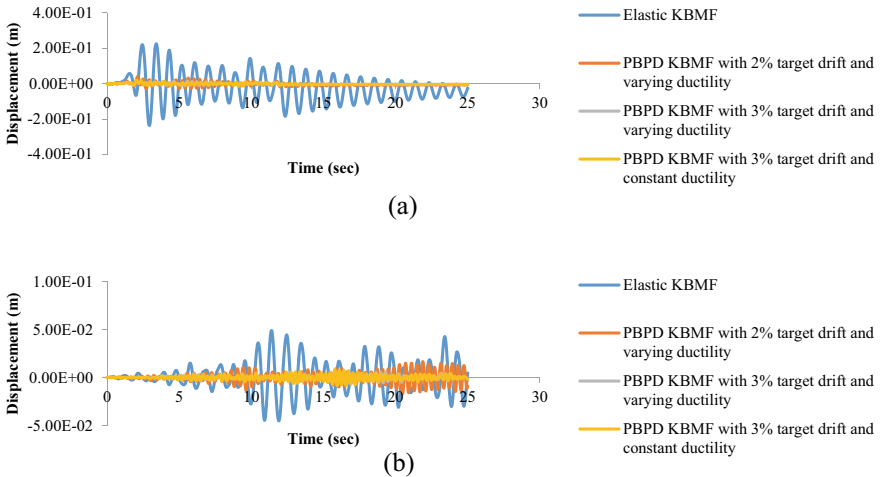


Fig. 10 Roof displacements of the KBMFs **a** El Centro earthquake; **b** Gujarat earthquake

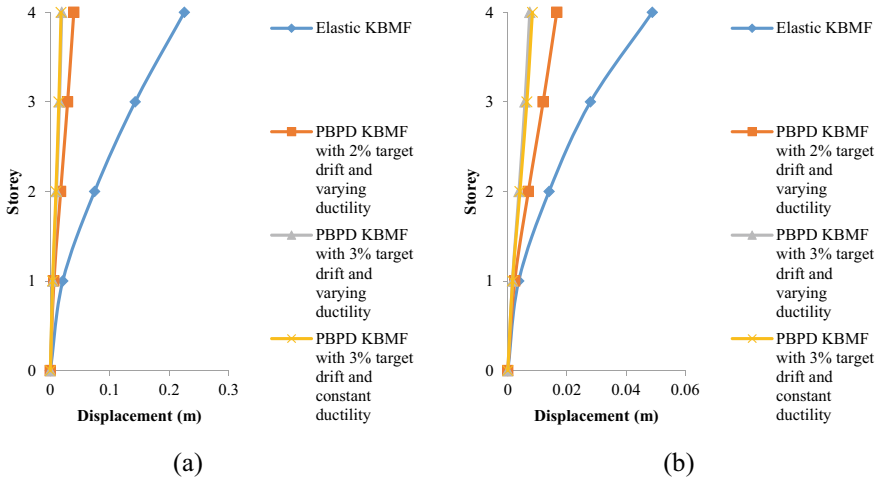


Fig. 11 Storey displacements of KBMFs **a** El Centro earthquake; **b** Gujarat earthquake

The maximum base force and corresponding displacement for the KBMF designed by elastic method are 5770.115 kN and 0.3594 m, for the KBMF designed by PBPD method with 2% target drift 23627.175 kN and 0.3745 m, for the KBMF designed by PBPD method with 3% target drift with varying ductility is 17299.842 kN and 0.1590 m and for the KBMF designed by PBPD method with 3% target drift with constant ductility is 16705.103 kN and 0.1256 m. The roof displacements of elastic KBMF, PBPD KBMF with 2% target drift, PBPD KBMF with 3% target drift-varying ductility and PBPD KBMF with 3% target drift-constant ductility under El Centro earthquake are 0.2254, 0.0395, 0.0192 and 0.0180 m and under Gujarat earthquake are 0.0489, 0.0166, 0.0074 and 0.0083 m, respectively. In terms of base force, PBPD frame with 2% target drift is superior to all other frames. Plastic hinges are formed in the columns of elastic KBMF randomly which is not desirable, for the PBPD KBMFs expected yield mechanism is achieved and the plastic hinges are evenly distributed throughout the frame. Inelastic activity is only observed under El Centro earthquake in elastic KBMF in all the other frames under both the earthquakes no inelastic activities are observed.

The PBPD KBMFs exhibit superior performance in terms of base force as they have effective energy dissipation throughout the height of the frame, the elastic KBMF has lower base force as inelastic activities are concentrated in the column regions. The pushover curves show linear increase for all the frames but for the elastic KBMF and PBPD KBMF with constant ductility a considerable fall at the collapse can be observed. The increase in ductility of the frame beyond certain limits, i.e. $\mu_s > 5$, reduces its flexibility and increases its stiffness, too much of stiffness in a frame can make it brittle, which can be justified by the results of the NSPA where the KBMF with 2% target drift collapses at 0.3734 m and the KBMFs with 3% target drift collapses at 0.1590 m and 0.1256 m. Increase in energy dissipation increases the

base force of a structure which can be justified by comparing the base forces of all the frames corresponding to a particular displacement; i.e. for a displacement of 0.12 m, the elastic frame has base force of 2300 kN, PBPD frame with 2% target drift has base force of 11,000 kN, PBPD frame with 3% target drift and varying ductility has base force of 15,000 kN and PBPD frame with 3% target drift and constant ductility has base force of 16,600 kN. As it is observed from the plastic hinge formations of the frames under NSPA at collapse frames with higher ductility has higher energy dissipation and intern have higher base force at particular displacements. The inelastic activities in first and second storey beams of PBPD KBMF can be attributed to the higher ductility ratio, i.e. greater than 5 ($\mu_s > 5$) as no performance point exists for members designed with ductility factor 6, i.e. $\mu_s = 6$ [3]. In order to achieve desirable yield mechanism of fully elastic beams even at collapse condition strict drift controls such as 1.5% target drift can be employed in the design which restricts the ductility in frame to desired limit, i.e. $\mu_s < 5$.

6 Conclusions

This study evaluates KBMFs designed with current codes and by ductility-based seismic design approach. Steel structures have good ductile behaviour, the response of the frames under different target drifts and ductility conditions has been studied and the main findings are presented below.

- Knee-braced moment frames designed using ductility-based seismic design approach exhibit expected outcomes in terms of desired yield mechanism and effective drift control under strong ground motions.
- KBMFs designed using ductility-based seismic design approach exhibit global ductile behaviour as inelastic activities are thoroughly distributed throughout the height of the frame, but the elastic KBMF exhibit global brittle behaviour as the inelastic activities are concentrated in certain regions.
- Increase in ductility of the frame increases its strength and provides desirable and predictable structural response, but care should be taken to restrict the ductility to certain limit beyond which inelastic activities are observed in non-designated yielding members and it also causes adverse effect on the frame by making it stiffer which leads to brittle failure.
- Varying the ductility ratio (μ_s) throughout the frame leads to economical design of the frame.
- In the ductility-based seismic design of steel structures, for regions with high seismic activity low target drifts have to be used and for regions with moderate and low seismic activities relatively higher target drift values can be used.

References

1. Banihashemi MR, Mirzagoltabar AR, Tavakoli HR (2015) Performance-based plastic design method for steel concentric braced frames. *Int J Adv Struct Eng* 7:281–293
2. Belaladavar SC, Patil VB, Kharmale SB (2018) Ductility-based seismic design of knee-braced moment frame (KBMF). In: 16th symposium on earthquake engineering, vol 61
3. Dalal SP, Dalal PD, Desai AK (2017) Effect of increasing ductility factors on the performance of a steel moment resisting frame designed by performance based plastic design method attuned with Indian code of practice. *Proc Eng* 173:1862–1869
4. Goel SC, Liao WC, Bayat MR, Chao S (2010) Performance-based plastic design (PBPD) method for earthquake-resistant structures: an overview. *Struct Design Tall Spec Build* 19:115–137
5. Goel SC, Chao S (2008) Performance-based plastic design: earthquake-resistant steel structures. International Code Council, USA
6. Leelataviwat S, Suksan B, Srechai J, Warnitchai P (2011) Seismic design and behaviour of ductile knee-braced moment frames. *J Struct Eng* 137(5):579–588

Prequalifying Criteria for Hollow Structural Steel [HSS] Truss Connections



S. Arul Mary and T. Rama Sindhia

Abstract This paper presents prequalifying criteria for hollow structural steel [HSS] truss connections. The criteria were derived based on the parametric study on T, Y, X, N and K type hollow structural steel truss connections. The parametric study was undertaken with reference to the recommendation of CIDECT design guide-3. The more influencing geometric parameters taken in this study were the ratio of brace width to chord width (β parameter), ratio of brace thickness to chord thickness (τ parameter), chord and brace slenderness values, chord and brace aspect ratios. An experimental investigation on welded T and X type truss connections was conducted to validate the prequalifying criteria which were obtained through the parametric study on these connections. The most influencing geometric parameter found in this experimental validation was the ratio of brace width to chord width. The prime objective of this prequalifying criteria is that it qualifies the HSS truss connection such that at its ultimate it governs the chord face plastification connection failure.

Keywords Hollow structural steel connections · T joint · X joint · Prequalifying criteria · β Parameter · τ parameter · Chord face plastification

1 Introduction

Generally, steel hollow sections are categorised into circular hollow sections and non-circular hollow sections, in which the former are called tube sections and the latter, are called box sections. The non-circular hollow sections are further divided into square hollow sections and rectangular hollow sections. The connection of two or more hollow sections leads to the various type of joints, namely T joint, Y joint, X joint, N gap joint and K gap joint. In connection, the main member is a chord and the branching member is the brace.

S. A. Mary (✉) · T. R. Sindhia
Department of Civil Engineering, Thiagarajar College of Engineering, Madurai, India
e-mail: samciv@tce.edu

© The Author(s), under exclusive license to Springer Nature Singapore Pte Ltd. 2023
M. Madhavan et al. (eds.), *Proceedings of the Indian Structural Steel Conference 2020* (Vol. 2), Lecture Notes in Civil Engineering 319,
https://doi.org/10.1007/978-981-19-9394-7_35

437

In the T joint, the force acting in the brace is equilibrated by shear and bending in the chord member. The Y joint is similar to T joint, in which the brace is not perpendicular to the chord. In X joint, the force acting in the brace is resisted by the force in the opposite side brace. In K joint, the force in one brace is equilibrated by the force in the brace of the same side. The N joint is similar to K joint, in which one brace is perpendicular to the chord. The K and N joints can be gap joints if there is a gap distance between the two braces and can be overlapped joints if one brace overlaps with the other. The welded connections between the hollow sections are complicated. The general failure which occurs in these connections is local brace failure, chord face yielding, chord sidewall failure, punching shear failure, chord shear failure, rupture of tension member failure, local buckling of chord side walls and chord face, local buckling of compression bracing member. But the joint strength is based on the failure modes.

The effective width failures such as local brace failure and rupture of a tension member occur due to cracking in the welds or non-uniform stress distribution in the brace that leads to a reduction in effective brace width. The chord face plastification occurs due to the plastification of the face of the chord or the entire cross section. The chord punching shear failure is caused by the initiation of a crack in the face of the chord due to a load of the brace, acting perpendicular to the chord, leading to the rupture of the chord. The chord sidewall failure also called chord web failure occurs due to instability, crushing or yielding under the bracing member. The local buckling failure occurs at the joints due to chord instability, and it can be limited by using appropriate flat width-to-thickness ratios. The weld failure in the joints can also be limited by providing stronger welds than the connected braces and throat thickness satisfying the requirements. The chord shear failure occurs due to shear forces in the chord sidewall, and it becomes critical on using rectangular hollow sections having width more than the depth. Among these failure modes, the chord face yielding mode utilises the entire cross-sectional properties. Hence in the hollow section connections, this yielding failure mode is recommended for its design.

2 Literature Review

Many kinds of research were done on the study of the strength and behaviour of connections in hollow structural steel sections. The connections had been reported between hollow sections and open sections. Limited research works are available on the hollow steel sections connections tested under static conditions. The design guides proposed by CIDECT [DG3] provide enough guidelines for welded connections in frame and truss applications. Wardenier et al. research on hollow sections in structural applications provides an outline of the static and fatigue behaviour of HSS connections and their mode of failure.

Yura et al. [6] studied the ultimate capacity and found that the branch moment capacity can be converted into axial capacity by dividing with a factor of 0.8. Packer Davies [3] studied that the local buckling of the compression brace was observed

to be the most common failure mode in determining the ultimate strength. Packer [2] studied the connections in concrete-filled and unfilled HSS and compared their mode of failure. Zhao and Hancock [7] found that the CIDECT model and Kato model underestimate the section strength. Dawe et al. [1] conducted sixteen full-scale tests on welded T and N type offset connections to study their structural behaviour. IN both the connections one member was laterally offset from the plane of connection. The experimental results reveal that in T type a reduction in capacity due to offsetting a member by 17% of the width of the chord but in N type, the offsetting of the diagonal member by 8% of the width of chord showed a small increase in ultimate capacity.

Feng [4] presented numerical analysis and experimental investigation of cold-formed stainless steel tubular T joints and X joints. The results of the parametric study showed that the design rules are not conservative for the specimens which failed by chord face failure and are conservative for the specimens which have failed by chord sidewall. The validity range for the important parameters in the design equation was also discussed. Beque presented a new design methodology for equal width RHS X joints which were failing by sidewall buckling. A reliability analysis is performed within the framework of both Eurocode and the AISI standards to ensure that the proposed design equation possesses the required level of safety. The newly proposed equation outperforms the current CIDECT design rule for sidewall buckling and also extends the range of applicability to a wall slenderness ratio of up to 50. Packer studied the strength of a welded hollow structural steel connection situated near an open chord member. Based on the experimental investigation and followed by a numerical study by varying the connection geometrical parameters. From this study, a minimum chord end distance was proposed. Sun et al. [5] developed specific design guidelines for hollow structural steel connections located near the truss/girder end with rigid cap plates and also concluded that the existing stress concentration factors in CIDECT design guide-8 were found to be inaccurate. The author also extended the study to estimate the stress concentration factors in circular hollow X type connections. Published another paper in the same year by quoting the inaccuracy of the CIDECT design guide-8.

In the referred literature, the study has been done by connecting the members using appropriate β ratio and thereby various failure modes have been obtained. In this literature, the limits for the failure modes are discussed based on the β parameter only. This study mainly focuses on the connection of members in T and X joints to attain ductile failure. It also shows the ranges of member dimensions to enable ductile failure based on other dimensional parameters.

3 Parametrical Study

The failure modes other than chord face plastification lead to a sudden failure without any warning. Hence, chord face plastification is identified as a ductile failure mode which is recommended for the connection design. To enable the governing failure as a ductile failure in the HSS connections, a parametric study was done on T, Y, X, K and

N connections based on CIDECT guidelines. Indian standard HSS given in IS: 4923 were taken for the study. All possible combinations of Indian standard sections were tried on the considered connections. Based on the parametric study, prequalifying parameters were identified for the HSS connection and the same was presented in Table 1. These parameter limits ensure yielding failure in the HSS connection. The dimension details of the HSS connection were illustrated in Fig. 1. The table values provide an inference that to initiate a yielding failure in all types of HSS connections, the ratio of brace width to chord width (β) value has to be less than 0.82. Among all parameters, the β and τ are found to be more effective than other parameters. The other failure modes of HSS connections are also categorised based on the β ratio. The categories are shown in Table 2.

Table 1 Prequalifying parameters for HSS connections

Prequalifying parameters	Expected failure mode in HSS connection—Chord face yielding				
	T connection	Y connection	X connection	K gap connection	N gap connection
$\beta = b_1/b_0$	< 0.82	< 0.82	< 0.82	< 0.82	< 0.82
$\tau = t_1/t_0$	0.71–0.62	0.71–0.62	0.71–0.62	1–0.83	1–0.83
t_0/b_1	0.13–0.15	0.13–0.15	0.13–0.15	0.08–0.13	0.08–0.13
t_0/b_0	0.11–0.14	0.11–0.14	0.11–0.14	0.06–0.1	0.06–0.1
t_0/h_0	0.04–0.06	0.04–0.06	0.04–0.06	0.03–0.05	0.03–0.05
t_1/b_0	0.1–0.15	0.2–0.15	0.3–0.15	0.05–0.1	0.05–0.1
θ	90°	60°–120°	75°–100°	70°–80°	90°, 70°–80°

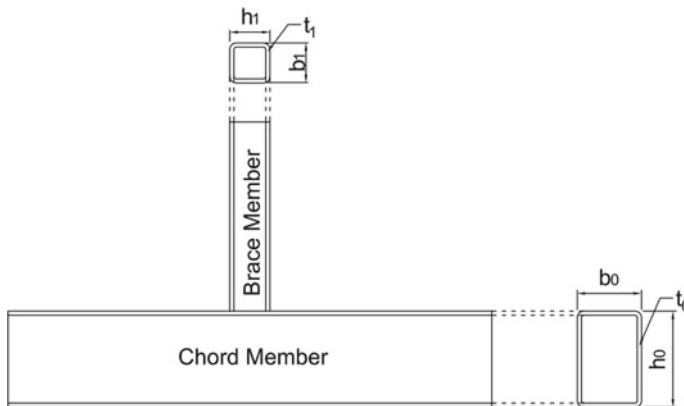


Fig. 1 Dimension details of HSS connection

Table 2 HSS connection failures based on β values

β (brace width/chord width)	Mode of failure
< 0.82	Chord face yielding
to 1	Punching shear
> 0.85	Chord sidewall
> 0.82	Chord shear failure
> 0.9	Effective width failure

4 Validation of the Prequalifying Parameters

Through the detailed parametric investigation, the effective prequalifying dimension limits were derived to ensure yielding failure in the HSS connection. Among these limits, the β and τ limits were found to be more influencing than others. To validate these β and τ limits, experimental programme was conducted. Two main types of connection such as T type and X type connections were considered for the experimental validation. The experimental programme was planned in such a way that the test specimens for the two types of connections were configured to study the prequalifying limits. The tests were performed on specimens having values of $\beta \leq 1$ and τ ranging from 0.6 to 0.9.

5 Experimental Programme

5.1 Specimen Details

The experimental programme was performed on three T type connections and three X type connections. Each of the types of connections has three test samples, and hence, a totally of 18 tests were conducted. The joints were made of structural steel hollow sections manufactured by TATA STRUCTURA with a yield stress of 310 MPa. In T and X connections, the chord was rectangular hollow steel sections and the brace was square hollow steel sections. Among three T connections, one connection was selected to have the same width of chord and brace. The other two T connections were selected to have different widths of chord and brace. Similarly in X connections, one X connection was selected to have equal width of chord and brace. The other two X connections were selected to have different chord and brace widths.

Based on their availability in the market, the width of the chord and brace were selected for the proposed β parameter. The thickness of the chord and brace was selected based on the τ parameter. The sizes of chords used were $60 \times 40 \times 2$, $60 \times 40 \times 2.6$ & $80 \times 40 \times 2.6$ mm and brace were $25 \times 25 \times 1.6$ mm & $40 \times 40 \times 2$ mm. The section dimension details were given in Table 3. In each connection, the

Table 3 Hollow structural steel section for experiment study

Section designation		<i>b</i> (mm)	<i>h</i> (mm)	<i>t</i> (mm)
Chord member	C1	40	60	2
	C2	40	60	2.6
	C3	40	80	2.6
Brace members	B1	25	25	1.6
	B2	40	40	2

chord and brace were connected such that $\beta \leq 1$ and $0.6 < \tau < 0.9$ to study the mode of failure. The connections were checked to act as T or X joints as per CIDECT requirements.

5.2 Mechanical Property of the Test Specimen

A coupon test was conducted on the chord and brace HSS as per IS: 2062 and ASTM A370/E8/E8M-13a standards. The C2 chord member coupon result was illustrated in Fig. 2. The complete coupon results of all HSS members were presented in Table 4. From the coupon test, the yield stress and Young’s modulus were fixed as 375 MPa and 200 MPa, respectively, to compare the experiment result with the analytical results.

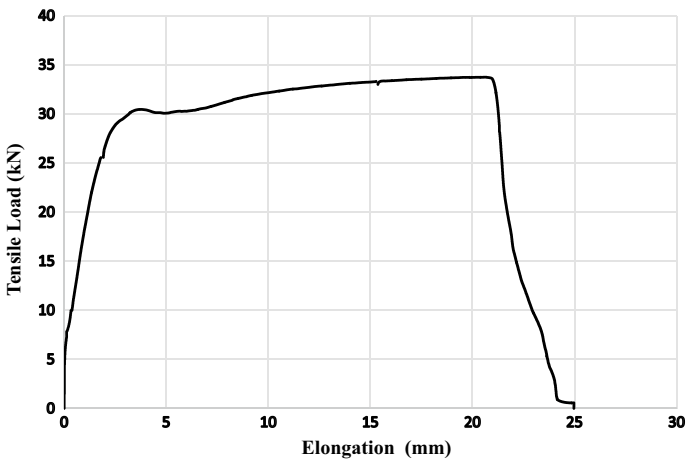


Fig. 2 Coupon test results of the C2 chord member

Table 4 Mechanical properties of the HSS from coupon test

Specimen details	Young's modulus GPa	Yield stress MPa	Ultimate stress MPa	Elongation %
C1	214	380	495	8
C2	215	375	430	9.2
C3	215	375	430	9.2
B1	213	415	515	10
B2	214	380	490	8

Fig. 3 Machine cut of the hollow section

5.3 Fabrication

Connections were fabricated with a rectangular hollow section of 1000 mm length as chord member and square hollow sections of length 220 mm as brace member. End plates of size 250 × 300 × 10 mm were used at the ends of the member to facilitate the application of load and support. All the cutting was done using the machine as shown in Fig. 3. The brace was placed at the midsection of the chord and was welded using a welding machine confirming the standards of IS: 816-1998. In T connection, the brace was welded to one side of the chord. In X connection, the brace was welded to the top and the bottom face of the chord. The connection is then welded to the end plate on one side of the brace in T connection and both the sides of the brace in X connection. Additional stiffeners were used near the supports as shown in Fig. 4 to avoid local failure.

5.4 Specimen Designation

The specimens were labelled based on joint type, nature of the load, chord and brace dimensions and presented in Table 5. For the specimen with designation TC_C2-B1, the first letter 'T' denotes the T joint, the second letter 'C' denotes the loading

Fig. 4 Welding of additional stiffeners near the support



Table 5 Specimen designation and parameter details

Specimen designation	Chord dimensions (mm)			Brace dimensions (mm)			$\beta \left(\frac{b_1}{b_0} \right)$	$\tau \left(\frac{t_1}{t_0} \right)$	$\frac{t_0}{b_1}$	$\frac{t_0}{b_0}$	$\frac{t_0}{h_0}$	$\frac{t_1}{b_0}$
	b_0	h_0	t_0	b_1	h_1	t_1						
TC_C1-B1	40	60	2.0	25	25	1.6	0.63	0.80	0.08	0.05	0.033	0.04
TC_C2-B1	40	60	2.6	25	25	1.6	0.63	0.62	0.104	0.065	0.043	0.04
TC_C3-B2	40	80	2.6	40	40	2.0	1.00	0.77	0.065	0.065	0.033	0.05
XC_C1-B1	40	60	2.0	25	25	1.6	0.63	0.80	0.08	0.05	0.033	0.04
XC_C2-B1	40	60	2.6	25	25	1.6	0.63	0.62	0.104	0.065	0.043	0.04
XC_C3-B2	40	80	2.6	40	40	2.0	1.00	0.77	0.065	0.065	0.033	0.05

in compression, C2 denotes the chord dimension of $60 \times 40 \times 2.6$ mm and ‘B1’ denotes the brace dimension of $25 \times 25 \times 1.6$ mm. For the specimen with designation XC_C1-B1, the first letter ‘X’ denotes the X joint, the second letter ‘C’ denotes the loading in compression, ‘C1’ denotes the chord dimension of $60 \times 40 \times 2$ mm and ‘B1’ denotes the brace dimension of $25 \times 25 \times 1.6$ mm.

5.5 Test Setup

The T and X connection arrangements were tested in a column tester having a capacity of 2000 kN. The load was applied through the loading ram using the 2000 kN hydraulic jack. The 100 kN load cell and linear variable differential transducers (LVDT) connected to a 16 Channel data logger system measured the displacement readings.

The column tester has four rigid frames with an upper movable part. The upper movable part was moved to the required height and was levelled using a spirit level and plumb bob. The load cell was placed above the loading ram, upon which a plate was placed to provide uniform distribution of load to the specimen. The specimen was placed between the load cell and the upper movable part of the column tester. The typical arrangement is shown in Fig. 5. Initially, the load was applied in small

Fig. 5 Connection setup of X type



amounts until the specimen makes contact with the upper movable part. The linear variable differential transducers (LVDT) were used to measure the displacement readings of axial shortening, chord side wall and chord face.

The axial compressive load is applied to the specimen through the loading ram using the hydraulic jack. The load is applied in small increments until failure. In the X connection, the load applied to one brace is transferred to the other brace through the sidewall. In the T connection, the load applied to the brace is resisted by the chord shear of the specimen.

6 Results and Discussions

6.1 T Sections

Three connection responses such as the axial deformation at the joint, chord face yielding at the joint and chord side wall buckling near the joint for the given axial compressive load through the brace were presented in Figs. 6, 7 and 8, respectively. It was inferred that the influence of β is more predominant than τ . The failure loads and the failure modes of three cases of T connection were presented in Table 6. The chord face yielding of the connection is clearly shown in Fig. 9, and the joint weld failure is presented in Fig. 10.

From the experimental investigation, it was observed that the connection failure is initiated as chord face yielding and followed by chord side wall buckling when β is less than unity. When β is 0.63 and τ is 0.62, i.e. the brace dimension is 62%

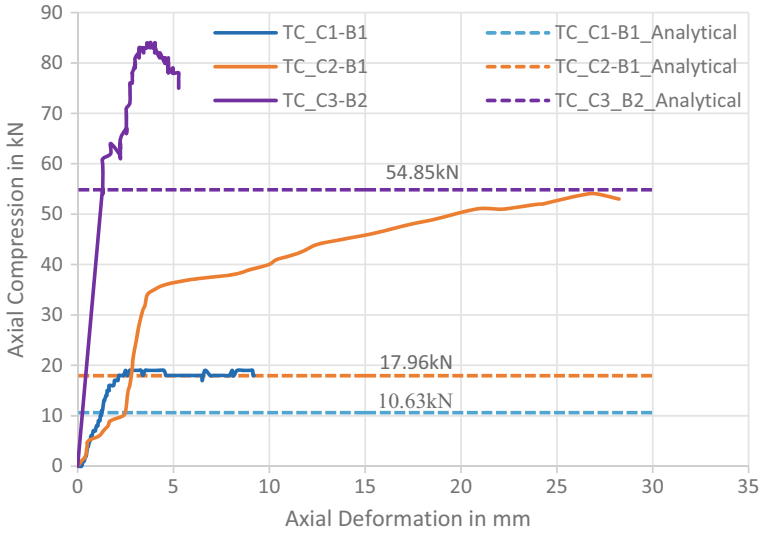


Fig. 6 Axial compression versus axial displacement of T connection

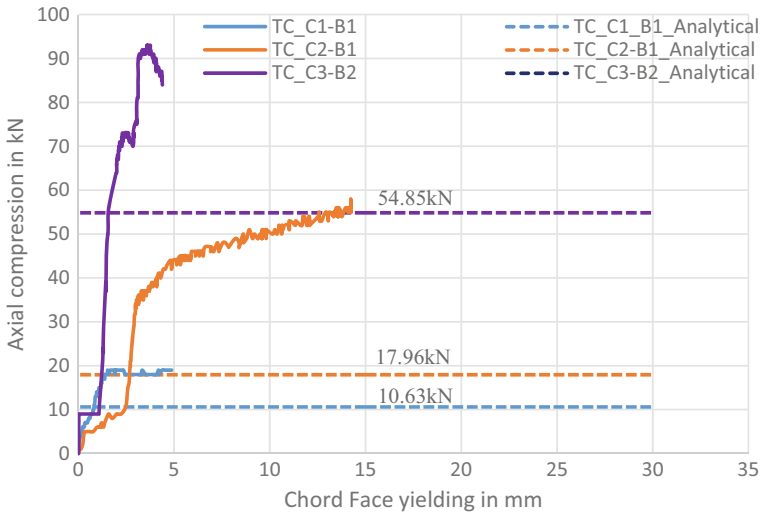


Fig. 7 Axial compression versus chord face displacement of T connection

(approximately) of chord dimension, then the connection shows a significant chord face yielding and joint yielding by reaching the yield point at 35 kN and ultimate at 54 kN. Chord sidewall yielding was also observed in this case. The test result of the case β is 0.63 but τ is 0.8; i.e. the increase in the thickness of bracing the connection failures at 19 kN proves that there is no increase in capacity as the increase in brace

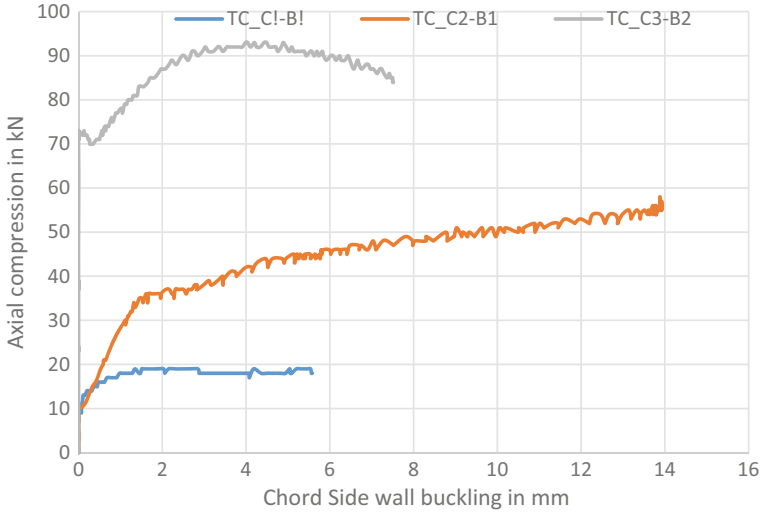


Fig. 8 Axial compression versus chord side wall displacement of T connection

Table 6 Failure loads and modes of T connections

Specimen designation	β	τ	Analytical results from parametric study		Results from experimental investigation	
			Failure load (kN)	Mode of failure	Failure load (kN)	Mode of failure
TC_C1-B1	0.63	0.8	10.63	Chord face yielding	19	Chord face yielding followed by chord sidewall failure
TC_C2-B1	0.63	0.63	17.96	Chord face yielding	54	
TC_C3-B2	1	0.77	54.85	Chord sidewall failure	84	Connection weld failure

Fig. 9 Chord face yielding of TC_C1-B1_2

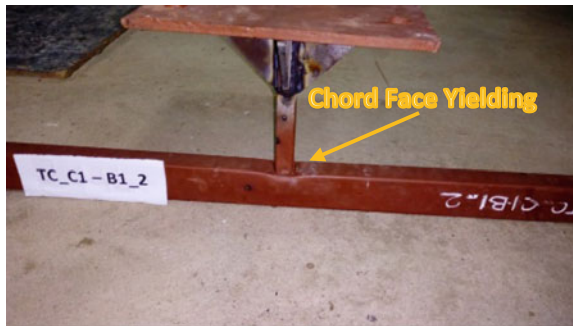
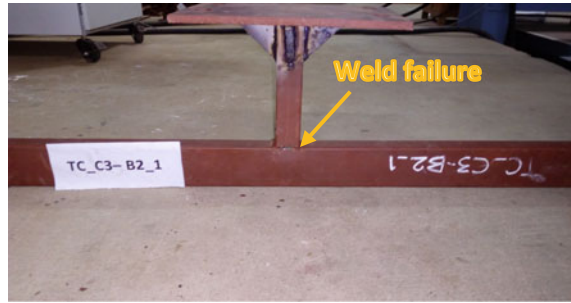


Fig. 10 Weld failure of TC_C3-B2_1



thickness. If the β is kept as a unit and τ is 0.77, the connection shows a rigid behaviour with the ultimate capacity of 84 kN and a reduced deformation, finally failing in joint weld failure. The failure was found to be very sudden.

The connection behaviour is influenced more by the ratio of brace to chord width than its thickness. If the ratio of brace to chord width increases, the connection capacity increases but the increase in the ratio of brace to chord thickness doesn't influence the connection capacity. The analytical estimation of the connection capacities of the above cases was also plotted along with the experimental results in Figs. 4 and 5. From the plot, it was observed that the analytical values were much more conservative than the experimental prediction.

6.2 X Connections

Similar to T connection, in X connections also the three responses were observed during the experimental investigation and the same were shown in Figs. 11, 12 and 13. The failure loads and the failure modes were presented in Table 7 which were compared with the analytical results obtained from the parametric study. The illustration of chord face yielding and weld failure of X connection was presented in Figs. 14 and 15, respectively.

When β is 0.63 and τ is 0.62, the connection shows a ductile behaviour reaches its ultimate at 31 kN. If the thickness of the bracing to the chord is increased, the connection capacity reduces. In the case of β unity and τ is 0.77, the connection behaviour is found to be very stiff and has an ultimate capacity of 95 kN. But the connection fails at the joint weld. Hence, the β ratio is a very much influencing parameter than the τ parameter.

The analytical estimation of the three cases was presented along with the experimental results in Figs. 9 and 10. As mentioned in the T connection, the analytical results are very much conservative in comparing the experimental estimation. Both the connection shows very similar behaviour. With the increase of thickness, the ratio doesn't enhance the connection capacity.

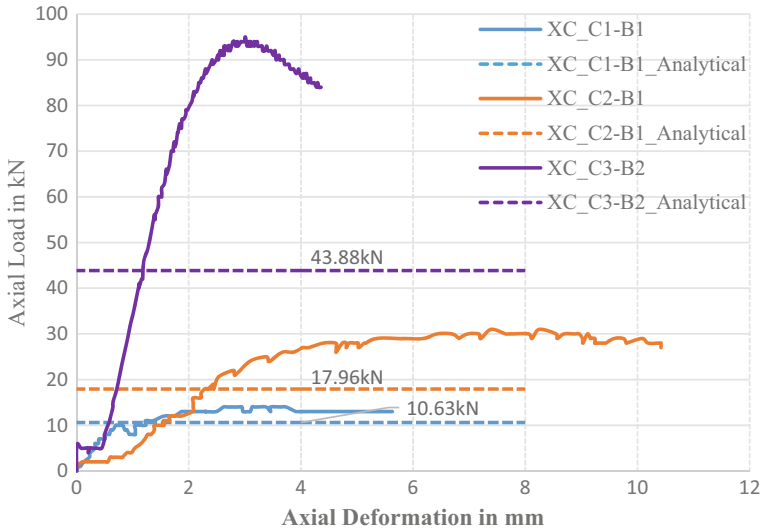


Fig. 11 Load versus axial displacement of X sections

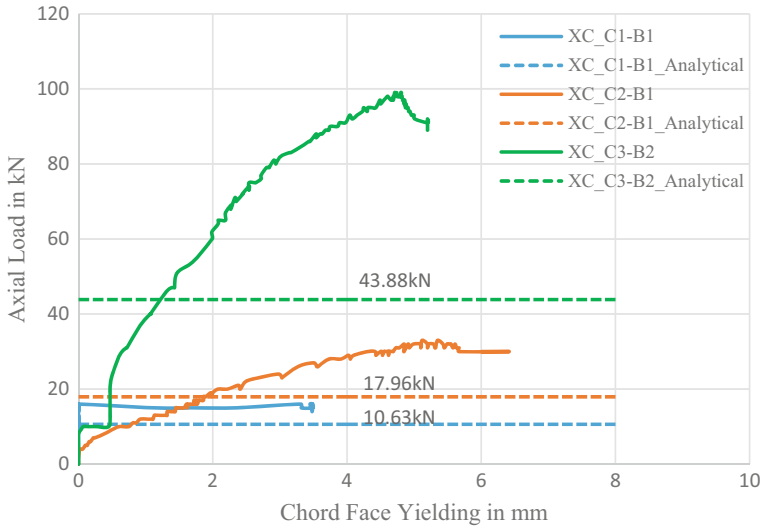


Fig. 12 Load versus chord face displacement of X sections

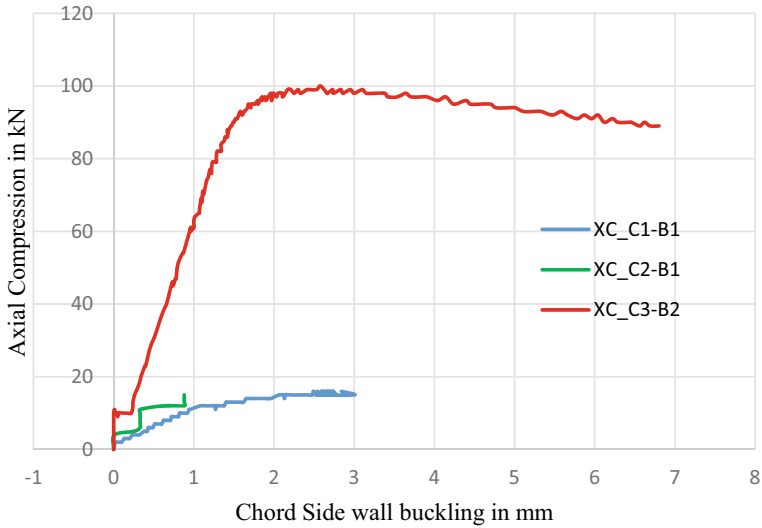


Fig. 13 Load versus chord side wall displacement of X sections

Table 7 Failure loads and modes of X connection

Specimen designation	β	τ	Analytical results from parametric study		Experimental investigation	
			Failure load (kN)	Mode of failure	Failure load (kN)	Mode of failure
XC_C1-B1	0.63	0.8	10.63	Chord face yielding	14	Chord face yielding followed by chord sidewall failure
XC_C2-B1	0.63	0.62	17.96	Chord face yielding	31	
XC_C3-B2	1	0.769	43.88	Chord side wall failure	95	Connection weld failure

Fig. 14 Chord face yielding of XC_C2-B1



Fig. 15 Weld failure of XC_
C3-B2_1



7 Conclusions

HSS T and X joints behaviour were studied for different failure modes, and a parametric study was undertaken to determine the dimension limits which govern ductile failure. The conclusions are obtained based on the connection resistance. The following conclusions were drawn out from the study.

- Among the various failure modes occurring in the hollow section joints, the chord face plastification is recommended as the governing failure mode, as it furnishes a yielding behaviour.
- The influence of brace to chord width ratio and the brace to chord thickness ratio on the behaviour of the HSS truss connection were studied.
- As the thickness of the chord increases, the connection capacity increases.
- In T as well as X connection when the β is less than 0.82 and τ is between 0.6 and 0.9, the failure was initiated in the form of yielding in the chord face region and then extending to the chord sidewall. The load transfer was based on the yield line mechanism formed in the connection region of the chord and brace.
- When β is 1 and τ between 0.6 and 0.9, there was no ductile failure was observed during the experimental investigation. The failure occurred in the weld region connecting the chord and brace.
- It was also observed that the prediction of connection behaviour and failure pattern from the parametric study was found to be the same in the experimental investigation. But the analytical estimation of connection capacity was found to be very much conservative.

- This study provides a prequalifying criterion for T and X type connection for the HSS truss. In T type as well as X type connections, to initiate ductile failure, qualify the brace and chord member such that the ratio of brace width to be 63% of chord width and the brace thickness to be 62% of chord thickness.
- Matching of the brace width with the chord width leads to a stiff connection governed by brittle failure.

Acknowledgements This research was sponsored by TATA STEEL. The authors wish to acknowledge TATA STRUCTURA for supplying the steel specimens for testing.

References

1. Dawe JL et al (2006) Experimental Study of Offset HSS Connections. *J Struct Eng* 132(5):717–725. [https://doi.org/10.1061/\(asce\)0733-9445\(2006\)132:5\(717\)](https://doi.org/10.1061/(asce)0733-9445(2006)132:5(717))
2. Packer BJA (1995) Connections. *J Struct Eng* 121(3):458–467 [ASCE]
3. Packer J, Davies G (1982) Ultimate strength of overlapped joints in rectangular hollow section trusses. *Proc Inst Civil Eng* 73(2):329–350. <https://doi.org/10.1680/iicep.1982.1704>
4. Ran Feng BY (2011) Design of cold-formed stainless steel tubular T- and X-joints. *J Constr Steel Res* 67:421–436
5. Sun M et al (2021) Chord-end RHS-to-RHS and CHS-to-CHS X-connections with rigid cap plates: stress concentration factors. *J Constr Steel Res* 179:106567. <https://doi.org/10.1016/j.jcsr.2021.106567>
6. Yura JA, Zettlemoyer NA, Edwards IF (1980) Ultimate capacity equations for tubular joints. In: Proceedings of the offshore technology conference. American Society of Civil Engineers
7. Zhao X-L, Hancock GJ (1991) T-Joints in rectangular hollow sections subject to combined actions. *J Struct Eng* 117:2258–2277

Cold-Formed Steel Frames Using Self-Drilling Screw Connections



Jikhil Joseph and S. R. Satish Kumar

Abstract This paper analytically and numerically verifies the new design approach for cold-formed steel connections. The need of an easy and rapid construction of moment-resisting frames in cold-formed steel resulted in the screwed connections which are good in taking bearing and shearing forces. The closed cold-formed rectangular box sections are used as the main frame member. The connection idea is to symmetrically distribute the beam moments to column moments through the gusset plates which are screw fastened to the structural members. To begin with, the structural members are sized based on the structural loading. The optimum shape of the gusset plate was found based on the numerical formulations. The size of the gusset plates is formulated based on the beam and column sizes, possibility of assembling the required number of screws and also on the aesthetic sense. The thickness of the gusset plates is arrived based on the numerical simulations by modelling the screws as ties, and the research has progressed towards formulating the expressions for the minimum thickness of the gusset plates based on the moments. The availability of the sheets in the market and also the possible drilling thickness of self-drilling screw also affects the thickness of gusset plates for the practical works.

Keywords Cold-formed steel · Screwed connections · Gusset plates · Local buckling · Rapid constructions

J. Joseph (✉)

Department of Civil Engineering, IIT Madras, Chennai, India
e-mail: jikhil16@gmail.com

S. R. S. Kumar

Structural Engineering Division, Department of Civil Engineering, IIT Madras, Chennai, India
e-mail: kim@iitm.ac.in

1 Introduction

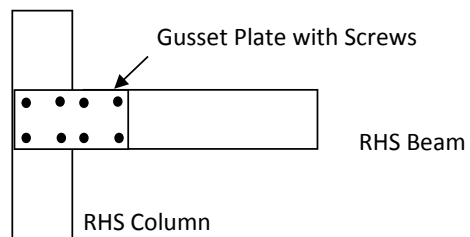
Cold-formed steel members are lightweight structural elements which can be assembled to make frames. The members can be connected by various methods such as gluing, welding and bolting [1, 2]. Screw connections between the cold-formed steel members are generally used as the shear connections [3, 4] and its applicability for the moment connections are checked in this work. Here the proposal is made to connect the beam to column by gusset plates fastened with self-drilling screws. The gusset plates are placed on the both sides of the column for a symmetric distribution of the moments. This connection system is aimed to develop rapid and easy construction technique for the framed structures [5, 6]. The main structural components in this frames include cold-formed steel beams, columns, gusseted plates and self-drilling screws as the fasteners. The self-drilling screws are preferred over self tapping screws because it can drill their own hole and penetrate into the steel thickness. As screws are good in taking shear and bearing [7, 8], the connection is designed for this load and the chances of pull-out load are avoided. The gusset plate acts as the structural member that transfers the moment from the beam to the columns using the screws. The numerical computations of the connections will give some idea on the behaviour of individual connection elements and the whole assembly. The cyclic experimental testing of the proposed model and its realistic numerical simulations are required for the in-depth study on the behaviour of connections and its quality assessment. The CFS members show various types of buckling [9–12] Connections design has to be taken due care as retrofiting methods are always costly [13, 14]. As the self-drilling screws do not need access from both sides of the connection area, the development of this connection gives wider applications.

The proposed model is shown in Fig. 1.

2 Design Idea

The entire frame out of cold-formed steel is planned to build with rectangular box sections and to connect it with gusset plate—self-drilling screw combinations.

Fig. 1 Proposed connection configuration



As in the design of regular frames the first step is analysing a 3D frame model for the expected loads. The span of beam and column members is taken as 3 m for the analysis, and members are designed accordingly.

The process involved in the design of CFS frames is:

- (1) Analyse the 3D frame and find the member forces.
- (2) Design the rectangular hollow beam and column members for the member forces.
- (3) Fix the dimensions of gusset plate as depth of gusset plate (d) = depth of beam, length of gusset Plate = two times the width of column.
- (4) Find the array of screw groups, i.e. number of screws required for the proposed connection.

2.1 Design of Beam

Beams are designed based on the loads acting on the member. Rectangular box section with required section modulus is selected as the member [9]. $Z_{\text{breq}} = \frac{M}{f_{\text{eff}}}$, where the Z_{breq} is the required section modulus for the beam, M is the applied moment and f_{eff} is the effective bending stress.

2.2 Design of Column

The columns are designed for twice the section modulus of the beams. $Z_{\text{creq}} = 2 \times Z_{\text{breq}}$ (columns are designed for 2 times the elastic section modulus of the beam), where the Z_{creq} is the required section modulus for the column.

3 Preliminary Analytical Computations

3.1 Size of the Gusset Plate

The size of the gusset plate is fixed based on the beam and column sizes. The array screws to establish the connection and aesthetics also play a major role.

3.2 Thickness of the Gusset Plate

Thickness of the gusset plate is finalized based on the finite element computations. It's also limited with the availability of the sheet thickness in the market.

3.2.1 Thickness Prediction of Gusset Plate

Gusset plates are to be designed for transferring the moments from beam to the column. Gusset plates can be stiffened by increasing its size as well as the thickness. Both the options has got a limitation in itself. Here the depth of gusset plate is made equal to the depth of beam and the length of gusset plate is made equal to twice the width of column. Increasing size beyond this is an aesthetic issue. Regarding the thickness of the gusset plate, the maximum thickness of cold rolled sheets available are 3 mm. Hence, if higher thickness are required one should go for the sandwich plates as per the requirement.

In the present connection configuration, the gusset plates will behave as in a simple plate bending theory. In addition to this, the bearing stiffness provided by the self-drilling screws adds to the bending capacity of the plate.

For finding the bending capacity of the gusset plate, we can divide the total capacity into two.

- (1) In plane bending capacity of the plates
- (2) Screw group rotational stiffness.

To find the in plane bending capacity of the gusset plate, let's recall the simple plate bending theory (Fig. 2).

Simple Bending Equation

$$\frac{M}{I} = \frac{E}{R} = \frac{\sigma_y}{y},$$

where $M = \frac{\sigma_y}{y} * I$

Plate Buckling Equation $\sigma_b = \frac{K * \pi^2 * E}{12(1-\mu^2) * (\frac{b}{t})^2}$, where $k =$ support constant, $E =$ modulus of elasticity, b and t are width and thickness of the plate, respectively.

We have $M = f * Z = \sigma_b * Z$.

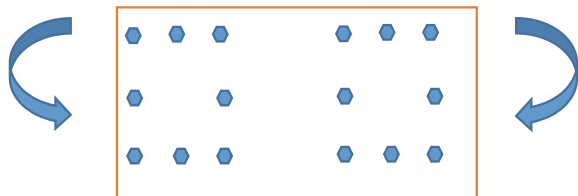
Hence, $M = \frac{K * \pi^2 * E * t * b^2}{12(1-\mu^2) * (\frac{b}{t})^2 * 6}$

We have $K = 24$, and giving values for other constants we have, $(t) = \sqrt[3]{1.3M}$. Hence, we can moment capacity for various thicknesses as given below.

1 mm Gusset Plate Are Able to Give in Plane Bending Strength of 0.723 kNm

2 mm Gusset Plate Are Able to Give in Plane Bending Strength of 5.78 kNm

Fig. 2 Gusset plate with screws



3 mm Gusset Plate Are Able to Give in Plane Bending Strength of 19.53 kNm
4 mm Gusset Plate Are Able to Give in Plane Bending Strength of 46.275 kNm

3.3 Shape of the Gusset Plate

The various shapes of gusset plates were explored such as rectangular, trapezoidal and stiffened gusset plates. Rectangular plates are good at aesthetics and easy to fabricate. Trapezoidal gusset plates provide good stress distribution and efficient use of steel sheet. Stiffened gusset plates are provided if the thickness required is more than available in the market and to enhance plate local buckling strength.

4 Gusset Plate Modelling

Gusset plate forms a major connection element that transfers the moment from the beams to the columns with the help of self-drilling screw fasteners. In the connection element, the screw group size and gusset plate size are mutually dependent. So from the practical design considerations, it was planned to size the gusset plate first and then provide it with required number of self-drilling screws. Trapezoidal or rectangular shapes for gusset plates were the competent options. An extensive numerical study was carried out on the proposed connection between $100 \times 150 \times 2$ mm beam and $100 \times 150 \times 3$ mm column sections. Length of both beam and column was taken as 1 m. Grade of steel is taken as 310 N/mm^2 . The connection assembly is analysed for point loads at the free ends.

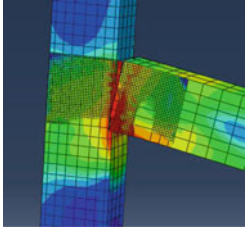
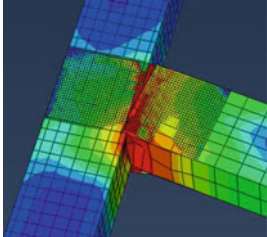
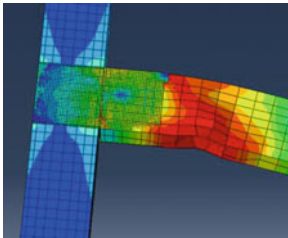
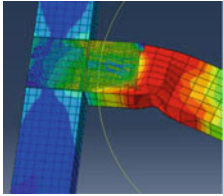
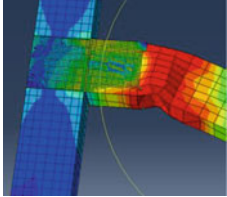
Assumption

All the numerical studies on fixing the size/shape of the gusset plates were performed by Abaqus software. Here the proposed connections are simulated with shell elements (S4R) for the beam, column and gusset plates. The screws are idealized as the tie constraints, assuming that the screws won't undergo any sort of failures.

4.1 Rectangular Plate

The initial idea was to go for a rectangular plate which has got depth same as the beam and width twice the column width. It was found that a gusset plate of 6 mm is required to make the connection safe and to initiate local buckling failures in the beams (Table 1).

Table 1 Rectangular plates

Thickness of gusset plate	Failure pattern	Type of failure
2 mm		Gusset plate
3 mm		Gusset plate
4 mm		Gusset plate
5 mm		Gusset + beam local buckling
6 mm		Beam local buckling

4.2 Trapezoidal Gusset Plates

The depth of plate was assumed to be 300 mm (twice the depth of the beam) on the column and tapered to the beam depth for a width equals the column width. This ensures a smooth stress flow from the beam to the column. From the finite element analysis, it was found that min 5 mm thickness is required for the gusset plates to be strong by itself.

The various failure modes of all thicknesses of gusset plates are shown in Table 2.

4.3 The Idea of Stiffened Gusset Plate

By the finite element analysis, it was found that the gusset plate compression at the beam–column junction is the major reason for gusset plate buckling. The various parameters affecting the gusset plate local buckling are the depth of gusset plate at the beam–column junction, thickness of gusset plate and the unsupported length in the junction. So if the initiation of compression buckling is avoided, the gussets can take a large moment. The various ways of achieving this include increasing the depth (aesthetics issue), increasing the thickness (cost, availability) decreasing the unsupported length (practical/economic considerations).

This drawbacks led to the development of stiffened end gusset plates which leads to great savings and feasible solutions (Table 3).

Hence from the numerical analysis, it's concluded that stiffened gusset plates are the economical shapes for the gusset plates.

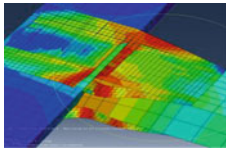
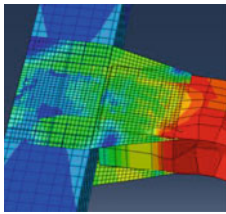
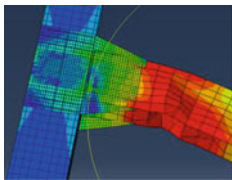
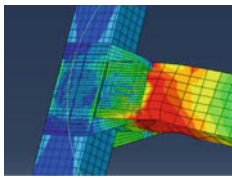
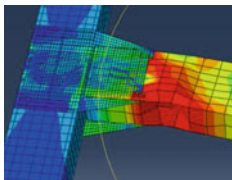
5 Screw Design

5.1 Screw Connections

Self-drilling screws can provide a rapid, effective and economical means to fasten thin-walled steel members. The screws that are available in the market can be classified into two self-drilling and self tapping screws.

Self tapping screws require a pilot hole for advancing the screw. Self-drilling screws have a set of opposing vertical cutting blades at the tip of drill bit, which will facilitate the fastening. Self tapping screw needs a pilot hole to pierce into the steel thickness.

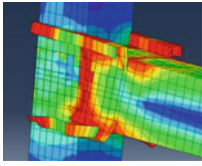
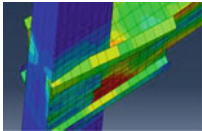
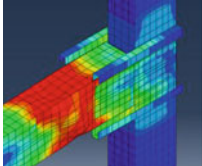

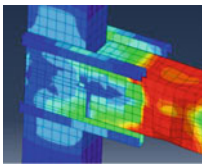
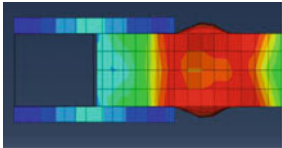
Table 2 Trapezoidal plates

Thickness	Failure pattern	Type of failure
2 mm		Gusset plate failure
3 mm		Gusset plate failure
4 mm		Gusset + beam failure
5 mm		Beam local buckling
6 mm		Beam local buckling

5.2 Various Failure Modes in Screw Connections

Various international codes such as AISI 2007, BS-5950-Part3, EN 1993-1-3 (2006), AS/NZS 4600:2005 provide expressions for the bearing, shearing, pull-out and tilting failures of the self-drilling screws.

Table 3 Stiffened plates

Thickness	Failure pattern	Type of failure
2 mm		Gusset plate failure
3 mm		Gusset plate failure
4 mm		Gusset plate bending + beam buckling
4 mm		Gusset plate failure
5 mm		Beam buckling
5 mm		Beam buckling

5.2.1 Shear Failure

The shear failure is also an important mode of failure which cuts the screw transversely into two pieces.

5.2.2 Excessive Screw Tilting

The screw tilting is also identified as a mode of failure which will allow a slip between the adjoining plates.

5.2.3 Bearing Strength

Bearing failure is mainly the piling up of steel sheet behind the screws. The bearing strength of connected plate depends upon several parameters including thickness of plates, tensile strength of the connected plates, etc.

5.3 Spacing of Screw Connections

As per the AISI 2007 the minimum *c/c* distance between the screws shall be not less than 3times the diameter of the screw. Similarly, the edge-to-end distance should not be less than the 1.5 days.

6 Design of Screw Connections

The self-drilling screws are used for connecting the beam to column using the gusset plates. The in plane action of moments will make the screws to undergo bearing, shearing and pull-out/pullover modes of failure. The tensile yielding of the screws is not a significant case. In the proposed connections, the screws are designed and arranged in a view to take the moment and shear and bearing action. Screw groups are arranged on the both sides of column, and the load is transferred from the beam through gusset plates. The screws are arranged farther from the centroid to take moment and shear loads. The screws near to the centroid are removed as they are unable to take up the moments (Fig. 3).

Figure 4 shows the arrangement of screw groups on beam and column. A spreadsheet was prepared to find the shearing/bearing capacity of the connections for the desired performance.

The screw groups in twisting moment + shear connections can be analysed or designed by two methods such as elastic (vector) analysis and strength (plastic analysis). As per the former analysis, the force in a screw is proportional to the distance from the centroid of the bolt group. Similarly, the direction of force will be perpendicular to the line radiating from the centroid to the bolt group.

In the case of plastic analysis, the instantaneous centre of rotation is differently located from the centroid of the screw group. And the estimation of instantaneous centre of location is a trial-and-error procedure which makes it tedious. When there is lack of fit in the connection, the plastic method may be oversensitive and not

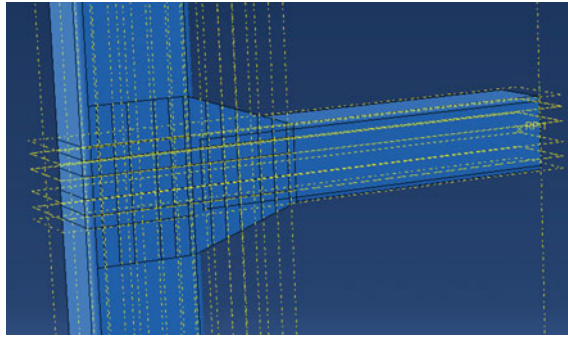


Fig. 3 Trapezoidal plates

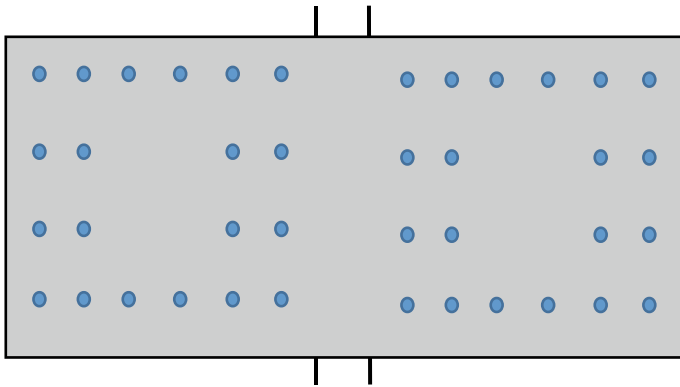


Fig. 4 Gusset plates with screws

recommended. The elastic analysis always gives a lower bound result and always preferable.

6.1 *Strength Prediction of Screws Due to Various Structural Actions*

The screw capacity check is performed on the weaker region between beams—gusset plate connection. The beam thickness is taken as 2 mm and the gusset thickness as 4 mm. The ultimate tensile capacity of the plate is taken as 280 N/mm² (Table 4).

Table 4 Screw capacities based on various design codes

	Shear capacity	Bearing capacity	Pull-out	Pullover	Net section failure
AISI 2007	7.6 kN	–	2.5 kN	28.4 kN	72 kN
AS/NZS	7.6 kN	–	2.5 kN	28.4 kN	
CSA	–	–	–		
EUROCODE	–	5.82 kN	2 kN		
IS 801	–	5.82 kN	2 kN		

The arrangement of screws was made such that no screws in the group exceeds codal values. This satisfies the strength requirement of screw groups.

7 Group Rotational Stiffness Assessment

7.1 Stiffness Design

$$K_B = kb \sum d_i^2$$

$\sum d_i^2 = \frac{M}{K_B * \Theta_r}$. The equations are provided by the Lim et al. [5] (Table 5).

The rotational stiffness (K_B) of various screw group sizes is tabled here for quick estimations. Here in Table 1 represents total length of screw group and the d represents the depth of the screw group. The required rotational stiffness can be computed and provided as an array of screws as per the tabular values for establishing desired rigidity in the connections.

Table 5 Screw sizes and rotational stiffness

Screw group size	Rotational stiffness
2 × 2	$(l^2 + d^2)$
3 × 3	$1.5 (l^2 + d^2)$
4	$2.22 (l^2 + d^2)$
5	$3.125 (l^2 + d^2)$
6	$4.2 (l^2 + d^2)$
7	$5.444 (l^2 + d^2)$
8	$6.857 (l^2 + d^2)$
9	$8.4375 (l^2 + d^2)$
10	$10.185 (l^2 + d^2)$

8 Conclusion

The primary development of moment-resistant cold-formed steel frames is detailed in this paper. It was found that the moment transfer from beam to column through the gusset plate and self-drilling screw combinations works well and is numerically proven. A series of detailed experimental works were performed at the IITM lab and support the connection idea.

References

1. Lee YH et al (2014) Review on cold-formed steel connections. *Sci World J.* <https://doi.org/10.1155/2014/951216>
2. Lennon R, Pedreschi R, Sinha BP (1999) Comparative study of some mechanical connections in cold formed steel. *Constr Build Mater* 13(3):109–116 (Elsevier Science Ltd)
3. Fiorina L, Della Corte G, Landolfo R (2007) Experimental tests on typical screw connections for cold-formed steel housing. *Eng Struct* 29(8):1761–1773. <https://doi.org/10.1016/j.engstruct.2006.09.006>
4. Wang L, Young B (2018) Behaviour and design of cold-formed steel built-up section beams with different screw arrangements. *Thin-Walled Struct* 131:16–32
5. Lim JBP, Nether Cot DA (2004) Finite element idealization of a cold-formed steel portal frame. *J Struct Eng* 130:78–94
6. Mills J, Laboube R (2004) Self-drilling screw joints for cold-formed channel portal frames. *J Struct Eng* 130:1799–1806
7. Rautenbach E, van Rensburg BWJ (2016) Finite element modelling of thin sheet steel screw connections. In: *Insights and innovations in structural engineering, mechanics and computation—proceedings of the 6th international conference on structural engineering, mechanics and computation, SEMC 2016*, pp 1253–1258. <https://doi.org/10.1089/wound.2014.0603>
8. Serrette R, Peyton D (2009) Strength of screw connections in cold-formed steel construction. *J Struct Eng* 135(August):951–958. [https://doi.org/10.1061/\(ASCE\)0733-9445\(2009\)135:8\(951\)](https://doi.org/10.1061/(ASCE)0733-9445(2009)135:8(951))
9. Foster ASJ, Gardner L (2016) Stability of steel beams using the continuous strength method. *Thin-Walled Struct* 100:1–13
10. Niu S, Rasmussen KJR, Fan F (2015) Local–global interaction buckling of stainless-steel I-beams. I: Experimental investigation. *J Struct Eng* 141(8):04014194
11. Selvaraj S, Madhavan M (2019) Structural design of cold-formed steel face-to-face connected built-up beams using direct strength method. *J Constr Steel Res* 160:613–628
12. Selvaraj S, Madhavan M (2018) Geometric imperfection measurements and validations on cold-formed steel channels using 3d noncontact laser scanner. *J Struct Eng* 144(3):04018010
13. Selvaraj S, Madhavan M (2018) Retrofitting of structural steel channel sections using cold-formed steel encasing channels. *J Perform Constr Facil* 32(4):04018049
14. Selvaraj S, Madhavan M (2019) Strengthening of laterally restrained steel beams subjected to flexural loading using low-modulus CFRP. *J Perform Constr Facil* 33(3):04019032

Finite Element Modelling of Screw Connections in Cold-Formed Steel



Jikhil Joseph and S. R. Satish Kumar

Abstract The idea of this paper is to critically review the various finite element modelling methods of screw connections in cold-formed steel. To have a detailed study, the finite element modelling of gusset plates with screws as the fastener has been taken. In the real model, the screws are subjected to bearing, shear and pullout forces. The various methodologies for modelling screw connections include tie constraint model, spring model and screw solid model with interactions. The modelling procedure, assumptions, merits and demerits of each finite element model are deeply studied. In the tie constraint model, the screws are modelled as ties which connects the two adjacent nodes. In this model, the behaviour of screws cannot be studied and are intended for studying the behaviour of connecting elements treating the screws as rigid. The spring model is an advanced model which accounts the bearing, shearing and pullout strengths of the screws which has to be programmed based on the experimental results. The more realistic one is the real solid modelling of screws in the connections. This numerical analysis does not need any input data's other than the material properties. Even the model is computationally time consuming, the results give accurate screw stresses at the element level.

Keywords Cold-formed steel · Screwed connections · Tie constraints · Spring modelling · Solid modelling of screws

J. Joseph (✉)

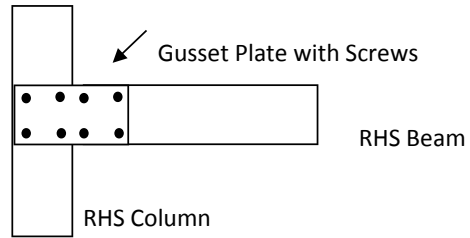
Assistant Professor, Department of Civil Engineering, Government Engineering College, Thrissur, India

e-mail: jikhil16@gmail.com

S. R. S. Kumar

Professor, Structural Engineering Division, Department of Civil Engineering, IIT Madras, Chennai, India

e-mail: kim@iitm.ac.in

Fig. 1 Finite element model

1 Introduction

Cold-formed steel sections provide numerous possibilities of connections such as bolts, self-drilling screws, blind rivets, various welding techniques, gluing, clinching, nailing [1]. Among the various connections, the screw connections which aids the faster constructions are possible only in the cold-formed steel members. A lot of works has been done on the screw connections and the design equations have been developed [2, 3]. The researches are ongoing with this connection, trending towards the fire resistance and seismic designs.

As the full-scale connection test is very costly, the researchers are more focusing on developing the finite element models which will represent the actual test behaviour [4, 5]. When it comes to the screw modelling, tilting of fasteners in the hole, pullover of the screws, distortion of the sheet metal around the hole in tension and so forth contribute to this distinction as well. Other important factors to be considered in finite element modelling are boundary conditions, load paths and large displacement of any structural part because of buckling/bending/rotation. To incorporate such large local displacements and rotation of screws, a geometrically and materially nonlinear finite element formulation was used. The CFS member exhibits various buckling modes [5, 6] and its design is always complex [7, 8]. As the retrofitting methods are always costly especially in CFS [9, 10], the same has to be properly addressed.

The most frequently used iteration scheme Newton–Raphson is preferred for the solution of nonlinear finite element equations. Finite element modelling ideas of the screws [2] were studied taken as a single case study in this paper. The connection between rectangular beam to the column with gusset plate–self-drilling screw combination were taken for the connection modelling. The study model is shown in the Fig. 1.

2 Validation of the Finite Element Model of the Beam

To have a detailed study on the model, the finite element modelling of the structural elements has to be validated. As this connection is critical at beam level and connection level, the rectangular hollow cold-formed steel beam is validated here.

Fig. 2 FE model proposed by Wilkinson [11]

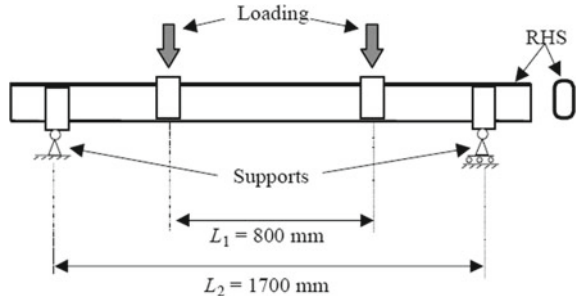
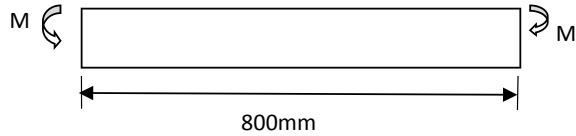


Fig. 3 Schematic representation of the simplified FE model used



In the studies by Wilkinson [11], the cold-formed RHS beam was loaded with four point loading. Hence, out of 1700 mm length, only 800 mm was under pure bending. In the experimental setup, loading was applied through two welded plates enabling the load to be applied as two point loads. The FEM model used by Wilkinson was an exact replication of the experimental model. The normalised moment curvature plots obtained from the experiments were compared with the FEM prediction of the simplified model (Fig. 2).

A simple model is used in the current study by taking exact beam bending length and uniform moments were applied on both the ends of the beam. The beam is simply supported, allowing nodal displacement in the axial direction. The beam is prevented from lateral buckling by giving adequate lateral supports (Fig. 3).

The finite element studies revealed that the ABAQUS model used adequately predicts the initial stiffness, peak load and post buckling behaviour obtained from the experimental studies. The ABAQUS model with S4R shell elements is meshed (Fig. 4) appropriately and analysed using RIKS algorithm to exactly predict the CFS beam response as shown in Fig. 5.

3 Validation of the Gusset Plate

Similar to the cold-formed steel beam, the finite element modelling of gusset plates has also to be validated. The gusset plates are validated for the in plane bending for the theoretical equations available. Here, the size of gusset plate is taken as 300X150mm and subjected to uniform moment. All the boundaries were simply supported and plate bending stress is given by

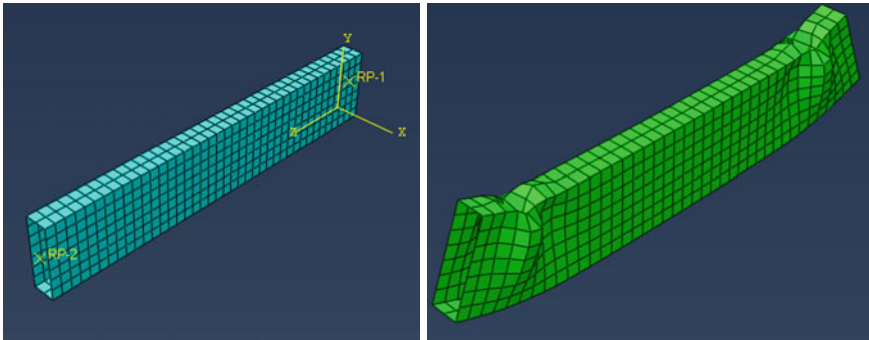


Fig. 4 S4R rectangular box beam mesh and failure mode

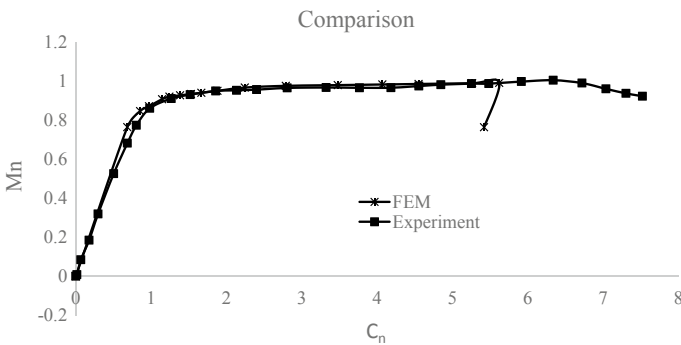


Fig. 5 Comparison between experimental and simplified FE model results

$$F_{cr} = \frac{\pi^2 k E}{12(1 - \eta^2)} \left(\frac{t}{b}\right)^2,$$

where t, b are thickness and width of the plates. K is the bending coefficient and for simply supported plates with uniform bending its 24. The elastic in plane bending moment is compared with numerical modelling (S4R shell element) and theoretical expressions and is given below (Figs. 6, 7 and Table 1).

This plot on comparison between theoretical and numerical results with thickness as a parameter shows that for smaller thicknesses, the values are near and fem model works well (Fig. 8).

Fig. 6 Numerical model of plate

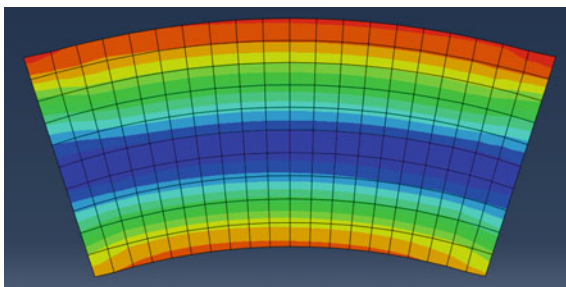


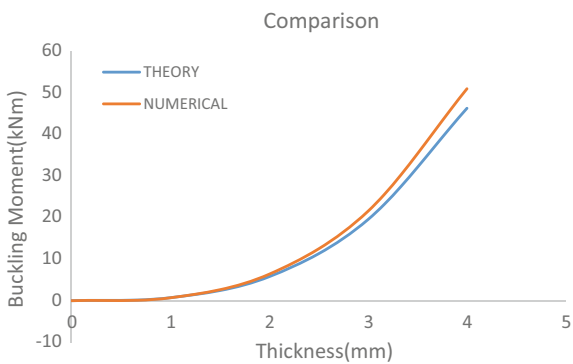
Fig. 7 Support conditions of plate



Table 1 Comparison of numerical and theoretical moments for in plane plate bending

Thickness	Theoretical	Numerical	Numerical/theoretical
1	0.723	0.698	0.96
2	5.78	6.377	1.10
3	19.53	21.53	1.10
4	46.27	50.96	1.10

Fig. 8 Variations in results upon thickness



4 Screws

In the construction industry, mainly two types of screws are used self-drilling and self-tapping screws. In the case of self-drilling screws, the drill bits on the end portion facilitate the easy driving of screws into the cold-formed steel plates. The self-drilling screws with maximum thickness of penetration available in the market are 12 mm. Here for the screwing purpose, there is no need to make a pilot hole. On the other hand, the self-tapping screws are not provided with any drill-bit, and it requires a pilot hole to pierce into the cold-formed steel plate.

4.1 *Various Modes of Failure of Screw Connections*

The screws undergo various modes of failure such as bearing, shearing, pull-out, pullover and tilting modes of failures. The self-drilling screws are efficient in taking bearing and shearing stresses. Hence, most of the screw connection designs were made to undergo these stresses.

5 Finite Element Modelling of Screw Connection Assembly

Considering the behaviour of self-drilling screws and various modes of failures in structural actions, three methods of finite element modelling of screws are studied.

5.1 *Tie Constraint/Fastener Modelling*

In the tie constraint modelling of screws, the real behaviour of screws is not taken into account. Here, two nodes are tied together so that during the analysis, the slave node moves with the master node. The tie constraint model was adopted to find out the minimum thickness of the gusset plate required to prevent the premature buckling of plates. Here, hard contact is given between the beam and column (Fig. 9).

Once the stresses in the screws are within the limits, the next mode of failure is gusset plate buckling. This model can be used for checking the adequacy of the gusset plate thickness assuming the screws are safe. Once the gusset plates have the desired thickness, the connection will remain strong, and the failure will be visible in the structural members especially the beam local buckling.

In the ABAQUS programme, the tie constraints are available in the Interactions module. This study was mainly made to study the effect of shape and size of gusset plates on the failure modes of connections assuming screws are intact.

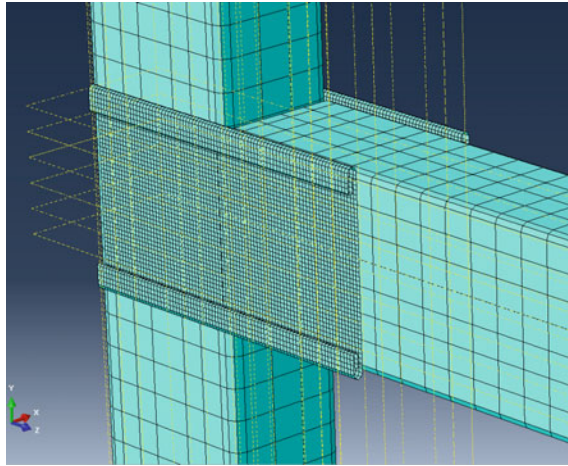


Fig. 9 Tie constraint model

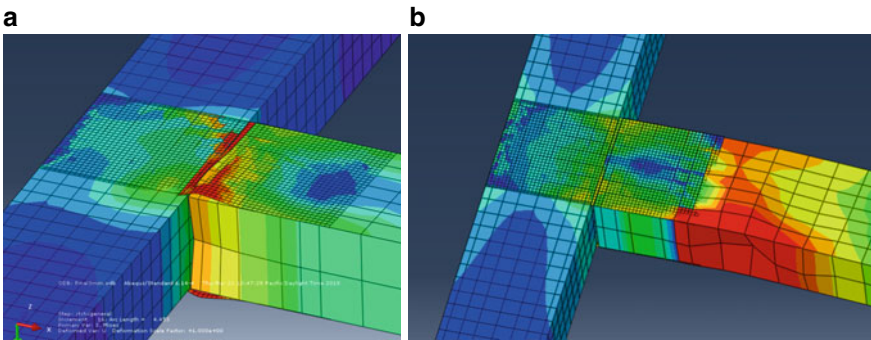


Fig. 10 a 3 mm gusset plate. b 6 mm gusset plate

The various shapes of gusset plates such as rectangular, trapezoidal and stiffened (in order as shown below) are analysed for finding the minimum thickness to change the mode of failure from connection to beam buckling as shown in Figs. 10, 11 and 12.

5.2 Spring Modelling

In the case of spring modelling, the screws are modelled as springs to add the effect of screws to the numerical model. The spring behaviour is idealised by the rotational spring and rotational stiffness's to account for the tilting and pullout behaviour of

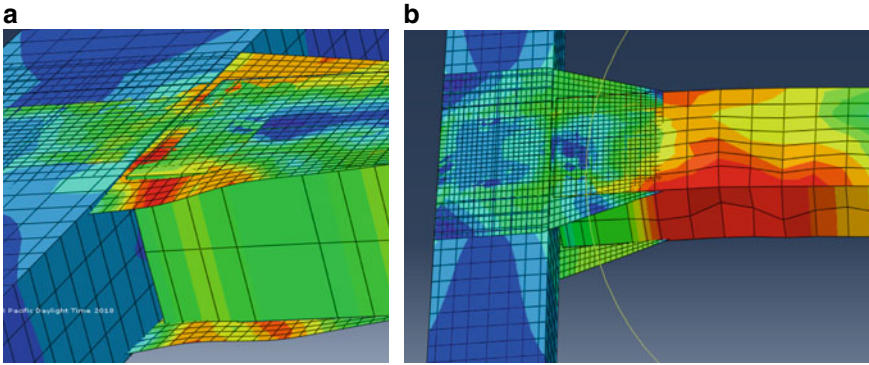


Fig. 11 a 2 mm thickness. b 4 mm thickness

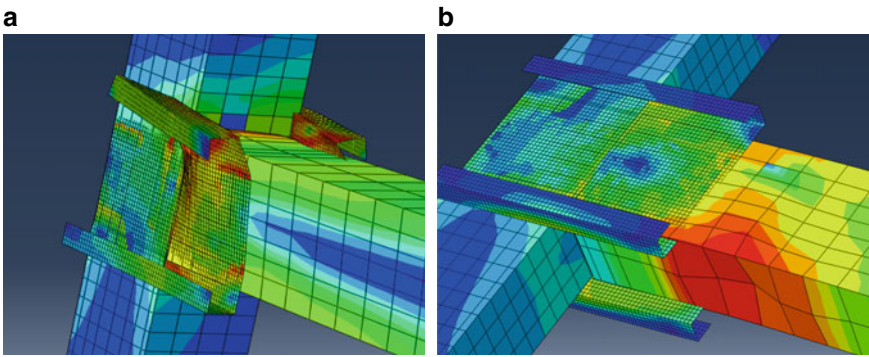


Fig. 12 a 2 mm thickness. b 3 mm thickness

the screws. The axial springs in linear and transverse directions take into account the bearing, shearing and pullout behaviours (Figs. 13 and 14).

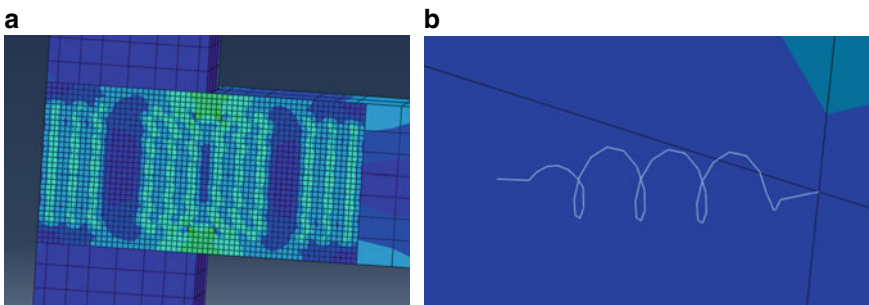


Fig. 13 a Rectangular connection assembly. b Spring in the numerical model

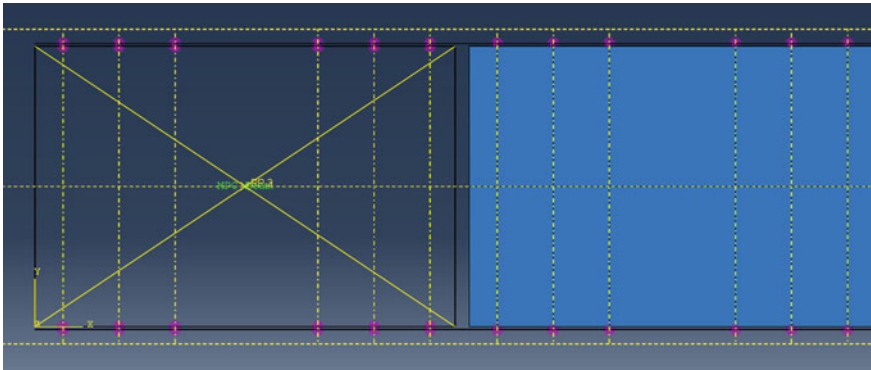


Fig. 14 Top view of spring modelling

On comparison with the tie constraint model, where the screw was just considered as a rigid element, here in the spring model, the effect of screws in the connection is considered. In the ABAQUS model, the spring model is available under the connectors tab, and options are provided to input various spring stiffnesses. But the drawback of this model is that this model is not capable of analysing the stresses induced in the screws at the element level. For a detailed study of the screw connections, one has to go for the full-scale solid modelling, and significant advances have made in the numerical model as detailed in the next section.

5.3 Screw Solid Modelling

Before proceeding to an in-depth analysis of solid screw model, a small case study has been considered. Here, two steel plates connected with single screw are numerically modelled, and its behaviour is studied (Fig. 15).

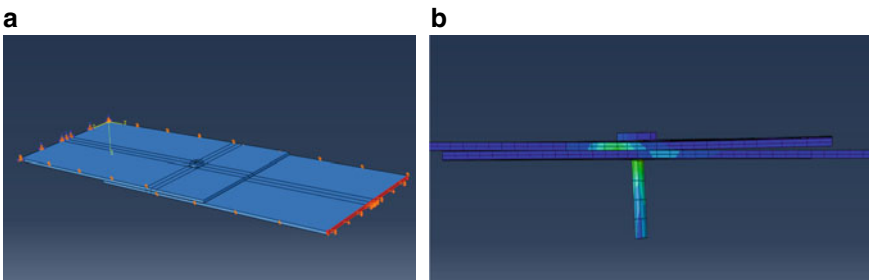


Fig. 15 a, b Preliminary model for self-drilling screws

In the model, the interactions between the plate holes and screws were given as hard contact, and the analysis shows that the model is good enough to catch the screw failures.

The analysis was extended to full solid modelling to simulate the exact behaviour of screws and the element interactions. In this model, all the adhering elements such as beams, columns and gusset plates are modelled as S4R elements and screws are modelled as 3D solid elements (Fig. 16).

The full solid modelling of screws in the cold-formed connections is progressing, and now, the model is able to predict the realistic failure model. Numerical works are advancing towards the proper interaction between the elements for an realistic load deflection and hysteresis curves of the connection. A comparison on the failure model between the numerical and experimental results as shown in the following Fig. 17.

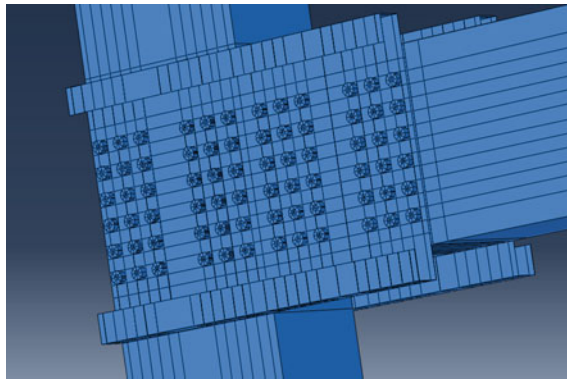


Fig. 16 Full-scale model of self-drilling screw connections

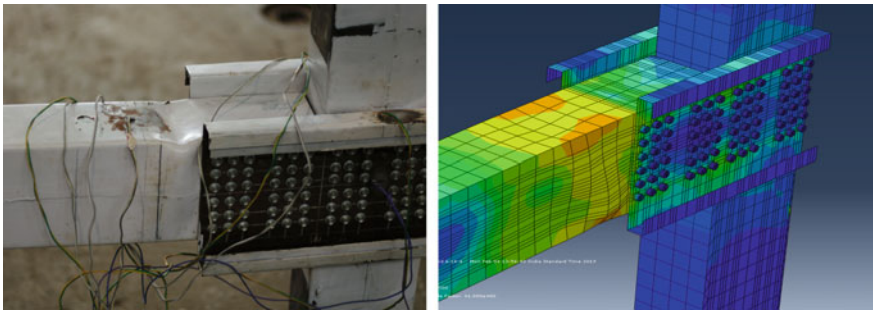


Fig. 17 Failure comparison of gusset plate screw connections

6 Conclusion

All the listed finite element modelling procedures are purpose oriented. If the researcher is focused on the behaviour of connections assuming the screws are rigid, the tie constraint model is a computationally better model. If the interest is to analyse the connection by taking into the account of the behaviour of screws, the spring model seems to be a better choice. A complex model such as solid screw modelling is required if one intends to study the behaviour of screws in the connection and when one wants to study the ductility/energy dissipations' of the connections.

References

1. Lennon R, Pedreschi R, Sinha BP (1999) Comparative study of some mechanical connections in cold formed steel. *Constr Build Mater Elsevier Sci Ltd* 13(3):109–116
2. Rautenbach E, van Rensburg BWJ (2016) Finite element modelling of thin sheet steel screw connections. In: *Insights and innovations in structural engineering, mechanics and computation—proceedings of the 6th international conference on structural engineering, mechanics and computation, SEMC 2016*, pp 1253–1258. <https://doi.org/10.1089/wound.2014.0603>
3. Wang L, Young B (2018) Behaviour and design of cold-formed steel built-up section beams with different screw arrangements. *Thin-Walled Struct* 131:16–32
4. Lim JBP, Nether Cot DA (2004) 'Finite element idealization of a cold-formed steel portal frame. *J Struct Eng* 130:78–94
5. Foster ASJ, Gardner L (2016) Stability of steel beams using the continuous strength method. *Thin-Walled Struct* 100:1–13
6. Niu S, Rasmussen KJR, Fan F (2015) Local–global interaction buckling of stainless-steel I-beams. I: experimental investigation. *J Struct Eng* 141(8):04014194
7. Selvaraj S, Madhavan M (2019) Structural design of cold-formed steel face-to-face connected built-up beams using direct strength method. *J Constr Steel Res* 160:613–628
8. Selvaraj S, Madhavan M (2018) Geometric imperfection measurements and validations on cold-formed steel channels using 3d noncontact laser scanner. *J Struct Eng* 144(3):04018010
9. Selvaraj S, Madhavan M (2018) Retrofitting of structural steel channel sections using cold-formed steel encasing channels. *J Perform Constr Facil* 32(4):04018049
10. Selvaraj S, Madhavan M (2019) Strengthening of laterally restrained steel beams subjected to flexural loading using low-modulus CFRP. *J Perform Constr Facil* 33(3):04019032
11. Wilkinson T, Hancock GJ (2006) Predictions of rotation capacity of Rhs beams using finite element analysis. In: Chan SL, Teng JG (eds) *Advances in steel structures, Proceedings, 2nd international conference on advances in steel structures, (ICASS'99)*, Hong Kong, China, Elsevier, December 1999, ICASS 99, pp 261–268

Behaviour of Self-Tapping Screws Under Shear



M. Divya, R. Senthilkumar, and Prince George

Abstract Fasteners are the backbone of steel construction industries. Various researches are being done on the different types of connectors. Self-tapping screws are one fastener used widely in cold-formed steel frame construction industries. Self-tapping screws are designed to cut their hole as it is screwed into the materials. This study presents an experimental investigation on static behaviour of self-tapping screw subjected to shear by varying the orientation, number of screws and thickness of material on which it is driven. In this experiment, two plates were connected by the self-tapping screw in a single lap connection. The tensile force was applied on the plates so that the screws were made to undergo shear failure. The group effect of screws and the reduction factor adopted in multiple screw arrangements have been studied. The stiffness of the connectors was analysed. The connection with more screws and thicker plates was found to be stiffer.

Keywords Self-tapping screw · Shear strength · Bolted connection · Fasteners

1 Introduction

A wide variety of connections are in existence for steel structures. The type of connection determines the behaviour of the joint, construction cost and speed of the construction. Bolts, screws, rivets and pins are the most prevalent fasteners [1]. The self-drilling screw is another type of fastener which is widely used to fasten sheet metal cladding and roofing to frame members and make joints in cladding and

M. Divya (✉) · R. Senthilkumar · P. George
Department of Civil Engineering, NIT Tiruchirapalli, Tiruchirapalli, Tamil Nadu, India
e-mail: 403117052@nitt.edu

R. Senthilkumar
e-mail: senthilr@nitt.edu

P. George
e-mail: 203218021@nitt.edu

© The Author(s), under exclusive license to Springer Nature Singapore Pte Ltd. 2023
M. Madhavan et al. (eds.), *Proceedings of the Indian Structural Steel Conference 2020*
(Vol. 2), Lecture Notes in Civil Engineering 319,
https://doi.org/10.1007/978-981-19-9394-7_38

roofing. These are externally threaded fasteners that, when driven with a screw gun, drill their hole and form their threads in steel sheet. It ensures the correct hole size and tighter clamp. It reduces the fabrication time and eliminates pre-drilling of the hole for the fastener. Since the fastening process does not require any power drills and drill bits or any costly equipment, they are economical [2]. Thus, self-drilling screws can be an alternative to provide a rapid, economical and cost-effective method to fasten thin-walled steel members such as cold-formed steel structural members [3].

Though it has more advantages, very limited studies have been undertaken so far in the field of self-tapping screws [4, 5]. Rogers et al. [6]. showed that the design standards provide accurate load predictions for single overlap screwed connections. But more detailed studies are required for group effects. When the two joined sheet plates of steel are of a similar thickness, the failure is more likely to depend on the tilting of the screws. Shan et al. [7]. showed that the ductility capacity was greatly affected by the thickness of the base steel plate, the fastener number and the spacing of fasteners. Ductility increases with the increasing thickness of the base steel plate. The ultimate displacement increases with the increasing thickness of the base steel plate while the yield displacement remains unchanged [8]. In group effect, the ductility is reduced when the fasteners are placed closer to each other. However when the spacing is increased the ductility also increased [9]. Huynh et al. [10] conducted a test on screws by varying the diameter of the screws and thread length. During the experiments, two different limit states were observed. These were screws failing in shear as well as in bearing and tilting. Bearing failure of the plate was observed when the thickness of the plate used was less. Sokol et al. [11] studied the effect of screw connections by varying sheet thickness, screw size, screw pattern, number of screws and screw spacing. Thicker sheets and larger screws gave larger bearing capacities. Screw arrangement did not cause a significant variation in strength. Also, the number of screws didn't give a direct multiplier of strength compared to single-screw strength. Bearing failure was found to be a combination of tilting, bearing, and tearing or fracture. A better understanding of the behaviour of screw connection is very much important to get the cost-effective optimum design of screw connection. This study presents an experimental investigation of the static behaviour of self-tapping screws subjected to shear. A series of 36 specimens were tested with variation in the number of screws, the orientation of screws and thickness of the connected plates.

2 Experimental Investigation

This study deals with the behaviour analysis of connections made by self-tapping screws. Thirty-six specimens were fabricated and tested. Each specimen consists of 2 steel plates of 300 mm length and 70 mm width. These plates were connected through 5 mm self-tapping screws. The connections have been studied for four different screw arrangements and in three different plate thicknesses. The thickness of the plate adopted were 1.6, 3 and 5 mm; the thickness of more than 5 mm was not adopted

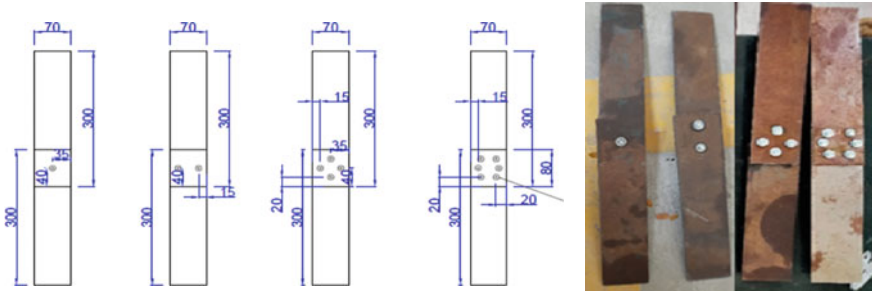


Fig. 1 Screw patterns in the connection

since it was difficult to drill a 5 mm self-tapping screw into the plates, and also, it was difficult to drill with 500 watts drilling machine. The screws were arranged in point, chain, diamond and hexagon. A single screw was arranged as to point, double as chain, four as diamond, six as hexagon, as shown in Fig. 1. The nomenclature of specimen was adopted as SP 1-1.6, SP 2-1.6, SP 4-1.6, SP 6-1.6, SP 1-3, SP 2-3, SP 4-3, SP 6-3, SP 1-5, SP 2-5, SP 4-5 and SP 6-5. SP denotes specimen, and the first digit denotes the number of screws in the connection, whereas the second digit denotes the thickness of plate used in mm. For example, SP 4-6 denotes the plate of 6 mm connected using four screws. Three specimens were made and tested to check the accuracy for each variation, and the trial number is given as the last digit in the specimen name. So, SP 4-6-1, SP 4-6-2, SP 4-6-3 denotes the first, second and third of SP 4-6.

3 Material Properties

3.1 Tensile Coupon Test of the Steel Plate Materials

Flat coupons from the cold-formed steel sections were extracted and tested to determine the material characteristics of the steel plate—the dimensions of the tensile coupons are 100mm length 6 mm width. The tensile coupon tests were performed for all three thicknesses of the plate. The extracted specimens and test setup were shown in Figs. 2 and 3, respectively. The yield and ultimate stress of the coupon are listed in Table 1.

Fig. 2 Tensile coupon test of steel joists



Fig. 3 Tensile coupon test setup

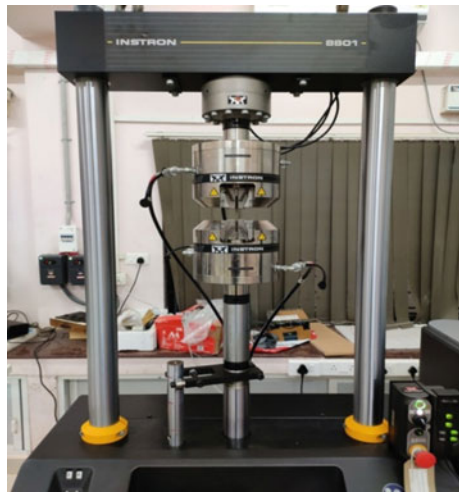


Table 1 Properties of steel plates

Steel plate thickness in mm	Yield stress (MPa)	Ultimate stress (MPa)
1.6	319.39	429.17
3	323.95	413.74
5	314.04	441.35

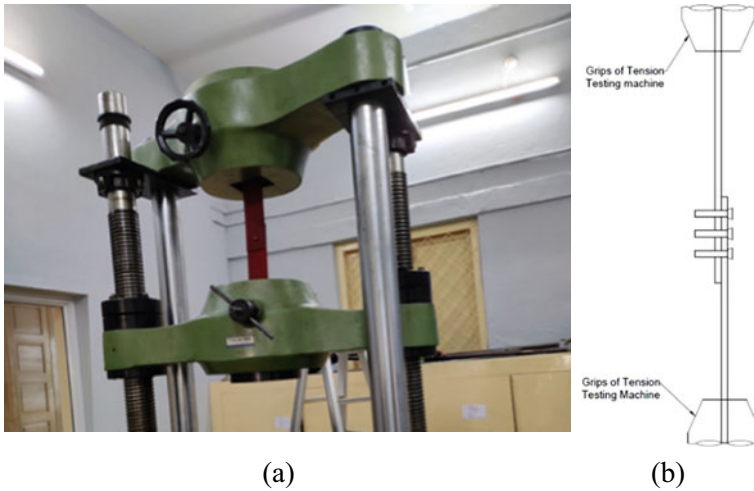


Fig. 4 a Experimental setup, b schematic diagram

4 Experimental Setups

Each specimen was fabricated using two steel plates of length 300 mm, width 70 mm and thickness of 1.6, 3 and 5 mm connected through the self-tapping screw. The plates were arranged as a single lap connection [12]. The screws were drilled in four different patterns. Totally 36 specimens were prepared to study the effect of screw number and thickness of connecting plates. Plates and screw arrangements were designed in such a way as to avoid the yielding of plates before the failure of connection. In this experiment, a tensile force was applied on plates with a universal testing machine (UTM) capacity of 100 tonnes. The load was kept at a constant loading rate of 5kN/min, and the slip between the plates was recorded by DAQ attached to UTM. The DAQ automatically records the reading for every second of loading. The tensile force was applied on the plates, which shears the screws. The testing arrangement and schematic diagram are shown in Fig. 4a and b.

5 Mode of Failure

The plates were subjected to axial loading while the screws experienced shear force between the plates. These experimental studies show that the connection fails by three types of failure: tearing of plates, shearing of screws and rotation of plates. Table 2 lists the results obtained from experimental observation. The tearing and rotation of plates are highly evident in the plates with lesser thickness, while the plates with higher thickness directly shear off the screws. From Figs. 5b, c, 6b, c and 7b, c, it is highly evident that the specimen SP 1-1.6, SP 2-1.6, SP 4-1.6, SP 6-1.6

failed by rotation and tearing of plates. The specimen SP 1-1.6 allowed the rotation of the screw; however, there was not much separation of plates witnessed. But, the specimens SP 4-1.6 and SP 6-1.6 were allowed rotation of screws, and there was a huge separation of plates witnessed as the specimen reached its ultimate load.

The specimen with medium thickness, SP 1-3, SP 2-3, SP 4-3, SP 6-3, experiences both tearing and shearing of screws. The separation was not witnessed; however, mild rotation of screws was observed in all the specimens. As the loading propagates, mild tearing occurs, the specimen fails by complete shearing of screws. The failure pattern of 3 mm plate specimen is shown in Fig. 5d, 6d and 7d.

The specimen with an equal thickness of screws diameter such as SP 1-5, SP 2-5, SP 4-5, SP 6-5 fails by shearing off screws. The specimen with single and double screws does not allow much rotation, while four and six screwed specimens experience little rotation. As the load increases, the tearing of the plate increases, which in turn provides room for the rotation of screws; thus, rotation of screws

Table 2 Experimental results of specimens

Sl. No	Specimen	Ultimate slip in mm	The average strength of specimen in kN	Group effect
1	SP 1-1.6	12	6.95	1
2	SP 1-3-1	7	10	1
3	SP 1-5-1	8	10.5	1
4	SP 2-1.6-1	10.2	6.25	0.89
5	SP 2-3-1	7	9.75	0.975
6	SP 2-5-1	9	9.6	0.96
7	SP 4-1.6-1	14	5.28	0.76
8	SP 4-3-1	8.65	9.56	0.95
9	SP 4-5-1	8.29	9.48	0.90
10	SP 6-1.6-1	15.6	4.83	0.69
11	SP 6-3-1	8.62	8.9	0.89
12	SP 6-5-1	10.1	8.4	0.88

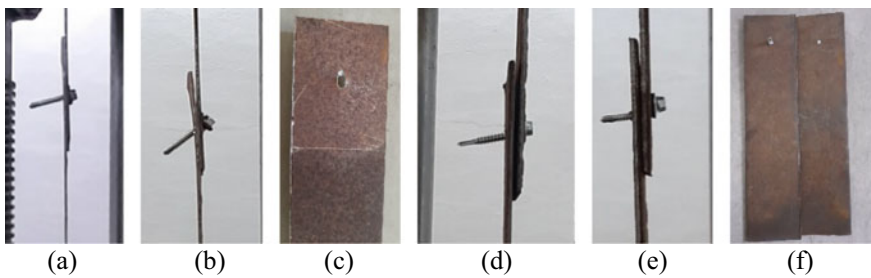


Fig. 5 Mode of failure of the specimen

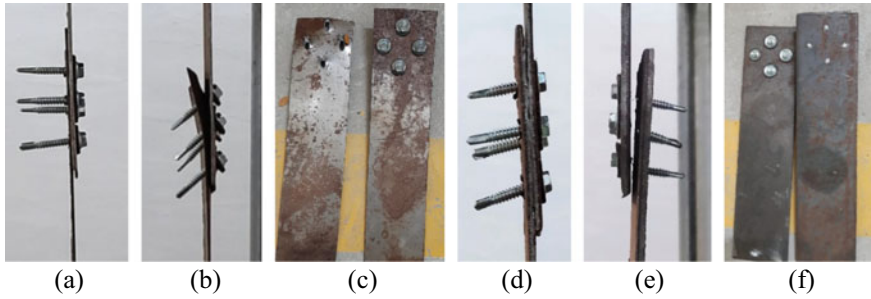


Fig. 6 Failure of four screwed specimen

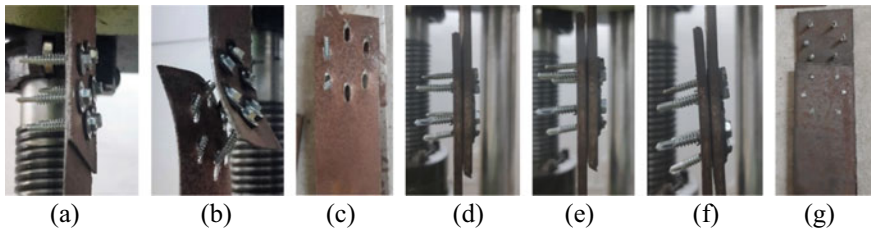


Fig. 7 Failure of six screwed specimen

increases as load taken by the connection increases can be inferred. For example, SP 1-5 and SP 2-5 specimens take less load and do not allow any rotation (as shown in Fig. 5g). However, SP 4-5, SP 6-5 take a relatively higher load than other specimens; hence, little rotation was observed as shown in Figs. 5e, f, 6e, f and 7f, g.

6 Results and Discussions

The specimens with less thickness (1.6 mm) were failed by tearing followed by shear off, and relatively higher thickness specimens (3 mm and 5 mm) were failed by the direct shear failure of screws only. Hence, 1.6 mm thickness specimens have relatively less capacity than higher thickness specimens, as given in Table 2. For example, the specimen SP 1-1.6 failed at 6.95 kN, whereas SP 1-3 and SP 1-5 failed at 10kN,10.5kN. In this case, the capacity of SP 1-1.6 is lesser than counter specimens due to the tearing failure of the plate. In the higher thickness plates, the specimen failed by the shear failure of the screw; hence, there is not much difference in the capacity.

As the number of screws increases, the connection capacity also increases for the particular thickness of the plate, which is clearly shown in Fig. 8. But, the connection strength is not proportionate to the thickness of the plate after 3 mm. The failure mode

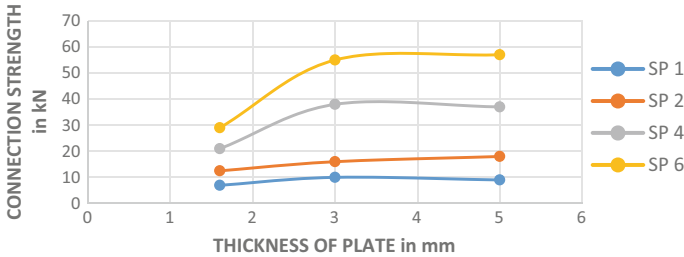


Fig. 8 Capacity of connection

governed by the 3 and 5 mm specimens is similar, where the failure of screw alone governs the failure of the connection.

Like connection strength, group effect is also one of the main parameters in connection design. As the number of screws increases, the individual screw capacity in the group decreases, known as group effect. In this study, the group effect is defined as the ratio of strength per screw for a given connection to the connection strength for a single-screw connection with the same sheet thickness and screw size. The strength per screw was calculated based on the failure load and the number of screws in the screw pattern. If all screws in a connection acted and contributed equally, the group effect would be 1.0. The connection capacity with more screws will not be the exact multiplication of the number of screws and individual screw capacity. There will be some reduction in strength for every screw in the connection—this reduction of capacity increases as the number of screws in the specimen increases. The reduction in individual screw capacity is shown in Fig. 9. Due to the group effect, the strength per screw may reduce, but the connection stiffness increases considerably. The specimen SP 1-1.6, SP 1-3, SP 1-5 show the same stiffness because of the presence of only one screw. As the number of screws increases, the stiffness increases relatively. The increase in stiffness also depends on the thickness of the plate. The specimen SP 2-3, SP 4-3, SP 6-3 witnesses an increase in stiffness, and the rate of change of stiffness is high for the specimen with higher thickness, as shown in Fig. 10. Hence, it is evident stiffness depends on two factors, such as the thickness of the plate and the number of screws.

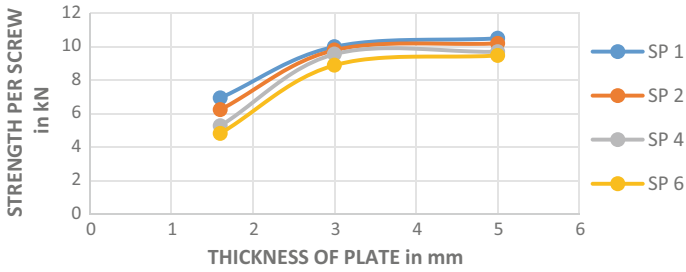


Fig. 9 Group effect of screws

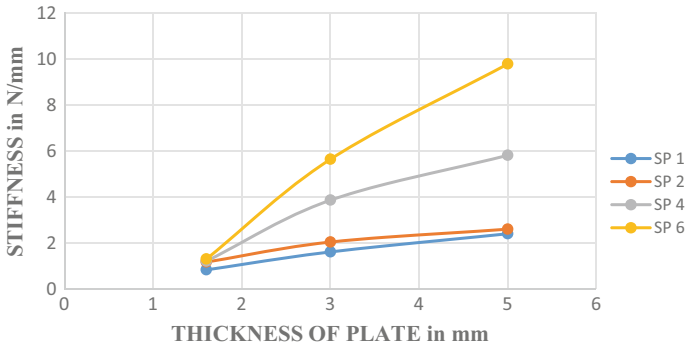


Fig. 10 Stiffness of the connections

7 Conclusion

Based on the results obtained from a test program that consisted of 36 single lap shear connections, a better understanding of the behaviour of screw connections was obtained. The research findings demonstrated that the thinner plates fail by tearing and shear off, and thicker plates fail directly. So, the minimum plate thickness is suggested as 2 mm less than the diameter of the screw to utilize the full screw capacity. Also, the assumption that the connection strength for a multiple screw connection is proportional to the number of screws in the connection pattern was unconservative. Hence, the design’s reduction factor must be considered to incorporate the group effect. The stiffness variation of the connection has been observed, and it is found that the connection with more number of screws and higher thickness has more stiffness than a thinner plate with fewer screws.

References

1. Xue D, Liu Y, Yu Z, He J (2012) Static behavior of multi-stud shear connectors for steel-concrete composite bridge. *J Constr Steel Res* 74:1–7
2. Selvaraj S, Madhavan M (2020) Influence of sheathing-fastener connection stiffness on the design strength of cold-formed steel wall panels. *J Struct Eng* 146:04020202
3. Mahlknecht U, Brandner R (2019) Block shear failure mechanism of axially-loaded groups of screws. *Eng Struct* 183:220–242
4. Cai Y, Young B (2020) Effects of end distance and temperature on thin-sheet steel double shear-bolted connections. *J Struct Eng* 146:04020120
5. Cai Y, Young B (2020) Effects of end distance on thin sheet steel single shear bolted connections at elevated temperatures. *Thin-Walled Struct* 148:106577
6. Rogers CA, Hancock GJ (1998) Bearing design of thin sheet steel screwed connections. In: International specialty conference on cold-formed steel structures—recent research and developments in cold-formed steel design and construction, pp 481–494
7. Shan ZW, Su RKL (2019) Behavior of shear connectors joined by direct fastening. *Eng Struct* 196:109321
8. Daudet LR, LaBoube RA (1996) Shear behavior of self drilling screws used in low ductility steel. In: International specialty conference on cold-formed steel structures—recent research and developments in cold-formed steel design and construction, pp 595–613
9. Ataei A, Chiniforush AA, Bradford M, Valipour H (2019) Cyclic behaviour of bolt and screw shear connectors in steel-timber composite (STC) beams. *J Constr Steel Res* 161:328–340
10. Huynh MT, Pham CH, Hancock GJ (2020) Experimental behaviour and modelling of screwed connections of high strength sheet steels in shear. *Thin-Walled Struct* 146:106357
11. Sokol MA, LaBoube RA, Yu W-W (1998) Determination of the tensile and shear strengths of screws and the effect of screw patterns on cold-formed steel connections
12. IS 800 (2007) I. IS 800–2007 General construction in steel—code of practice, third revision

Spirally Welded Steel Hollow Columns—A Numerical Study



K. M. Bharathi, B. Vignesh, and H. Jane Helena

Abstract Cold-formed steel (CFS) columns are increasingly used in structures for their high strength-to-weight ratio. CFS tubular columns of square, rectangular, circular, and various innovative cross-sections are being experimented worldwide. Also, spirally welded (SW) pipes, which have a massive usage in pipeline industry, have their room of experimentation as a column. Longitudinal welded columns necessarily require steel sheets/coils of certain height to avoid coil girth welding, but available sizes are limited. Spiral turning and welding of steel sheet allow manufacturing of different sized columns with the same width of the sheet. Unlike longitudinal pipes, continuous and very long spiral-welded columns can be manufactured using compact coil strips. In spiral welding, with the same width of the sheet by varying the revolving radius small to large diameter columns can be produced. Also by varying the pitch, with the same length of the sheet, columns of different lengths can be produced. In this paper, SW columns with varying pitch and L/D ratios are modeled and analyzed using finite element program ABAQUS and their buckling behavior is studied.

Keywords Spirally welded column · Buckling · Pitch

K. M. Bharathi (✉) · B. Vignesh · H. J. Helena
Anna University, Chennai, India
e-mail: bharathi.structural@gmail.com

B. Vignesh
e-mail: vignesh280689@gmail.com

H. J. Helena
e-mail: jane@annauniv.edu

1 Introduction

Cold-form steel (CFS) columns are gaining increased use in all forms of structural members. CFS circular hollow columns are one of the prominent structural compression members. Material and geometric properties affect the ultimate capacity of CFS columns under axial compression [2]. Steel hollow columns are being made in different cross-sections, with/without seam welding. Hollow steel tubes without seam welding are manufactured in factories by casting method. Seam welded steel tubes are categorized as longitudinal welded (LW) and spirally welded (SW).

Spirally welded (SW) columns are also columns with circular cross-sections, whereas the making process differs. Unlike in other welded circular steel columns, SW columns are fabricated by revolving a steel sheet with respect to a central axis at a certain pitch value. Welding is provided on both sides of the column along the revolution pitch. SW columns have the advantage that, column of any diameter and length can be made in a continuous manner. Spiral is formed through three roll bending system [5]. Spirally welded columns can be accurately modeled and analyzed using finite element (FE) program to check its adequacy. Hence, in this paper eigenvalue buckling analysis with an incremental loading pattern is carried out to find the critical buckling load and then a static nonlinear analysis is performed by incorporating the imperfections.

Columns are characterized as short and long columns based on their slenderness ratio. Short column tends to carry loads in proportion to their size and long column tends to buckle depending on the effective length. This study compares the behavior and capacity of SW columns with varying slenderness ratio and with distinct pitch values. SW columns of three different lengths (600 mm, 750 mm, 900 mm), four different pitches ($P_1 = 300$ mm, $P_2 = 250$ mm, $P_3 = 200$ mm, $P_4 = 150$ mm), and two different diameters ($D_1 = 200$ mm, $D_2 = 300$ mm) for a constant sheet width (300 mm) and constant thickness (2 mm) are studied. The columns having D/t ratio greater than 100 buckles quite suddenly [10]. The columns with different pitch are shown in Fig. 1. The optimum pitch considering the strength, weight, manufacturing process, and cost of the column is arrived.

2 Finite Element Analysis

The finite element program ABAQUS is used to develop the column models for the study. FE models can predict the results with more than 98% accuracy and are consistent with less than 4% scatter [1]. To ensure the accurate modeling, the spirally welded columns are modeled with revolution and pitch as if it is done in experimental fabrication. The welding simulation is done with solid element and compared with tie

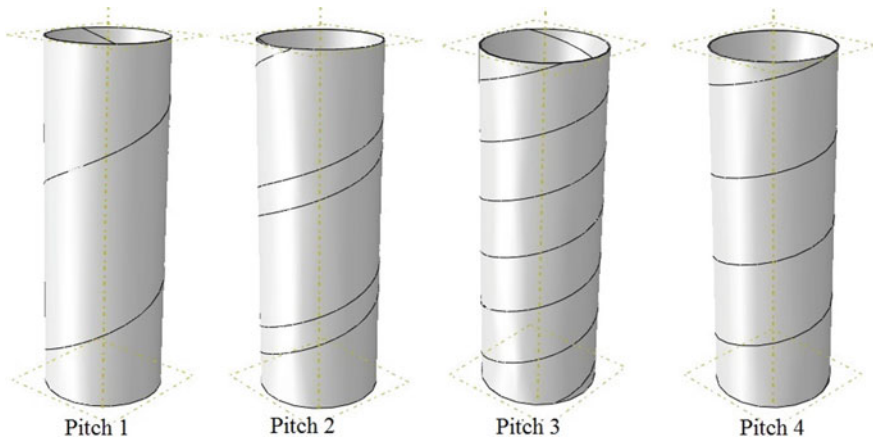


Fig. 1 Spirally welded column with different pitch

constraint properties. The constrained spiral comparatively takes lesser load, which the weld material has bridged. Still the grains are arranged diagonally, and hence, the tied spiral behaves almost similar to the solid element welding. In this paper tie constraint property is used to simulate the weld connection between the spiral turns. All the modules such as developing model, assigning material properties, creating constraints, meshing with proper element type, loading and boundary conditions are considered.

2.1 Modeling and Material Properties

Modeling of the steel hollow column involves shell revolution with angle of revolution and revolving direction. Mechanical properties for the created shell section are provided with elastic modulus $E = 199,856 \text{ N/mm}^2$ and Poisson ratio $\nu = 0.3$. Isotropic plastic hardening of steel with initial plastic strain value of zero is assigned. Shell thickness value with Simpson thickness integration module has been adopted.

2.2 Constraint and Loading

In FE analysis to eliminate the end plates and to create accurate loading condition, boundary nodes of the end circular regions are tied with the center reference point where the load is acting, using the tie constraint. The spiral pitches were tied to each other to ensure continuity in the joints. Proper boundary conditions are ensured by providing encastre condition for fixed end at the bottom of the column and arresting all the degrees of freedom except the longitudinal direction displacement at the top

end of the column. Concentrated force is applied at the reference point to act at all the tied nodes. Pitch angle with respect to the axial loading has negligible influence on the behavior of the columns [2].

2.3 Meshing

In finite element analysis, mesh refinement produces results of closer accuracy. Mesh element is also a factor, which influences the result. It is necessary to adopt proper mesh element and size for improving the accuracy and to reduce the computational time. In past research, FE analysis with solid material used 3D eight-node linear hexahedral solid elements with reduced integration (C3D8R) and conventional eight-node linear isoparametric element (C3D8). Eight-node linear solid element with incompatible modes (C3D8I) produced results of similar accuracy to the C3D8R elements [2]. This study includes model with shell material and four-node doubly curved thin or thick shell, reduced integration (S4R) mesh element.

3 Column Capacity

The strength of the columns is calculated based on EC 3 formula for CFS columns and compared with the results obtained in FE analysis. The comparison of values is given in Table 1. It can be seen that the analytical values closely match the theoretical results within a margin of $\pm 3\%$. EC 3 does not have any provision for spirally welded columns. As this is a limited study, more elaborate research is needed in this area. To check the adequacy of the FE model, experimental investigation is needed.

In the FE models developed, the columns having 300 mm pitch have no overlapping, 250 mm pitch has a 50 mm overlapping on each revolution. Similarly, 200 mm and 150 mm pitch have 100 mm and 150 mm overlapping, respectively. The increase in capacity due to extra material is found to be 2–3%. Moreover, this study shows that overlapping of steel sheet on welding tends to reduce the capacity of the column and chances is that the column may also tend to fail prematurely. With an increase in D/t ratio, initial stiffness and ultimate strength decrease, while ductility increases [7].

Table 1 Load comparison between FEM and Eurocode

Specimen	L (mm)	L/D	t (mm)	$P_{u(FEM)}$ (kN)	$P_{u(Eu)}$ (kN)	$P_{u(FEM)}/P_{u(Eu)}$
HSS P1-600D1	600	3	2	306.42	307.33	0.99
HSS P1-600D2	600	2	2	454.01	471.68	0.96
HSS P1-750D1	750	3.75	2	304.76	305.242	0.99
HSS P1-750D2	750	2.5	2	447.02	466.18	0.95
HSS P1-900D1	900	4.5	2	300.86	301.45	0.99
HSS P1-900D2	900	3	2	417.75	464.6	0.89
HSS P2-600D1	600	3	2	307.51	306.58	1
HSS P2-600D2	600	2	2	455.19	469.86	0.96
HSS P2-750D1	750	3.75	2	308.84	302.58	1.01
HSS P2-750D2	750	2.5	2	452.59	467.7	0.96
HSS P2-900D1	900	4.5	2	302.39	299.64	1
HSS P2-900D2	900	3	2	442.82	462.37	0.95
HSS P3-600D1	600	3	2	329.32	303.9	1.08
HSS P3-600D2	600	2	2	454.7	467.4	0.97
HSS P3-750D1	750	3.75	2	309.59	300.2	1.03
HSS P3-750D2	750	2.5	2	453.84	463.78	0.97
HSS P3-900D1	900	4.5	2	305.61	296.83	1.02
HSS P3-900D2	900	3	2	448.67	460	0.97
HSS P4-600D1	600	3	2	358.27	301.41	1.18
HSS P4-600D2	600	2	2	455.98	464.7	0.98
HSS P4-750D1	750	3.75	2	311.41	297.95	1.04
HSS P4-750D2	750	2.5	2	454.4	461.1	0.98
HSS P4-900D1	900	4.5	2	310.98	294.36	1.05
HSS P4-900D2	900	3	2	452.26	457.2	0.98

4 Buckling Mode

The first eigenvalue mode is taken as the critical mode and used in the geometrically nonlinear static Riks analysis. The typical buckling mode of spirally welded columns with solid element weld is shown in Fig. 2. In the eigenvalue analysis, all the 24 models with tie joint welding simulation showed a similar buckling mode as shown in Fig. 3.

Fig. 2 Typical buckling of spirally welded columns with solid element weld

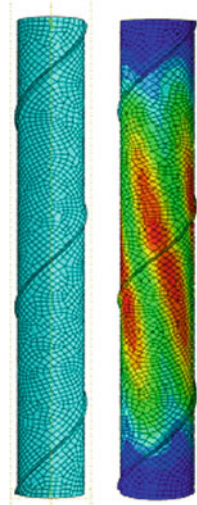
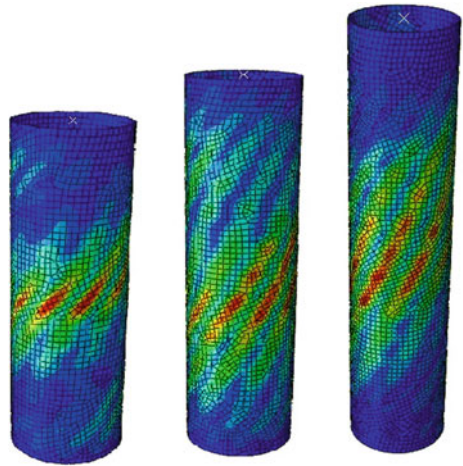


Fig. 3 Buckling mode of spirally welded columns with tie joints



5 Residual Stress

Residual stress is the preexisting stress developed in the member before loading. In SW columns, three-dimensional residual stress develops near the weld. Since in SW columns, welding is helical, the stress developed is compressive causing confinement, and this will act as positive residual stress. All specimens were mainly subjected to tensile and compressive longitudinal residual strains on the outer and inner surfaces, respectively. Residual stress is largely due to the mechanical load during turning process and thermal effect of welding [4, 6, 9]. Residual stresses are (a) macroresidual stress, larger than the grain size of the material (b) microresidual

stress of size about one grain size (c) microresidual stress, size less than a grain size. Residual stress can be reduced by optimizing the welding [3]. High-frequency electric resistance welding caused a negligible effect on residual stresses [11]. The residual stress involves two parts, including (1) variation of the residual stress through cross-section wall thickness and (2) magnitude and distribution of the residual stress around the cross-section. Three components of through-thickness residual stress in each direction exist, including (1) membrane, (2) bending, and (3) layering residual stress [8].

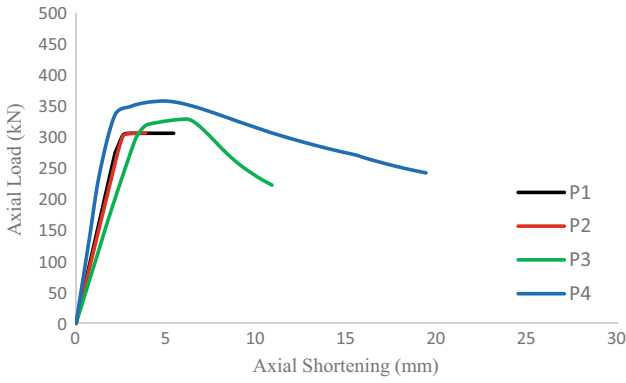
6 Load Versus Axial Shortening

From the nonlinear geometric analysis in FE, the load and displacement values are obtained in the history output and field output data, in unique nodal point module. The displacement values are used to calculate the axial shortening and plotted to compare and study the effect of pitch on spiral-welded columns. Figure 4 shows the load versus axial shortening behavior of all the columns analyzed.

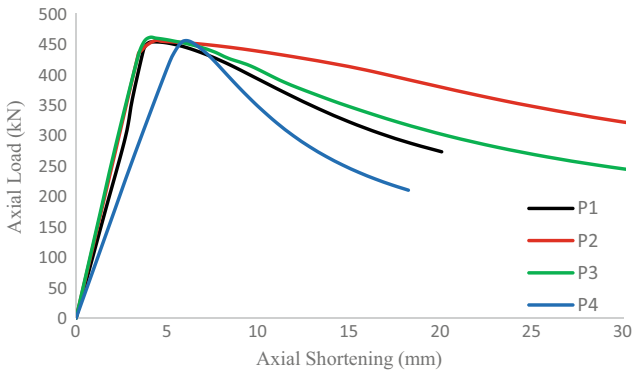
7 Conclusions

Comparison of the load versus axial shortening, for columns of same dimension with different pitch shows that, for each length and diameter, a particular pitch behaves well. However, on average, it is clear that for any length of the column; the maximum pitch can be fixed based on the width of the sheet. The angle of the spiral rolling varies based on the diameter of the column and pitch of the spiral.

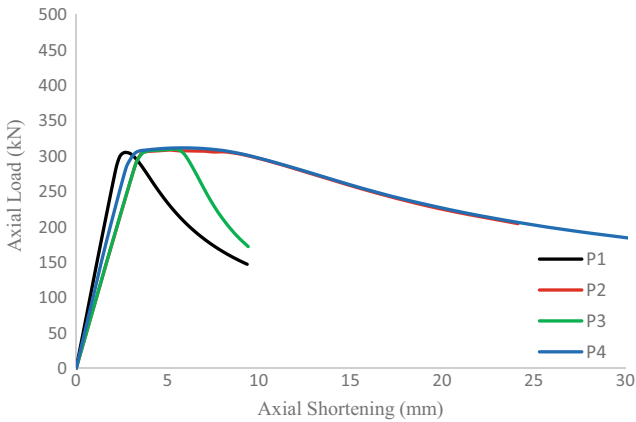
- The failure modes of column show local buckling.
- No column forms any sign of failure near the spiral joints.
- Increase in pitch does not contribute much to the strength.
- EC3 results are capable of predicting the design capacity within a margin of $\pm 3\%$.



(a) $L = 600\text{mm}$ $D = 200\text{mm}$ $L/D = 3$

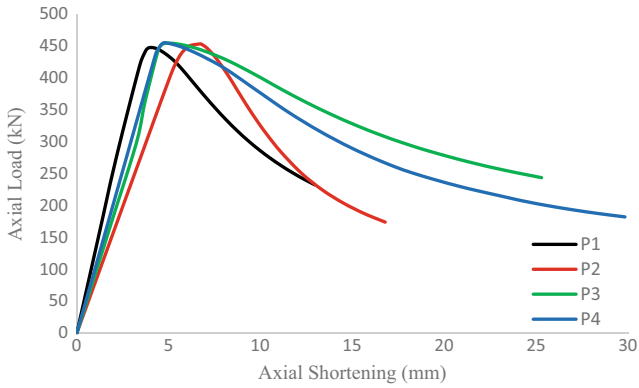


(b) $L = 600\text{mm}$ $D = 300\text{mm}$ $L/D = 2$

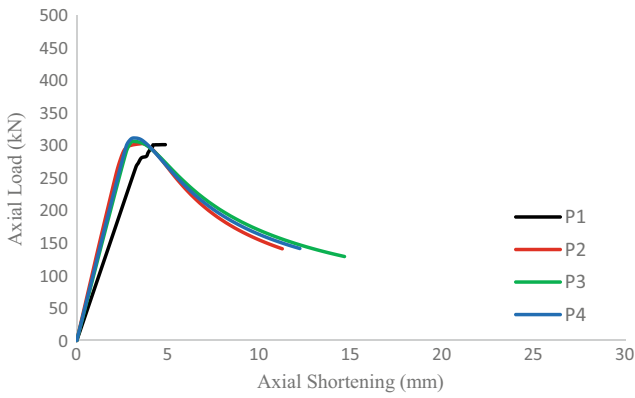


(c) $L = 750\text{mm}$ $D = 200\text{mm}$ $L/D = 3.75$

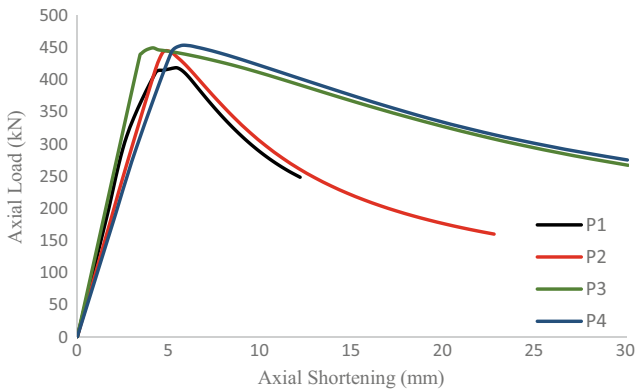
Fig. 4 Load versus axial shortening



(d) $L = 750\text{mm}$ $D = 300\text{mm}$ $L/D = 2.5$



(e) $L = 900\text{mm}$ $D = 200\text{mm}$ $L/D = 4.5$



(f) $L = 900\text{mm}$ $D = 300\text{mm}$ $L/D = 3$

Fig. 4 (continued)

References

1. Anbarasu M, Ashraf M (2017) Interaction of local-flexural buckling for cold-formed lean duplex stainless steel hollow columns. *Thin-Walled Struct* 112:20–30
2. Aslani F, Uy B, James Hur J, Carino P (2017) Behaviour and design of hollow and concrete-filled spiral welded steel tube columns subjected to axial compression. *J Constr Steel Res* 128:261–288
3. Aslani F, Uy B, Hicks SJ, Kang WH (2015) Spiral welded tubes—imperfections, residual stresses, and buckling characteristics. *Int Conf Adv Steel Struct*, Lisbon, Portugal, July 22–24, 2015
4. Chen TM, Young B (2019) Structural performance of cold-formed steel elliptical hollow section pin-ended Columns. *Thin-Walled Struct* 136:267–279
5. Van Es SHJ, Gresnigt AM, Vasilikis D, Karamanos SA (2016) Ultimate bending capacity of spiral-welded steel tubes—part I: experiments. *Thin-Walled Struct* 102:286–304
6. Fang H, Chan TK, Young B (2018) Structural performance of cold-formed high strength steel tubular columns. *Eng Struct* 177:473–488
7. Li D, Uy B, Aslani F, Hou C (2018) Numerical analysis of concrete-filled spiral welded stainless steel tubes subjected to compression. In: *International conference on advances in steel-concrete composite structures*
8. Liu W, Rasmussen JRK, Zhang H (2017) Modelling and probabilistic study of the residual stress of cold-formed hollow steel sections. *Eng Struct* 150:986–995
9. Ma JL, Chan TM, Young B (2015) Material properties and residual stresses of cold-formed high strength steel hollow sections. *J Constr Steel Res* 109:152–165
10. Vasilikis D, Karamanos SA, Van Es SHJ, Gresnigt AM (2016) Ultimate bending capacity of spiral-welded steel tubes – part II: predictions. *Thin-Walled Struct* 102:286–302
11. Yao Y, Quacha W, Young B (2019) Finite element-based method for residual stresses and plastic strains in cold-formed steel hollow sections. *Eng Struct* 188:24–42

Effect of Braking Load on Longitudinal Forces in Continuous Welded Rail Considering the Presence of Bridge



C. K. Ali Mubarack and Akhil Upadhyay

Abstract Need for a high-speed rail demands the continuous welded rail (CWR) to be continued on the bridge to make a smooth track eliminating special expansion joints (SEJs). Braking load is an important consideration for the design of railway bridges. Being a slender steel structure, CWR is prone to buckling and fracture due to compressive and tensile rail stresses, respectively. Track bridge interaction (TBI) phenomenon results in additional rail stress, which varies along the track–bridge portion of CWR. This paper investigates TBI due to braking load. Effect of braking load on the rail stress and the longitudinal support reaction of the bridge pier have been investigated. A numerical model developed for track–bridge interaction in SAP2000 is extended to study the effect of braking load in the presence of ballasted CWR track. UIC 774-3R Code guidelines are followed while modeling the phenomenon. When compared to a bridge with special expansion joints, a significant portion of the braking load is dissipated in the approach zone of the bridge as a result of track–bridge interaction for all span lengths. The longitudinal support reaction at the fixed end pier of the bridge support is also affected significantly.

Keywords Track–bridge interaction · Braking load · Continuous welded rail · High-speed rail · Additional rail stress

1 Introduction

The track forms the heart of railway traffic. Unlike the jointed rail track, continuously welded rail (CWR) reduces the maintenance cost, enhances track and vehicle service life, improves the passenger comfort, reduces the tractive effort, and decreases the noise pollution. Generally, this essential part of the railway construction rests on

C. K. A. Mubarack (✉) · A. Upadhyay
Department of Civil Engineering, Indian Institute of Technology Roorkee, Roorkee, India
e-mail: alimubarackck@gmail.com; ak@ce.iitr.ac.in

A. Upadhyay
e-mail: akhilfce@iitr.ac.in

© The Author(s), under exclusive license to Springer Nature Singapore Pte Ltd. 2023
M. Madhavan et al. (eds.), *Proceedings of the Indian Structural Steel Conference 2020* (Vol. 2), Lecture Notes in Civil Engineering 319,
https://doi.org/10.1007/978-981-19-9394-7_40

499

the subgrade. CWR inherently develops thermal stress on account of temperature changes in the surrounding environment (see Fig. 1). Any change in track temperature with respect to neutral temperature (the temperature at which track develops no thermal stress) induces thermal strains in CWR, and the track tends to move longitudinally. Restraintment of this thermal movement leads to the development of track forces as shown in Fig. 1, where F is the track force, the parameter α is the coefficient of thermal expansion, ΔT_R is the rail temperature change relative to the neutral temperature, E is Young’s Modulus (steel), and A is the cross-sectional area of two rails combined. The central portion of CWR is completely restrained against longitudinal thermal movements and forms an immobile part of the track, whereas the ends of CWR move with temperature changes. The support of the CWR track by a bridge needs special situation. Here, the rail, sleeper, ballast, and fastenings are supported directly by the bridge structure. In this situation, the loads acting on the track–bridge system causes the bridge to move relative to CWR. These can be caused by uniform temperature change, vehicle braking, and vehicle acceleration, changes of the supporting structure, or the flexural deformation of the bridge deck under vertical loads [6]. The relative displacement between the track and the bridge results in track–bridge interaction (TBI) phenomenon.

The investigation of longitudinal loads and their influence on the forces in CWR and bridge has been much demanding for the last 15 years. The importance of TBI is substantiated by the numerical results presented by previous studies [3–5, 7, 8]. UIC Leaflet [6] has been developed in Europe based on the earlier research on TBI. UIC Code discretely treats the loading cases—traction, braking, and temperature changes—and the maximum longitudinal stresses follow from a subsequent summation of the results corresponding to various loading cases. This approximate approach neglects the history of previous load events on the structure. A more realistic combination of loading cases is essential to obtain correct results. For this purpose, a nonlinear track–bridge interaction (TBI) model needs to be developed considering the correct combination of loading cases.

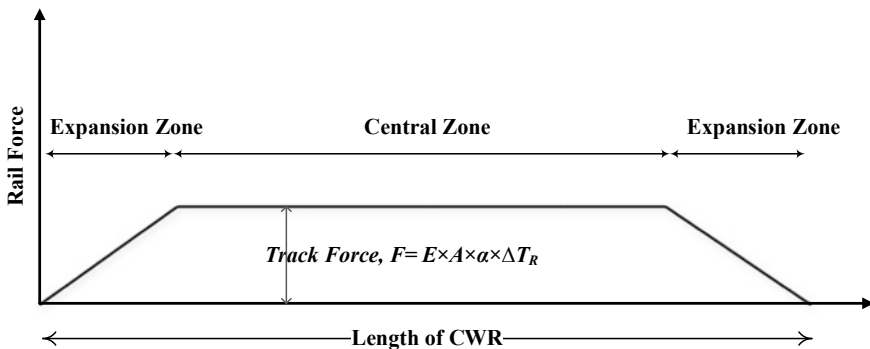


Fig. 1 Variation of longitudinal rail force in CWR

In this paper, numerical model developed for TBI in SAP2000, a general-purpose structural modeling and analysis software, is discussed considering the effect of braking load. Ballasted track on the simply supported bridge is considered. Nonlinearity associated with the ballast is taken into account. A single rail track supported on bridge is considered. UIC 60 rail section is utilized to model CWR. The model is validated for rail stress and support reaction. The effect of braking load on the rail stress and the longitudinal support reaction of the bridge pier has been investigated. Continuation of CWR on bridge is studied against the provision of special expansion joint (SEJ).

2 Track–Bridge Interaction

Track–bridge interaction (TBI) is inevitable as track and bridge are mutually coupled through ballast and fasteners, and the relative movements and deformations of one structure affect the other. Figure 2 shows a track–bridge system with a single-span bridge, where CWR is passing over a bridge with fixed-elastic support at one end and movable (free support) support at the other end. The bridge is located in the central zone of CWR. CWR over subgrade is continued over bridge deck without providing expansion joints. As CWR does not contract or expand, except at the ‘breather’ zone (Fig. 1), it stays the same length irrespective of the ambient temperature. Due to thermal expansion and contraction, bridge decks are longer on hot days than on cold days. Since CWR is continued over bridge, due to the coupling between track and bridge, displacement of one structure affects the other, and the track is subjected to axial stress in addition to the pre-existing stress [6].

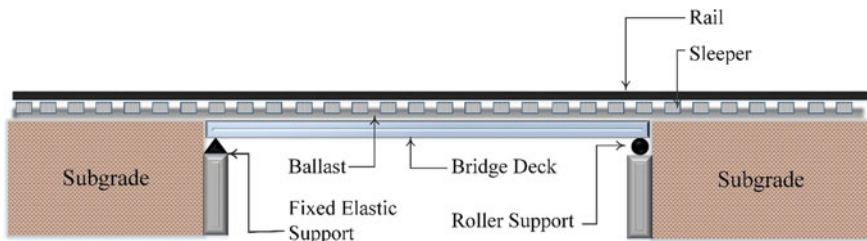


Fig. 2 CWR passing over a single-span bridge

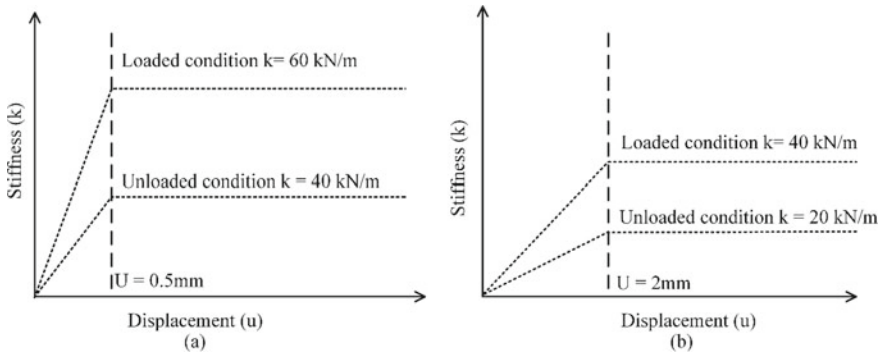


Fig. 3 Track stiffness parameters **a** Frozen ballast, **b** Normal ballast

2.1 Parameters Affecting the Phenomenon

The interaction between track and bridge is affected by track and bridge parameters and also by different loading conditions including:

- Temperature variation
- Horizontal braking and acceleration
- Vertical traffic-induced end rotation of the bridge deck
- Deformations and settlements due to creep and shrinkage.

Rolling stock moving on bridge will introduce horizontal braking and acceleration forces in addition to causing vertical bending in the bridge deck. Bridge parameters account for geometry and structural configuration of the bridge. Expansion length (L_T), support stiffness (K_{support}), bridge deck bending stiffness, and height of the deck are the important bridge parameters. Expansion length (L_T) of the bridge deck is defined as the greatest distance from the fixed bearing (fixed support) to the farthest end of the structure that can freely move. It is the largest distance between the thermal central point and the opposite end of the bridge deck. Support stiffness is a collective property of bearings, piers/abutment, and soil strata beneath [6]. Track stiffness is an important parameter that affects the phenomenon (see Fig. 3). The track will be under the loaded condition under braking load due to the presence of the rolling stock. The normal ballast is considered in this work.

2.2 Modeling the Phenomenon for Braking Load

For numerically modeling the track–bridge system in SAP2000, the beam element is utilized to model the bridge girder and the rail elements, and link elements are used to connect the bridge girder to the rails serving as support elements. The braking force which acts at the top of the rails in the longitudinal direction of the rails is commonly

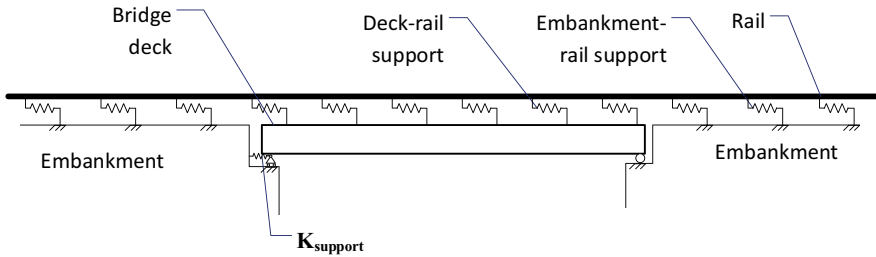


Fig. 4 Model for track–bridge interaction

assumed as constant distributed force along each wagon [2]. As TBI phenomenon is influenced by numerous parameters, the evaluation of various forces and stresses are computationally intensive. A numerical model has been developed in SAP2000 [1]. Figure 4 shows the model for the track bridge system for a single-span bridge, where CWR is passing over a bridge which is located in the central zone of CWR. The model is developed by considering the track as a continuous beam supported on a number of discrete springs (beam on elastic foundation). The single-span bridge modeled with fixed-elastic support at one end and a movable (roller support) support at the other end.

The model has incorporated material nonlinearity associated with the ballast bed, which supports the track and fasteners, through the nonlinear link elements. Figure 3 shows the track stiffness parameters. Track resistance is approximated to be bilinear, which takes into consideration the nonlinear constitutive behavior of the ballast [8]. This bilinear approximation is valid over a reasonable track displacement [6].

The line model reduces the total number of elements in the model significantly, and also it simplifies the model. Support stiffness of the bridge (K_{support}) incorporates the influence of following: stiffness of the foundation, stiffness against the rotation of the foundation at the top of the support, and stiffness of the piers.

2.3 Validation of the Present Model for Braking Load

UIC Code recommends the numerical model for TBI to be validated for rail stress and support reaction before conducting numerical studies on them [6]. In this study, the ballast is assumed to be well maintained. The track stiffness is taken as 40 kN/mm as in Fig. 3b. The model described in the previous section has been used to find the effects of braking load on TBI. UIC 60 rail section is utilized with 1540 mm² as the combined cross-sectional area. The bridge deck has the following specification: Young modulus, $E = 2.1 \times 10^5$ N/mm², coefficient of thermal expansion $\alpha = 1.0 \times 10^{-5}$ °C⁻¹. Length of the bridge deck considered is 15 m, 30 m, 45 m, 60 m, and 90 m, respectively. K2L is taken as the support stiffness, and the corresponding

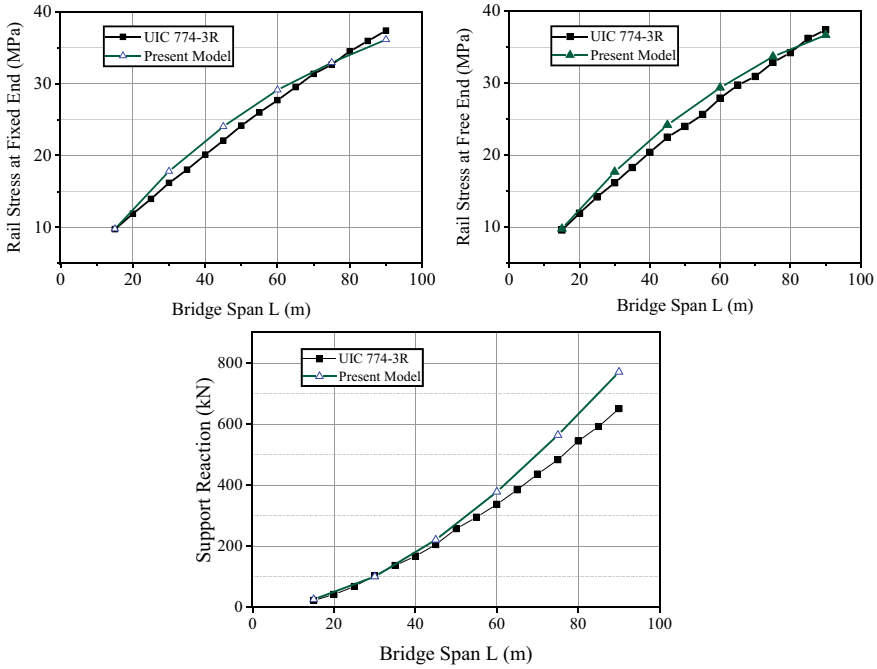


Fig. 5 Comparison of the present model values with UIC 774-3R Code

bridge deck properties are obtained from UIC Code [6]. Braking load = 20 kN/m is applied on the entire span of the bridge.

Figure 5 shows the compares the present model values with UIC 774-34 for braking load. Rail stress the fixed end, rail stress at the movable end, and the corresponding support reaction are compared. It is evident from Fig. 5 that the present model values hold a good agreement with the corresponding UIC codes values.

3 Numerical Study on Braking Load Induced TBI

The numerical study is carried out on the present model to assess the effect of TBI effects due to braking load. TBI effects are controlled by the relative displacement between track and bridge along the length of the track. Effect of continuation of CWR on bridge is studied against the provision of special expansion joints (SEJs) for the longitudinal force distribution in the rail (in terms of rail stress) and the support reaction.

3.1 Effect of SEJs on the Rail Stress Due to Braking Load

The provision of SEJs is undesirable for a high-speed rail track as the riding quality and the maximum vehicle speed are reduced. SEJs modifies the relative displacement between track and bridge. Continuous track eliminates SEJs and results in full track–bridge interaction. The provision of SEJ results in the release of rail forces near SEJ. For understanding the effect of braking load on track bridge system, the four cases considered are given by:

1. No SEJs: CWR over bridge forms a continuous immovable structure. Thermal stress is fully developed in CWR.
2. SEJ provided at the fixed end: Rail stress is released near the fixed support end of the bridge.
3. SEJ provided at the free end: Rail stress is released near the fixed support end of the bridge.
4. SEJ provided at both ends: The portion of the rail on the bridge is isolated from the rest of the track. No thermal stress is developed in the rail.

It should be noted that the presence of SEJs can result in the release of rail forces near these joints. Therefore, in in Case 2, the rail stress at the fixed end of the bridge is also zero for all span lengths due to the presence of SEJ, and in Case 3, the rail stress at the free end of the bridge is zero and due to the presence of SEJ. Simply supported bridges with different span lengths were investigated for the above cases considering the impact of a uniformly applied braking load of 20 kN/m across the entire span from hinged side to roller side. Figure 6(a) compares the rail stress developed at the fixed end of bridge for Case 1 and Case 3. The stress developed is tensile in nature. In case 3, for all the span lengths, the rail stress at the free end of the bridge is zero due to the presence of SEJ. It can be observed from Fig. 6a that a continuous system develops lesser rail stress for all span lengths. Figure 6(b) shows the comparison of the rail stress developed at the free end between Case 1 and Case 2. The stress developed is compressive. In case 2, for all the span lengths, the rail stress at the fixed end is zero due to the presence of SEJ. Again it can be observed that a continuous system develops lesser rail stress for all span lengths.

3.2 Effect of SEJs on the Support Reaction Due to Braking Load

Figure 7 compares various cases for the horizontal bridge support reaction due to braking load. If SEJs are provided at both the ends of the bridge, the entire braking load is transferred to the bridge support. The provision of SEJ at only one end of the bridge results in partially transferring the braking load to the embankment. From Fig. 7, it is observed that the continuous system results in the maximum reduction of the horizontal force in the bridge support among all the scenarios. This analysis

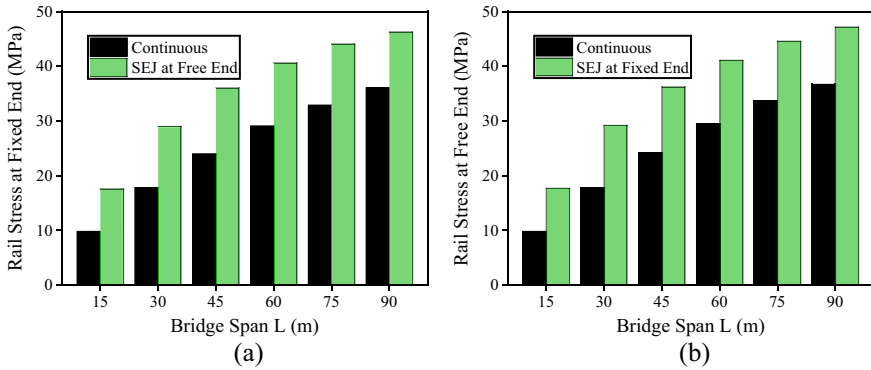


Fig. 6 Effect of providing SEJ on rail stress

highlights the beneficial aspect of track-bridge interaction (TBI) by emphasizing the importance of maintaining continuity of continuously welded rail (CWR) in relation to braking load.

Compared to a bridge with special expansion joints, a significant portion of the braking load is dissipated to the approach zone of the bridge as a result of track-bridge interaction for all span lengths. In small span bridges ($L < 45$ m), the reduction is very steep, and only less than one-third of the total braking load is transferred to the bridge support. And the reduction in support reaction is more than 50% in all the span lengths. This could be advantageous while providing CWR over the existing bridge structures.

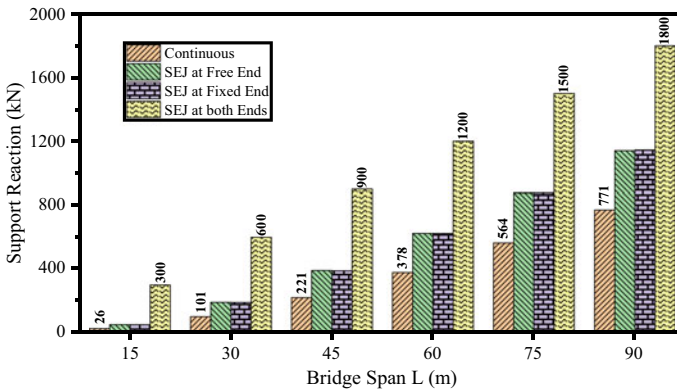


Fig. 7 Comparison of variations in support reaction for different span lengths

4 Conclusion

CWR is gaining popularity over jointed rail because of its inherent advantages. But the designer should have a good amount of understanding of the TBI-related issues for the safe and efficient design of the system. A simplified numerical model developed TBI has been extended to study the effect of braking load on the track–bridge system. The model has been validated for the rail stress and support reaction with UIC Code. A comparative study has been performed comparing the continuous and the discontinuous rail system. This present study highlights the beneficial aspect of track–bridge interaction (TBI) with respect to braking load by emphasizing the importance of maintaining continuity of continuously welded rail (CWR) over bridge. Due to braking load, maximum rail stress developed in the continuous rail system is less compared to the maximum rail stress developed in the presence of SEJ. Also, the longitudinal support reaction at the fixed end pier of the bridge support is affected significantly. When compared to a bridge with special expansion joints, a significant portion of the braking load is dissipated to the approach zone of the bridge as a result of track–bridge interaction for all span lengths. With provision of CWR, the reduction in support reaction is more than 50% in all the observed span lengths. In small span bridges ($L < 45$ m), the reduction is even more steep, and only less than one-third of the total braking load is transferred to the bridge support. It is recommended that one should look into the other causes of TBI before concluding the final state of stress in CWR.

References

1. Ali Mubarak CK, Upadhyay A (2021) Stability of continuous welded rail on steel bridge subjected to thermal loading. *Structures*. <https://doi.org/10.1016/j.istruc.2021.10.050>. <https://www.sciencedirect.com/science/article/pii/S2352012421010079>
2. Eurocode 1: Basis of design and actions on structures, part 3: traffic loads on bridges, ENV 1991-3:1994. European Committee for Standardization
3. Fryba L (1985) Thermal interaction of long welded rails with railway bridges. *Rail Int* 16:5–24
4. Kumar R, Upadhyay A (2012) Effect of temperature gradient on track–bridge interaction. *Interact Multiscale Mech* 63(1):1–12
5. Ruge P, Birk C (2007) Longitudinal forces in continuously welded rails on bridgedecks due to nonlinear track–bridge interaction. *Comput Struct* 85(7–8):458–475
6. UIC (International Union of Railways) (2001) UIC 774-3R track/bridge interaction recommendations for calculations, 2nd edn. International Union of Railways, Paris
7. Yang SC, Hwang SH (2016) Train-track–bridge interaction by coupling direct stiffness method and mode superposition method. *J Bridg Eng* 21(10):04016058
8. Yang SC, Jang SY (2016) Track–bridge interaction analysis using interface elements adaptive to various loading cases. *J Bridg Eng* 21(9):04016056

Assessment of Efficiency of Steel X-Bracings and Steel Plate Bonding Applied as a Retrofit Measure to Enhance the Seismic Resistance of RC Structures



Mohammed Mazharuddin and Y. K. Guruprasad

Abstract Damage or distress caused due to earthquakes need to be retrofitted to enhance the load carrying capacity of distressed structural members. This study focuses on the behavior of a L-shaped Flat slab structure having $10 \times 10 \times 2$ bays in plan and 9 stories to seismic loads using ETABS. One set of models for study are carried out with steel X-bracings between the columns vertically at various locations in the plan of the structure. A second set of models for study are carried out by providing steel plate bonded columns at all stories for different columns in the plan of the structure. The performance of the structural models in earthquake and comparison with that of reference model without any lateral load resisting system is studied. The comparative study between the two sets of models is carried out to check the performance of steel X-bracings as compared to steel plate bonded columns.

Keywords Seismic resistance · Flat-slab structure · Torsional irregularity · Retrofitting · X-bracing · Steel plate bonding

1 Introduction

The earthquakes occurring in a region are difficult to effectively predict before the occurrence. The additional loads induced on the structure due to earthquakes are necessary to be included in the analysis of a structure as this may lead to considerable damage to the structure. The structures subjected to the Seismic loads dissipate the energy due to the lateral forces leading to the formation of plastic hinges at some locations in the structural elements [1]. Various codal provisions are available in order to predict the effect the earthquake on structures based on different earthquake zones. Based on the structural importance and type of the structure the seismic design of the structure varies.

M. Mazharuddin (✉) · Y. K. Guruprasad
Department of Civil Engineering, Ramaiah Institute of Technology, Bengaluru, India
e-mail: mazharuddin191@gmail.com

© The Author(s), under exclusive license to Springer Nature Singapore Pte Ltd. 2023
M. Madhavan et al. (eds.), *Proceedings of the Indian Structural Steel Conference 2020*
(Vol. 2), Lecture Notes in Civil Engineering 319,
https://doi.org/10.1007/978-981-19-9394-7_41

509

The static and dynamic analysis of a structure can be easily carried out using soft computing tool such as ETABS. The codal provisions specified in IS 1893:2016 [2] can be used for response spectrum analysis in order to check the stability of the structure to seismic loads.

The structures that shows instability or large displacements preferably in lateral directions can be provided with lateral load resisting systems such as bracings, dampers, isolators, etc. Torsional irregularity arrives in the structure due to twisting action of structure about its vertical axis. This twisting action may be due to the eccentricity between centre of mass and centre of stiffness. It can also be reduced effectively by locating optimal position of lateral load resisting systems in the plan of structure. The bracings are usually provided as diagonal members in order to resist lateral forces on the structural elements and helps in effective transfer of loads to the other structural elements reducing damage or distress on the structural elements. Torsional irregularity coefficient of a structure is calculated as the ratio of maximum story displacement to the average story displacement. If this ratio is above 1.2 then structure is subjected to torsion in plan and if the ratio is greater than 1.4 then very large torsional moment exists in the plan of the structure [3].

2 Literature Review

Dia et al. [4], carried out analytical work using ETABS for seismic analysis of steel structure of varying stories and different types of bracings. The maximum base shear can be observed for the structures with X-bracing for different storey models. The least displacements are observed for VBF, IBF and ZBF for 12 and 16 stories, VBF and IVF for 4 stories and ZBF and XBF for 8 stories. IVF, VBF and ZBF structures are considered to perform better than other structures.

Raheem et al. [3], carried out comparative analytical work using ETABS for different structures with L-shaped plan irregularities for earthquakes by response spectrum method. The story responses shows the increase in the displacement of irregular plan of about 54% more than the regular plan building. Torsional irregularity developed is plotted for different plans that shows the value of 1.5 for maximum eccentricity in the plan which results in the more stress concentration due to increased forces. High irregularity in the plan leads to instability and non-uniform damage of the structure.

Rishab et al. [5], carried out seismic analysis of the RC frame structure using ETABS adopting different types of bracings as lateral load resisting system. X-bracings resulted in maximum reduction of lateral displacements of about 64.78% at roof as compared to other types of bracings used for analysis. The values of reduction in storey drift and drift ratio were highest for X-bracing. Performance of V-bracing, inverted V-bracing and combined V-bracing is almost similar with similar values of displacement, storey drift and drift ratio. The base shear value for the structure with X-bracing is higher than other types of bracings.

Xiao and Wu [6], carried out experimental research on cyclic loading of RC columns retrofitted with steel jackets and partially stiffened at the ends. The thickness of jacket plate required for confinement is determined by following ACI codal provisions. The failure of RC column is found to be brittle in nature. For columns stiffened with steel plate throughout showed bulging at the ends showing shear deficiency whereas stiffening columns at the ends increases the shear capacity of the columns.

3 Methodology

The current study involves modeling of a 9-storey flat slab building with irregular L-shape having $10 \times 10 \times 2$ bays in plan with each bay having a span of 5 m in length, total height of structure is 28 m in elevation with typical storey height of 3 m and bottom storey height as 4 m using ETABS as shown in Fig. 1 [3].

The material and sectional properties used for the purpose of structural modeling are as shown in Tables 1 and 2 respectively [3]. The compressive strength of concrete and yield strength of steel rebar are calculated considering material strength for particular grade of concrete and steel as per Code No. (205) [7].

The loads applied to the existing structure are as shown in Table 3 [3].

For linear seismic analysis, Response spectrum method as defined in IS 1893:2016 [2] is adopted. Response reduction factor of 3 is considered for analysis.

The seismic forces are defined separately in X-direction and Y-direction and envelope of load combinations is adopted to obtain maximum response of the structure.

The model analyzed by dynamic method needs to be enhanced for lateral load carrying capacity which may tend to reduce the storey drifts and storey displacements.

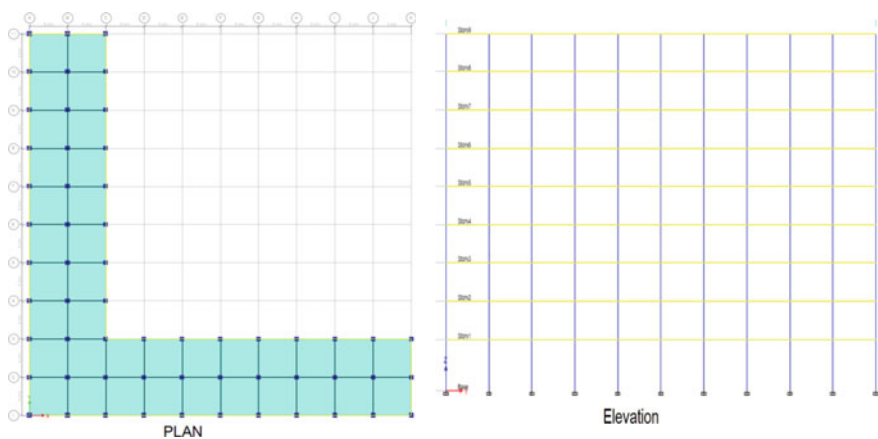


Fig. 1 Building plan and elevation for existing model

Table 1 Material properties of the existing structural model

Materials				
Concrete		Rebar		
Grade	Compressive strength (MPa)	Grade	Tensile strength (MPa)	Yield strength (MPa)
C400	28	St40	400	348
		St24	240	209

Table 2 Sectional properties of the structural elements of existing structure

Sections		
Beam (mm)	Column (mm)	Flat Slab (mm)
250 × 600	600 × 600	160

Table 3 Loading details on the structure

Importance factor	Seismic zone	Zone factor	Damping ratio	DL (kN/m ²)	Partition wall load (kN/m ²)	LL floor (kN/m ²)	LL roof (kN/m ²)	SDL (kN/m ²)
1	V	0.36	0.05	4	1.5	2.5	1	3.5

One set of study is carried out by providing steel X-bracing between the columns. Second set of study is carried out by providing steel plate bonding around the existing columns of the structure.

3.1 Set 1: With Steel X-bracings Between Columns

The steel X-bracings of section ISA 100X100X10 as defined in SP: 6(1)—1964 [8] are provided between the columns at various positions in the plan at all stories. The location of X-bracings is adopted based on different combinations where the X-bracings are located such that, the lateral drifts in the structure are reduced predominantly and the torsional resistance of the structure is improved significantly due to overall increase in stiffness of the structure. A set of models having X-bracings are named from B1 to B9 as shown in Fig. 2.

These models are then analyzed by response spectrum method. Response reduction factor is considered as 4 for braced structures as per IS 1893:2016 [2]. The analysis results of each model is checked for storey displacements, inter-storey drifts and torsional irregularity coefficient.

The values obtained for different models are plotted against stories in order to understand the performance of the structures and the results obtained are compared with reference model.

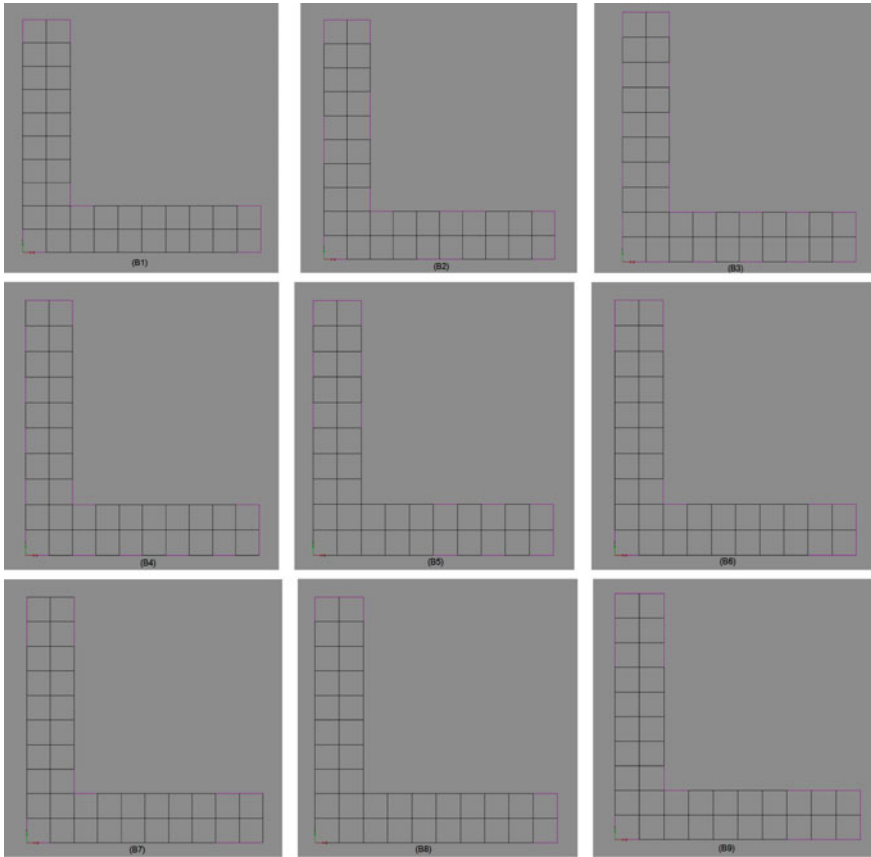


Fig. 2 Plans of first set of models (B1 to B9) with different locations of bracings. Pink line—Bracings; Frame—black line

The structural model without bracings and the model with optimum location of bracings (model B8) are analyzed by non-linear static or pushover analysis method for the target displacement of 930 mm which is calculated approximately as $H/30$ where H is total height of the structure.

3.2 Set 2: With Steel Plate Bonding Around the Columns

The steel plate bonding of thickness 10 mm and yield strength of 345 MPa is defined around the column section using section designer in ETABS as shown in the Fig. 3.

A set of models are created with different locations of steel plate bonded columns in the plan of the structure at all stories named from S1 to S5 as shown in the Fig. 4. Response reduction factor of 3 is considered for analysis as per IS 1893:2016 [2].

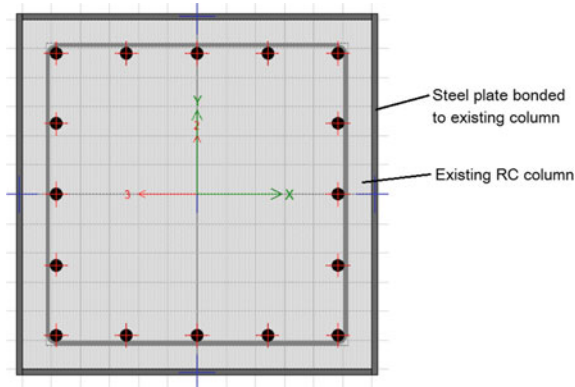


Fig. 3 Cross-section of steel plate bonded column

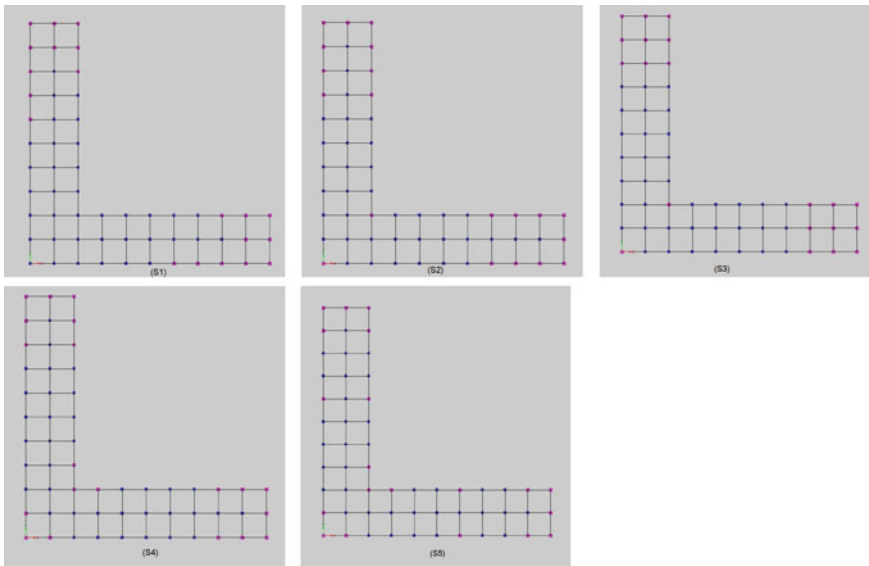


Fig. 4 Plans of second set of models (S1 to S5) with various locations of bracings. Steel plate bonded column—pink box; RC column—blue box

These models are analyzed using response spectrum method and results are compared for storey displacements, inter-storey drifts and torsional irregularity coefficient.

4 Results and Discussions

The maximum storey displacements of the structure with and without X-bracings for first set of models are as shown in the Table 4 and the same results are plotted against the stories are shown in Fig. 5.

The above results shows a considerable decrease in the values of maximum storey displacements for steel bracings adopted. The results observed for the model B5 suggests that this configuration has reduced story displacement to the maximum. The reduction in storey displacement in model (B5) is about 72% as compared to reference model (WB). Agreeable values are observed in the other models. Relatively higher values which are close to the values of model B5 are observed for model B7 and B8.

Table 4 Maximum storey displacements for the set of models with and without bracings

Stories	Maximum storey displacements for first set									
	WB	B1	B2	B3	B4	B5	B6	B7	B8	B9
9	152.8	47.1	56.6	64.0	57.9	42.4	50.4	107.2	48.7	57.0
8	145.1	44.4	53.4	60.4	54.5	40.0	47.6	102.0	46.3	54.0
7	134.4	40.8	49.2	55.6	50.0	36.8	43.9	94.6	42.9	50.0
6	120.5	36.3	43.9	49.6	44.4	32.9	39.2	84.8	38.5	44.7
5	103.5	31.0	37.7	42.6	38.0	28.2	33.7	73.0	33.2	38.5
4	83.9	25.2	30.7	34.7	30.9	23.0	27.5	59.3	27.2	31.5
3	62.1	18.9	23.2	26.3	23.2	17.3	20.8	44.1	20.6	23.9
2	39.2	12.4	15.3	17.4	15.2	11.4	13.7	28.0	13.5	15.8
1	17.3	5.8	7.4	8.4	7.3	5.5	6.5	12.5	6.4	7.6

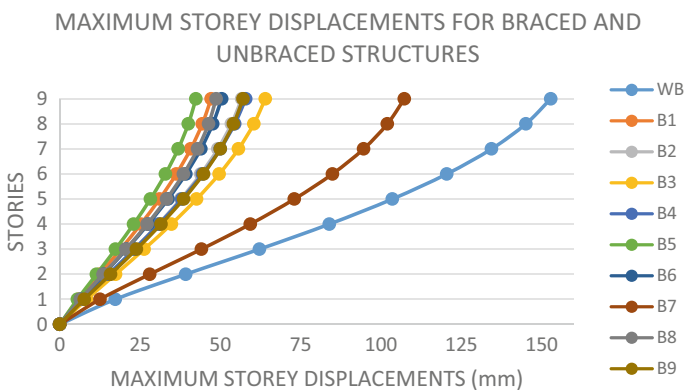


Fig. 5 Maximum storey displacements versus stories for the set of models with and without bracings

Similarly, the maximum storey displacements for second set of models with and without steel plate bonding to columns are as shown in the Table 5 and same results are plotted against the stories are shown in Fig. 6.

Comparatively lesser values of maximum storey displacement is observed for S1 and S3 models, whereas model S5 does not show any considerable change in the values as compared to the reference model.

The inter-storey drifts of the structures for the first set of models are as shown in Table 6 and plotted results are shown in Fig. 7.

The least values of inter-storey drifts can be observed in the model B8 and closer values to model B8 can be observed in the models B1, B5 and B6 suggesting similar behaviour of the structure with different locations of X-bracings. Highest values are found for the model B7.

Table 5 Maximum storey displacements for set of models with and without steel plate bonding

Stories	Maximum storey displacements for second set					
	WB	S1	S2	S3	S4	S5
9	152.796	143.307	144.36	143.73	145.391	152.917
8	145.057	134.895	135.966	135.276	137.078	145.399
7	134.376	123.958	125.01	124.295	126.153	134.857
6	120.453	110.131	111.129	110.422	112.255	120.921
5	103.513	93.567	94.479	93.809	95.544	103.912
4	83.905	74.658	75.45	74.848	76.411	84.215
3	62.134	54.074	54.709	54.21	55.511	62.348
2	39.2	33.046	33.484	33.127	34.061	39.321
1	17.299	13.907	14.121	13.938	14.416	17.341
0	0	0	0	0	0	0

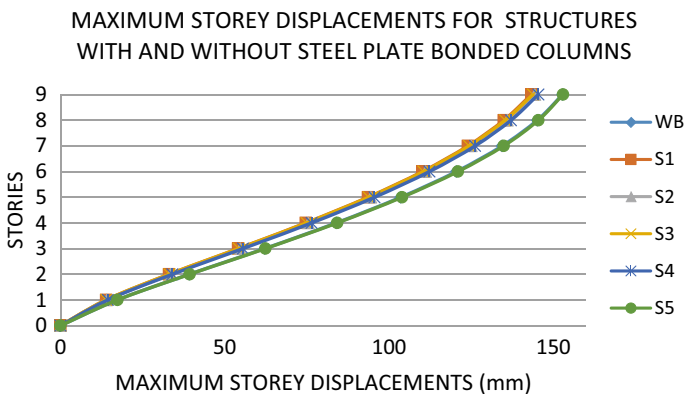


Fig. 6 Maximum storey displacements for set of models with and without steel plate bonding versus stories

Table 6 Maximum inter-storey drifts for the set of models with and without bracings

Storey	Maximum inter-storey drifts for first set (mm)									
	WB	B1	B2	B3	B4	B5	B6	B7	B8	B9
9	9.154	2.893	3.328	3.728	3.59	2.924	2.907	6.162	2.601	3.144
8	12.393	3.826	4.449	4.998	4.716	3.899	3.916	8.463	3.713	4.301
7	15.6	4.724	5.546	6.237	5.794	4.853	4.914	10.748	4.745	5.456
6	18.296	5.437	6.432	7.243	6.651	5.618	5.724	12.675	5.577	6.409
5	20.502	5.979	7.117	8.02	7.297	6.207	6.355	14.259	6.24	7.162
4	22.239	6.365	7.61	8.578	7.748	6.633	6.819	15.508	6.751	7.725
3	23.111	6.588	7.906	8.909	7.998	6.892	7.108	16.177	7.086	8.086
2	21.94	6.554	7.958	8.983	7.983	6.918	7.157	15.513	7.08	8.198
1	17.3	5.847	7.357	8.406	7.274	6.295	6.537	12.53	6.442	7.633

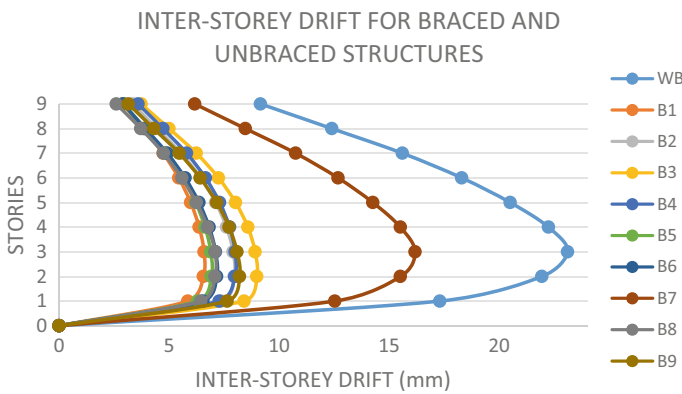


Fig. 7 Maximum inter-storey drifts for the set of models with and without bracings versus stories

Similarly, the storey drifts of the structures for the second set of models are as shown in Table 7 and results plotted are as shown in Fig. 8.

Almost similar values are observed in all models with no considerable change as compared to that of reference model.

The torsional irregularity coefficient of the first set of structural models are as shown in Table 8 and plotted results for the same are shown in Fig. 9.

Least values are observed for models B1, B5 and B8 which suggest higher resistance to torsion in plan of the structure can be achieved by adopting these locations of X-bracings and highest values are found for model B7 which suggests existence of high torsional irregularity in the structure.

Similarly, the torsional irregularity coefficient of the second set of structural models are as shown in Table 9 and Fig. 10.

All the models have similar values of torsional irregularity coefficient which shows no considerable variation in torsion occurring in plan of the structure.

Table 7 Maximum inter-storey drifts for the set of models with and without steel plate bonding

Storey	Storey drifts for second set					
	WB	S1	S2	S3	S4	S5
9	9.154	9.597	9.605	9.649	9.547	8.881
8	12.393	12.287	12.336	12.343	12.338	12.243
7	15.6	15.096	15.179	15.153	15.229	15.621
6	18.296	17.555	17.665	17.612	17.753	18.378
5	20.502	19.546	19.682	19.603	19.806	20.603
4	22.239	20.91	21.075	20.967	21.246	22.341
3	23.111	21.15	21.35	21.206	21.579	23.207
2	21.94	19.166	19.391	19.216	19.674	22.019
1	17.3	13.907	14.121	13.938	14.416	17.341
0	0	0	0	0	0	0

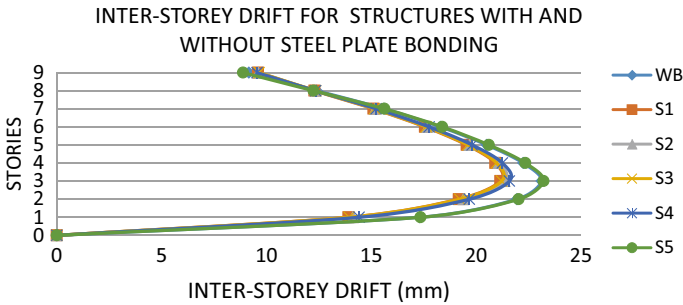


Fig. 8 Maximum inter-storey drifts for the set of models with and without steel plate bonding versus stories

Table 8 Torsional irregularity coefficient for the set of models with and without bracings

Stories	Torsional irregularity coefficient for first set									
	WB	B1	B2	B3	B4	B5	B6	B7	B8	B9
9	1.4	1.087	1.267	1.319	1.26	1.175	1.193	1.399	1.054	1.301
8	1.365	1.073	1.254	1.31	1.247	1.161	1.179	1.398	1.069	1.281
7	1.349	1.067	1.253	1.311	1.245	1.16	1.177	1.402	1.074	1.275
6	1.34	1.064	1.253	1.312	1.245	1.159	1.177	1.406	1.077	1.272
5	1.333	1.062	1.254	1.313	1.244	1.158	1.177	1.411	1.08	1.27
4	1.326	1.06	1.254	1.314	1.245	1.158	1.176	1.417	1.083	1.268
3	1.317	1.059	1.255	1.316	1.246	1.159	1.176	1.418	1.085	1.267
2	1.301	1.058	1.254	1.315	1.246	1.16	1.175	1.402	1.087	1.263
1	1.269	1.047	1.238	1.294	1.231	1.149	1.163	1.349	1.099	1.244

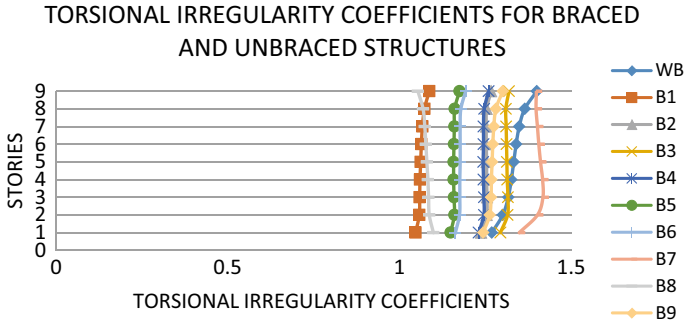


Fig. 9 Torsional irregularity coefficient for the set of models with and without bracings versus stories

Table 9 Torsional irregularity coefficient for the set of models with and without steel plate bonding

Stories	Torsional irregularity coefficient for second set					
	WB	S1	S2	S3	S4	S5
9	1.4	1.413	1.411	1.409	1.405	1.397
8	1.365	1.372	1.37	1.369	1.368	1.363
7	1.349	1.348	1.348	1.347	1.347	1.349
6	1.34	1.337	1.337	1.335	1.337	1.34
5	1.333	1.328	1.328	1.327	1.329	1.333
4	1.326	1.318	1.318	1.316	1.32	1.327
3	1.317	1.303	1.304	1.302	1.307	1.318
2	1.301	1.279	1.282	1.278	1.287	1.302
1	1.269	1.238	1.243	1.239	1.25	1.269

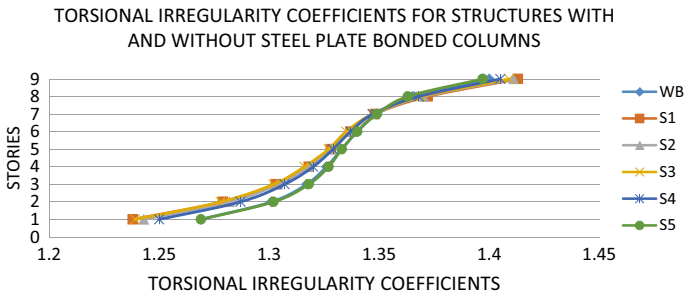


Fig. 10 Torsional irregularity coefficient for the set of models with and without steel plate bonding versus stories

The pushover curves for the model WB and the model B8 are represented in the Figs. 11 and 12 respectively.

The above pushover curves for the models suggests that, model WB has entered into the non-linear stage where potential plastic hinges are formed in the structural members with considerable damage, while in the model B8 the structural members have least levels of damage.

The maximum storey displacements, inter-storey drifts and torsional irregularity coefficients for different stories of the structure with steel X-bracings (model B8) and without bracings (model WB) are shown in Table 10.

The above results shows that, the response of the structure for pushover analysis in terms of Maximum storey displacements, inter-storey drifts and torsional irregularity

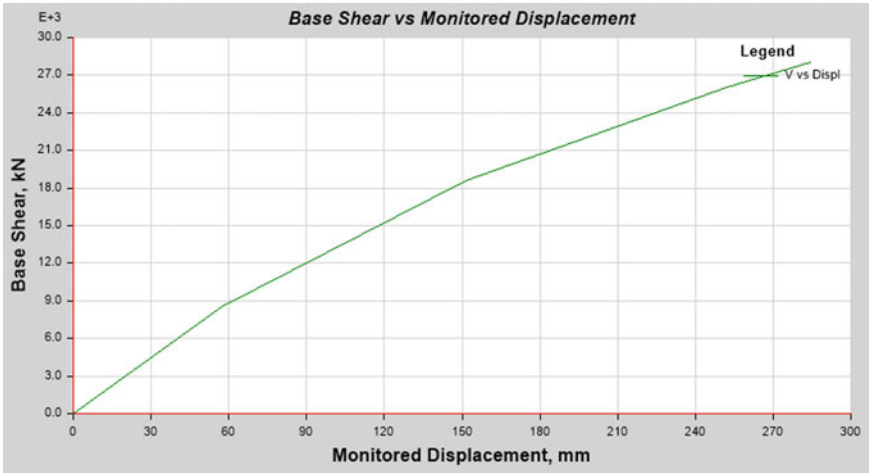


Fig. 11 Pushover curve at 930 mm target displacement of model WB

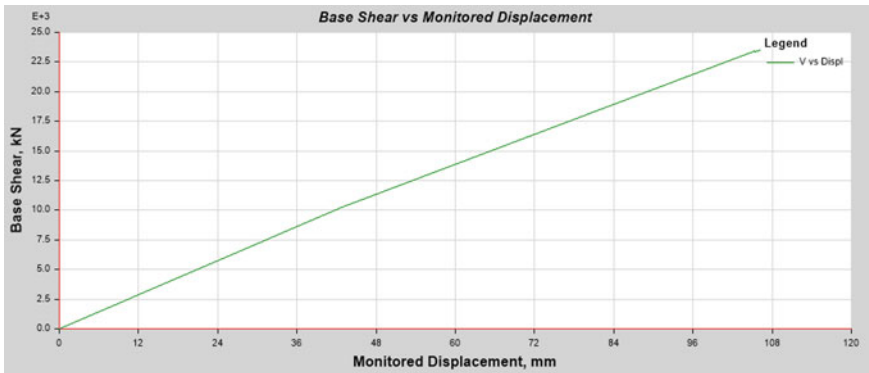


Fig. 12 Pushover curve at 930 mm target displacement of model B8

Table 10 Maximum storey displacement, inter-storey drift and torsional irregularity coefficient for structure subjected to a target displacement of 930 mm by pushover analysis method

Stories	Maximum storey displacement (mm)		Inter-storey drift (mm)		Torsional irregularity coefficient	
	B8	WB	B8	WB	B8	WB
9	123.785	284.129	4.843	6.837	1.021	1.292
8	119.14	277.292	6.634	10.545	1.019	1.244
7	112.506	266.747	8.83	15.143	1.038	1.226
6	103.675	251.605	11.04	20.2	1.05	1.218
5	92.635	231.404	13.228	25.773	1.06	1.208
4	79.407	205.631	15.445	32.208	1.07	1.183
3	63.962	173.423	17.761	39.802	1.083	1.148
2	46.201	133.621	20.336	51.039	1.1	1.101
10	25.8640	82.5820	25.8640	82.5820	1.140	1.0250

coefficients at different stories for the model B8 with bracings are significantly less when compared to the model WB without bracings. It shows significant reduction in lateral response and greater resistance to torsion in plan of the structure at different stories.

5 Conclusions

1. Seismic response (storey displacements) of the structure can be effectively reduced by retrofitting adopting steel plate bonding and steel X-bracing by increasing the lateral stiffness of the columns and the frame respectively.
2. By carrying out a comparative study of the structural responses of all the structural models it was found that, model B8 gave the optimum number and location of steel X-bracings in the plan that reduced the storey displacements to the maximum and also reduced the possibility of torsion taking place in the structure.
3. It was learnt even by carrying out the pushover analysis separately, model B8(model with bracings) performed well in resisting the lateral loads in the pushover analysis by showing lesser degree of damage in it (damage within repairable limits) when compared to the damage taken place in the model WB (without bracings) that had developed considerable damage.
4. The steel plate bonded columns adopted for the study in the structure did not efficiently reduce the storey displacement, thereby not improving the lateral stability of the structure when compared to the steel X-bracings. However the steel plate bonded columns are good in enhancing the axial load carrying capacity of the distressed columns.

References

1. Jenn-Shin H (2002) Seismic design of structures with viscous dampers. In: International training programs for seismic design of building structures, pp 124–138
2. IS 1893 (2016) Criteria for earthquake resistant design of structures. Part-1: general provisions and buildings. Bur Indian Stan
3. Raheem SEA, Ahmed MMM, Ahmed MM, Abdel-shafy AGA (2018) Evaluation of plan configuration irregularity effects on seismic response demands of L-shaped MRF buildings. *Bull Earthq Eng* 16(9):3845–3869
4. Dia EN, Hussein AK, Mohammed AH (2017) Comparative response assessment of steel frames with different bracing systems under seismic effect. *Structures* 11:229–242
5. Rishab S, Tiwary SK, Mangla S, Husain MT (2018) Seismic analysis and retrofitting of a multi-storey RC building. *Int Res J Eng Technol* 5(5):2988–2992
6. Xiao Y, Wu H (2003) Retrofit of reinforced concrete columns Using partially stiffened steel jackets. *J Struct Eng* 129(6):725–732
7. Code No. (205) (2001) Egyptian code of practice for steel construction and bridges: allowable stress design—ASD. Ministerial Decree No 279-2001
8. SP: 6(1) (1964) Handbook for structural engineers—structural steel sections

Static and Cyclic Behaviour of Beam-Column Endplate Connection with Cellular Beam



Dondeti Manideep Reddy, C. Arunkumar, and N. Umamaheswari

Abstract The present study focused on numerical investigation on beam-column end plate connection provided with cellular beam. If the beam possesses openings in the web portion it is referred as cellular beam. The perforation in the cellular beam tries to shift the position of plastic hinge away from the beam-column connection under cyclic load conditions. The finite element analysis was carried out for cellular beam provided with circular opening in the web portion. The radius of web opening was varied as 30, 40, 50, 60 mm in order to assess the performance of the connection in terms of rotational stiffness, failure mode etc.. The moment-rotation behaviour of the connection was analysed under static and cyclic load conditions. The loading history for cyclic load condition was given as per FEMA 350 guidelines. While increasing the radius of web opening of cellular beam, the moment capacity was found to be increased. The plastic region is extended before failure which was observed from the moment-rotation behaviour of beam-column end plate connection under consideration.

Keywords Cellular beam · Plastic hinge · Cyclic load · Circular opening · Stiffness

1 Introduction

Steel structures have been vastly used in the Architecture, Construction and Engineering (ACE) industry over the past few decades. Use of these structures results in a drastic reduction in the amount of formwork and promotes the speed during construction. Metal structures have the advantage of a uniform ductile cross-section.

D. M. Reddy · C. Arunkumar · N. Umamaheswari (✉)
Department of Civil Engineering, SRM Institute of Science and Technology, Kattankulathur,
Chennai 603203, India
e-mail: umamahen@srmist.edu.in

C. Arunkumar
e-mail: arunkumc2@srmist.edu.in

© The Author(s), under exclusive license to Springer Nature Singapore Pte Ltd. 2023
M. Madhavan et al. (eds.), *Proceedings of the Indian Structural Steel Conference 2020*
(Vol. 2), Lecture Notes in Civil Engineering 319,
https://doi.org/10.1007/978-981-19-9394-7_42

523

The steel beam provided with a web opening is termed as cellular beam which is found to be advantageous in smooth distribution of stress near opening as well as increased stiffness. Due to reduction of cross-section, it is also economical. In order to retard the failure of connection by plastic hinge formation, the end plate connection is used with cellular beam.

In this research work, beam-column endplate connections with cellular beam have been analysed using ABAQUS finite element analysis (FEA) software. The numerical investigation has been conducted keeping radius of cellular beam as parameter. The parametric study deals with the stiffness of the connection under static and cyclic loading.

2 Literature Review

After the occurrence of Northridge earthquake in the United States during the year 1994, it was observed that the failure caused in steel structures occurred due to failure of beam-column connections [2, 7]. Taking this incident into consideration, across the globe, many studies were carried out on the mechanical behaviour of beam-column connection under various loading conditions [9, 10]. The easiest way of connection is by welding the beam to periphery of the column with an endplate. But beam should not be welded directly to the metal column in a moment resisting frame (MRF) [1]. The use of bolted connection or combination of field bolt-shop weld connection are alternatives of field weld.

In moment resisting frames, a strong column-weak beam concept is applied due to a viable alternative to the sophisticated dampers under earthquake conditions [9]. Also, the plastic hinge shift away from connection is achieved by the reduced web section [3]. Perforated beams are used as weak beam members in steel structures because of lower cross-sectional area and a high moment carrying capacity of the connection [5]. Due to high moment of inertia, these beams will possess high stiffness. Different shapes of perforated beams like rectangular, circular, hexagonal, etc., are selected based on design procedure and availability. Circular perforated beam is commonly known as cellular beam which has more uniform stress distribution compared to any other perforated beams [4, 8].

Early twenty first century, study on seven different moment resisting composite connection was conducted experimentally under cyclic loading. All seven connections are highly complex in nature during the time of construction. Six out of seven connections have extended flange section which is considered to be an alternative to the reduced section. But later, with research it was observed that very high stress region occurred in and around the toe of extended flange section. So, the other alternative is reduced section in beams [9].

Boushehri et al. [3] carried on reduced web section (RWS) moment connection to the deep column, the effect of web opening size and the location of RWS on the connection was experimented through numerical investigation. It was observed that due to web opening the ductility of the connection is enhanced. Also, the location

of plastic hinge was influenced by the web opening size and the location. In the year 2018, Sherif A. Elsayaf conducted a study on steel beam with web openings under fire conditions. Seven different web opening configurations were exposed to fire condition using ABAQUS finite element analysis software. It was noted that the circular and castellated web opening configurations excelled in the test results. The highest limiting temperature difference was 176°C for rectangular configuration. This result explains that the change in shapes has an impact in the performance of steel structures.

3 Numerical Investigation

The finite element analysis has been conducted on the cellular beam with variation in the radius of opening in the beam. The specimen configuration used for the analysis is shown in Table 1.

The connection components were made with C3D8R solid element as individual elements (beam, column, end plate, bolt) and assembled as beam-column connection as shown in Fig. 1. The material properties such as modulus of elasticity (2×10^5 N/mm²) and Poisson's ratio (0.3) were assigned. The interaction between column flange and end plate has been modelled with surface to surface contact in which tangential contact was considered with coefficient of friction value of 0.3. The interaction between bolt head and endplate as well as nut and column flange has been modelled with tie constraint. The column ends are fixed using boundary condition ENCASTRE as shown in Fig. 2. The bolt load was applied through inner surface of the shank portion along centroidal axis in order to simulate the tightening effect as shown in Fig. 3.

The displacement approach is used for both static and cyclic loading. The loading history for cyclic loading is shown in Fig. 4. The meshing has been done by the aspect ratio of elements (ratio of length to width) as small as possible as shown in Fig. 5.

Table 1 Details of specimen used in FE analysis

Specimen ID	Column section	Beam section	Radius of the opening	Loading type
Specimen 1	ISMB300	ISMB 200	30	Static
Specimen 2	ISMB300	ISMB 200	40	Static
Specimen 3	ISMB300	ISMB 200	50	Static
Specimen 4	ISMB300	ISMB 200	60	Static
Specimen 5	ISMB300	ISMB 200	30	Cyclic
Specimen 6	ISMB300	ISMB 200	40	Cyclic
Specimen 7	ISMB300	ISMB 200	50	Cyclic
Specimen 8	ISMB300	ISMB 200	60	Cyclic

Fig. 1 Assembled model of cellular beam end plate connection

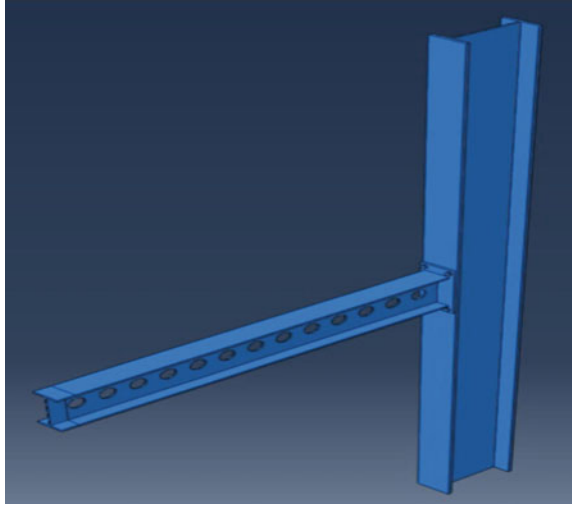
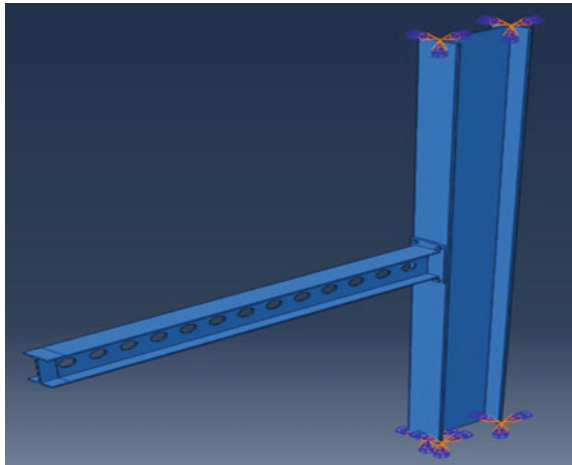


Fig. 2 Boundary condition considered



The local and global seeds were used for dividing the element finite and meshed with tetrahedron mesh.

4 Results and Discussion

The finite element analysis has been conducted for the cellular beam connected to column through end plate connection, with varying radius of opening of beam. The displacement approach was used for both static and cyclic loading. The

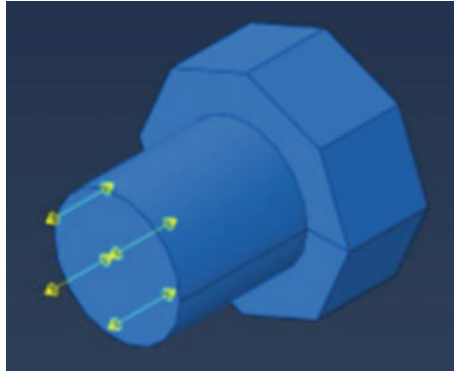


Fig. 3 Application of Bolt load

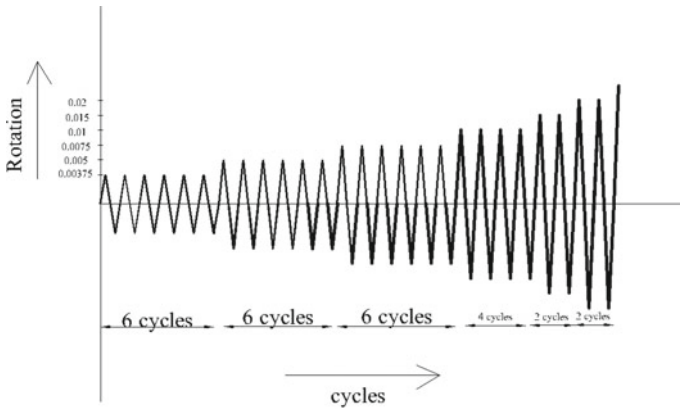


Fig. 4 Loading history based on FEMA 350

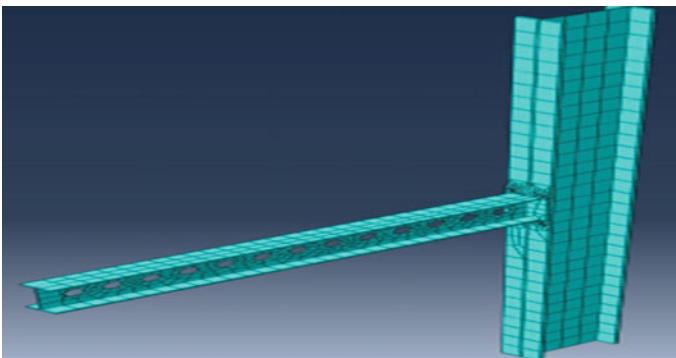


Fig. 5 Meshing

Table 2 Connection stiffness in static condition

Specimen ID	Ultimate moment (kNm)	Ultimate rotation (rad.)	Connection stiffness (kNm/rad)
Specimen 1	22.50	0.0966	232.80
Specimen 2	23.08	0.1358	169.99
Specimen 3	23.07	0.1358	169.91
Specimen 4	23.12	0.1372	168.51

loading history for cyclic loading was given as per FEMA350. The moment-rotation behaviour was observed for static and cyclic loading condition. Identical connection specimen configuration was adopted for cyclic load analysis. Because of reversal of load, moment was observed in both positive and negative moment regions. The discussions on the results obtained for static and cyclic load analysis is given in the following sections.

4.1 Static Load Behaviour of Cellular Beams

Four specimens were modelled with different radius (30R, 40R, 50R, 60R) of web opening and analysed under incremental static load. The displacement approach was used in order to find the maximum moment and rotation. The connection stiffness obtained under static load condition is shown in Table 2.

The moment versus rotation characteristics of all four specimens were plotted (Fig. 6). Large inelastic deformation was observed in moment-rotation curve, when the web opening was increased. This is due to the shift of plastic hinge away from the connection. Ductile behaviour of connection was observed, when increasing the web opening radius from 30 to 40 mm with 2.5% increase in moment capacity whereas 2.8% increase was observed for increase in radius from 30 to 60 mm. Also connection rotational stiffness has been reduced upto 27%. As per Eurocode 3, the connection was categorized as pinned connection, since the connection stiffness is less than $0.5 EI_b/L_b$. There was no significant variation in moment capacity and connection stiffness, when the radius of web opening was increased from 40 mm to 60 mm. When increasing the radius from 30 to 60 mm, the ultimate rotation has been increased by 42%.

4.2 Cyclic Load Behaviour of Cellular Beams

For cyclic load analysis, identical specimen configuration was adopted as in static condition. Because of reversal of load, positive and negative moment region was observed. The ultimate moment in tension and compression region is shown in Table

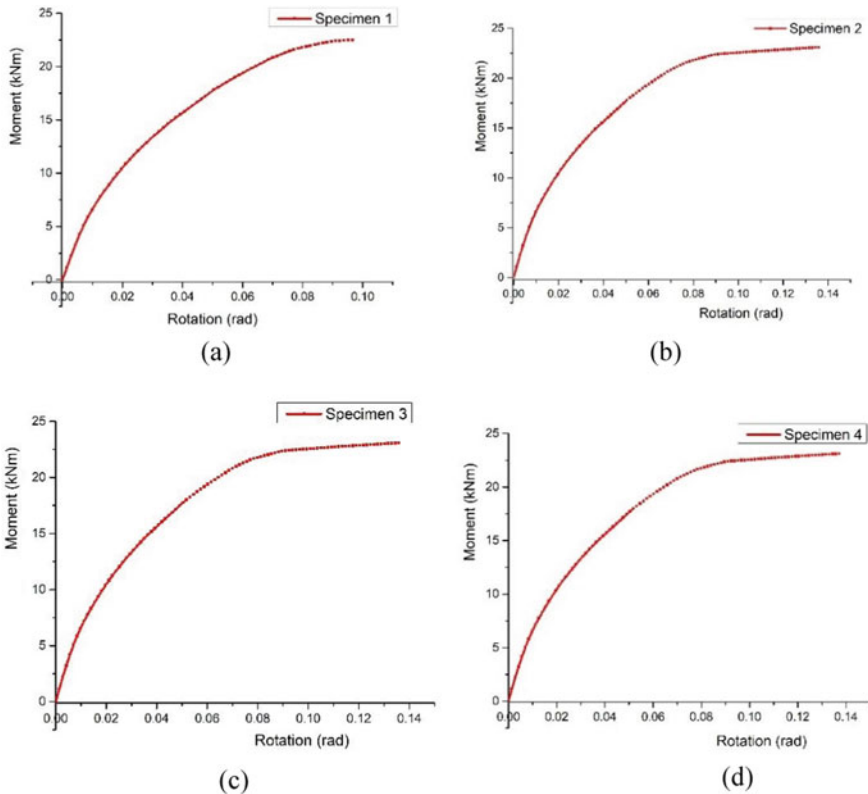


Fig. 6 Moment-rotation curve of **a** 30 R web opening, **b** 40 R web opening, **c** 50 R web opening, **d** 60 R web opening

3. There is some deviation in stiffness due to variation in yielding of beam in the inelastic region. With the results of cyclic load analysis, it was found that the ultimate moment capacity has been increased by upto 2.97% comparing the performance of all beam-column end plate connection specimens. When increasing the radius of web opening beyond 50 mm, the moment capacity started decreasing. The variation in connection rotational stiffness with respect to change in radius of web opening is marginal only.

The hysteresis behaviour of cellular beam end plate connection with different radius of web opening is plotted (Fig. 7). The shape of the hysteresis curve depends on both moment and rotation values. The shape of hysteresis curve is found to be directly related to the radius of web opening. It was observed that the hysteresis loop is flattened in the elastic region due to lesser resistance of connection. After reaching the inelastic region, the loading and unloading followed different path and exhibited hysteresis behaviour. When increasing the radius of web opening, the strain hardening portions are extended as in Fig. 7b and c.

Table 3 Connection stiffness in cyclic condition

Specimen ID	Ultimate negative moment (kNm)	Negative connection stiffness (kNm/rad)	Ultimate positive moment (kNm)	Positive connection stiffness (kNm/rad)
Specimen 5	10.09	351.40	13.86	463.92
Specimen 6	10.15	342.81	13.52	445.31
Specimen 7	10.39	347.49	13.88	462.67
Specimen 8	10.36	345.67	12.75	489.13

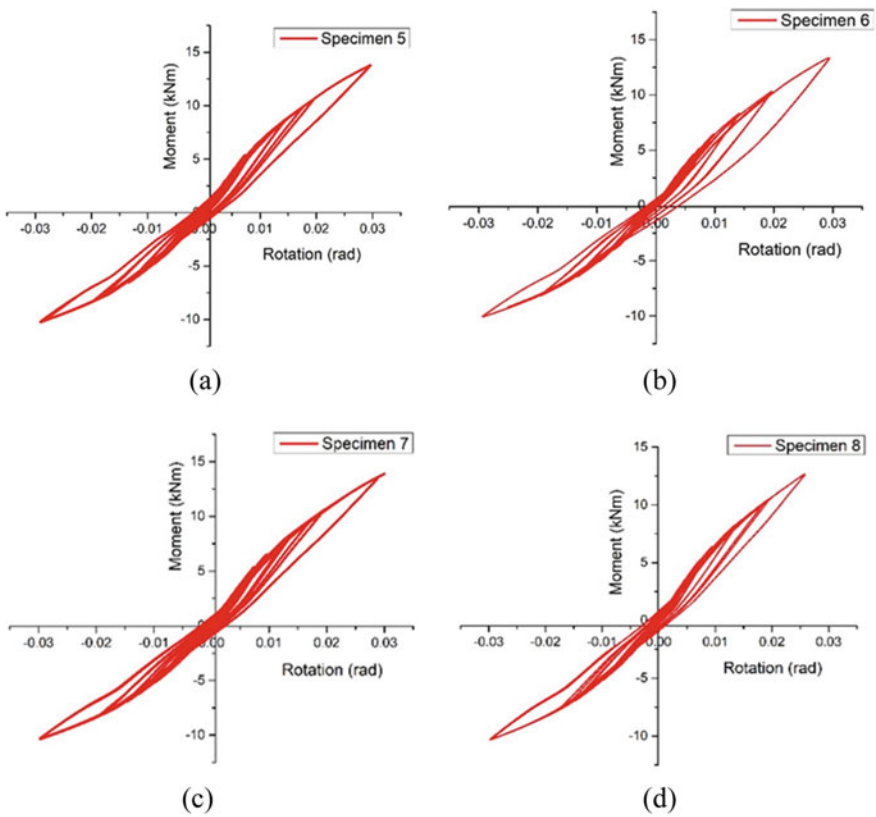


Fig. 7 Hysteresis curve of **a** 30 R web opening, **b** 40 R web opening, **c** 50 R web opening, **d** 60 R web opening

4.3 Failure Modes

Failure modes under static and cyclic load is shown in Figs. 8 and 9, respectively. Upon observing failure mode of beam-column end plate connection with cellular beam, subjected to static loading, it was found that the increase of web opening size leads to shifting of stress concentration from web to flange of beam section. All specimens exhibited bolt failure with yielding of flange which is Mode 2 failure as per Eurocode 3. The separation of end plate has not occurred due to adequate tension zone resistance. With cyclic load analysis (Fig. 9), all specimen components were found to be affected, column web in tension, column web in compression, column web in shear, bolt tension and end plate local buckling.

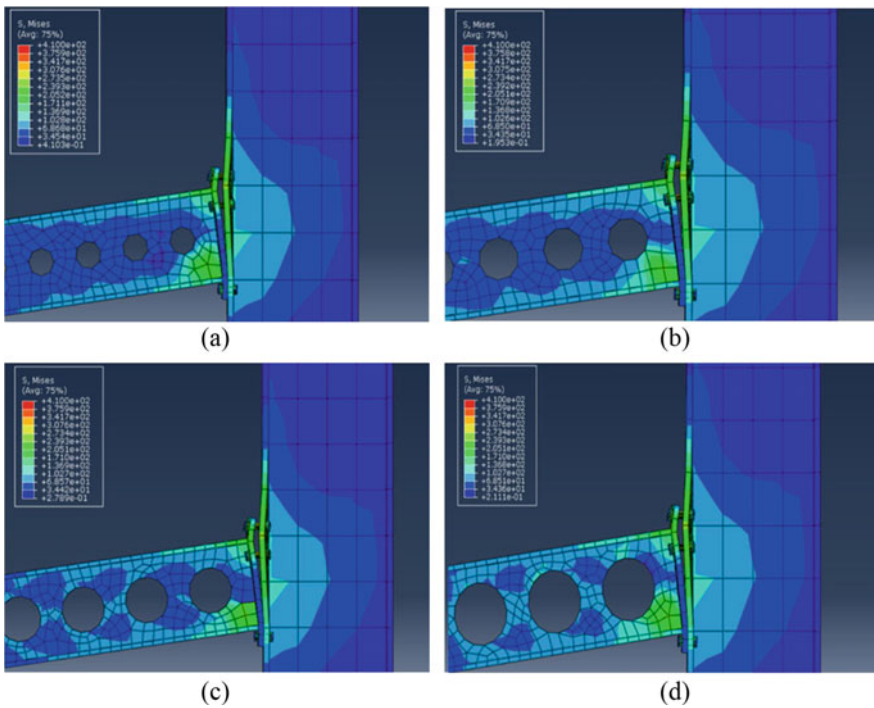


Fig. 8 Failure mode under static load of **a** 30 R web opening, **b** 40 R web opening, **c** 50 R web opening, **d** 60 R web opening

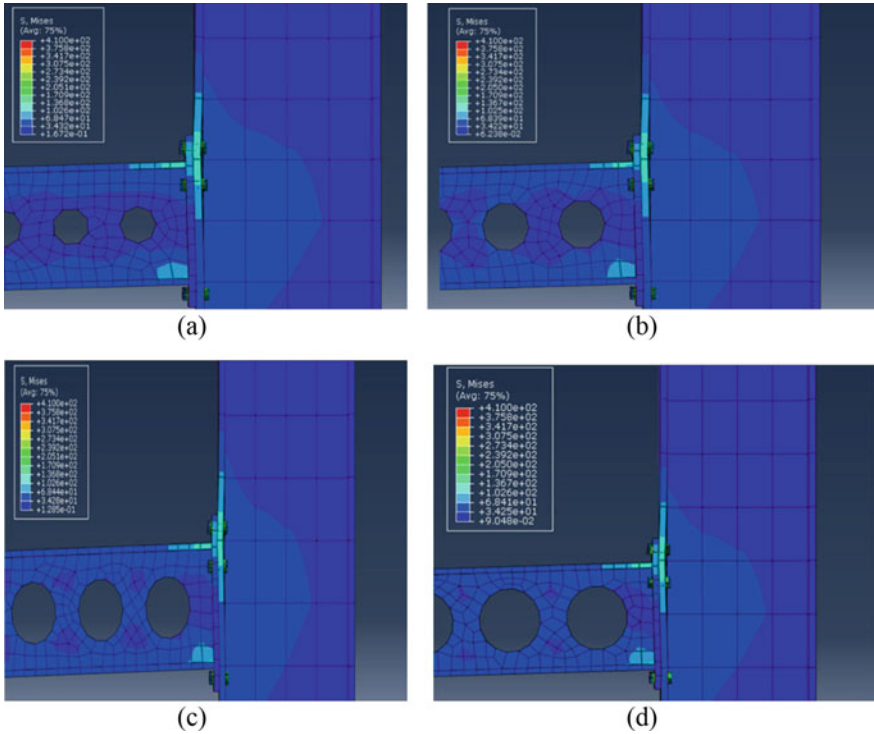


Fig. 9 Failure mode under cyclic load of **a** 30 R web opening, **b** 40 R web opening, **c** 50 R web opening, **d** 60 R web opening

5 Conclusions

From the finite element analysis of end plate connection with cellular beam, influence of the radius of web opening has been investigated and the following conclusions are arrived,

- (i) Upon observing failure mode of beam-column end plate connection with cellular beam, subjected to static loading, it was found that the increase of web opening size leads to shifting of stress concentration from web to flange of beam section. The separation of end plate was not happened in the tension zone because of adequate number of (four) bolts placed in the tension zone.
- (ii) Large inelastic deformation was observed in moment-rotation curve in static load analysis. There was no significant influence in the moment capacity or connection stiffness was observed, when increasing the web opening radius from 40 to 60 mm, whereas 2.8% increase in moment capacity was observed for 30 to 60 mm increase in radius. And rotation capacity has been increased by 42%.

- (iii) With the results of cyclic load analysis, it was found that the ultimate moment capacity has been increased by upto 2.97%, comparing the performance of all beam-column end plate connection specimens.
- (iv) It is suggested that, for ISMB 200 beam profile the radius of web opening is restricted to 50 mm. When increasing the radius of web opening beyond 50 mm, the moment capacity started decreasing.

References

1. Alostaz YM, Schneider SP (1996) Analytical behavior of connections to concrete-filled steel tubes. *J Constr Steel Res* 40(2):95–127
2. Bertero VV, Anderson JC, Krawinkler H (1994) Performance of steel building structure during the Northridge earthquake. Report No. UCB/EERC-94/09
3. Boushehri K, Tsavdaridis KD, Cai G (2019) Seismic behaviour of RWS moment connections to deep columns with European sections. *J Constr Steel Res* 161:416–435
4. ElSawaf SA, Hassan MM (2018) Behaviour of structural sub-assemblies of steel beams with openings in fire conditions. *J Constr Steel Res* 148:627–638
5. ElSabbagh A, Sharaf T, Nagy S, ElGhandour M (2019) Behavior of extended end-plate bolted connections subjected to monotonic and cyclic loads. *Eng Struct* 190:142–159
6. FEMA-350 (2000) Recommended seismic design criteria for new steel moment-frame buildings. Federal Emergency Management Agency, SAC Joint Venture
7. Popov EP, Yang TS, Chang SP (1998) Design of steel MRF connections before and after 1994 Northridge earthquake. *Eng Struct* 20(12):1030–1038
8. Pachpor PD, Mittal ND, Gupta LM, Deshpande NV (2011) Finite element analysis and comparison of castellated and cellular beam. *Adv Mater Res* 264:694–699
9. Ricles JM, Peng SW, Lu LW (2004) Seismic behavior of composite concrete filled steel tube column-wide flange beam moment connections. *J Struct Eng* 130(2):223–232
10. Wu LY, Chung LL, Tsai SF, Shen TJ, Huang GL (2005) Seismic behavior of bolted beam-to-column connections for concrete filled steel tube. *J Constr Steel Res* 61(10):1387–1410

Numerical Study of a Novel Self-lock Connection for Modular Tall Buildings



Huu-Tai Thai

Abstract Compared with conventional onsite construction, modular construction provides significant benefits such as faster and safer manufacturing, better quality control, and less environmental impact due to allowing up to 95% of a building to be prefabricated in a controlled factory environment. These benefits can be maximised in high-rise buildings due to the increased number of repeated modules. However, most of the success stories of adopting modular construction are limited to low-rise buildings due to a lack of a joining technique which can ensure lateral resistance, structural integrity, overall stability, and robustness of the whole modular building. This paper presents a numerical study of a novel joining technique which not only enables easy and quick installation, but also provides adequate strength and stiffness for use in modular tall buildings. A detailed finite element (FE) model is developed in ABAQUS to simulate the complex behaviour and failure mode of the connector. It is also verified with available experimental results. A parametric study is then performed to examine the effects of a wide range of geometric and material parameters on the behaviour of the connector.

Keywords Modular building · Inter-module connection · Finite element modelling · ABAQUS

1 Introduction

Modular construction can allow up to 95% of a building to be prefabricated in a controlled factory environment before transporting to a construction site for installation. Therefore, it can save construction time by 50%, cut cost by 20% (equivalent to 22 billion dollars globally), and reduce onsite construction waste up to 90% compared to traditional onsite construction [16]. Modular construction also offers

H.-T. Thai (✉)

Department of Infrastructure Engineering, The University of Melbourne, Parkville, VIC 3010, Australia

e-mail: tai.thai@unimelb.edu.au

sustainability benefits in terms of material efficiency, reduced waste, and improved working conditions [11]. These benefits can be maximised in high-rise buildings due to the increased number of repeated modules. Therefore, modular construction is believed to shape the future of the construction industry and can tackle the housing shortages on a large scale [24].

There has been a growing trend in the use of modular construction in UK, Singapore, Australia, and USA, where labour costs and affordable housing crisis are of significant concern [16]. However, most of the success stories of adopting modular construction are limited to low-rise buildings as shown in Fig. 1. It is worth of noting that less than 1% of high-rise modular buildings were constructed recently using the panelised method (60-storey Collins House in Melbourne as shown in Fig. 2a) or volumetric method (40-storey Clement Canopy tower in Singapore as shown in Fig. 2b) with wet joining techniques for inter-module connections which require site labour for laying of rebars and site grouting, and consequently, reduce the speed and efficiency of modular construction [14]. A critical review of recent advancements in modular construction technologies conducted by Ferdous et al. [9] confirmed that one of the current challenges that hinder the widespread adoption of modular construction is the lack of a reliable joining technique that can ensure the integrity, stability, and robustness of the whole building.

An increased number of joining techniques have been recently developed for inter-module connections of modular buildings [12]. These connections can be classified into three different types: (i) inter-module connection using tie rod with shear block [1], steel box [20], and shear key [13]; (ii) inter-module connection using connector, e.g. Vectorbloc [7], self-lock [5], and rotary [4]; and (iii) inter-module connection using bolt with plug-in devices [2] and cover plates [6]. The tie rod connection has limited moment resistance and stiffness, and thus, it is not suitable for high-rise buildings. Bolted connection can provide more strength and stiffness suitable for high-rise buildings, but it is only suitable for connecting steel modules. The connector is the most simple and easy installation technique, but its application is limited to low-rise and mid-rise buildings. Hence, it is crucial to develop a stronger connector technique for high-rise buildings.



Fig. 1 Typical applications of modular construction in Australia, UK, Singapore, and USA

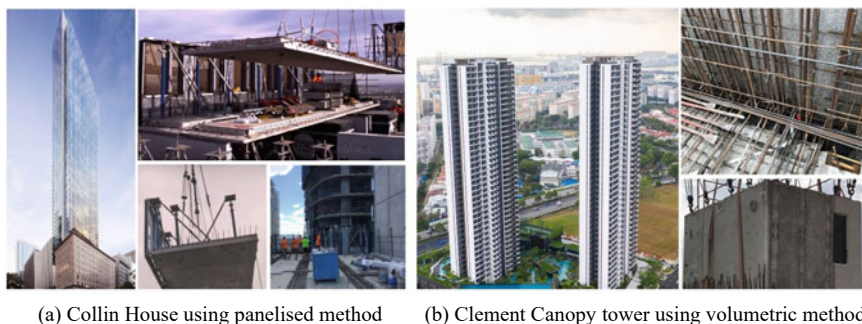


Fig. 2 Typical high-rise modular buildings using wet joint

This paper presents a numerical study of a novel self-lock connector recently tested by Dai et al. [5]. A detailed FE model was developed using ABAQUS/Explicit to simulate the behaviour of the tested specimen. In order to accurately simulate the failure mode of the tested connector due to stud necking, ductile damage models in ABAQUS were used to account for element removal. The accuracy of this model was verified with the experimental result reported by Dai et al. [5]. Finally, a parametric study was performed to explore the effects of geometric and material parameters on the behaviour of the connector and to confirm the applicability of this joining technique to high-rise modular buildings.

2 Inter-module Connections of Modular Buildings

The connections between modular units in modular buildings as shown in Fig. 3 play a very important role because they ensure the structural integrity, overall stability, and robustness of the whole building. Although welded connection can provide rigid stiffness between adjacent modules, it is not preferred onsite due to requiring highly skilled labour, working space, and time-consuming inspection after welding [14]. Therefore, a large number of joining techniques have recently been developed an alternative solution to onsite welding. These connections have their own advantages and disadvantages, and they can be classified into three different types: (a) inter-module connection using tie rod, (b) inter-module connection using bolt, and (c) inter-module connection using connector. A review of bolting techniques can be found in [12, 17].

Tie rod joining techniques: In this connection, a vertical rebar as shown in Fig. 4 is used to provide the vertical tying between lower and upper modules, whilst the shear force between adjacent modules is resisted by means of shear keys. The advantage of this connection is that it can be done outside the modules and thus will not cause any potential damages to internal finishes [14]. In addition, this joining technique can be used for columns with both hollow bare steel sections and composite sections.

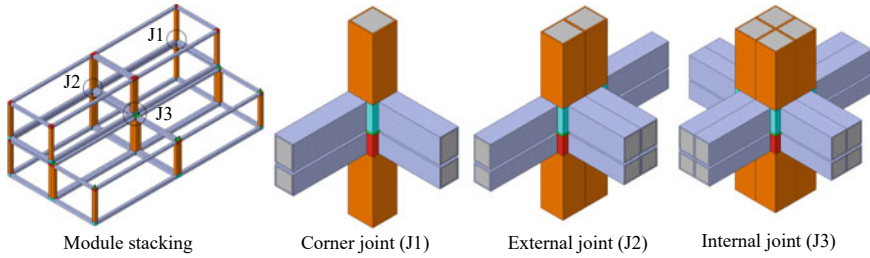


Fig. 3 Typical inter-module joints of modular buildings

However, it has low moment resistance and thus is not suitable for high-rise buildings. Different versions of this technique were proposed by Sanches et al. [20] using a steel box instead of a shear key and recently by Lacey et al. [13].

Bolting joining techniques: Instead of using a rebar as in the tie rod method, this technique uses a bolt to vertically connect the upper and lower modules as shown in Fig. 5. Different versions of this technique have been developed using different methods for shear connections between adjacent modules such as a plug-in device (Fig. 5a), a gusset plate (Fig. 5b), and extended endplates (Fig. 5c). The seismic performance of this technique was experimentally tested, and the results indicated that this joining technique can provide satisfactory connection ductility, but its strength and stiffness are still limited for mid-rise buildings [2, 3].

Connector joining techniques: In this technique, all beams and columns will be offsite welded to a connector at eight corners of the module as Fig. 6. Therefore, the onsite installation of this technique is quite simple and flexible compared with bolting and tie rod methods. Other advantages of this method are of its flexibility and robustness because it is applicable to various cross-sectional areas of steel and

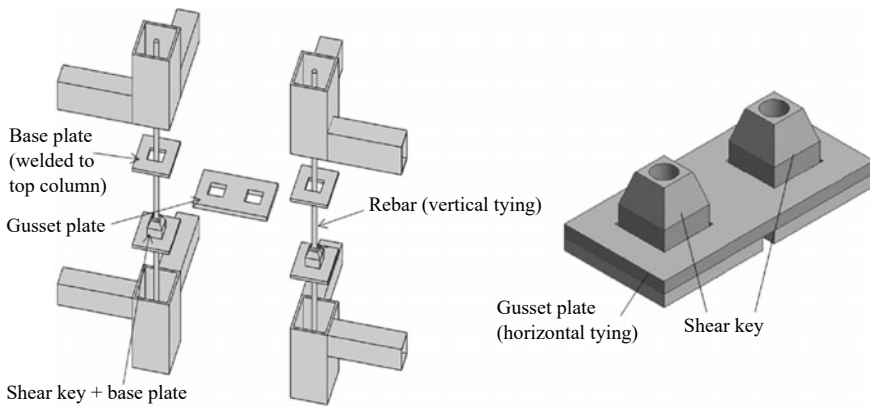


Fig. 4 Tie rod connection with shear keys and gusset plate [14]

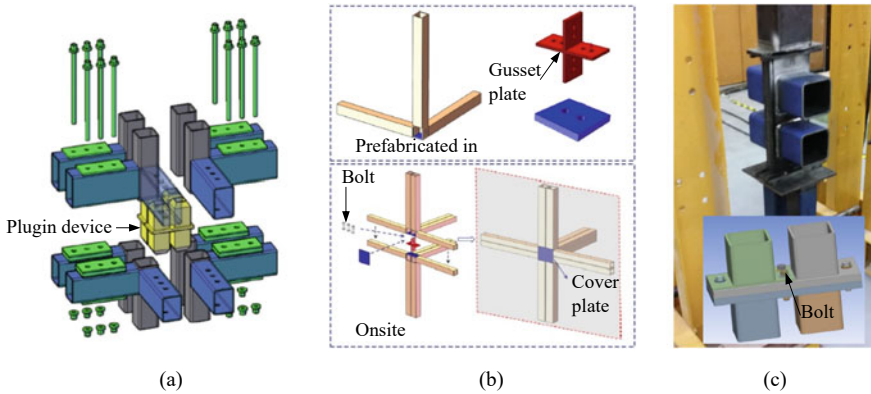


Fig. 5 Bolted connection with **a** plug-in device [2]; **b** welded cover plate [6]; and **c** extended endplate [10]

composite modules, as well as different joint configurations. Various versions of the connectors have been developed such as Vectorbloc (Fig. 6a), rotary (Fig. 6b), bracket (Fig. 6c), and self-lock. The connector will ensure the vertical connection between the lower and upper modules, whilst the horizontal connection between adjacent modules can be achieved by means of a gusset plate (Vectorbloc, self-lock) or bolt (in bracket).

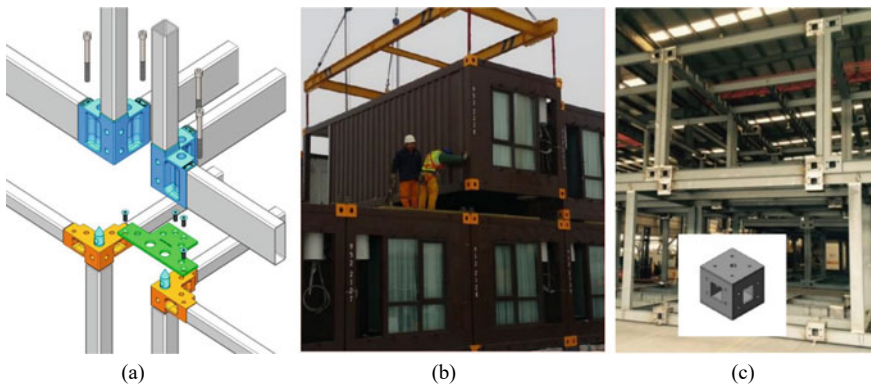


Fig. 6 Connector connection using **a** Vectorbloc [7], **b** rotary [4], and **c** bracket [8]

3 Novel Self-lock Connectors for Modular Tall Buildings

This novel self-lock joining technique was recently developed and experimentally tested by Dai et al. [5]. In this technique, the vertical connection between lower and upper modules is provided by means of a stud, which is screwed between the top plate of the top joint box of the lower module (the red box in Fig. 7) and the connector inside the bottom joint box of the upper module (the cyan box in Fig. 7). The horizontal connection between adjacent modules is secured by a gusset plate. An assemble hole will be cut on the bottom plate of the bottom joint box of the upper module. During onsite erection, the upper module will be lifted above the lower module. It will then align with the lower module via the assemble hole and the stud which is fixed to the top plate of the top joint box of the lower module. After inserting the gusset plate into the stud, the top module is laid down, so the stud is plugged into the connector.

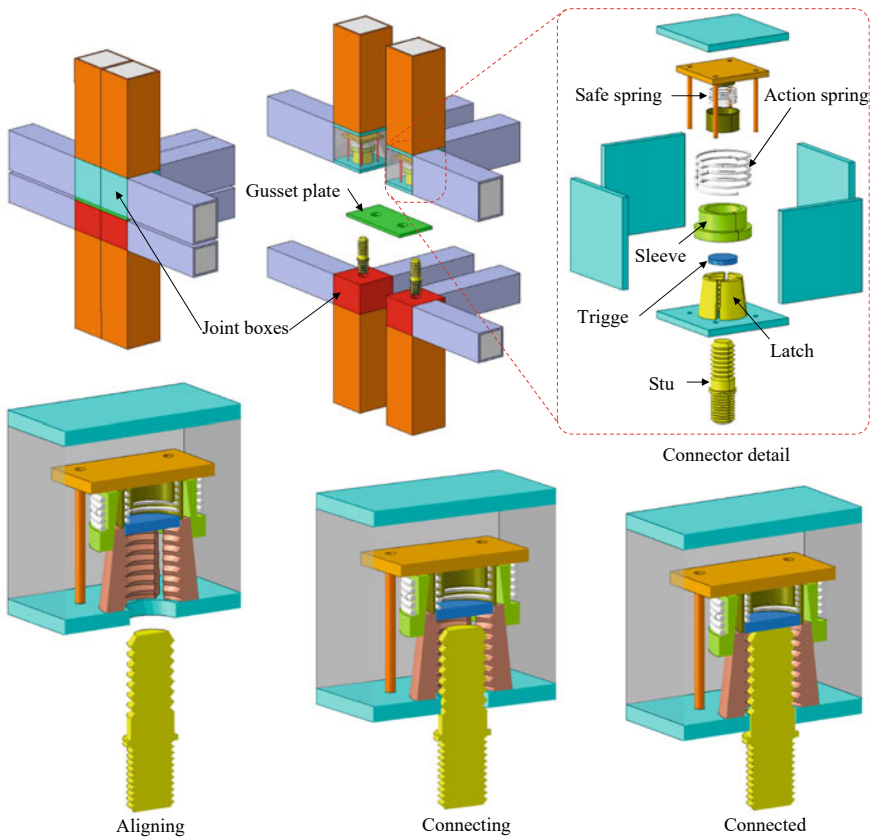


Fig. 7 Self-lock joining technique for inter-module connections of modular buildings

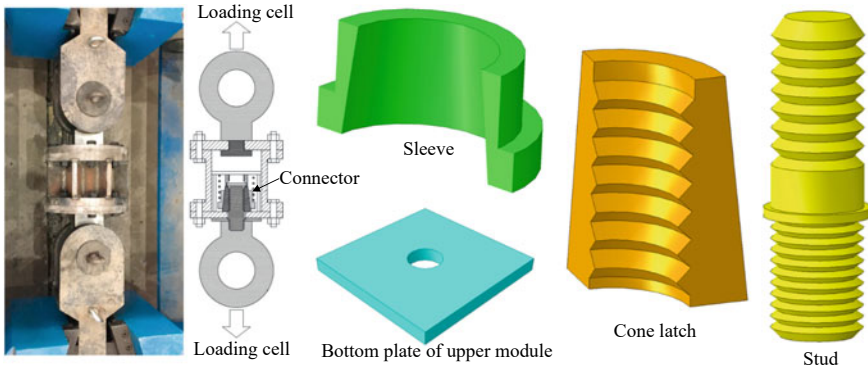


Fig. 8 Connector specimen under pull-out test (geometric details can be found in [5])

The innovation of this technique is a plug-in connector which enables self-lock mechanism via an action spring when the top surface of the stud is in contact with the trigger plate as shown in Fig. 7. This joining technique enables faster and easier onsite installation since all beams and columns of modules are welded to a joint box offsite (see Fig. 7). This technique can also apply to a wide range of joint configurations via different gusset plates and different types of cross-sections of modular units (with joint boxes).

4 Finite Element Modelling

The tensile capacity of the connector was tested by Dai et al. [5] under pull-out loading from two loading cells (one fixed on the stud, the other fixed on the flange barrel) as shown in Fig. 8. The diameter of the stud is 50 mm with the weakest section at the ring-teeth being 40 mm. In the test, the connector was placed inside a flange barrel. However, for simplicity, only parts of the specimen (i.e. cone latch, sleeve, stud, and bottom plate) were modelled in the simulation. ABAQUS/Explicit was employed to overcome the convergence problems which are usually encountered in ABAQUS/Implicit analysis due to large deformations and multiple contact interactions between joint components [23].

5 Modelling Technique

All components of the simplified connector (sleeve, latch, stud, bottom plate) were modelled with brick elements (C3D8R). Mesh convergence study was also conducted to obtain the final mesh as shown in Fig. 9 including 26,738 nodes and 20,464 C3D8R

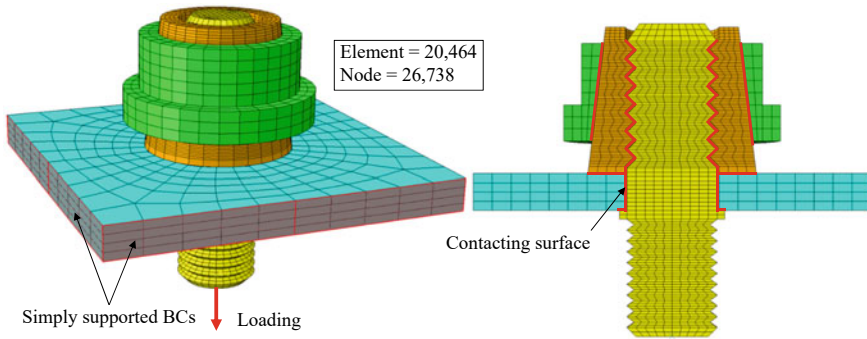


Fig. 9 Finite element mesh and constraint conditions

elements. Simply supported boundary conditions (BCs) were applied to the end face of the bottom plate as shown in Fig. 9, whilst the pull-out loading was applied to a reference point located at the centre of the end section of the stud, which was tied to the bottom part of the stud via rigid body constraints [22]. The general contact option was used to model the interaction between contacting surfaces as shown in Fig. 9. More details about defining contact and loading can be found in [21, 23].

6 Material Model

In order to simulate necking in the stud, ductile damage models in ABAQUS (see Fig. 10a) were used to account for failure modes and element removal [19]. The damage initiation and the damage evolution criteria were determined from [25]. Since the stress–strain relationships of steel and stud are not available in the tested specimen by Dai et al. [5], they are obtained in this study (see Fig. 10b) by calibrating the predictions with the experimental results. It should be noted that Fig. 10b plots the true stress and true plastic strain which can directly input into ABAQUS material models.

7 Verification

The accuracy of the developed FE model was verified with experimental test carried out by Dai et al. [5] as shown in Fig. 11. A very excellent agreement of the load–displacement behaviour of the connector as shown in Fig. 11a indicated that the developed model can accurately predict the complete response of the connector including the initial stiffness, ultimate load-carrying capacity, and ductility. As shown in Fig. 11b, von Mises stress and plastic strain are concentrated in the body of the stud near the bottom plate (the first ring-teeth) at the ultimate state and thus resulting

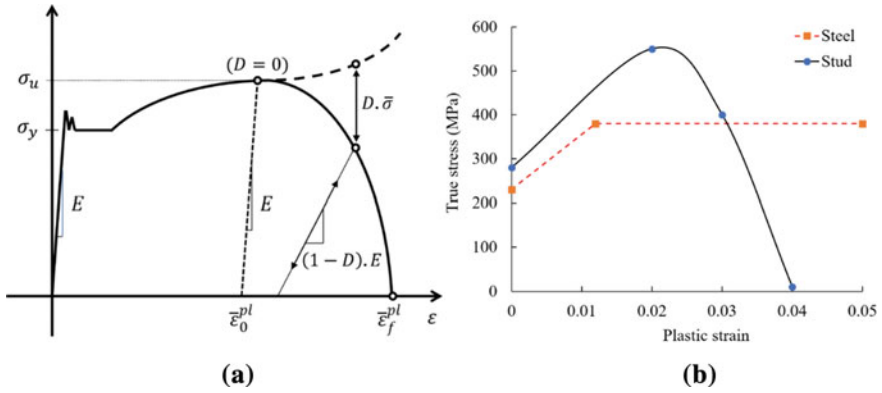


Fig. 10 a Ductile damage model in ABAQUS; b calibrated true stress–plastic strain

necking failure of the stud as shown in Fig. 11c. The FE model also predicts very well the failure mode of the connector due to stud necking as demonstrated Fig. 11c. The maximum elastic load and the ultimate load-carrying capacity of the connector are approximately of 350 kN and 690 kN, respectively, which are almost equal to the yielding and ultimate capacities of the stud (the product of the weakest cross-sectional area of stud ($\phi 40$) and the yield stress of 280 MPa and ultimate stress of 550 MPa). This means that the tensile strength of the connector is mainly dependent on the material and geometric properties of the stud.

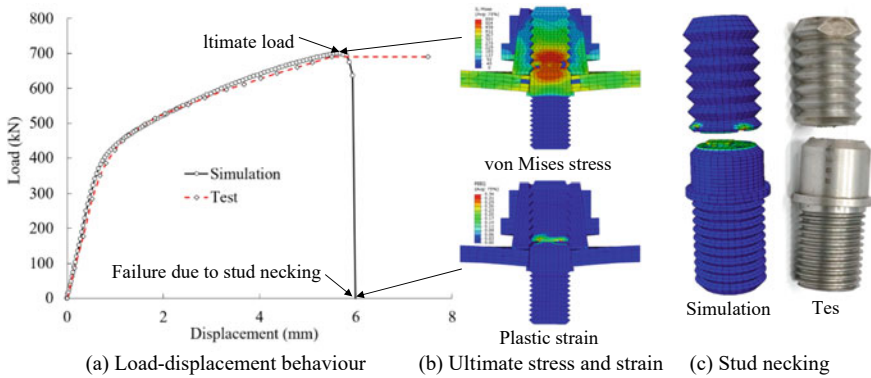


Fig. 11 Comparison between test and simulation

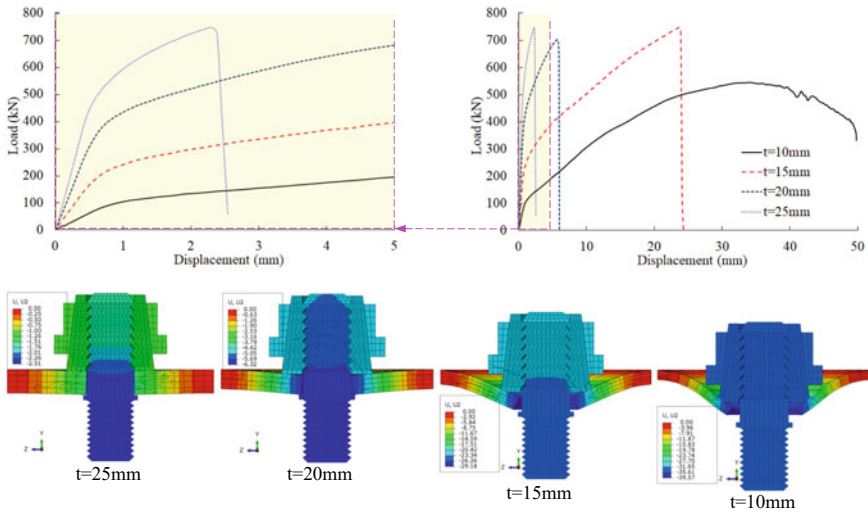


Fig. 12 Load–deflection curves and vertically deformed shapes

8 Parametric Study

8.1 Effect of the Plate Thickness of the Joint Box

Figure 12 shows the effect of the thickness of the bottom plate to the load–deflection behaviour and the failure mode of the connector. Four different cases of thickness of 10, 15, 20, and 25 mm were considered. The case of thickness equal to 20 mm is corresponding to the test specimen. A plate under a concentrated load is acting at the plate centre. In the design, the bending failure mode is not expected as it has low load-carrying capacity. Therefore, the thickness of the joint box should be determined to ensure the necking failure mode of the connector.

8.2 Effect of Stud Material

In order to explore the effect of material properties of the stud on the load-carrying capacity of the connector, the bottom plate is assumed to behave elastically to ensure necking failure of the stud. Three types of commonly used high-strength bolts Grades 8.8, 10.9, and 12.9 are used for the stud materials. The stress–strain behaviours of these high-strength bolts are taken from the coupon tests conducted by Pang et al. [18] as shown in Fig. 13a. The key parameters of these stress–strain curves including elastic modulus, yield stress, ultimate stress, yield strain, ultimate strain, and fracture strain corresponding necking are summarised in Table 1.

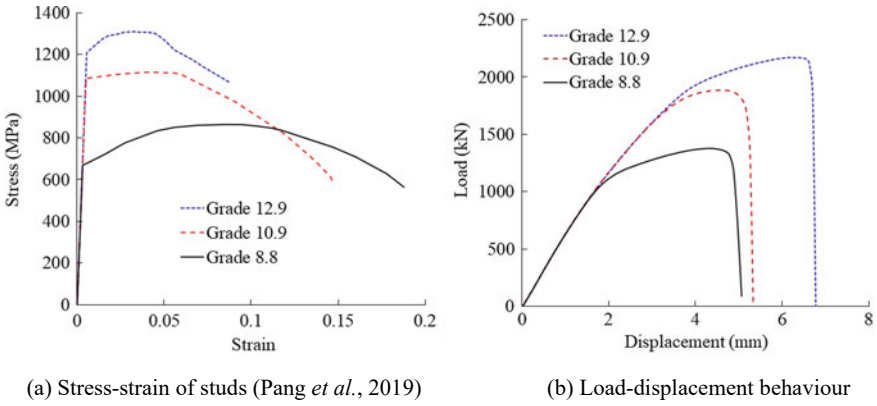


Fig. 13 Effect of material properties of stud

Table 1 Material properties of studs referred from [18]

Property	Grade 8.8	Grade 10.9	Grade 12.9
Elastic modulus (GPa)	212	214	211
Yield stress (MPa)	668	1085	1210
Ultimate stress (MPa)	865	1114	1310
Yield strain	0.00315	0.00507	0.00573
Ultimate strain	0.08235	0.04455	0.03250
Fracture strain	0.1879	0.1472	0.087

Figure 13b shows the comparison of the load–deflection behaviours of three bold grades. It can be seen that the ultimate load-carrying capacity of the connector is proportional with the ultimate stress of the stud. This is expected since all connectors are failed by stud necking. In addition, all cases have the same initial stiffness as expected since they have the same geometric data and similar elastic modulus. With a standard stud of 50 mm diameter having the weakest diameter of 40 mm, a high-strength stud Grade 8.8 can provide a tensile strength up to 1377 kN as shown in Fig. 13b which is adequate for a building well over 50 storeys.

9 Conclusions

A numerical model has been developed in this paper to investigate the behaviour of a novel self-lock connector for possible use in inter-module connections of high-rise modular buildings. The developed FE model can accurately capture the load–deflection response of the connector in terms of initial stiffness, ultimate load-carrying capacity, and ductility. By using ductile damage model available in ABAQUS, the present model is capable of accurately simulating the failure mode due to stud

necking. This novel joining technique not only offers a quick and easy installation process by means of a self-lock connector, but also provides adequate tensile strength for tall buildings well over 50 storeys as demonstrated in the parametric study. In addition, this type of joining technique can be applied to both steel and composite modules with hollow and composite sections thank to the use of a joint box. It is also applicable to all inter-module joint configurations by means of a gusset plate with different shapes. This is a promising joining technique that can revolutionise the modular construction industry. Further study is carrying out to develop design equations and design models (on the basis of the component method recommended in Eurocode 3) for estimating the strength and stiffness of the connector because they are necessary for advanced analysis and design of the whole modular building, as well as for the progressive collapse analysis to investigate the structural robustness of the whole modular building [15].

References

1. Chen Z, Li H, Chen A, Yu Y, Wang H (2017) Research on pretensioned modular frame test and simulations. *Eng Struct* 151:774–787
2. Chen Z, Liu J, Yu Y (2017) Experimental study on interior connections in modular steel buildings. *Eng Struct* 147:625–638
3. Chen Z, Liu J, Yu Y, Zhou C, Yan R (2017) Experimental study of an innovative modular steel building connection. *J Constr Steel Res* 139:69–82
4. Chen Z, Liu Y, Zhong X, Liu J (2019) Rotational stiffness of inter-module connection in mid-rise modular steel buildings. *Eng Struct* 196:109273
5. Dai X-M, Zong L, Ding Y, Li Z-X (2019) Experimental study on seismic behavior of a novel plug-in self-lock joint for modular steel construction. *Eng Struct* 181:143–164
6. Deng E-F, Zong L, Ding Y, Dai X-M, Lou N, Chen Y (2018) Monotonic and cyclic response of bolted connections with welded cover plate for modular steel construction. *Eng Struct* 167:407–419
7. Dhanapal J, Ghaednia H, Das S, Velocci J (2019) Structural performance of state-of-the-art VectorBloc modular connector under axial loads. *Eng Struct* 183:496–509
8. Doh J-H, Ho NM, Miller D, Peters T, Carlson D, Lai P (2016) Steel bracket connection on modular buildings. *J Steel Struct Constr* 2(2):121–127
9. Ferdous W, Bai Y, Ngo TD, Manalo A, Mendis P (2019) New advancements, challenges and opportunities of multi-storey modular buildings—a state-of-the-art review. *Eng Struct* 183:883–893
10. Gunawardena T (2016) Behaviour of prefabricated modular buildings subjected to lateral loads. PhD thesis, Department of Infrastructure Engineering, The University of Melbourne
11. Hough MJ, Lawson RM (2019) Design and construction of high-rise modular buildings based on recent projects. *Proc Inst Civil Eng—Civil Eng* 172(6):37–44
12. Lacey AW, Chen W, Hao H, Bi K (2019) Review of bolted inter-module connections in modular steel buildings. *J Build Eng* 23:207–219
13. Lacey AW, Chen W, Hao H, Bi K, Tallwin FJ (2019) Shear behaviour of post-tensioned inter-module connection for modular steel buildings. *J Constr Steel Res* 162:105707
14. Liew JYR, Chua YS, Dai Z (2019) Steel concrete composite systems for modular construction of high-rise buildings. *Structures* 21:135–149
15. Luo FJ, Bai Y, Hou J, Huang Y (2019) Progressive collapse analysis and structural robustness of steel-framed modular buildings. *Eng Fail Anal* 104:643–656

16. McKinsey (2019) Modular construction: from projects to products. Available from <https://www.mckinsey.com/industries/capital-projects-and-infrastructure/our-insights/modular-construction-from-projects-to-products>
17. Pang SD, Liew JYR, Dai Z, Wang Y (2016) Prefabricated prefinished volumetric construction joining techniques review. In: Proceedings of the modular and offsite construction (MOC) summit, pp 249–256
18. Pang X-P, Hu Y, Tang S-L, Xiang Z, Wu G, Xu T, Wang X-Q (2019) Physical properties of high-strength bolt materials at elevated temperatures. *Results Phys* 13:102156
19. Pavlovic M, Marković Z, Veljković M, Buđevac D (2013) Bolted shear connectors vs. headed studs behaviour in push-out tests. *J Constr Steel Res* 88:134–149
20. Sanches R, Mercan O, Roberts B (2018) Experimental investigations of vertical post-tensioned connection for modular steel structures. *Eng Struct* 175:776–789
21. Thai HT, Uy B (2015) Finite element modelling of blind bolted composite joints. *J Constr Steel Res* 112:339–353
22. Thai HT, Uy B, Khan M, Tao Z, Mashiri F (2014) Numerical modelling of concrete-filled steel box columns incorporating high strength materials. *J Constr Steel Res* 102:256–265
23. Thai HT, Vo TP, Nguyen TK, Pham CH (2017) Explicit simulation of bolted endplate composite beam-to-CFST column connections. *Thin-Walled Struct* 119:749–759
24. Thomson J (2019) Modular construction: a solution to affordable housing challenges. *Cornell Real Estate Rev* 17(21):90–97
25. Wang J, Uy B, Thai HT, Li D (2018) Behaviour and design of demountable beam-to-column composite bolted joints with extended end-plates. *J Constr Steel Res* 144:221–235

Sustainability by Reverse Joints in Steel Structures (Demountable Modular Shear Connection)



Shashidhar S. Shilavantar, Savai Suthar, B. Chaitanya, A. Chiranth, and R. Ravindra

Abstract Mankind is facing significant burden due to production of large quantities of construction and demolition waste. Therefore, new approaches in design and construction need to be found to increase recycling and reuse rates—use of reusable joints will contribute to an integral approach in construction. This paper focuses on reuse of steel joints which promotes the reduction in carbon emissions. It gives an overview of the advantages of the joint and challenges and provides recommendations. It also gives examples of successful applications with an overview of possible environmental savings and introduction of a new joint with its technical aspects as well as its merits and demerits over conventional joints. Experiments are performed to assess the structural characteristics and ultimate capacity of the connection. Physical and chemical tests are conducted on the reused steel and further analysis of channel sections is done using STAADPRO and the simulation of the whole assembly is done through Ansys to assess its behavior. FEM analysis is conducted on the connection joint to know the stress concentration and deformation in the joint. The connection shows maximum deformation of 31 mm at 400 kN load on the beam and maximum shear stress of 1778.9 Mpa at load applied much part of the connection shows shear stress of 290 Mpa. It is clear that for 400 kN load at beam end forming 160 kN-m moment, the vertical plates in the joint are deformed. Moreover, the plates in the center joint plate's contribution to the load transfer mechanism is higher than the beam plates and equivalent strain in the connection. It is found that through proper design and detailing the reused joint will behave as per the design. Study also carried out to investigate the parameters that influence the stiffness, strength and rotation

S. S. Shilavantar · S. Suthar · B. Chaitanya (✉) · A. Chiranth · R. Ravindra
Department of Civil Engineering, RVCE, Bengaluru, India
e-mail: chaitanyab.cv16@rvce.edu.in

S. S. Shilavantar
e-mail: shashidharss.cv16@rvce.edu.in

S. Suthar
e-mail: sawaihsuthar.cv16@rvce.edu.in

A. Chiranth
e-mail: chiranthanandsp.cv@rvce.edu.in

capacity of modular block shear connection. The joint is also validated for reusability through various parameters like elastic behavior, damages and traceability. It can be concluded that the material is totally fit for reuse based on the results obtained from chemical test and tensile test which satisfies the IS codes. Staadpro analysis and FEM analysis gives us the load carrying capacity of the joint and stress concentrations for testing purposes.

Keywords Reverse joint · Sustainable development · CO₂ emission · Modular shear connector · Fem analysis

1 Introduction

Energy is the utmost requirement for mankind—our primary use of materials such as Metals, Ceramic and Polymers helps to live in comfort and gives a way for the future.

Unfortunately, the ever usage of these materials is causing:

- Resource shortage
- Water stress
- Land stress
- Chemicals and toxic byproducts
- Climate change
- The list has been growing and causing severe damage to the Earth.

Every structure built has an age range regardless of how better it is built. Long back engineers introduced the idea of “service life”, where a structure is designed for a certain design period (structurally durable for a given number of years after construction) usually 50 years [1]. But modern building fail to meet the design period due to various demands of owners and the successive renovations in the building. In fact, a study done in USA shows that the lifetime of building to be under 35 years [1].

Complexity is involved in the current building connections therefore it becomes difficult to dismantle the members, only solution is demolition and dumping waste to landfills.

Sustainable development is one that meets the needs of the present generation without compromising the ability of the future generations to meet their own needs.

For any building material there are only three end of life scenarios, among them the most conventional one is the landfill for dumping. The second one is recycling which is always a better solution than dumping and landfill. The third and most innovative and sustainable solution is the reuse of the material which consumes the least energy among all.

Among all the building materials steel is one such material which does not lose any of its material properties when it is recycled, i.e., melted and remolded into

any shape, and also recycling steel is less expensive and consumes only 25% of the energy compared to fabricating steel from scratch (Steel Recycling Institute).

In today's world 87% of the structural steel is recycled and only 2% is sent to landfills and remaining 11% is reused which is the most suitable and sustainable end of life solution to steel, although the recycling process saves a lot of raw material and energy input but still if steel is simply salvaged and reused it will substantially consume the least energy compared to recycling process and the only energy input involved is the transportation of demounted steel to new site [2].

According to the design for deconstruction movement, the steel is manufactured in such a way that a great proportion of steel can be reused from one building to another, the design concept ensures that most of the steel elements can be reused besides recycling through proper design of joints [3].

The use of steel to emphasize scale and impact is as follows [all US figures]:

- Construction-BUILDINGS-42%
- Construction-Infrastructure-14%
- Cars and Trucks-9%
- Electrical Equipment-3%
- Mechanical Equipment-13%
- Metal Goods-12%
- Domestic Appliances-3%
- Others-remaining.

2 Literature review

Out of all global manufacturing sectors steel manufacturing contributes to the highest level of CO₂ emission, this is because of a large amount of coal used as a main energy source and a very large volume of steel produced [4]. For the steel industry the average CO₂ emission per ton of steel is 1.9 tons [5–7]. The process of iron making emits 70–80% of CO₂ which makes it to be most emission intensive steel production process, the same involves the reaction of iron ore with reducing agent such as coking coal which emits a large amount of [8, 9]. The intensity of CO₂ for iron and steel production varies from a range of 0.4 tons CO₂ per ton of crude steel for scrap/EAF and 1.7–1.8 tons of CO₂ per ton of crude steel for integrated BF BOF and also up to 2.5 tons of CO₂ per ton of crude steel for DRI (Direct reduced iron) process [4, 10]. The process of iron making emits 70–80% of CO₂ which makes it to be emission intensive steel production process. The reaction of iron ore with reducing agents such as coking coal in iron production produces huge amounts of CO₂ in steel plants. The iron production system consists of several processes—coking plant, sinter plant, iron making, steel making and rolling mills, etc. CO₂ is emitted at various stages of the process which is indirect and negligible but sintering machines, coke oven, blast furnace, converter, rolling mills, shaft kiln and power generation boilers results in direct emission of CO₂ [8, 9, 11].

Mohammed [12] analyzed numerical investigations which was conducted on the stainless-steel beam column joint and also the behavior was simulated using finite element method (FEM) analysis, then the results were verified against full scale tests on the bolted connection. The specimen failed by inelastic deformation of the top angle and clear failure pattern and high accuracy in moment rotation prediction is observed.

The study was conducted on two precast beams to column connections with steel box and peripheral plates. Downscale models of 2/3rd. scales were tested under cyclic load test and hence the results showed that the post beam corner connectors (PBC) had higher load carrying capacity, energy dissipation and ductility compared to industrialized building systems and met all seismic requirements [13].

In conventional moments resisting connections like box columns to beam joints there was difficulty in accessing the inside of the column for developing reliable load paths. Syed **Mirghadri et al.** studied the load transfer mechanism and design methods are proposed to find the dimensions of the through plates.

Cyclic load tests were conducted on two specimens to evaluate the seismic performance and hence the specimen reached at least 0.06 rad total story drift before strength degradation and this obtained value was more than 0.04 rad as specified by American Institute of Steel Construction (AISC) seismic provisions. [14].

Moghadam et al. [15] studied the characteristics of proposed partially restrained (PR) connections of steel moment resisting frames and seismic performance of these structural systems were determined using nonlinear time history analysis. This experiment was done to compare the results of plastic hinge rotation of PR connection with other type connection Fully Restrained (FR) Moment Connection and Pin connection. Results showed that PR connections can reduce the moment rotation which was present in columns and high performances can be achieved.

Erfani et al. [16] conducted an experiment where I-beam was connected to a box column for numerical investigation on cyclic behavior by using the finite element method (FEM). A stub I-beam was connected to the box column and an end plate is connected to the stub beam through shop welding. This experiment was done to compare the numerical results of an end plate connection with experimental data, regarding material properties, element types and contact elements. All specimens tested have undergone 0.05 rad total story drift which satisfies the American Institute of Steel Construction (AISC) seismic requirements.

Rofoeia and YadegariFarzanehb [17] SMA conducted an experiment where (shape memory alloys) bolts were used in moment resisting frame (MRF) structures for improving the seismic behavior of connections. Nonlinear dynamic time history analysis was conducted to determine the efficiency of the steel and SMA-based connections, therefore enhancing the seismic performance of the structural model. This experiment was carried out to reduce the seismic parameters of the structure. A semi-rigid end plate beam column connection was introduced which was based on parallel application of steel. Story drifts and induced forces were reduced from parallel application of steel and SMA bolts. The results obtained showed that application of end plate connection with parallel application of steel and SMA bolts reduces

structural responses with comparison of conventional rigid connections. An increase in refractive index (RI) of steel and mass eccentricity increases the base shear force.

Studies made by University of Cambridge said that ATLSS joints hold the drawback of easy detachability due to shaped cast pieces. QUICON joints allow fast assembly of joints, due to the presence of bolt holes and structural weakness this connection is not suitable for seismic zones. In CONX connections collars exhibit less yielding and redundant beam sections forms flexural hinging [18].

QUICON joints speed up the construction, and have shown some defects in its second project. Which are: Deflection, Twisting of primary beams. CONX joints achieved a total of 7 LEED points. This joint reduced steel mass by 30%, cost by 30% and erection time by 50%. GIRDER CLAMPS connections have a tension capability of 25te which is more than the British standard specification 7.5te [19].

Bogatinoski et al. [20] analyzed rigid and semi-rigid connections of eight types of specimens were analyzed using experimental and theoretical methods. It consists of IPE-profile (European I Beams) connection of four in number and tube sections connection of 4 in number for the beam. The experiment was conducted to find which of the eight types of specimen had ideal beam column connection and high strength and deformation characteristics which means to have higher bending moments with higher rotational capacity at the same time. The experiment consists of characteristic diagrams (force–displacement) and bending moment rotation in the end of the beam. For adding and transferring force axial piston was there, i.e., placed from steel frame. From the experiment conducted we can say that the bending of rigid connection was greater than semi-rigid connection. Semi-rigid connection has higher plastic deformation and higher rotation but have smaller load capacity compared to rigid connection.

Salem et al. [21] designed the equation of end plate thickness and bolts was studied for rigid beam to column connections which are subjected to axial and shear forces with bending and torsional movements. For these connections finite element method was developed and it was composed with experimental results for verification. A parametric connection was carried out to study the various parameters regarding connection behavior. To develop the design charts these experiments were conducted which enables the designers to calculate connection capacity for specific bolt diameter, edge distance and end plate thickness without performing complicated calculations as currently adopted by many Codal practices. From experiment conducted we can conclude that end plate connections undergo biaxial bending because of plate deformation. The analysis showed that American Institute of Steel Construction (AISC) design guide 16(no) overestimates the connection capacity for bolt rupture and underestimates plate failure connections.

Hawxwell and Tsavdaridis [22] conducted an experiment where eccentric end plate (EEP) beam to beam connection was studied for its rotational behavior with a series of rotational behavior experiments, then compared it with fin plate (FP) connection and partial-depth end plate (PDEP) connection. A testing rig was made on 3 types of connections and each test was repeated thrice to confirm the performance therefore 9 specimens were fabricated to study. The connections were test 1 (eccentric and plate connection), test 2 (fin plate connection) and test 3 (partial-depth end plate

connection). Nine beam to beam connection of 3 types was tested experimentally to give comparison and classify them against design specification. The conclusions were 1. EEP connection was semi-rigid with higher stiffness and strength than FP and PDEP connection which acts as normally pinned connection. The EEP connection has higher forces and results in more deformation which was obtained on the supporting member with comparison of FP and PDEP connections. Finally, it was recommended to use only reconnection.

Nagao et al. [23] studied the moment connection post-Kobe details which was developed for the prevention of brittle fractures. Investigation was not only carried in the view of structural behavior; it was studied through cost aspects. Brittle fractured around the welding metal was observed. Improvement of these brittle fractures were taken into account by welding procedures, material properties, composite actions with slabs. Based on the result there were two ways by which cost could be reduced namely material cost saving and process cost saving. By categorizing the details in the design document helped for steel fabrication.

Justin and Joy [24]. A research which was done to improve the beam column joint by strengthening the materials and selecting them correctly. Here cross inclined bars were used at the beam column joint, Fiber-Reinforced Plastic (FRP) fibers can also be used. Compression testing machine was used for experimental analysis in which basalt fiber was put on the beam column joint for experimental observations. Finite element model (FEM) analysis was done, from the results cross inclined column bars possess high resistance to deformation and displacement under static and dynamic loadings.

Abishek and Karthikeyan [25]. In a theoretical and experimental analysis which was done on different types of beam to column connections by reduced beam section concept six different models were analyzed using Ansys software and stiffeners were provided to prevent collapse in the structure. This experiment was done to check total deformation. A 3 story frame was developed for which pushover analysis was done using E-TABS. Pushover curve was plotted by observing the building at different stages from hinge formation. From the results obtained we can say that reduced beam section was more effective through welded joint when compared to bolted joint.

Elmasry et al. [26]. Finite element model (FEM) analysis which was done for exterior beam column joints to analyze Reinforced Concrete (RC) frame structures. Many specimens were studied one for un-strengthen case and others for strengthening case with multiple techniques. Carbon Fiber-Reinforced Polymer (CFRP) and Reinforced Polymer (RP) were used to strengthen the beam column joint. Models were prepared and analyzed by adding loads till failure. Stress and deformation were analyzed and compared for each case. The results showed that beam column joint strengthened with CFRP increases structural stiffness, strength and energy dissipation compared to other techniques.

Iannone et al. [27]. Studied the ultimate behavior of bolted beam to column connection by cyclic actions. To prevent yielding the components has to be strengthened by proper design. Component approach was adopted as the design tool. The aim of this experiment was to compare the component approach and cyclic action results regarding beam to column joints. The aim was to evaluate the overall energy

dissipation, based on the results obtained we can conclude that overall energy dissipation can be obtained by adding the energy emitted from single joint components. The results obtained were confined to Euro code 3.

Anju Das and Johny [28]. Analysis on a beam column joint was done under seismic loading with bolts and end plates. The work was carried in the location where joints have flush plate and end plate with different thickness and seismic loading. Diameters of bolts were varied and further study was carried on optimum thickness of plates. The software used was Ansys workbench. The parameters studied are total deformation, maximum stress and maximum strain by the Ansys software. Based on the results obtained it is clear that initial stiffness of joint was sensitive to the thickness of end plate and diameter of bolts.

Yang and Tan [29]. In an investigation on failure mode and ductility of composite beam column joints. Connections regarding flush end plate composite web cleat and flush end plate were studied. There were two types of tests conducted they are as follows: 1) Middle joint under sagging moment and 2) Side joints under hogging moment. Testing was done on five composite beam column joints. Flush end plate and composite web cleat connections were studied. Based on the results obtained we can conclude that ductility and load resistance were demonstrated in catenary action mode. Strengthen web cleat has higher load carrying capacity compared to normal web cleat connection. Composite slabs increase load carrying capacities at beam column joints. Pure tensile forces after undergoing large rotations was sustained by beam column joints.

3 Methodology

See Fig. 1.

3.1 Introduction

In introduction we have discussed about usage of materials, service life of building and reuse of steel.

3.2 Literature

Literature survey has been done on existing and innovative steel beam column connections and the results are studied. Through literature survey we came to know the literature gaps and for some of the problem statements observed in the literature we were able to come up with a new beam column joint which overcomes some of the problems in member connection and deconstruction.

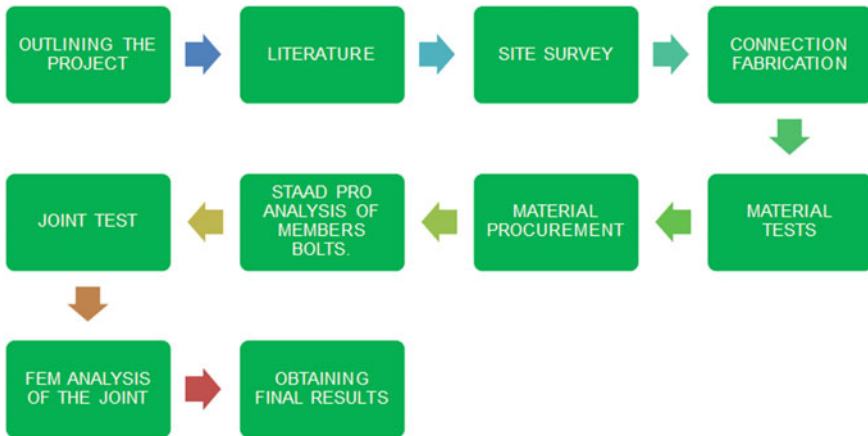


Fig. 1 Brief methodology

3.3 *Site Survey*

We have investigated 3 sites to observe the existing steel connections and to check the no of reusable and innovative joints used in the project and also to check whether any of the existing connection can be made reusable and the details of the observations made are described below in the paper and hence the idea of innovative Modular Shear connector came through.

3.4 *Material Procurement*

The material sheet has been procured from one of the existing sites based on the visual inspection to avoid corroded steel, dent free steel (i.e., steel which is in good state of condition for reuse) and the same has been used to fabricate Modular Shear connector and a sample of which was given for the chemical analysis test and tensile test.

3.5 *Material Tests*

A sample of material from which we have fabricated joint was given for chemical analysis test to know the composition of various constituents of steel and the tensile test to check whether the procured material lies in elastic limit and the results of the same have been mentioned in the paper.

3.6 Joint Fabrication

Modular Shear connector has been fabricated from used steel plates of thickness 10 mm and it is of size 225×225 mm and 2 perpendicular steel plates of dimension 222×100 mm has been provided based on the designer's suggestion to avoid buckling of plates.

3.7 Staadpro Analysis and FEM Analysis

Staadpro analysis and Fem analysis was done to find out the load capacity of the joint and stress concentrations of the joint for testing purposes.

4 Sankey Diagrams

Sankey diagrams show the flow of the quantities in proportions with respect to one another. The width of each band shows the flow of their magnitude. The below Sankey diagram shows the global carbon emissions in steel production and use, we can also depict arboreal depiction of the steel industry also.

Global energy inputs of steel:

Blast furnace: 16 EJ

Basic oxygen furnace: 0.2 EJ Direct reduction: 0.7 EJ Continuous casting: 0.4 EJ

Electric arc furnace:

2.7 EJ Coating: 0.6 EJ Rolling: 3.6 EJ

Forming: 0.2 EJ Shape casting: 2.1 EJ Fabrication: 6–11 EJ Overall Steel: 38 EJ (Fig. 2).

5 Existing Reusable Connections

5.1 Shear Block Connector: Use of BSCs

- Beam-beam connection
- Minor-axis H/I

BSC is a type of reverse joint which can be easily demounted and reused in another building. Standardization of length of structural elements like beams, rafters, cross beams can be easily done (Figs. 3 and 4).

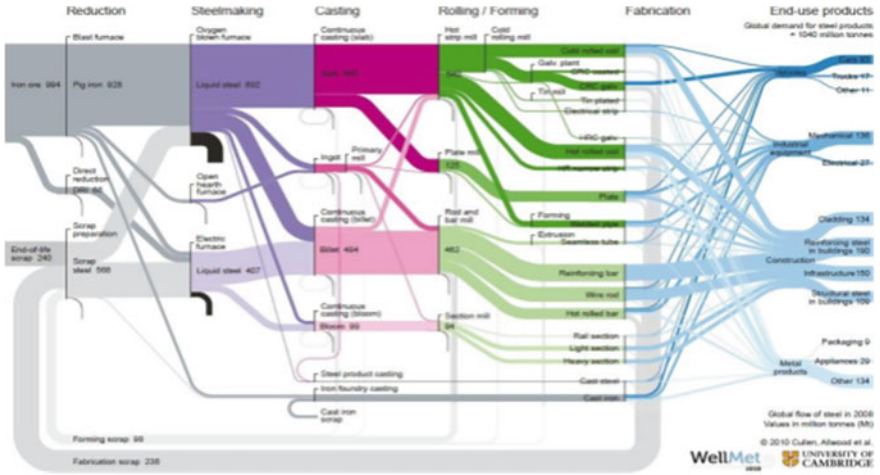


Fig. 2 Sankey diagram (global flow of steel in 2008 values in million tons)

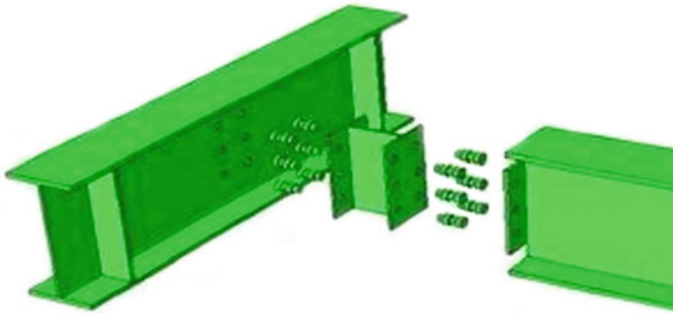


Fig. 3 Shear block connector

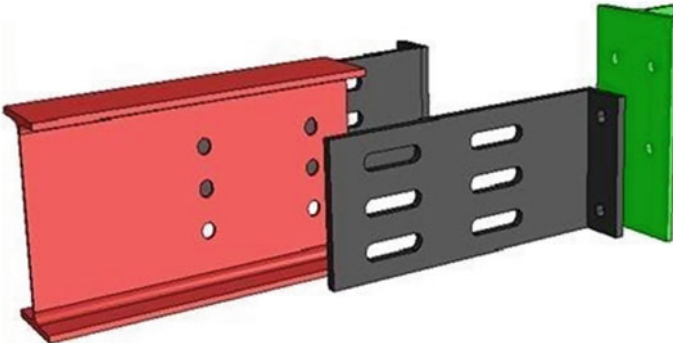


Fig. 4 Adjustable slotted hole connection

Advantages of BSCs:

- Eliminate coping cost
- Easy and economic fabrication
- Replaceable (Reuse of beams)
- Standardization (Length of beams)

5.2 Adjustable Slotted Hole Connection

ASHC is a type of reverse joint which can be reused again in a different building as it has a margin of safety because of the hole being slotted.

5.3 Quicon System

It is a steel frame connection. Quicon connection system was first used to construct a mezzanine floor in (2002). With this connection 50% construction procedure is reduced. It consists of T-piece (slotted) which is welded to beam or column inside factory (Figs. 5 and 6).



Fig. 5 Quicon system

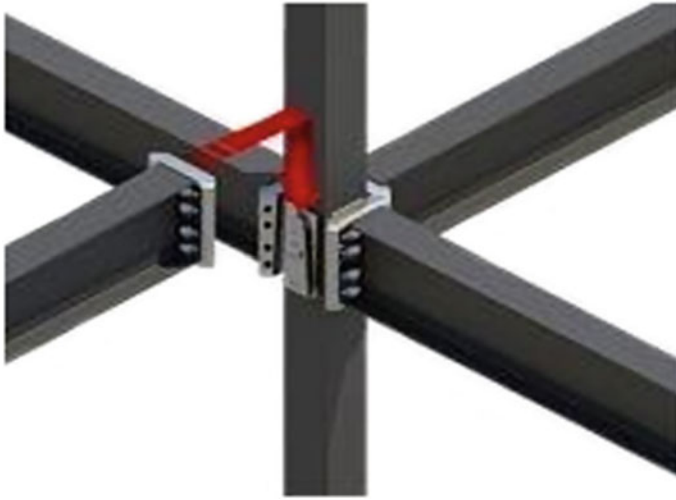


Fig. 6 ConX connection

5.4 ConX connection

ConX connection: ConX is bolted moment framed connection developed by ConX-tech space frame systems or seismic and structural integrity. It is shop welded, field bolted and self-guided collar system. ConXtech has developed 2 framing systems: 1. ConX-r 2. ConX-L [19].

5.5 Possible Uses of Reverse Joints

- Temporary modular construction (during floods).
- Permanent modular construction (habitation for flood, earthquake affected area).
- Precast concrete buildings.
- Sustainable and net energy buildings for office and commercial sites.

5.6 Examples of Use of Reverse Joints in International Market

- London Olympic stadium.
- University of Taranto.
- Park wood residence, Oshawa.
- Roy stabs elementary school.

6 Problem Statement

- Mismatch of supply and demand-both in terms in quality and quantity.
- Insufficient time allowed for deconstruction and careful packing of reusable items.
- Lack of facilities locally.
- Reluctance to use products without certification of tested performance.
- Health and safety risks of manual deconstruction are considered to be a key reason for the mechanical demolition techniques.
- Building technology is a mixture of traditional and rapidly changing techniques.
- Value of products and materials can be an opportunity or a barrier.

OPPOURTUNITY: Significant oppourtunities exist in the field of sustainable steel construction and to overcome the above problems itself is the biggest opportunity and hence there is huge scope for Reusable and Demountable connections (REVERSE JOINTS) in India because no company or research have tapped in to this.

7 Aims and Objectives

- Reduction of the carbon emissions by reusing the steel through a reverse joint approach instead of melting it and the nursing.
- Representation of CO₂ emissions through Sankey diagram and carbon footprints.
- Ease of demount ability and the reusability of steel components.
- Making of models of simple and moment connection using reverse joints and comparing the same with the existing connections (Rivet, weld, Bolted) from the strength, durability and reusability perspective.
- Compare new steel vs. reused steel for strength and durability
- Developing a marketing plan, business model and Revenue model to bring this innovative product in the current Indian market as a disruptive technology and convert our project into startup venture.

8 Site Investigation

Few site visits were done to look at the existing connection types. The sort of connections at helped us to think of a new type of joint which permits the connection of members in three axis and also can be used as a multipurpose joint (Figs. 7, 8 and 9).



Fig. 7 Pokarna site

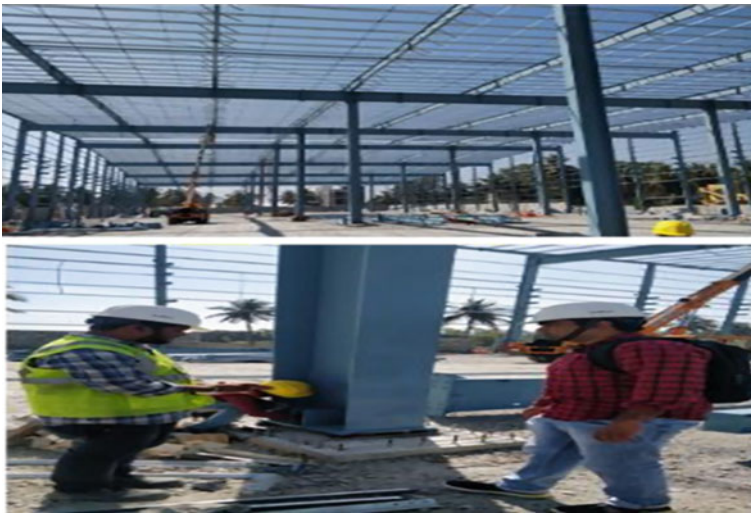


Fig. 8 Janamuki site

Observed connection at sites (Figs. 10, 11, 12 and 13):

- a. Purpose of the building:
 - Bial site (cargo and office)
 - Janamuki (croma warehouse)
 - Pokarna (stone factory)
- b. All are pre-engineered buildings where the buildings are engineered at a factory and assembled at site.



Fig. 9 Bial site



Fig. 10 Main beam to column connection



Fig. 11 Column to beam connection

Fig. 12 Multiple connection joint





Fig. 13 Beam column connection

Design Methodology:

- Method Used: Stiffness Matrix Method
- Standard Code used:
 - AISC
 - ASCE
 - IS: 800
- Software used: Staad.Pro v8i, ETABS, RAM Steel
- Load Considerations and their Calculations: Loads considered in the PEB design are same as for general building structure. These are as follows:
 - *Dead load Calculations:* It includes Self Wt. of Purlins, Roof and Wall Sheeting, insulation material and other structural component.
 - *Live/Imposed Load Calculations:* It should be Considered as per given in IS 875 (Part 2) for diff. type of Loads.
 - *Wind Load Calculations:* Consider the Basic Wind Speed as per Area of that particular structure. Design wind Pressure is calculated as per IS 875 (Part 3).
Wind Load on Roof can be UDL and calculation for this can be done as per IS875(Part 3)
 - *Seismic Load Calculations:* Earthquake Loads affect the design of structure in areas of great seismic activity. The seismic load can be calculated as per IS 1893-2002 (Part 1).
 - *Other Moving Loads:* It can be Moving EOT Crane load or Mono Rail etc.

It includes rigid joint like column to rafters, column to base, bolted connections, built up members, etc.

c. Observation of the joints:

We observed few joints like fly joints, adjustable slotted hole connection, column to base joint, column to rafters joint, rafters to purlins joint, standing seam clip, wall grit fixing. These joints were located at the base, roof top, near walls, etc. we found that adjustable slotted hole connection and rafter to purlin joints are reusable joints.

d. Safety-Induction [who gave you the induction]

Safety induction was given by site engineer santosh (janamuki site), subhasish site engineer (bial site) and site engineer Rajshaker reddy for pokarna site.

Minimum Safety requirement at worksite

- Workers should have the knowledge about the hazards on the construction site.
- Protective equipment must be used while working on the site like jackets, helmets, shoes.
- Personal protective equipment must be checked before use.
- Employees and workers must be checked if they are physically fit.
- Strong supervisor is necessary.

9 Experimental Program: Modular Shear Joint (Our Innovation)

Modular means the dimensions are standardized and shear means the angle of deflection when subjected to load is always 90 degrees, therefore it is classified as a rigid joint.

This type of joint can be used for temporary modular construction like labor camps, storages, temporary housing for people in flooded areas, etc. The joint is made up of used steel and then the tests will be performed to check for reusability. Dimensionality: 10 mm thick plate 230×230 mm plates 10 mm fillet weld is given.

For considered beam/column members ISMC 125 welded face to face, and bolt values 8 bolts of 18 mm diameter which requires 34 mm edge distance and 81 mm pitch, the plates of 230×230 mm holds perfect assembling of the beam column members and bolt holes. If size of the plates are reduced for same dimensions of beam column members and bolt values, the bolt holes and beam column members merge/overlap each other which makes it impossible to assemble the members. Instead the dimensions lesser than 230 mm can be used to assemble the members through welding the beam column members to the Modular Shear joint which does not satisfy the main objective (reusability) of the project.

Advantages of ISFG 12.9 s grade 18 mm diameter bolt are:

- a. Easy demount ability and reusability within the life cycle of steel.
- b. Significant cost reduction up to 50% can be achieved.
- c. Promotes sustainable development.
- d. Triaxial joint, up to five members can be connected (multi connection joint).

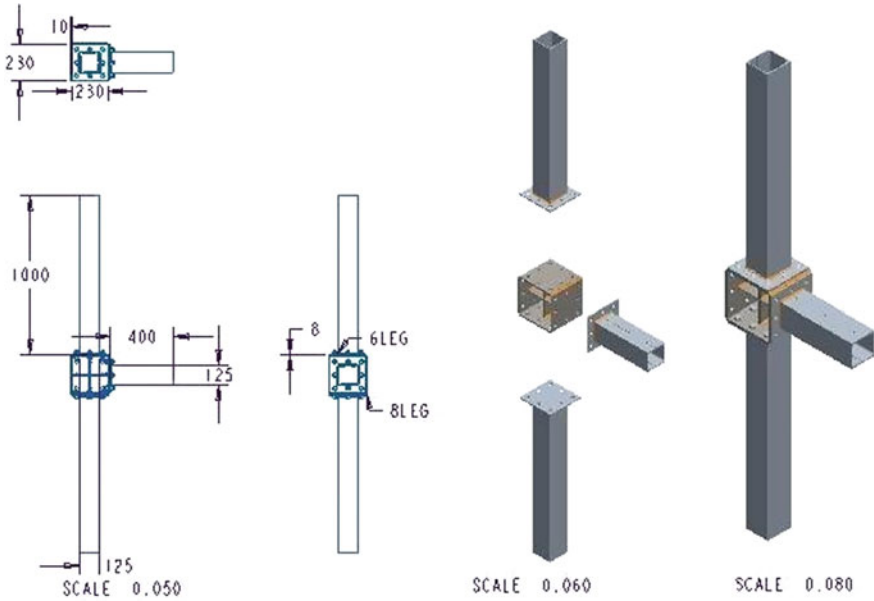


Fig. 14 Modular shear joint assembly

- e. Significant carbon reduction because it's reusable.
- f. Green building concept.

Figures 14 and 15 are the dimensions and assembling of the beam column connection and bolts used in the finite element module analysis. The scales of the assembly is 0.080 and the bolt, nut scale is 1.5 (Figs. 14, 15, 16, 17 and 18).

9.1 Design Strength of the Joint

Calculation of the compressive strength of the joint: Dimensions: (230*230*10) mm.

$$\text{Compressive strength } p * d = A_c * F_{cd}$$

where

A = effective sectional area as defined in 7.3.2, and

F_{cd} = design compressive stress, obtained as per 7.1.2.1, from IS 800-2007.

$$\text{Slenderness ratio}(\lambda) = K * l/r = 0.67 * 230/vI/A$$

where

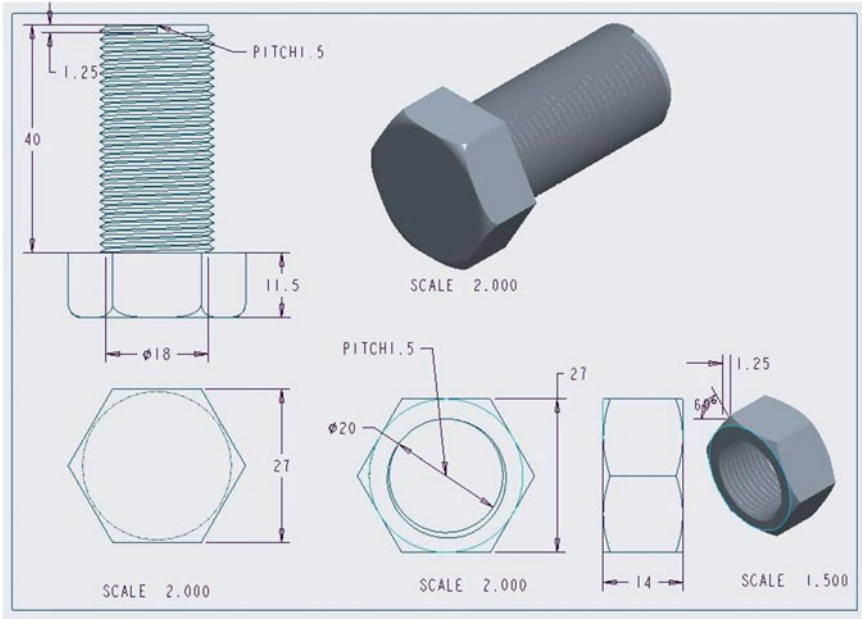


Fig. 15 Bolt dimensions used in the analysis



Fig. 16 Modular shear joint



Fig. 17 Modular shear joint

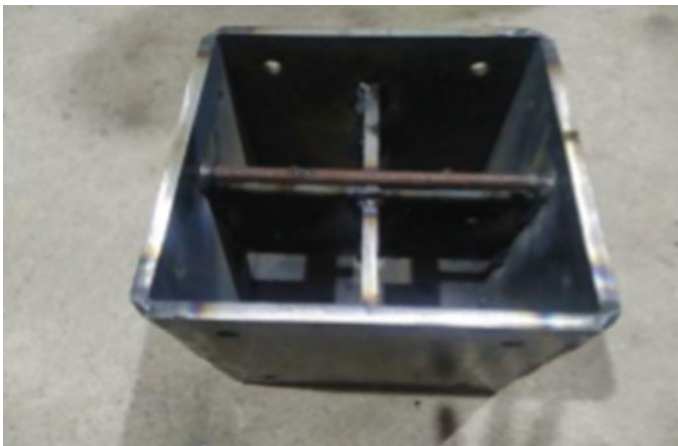


Fig. 18 Modular shear joint

$K * l/r$ = effective slenderness ratio or ratio of effective length, KL to appropriate radius of gyration, E

Moment of inertia (I) = 18,750 mm², Area of the plate (A) = 2300 mm²

$$\text{Slenderness ratio } (\lambda) = 52.22$$

The plate comes under buckling class c from Table 9c IS-800 $F_{cd} = 179.67 \text{ N/mm}^2$ $P * d = 40.22 \text{ tons}$.

Load carrying capacity of joint = $3 * 40.22 = 121.2 \text{ tons} = 1212.78 \text{ kN}$.

9.1.1 Bolt Value Calculations

Calculation of bolt value and number of bolts required for connection:

$$\begin{aligned} \text{Bolt diameter} &= 18\text{mm.} & \text{HSFG grade 12.9s.} \\ \text{Hole diameter} &= 20\text{mm} & \text{Edge distance } (e) = 34\text{mm.} \\ \text{Pitch } (P) &= 81\text{mm.} \end{aligned}$$

Design for friction type bolting in which slip is required to be limited, a bolt subjected only to a factored design shear force, V_{sf} the interface of connections at which slip cannot be tolerated, shall satisfy the following:

$$V_{sf} < V_{dsf}.$$

where

$$V_{dsf} = V_{nsf}/\gamma_{mf}$$

V_{nsf} = nominal shear capacity of a bolt as governed by slip for friction type connection, calculated as follows:

$$\text{Shear strength} = \mu_f * n_e * k_h * F_o.$$

where

μ_f = coefficient of friction (slip factor) as specified in Table 20 IS 800-2007. ($\mu_f = 0.55$),

n_e = number of effective interfaces offering frictional resistance to slip, $K_h = 1.0$ for fasteners in clearance holes,

= 0.85 for fasteners in oversized and short slotted holes and for fasteners in long slotted holes loaded perpendicular to the slot,

= 0.7 for fasteners in long slotted holes loaded parallel to the slot,

Factor of safety = 1.10 (if slip resistance is designed at service load),

= 1.25 (if slip resistance is designed at ultimate load),

F_o = minimum bolt tension (proof load) at installation and may be taken as $A_{nb} * f_o$.

A_{nb} = net area of the bolt at threads, and f_o = proof stress (= 0.70 u_b).

$$\text{Shear strength } (V_{saf}) = 0.55 * 1 * 1 * 0.7 * 198.5 * 1220.$$

$$V_{saf} = 93.22\text{kN}.$$

$$\text{Bearing strength} = 2.5 * k_b * d * t * f_u e / 3d_o = 34/3(20) = 0.56.$$

$$P/3d_o - 0.25 = 81/3(20) * 0.25 = 1.11.$$

$$V_{dpb} = 2.5 * 0.056 * 18 * 8 * 410 V_{dpb} = 104\text{kN Bolt strength} = 93.22\text{kN}.$$

Moment = 160KN for 0.4 on beam (according to test floor dimensions).

Number of bolts (n) = sqrt (6 M/2V_d*P) = sqrt(6*160*10⁶/2*93.22*10³*81).

Number of bolts (n) = 8.

9.2 Test Results

(This test result was taken from Raghavendra Spectro metallurgical laboratory)

9.2.1 Chemical Analysis Test

The standard test method for analysis of carbon and low alloy steel (ASTM E415) is performed with optical emissions spectrometer (BAIRD-DV6) which gave us the composition of various constituents present in steel and are tabulated in the below given report. All the constituents (C, SI, Mn, P, S and CE) meet up the specifications of IS 2062-2011 and are within the maximum limits.

Sample dimensions : 40 × 350 × 10mm

9.2.2 Tensile Test

Tensile test is performed on the steel specimen as per the method of test mentioned in IS 1608-2018 at room temperature and the Yield Stress, Tensile Strength and % Elongation along with the Load (KN) vs. Cross Head Travel (CHT) graph is specified in the below report (Tables 1 and 2).

From the above test reports, it can be concluded that the material is in elastic limit and hence can be reused.

Table 1 Chemical composition

Content	Percent (%)	Specifications (IS 2062-2011 E250 Gr BR/BO)
C	0.131	0.22 MAXX
Si	0.141	0.40 MAXX
Mn	0.784	1.50 MAXX
P	0.021	0.045 MAXX
S	0.017	0.045 MAXX
CE	0.261	0.41 MAXX

Table 2 Output data

Elongation at Yield:	9.270 mm
Load at Yield	35.598 KN
Yield Stress	284.784 N/mm ²
Load at peak	56.256 KN
Elongation at peak	23.670 mm
Tensile Strength	450.048 N/mm ²
Load at Break	43.602 KN
% Elongation	33.88%

9.3 *Staadpro Analysis*

Staadpro analysis is done to determine the suitable member which can be connected to the joint to ensure that the member does not fail while carrying out the experimental program. It also gives the nodal displacements and the rotation of the joint on varying load applications. The members which have been analyzed based on the trial and error method in the Staadpro are confined to the availability in the Indian market. Based on the outputs of the analysis 2-ISM 125 are used in connection analysis as a suitable member for beam connected face to face and 2-ISM 125 as suitable member for columns connected face to face. The deformations in the beam column is shown in below tables. Maximum deformation in the beam at the point of load application is 21.044 mm and shear force of 400kN. Table 3 shows the nodal displacement of the connection after load application. Tables 4 and 5 gives maximum beam relative displacements and member end forces in the connection. Figure 22 is the connection of beam column channel sections used in the Staadpro analysis. Here top and bottom portion of columns are fixed and load is applied on the beam to know the deformations in the connection. In the Fig. 19 bottom part of the below column is Node 1, center connection is Node 2, top part of above column is Node 3 and beam end is the Node 4 (Figs. 20 and 21).

Table 3 Node displacement of the connection

Node	L/C	X (mm)	Y (mm)	Z (mm)	Resultant (mm)	rX(rad)	rY(rad)	rZ (rad)
1	1: Load case	0.000	0.000	0.000	0.000	0.000	0.000	0.000
2	1: Load case	0.000	-0.318	0.000	0.318	0.000	0.000	-0.000
3	1: Load case	0.000	0.000	0.000	0.000	0.000	0.000	0.000
4	1: Load case	0.000	-21.044	0.000	21.044	0.000	0.000	0.046

9.4 Fem Analysis of Connection

Finite Element Module analysis is conducted on the connection joint to know the stress concentration and deformation in the joint. In finite element module analysis upper and lower face will be restrained so that it is easy to know the behavior of the vertical plates on loads coming on it. 8 HSFG grade 12.9 s Bolts of 18 mm diameter are used to connect beam/column to joint.

The connection shows maximum deformation of 31 mm (Fig. 21) at 400 kN load on the beam and maximum shear stress of 1778.9 Mpa (Fig. 20) is applied at load and overall part of the connection shows shear stress of 290 Mpa. It is clear that for 400 kN load at beam end forming 160 kN-m moment, the vertical plates in the joint are deformed. Moreover, the plates in the center joint plate's contribution to the load transfer mechanism is higher than the beam plates. Equivalent strain in the connection is shown in (Fig. 22) and equivalent stress in the connection is 4.98e9 Pascal. Here only one beam is connected and simulated, and assumed that the other beams connected to the joint behave similarly to the analyzed beam.

In Fig. 20 shear stress analysis results of beam column connection the maximum shear stress at 400 kN load is 1778.9 Mpa and minimum value is -1569.2 Mpa. It is shown that the maximum and minimum values of shear stress are on the beam end which is the point of load application (Fig. 23).

Figure 21 is the total deformation of the beam under 400kN load applied at the end of the beam section. Maximum deformation is occurred in the beam at the point of load application and the minimum deformation is at the fixity of both the columns and the center joint plates which do not carry the beam sections. The maximum value of deformation is 31.8 mm at the beam end and minimum value is 0 mm at the column ends (Fig. 24).

Figure 22 is the equivalent elastic strain in the beam column connection analyzed at 400kN load applied at the beam end. Maximum equivalent strain in the connection is 0.029474 m/m experienced at the beam end and the minimum magnitude of equivalent elastic strain is 1.2242e-8 which is shown in column sections and center joint plates without beams (Fig. 25).

When the analysis results of Staadpro and finite element module analysis are compared, and it is found that there is a diminutive difference in the deformation values, i.e., in case of Staad analysis the beam deformed to a value of 21mm and

Table 4 Beam maximum relative displacements

Beam	Node A	Length (m)	L/C	y (mm)	d (m)	z (mm)	d (m)	Resultant (mm)	d (m)	Span Max z
1	1	1.200	1:Load case	2.047	0.800	0.000	0.000	2.047	0.800	586
2	2	1.200	1:Load case	-2.047	0.400	0.000	0.000	2.047	0.400	586
3	2	0.500	1:Load case	2.047	0.208	0.000	0.000	2.179	0.208	299

Table 5 Member end forces structure type = plane-all units are Kn Mete (local)

Member	Load	JT	Axial	Shear-Y	Shear-Z	Torsio <i>N</i>	MOM-Y	MOM-Z
1	1	1	200.38	-118.77	0.00	0.00	0.00	-42.51
		2	-200.04	118.77	0.00	0.00	0.00	-100.0
								1
2	1	2	-200.04	-118.77	0.00	0.00	0.00	-100.0
		3	200.38	118.77	0.00	0.00	0.00	1
								-42.51
3	1	2	0.00	400.07	0.00	0.00	0.00	200.02
		4	0.00	-400.00	0.00	0.00	0.00	0.00



Fig. 19 Modular shear joint

the analyzed connection in FEM shows maximum deformation of 31.8mm in the direction of load applied (Table 6).

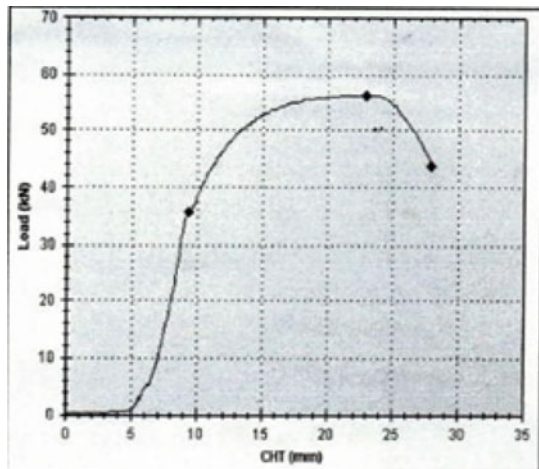
10 Conclusions

In the present work reusable joint has been fabricated and experiments are performed upon it to determine its tensile strength (elastic modulus), chemical composition of various constituents and compressive strength and the results are in the range as specified by IS codes. Materials used to fabricate this joint is used/reclaimed steel procured from one of the projects in Bangalore, the dimensions of the joint are 230 × 230 mm, the thickness of the joint is 10 mm and the dimensions of the inner plates are 230 × 100 mm and nut bolt are of HSFG 12.9 s grade.



Fig. 20 Material test specimen

Fig. 21 Material test specimen graph



From the tensile test performed on the reclaimed steel it can be concluded that the material is completely fit for reuse in accordance with IS 1608-2018 the tensile strength of material is found to be 450.048 N/mm^2 and the yield strength is found to be 284.784 N/mm^2 which are within the elastic limits.

From the chemical composition test of reclaimed steel specimen of size $(40 \times 350 \times 10) \text{ mm}$ when tested under optical emission spectrometer (BAIRD-DV6) it can be concluded that the composition of various constituents (Carbon, Silicon, Manganese,

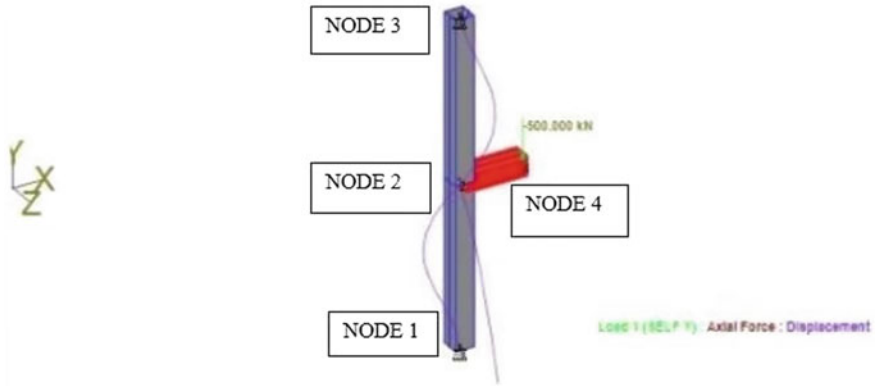


Fig. 22 Staadpro analysis mode

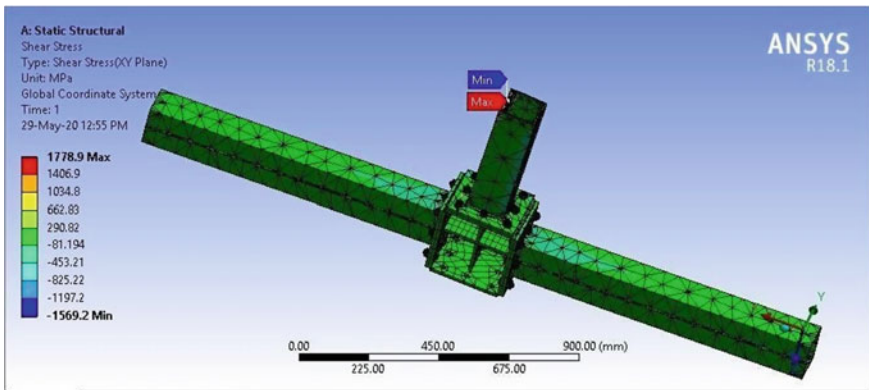


Fig. 23 Shear stress distribution in beam column connection

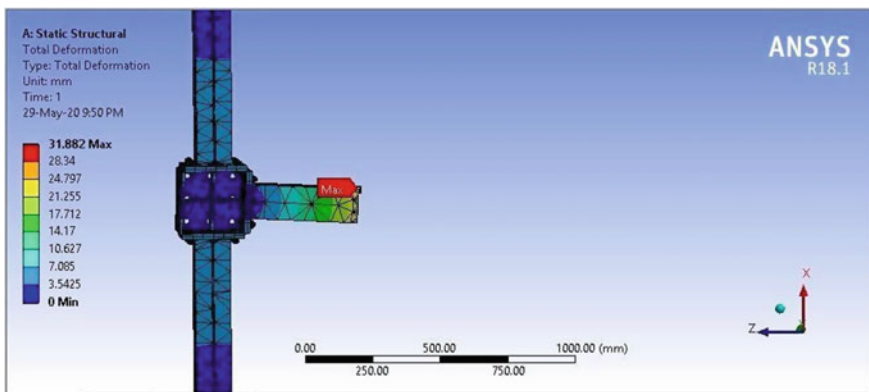


Fig. 24 Total deformation in the connection

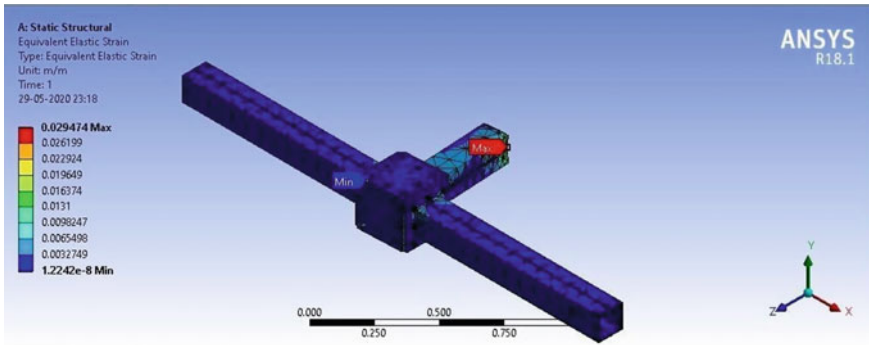


Fig. 25 Equivalent elastic strain in the connection

Table 6 Staadpro and FEM analysis results comparison

Sl. No.	StaadPro	FEM Analysis
1	Deformation:21 mm	Deformation: 31.8 mm
2	Shear force: 118 kN-m	Shear stress: 1776.9 Mpa

Phosphorus, Sulfur, C. E-Equivalent Carbon Content) meet up the specifications of IS 2062-2011 are within the maximum limit.

The joint has also been analyzed using finite element modeling (FEM) to determine stress concentrations, deformations and elastic strain etc., and Staadpro analysis of the joint has also been carried to determine the load carrying capacity of the channel sections (beams and columns) to avoid failure during floor test.

It can be concluded from the experiments that the material is totally fit for reuse because tensile strength of steel is in elastic limit and chemical composition of various constituents are within limits according to IS codes. The angle of deflection when subjected to load is always 90 degrees, therefore it is classified as a rigid joint.

10.1 Scope for Future Work

The project can further be extended to in-depth technical analysis of the Modular Shear Joint:

- a. Experimental test like the tensile test, compressive test for varying load ranges can be carried out to understand the behavior of the joint, failure pattern and type of failure. Pull out test of the joint can also be carried out to determine the soundness/strength of the fillet weld. The steel material and joint has to be tested for fatigue and the required modifications have to be done before reuse.

- b. Once the Modular Shear Joint is technically tested and certified for practical use through third party certification, it can be used in real-time steel projects and reused till the end of life.
- c. Once all technical outcomes are attained, the project has the scope for a manufacturing startup/business as it would be a new and innovative joint in the market which would destruct the market.

Acknowledgements We would like to thank our guide, **R. Ravindra**, Associate Professor, Department of Civil Engineering R V College of Engineering, Bengaluru, for his continuous support, encouragement and insightful suggestions which helped us to do the project work successfully.

We would like to thank **Mr. Govind Ramesh**, Chief Mentor, AGRIMA Roof and Facade Systems, Bengaluru for your undying enthusiasm for giving quality insights and for scheduling progress meetings and setting deadlines and acting as a catalyst to take our project forward.

We would like to thank, **Somanath M B**, Assistant Professor, Department of Civil Engineering R V College of Engineering, Bengaluru, for his valuable suggestions.

We would like to thank **Dr. Mahendrakumar Madhavan**, Associate Professor, Department of Civil Engineering, IIT Hyderabad, for his valuable suggestions and guidance.

We are thankful to **Dr. Radhakrishna**, Head of Department of Civil Engineering, R V College of Engineering, Bengaluru, for providing valuable feedback and suggestions. He was supportive which enabled us to carry out this project.

We express sincere gratitude to our beloved Principal, **Dr. K. N. Subramanya** for his appreciation towards this project work.

Lastly, we take this opportunity to thank our **family** members and **friends** who provided all the backup support throughout the project work.

References

1. Sarja A (2002) Integrated life cycle design of structures. UK Spon Press, London, pp 1–130. ISBN: 0-203-030234-6
2. Webster MD (2007) Structural design for adaptability and deconstruction: a strategy for closing the materials loop and increasing building value. In: Proceedings of the 2007 ASCE structures conference, Long Beach, USA, pp 1–6
3. Elma D, Noort N (2003) Reuse potential of steel in building construction. In: Proceedings of the CIG TG-39 design for deconstruction and material reuse conference, Delft, Netherlands, p 3
4. Carpenter A (2012) CO₂ abatement in the iron and steel industry. IEA Clean Coal Centre London, pp 7–100. ISBN: 978-92-9029-513-6
5. IEA (International Energy Agency) (2007) Tracking industrial energy efficiency and CO₂ emissions, Chapter 5 (Iron and Steel Industry). Paris, France IEA-2007, pp 95–138
6. Kundak A, Lazic L, Črnko J (2009) CO₂ emissions in the steel industry, pp 193–197. ISSN: 0543-5846
7. Quader MA, Ahmed S, Ghazilla RR, Ahmed S (2014) CO₂ capture and storage for the iron and steel manufacturing industry challenges and opportunities. J Appl Sci Agric 9:60–67. ISSN: 1816-9112
8. Siitonen S, Tuomaala M, Ahtila P (2010) Variables affecting energy efficiency and CO₂ emissions in the steel industry. Energy Policy 38:2477–2485
9. Lisienko VG, Lapteva AV, Chesnokov YN, Lugovkina VV (2015) Greenhouse-gas (CO₂) emissions in the steel industry. Steel Transl 45:623–626. Allerton Press. ISSN: 09670912

10. Van Ruijven BJ, Van Vuuren DP, Boskaljon W, Neelis ML, Saygin D, Patel MK (2016) Long-term model-based projections of energy use and CO₂ emissions from the global steel and cement industries. *Resour Conserv Recycl* 112:15–36
11. Jin P, Jiang Z, Bao C, Hao S, Zhang X (2017) The energy consumption and carbon emission of the integrated steel mill with oxygen blast furnace. *Resour Conserv Recycl* 58–65
12. Mohammed ME (2020) Behavior of steel beam to column bolted connection part I. *Const Steel Res* 164, Article No. 105784
13. Esmaeilli J, Ahooghalandary N (2020) Introducing an easy install precast concrete beam to column connection strengthened by steel box and peripheral plates. *Eng Struct* 205:1–20
14. Mirghadri SR, Torabian S, Keshaoarzi F (2010) I-beam to column connection by a vertical plate passing through the column. *Eng Struct* 32:2034–2048
15. Moghadam A, Estekanchi HE, Yekrangnia M (2018) Evaluation of PR steel frame connection with torsional plate and its optimal placement. *Sci Iranica A* 25:1025–1038. Sharif University of Technology
16. Erfani S, Asnafi AA, Goudarzi A (2016) Connection of I-beam to box-column by a short stub beam. *J Constr Steel Res* 127:136–150
17. Rofooeia FR, Yadegari Farzanehb A (2016) Numerical study of an innovative SMA based beam-column connection in reducing the seismic response of steel MRF structures. *Sci Iranica A* 23:2033–2043. Sharif University of Technology
18. Pongiglione M et al. (2017) A new demountable seismic resistant joint to improve industrial building reparability. Department of civil, chemical and environmental engineering, University of Genova, vol 8, pp 520–600. ISSN: 1759-5908
19. Novel joining techniques to promote deconstruction of buildings. University of Cambridge, pp 1–10
20. Bogatinoski Z, Trajanoska B, Arsova-Milosevska G (2014) Design of steel beam-column connections. University in Skopje, vol 3, pp 151–161
21. Salem AH, Sayed-Ahmed EY, El-Serwi AA, Aziz RA (2014) Behavior and design of I-beam-to-column connections, flushed rigid bolted connections. The American University in Cairo Egypt, pp1–6
22. Hawxwell DA, Tsavdaridis KD (2019) Beam-to-beam eccentric end plate connections—experimental comparison to fin plate and partial-depth end plate connections. University of Leeds UK, pp 1–30
23. Nagao T, Tanaka T, Nanba H (2004) Performance of beam-column connections in steel structures. Kobe University Canada, Paper No.1235, pp 1–6
24. Justin AM, Joy EN (2016) Behavioral study of beam column joint strengthened with cross inclined column bars and FRP fibres Christ knowledge city, Ernakulum, Kerala, India, vol 4, pp 1–3. ISSN: 2278-0181
25. Abishek P, Karthikeyan G (2018) Study on steel beam column joint with different types of connections. *Int J Innov Technol Explor Eng (IJITEE)* 8:320–323. ISSN: 2278-3075
26. Elmasry MIS, Abdelkader Essam AM, Elkordy A (2018) An analytical study of improving beam-column joints behavior under earthquakes. Alexandria University EGYPT, pp 488–500
27. Iannone F, Latour M, Piluso V, Rizzano G (2011) Experimental analysis of bolted steel beam-to-column connections component identification. University of Salerno, Italy, pp 214–244. ISSN: 1363-2469
28. Anju Das K, Johny A (2019) Study on performance of beam-column joint with endplates and bolts under seismic loading Saintgits College of Engineering, Kerala, India, vol 6, pp 484–487. ISSN: 2395-0056
29. Yang B, Tan KH (2014) Behavior of composite beam-column joints in a middle- column-removal scenario experimental tests. Florida Atlantic University, pp 1–20. [https://doi.org/10.1061/\(ASCE\)ST.1943-541X.0000805](https://doi.org/10.1061/(ASCE)ST.1943-541X.0000805)